Particle transportation in turbulent non-Newtonian suspensions in open channels

A thesis submitted in fulfilment
of the requirement for the degree of
Doctor of Philosophy

Raymond Guang

B.E (Chemical)

School of Civil, Environmental and Chemical Engineering

RMIT University

March 2011

STATEMENT OF ORIGINALITY

I certify that except where due acknowledgement has been made, the work is that of the author alone. The work has not been submitted previously, in whole or in part, to quality for any other academic award. The content of the thesis is the result of work which has been carried out since the official commencement date of the approved research program. Any editorial work, paid or unpaid, carried out by a third party is acknowledged.

Raymond Guang
09/09/2011

DEDICATION

I dedicate this to my wife, Hui and my parents.

ACKNOWLEDGMENT

I would like to express my deepest gratitude to my supervisor Professor Sati Bhattacharya from RMIT University for proofreading this thesis and providing guidance throughout my study.

I would like to show my sincerest appreciation to my second supervisor Dr Murray Rudman from Commonwealth Scientific and Industrial Research Organisation (CSIRO) for his guidance, constant criticism and supervision of this project. I would like to thank Professor Paul Slatter from RMIT Univeristy for his guidance and suggestions and his continuous kindness.

I would like to thank my project consultant Dr Andrew Chryss for the first two and half years of the project. I am very indebted to the laboratory technician Mr Mike Allan for his development of the experimental apparatus.

I would like to thank Dr Raj Parthasarathy, Dr Rahul Gupta, Dr Nhol Kao and Dr Sumanta Raha for their frequent technical support. I would like to thank Associate Professor Margaret Jollands and Professor Douglas Swinbourne for their support whenever I needed it.

I would like to thank Ms Sharon Taylor for her never-ending email reminders.

I would like to thank the Australian Research Council for their support of this discovery project.

Finally I like to thank all the postgraduate students and staff from Rheology and Materials Processing Centre (RMPC) for their constant support. I would like to thank the people from room 7.2.14 for the enjoyable daily entertainment.

Raymond Guang
March 2011

PUBLICATIONS ARISING FROM THIS THESIS

Guang, R., Rudman, M., Chryss, A., Slatter, P., Bhattacharya, S., 2011, Direct numerical simulation investigation of turbulent open channel flow of a Hershel-Bulkley fluid, in Proceedings 14th International Seminar on Paste and Thickened Tailings (Paste2011), R.J. Jewell and A.B. Fourie (eds), 5-7 April 2011, Perth, Australia, pp 439-452, ISBN 978-0-9806154-3-2.

Guang, R., Chryss, A., Rudman, M., Slatter, P., Bhattacharya, S., 2011, A DNS investigation of the effect of yield stress for turbulent Non-Newtonian suspension flow in open channels, *Particulate Science and Technology*, vol.29, pp209-228.

Guang, R., Rudman, M., Chryss, A., Bhattacharya, S., Slatter, P., 2010, A Direct numerical simulation investigation of rheology parameter in Non-Newtonian suspension flow in open channels, Paper 147, *17th Australasian Fluid Mechanics Conference,* Auckland, New Zealand, December, 2010.

Guang, R., Rudman, M., Chryss, A., Bhattacharya, S., 2010, Yield stress effect for Direct numerical simulation in Non-Newtonian flow in open channels, ID 287, *CHEMECA 2010,* Adelaide, Australia, ISBN 978-085-825-9713.

Guang, R., Rudman, M., Chryss, A., Slatter, P., Bhattacharya, S., 2009, A DNS investigation of Non-Newtonian turbulent open channel flow, *The 10th Asian International Conference on Fluid Machinery,* paper ID 155, Malaysia, AIP Conference Proceeding pp180-185, ISBN 978-0-7354-0769-5.

Guang, R., Rudman, M., Chryss, A., Bhattacharya, S., 2009, DNS of Turbulent Non-Newtonian Flow in An Open Channel, *7th International Conference on CFD in the Minerals and Process Industries,* Melbourne, Australia.

Guang, R., Chryss, A., Rudman, M., Bhattacharya, S., 2009, Non-Newtonian Suspension Flow in Open Channel with Direct Numerical Simulation, *CHEMECA 2009*, Perth, Australia.

Guang, R., Chryss, A., Rudman, M., Bhattacharya, S., Slatter, P., 2009, Non-Newtonian Suspension Flow in Open Channels, *6th International Conference for Conveying and Handling of Particulate Solids,* Brisbane, Australia, pp447-452.

ABSTRACT

The turbulent behaviour of non-Newtonian suspensions in open channel conditions is investigated here. There is a lack of fundamental understanding of the mechanisms involved in the transport of suspension particles in non-Newtonian fluids, hence direct numerical simulation into the research is a useful validation tool. A better understanding of the mechanism operating in the turbulent flow of non-Newtonian suspensions in open channel would lead to improved design of many of the systems used in the mining and mineral processing industries.

Direct numerical simulation (DNS) of the turbulent flow of non-Newtonian fluids in an open channel has been modelled using a spectral element-Fourier method. The simulation of a yield–pseudoplastic fluid using the Herschel-Bulkley model agreed qualitatively with experimental results from field measurements of mineral tailing slurries. The effect of variation of the flow behaviour index has been investigated and used to assess the sensitivity of the flow to this physical parameter. This methodology is seen to be useful in designing and optimising the transport of slurries in open channels.

The aim of this work is to understand the underlying phenomena and mechanisms operating in the turbulent flow of non-Newtonian suspensions in open channels, in particular their ability to transport suspended particles. It is intended to achieve the following objectives:

- Demonstrate how the rheological characteristics of the continuous medium carrier fluid influence the transport of solid particles in the suspension
- Carry out modification of existing computational model to describe the non-Newtonian open channel flow and validate by experimental measurements
- Establish relationships between rheology of the fluid and turbulent characteristics of the flow
- Establish relationships between rheology of the fluid and particle suspension in an open channel flow

There is a substantial amount of literature on turbulent flow in pipe and open channel flow. In this thesis, both experimental and computational studies for channel flow of non-Newtonian fluids have been carried out. The prediction of the velocity profile and other parameters such as Reynolds stresses and velocity fluctuations were compared with measurements of the same obtained in an open channel. These results addressed the question of size, intensity and frequency of the turbulent structures.

The existing computational code could not be used for open channel flow. It was therefore modified by introducing new boundary conditions on free surface. Rheological parameters were also incorporated in the computational code. Computational simulation was then validated against a number of different experimental and computational results. Different velocity distributions were tested to see the validity of the simulation.

Major investigations have been conducted to observe the effect of different rheological parameters on the simulation results. The major contribution from this study is that the simulation method provided the opportunity to examine the effect of changing one rheology parameter while keeping the other parameters constant. The relationship between rheological parameters and flow characteristics is Reynolds number dependent. It is concluded that the simulation can simulate non-Newtonian turbulent open channel flow reasonably well. A further investigation on secondary current was also conducted. It appears that with a smaller Reynolds number, weak and large size turbulent structures appear in the middle region of the channel.

Furthermore, Stokes number, low velocity streaks intensities and sizes have been studied. It is determined that the Reynolds number has more effects than rheological parameters on the low velocity streak size. It is found that the largest percentage of ejection and sweep events occurred away from the centreline and close to the wall at a height 10-20 cm from the bottom. It is already known that particles are easier to be suspended and re-suspended in those areas. In addition, it is also reinforced that the secondary current cell can assist the re-suspension of particles.

This study of non-Newtonian suspension flow in open channel will provide fundamental information for understanding the behaviour of fluid structure and the relationship between fluid and particles. This information will also be applicable to the design and operation of industrial

channels for the transport of mineral suspensions leading to improved channel management and economic outcomes.

TABLE OF CONTENT

LIST OF FIGURES

LIST OF TABLES

NOMENCLATURE

Symbol	Description	Unit
A	Cross sectional area	m^2
a, b	Geometric coefficients from equations (28) and (29)	
B	Channel width	m
B_s	Dimensionless property of the flow in the vicinity of the bed (Yalin, 1977)	
C	Chezy's flow resistance	
D	Diameter	m
f	Fanning friction factor	
F	Force	N
Fr	Froude number	
g	Gravity, acceleration	m/s^2
h	Height of the channel	m
H_b	Herschel-Bulkley number	
K	Fluid consistency index	$Pa.s^n$
k	Von Karman constant	
k_s	Roughness height	m
L	Channel length	m
M	Parameter of velocity distribution equation (60)	
n	Flow behaviour index	
N	Number of measurement	
P	Wetted perimeter	m
P_{zr}	Turbulence production	
Q	Flow rate	l/s
r	Radius	m
Re	Reynolds number	
R_h	Hydraulic radius	m
S	Slope	
St	Stokes number	
Sm	Relative density	

U	Axial velocity	m/s
U^*	Friction velocity	m/s
U^+	Normalised axial velocity	
u_0	Average slip velocity at the wall	m/s
u'	Axial velocity fluctuation	m/s
U, V	Average velocity	m/s
V	Radial velocity	m/s
v'	Radial velocity fluctuation	m/s
W	Azimuthal velocity	m/s
$w(\xi)$	Wake function	
w'	Azimuthal velocity fluctuation	m/s
Y	Distance	m
y^+	Distance from the wall, wall unit	
α, β	Angle	degree
α_s, β_s	Constant in equation (75)	
α_c	Critical value for secondary current generation	
α_y	Factor to predict secondary current in equation (49)	
$\dot{\gamma}$	Shear rate	s^{-1}
Γ	1-exp ($-y^+ / 26$)	
η	Apparent viscosity	Pa.s
η_r	Reference viscosity	Pa.s
λ	Aspect ratio of the rectangular channel	
μ	Viscosity	Pa.s
ν	Kinematic viscosity	m^2/s
ξ	Constant on an isovel on which the velocity is equal to the mean velocity	
Π	Cole's wake strength parameter	
ρ	Density	Kg/m^3
σ	Standard deviation	
τ	Shear stress	Pa
τ_s	Aerodynamic response time	

τ_F	Particle response time	
τ_w	Wall shear stress	Pa
τ_y	Yield stress	Pa
φ	Function defined by equation (29)	

Chapter 1: Introduction

1.1 Purpose and scope

The flow of non-Newtonian fluids in open channels has great implications for mining industry. When self-formed channels flow at a sufficient gradient or slope, it can generate a certain level of turbulence. This turbulent behaviour of the transportation material can keep the particles in suspension. From literature (Chryss *et al*, 2006) and industrial experience, it is concluded that if the slope reduces, the intensity of turbulence will decline as well. Therefore the particles will not be fully suspended in the channel and consequently the channel will slow its transportation rate and fill with tailing residues.

Particle transportation in the turbulent channel flow is often poorly understood. The addition of particles in turbulent flow increases the complexity of the turbulent phenomena. The mechanism governing particle transportation in turbulent flow has been studied in the past; however they are not completely comprehended. The Centrally Thickened Discharge (CTD) process is a good example of turbulent channel flow where mine waste is discharged as thickened slurry at a fixed location, forming low stacks of settled tailings. In this particular circumstance, the open channels of non-Newtonian suspensions arise spontaneously on the tailings stacks. A better understanding of the mechanisms operating in the turbulent flow of non-Newtonian suspensions in the open channels can well improve the operation in financial terms as well as in sustainability terms.

Over the past fifty years, the study of turbulent non-Newtonian suspension in pipes has received considerable attention because of its industrial relevance. In the 1960s, experimental flow visualization techniques were used to investigate the structure of a Newtonian turbulent boundary layer. In recent times, there has been a significant improvement in understanding turbulent flow in pipes as a result of improved instrumentation (e.g. Electro-Resistive Tomography, Particle image velocimetry and Rheometric methods) and computational techniques (Fluent, CFX and DNS). Although open channel flows are encountered frequently in industrial and natural circumstances, there has not been the same level of improved

understanding. Open channels present a complex scenario for analysis because they show asymmetric velocity and concentration gradients. Moreover, open channels often produce secondary flows. Usually, open channel flow of water can be described by simple equations such as Manning's equation as water has a constant viscosity under isothermal conditions. However, when water is admixed with a fraction of fine particles, its viscosity becomes increasingly non-Newtonian. Therefore the velocity distribution in an open channel is usually difficult to predict.

In open channel flow, a sufficient gradient can generate a level of turbulence that is able to maintain all the tailings particles in suspension. Shallower gradient will reduce the turbulence intensity; hence allow more solids to settle in the channel bottom. The channel gradient is believed to dictate the beach slope of CTD. The CTD process is extremely important to the mining industry in Australia. With a better understanding of CTD process, there is an improved possibility to recovering process water, a reduced likelihood of ground water contamination and more rapid environmental regeneration compared to standard tailing dams. From previous researches, there is a lack of fundamental understanding about the mechanisms involved in how a turbulent flow of a non-Newtonian fluid keeps particles in suspension.

1.2 Methodology

Experimental measurement of velocity profiles and turbulence statistics can be used to determine the state of channel flow. If the rheology of the suspension is known, then computational simulation can be used to simulate the flow patterns. In earlier years of research, Kim *et al* (1987) have simulated turbulent channel flow of Newtonian fluids with Reynolds number up to 3300. There have been some DNS of the turbulent flow of polymer solutions as well (Sureskumar *et al*, 1997). The study considered the drag reduction that arises in dilute polymer solutions in which shear-thinning behaviour was unimportant. Dimitropoulos *et al* (2004) have also used DNS to simulate viscoelastic turbulent boundary layer flow. It was found that as drag reduction increases, the streamwise velocity fluctuations are decreased. Furthermore, Rudman and Blackburn (2003, 2006) have used spectral element method to simulate non-Newtonian flow in pipes. The velocity distribution resulting from the present approach of adopting the Herschel-Bulkley model showed good agreement in terms of

shape and magnitude when compared with the experimental data. This indicates that the same simulation method could also be tested on channel flow with a change of boundary condition.

Experimental data on large scale channels has been obtained for non-Newtonian channel flow (Fitton, 2007). However, with limitations on equipments, most details of the turbulent structure are missed, and measurements close to the channel wall are impossible. With the comparison from both experimental result (Fitton, 2007) and simulation result, more detailed turbulence characteristics of the flow can be obtained from simulation. Wall velocity streaks sizes and frequency then can be closely investigated. Therefore it is possible to explore the possible relationship between rheology of the fluid, turbulence characteristics of the flow and particle behaviour. Consequently by relating turbulence characteristics to particle behaviour; a set of new knowledge can be gained from the research. The knowledge will also be significant for the design and operation of flumes in the process industries.

The study of non-Newtonian suspensions in open channels will provide the additional fundamental information for understanding the behaviour of self-formed channels in situations such as CTD stack. The same information will also be applicable to the design and operation of industrial channels for the transport of mineral suspensions with expected advantages in management and economic outcomes.

1.3 Aim and objectives

The aim of this project is to understand the underlying phenomena and mechanisms operating in the turbulent flow of non-Newtonian suspensions in open channels, in particular their ability to transport suspended particles. It is intended to achieve the following objectives:

- Demonstrate how the rheological characteristics of the continuous medium carrier fluid influence the transport of solid particles in the suspension
- Carry out modification of existing computational model to describe the non-Newtonian open channel flow and validate by experimental measurements
- Establish relationships between rheology of the fluid and turbulent characteristics of the flow

- Establish relationships between rheology of the fluid and particle suspension in an open channel flow

1.4 Thesis structure

The work presented here is structured in the following manner:

- Literature Review (Chapter 2). The literature that specifically addresses the topic of open channel flow, turbulence characteristic of flow, particle interactions and other relevant literatures.
- DNS studies review (Chapter 3). The literature addresses the previous DNS researches on turbulent pipe/duct flow and turbulent channel flow.
- Experimental work (Chapter 4)
    - Ultrasound velocity probe principles
    - Calibration of velocity probe
    - Experimental setup
- Numerical modelling of turbulent flow in open channels using Semtex (Chapter 5)
    - More detailed numerical method
    - Detailed simulation procedures
- Validation of open channel models presented in the literature (Chapter 6). The simulation results were validated with five different sets of data.
    - Presentation of current results
    - Validation of simulation results
    - Explore the effects of different simulation variables, it includes: Three different rheological parameters, change of depth, change of measurement positions, and change of mesh resolution.
    - Discussion of secondary current
- Discussion of particle transportation (Chapter 7)
    - Establishment of a relationship between fluid rheology and Stokes number
    - Establishment of a relationship between fluid rheology and wall velocity streaks and their sizes

- Discussion of particle suspension with the assistance of quadrant analysis
- Establishment of a relationship between secondary current and particle suspension and re-suspension

- A summary of new contributions and findings arising from the work is presented (Chapter 8)
- Conclusions drawn from the work are presented (Chapter 8)
- Recommendations are presented for future research (Chapter 8)

Chapter 2: Literature Review

2.1 Outline

There is a substantial amount of literature on turbulent flow in pipe and open channel. Experimental research on turbulent boundary layer and pipe flow has been conducted mainly in air flow since 1950s using hot wire anemometry. In the late 1960s, experimental flow visualization techniques were used to probe the structure of a Newtonian turbulent boundary layer. The basic research on open channel flow has only been investigated from the 1970s. Since 1980s, laser anemometry has made experimental studies in open channel turbulence much easier. In recent times, there has been a significant improvement in understanding turbulent flow in pipes as a result of improved instrumentation (e.g. Electro-Resistive Tomography, Particle image velocimetry and rheometric methods) and computational techniques. There is also a large amount of related literature that is extremely relevant to this work. The literature is presented in the following order:

- Flow behaviour
    - Non-Newtonian flow behaviour
- Open channel flow
    - Open channel flow categories
    - Equations for Newtonian turbulent open channel flow
    - Open channel flow review
- Turbulence characteristics of channel flow
    - Velocity profile in channel flow
    - Secondary current in channel flow
    - Quadrant analysis
- Particle interactions
    - Particle characteristics
    - Turbulence and particle interaction

2.2 Flow Behaviour

In this section, the flow characteristic of single-phase liquids and pseudo-homogeneous mixtures is described.

2.2.1 Non Newtonian behaviour

The flow behaviour of a fluid can be classified on the basis of the shear stress-shear rate relations. If the relationship between shear stress and shear rate is not linear, then the material is called a non-Newtonian fluid. Sometimes, rheological behaviour of solid-liquid suspensions is dependent on the interactions between the dispersed components and the suspending medium which cause the deviation of the shear stress versus shear rate relation from the linearity observed in Newtonian fluids. Typical tailing slurry may exhibit both yield stress as well as change in viscosity at different shear rates.

The graphical presentation of some relationships between shear stress and shear rate are shown in Figure 1.

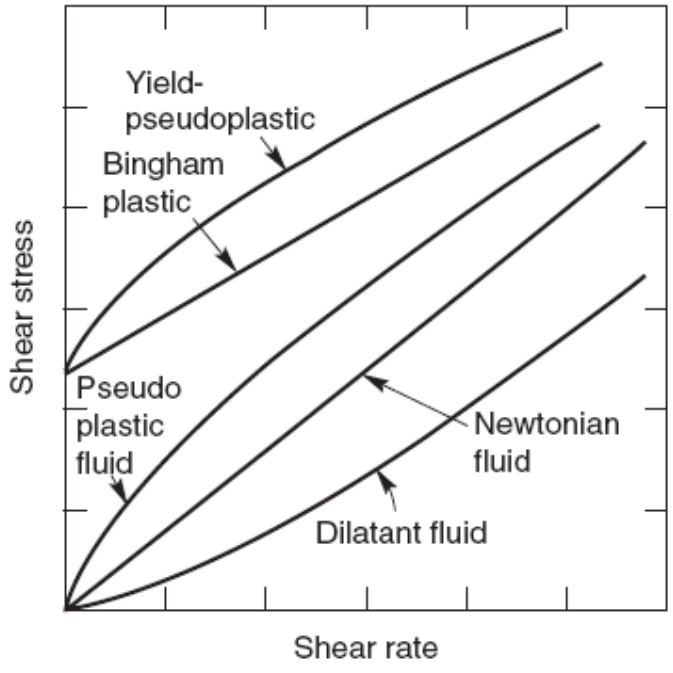

Figure 1 Types of time-independent flow behaviour (Chhabra and Richardson, 2008)

2.2.1.1 Non-Newtonian models

Three commonly used rheological models are Power law model, Bingham plastic model and Herschel-Bulkley model.

Power law model

This model suits a fluid flow that exhibits non-linear behaviour without yield stress. The equation for the power law model is presented below:

$$\tau = K\dot{\gamma}^n \quad \textbf{(1)}$$

Where τ is the shear stress (Pa), K is the power law consistency index (Pa.S^n), n is a power and $\dot{\gamma}$ is shear rate applied to the fluid (1/s).

A shear thinning fluid is characterised by an apparent viscosity which decreases with an increase of shear rate.

Bingham plastic model

This model is the simplest way to describe a flow behaviour with a yield stress. The equation is as follows:

$$\tau = \tau_y + K\dot{\gamma} \quad \textbf{(2)}$$

Where τ_y is the yield stress (Pa), K is the Bingham plastic viscosity (Pa.S) and $\dot{\gamma}$ is shear rate applied to the fluid (1/s).

This equation is linear and shear stress intercept is the yield stress. It is often used to represent many concentrated dispersions, emulsions and multiphase mixtures over a range of shear rates (Bhattacharya, 2001).

Herschel-Bulkley model

If a yield stress fluid exhibits a non-linear relationship between the shear stress and shear rate, then the yield pseudoplastic three constant models can be used. The equation is presented below:

$$\tau = \tau_y + K\dot{\gamma}^n \quad \textbf{(3)}$$

Where τ_y is the yield stress (Pa), K is the power law consistency index (Pa.S^n), n is a power and $\dot{\gamma}$ is shear rate applied to the fluid (1/s). It will be noted that the Herschel-Buckley model can be easily modified to describe the previously mentioned models.

If τ_y= 0, the equation becomes the power law equation.

If n = 1, the equation becomes the Bingham equation.

If n = 1, and τ_y= 0, the equation becomes the Newtonian flow equation.

2.3 Open channel flow

Open channel flow of water is a popular topic and has been studied extensively in the past (Chanson, 1999; Henderson, 1966). The physical conditions in open channels are quite different from that in pipes. The cross section of pipes is always round; for open channel the cross section can be of any shape. Open channel flow tends to be more complicated to predict because of the free surface which will change with time and space. Moreover, the depth of the flow, the discharge rate, the slopes of the channel and the free surface are all interdependent. In addition, an open channel flow is usually driven by gravitational force whereas a pipe flow is driven by a pressure gradient along with some gravitational effects. Secondary currents exist in open channel flows, which can cause the maximum velocity to exist somewhere below the free surface.

Table 1 Difference between pipe flow and open channel flow

	Pipe Flow	**Open channel flow**
Flow driven by	Pressure	Gravity
Flow cross section	Known, fixed	Unknown, as flow depth is unknown
Characteristics flow parameters	Velocity deduced from continuity	Flow depth deduced simultaneously from solving both continuity and momentum equations
Specific boundary condition		Atmospheric pressure at the free surface

2.3.1 Open channel flow categories

Open channel flow can be categorised into different types.

- Steady and unsteady flow

  Flow in an open channel is steady if the depth of flow does not change or if it can be assumed to be constant during the time interval under consideration. Therefore in this category, time is the important criterion.

- Uniform flow and varied flow

  If it is a uniform flow, then the depth of the flow is the same at every section of the channel. The flow is varied when the flow depth varies over the length. A uniform flow may be steady or unsteady, depending on whether or not the depth changes with time. In this category, space is the important criterion.

  (Chow, 1959)

The open channel flow under investigation for this study is expected to be a steady flow, as the depth of flow does not change over time. The depth of the flow will be same at every section of the channel.

Like any fluid mechanical problem, dimensional analysis can play a key role. In open channel flow, there are a few variables that are needed to describe the transportation of fluid or suspensions. They are as follows:

Table 2 Open channel flow variables

Symbol	Description	Unit
V	Velocity	m/s
L	Relevant length scale	m
μ	Dynamic viscosity	Pa.s
ρ	Density	m^3/kg
g	Gravity	m/s^2

There are two dimensionless parameters commonly related to open channel flow. They are Reynolds number and Froude number. Reynolds number is the ratio of the inertial to viscous forces and is calculated using:

$$\mathrm{Re} = \frac{\rho V L}{\mu} \quad \textbf{(4)}$$

For open channel flow, L becomes the hydraulic radius R_h, where the hydraulic radius is the ratio of area over the wetted perimeter of the flow cross-section (Chow, 1959). Then (French, 1982):

$\mathrm{Re} \leq 500$	Laminar flow
$500 \leq \mathrm{Re} \leq 12500$	Transitional flow
$12500 \leq \mathrm{Re}$	Turbulent flow

A dimensionless parameter Froude number (Fr) is commonly associated with open channel flow (Chow, 1959; Henderson, 1966; Yalin, 1977).

$$Fr = \frac{V}{\sqrt{gL}} \quad \textbf{(5)}$$

Where V represents the average velocity in the channel while g represents the local acceleration due to gravity. L is the characteristic length of the channel; it can be the depth of flow or hydraulic radius. The value of the Froude number (Equation (5)) indicates whether the flow is critical ($Fr = 1$), subcritical ($Fr < 1$), or supercritical ($Fr > 1$). For Froude numbers greater than 1, the flow is said to be supercritical. In open channel flow, it means that the flow

can only be controlled by an upstream weir or height control device (Henderson, 1966). For Froude numbers less than 1, the flow is said to be subcritical. This means that the flow can only be controlled by downstream devices. Froude number is readily used in Newtonian flows; however the application for non-Newtonian flow is not fully discovered.

In Figure 2, the flume is inclined at an angle θ from the horizontal plane. Figure 3 shows the cross sectional area of the flow, the depth of the flow and the angle β, which describes the location of the free surface relative to the location of the centre of the pipe.

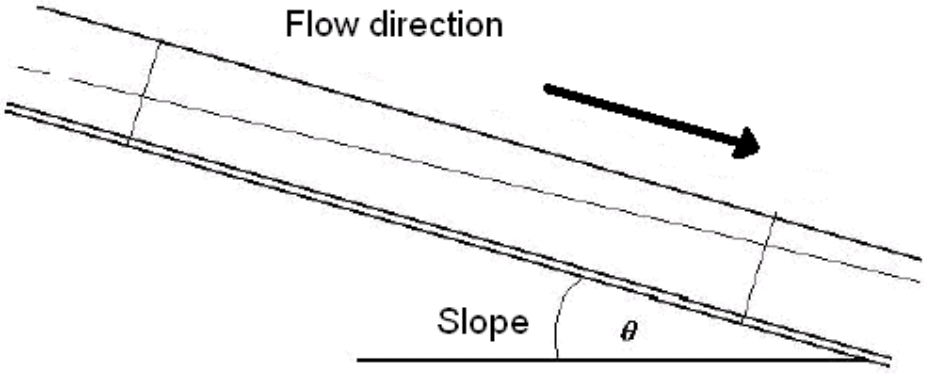

Figure 2 Schematic illustration of non-uniform, axial flow in a flume

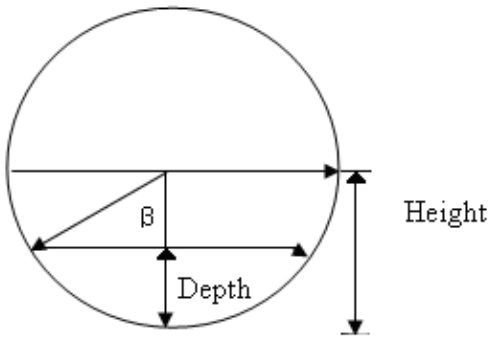

Figure 3 Schematic illustration of the cross-sectional view of open channel flow in a circular flume

For flow in an open channel, the wall shear stress is dependent upon the flume slope angle, the flow rate and cross-sectional area of flow. The bulk velocity at any location in a steady flow can be calculated by:

$$V = \frac{Q}{A} \tag{6}$$

The average wall shear stress in the channel can be determined by a force balance on the system. When uniform flow occurs gravitational forces exactly balance the frictional resistance forces which apply as a shear stress along the wall. Considering the gravity force resolved in the direction of the flow is

Gravity force $= \rho g A L \sin\theta$ **(7)**

And the boundary shear stress resolved in the direction of flow is

$$\tau = \tau_w P L \tag{8}$$

In uniform flow these balance

$$\tau_w P L = \rho g A L \sin\theta \tag{9}$$

So

$$\tau_w = \frac{\rho g A \sin\theta}{P} = \rho g R_h \sin\theta \tag{10}$$

The wall shear stress varies along the wetted perimeter of the flow and the value calculated in Equation (10) is the average shear stress in the open channel.

2.3.2 Equations for Newtonian turbulent open channel flow

There are a number of open channel flow models; some of them are adapted from pipe flow. A few of the models will be discussed in the next section.

2.3.2.1 Chezy's equation for channel flow

Most of the existing formulas and theories for pipe flow are not applicable to open channel flow. As mentioned previously, pipe flow is bounded in all directions by walls which fix the velocity based on the local cross-section area. In open channel flow, the velocity is not fixed

as the conditions dictate the depth of flow. Antoine Chezy developed the very first uniform-flow formula, which is defined as follows (Chow, 1959):

$$V = C\sqrt{R_h S} \quad \textbf{(11)}$$

Where V is the mean velocity, R_h is the hydraulic radius, S is the slope and C is a factor of flow resistance called Chezy's C. This formula applies to turbulent flow. It is also defined as follows by (Chanson, 1999)

$$V = C_{Chezy}\sqrt{R_h \sin\alpha} \quad \textbf{(12)}$$

H. Bazin proposed a formula to predict C (Chow, 1959).

$$C = \frac{157.6}{1 + \frac{m}{\sqrt{R}}} \quad \textbf{(13)}$$

The value of Bazin constant varies from 0.11 for very smooth cement of planed wood to 3.17 for earth channels in rough conditions (Chow, 1959).

2.3.2.2 Manning's equation

Robert Manning presented a different equation, which is presented as follows:

$$V = \frac{1.49}{n} R_h^{2/3} S^{1/2} \quad \textbf{(14)}$$

(Chow, 1959)

Where V is the mean velocity, R_h is the hydraulic radius, S is the slope and n is the coefficient of roughness. This particular formula applies to turbulent flow and is widely used for open channel flow.

2.3.2.3 Colebrook and White equation

Colebrook and White have designed an equation for pipe flow

$$\frac{1}{\sqrt{4f}} = -2\log\left(\frac{k}{3.7D} + \frac{2.51}{\mathrm{Re}\sqrt{4f}}\right) \quad \textbf{(15)}$$

In open channels, the equation can be modified by substituting the diameter with the hydraulic radius.

$$\frac{1}{\sqrt{4f}} = -2\log\left(\frac{k}{14.84R_h} + \frac{2.51}{\mathrm{Re}\sqrt{4f}}\right) \quad \textbf{(16)}$$

The *k* value is the equivalent roughness height. This particular equation can be transformed to an explicit equation in terms of the velocity to be:

$$V = \sqrt{32R_h \sin\alpha}\log\left(\frac{k}{14.84R_h} + \frac{1.255\mu}{R_h\rho\sqrt{32gR_h\sin\alpha}}\right) \quad \textbf{(17)}$$

This equation is used to calculate the flume roughness, and is regarded as one of the more sophisticated approaches to open channel design (Wallingford and Barr, 1994).

2.3.3 Open channel flow review

The flow of non-Newtonian fluid in open channels is quite common in mineral processing industry. However, it is not well presented in the literature and textbooks. A significant amount of research has been applied to the study of the water flow behaviour in open channel. The other area which attracts research interests is the transportation of sediments in open channel.

Coussot (1994) investigated flow of concentrated mud suspension in open channels. He used kaolin as the non-Newtonian suspension which had a particle diameter of less than 40 μm. He characterised the suspension as a Herschel-Bulkley fluid. The flow behaviour index was fixed to be 0.333.

The author defined the Herschel-Bulkley number as follows:

$$H_b = \frac{\tau_y}{K}\left(\frac{h}{V}\right)^n \quad \textbf{(18)}$$

Then the author proposed the empirical formula of the average wall shear stress:

$$\tau_w = \tau_y (1 + a(H_b)^{-0.9}) \quad \textbf{(19)}$$

With '*a*' being the shape factor and differing for different channel shape. For this particular paper, the wall shear stress equation is only designed for rectangular and trapezoidal channel shapes. These formulas are only valid for the Herschel-Bulkley fluids and the value of *n* needs to be fixed to 0.333. Furthermore the flow needs to be in the laminar region in order to be valid.

Haldenwang *et al* (2002, 2003, 2004) investigated a range of non-Newtonian fluid flows in open channel. Laminar and transitional flows were both achieved. The author used different concentrations of CMC solutions, kaolin and bentonite suspensions in the experiment. He characterised the CMC solution as a power law fluid, the kaolin suspension as a Herschel-Bulkley fluid and bentonite suspension as a Bingham fluid. The author conducted experiments in three different sizes of rectangular flumes, which were 75 mm, 150 mm and 300mm wide. The 75 mm flume was 4.5 m long and the 150 mm and 300 mm flumes were 10 m long. The author used five different slopes in the experiments, from 1 to 5 degrees.

The author defined Reynolds number as follow:

$$\mathrm{Re} = \frac{8\rho V^2}{\tau_y + K\left(\frac{2V}{R_h}\right)^n} \quad \textbf{(20)}$$

He modified the Slatter's Reynolds number to open channel flow (Slatter, 1995) by substituting the pipe diameter with hydraulic radius.

For power-law fluids, the equation reduces to:

$$\mathrm{Re} = \frac{8\rho V^2}{K\left(\frac{2V}{R_h}\right)^n} \quad \textbf{(21)}$$

For the Bingham fluids the equation reduces to:

$$\mathrm{Re} = \frac{8\rho V^2}{\tau_y + K\left(\frac{2V}{R_h}\right)} \quad \textbf{(22)}$$

Further, Haldenwang (2003) developed a new model for predicting the onset of transition and the onset of turbulence for non-Newtonian open channel flow. The author stated that the flow behaviour could be characterised by the Froude number and the Reynolds number. Haldenwang (2003) plotted Reynolds number against Froude number to establish the correlation between the two dimensionless numbers. He found that there is a linear relationship between the tested slopes. Then the linear relationship was plotted against the apparent viscosity. A critical Reynolds number was established by using the Froude number to predict the onset of transition. The Reynolds number was found to have a linear relationship with the Froude number for an apparent viscosity at 100 s^{-1}.

This critical Reynolds number is as follows:

$$\mathrm{Re}_c = \frac{200}{\left(\mu_{app(100s^{-1})}\right)^{0.21}} Fr + \frac{71}{\left(\mu_{app(100s^{-1})}\right)^{0.75}} \quad \textbf{(23)}$$

To predict the onset of transition the following procedure is followed:

- Select the Reynolds number
- Calculated f with laminar flow friction factor, which is: $f = 16/Re$
- Guess the flow depth
- Calculate the velocity using Darcy friction factor equation $f = \frac{2SR_h g}{V^2}$
- Calculate Re using equation (20).
- Optimise the flow depth until the two Reynolds numbers are the same
- Calculate the Froude number
- Calculate the Re transition using equation (23)
- Optimise the flow depth until Re is the same as Re_c for onset of transition

To predict the onset of turbulence, the author used similar procedure as for the onset transition prediction. The only difference is that the linear relationship was at an apparent viscosity at 500 s^{-1}. This critical Reynolds number is as follows:

$$\mathrm{Re}_c = \frac{105}{\left(\mu_{app\left(500\,s^{-1}\right)}\right)^{0.52}} Fr + \frac{108}{\left(\mu_{app\left(500\,s^{-1}\right)}\right)^{0.65}} \quad \textbf{(24)}$$

To determine the onset of turbulence, the procedure is as follows:

- Complete the first seven steps used when predicting the onset transition as above
- Calculate the critical turbulent Reynolds number using equation (24)
- Optimise the depth until Re is the same as Re_c for onset of turbulence

However, there is no mention of coarse particle transportation in laminar or turbulent flow in any of those works. Moreover the author did not include any turbulence characteristics in the paper and there is no measurement of local velocities as well. The prediction of transition and turbulence is purely based on Reynolds number and Froude number relationship. In Chapter 6, these methods will be used for the prediction of turbulence.

The shape factors were first defined by Straub *et al* (1958) in their open channel investigation. Kozicki and Tiu (1967) investigated the effect of shape in laminar flow in open channels further in their work. They proposed an analytical method by which frictional effects resulting from non-Newtonian fluid flow can be predicted in ducts of arbitrary cross-section (Kozicki and Tiu, 1967). Additional relevant research included the work of Metzner and Reed (1955) and Straub *et al* (1958) who attempted to correlate data and create a method for predicting wall shear stress and turbulent transition for non-Newtonian fluids in ducts of different cross sections.

Kozicki and Tiu (1967) showed that the method can be applied to open channel gravity flows with the following flow conditions.

1. Incompressible, time independent, non-Newtonian fluid
2. Isothermal, stead, one-dimensional, laminar, gravity flow
3. No-slip at channel walls
4. Zero shear free surface

5. Flow is uniform (free surface height does not change with axial position), no ripples or waves
6. Smooth channel wall

Kozicki and Tiu (1967) proposed a Reynolds number for a power-law fluid in rectangular flume as follows:

$$\mathrm{Re} = \frac{\rho\left(U-u_0\right)^{2-n} R_h{}^{n}}{2^{n-3} K\left(\frac{a+bn}{n}\right)^{n}} \tag{25}$$

This Reynolds number includes the shape factors '*a*' and '*b*'. With a semi-circular open channel, $a = ¼$ and $b = ¾$, and for rectangular open channel $a = 0.21$ and $b = 0.68$.

For a rectangular open channel '*a*' and '*b*' are as follows:

$$a = \frac{1}{2}\left(\frac{\lambda}{1+\lambda}\right)^{2}\left[1-\frac{32}{\pi^3}\sum_{0}^{\infty}\frac{(-1)^n}{(2n+1)^3}\frac{1}{\cosh\frac{(2n+1)}{2}\pi\lambda}\right] \tag{26}$$

With

$$\lambda = B/h \tag{27}$$

$$b = a[3\varphi-1] \tag{28}$$

Where

$$\varphi = \frac{1-\frac{32}{\pi^3}\sum_{0}^{\infty}\frac{(-1)^n}{(2n+1)^3}\frac{1}{\cosh\frac{(2n+1)}{2}\pi\lambda}}{1-\frac{192}{\pi^5}\frac{1}{\lambda}\sum_{0}^{\infty}\left(\frac{1}{(2n+1)^5}\right)\tanh\left(\frac{(2n+1)}{2}\pi\lambda\right)} \tag{29}$$

These shape factors however have not been tested against any valid experiment dataset. In fact, Kozicki and Tiu's shape factor can only predict the flow rate and maximum velocity in

laminar flow of an incompressible, time-independent non-Newtonian fluid in a straight open channel (Kozicki and Tiu, 1967). In Chapter 5, these models will be tested with data compiled for this thesis.

2.4 Turbulence characteristics of channel flow

Velocity distribution and turbulence characteristics in open channel flow have been studied theoretically and experimentally by many researchers. The following section reviews some interesting aspects of turbulence research in open channels.

2.4.1 Velocity profile in channel flow

In open channel flow, the velocity is not constant with depth. It usually increases from zero at the invert of the channel to a maximum value close to the surface. The velocity difference results from the resistance to flow at the bottom and sides of the channel. Theoretical exploration used the statistical theory of turbulence for uniform and fully developed flows in wide open channels. Some of the most definite data in 2-D open channel flow are velocity distributions. All the flows referenced in this section are fully developed turbulent flows.

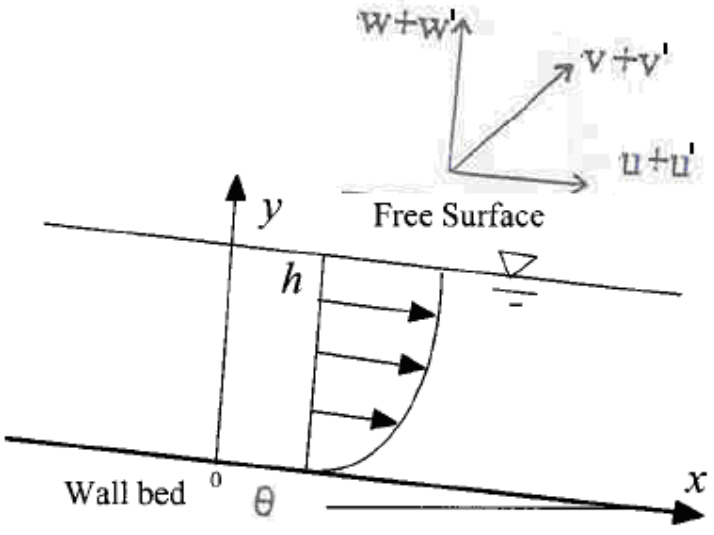

Figure 4 Definition sketch for steady 2D uniform open channel flow

Figure 4 shows the coordinate system in open channel flows. As shown in the figure, u, v, and w denote the components of mean velocity; u', v' and w' denote the velocity fluctuations.

Turbulent flow along a wall can be considered to consist of three regions, characterized by the distance from the wall. The very thin layer next to the wall where viscous effects are dominant is the viscous (or laminar or linear or wall) sublayer. Next to the viscous sublayer is the buffer layer, in which turbulent effects become significant, but the flow is still dominated by viscous effects. Above the buffer layer is the outer (or turbulent) layer where turbulent effects dominate over molecular diffusion effects (Cengel and Cimbala, 2006).

Experimental evidence shows that all wall shear turbulent velocity profiles, such open channel flow and boundary layer flows can be divided into two regions (Coles, 1956). These two regions are: an inner region where turbulence is directly affected by the bed; and an outer region where the flow is only indirectly affected by the bed through its shear stress. The inner region can be divided into a viscous sublayer, a buffer layer and an overlap. Also the outer region can be further divided into the overlap and a wake layer. In summary, the flow domain in a wall shear turbulence can be divided into four layers: viscous sublayer, buffer layer, overlap layer (or intermediate layer), and wake layer, shown in Figure 5.

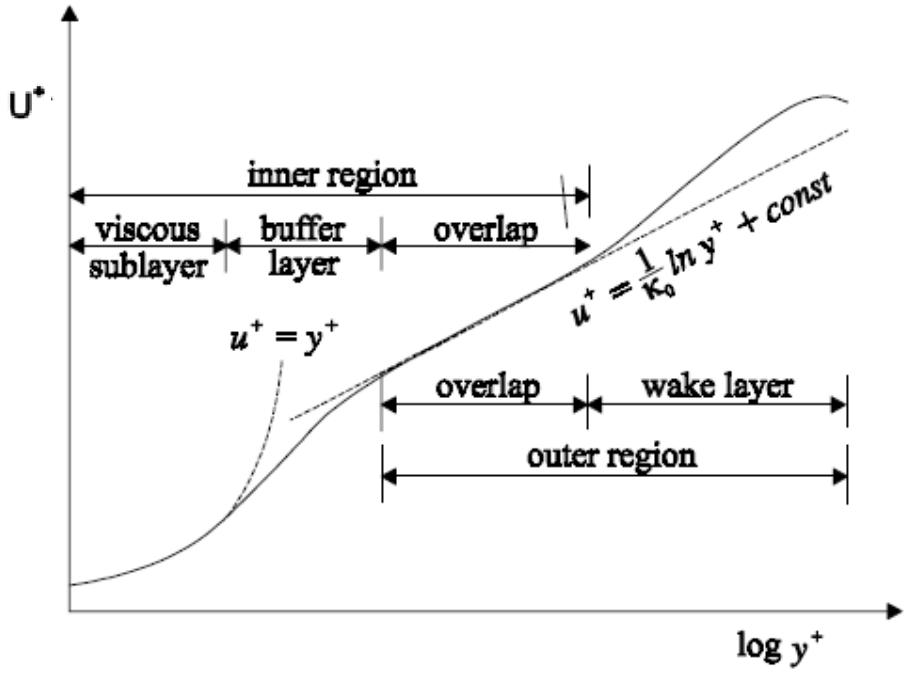

Figure 5 Sketch of a representative velocity profile in open channels

The mean velocity distribution for fully developed turbulent flow could be expressed by the logarithmic velocity distribution equation of von Karman-Prandtl (Cengel and Cimbala, 2006):

$$U^+ = \frac{1}{k}\ln\left(y^+\right) + A \qquad \textbf{(30)}$$

Where

$$y^+ = \frac{yU^*}{\nu}\ ,\ U^+ = \frac{U}{U^*} \text{ and } U^* = \sqrt{\tau_w / \rho} \qquad \textbf{(31)}$$

In equation (31), where U^* is the friction velocity, A is a constant of integration and k is the von Karman constant. A and k values are determined experimentally to be about 5.29 and 0.41 respectively (Nezu, 2005), regardless of the Reynolds number and Froude number. Nezu and Nagakawa (1993) reviewed results in other smooth-wall-bounded shear flows and found the following values for the constants in the log-law profile: k = 0.41 and A = 5.0 in boundary layers by Coles (1968); k = 0.41 and A = 5.17 in closed channel flow by Dean (1978). The von Karman constant is concluded to be 0.41 irrespective of flow configuration. However,

constant *A* may weakly depend on main flow properties but is nearly constant. i.e. between *A* = 5.0 - 5.3 on smooth beds. It is seen that the constants for 'plane' boundaries do not seem to differ much from those found for channel of circular cross section. It is indicating the similarity of the flow in the near-wall region of both cases.

In the viscous sublayer,

$$U^+ = y^+ \tag{32}$$

Equation (32) is the 'log-law' and is valid only in the wall region of the flow. Equations (30) and (32) are the 'law of the wall'. It is viewed as a universal velocity profile for turbulent flow in pipes and is also readily used in channel flow cases.

Van Driest (1955) provides a different *A* and *k* value for the logarithmic velocity distribution equation.

$$U^+ = \frac{1}{0.174}\log_{10}\left(y^+\right) + 5.24 \tag{33}$$

In this case, the author used a $\log_{10}$ rather than the natural log.
However, in buffer layer, there is no analytical solution available. Clapp (1961) proposed a velocity distribution equation for power law fluid which included an equation for buffer layer

Viscous sublayer $$U^+ = \left(y^+\right)^{1/n},\ 0 < y^+ < 5^n \tag{34}$$

Buffer sublayer $$U^+ = \frac{5}{n}\ln y^+ - 3.05,\ 5^n < y^+ < y^+_2 \tag{35}$$

Turbulent layer $$U^+ = \frac{G}{n}\ln y^+ + H,\ y^+ > y^+_2 \tag{36}$$

Where *G* and *H* are empirical constants to be obtained by experiment. y^+_2 = 30 is used for Clapp's (1961) paper and also in Chapter 6 of this work. The observed velocity distributions by the author were correlated by the equation:

$$U^+ = \frac{2.78}{n}\ln y^+ + \frac{3.8}{n} \quad \textbf{(37)}$$

Investigations (Coles, 1956) have shown that the deviation of the velocity distribution in the outer region of open channel flows from the log-law can be accounted for by adding a wake function.

$$U^+ = \frac{1}{k}\ln y^+ + A + w(\xi) \text{ with } w(\xi) = \frac{2\Pi}{k}\sin^2\left(\frac{\pi}{2}\xi\right) \quad \textbf{(38)}$$

Where $w(\xi)$ accounts for the deviation and termed the wake function, and Π is termed the Coles' wake strength parameter. Equation (38) is known as 'the velocity defect law' or 'the log-wake law'. Experiments conducted by Eckelmann (1974) and Nezu (2005) showed that Π is about zero at low Reynolds number < 500. At small values of *Re* greater than 500, Π increases rapidly with *Re* and it remains nearly constant, i.e. Π =0.2 for *Re* > 2000.

Barenblatt (1993) introduced a specific power law for the velocity profile in pipe flow. This law fits data in the inner part of the wake region and the outer part of the log region.

$$U^+ = Ay^{+\alpha} \quad \textbf{(39)}$$

$$A(\mathrm{Re}_d) = \frac{5}{2} + \frac{1}{\sqrt{3}}\ln \mathrm{Re}_d \quad \textbf{(40)}$$

$$\alpha(\mathrm{Re}_d) = \frac{3}{2\ln \mathrm{Re}_d} \quad \textbf{(41)}$$

Where $Re_d = VD/\upsilon$. The Re_d is based on the average pipe velocity *V* and the pipe diameter $D = 2r$. However, it is uncertain that if this power law fits for open channel flow.

Yalin (1977) introduced a set velocity distribution equation in turbulent flow with roughness of the channel considered. The author stated that:

- if $U^*k_s/\upsilon < \approx 5$, then the velocity distribution is

$$U^+ = \frac{1}{k}\ln\frac{y}{k_s} + B_s,\ B_s = 2.5\ln\frac{U^*k_s}{\nu} + 5.5 \quad \textbf{(42)}$$

- if $U^*k_s/\upsilon > \approx 70$, then the velocity distribution is

$$U^+ = \frac{1}{k}\ln\frac{y}{k_s} + B_s,\ B_s = 8.5 \quad \textbf{(43)}$$

Where U^* is the friction velocity, v is the kinematic viscosity. k_s is Nikuradse's original uniform sand grain roughness, it represents the equivalent sand roughness for any type of rough surface. B is a dimensionless property of the flow in the vicinity of the bed; in general, it must be a certain function of U^*k_s/υ. Kirkgoez (1988) conducted experiments with different rough surfaces in open channel flows. Experiments were performed in a glass-walled channel about 12 m long. Laser-Doppler anemometer was used to measure the flow velocities. The author found that on rough beds, the law-of-the-wall fits quite well for different roughnesses. However, the velocity-defect distribution shows some scatters.

Chiu and Tung (2002) proposed a method to predict the position of maximum velocity under water surface. The author derived the following velocity distribution equation:

$$U = \frac{U_{\max}}{M}\ln\left[1+\left(e^M-1\right)\frac{\xi}{\xi_{\max}}\right] \quad \textbf{(44)}$$

In which U = velocity; U_{max} = maximum velocity in a channel cross section; M = parameter; ξ_{max} = maximum value of ξ and occurs at the location of U_{max}; and ξ = constant on an isovel on which the velocity is equal to U. $\xi/\ \xi_{max}$ is equivalent to the probability of velocity, randomly sampled in a channel section, being less than or equal to U. M can be calculated by the ratio of the mean and maximum velocity:

$$\frac{\overline{U}}{U_{\max}} = \frac{e^M}{e^M-1} - \frac{1}{M} \quad \textbf{(45)}$$

ξ can be expressed as a function of y:

$$\xi = \frac{y}{Depth-h}\exp\left(1-\frac{y}{Depth-h}\right) = \frac{\frac{y}{Depth}}{1-\frac{h}{Depth}}\exp\left(1-\frac{\frac{y}{Depth}}{1-\frac{h}{Depth}}\right) \quad \textbf{(46)}$$

In which y = vertical distance from the bed. There are three cases for ξ, but only the following one is considered to be applicable for this research.

- The maximum velocity U_{max} occurs at a vertical distance h below the water surface, or y = Depth - h. In this case, $h > 0$ and ξ_{max} as well as U_{max} occurs at y = Depth - h. therefore

$$\frac{\xi}{\xi_{\max}} = \xi = \frac{y}{Depth - h} \exp\left(1 - \frac{y}{Depth - h}\right) \quad \textbf{(47)}$$

Since h represents the distance of U_{max} from the water surface, the upper limit of h/Depth is unity. In Chapter 6, these velocity profile equations will be tested with data compiled for this thesis.

2.4.2 Secondary current in channel flow

In 1878, Francis (cited in Gulliver and Halverson, 1987) first hypothesized the secondary currents concept. His explanation for secondary current was the depression of the point of maximum velocity from the free surface. Nikuradse (cited in Yang, 2009) first made the observations of secondary currents that appeared near the corners of the duct cross section. There are two kinds of secondary currents described in the literature. If the flow is not uniform in the streamwise direction, streamwise vorticity is generated by vortex stretching (Nezu and Nakagawa, 1993). Secondary currents generated by this particular mechanism are called 'secondary currents of Prandtl's second kind'. The first kind of secondary current has been widely investigated in curved channels and river ways. The other type of secondary currents is caused by the sidewall effect. These secondary currents of Prandtl's second kind are often termed turbulence-driven secondary currents. This particular secondary current can not arise in laminar straight channel flow (Nezu, 2005). The presence of secondary current displaces considerably the velocity contours.

In fact the secondary currents in open channel flows remained comparatively unknown until recently. The most important feature is that the maximum velocity appears not at the free surface, but just below the free surface in open channel flows. It is also suggested by Nezu and Nakagawa (1993) that this phenomenon is called the "velocity-dip", and it is peculiar to open channel flows. According to Nezu and Nakagawa (1993) and Nezu (2005), a secondary current is where the lower velocity/momentum material has been dumped into the high velocity/momentum region. Therefore there is a dip in the axial velocity profile after

maximum velocity has been reached. This happens regularly in non circular channel flow. Only this second kind of secondary currents is studied in the present research.

Nezu and Rodi (1985) used a two-colour LDV system to measure the longitudinal velocity and vertical velocity in an open channel. Figure 6 shows the velocity vectors of the secondary currents measured by Nezu and Rodi (1985) in a narrow open channel. It is quite obvious that a strong vortex occurs near the free surface. This vortex is called the 'free-surface vortex', and its pairing vortex near the bottom of the channel is called 'bottom vortex'. This free-surface vortex is much stronger than the bottom vortex. Free-surface vortex transports momentum and energy from the side of the channel toward the centre of the channel. The strong down flow that occurs at the channel centre causes the so called velocity dip as momentum is transported from the free surface to mid-depth.

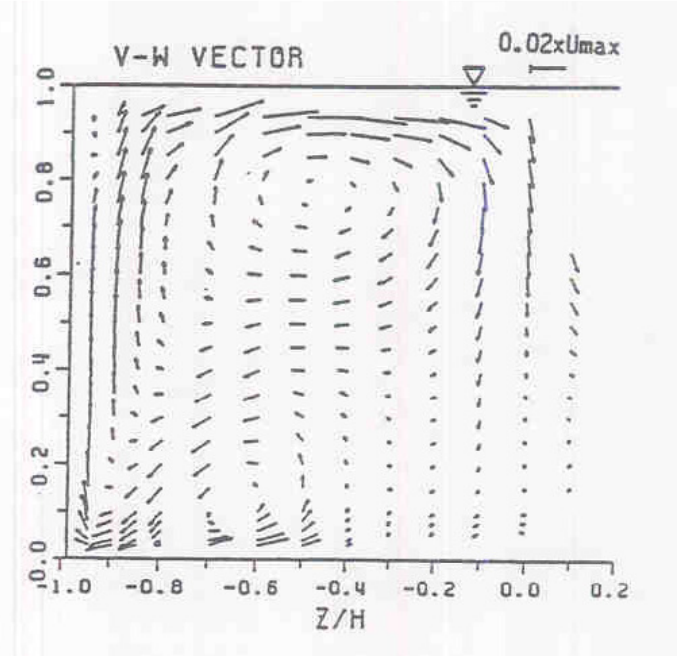

Figure 6 Vector description of secondary currents in open channel by Nezu and Rodi (1985)

Einstein and Li (1958) first deduced the equation of relation between the longitudinal vorticity and Reynolds shear stress. It is quite accepted that secondary flows are induced by the imbalance of normal Reynolds shear stress. In Gessner (1973), the author stated that the anisotropy of turbulent normal stresses, $\overline{v^2}$ and $\overline{w^2}$, did not play a major role in the generation of secondary currents. Knight and Sterling (2000) conducted experiments in circular conduits, with and without a smooth flat bed, and flowing partially full. The author discovered that the

secondary current appeared in both near the free surface and in the corner regions, particularly when a deposited sediment bed is presented.

In Nezu (2005), the author summarised that the velocity-dip phenomenon occurs if $b/h \leq \alpha_c$. The value of α_c is equal to 5 or slightly larger. It is then classified into two categories:

- Narrow open channels, $b/h \leq \alpha_c$. Corner flows are generated in flows because the side wall produces anisotropy of turbulence in the same manner as for closed-channel flows. The velocity-dip is also caused by the free-surface effect whereby the anisotropy of turbulence differs from that for closed-channel flows (Nezu, 2005).
- Wide open channels, $b/h > \alpha_c$. The side-wall effect disappears. But if any spanwise variation of bed shear stress occurs that is periodic, cellular secondary currents are generated. However, it is not investigated in this research.

Yang *et al* (2004) proposed a velocity distribution profile for secondary current in rectangular open channel as follows.

$$U^+ = \frac{1}{k}\ln\left(\frac{y}{y_o}\right) + \frac{\alpha}{k}\ln\left(1-\frac{y}{h}\right) \quad \textbf{(48)}$$

Where α_y is the factor to predict secondary current given by

$$\alpha_y = 1.3\exp\left(-\frac{B}{2h}\right) \quad \textbf{(49)}$$

In $\alpha_y = 0$, the above equation will become the classical log law. The second term on the RHS plays an important role in the outer region. However, it is negligible in the inner region as $\ln(1-y/h) \approx 0$. This will be tested in the Results section.

2.4.3 Quadrant analysis

This particular method is used in various journal papers to investigate the Reynolds stress structures and features of the large eddy. In this research, quadrant analysis is used as a tool to quantify the near boundary behaviour of the fluid.

The quadrant analysis technique is introduced by Willmarth and Lu (1972) for a turbulent boundary layer. This technique sorts out contributions to the Reynolds shear stress $u'v'$ into quadrants of the u-v plane. The largest positive contributions to the turbulent energy were provided by the ejection ($u'<0$, $v'>0$) and sweep quadrants ($u'>0$, $v'<0$), while small and negative contributions were made by the interaction quadrants ($u'<0$, $v'<0$ and $u'>0$, $v'>0$). The first quadrant $u'>0$, $v'>0$, contains outward motion of high-speed fluid. The second quadrant $u'<0$, $v'>0$ contains the motion associated with ejections of low-speed fluid away from the wall. The third quadrant $u'<0$, $v'<0$ contains inward motion of low-speed fluid. The fourth quadrant $u'>0$, $v'<0$ contains an inrush of high-speed fluid; this is usually referred to as the sweep event (Kim *et al,* 1987).

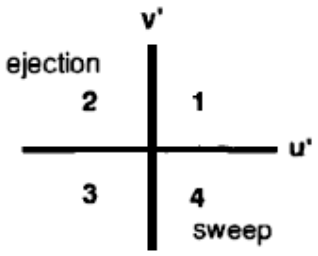

Figure 7 Quadrants of the instantaneous $u'v'$ plane

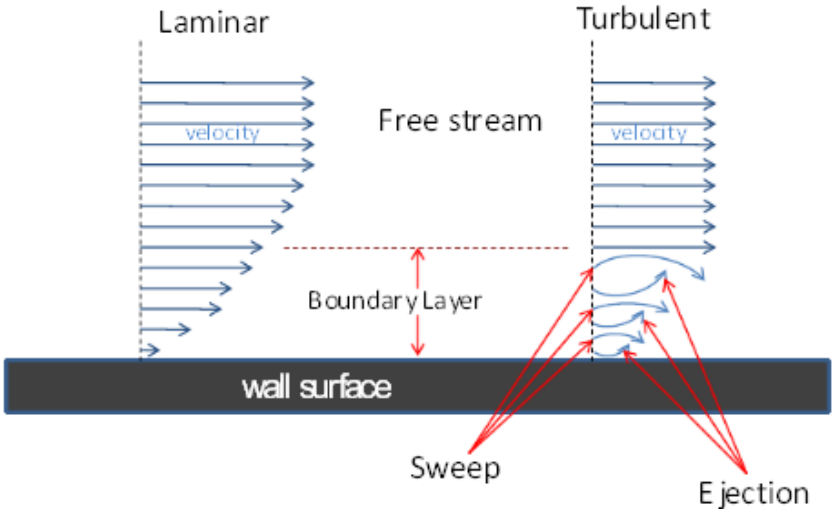

Figure 8 Sweep and ejection in turbulent boundary layer (Biddinika, 2010)

In Wallace *et al* (1972), the author used Hot-film measurement to measure Reynolds stress in a full developed channel flow. The Reynolds number based on the width of the channel and the centre-line velocity is 7150. This is equivalent to a pipe Reynolds number of 11000 (Wallace *et al,* 1972). Under these turbulent conditions, the author concluded that turbulent energy dissipation is associated with the Reynolds stress producing motions i.e. sweep and ejection. However, the author did not comment on the actual position of sweep and ejection. The investigation is been limited by equipment measuring ability. It has been discovered in Kim *et al* (1987) that the ejection event dominated away from the wall region whereas the sweep event dominated in the wall region. In Kim *et al* (1987)'s study, the author only used direct numerical simulation to produce Reynolds stress in a turbulent channel flow.

Rajagopalan and Antonia (1982) conducted X-wire/cold wire arrangement to measure velocity fluctuations in a wind tunnel. Their quadrant analysis technique is based on instantaneous products of longitudinal, normal velocity fluctuations and the temperature fluctuation. They found that the frequency of ejections is nearly equal to sweeps. Yet, they also did not comment on the place where sweep or ejection most likely to happen.

Antonia and Browne (1987) investigated the average momentum and heat transfers in the self-preserving region of a turbulent wake. Similar to Rajagopalan and Antonia (1987) they used X-wire/cold wire technique to measure velocities in a wind tunnel. The main focus of this research is on the vortex motion of a turbulent wake. In this case, the author identified ejections with the outer downstream part of a spanwise vortex and sweeps with the inner upstream part of the same vortex.

Shvidchenko and Pender (2001) presented a paper on the macro-turbulent structure of open channel flow. The author conducted the experiment with water in an 8 m long rectangular flume. They used SONTEK acoustic Doppler velocimeter to measure the velocity of the fluid. They also used a flow visualization technique to study the large scale turbulent structure of the flow. They used quadrant analysis and ADV to show the existence of sweeps and ejections in the channel. It is concluded that the upwelling (ejection) and high forward speed downwelling (sweep) fluid motions significantly increase the local Reynolds stress. This finding is parallel to Kim *et al* (1987)'s conclusion. Moreover, Shvidchenko and Pender

(2001) stated that if the sweep and ejection motion are strong enough, then the motion could suspend the bed particles.

Klipp *et al* (2006) used quadrant analysis on atmospheric surface layer. They deployed an array of sonic anemometers mounted on five towers in Oklahoma City. The author studied the turbulent transport and dispersion in the atmospheric boundary layer within an urban environment. They actually focused only on the turbulent momentum transport on wind vectors. Moreover, the authors did not put any emphasis on sweep and ejection, but on quadrant 1 and quadrant 3 motion instead.

Robinson (1991) stated that the majority of the turbulence production in the entire boundary layer occurs in the buffer region. The near wall turbulence production process is considered to be an intermittent, quasi-cyclic sequence. It is usually referred to as 'bursting'. It has described as 'violent breakup of a low-speed streak after lifting', and 'shear-layer interface sandwiched between an upstream, high-speed sweep and a downstream, low-speed ejection' (Robinson, 1991). Most of the definitions about bursting process describe it as a highly intermittent, explosive event. It is a very satisfying concept for the production of turbulent motion.

Yalin (1977) also mentioned 'bursting' as an 'observable chain of events'. The total chain of the events mentioned is referred to as the 'burst'. It seems that the bursting process is regenerative. I.e. a 'recirculation cell' is formed by the sweep action, then it would disintegrate into a multitude of smaller eddies. Therefore the path of a module or a macro-turbulent eddy should end just on the downstream side of the location where the path of the next module begins. This is a vast area and is extremely relevant with regards to particle transportation in channels. In the next section, the interactions between particles and turbulent structure will be discussed in details.

2.5 Particle interactions

From the literature, there are two issues of fluid dynamics which are poorly understood: turbulence and two-phase flow. This section will review the interaction between these poorly understood areas. In the coming section, only the effect of the particles on the turbulence in a boundary layer will be discussed in some depths.

2.5.1 Particle characteristics

2.5.1.1 Stokes number

Crowe *et al* (1993) published some parameters which affect the particle dispersion in large scale and organized structures. The authors proposed a Stokes number defined as:

$$St = \frac{\tau_s}{\tau_F} \tag{50}$$

Where τ_s is the aerodynamic response time of a particle and τ_F is the time associated with the motion of the large scale structure. The particle response time is the time it takes for the particle to respond to changes in the local flow velocity. It depends on the particle's radius and density (Hogan and Cuzzi, 2001). The aerodynamic response time is scaled as:

$$\tau_s = \frac{\rho_p d^2}{18\rho_f \mu} \tag{51}$$

Where ρ_p is the material density of the particle, d is the particle diameter and μ is the dynamic viscosity of the carrier fluid. The flow time is modelled as

$$\tau_F = \frac{\delta}{\Delta U} \tag{52}$$

Where δ is the size of the structure and ΔU is the velocity difference across the shear layer. The size of the structure in fact is a very vague description. According to Nezu *et al* (2004), the size of the structure has also been described as mixing length. From Nezu *et al* (2004), the mixing length l^+ is obtained by using van Driest damping function:

$$l^+ = ky^+\Gamma \tag{53}$$

k is the von Karman constant and has an universal value of 0.412. y^+ is the distance from the wall and

$$\Gamma = 1 - \exp(-y^+/26) \quad \textbf{(54)}$$

Stokes number becomes:

$$St = \frac{\rho_p d^2 \Delta U}{18 \rho_f \mu \delta} \quad \textbf{(55)}$$

It is discovered that if the $St \ll 1$ then the particle response time is less than the flow time and the particles will follow the fluid path lines. If $St \sim 1$, the particles will probably be centrifuged by the vortices structures. For $St \gg 1$, the particles have insufficient time to respond to changes in the fluid velocity and will continue in near rectilinear trajectories (Crowe *et al,* 1993). In other words, particles generally become more fluid-like as Stokes number approaches zero and they are distributed more uniformly in an incompressible fluid flow. When St is greater than unity, particles become less responsive to the flow field.

This concept is based on particle dispersion rather than the particle transport. The paper only described particle dispersion in large scale turbulent structures generated by free shear flows. Free shear flow is the unbounded region of a large body of fluid flow, which have either excess momentum or momentum deficit (Sreenivas, N.D). The future experiment may not be a free shear flow as it does not have an unbounded region of large body of fluid. Thus the calculation of Stoke number may not be able to give a clear answer.

The question needs to be asked is whether it is possible to relate the rheological characteristics of the continuous medium carrier fluid to the transport of solid phase in the suspension. Thus determine the conditions that allow transported particles to stay in suspension in turbulent open channel flow.

2.5.1.2 Sediment transportation

Yalin (1977) made a very thorough review on the mechanisms of sediment transport. Nevertheless, the models presented in the book are empirical and only applicable to dilute systems. There is no theoretical correlation to accurately describe the mechanism associated with transportation of coarse particles to date.

The best-known and most widely used investigation on initiation of motion is Shields (Yalin, 1977). This parameter is very frequently used to relate the suspended sediment to the dynamic parameters of flowing slurry. Shields found that the dimensionless critical shear stress is:

$$\tau_c = \frac{\tau}{g(\rho_s - \rho_f)d} \quad \textbf{(56)}$$

This parameter addresses the critical stage of a mobile bed and the initiation of grain motion en masse, not the detachment of an individual grain. In most of the studies, this model is used in diluted sediment slurries. The Shield parameter is just a way to describe the incipient motion of particles. It is not equivalent to the critical deposition velocity condition described in pipelines for concentrated systems. It is not entirely sure whether this can be used in non-Newtonian suspensions.

Schaflinger *et al* (1995) used a factor which resembled the Shields parameter to study viscous re-suspension of settled particles in laminar flows. The author investigated viscous re-suspension for a two-dimensional Hagen-Poiseuille channel flow. The methods described in the paper are only applicable to viscous Newtonian carrier fluid.

Muste and Patel (1997) conducted experiment in a 30 metres long rectangular flume with a concrete bed. They used the sand from Iowa River in their experiment with a size range of 0.044-0.710 mm. The authors measured velocity profile and turbulence characteristics of the liquid and sediment particles. Unfortunately they did not mention any rheology parameters of the sediment or the relationship between the rheology parameters and turbulence characteristics.

2.5.2 Turbulence & Particle interaction

From literature, it is discovered that the behaviour of solid particles in the wall region of a turbulent boundary layer is extremely important for the understanding of deposition, entrainment and re-suspension in different industrial processes. Three different types of coherent wall structures have been observed by many researchers (Blackwelder and Kaplan, 1976; Robinson, 1991; Jeong *et al,* 1997; Kumar *et al,* 1998; Liu *et al,* 2001; Rouson and

Eaton, 2001; De Angelis *et al*, 2002; Nezu, 2005.). One type consists of low velocity streaks very close to the wall. The second are streamwise and quasistreamwise vortices and the third type are 'active' periods usually referred as 'bursts' (Kaftori *et al*, 1995).

Sumer and Oguz (1978) investigated particle behaviour during the bursts using photographic techniques. The authors found that the particles moved along the bottom of the channel and were randomly ejected into the flow up to heights of 100-200 wall units or more. They also discovered that the ejected particle was within a low-velocity streak prior to the ejection.

Sumer and Deigaard (1981) argued that the mechanism which prevents the particle from settling is closely associated with the turbulence structure near the bottom of the channel. The authors used particles with diameters between 2.9-3.1 mm and specific gravity between 1.0029-1.0258 in the experiment. The heavy particles have the highest specific gravity of 1.0258. They used stroboscope and high speed camera to record particle paths in three dimensions.

It was noted that the particle ejected from the wall region could reach y^+ of 54 on average. The particle ejected from the wall region falls out of the lifted fluid with the burst before the burst break up. Then the particle starts to return back near the bottom and finally swept into low speed wall streak from where it is ejected again into the flow (Sumer and Deigaard, 1981).

Rashidi and Banerjee (1988) have used oxygen bubble technique and video camera to capture and trace the turbulent structure in a channel. However oxygen bubble flow visualization was only employed at $Re < 10000$ since at a high Reynolds number the bubbles dispersed through the flow very fast. After analysing the velocity-fluctuation amplitude distributions, they have found out that "bursts" lead to an overall rotational structure in the liquid stream that rolls with the flow (Rashidi and Banerjee, 1988). By plotting the intensities of vertical fluctuations, the region near the interface showed higher intensities than the ejection events. It is interesting to see that after the burst fluid reaches the interface; the velocity field becomes more chaotic.

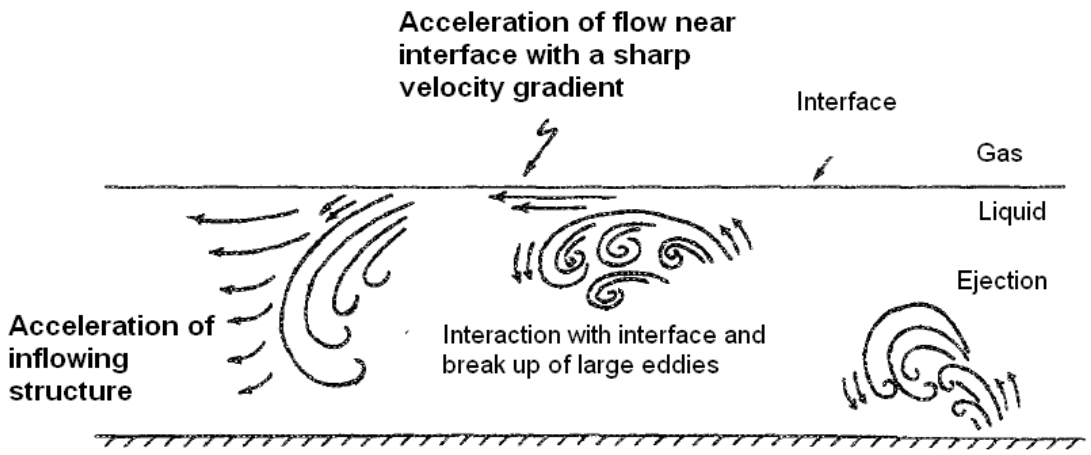

Figure 9 Sketch of burst evolution in a flowing liquid layer between a wall and a free surface (Rashidi and Banerjee, 1988)

In their next paper, Rashidi *et al* (1990) conducted experiments on particle-laden fully-developed pipe flow and free shear flow. They used a Plexiglas rectangular channel and liquid recirculating facilities. They have used water as the carrier fluid in the experiment. The solid particles were larger than 0.5 μm glass or polystyrene spheres. The structure of turbulence was visualized by the use of oxygen bubble tracers. The flow then was photographed using high-speed video analyser.

Fluid and particle velocity profile were obtained by image processing. Velocity of fluid as well as particle was then plotted against non-dimensional distance from the wall. The result showed that as the particle size increases, the particle response to the fluid velocity decreases giving rise to an increase in the relative velocities. Particles with Re_p (Particle Reynolds number) < 100 would suppress the turbulence and particles with $Re_p > 400$ would enhance the turbulence. They also showed that light particles rather than heavy particles can bring about significant modulation of turbulence through changing the number of wall ejections. The larger particles cause an increase in the number of wall ejections as well as an increase of turbulent intensities and Reynolds stresses. The lighter and smaller particles cause a decrease in the number of wall ejections, hence causing a decrease in the turbulent intensities and Reynolds stresses. Furthermore, it has also been observed that the low-speed region, is periodically broken off near the wall, and then is ejected into the main stream. However the author only used water as the transportation medium. With a small concentration of particles, the suspension can only be assumed to be Newtonian.

Rogers and Eaton (1991) investigated two-dimensional turbulent boundary layer particle-laden flow in air. The authors showed that particles damp fluid turbulence affecting all scales equally. There is a noticeable correlation of local particle concentration in the near- wall regions of high turbulent kinetic energy of the fluid and the suppression of the turbulence.

Pedinotti *et al* (1992) used DNS simulation to investigate the motion of small particles in the wall region of turbulent channel flow. They used the well known method by Kim *et al* (1987) to simulate the channel flow. The simulation indicated that particles were ejected from the wall due to upflow caused by quasi-streamwise vortices. The author commented that there was difficulty in simulating high Reynolds number numerically. The Reynolds number used in this simulation is only around 147.

Brooke and Hanratty (1993) presented that the flow-oriented vortical eddies were connected with large Reynolds stresses and the production of turbulence in the viscous region close to the wall. In their DNS simulation, the fluid velocity field for turbulent flow in a vertical channel was generated. According to the DNS velocity vector field, turbulence was generated by the unpaired vortices.

From the DNS study, it is shown that large Reynolds stresses and large turbulence production occurred in the viscous wall region where Rashidi *et al* (1990) also noted as an area of interest. Brooke and Hanratty (1993) found a new mechanism of how new vortex is born at the wall. This mechanism can be related to the particle suspension in this study.

Hetsroni (1993) described the coherent structure in more detail. He revealed that a boundary generates organized structures in the fluid. When the shear rate is increased at a boundary, either high speed or low speed regions can be observed near the boundaries. From the experimental data, the authors concluded that larger particles (about 500 to 1000 μm) enhance the turbulence of the fluid in a channel whereas the smaller particles suppress the turbulence. They claimed that in the boundary layer, the larger particles increase the frequency of ejections. This particular mechanism is associated with increasing velocity gradients in the flow, as the vortex may cause additional energy dissipation.

In their next paper Hetsroni and Rozenblit (1994) found experimentally that with particles of the order of 10 wall units, the particles tend to accumulate in the low velocity streaks. With the particles larger than 30 wall units, they were more randomly distributed on the bottom of the flume. However the method to calculate the wall unit or the definition of wall unit is not included in this paper.

It is also shown from a number of studies that suspended particles may affect turbulent parameters and eventually the transportation properties. Kaftori *et al* (1998) suggested that small particles tend to suppress turbulence and large particles enhance the turbulence. "Close to the wall, particles exhibit a tendency to preferentially accumulate in certain regions. Heavier particles which settle to the wall in horizontal flow tend to migrate into the low speed regions…" (Kaftori *et al*, 1998, p360). This finding is parallel with Hetsroni (1993) and Rashidi *et al* (1990).

The solid particles used in Kaftori *et al* (1998) were polystyrene with diameters of 100, 275, and 900 μm, with distributions of 90-106 μm, 212-300 μm, and 850-1000 μm, and specific density of 1.05. The investigated experiments were conducted at Reynolds numbers of 5000, 10000 and 14000. Hetsroni (1993) claimed that larger particles enhance the turbulence of the fluid. It is suggested that in the future experiment the point of interest would be the larger particle size. E.g. from 800 to 1000 μm.

Ljus *et al* (2002) investigated turbulent air flow with particles. The results showed that with spherical particles, the influence of the particles on the flow is significant. With a range of different velocities, the turbulent intensity data showed similar trend where at lower part of the pipe, the turbulence is attenuated by the particles. One of the possible reasons discussed by the author is that small particles can follow smaller scales in the turbulence. Therefore the turbulent energy is then transferred from the gas phase/liquid phase to the particles. The lower part of the pipe has a higher concentration of particles hence the turbulent intensity is reduced. The particles used in this experiment have a particle response time of 0.5 s. However it is still based on air flow rather than liquid flow. Further research needs to be done in order to discover a suitable formula for liquid flow particle response time.

Righetti and Romano (2004) indicated that in particle-laden flow, the fluid and solid phase mean velocities are reduced in the outer layer ($y^+ > 20$), but increased in the viscous sub-layer ($y^+ < 5$) in comparison to the clear water flow. In particle-laden flow, the flow velocity is smaller than the particle velocity close to the wall ($y^+ < 15$). In the outer layer, the opposite takes place. The authors also found that the Reynolds stress and turbulence intensities of the streamwise and vertical velocity are dampened for $y^+ > 20$, but enhanced in the near wall regions ($y^+ < 5$).

Nezu *et al* (2004) claimed the coherent structures such as ejections and sweeps will influence fluid-particle interactions. Moreover, the fluid-particle interactions and the bursting phenomena all occur most violently in the inner-wall region of $y/h < 0.2$. The difficulty is how to measure the velocity fluctuations or wall shear stress in the inner-wall region. Therefore in this study, DNS will be employed for this investigation.

2.6 Summary

To summarise, there are different areas of particle transportation in open channel flow that have not been adequately studied. Most of the studies presented in this chapter are investigations of Newtonian fluid such as water (Rashidi and Banerjee, 1998; Rashidi *et al*, 1990; Hestroni, 1993; Hestorni and Rozenblit, 1994; Righetti and Romano, 2004; Nezu *et al*, 2004) and pneumatic conveying (Ljus *et al*, 2002). Further, no paper in this area mentioned the visible secondary flow effect in the channel flow with non-Newtonian fluid. Some papers only discussed the secondary current in developing turbulent flow along a corner with water flow (Nezu *et al,* 2004; Yang *et al*, 2004; Yang, 2009).

All the works discussed in this chapter have focused on velocity distribution in channels with Newtonian fluids, turbulent characteristic and turbulence and particle interaction in Newtonian fluids and air. Further study is required to improve the existing models for velocity distribution in non-Newtonian channel flow. Furthermore, the turbulence characteristics should be related to fluid rheology and the channel geometry in order to improve the understanding of particle transportation in open channels.

Chapter 3: DNS studies

3.1 Introduction

A Large Eddy Simulation (LES) has been used in computational fluid dynamics simulations since the 1960s (Smagorinsky, 1965). However, there are few problems with LES techniques. Firstly, because of the complex nature of the physical systems involved in process industry applications, the turbulent closures involve many equations with many unknown cross-correlations having to be modelled. Secondly, the geometrically complicated nature of the application, simple computational meshes cannot be used. Finally, the computational expense of LES is significant when compared to many RANS techniques. Moreover, the near-wall regions cannot be properly resolved.

Direct Numerical Simulation (DNS), a computational fluid dynamics method with all the details of the complex turbulent fluctuating motion are governed by the unsteady 3D Navier-Stokes equation together with the continuity equation. This means that all the motions need to be resolved. The advantage of simulations relative for experiment is quite obvious as all quantities of interest can be obtained for the whole field (McIver *et al*, 2000). It basically means that velocity, pressure and their derivatives at any time and point in the instantaneous flow field can be obtained.

However, with all motions needed to be resolved, the size of the numerical mesh must by smaller than the size of the small-scale motion where dissipation takes place (Rodi, 2006). It is said in Rodi (2006) that DNS is possible only for flows with low Reynolds numbers. In this study, DNS is attempted to simulate turbulent channel flow. This will be described in Chapter 5.

3.2 Literature review for DNS simulations

Over the past fifty years, the study of turbulent non-Newtonian suspension flow in pipelines has received considerable attention because of its industrial relevance across a wide range of industries. In recent years, there has been a significant improvement in understanding of

pipeline flows as a result of improved instrumentation and computational techniques. The literature is presented in the following order:

- Turbulent pipe/duct flow
- Turbulent channel flow

3.2.1 Turbulent pipe/duct flow

In 1987, Kim *et al* applied DNS to investigate fully developed turbulent flow between two plates. They used almost 4 x 10^6 grid points in the simulation. The authors simulated the flow field at a Reynolds number based on mean centreline velocity at only around 3300. The turbulence statistics agreed with experimental results of Eckelmann (1974) except at the near-wall region. It was suspected that the disagreement might be due to the inaccurate measurement of the experimental values.

In Eggels *et al* (1994), the authors used DNS and experiments to study fully developed turbulent pipe flow at a Reynolds number ≈ 7000 based on the centreline velocity and pipe diameter. They made comparison between a plane channel flow and an axisymmetric pipe flow. It is discovered that the differences in the mean velocity profile are related to the geometry. The change of geometry may cause the change in mean velocity because of the absence of side walls in plane channel. However, the authors did not mention anything in regards to the rheology of the fluid. It is suspected that the authors used a Newtonian fluid in the simulation.

Shan *et al* (1999) simulated transitional pipe flow with direct numerical simulation at Reynolds number = 2200 and 5000. The authors mainly focused on the fluid structures presented in the simulation. The simulation was carried out with a spectral element method. In this study, the authors argued that puff has the characteristics of a wave phenomenon whereas the slug can be characterised as a material property which travels with the flow. The authors only used a Newtonian fluid for the simulation.

Rudman and Blackburn (1999) used large eddy simulation on turbulent pipe flow. In the pipe flow geometry, the streamwise dimension is based on the integral correlation lengths of turbulence. In the paper, the authors concluded that the simulation of turbulent pipe flow is in good agreement with the experimental measurement at the same Reynolds number which is

around 1920. Rudman *et al* (2001) and Rudman *et al* (2003) described non-Newtonian turbulent pipe flow in their recent works. Both the papers used the experimental method and Direct Numerical Simulation (DNS) to investigate the turbulent behaviour of non-Newtonian fluids in a pipe.

Rudman *et al* (2001) conducted the experiment in a 40m × 100mm diameter pipe loop. Laser Doppler velocimeter (LDV) was used to measure the axial velocity profiles across the horizontal and vertical diameter of the pipe. CMC solution was modelled using power law correlation. In conjunction with experiments, numerical simulation was also conducted to compare the results. It was discovered that CMC does not behave as a simple power law fluid. The simulation results showed some agreements as well as some differences with the experimental results. Authors argued that there might be a possibility of fundamental error in the numerical method, and also the power law model parameter fitting (Rudman *et al,* 2001). In the paper, the computer simulation revealed the contours of streamwise velocity.

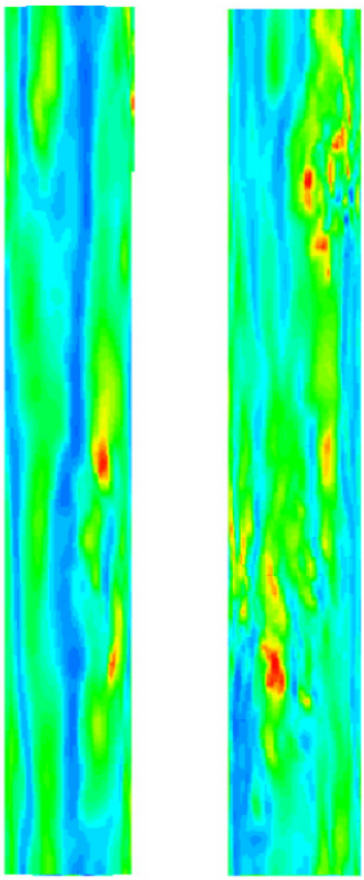

Figure 10 Near wall structure *Re* = 3964 (left) and *Re* = 5000 (right) (Rudman *et al,* 2001)

The above diagram showed some wall streaks and it revealed that there might be some bursting and not fully developed turbulence. The wall structure has some significant impacts on particle transportation. Therefore with current simulation method, a detailed wall structure can be simulated in order to examine the relationship between the structure and particle behaviour.

Rudman *et al* (2003) used the same approach to investigate turbulent pipe flow. In this paper, power law model was considered as well as Herschel-Bulkley model. The authors compared the simulation results to the correction proposed by Clapp (1961). The logarithmic velocity profile for the turbulent flow of power law fluids is a function of the flow index, *n*.

$$U^+ = \frac{A}{n} + \frac{B}{n} \ln y^+ \qquad \textbf{(57)}$$

Where

$$y^+ = \left[\left(\rho \tau_w^{\,2-n} \right)^{1/2} / K \right] y^n \qquad \textbf{(58)}$$

The results by adopting Herschel-Bulkley model showed good agreement in terms of shape and magnitude when compared with the experimental data. The simulated results predicted by friction factors were 10-15% higher than the Dodge and Metzner (1959) friction factor correlation. It was commented that the reason might be that elastic or elongational effects are influencing the results. In this paper, the authors paid more attention on the wall structure simulated by DNS. It is revealed when $n = 0.5$, the structure seemed more transitional, when $n = 1$ (a Newtonian fluid) the structure is more random and the streaks shorter; this may indicate that it is a more developed turbulent flow.

Rudman *et al* (2004) presented simulations on power law fluids as well as Herschel-Bulkley fluids. The rheology values were chosen to match some previous experimental results for a 0.05 wt% Ultrez 10 solution and were estimated from a curve fit to a rheogram. The generalised Reynolds number was 7027 for the simulation in this paper. The authors concluded that the simulations were in good agreement compared to the experimental result. The Herschel-Bulkley fluid simulation showed similar behaviour to the power law simulation result. Yet, the simulations from this paper were still based on pipe flow.

Rudman and Blackburn (2006) conducted further experiment on turbulent non-Newtonian pipe flow using a spectral element method. This paper is the extended and updated version of the previous studies. The paper showed that pipe flow of yield stress fluids can make transition to turbulence via intermittency and slugs and puffs observed in Newtonian flow. It was then claimed that the results were not conclusive because of the insufficient domain length of the simulation. In the simulation, the particular domain length was $5\pi D$. Therefore in the future computational experiment, it was suggested to increase the domain length in order to achieve a reasonable result. In this paper, the authors concluded that the simulation of a Carreau-Yasuda fluid showed very similar behaviour to the Herschel-Bulkley fluid result. Both of the fluids' log-law profiles lay above the Newtonian velocity profile which suggested undeveloped flow. However, the authors made comments that by using polymer solutions to approximate idealised rheologies, difficulties can be encountered due to some unwanted rheological effects.

Sharma and Phares (2006) made some interesting discoveries in their work. They simulated turbulent flow through a square duct. This particular study focused on DNS of turbulent particle transport through a square duct at a Reynolds number of 300 based on friction velocity. In the paper, the authors did not comment on the rheology of the fluid. It is then suspected that the author might have used a Newtonian fluid in the simulation rather than non-Newtonian fluid. It is pointed out by the authors that the off-axis secondary current in the square duct tends to enhance lateral mixing and turbulent dispersion of particles. Nevertheless, the authors only considered a closed duct in the investigation.

Joung *et al* (2007) simulated turbulent flow in a square duct for a Reynolds number based on bulk streamwise velocity and duct height equal to 4440. The main aim for this study is to investigate the secondary flow effect in corner of square duct. In Joung *et al* (2007), the Navier-Stokes equation were discretized in time and space by using the fully implicit velocity decoupling procedure proposed by Kim *et al* (2002). However, the author did not compare their velocity profile with any of the existing models.

3.2.2 Turbulent channel flow

Most of the DNS studies done on open channel flows are based on Newtonian fluid (i.e. water). Computational fluid dynamics methods such as DNS have not been readily used to examine the turbulent flow behaviour of non-Newtonian fluids.

Kim *et al* (1987) published their DNS result for turbulent channel flow. Their Reynolds number based on the friction velocity and channel half width was 180. Since then, DNS for channel has been regularly performed because of simple geometry and fundamental nature to understand the transport mechanism.

During that time, majority of the developed turbulent flow is simulated for flow between parallel walls. Since the geometry effect does not appear to have been taken into account in most of the turbulent pipe/duct flows, it is quite important to re-interpret the previous results. Therefore Antonia *et al* (1992) first examined turbulent channel flow at a Reynolds numbers of 3300 and 7900. They used numerical algorithm which was presented in Kim *et al* (1987). In their paper, it was found that both the DNS and experimental data show significant low Reynolds number effects. The original title of the paper is "turbulent channel flow", however, in the conclusion; it was mentioned as duct flow.

Sureshkumar *et al* (1997) simulated turbulent channel flow of a polymer solution with Reynolds number of 125 based on the friction velocity. The authors used an independently evaluated rheological model, the FENE dumbbell fluid model for the polymer chains (Sureshkumar *et al*, 1997). Reynolds number for this simulation equals 125 based on friction velocity due to computational constraints. The simulation results showed qualitative agreement with the experimental data associated with drag reduction. The author did not pay special interest in the geometry of the channel.

Baron and Sibilla (1998) reported an investigation of DNS on turbulent channel flow of a dilute polymer solution. The DNS code was based on a second order finite difference scheme, with explicit time advancement by a 3rd order Runge-Kutta Scheme. Continuity was then enforced at every Runge-Kutta step by solving a Poisson equation for pressure. The authors presented the findings to suggest that the polymer molecules could affect the bursting cycle of turbulence by weakening the streamwise vortical structure (Baron and Sibilla, 1998). Only

Warner's FENE dumbbell model was introduced to model the polymer's non-linear modulus of elasticity.

Wu *et al* (2000) conducted numerical modelling for sediment transport in open channels. They included free surface effect as well as the bed roughness to the original general-purpose flow solver FAST3D. The detail of their boundary conditions will be further discussed in Chapter 5. Moreover, Wu and his colleagues added a sediment transport model into the flow solver. This research is mainly a validation study for their new codes in sediment transport in open channels. The authors only used water as simulation fluid.

Mei and Yuhi (2001) investigated flow of Bingham fluid in a shallow channel. The authors actually considered a thin layer of Bingham fluid flowing down an open channel of finite width. They assumed that the fluid is homogeneous. The cross section was considered into three different zones: around the centre plane of the channel there was a shear zone at the bottom and plug flow zone at the top, separated by the yield surface. The dependence on the initial flow depth, bottom geometry and the fluid property was investigated in this particular research. This developed numerical model can be applied only on slow flows in an unbounded incline. Moreover, it has been reported that the model is quite simple to modify in order to suit other fluid models.

Abe *et al* (2001) performed DNS on fully developed turbulent channel for Reynolds number of 180, 395 and 640 based on friction velocity. They used finite difference method for the simulation. The authors obtained various turbulence statistics from the simulation and compared with DNS for turbulent boundary layer flow and experiments for channel flow. This particular paper is only based on air flow.

Rouson and Eaton (2001) presented results from a DNS of the passive transport of solid particles in turbulent channel flow. The Reynolds number for this paper was around 180 based on friction velocity and the channel half-width. The authors used DNS to resolve all the dynamically relevant scale of turbulence, and Lagrangian tracking for the particles. The authors found the particles tend to accumulate in the low-speed streaks which suppress the mean velocity below the fluid mean velocity in the near wall regions. It only indicated that particles slightly heavier than the fluid tend to segregate. This finding is extremely similar to

Hetsroni (1993) and Rashidi *et al* (1990) in their experimental work. This work however did not make any comments on the channel geometry or the rheological characters of the simulation fluid.

In Narayanan and Lakehal (2003), DNS of a turbulent open channel was combined with Lagrangian particle tracking to study the mechanisms of particle deposition onto the channel wall. The authors divided the deposited particles into two different populations: those with large wall-normal deposition velocities and the small near-wall residence times referred to as the free-flight population. The particles depositing with negligible wall-normal velocities and large near-wall residence time were referred to as the diffusional deposition population. They then concluded that the free flight is the dominant mechanism for particle deposition in wall-bounded flows. In this study, there was no discussion of the channel geometry or the rheology of the fluid.

Tsukahara *et al* (2005) investigated a DNS of fully developed turbulent channel flow for low Reynolds number of 64 based on friction velocity and channel half width. The authors stated that the Reynolds number dependence of the mean velocity profile is quite significant in the outer region of the channel. Nevertheless, Tsukahara and his colleagues did not use any rheology parameters in the simulation.

Li *et al* (2006) undertook DNS of dilute polymeric solutions in turbulent channel flow with Reynolds number of 125, 180 and 395 based on friction velocity. It was mentioned in this paper that for a given Reynolds number, the CPU-time and memory required for DNS of non-Newtonian flows are an order of magnitude higher as compared to Newtonian cases. Therefore, the DNS turbulent flows are mainly limited to small Reynolds numbers. In this paper, the authors mainly investigated drag reduction effect of the polymer solutions only. One of the interesting findings from this paper is that the eddy viscosity varies with the distance from the channel wall. This can be related to particle transportation in the channel in this study.

Kang *et al* (2007) simulated turbulent channel flows for Reynolds number up to 1270 based on friction velocity. They examined the clusters of vortices and their dynamics in the outer layer of the flow. The authors found that a large instantaneous Reynolds shear stress is carried

by the fine scale eddy structures. Further, a significant amount of turbulent kinetic energy is also dissipated in the eddy structure. They concluded that these eddy structures play a very important role in the production of the Reynolds shear stress. Yet, there are no comments made on the rheology of the simulation medium.

3.3 Summary

From the above review, it is quite obvious that computational fluid dynamics methods such as DNS have not (in the author's knowledge) been used to examine the turbulent flow behaviour of non-Newtonian fluids in open channel flow. Other than turbulent pipe/duct flows (Eggels *et al*, 1994; Shan *et al*, 1999; Rudman and Blackburn, 1999, 2006; Rudman *et al,* 2001, 2003, 2004; Sharma and Phares, 2006; Joung *et al,* 2007) most of the DNS turbulent studies are simulated assuming simple geometry (parallel plate) with relative low Reynolds number or using a diluted polymer solution which shows nearly Newtonian behaviour (Sureshkumar *et al*, 1997; Baron and Sibilla, 1998; Li *et al*, 2006). Also a number of studies investigated open channel flows (Kim *et al*, 1987; Antonia *et al*, 1992; Wu *et al*, 2000; Mei and Yuhi, 2001; Abe *et al*, 2001; Rouson and Eaton, 2001; Narayanan and Lakehal, 2003; Tsukahara *et al*, 2005; Kang, *et al*, 2007); however, all of them used Newtonian fluid as the transported medium.

Further, no paper in this area mentioned the visible secondary flow effect in the channel flow with DNS. No one used quadrant analysis for interpreting the results. Therefore there is a need to combine experiments with advanced application of mathematical computing techniques to give an insight into the problems of turbulent conveying in complex fluids in open channels.

Chapter 4: Experimental work

4.1 Introduction

Experimental and computational analyses have been attempted for Newtonian flows in channels (Kim *et al,* 1987) and non-Newtonian fluids in channel flow (Haldenwang *et al,* 2002, 2004). The overall approach to this research will be to examine channel flows under controlled conditions using a fluid analogue (which is rheologically similar to a typical fine particle suspension) and gather potential information on channel behaviour and turbulent properties.

This project used an established instrumented water flume built at CSIRO, Highett. The flume was then modified to fit the requirement of the current project. A set of experimental data were collected under different conditions of flow and channel slope. These data, combined with the fluid rheology were used as input to the DNS. The prediction of the velocity profile and other parameters such as Reynolds stresses and velocity fluctuations were compared with measurements of the same obtained on the open channel. This allowed refinements to the understanding of the nature of the turbulent flow that would not have been possible with physical measurements alone. These include the near wall velocity distribution and the characteristics of the near-wall turbulence structure. These results addressed the question of size, intensity and frequency of the turbulent structures.

4.2 Experimental programme

There are two experimental phases for this project. The first phase consisted of controlled laboratory experiments that were conducted at Highett, CSIRO. The second phase consisted of small scale flume laboratory work that was undertaken at RMIT University, Melbourne. DNS work was constantly running throughout the project.

4.3 First phase

4.3.1 Experimental objectives

The main objective for this phase of experimental work is to measure the necessary turbulent characteristics of non-Newtonian fluid flowing down a flume of known slope. There are a number of secondary objectives that were planned such as the measurement of velocity at different points within the flow. Depth measurements taken at different positions would indicate whether uniform flow conditions had been reached in the flume. Sample fluids from the flume were tested to check for rheology parameters. The test would allow the non-Newtonian fluid to be characterised with rheological models.

4.3.2 Test flume

A return-circuit testing flume located at CSIRO, Highett, Australia was used for the initial experiment. Fluid was pumped through a straight measurement section containing a calibrated orifice plate, through a diffuser, and into a settling chamber containing filter material and a honeycomb distributor. The fluid passed through a 4:1 contraction and a working section of the tunnel which was 1870 mm long, 244 mm high and 244 mm wide. The walls of the channel were made of transparent acrylic material. The velocity of fluid in the tunnel could be varied using a variable speed controller. Then water passed into an outlet reservoir tank.

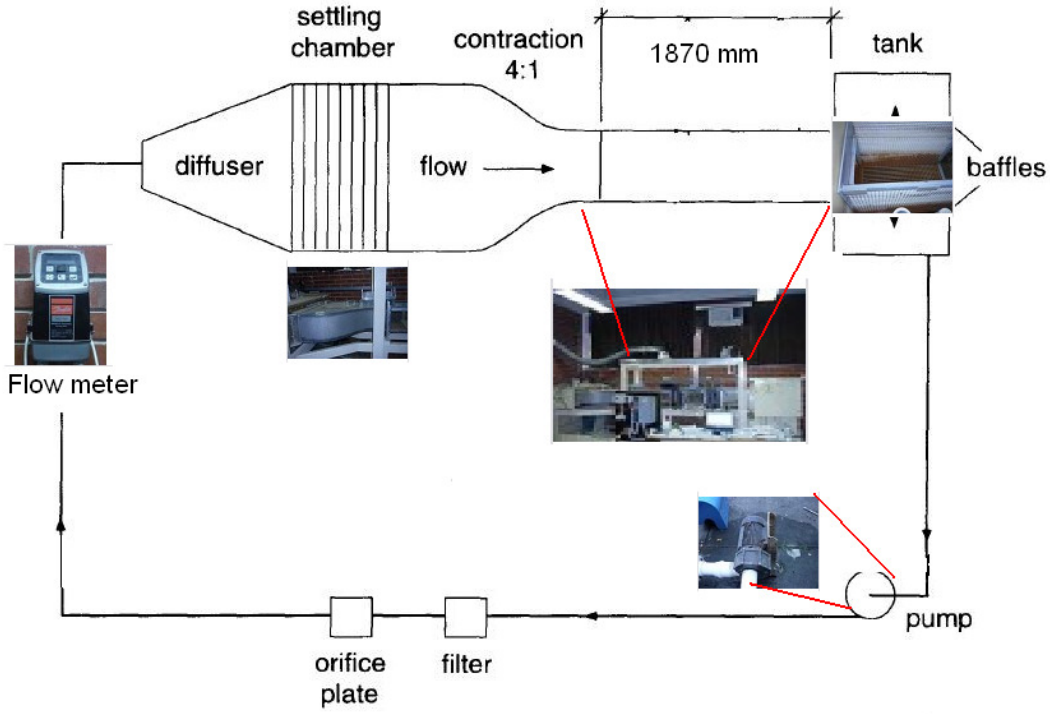

Figure 11 Closed-circuit test flume

4.3.3 Acoustic Doppler Velocimeter

In this experiment, Nortek Vectrino velocimeter was used to measure velocity fluctuations in the channel flow.

4.3.3.1 Basic of ADV

This type of velocimeter uses the Doppler effect to measure velocity. This is a versatile, high-precision instrument that measures all three flow velocity components. The measurements are insensitive to water quality which allows for a wide range of applications. These kinds of velocimeters are used in laboratories, wave basins, rivers, estuaries and oceanographic research.

In this case, the Doppler velocimeter measures three-dimensional flow velocities using the Doppler principle. The instrument consists of a sound emitter, three sound receivers and a signal conditioning electronic module (Garcia *et al*, 2005). The sound emitter generates an acoustic signal that is reflected back by sound-scattering particles present in the medium. Then the scattered sound signal is detected by the receivers and used to compute the Doppler

phase shift. In this case, the flow velocity in all three directions can be detected or calculated. A more detailed description of the velocimeter operation can be found in Nortek AS (2004).

4.3.3.2 Vectrino Principles

In contrast to the standard Doppler profilers, the Vectrino is a bistatic sonar. It means that the probe uses separate transmit and receive beams. It is obvious to see that it transmits through a central beam and receives through four beams displaced off to the side.

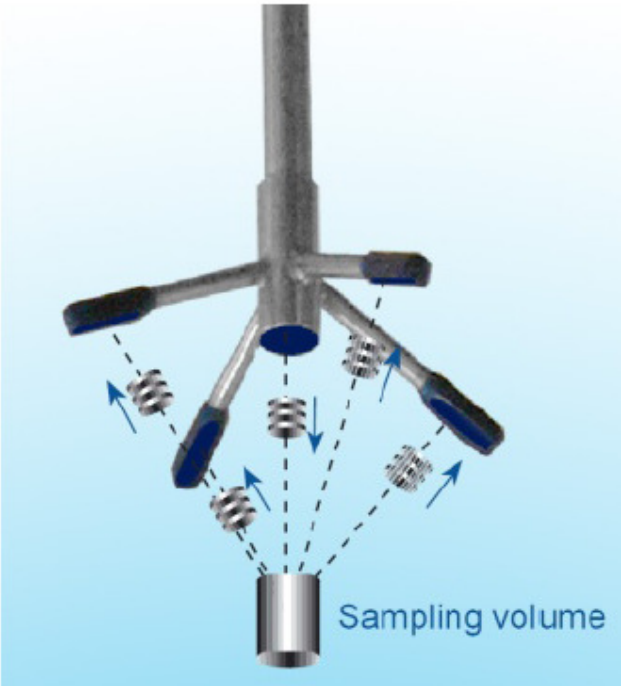

Figure 12 Operating principle (Nortek AS, 2004)

Figure 12 shows how the beams intersect each other 50 mm from the transmitter. The measurement volume is defined by this intersection (Nortek AS, 2004). The transmit transducer sends a short pulse that covers 3-15 mm vertically and receivers corresponds from this volume. The diameter of the volume is 6 mm (Nortek AS, 2004). The velocity probe uses four receivers and all receivers are focused on the same volume to obtain the three velocity components from that volume. It is stated that the velocity probe is more sensitive to the z-velocity than it is to the x- or y-velocity. Figure 13 shows the transmitter taking measurement from a flowing fluid.

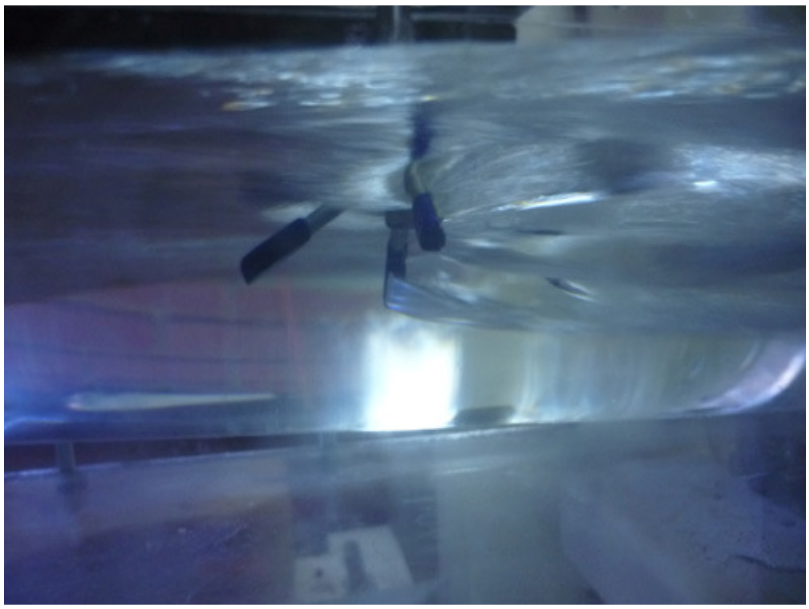

Figure 13 Photograph of velocity probe in the fluid

4.3.3.3 Velocity uncertainty

The velocity is an average of many velocity estimates. The uncertainty of each estimate is dominated by the short term error. The short-term error of a single estimate depends on the size of the transmit pulse and the measurement volume. It also depends on the beam geometry. From the user manual, it was stated that the error in the velocimeter is typically a fraction of 1 cm/s (Nortek AS, 2004).

4.3.4 Calibration of the test flume

Water was used as calibration for the loop. It was pumped through a straight measurement section containing a calibrated orifice plate and diffuser, and into a settling chamber containing filter material and a honeycomb. The fluid passed through a 4:1 contraction and a working section of the flume. Velocities were measured at specific points in order to avoid exit effect in the flume.

Velocity range was set to cover the range of the velocities anticipated during the data collection. It was said that a higher velocity range would give more noise in the data and vice versa. However, it was unknown that which velocity range is suitable in this experiment. Therefore, majority of the velocity ranges were tested in this experiment. For this probe, the

presence of a boundary close to the probe sampling volume may give rise to problems; especially when the boundary is hard (rocks, concrete, glass, etc).

From initial testing, it was discovered that for each velocity range, there are one or two distances that give rise to problems. The existence of these 'weak spots' can be identified in the data record by a decrease in the correlation and an increase in the velocity variance. The problem is mostly seen in flumes with a hard bottom but has also been observed in the field (Nortek AS, 2004), especially at the higher velocity ranges.

Table 3 Vectrino weak spots

Range	**Weak spots**
4 m/s	2 cm and 5 cm
2.5 m/s	3 cm and 10 cm
1 m/s	5 cm and 12 cm
0.3 m/s	10 cm and 23 cm
0.1 m/s	23 cm and 45 cm
0.03 m/s	38 cm and 75 cm

These weak spots are related to the spatial separation between the pulse pairs transmitted by the velocimeter. The weak spot usually occurs when the first pulse hits the bottom as the second pulse goes through the sampling volume.

Moreover, transmit length is also another variable in the velocimeter. The effect of increasing the transmit pulse length is that the signal-to-noise ratio is increased. It is said that as sampling volume decreases and/or get closer to boundaries, the transmit length needs to be reduced as well. However, the optimal combination of nominal velocity range and transmit length is not concluded previously.

Seeding particles also need to be added in water flow experiment as sound does not reflect from water. These particles move with the same average speed as water. Therefore the velocity that is measured is consequently the velocity of water. In this case, particles made up by Borosilicate glass (< 1 gram) were added as seeding particles. The mean particle size was around 8-13 μm, with density equals to 1000 kg/m^3.

The velocity –depth profiles presented in Figure 14 to Figure 17 show the axial velocity at 18.75 l/s of water flow, at a maximum depth of 154 mm. Due to the velocity probe's limitation, velocity probe's transmitter position needs to be at least 50 mm from the bottom of the flume. All the measurements were taken from the middle of the flow. NV stands for nominal velocity range (m/s) and TL stands for transmit length (cm).

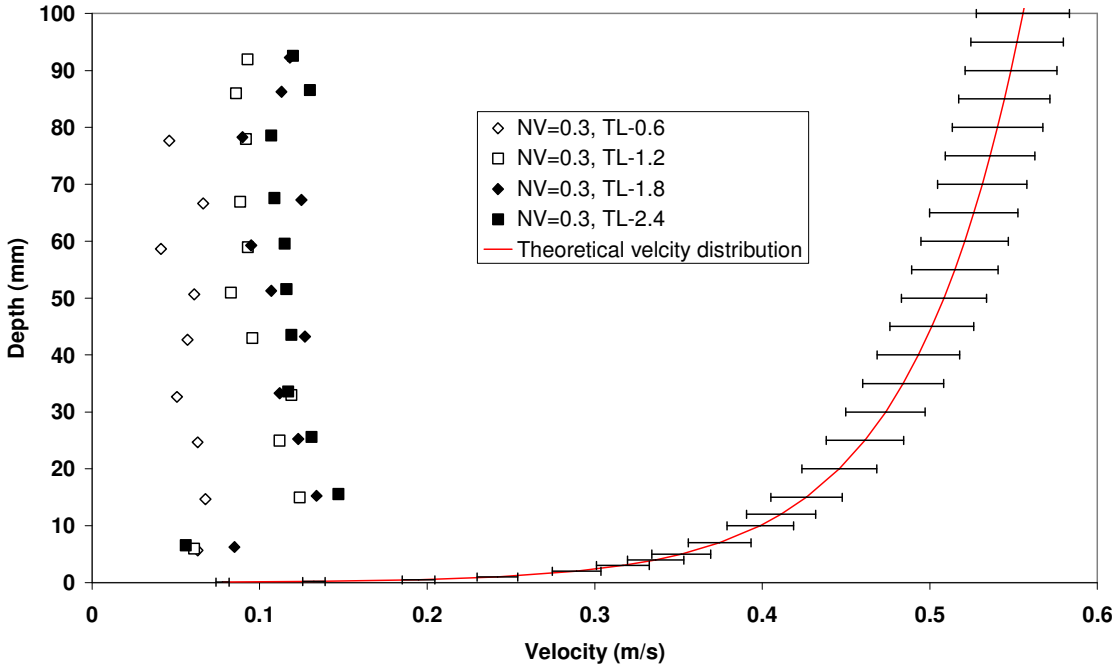

Figure 14 Axial velocity profile for nominal velocity range = 0.3 m/s and different transmit lengths

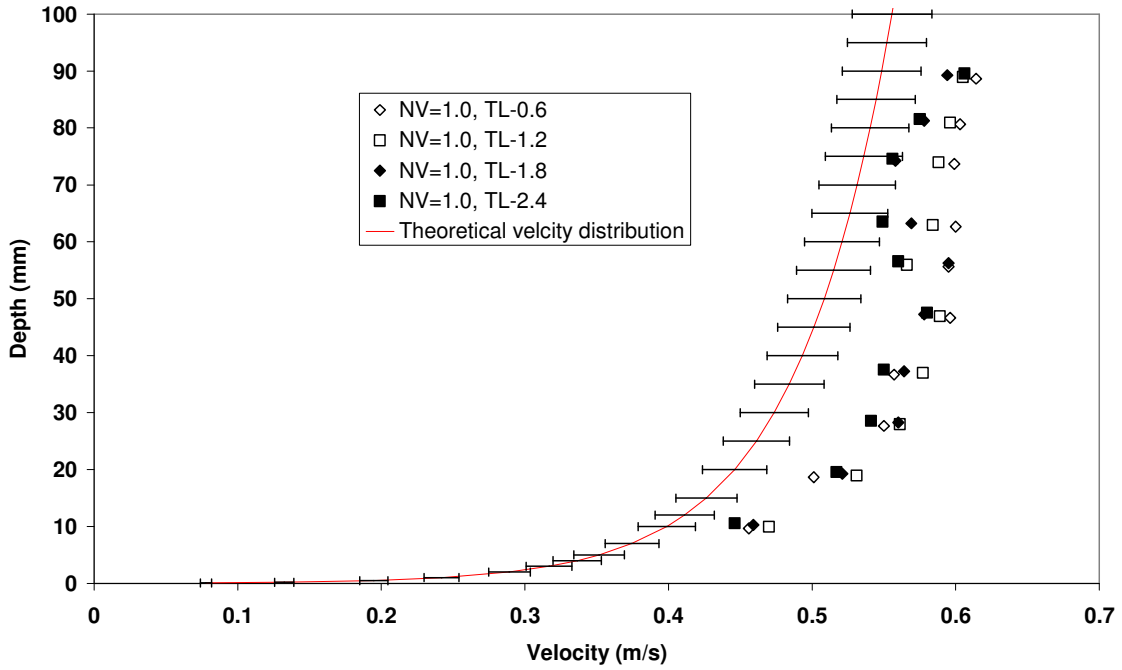

Figure 15 Axial velocity profile for nominal velocity range = 1.0 m/s and different transmit lengths

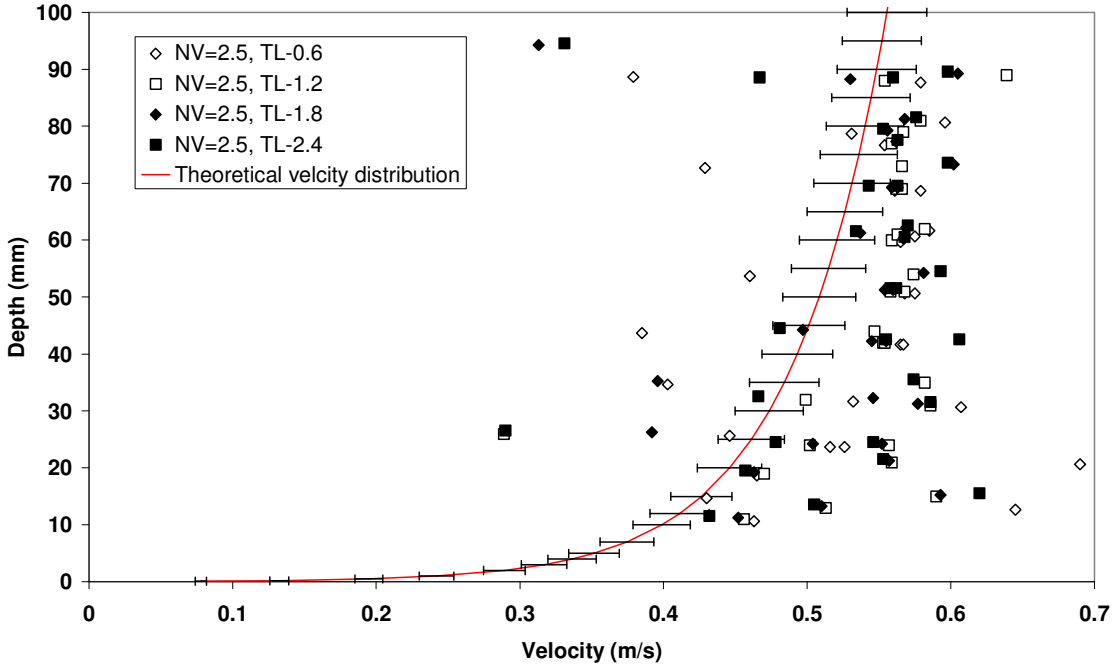

Figure 16 Axial velocity profile for nominal velocity range = 2.5 m/s and different transmit lengths

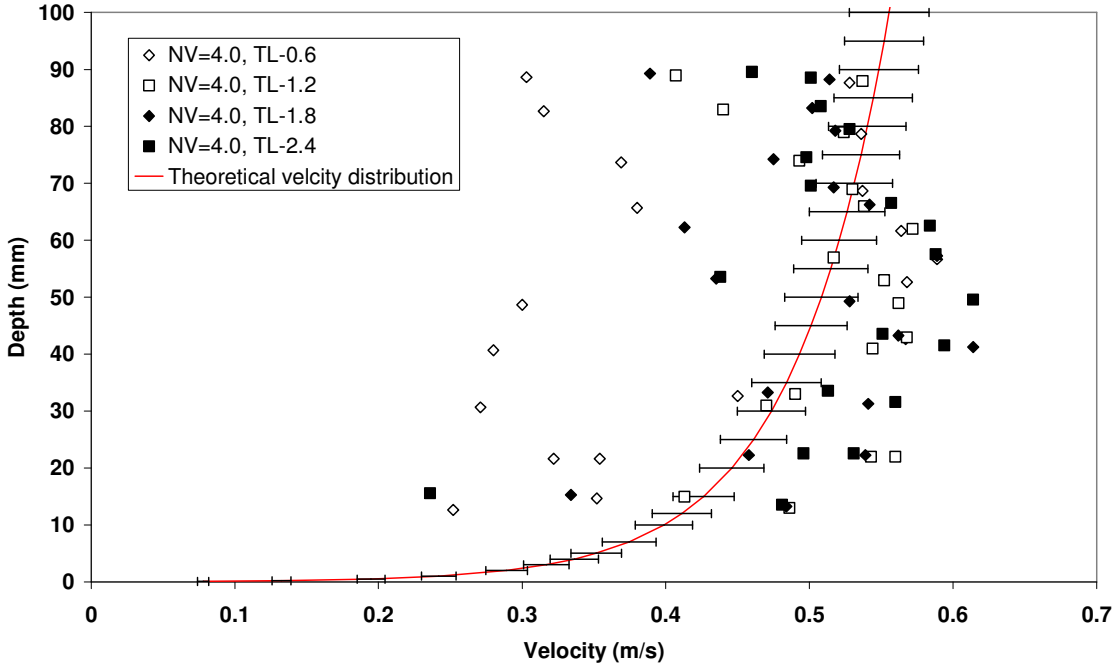

Figure 17 Axial velocity profile for nominal velocity range = 4.0 m/s and different transmit lengths

The theoretical velocity curve was calculated by the velocity distribution equation in equation (30). Figure 14 shows that with a nominal velocity of 0.3 m/s, none of the transmit lengths would work on the current flow conditions. The actual average velocity was around 0.5-0.6 m/s. It is very surprising that a nominal velocity range of 0.3 m/s is not suitable for this experiment. In Figure 15, the measured velocity profile is slightly higher than the theoretical velocity profile. However, all the data points are aligned in a similar way to the theoretical velocity profile. All four different transmit lengths gave similar velocity readings. In Figure 16, the measurements are somewhat scattered. When transmit length is set to 0.6 mm, the data points look more scattered. For transmit lengths 1.2 mm, 1.8 mm and 2.4 mm, the data points are closer to the theoretical velocity profile. It also shows that the axial velocity in the flume decreases with depth. Similarly in Figure 17, transmit length of 0.6 mm does not give a good indication of the velocity distribution. On the other hand, for the other transmit lengths, the measurements show that the maximum velocity in this flume occurs below the water surface.

Overall, the best nominal velocity range and the transmit lengths combinations are: Nominal velocity range = 2.5 m/s with transmit lengths = 1.2 mm and 1.8 mm. This is shown in Figure 18.

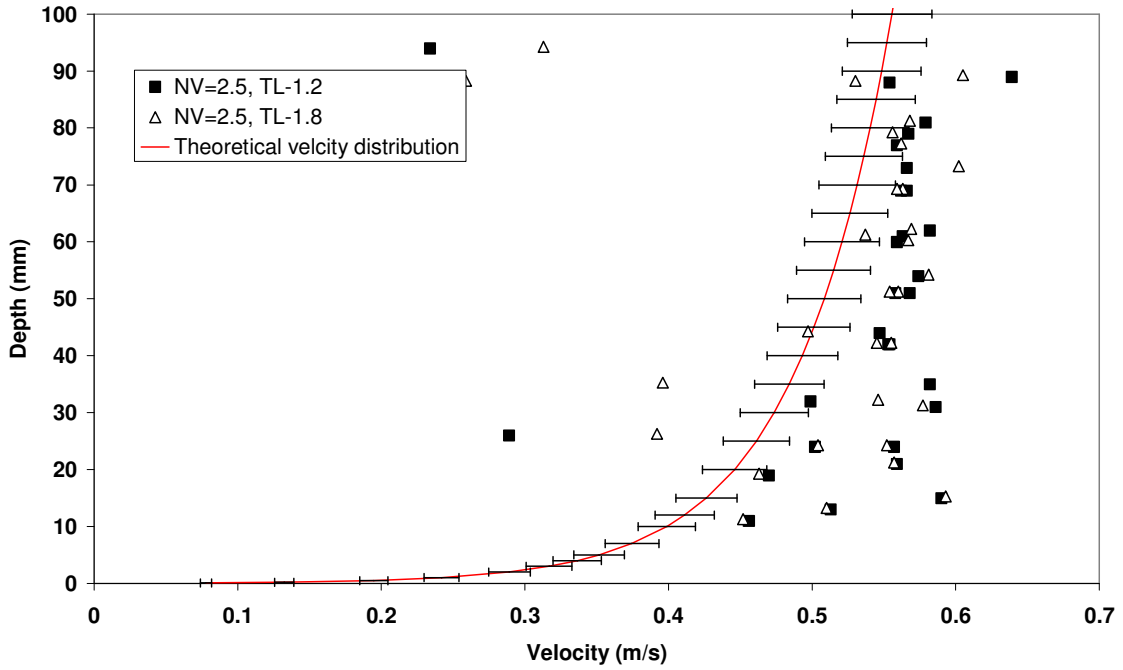

Figure 18 Axial velocity profile for nominal velocity range = 2.5 m/s and different transmit lengths = 1.2 mm and 1.8 mm

It would be useful if the maximum velocity in this investigation can be validated. Therefore Chiu and Tung (2002)'s method is used here for validation. The equation for predicting the maximum velocity that occurs below the surface is:

$$u_D = \frac{u_{\max}}{M} \ln\left[1 + \left(e^M - 1\right)\frac{1}{1-\frac{h}{D}} \exp\left(1 - \frac{1}{1-\frac{h}{D}}\right)\right] \quad \textbf{(59)}$$

Where M is parameter of velocity distribution equation. It can be calculated by

$$\frac{h}{D} = -0.2\ln\frac{fn(M)}{58.3} \quad \textbf{(60)}$$

The results of prediction of maximum velocity below water surface for nominal velocity range of 4.0 m/s is shown in Table 4.

Table 4 Comparison between actual velocity and calculated velocity

Transmit length (mm)	Actual velocity measurement (m/s)	Calculated velocity (m/s) (Chiu and Tung 2002)
1.2	0.486	0.553
1.8	0.484	0.568
2.4	0.481	0.581

It is seen from the table that the calculated maximum velocity below water surface is higher than the measured velocity. One possible reason for this is that particles other than seeding particles were detected by the receiver. Before the commission of the experiment, the whole set up was unused for number of years. Therefore there was a large amount of dirt stuck on the honeycomb structure. It was not viable to take the honeycomb structure out and there was no way to completely clean it within the limited time. These foreign matters not only caused the fluids to get discoloured, but also disturbed the signals from acoustic velocity probe. The dirt was mainly deposited in the honeycomb structure in the settling chamber. With a low volumetric flow rate, the dirt did not detach from the honeycomb. However, with a high volumetric flow rate at around 20 l/s, dirt and large particles were flushed out by the strong force and were floating into the system. This might have caused some inevitable error to the velocity measurements. Figure 19 shows considerable amount of dirt located in the upstream end of the flume. When the flow rate increased, some of the dirt would get suspended and transported itself through the channel. Such action would have caused large velocity uncertainties when measured by the velocimeter.

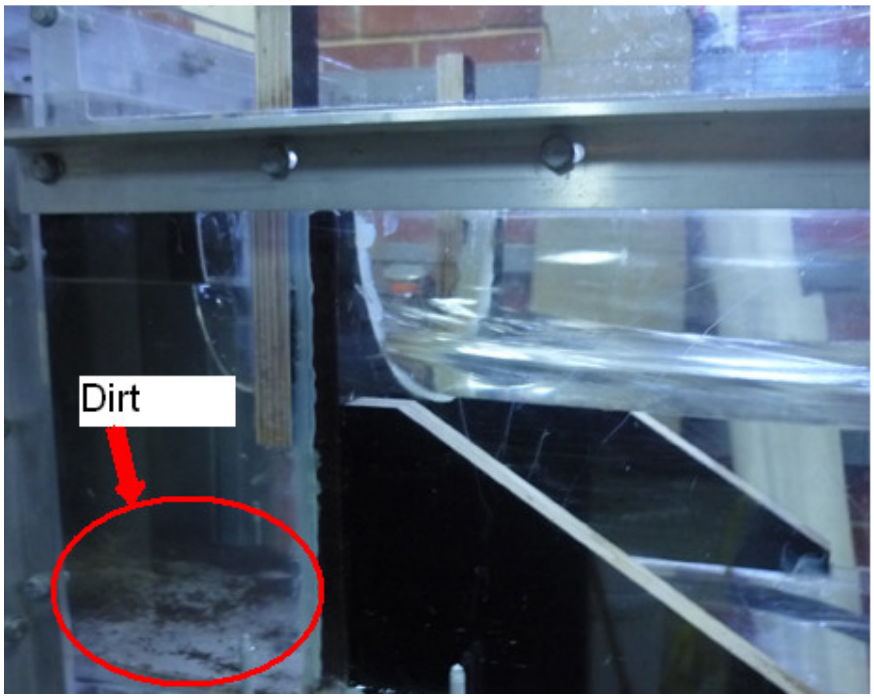

Figure 19 Photograph of dirt in the flume

The velocities presented here are time averaged points. These were measured over a minute period at the rate of 200 Hz. This is extremely important as the measured instantaneous velocities fluctuate as a result of the turbulence in the channel. An example of this can be seen in Figure 20.

In conclusion, Vectrino velocity probe can be used in measuring velocity in this particular set up. From water measurements, it is recommended that the following nominal velocity range should be used: 1.0 m/s, 2.5 m/s and 4.0 m/s. For transmit length, the following should be used: 1.2 mm, 1.8 mm, and 2.4 mm.

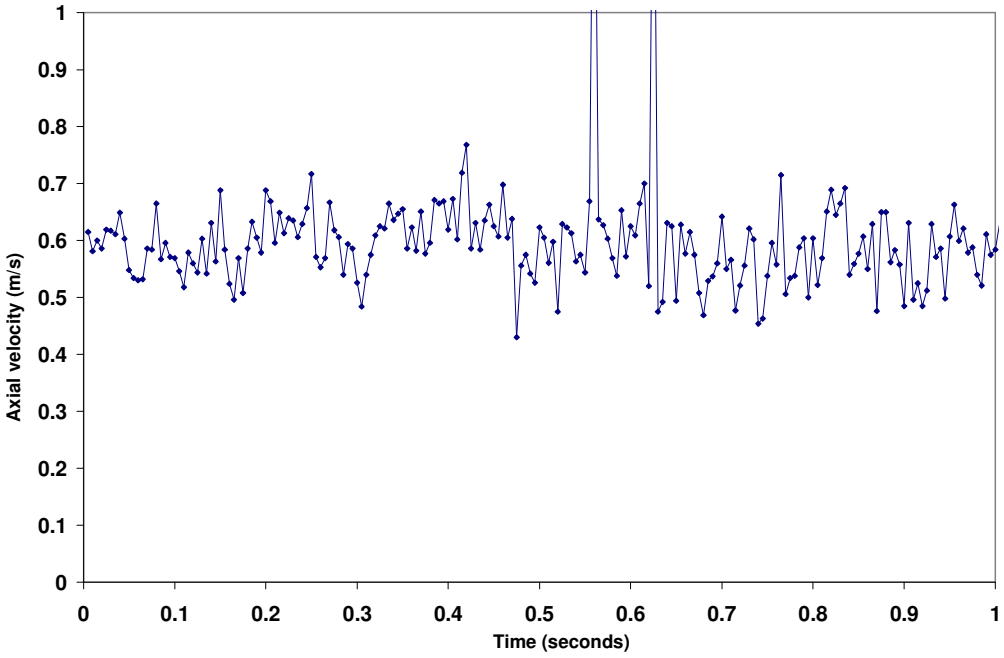

Figure 20 Raw axial velocity data at a rate of 200Hz

4.3.5 Channel for the flume

One semi-circular acrylic channel of 198 mm internal diameter was constructed by cutting a commercial pipe lengthwise in two halves. The semi-circular channel was inserted into the original square flume. The channel was then supported by three supports to prevent it from bending. Figure 21 and Figure 22 show the upstream end of the semi-circular insert. The insert was glued on the black shaped supporting structure by silicone gel. Therefore when fluid came out from the contraction, it would flow into the semi-circular insert instead of the original rectangular flume.

The bottom end of the insert however was not fixed to the square flume. Figure 23 shows a gap between the support and the bottom of the flume; hence blocks of wood could be inserted in order to change the slope. The gap was needed for adjusting the slope of the semi-circular channel. The calibration of the slope of the channel was achieved with the use of an automatic level.

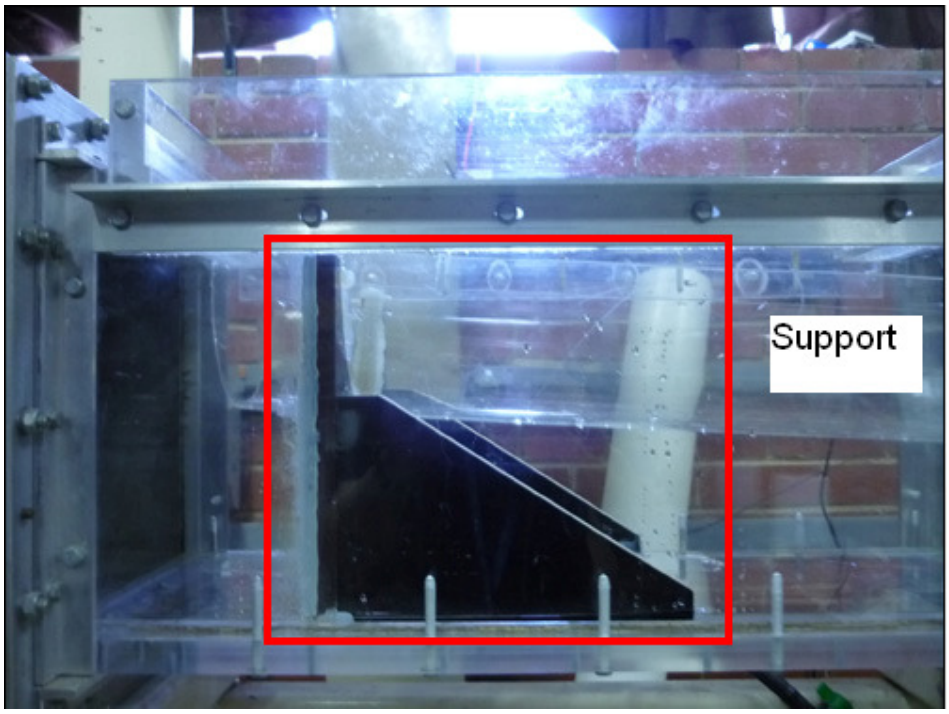

Figure 21 Photo of top stream end of the semi-circular insert

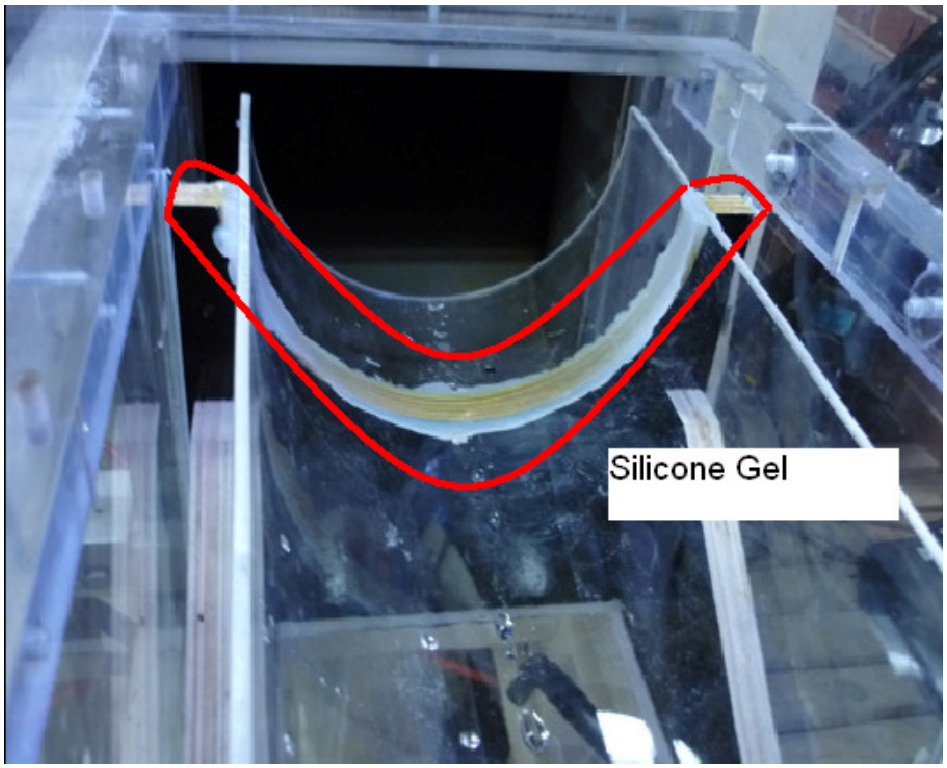

Figure 22 Photo of top stream end of the semi-circular insert 2

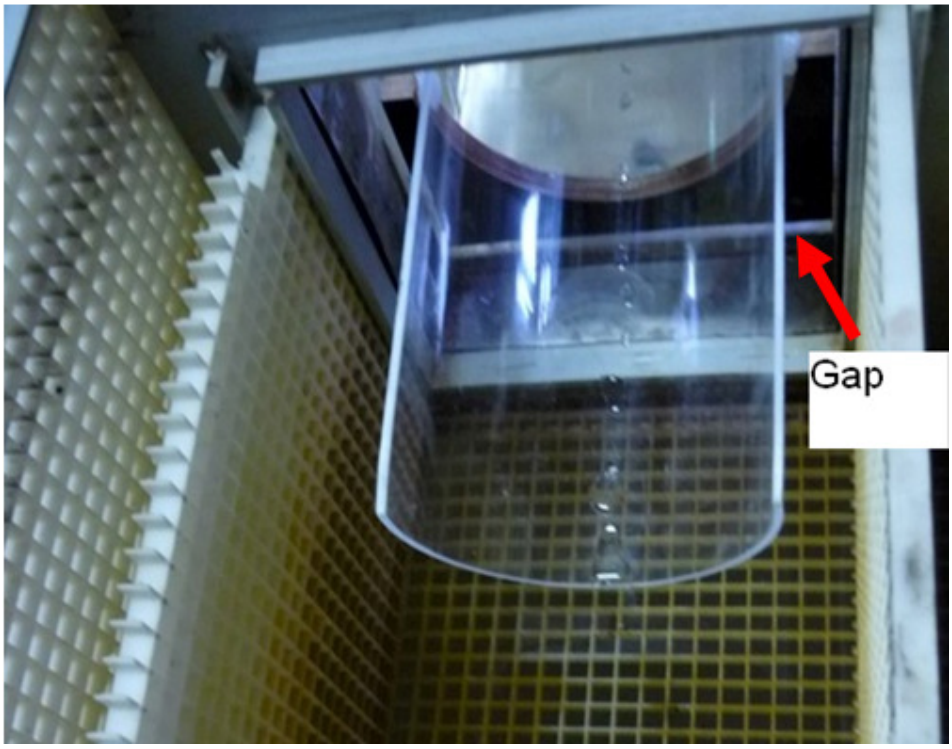

Figure 23 Photo of downstream end of the semi-circular insert

4.3.6 Test fluid

The actual test fluid consisted of a clear solution of carboxymethylcellulose sodium salt (CMC) (D.S. 0.9). The concentrations used were between 0.01% and 0.015% by weight. The fluid exhibited shear-thinning characteristics. Shear thinning behaviour means that the viscosity of the fluid reduces as shear rate increases. Slow viscosity degradation was observed as temperature increased (Cancela *et al,* 2005). It was also expected that the shearing experienced by the circulation of the fluid in the flume might cause a change in rheological parameters. Therefore samples were taken every hour and rheological measurements were conducted for each sample.

Preparation of CMC test fluid

1. Transfer known amount of water into the mixing tank
2. Set up mechanical stirrer, power on the stirrer
3. Pour known amount of sample slowly into the mixing tank

4. Wait till the solution has fully dissolved (this may take more than 24 hours)

Water was used for calibration purposes. Large volumes of tap water were used, but that was the only option.

4.3.7 Fluid Temperature

The temperature was also monitored to ensure that the experimental temperature was maintained within $20^{o}C \pm 1^{o}C$. This was measured by the Vectrino velocimeter. The velocimeter was directly linked to the computer that read the temperature in degrees Celsius. As the computer read the thermocouple directly, no signal calibration was required. The accuracy of the thermocouple is in the order of 0.1 degree Celsius. Most of the non-Newtonian fluid tests were done during autumn months. The fluid temperature during the tests varied from 15-20 degrees Celsius. Generally speaking, temperature increases rapidly only with outside weather as most of the pipe fittings are located outside of the lab. The pump did not heat up the fluid significantly. If the temperature increased to higher than $20^{o}C$ during the experiment, the pipe loop was then shut down in order to maintain a stable temperature.

4.3.8 Local velocity measurement

Velocities were measured at specific points within the flume. From previous sections, the limitation of the probe was discovered investigating water flow. The velocity probe senses fluid motion in a region reaching out about 50 mm from the receivers. It was also found that the angle and width of the receiver head of the probe prevented velocity measurements from being taken within 20 mm of the boundaries of the half pipe.

4.3.9 Local depth measurement

Depth measurements were made using a ruler. It was used to measure the distance from the fluid surface to fixed points above the fluid surface. The offset distances to the flume bed from the fixed points were recorded in order to calculate the true depth. This method enabled the measurements to be made without immersing the ruler into the testing fluid. Figure 24 shows an illustration of a ruler taking measurement by above method.

Another ruler was glued to the side of the channel to measure the depth of the velocity probe. This measurement was later compared to the automatic depth measurement by Vectrino software.

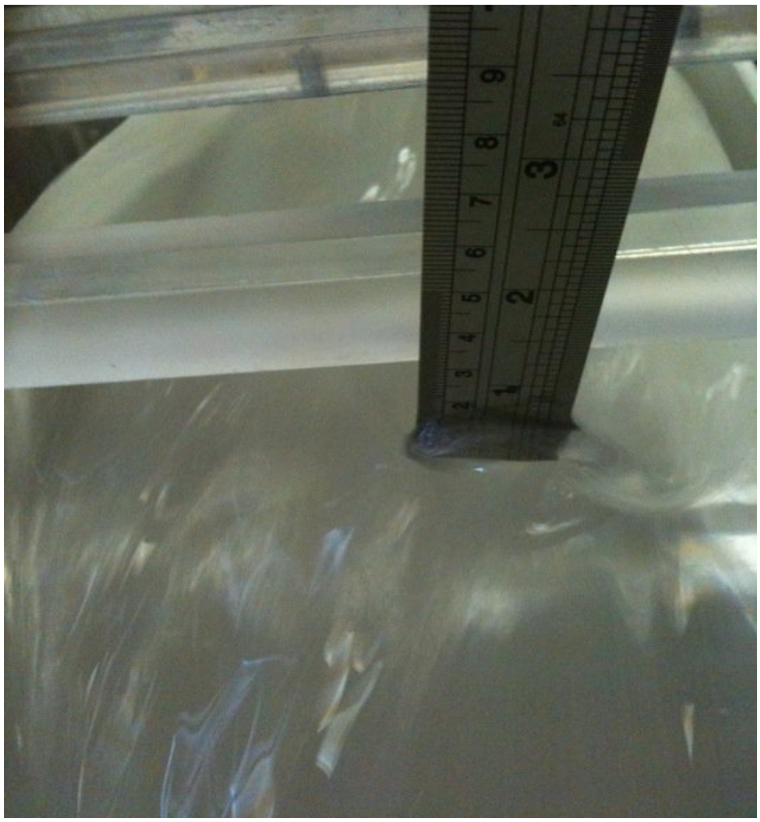

Figure 24 A depth measurement

4.3.10 Experimental procedure

A certain volume of fluid was pumped into the reservoir tank. The pump was then run at different speed settings. Six different measurements were recorded for each run:

- Volumetric flow rate
- Position of the velocity probe
- Temperature of the fluid
- Slope of the flume
- Depth of the fluid
- Velocity

With the pump running at a very high speed, the volumetric flow rate could reach 30 l/s. However, with a high flow rate, the fluid from the upstream would have splashed out of the

flume into the surroundings. This would cause a significant amount of surface disturbance. The maximum flow rate was kept used is less than 19 l/s in order to eliminate any obvious surface disturbance.

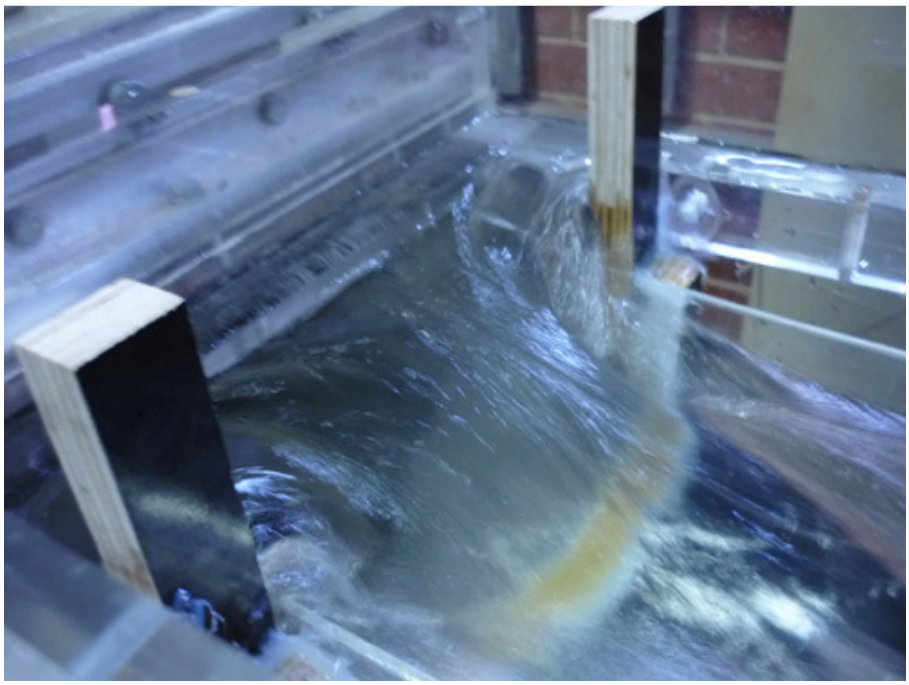

Figure 25 Photograph of flume entrance

4.3.11 Rheological analysis

Rheology test was performed on samples of the testing fluid to determine the fluid behaviour. A rheological model was then fitted for further use in the analysis of the fluid flow in relation to velocity distributions.

Rheological analysis for the testing fluid was done using the Rheosys Merlin II rheometer with cup and bob measurement system. This instrument is classed as a Couette rheometer (or concentric cylinder rheometer). It means that it shears a fluid sample in the annular space that is formed between a cup and a cylindrical bob that is inserted into the cup and rotated about the vertical axis. In this case, the bob has a vertical length of 36 mm and a diameter of 25 mm. The shear rates applied to the fluid ranged from 2 to 800 l/s. The testing fluid was kept at a temperature of 20^{o}C.

The rheological testing done on the testing fluid has been presented in the standard shear rate vs shear stress plots in Figure 26. The first four digits from the legend mean sample collection date. The last four digits mean the collection time. This rheogram shows that CMC exhibits shear thinning behaviour. It is interesting to see that the rheological behaviour of the fluid from the same day is similar in different time intervals. It was suspected that the rheological behaviour would vary because of the constant shearing of the fluid in the flume and pump.

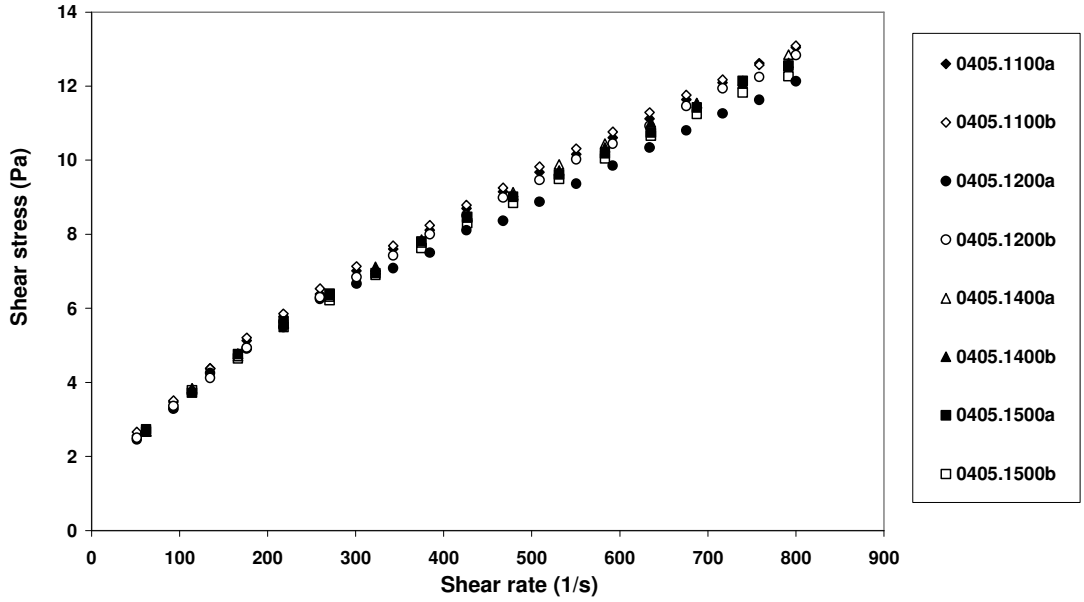

Figure 26 Rheogram for different samples on the same day

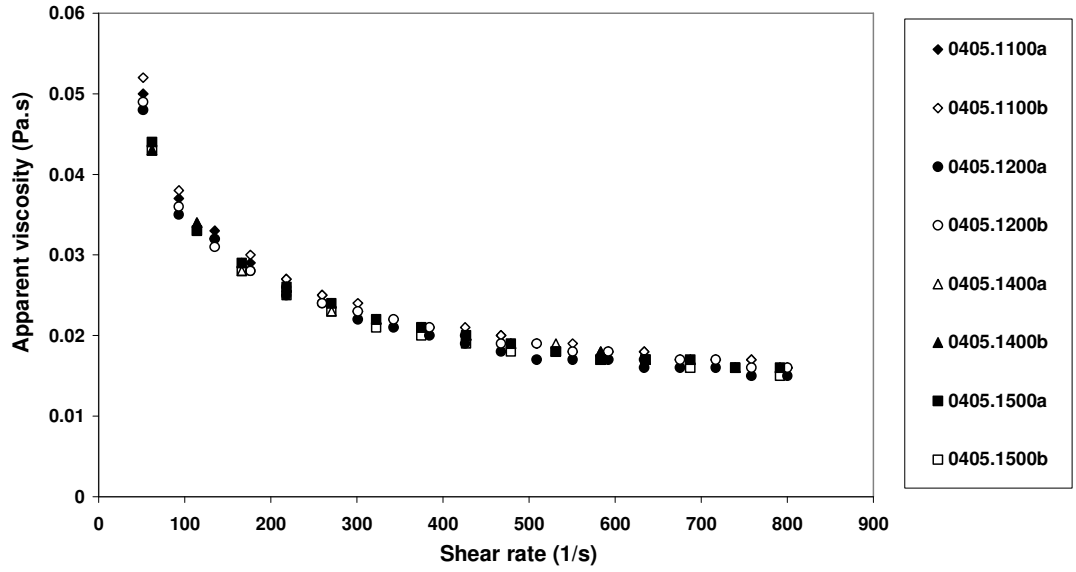

Figure 27 Apparent viscosity against shear rate for fluid tested on one day

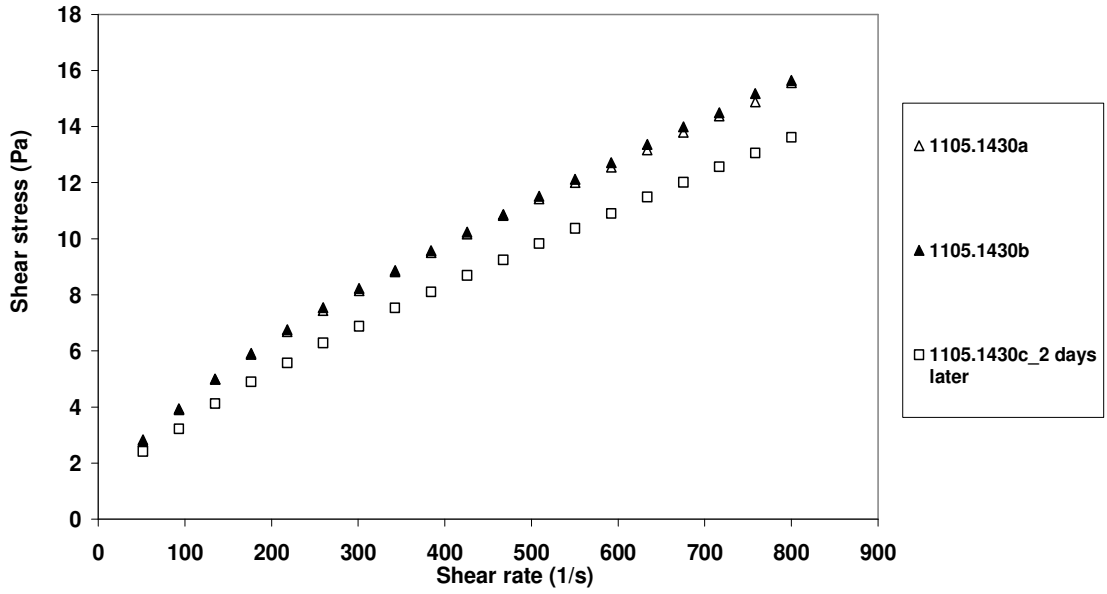

Figure 28 Rheogram for different samples on the same day but tested on a later date

4.3.11.1 Rheological modelling

Rheological parameters are used as inputs for semtex code. In this case, a power law model is applied to the rheology data measured for the testing fluid. Some introduction of the model can be found in Chapter 2. In this case, the power law rheological model was applied to the rheology data measured for the fluid.

Note that the concentration of the fluid was not important in this experiment. In the computational code, only the flow behaviour index and flow consistency index were used. Fitton (2007) used experimental data to calculate the effective shear rate region in open channel flows. The shear rate was found to by typically between 40/s and 140/s. This shows that the shear rate range used in the rheological measurement was adequate.

4.3.11.2 Power law model fit

CMC is often modelled as a power law fluid. This model suits a fluid without yield stress that exhibits non-linear behaviour. This was implied by the linear relationship shown in the log-log plot in Figure 29. The equation for the power law model is presented in equation (1). Where τ is the shear stress (Pa), K is the power law consistency index (Pa.S^n), n is a power and $\dot{\gamma}$ is shear rate applied to the fluid (1/s). Table 5 shows the summarised power law parameters for the non-Newtonian fluids tested in the Highett loop. The first half of the fluid ID means the date and month of the collection, the second half of the ID means the collection time.

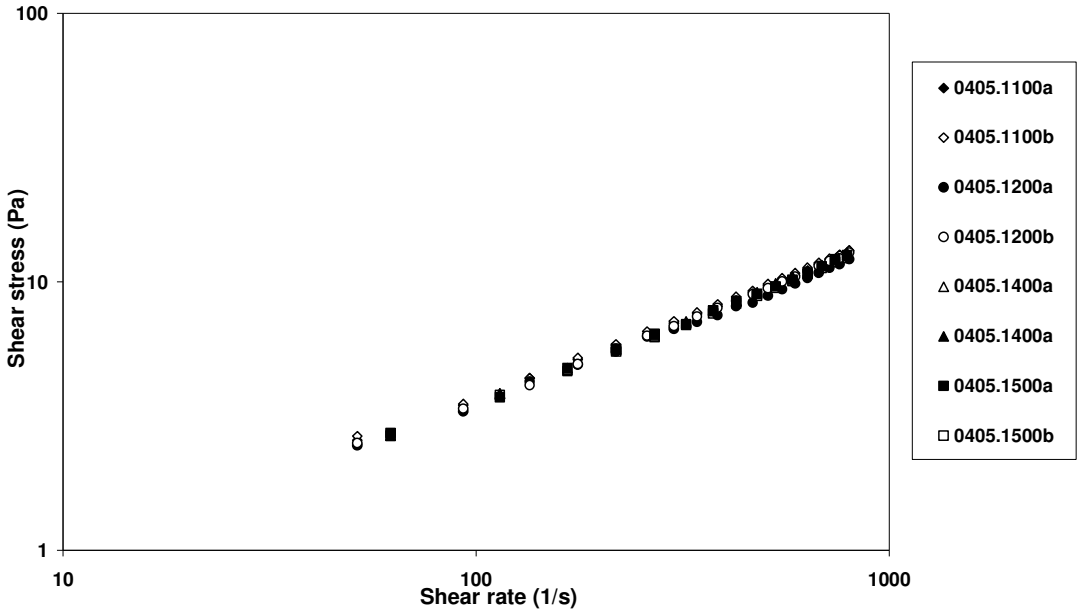

Figure 29 Rheology of CMC in log-log plot

Table 5 Power law parameters for the non-Newtonian fluids tested

Fluid test number	*K* (Pa.S^n)	n
0405.1100 (DD/MM.time)	0.237	0.596
0405.1200	0.230	0.594
0405.1300	0.197	0.623
0405.1500	0.204	0.615
0705.1015	0.186	0.624
0705.1140	0.177	0.630
1105.1030	0.239	0.620
1105.1140	0.227	0.629
1105.1400	0.228	0.630
1405.1145	0.238	0.655
1405.1400	0.244	0.653
1405.1430	0.247	0.651
1705.1130	0.127	0.716
1705.1400	0.134	0.706

1705.1530	0.132	0.712
1805.1015	0.168	0.675
1805.1140	0.157	0.688
2405.1300	0.159	0.703
2405.1430	0.158	0.703
2805.1100	0.094	0.758
2805.1230	0.256	0.702
2805.1330	0.122	0.713

4.4 Second phase

The objective for this smaller scale flume experiments was to check the particle behaviour in analogue non-Newtonian slurries by measuring the equilibrium slope. Winterwerp *et al* (1990) referred to a critical slope of the channel as the "equilibrium slope" where the slope is sufficiently steep to enable the transportation of all of the slurry particles. If the slope is lower than the equilibrium slope, it means that one or more particles will deposit in the flume. This experiment allows the observation of the particle behaviour in the transparent pipe. Each equilibrium slope with different flow rate will be recorded. This will produce some qualitative results for particle transportation.

4.4.1 Test flume

The pipe was 4 metres in length and had 50 mm internal diameter. The pipe was made of transparent glass thus it was possible to observe the flow behaviour qualitatively. A U-bend fitting was fitted on the upstream end of the glass pipe. The flume set up could be tilted to slopes between horizontal to 6^{o}. The holding tank had a capacity of 40 litres and was fitted with an electrically driven mixer that ran continuously during the tests. A progressive cavity pump was used to pump the fluid mixture through the pipe loop. The flow capacity of the pump was between 2 and 32 litres per minute.

Flow measurement and density measurement were made by a Micro motion F050 Mass and Volume flow and density sensor coriolis meter. The coriolis meter was located downstream of the pump. A schematic diagram of the set up is presented in Figure 30. Several other

photographs of the apparatus appear in Figure 31 to Figure 34. Figure 32 shows the flume entrance at the upstream end. Figure 33 shows the 40 litre holding tank and the smaller calibration tank. Figure 34 shows the inclinometer used to measure the angle of slope with respect gravity.

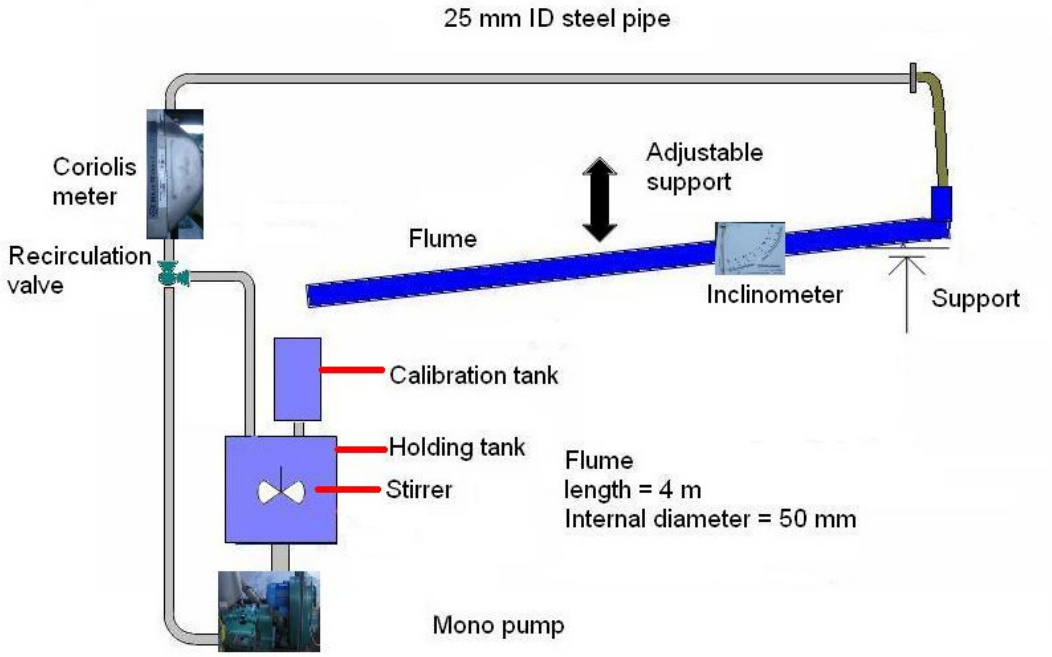

Figure 30 Diagram for small scale flume

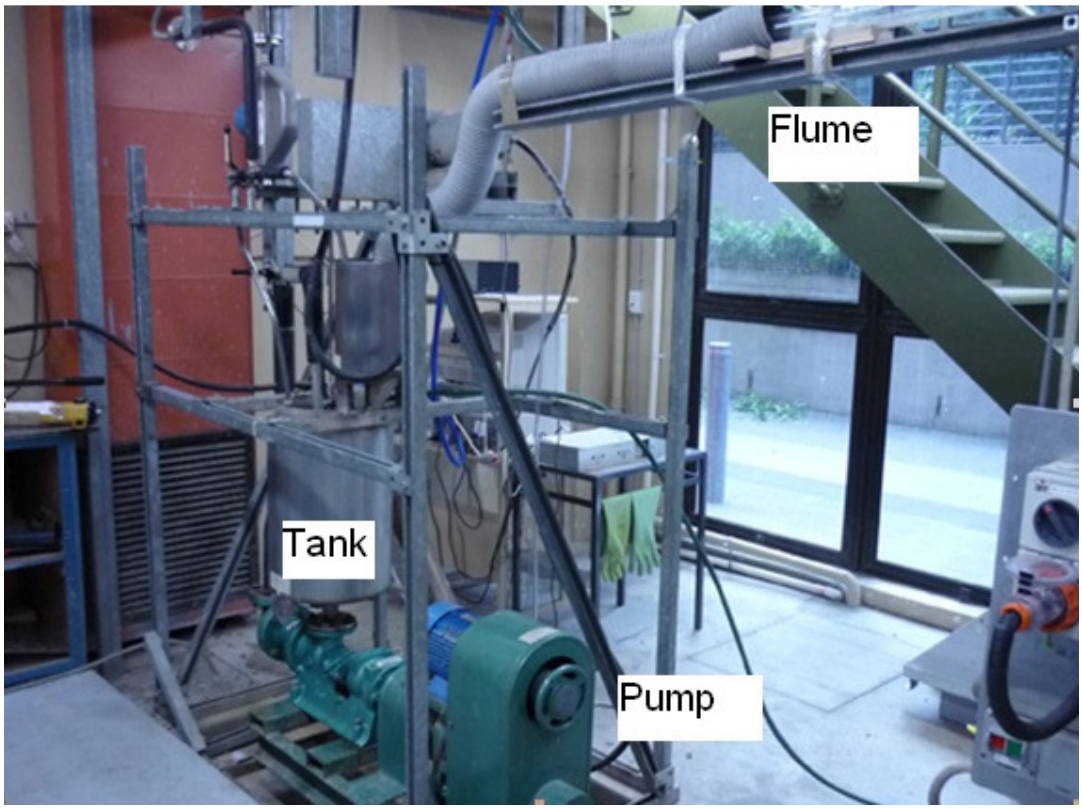

Figure 31 Small scale flume, downstream end

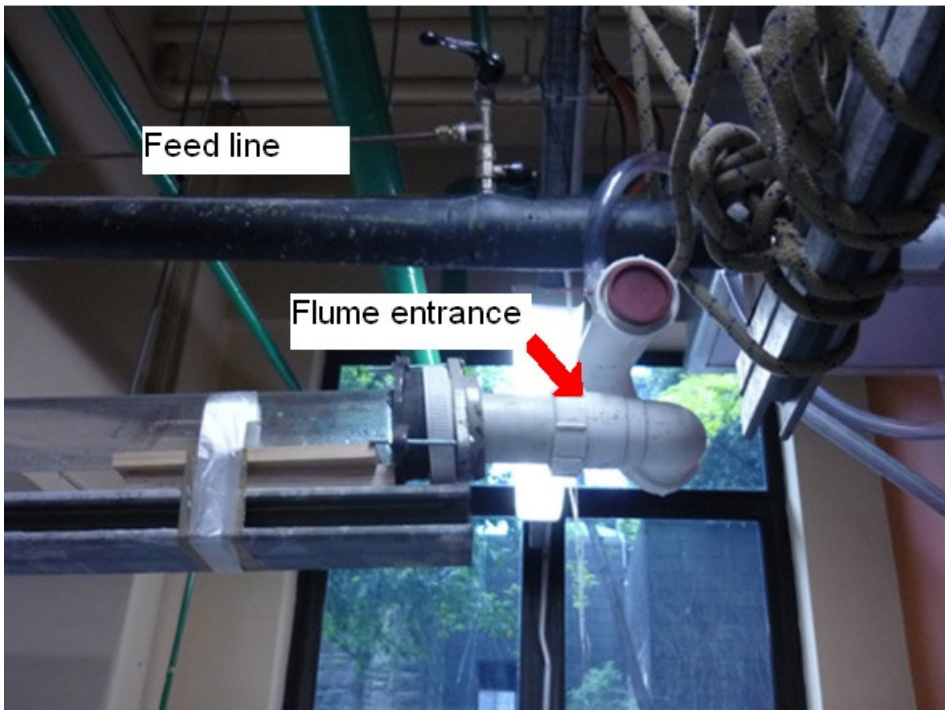

Figure 32 Photograph of flume entrance, taken from the upstream end

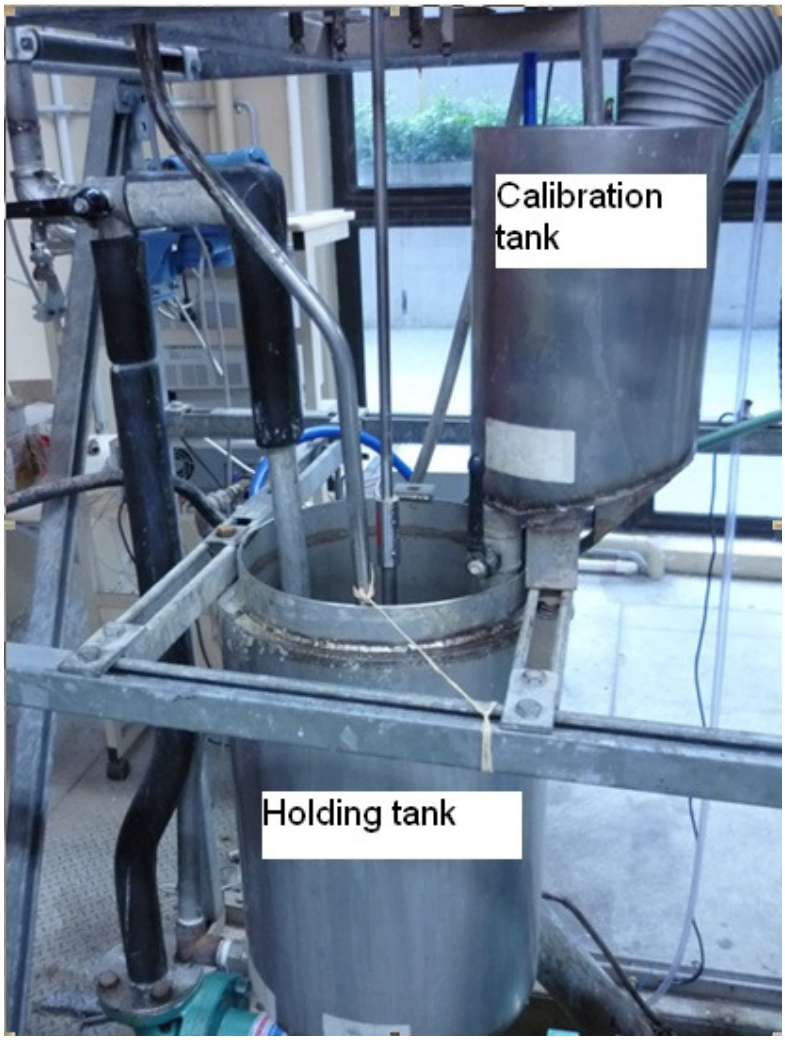

Figure 33 Photograph of calibration tank and holding tank

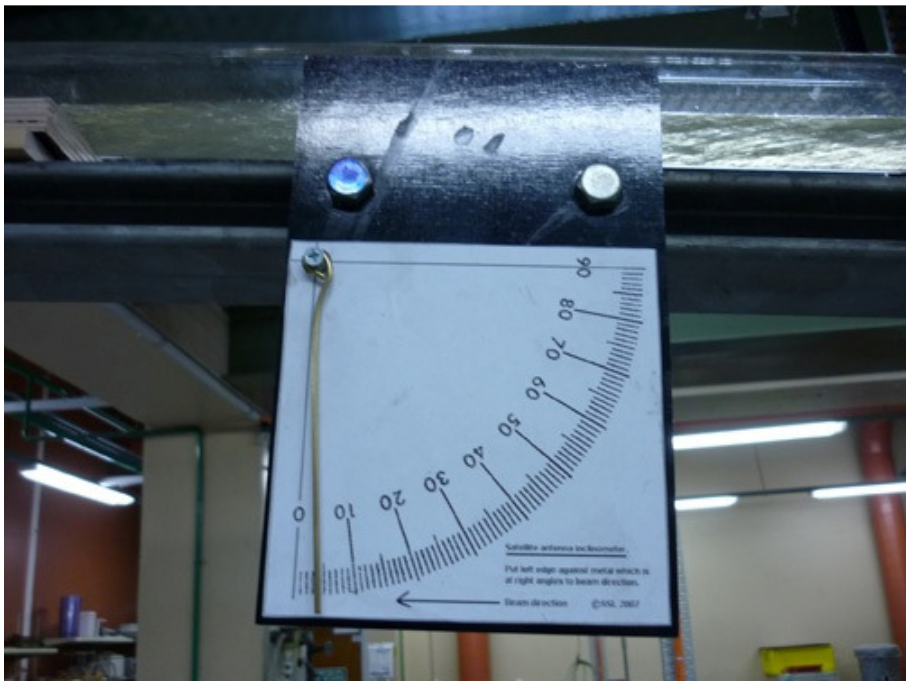

Figure 34 Photograph of inclinometer

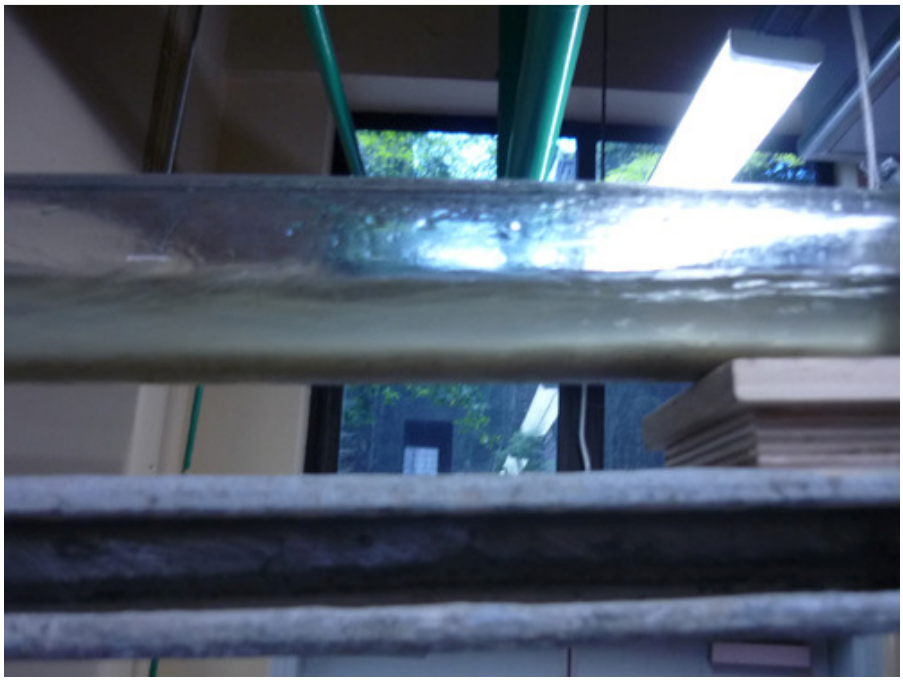

Figure 35 Photograph taken from side of the flume. Note: bed formed on the bottom of the pipe

4.4.2 Test fluid

The test fluid consisted of a clear solution of carboxymethylcellulose (CMC). Different concentration CMC solutions mixed with water were used in this experiment. Two different groups of sand particles (coarse and medium) were chosen for the experiment. Previously crushed glass particles were used for the same set up. However, it was discovered that the crushed glass particles damaged the rubber stator when the pump was running at a high speed. This allowed the introduction of foreign matter into the flume overtime. It was then confirmed other than actual foreign matters, rubber particles were also in the system because of the constant contact between rubber and glass particles. Hence, sand particles replaced the crushed glass particles in this experiment.

4.4.3 Fluid density

Fluid density ρ was calculated as follows

- Take a 100 ml beaker
- Take a fluid sample from the holding tank. This can be done by taking a few different samples from different places in the tank
- Fill the beaker with the fluid sample and weigh (A)
- Empty the beaker, clean and fill with water to the same mark, and weigh (B)
- The procedure is repeated at least three times to check the accuracy of testing
- The relative density (S_m) is defined as:

$$S_m = \frac{\rho}{\rho_w} \quad \textbf{(61)}$$

And this can also be written as:

$$S_m = \frac{MassA}{MassB} \quad \textbf{(62)}$$

From equation (61)

$$\rho_m = S_m \rho_w \quad \textbf{(63)}$$

4.4.4 Particle size analysis

Sieve analysis of the sand particles was carried out to generate a particle size distribution curve. All the sand particles went through the sieve. The coarse particles consisting of particles passing a 1000 μm sieve but caught in 850 μm sieve. The medium particles were the particles passing an 850 μm sieve but caught in 500 μm sieve. Figure 36 shows that the particle diameter (d_{50}) for the sand particles was about 560 μm.

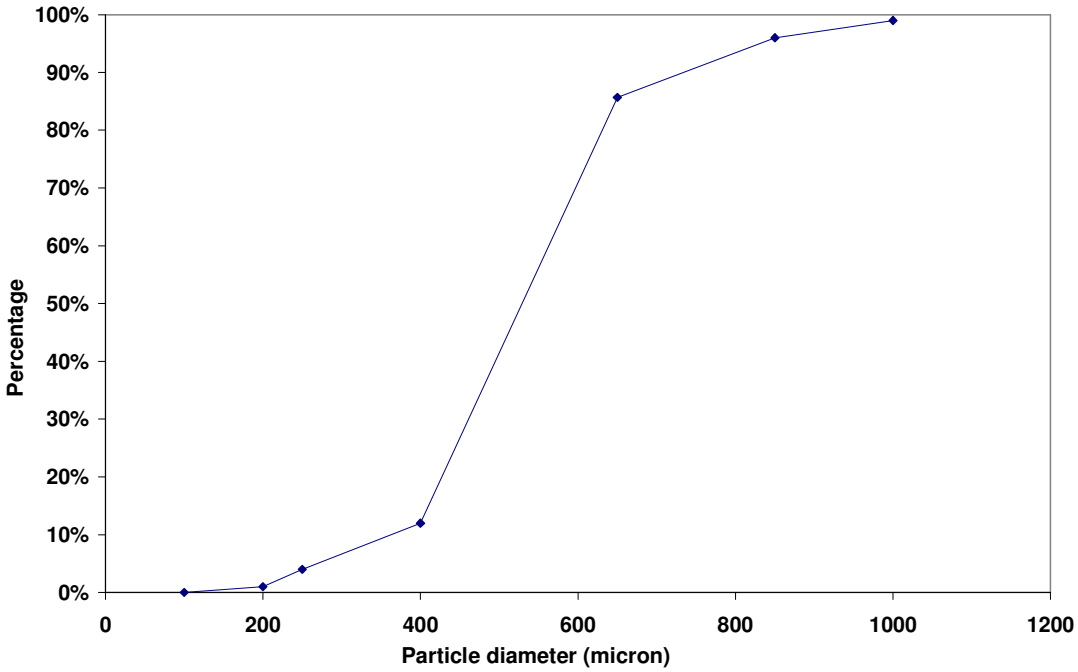

Figure 36 Particle size curve for sand particles

4.4.5 Experimental procedure

A certain volume of fluid was transferred into the holding tank. A measured quantity of sand particles was added to the fluid to create the analogue slurry. The pump was then run at a high speed setting. The recirculation valve was used to divide the flow to send part of the flow into the flume, the remainder into the holding tank. This was easier and more accurate to control the flow rate. With a lower pump speed, the pump tends to vary the speed because of small fluctuations. With a higher pump speed, the fluctuations were minimised. Therefore, it was decided to run the pump at higher speed setting to enable a more stable flow rate during the experiment. Equilibrium slope observation was then conducted through the transparent pipe.

To find an equilibrium slope, the flume was initially set at a steep slope, and then the flume was raised to yield flatter slopes. When the slope was flat enough to allow one or more stationary deposits of sand particles to form in the bottom of the pipe, then the slope was recorded as the equilibrium slope for the particular flow rate.

Four different measurements need to be recorded for each run.

- Volumetric flow rate
- Equilibrium slope of the flume
- Depth of the fluid
- Fluid sample for each equilibrium slope

The slope of the flume was measured by an inclinometer. The inclinometer was fixed to the support beam in order to measure the angle of the tilted pipe.

The depth of the flow in the glass pipe was measured from outside the glass pipe. In a previous study conducted by Fitton (2007), a mathematical expression was used to enable all the data to be corrected for refractive errors. In this current study, the same expression was also used to eliminate the errors. This expression was adopted throughout the depth measurement for determining the actual depth as a function of the apparent depth measurement from outside the pipe with a ruler. The expression is presented below:

$$ActualDepth = 0.90 \times MeasuredDepth + 1.71 \quad \textbf{(64)}$$

4.4.6 Equilibrium slope testing

Different particles and flow rates were used to measure the equilibrium slope for the small scale experiment.

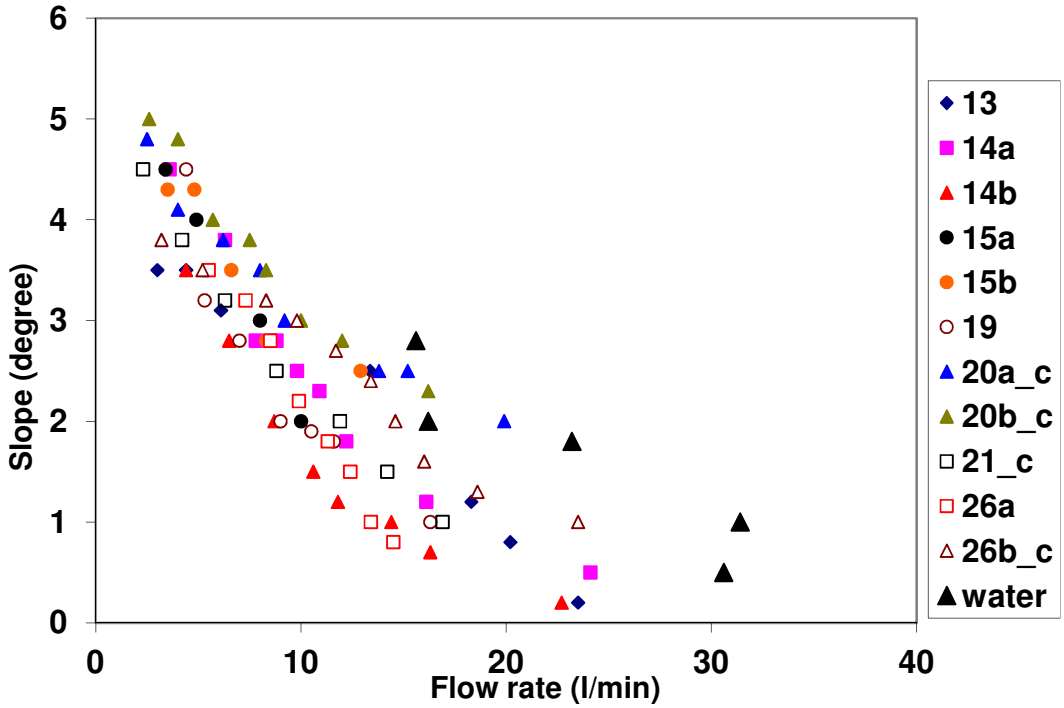

Figure 37 Plot of equilibrium slope data

Figure 37 shows the equilibrium slope for this experiment. It is very interesting to see that this graph shows some very different trend when compared to the previous experiment done by Fitton (2007). In Figure 37, the legends show the fluid name and particle size. The fluid name with a letter 'c' means coarse sand particle were used; the others were medium particles. In Figure 37, it is shown that an increased particle size produced steeper equilibrium slopes. For the data series 20a_c, 20b_c, 21_c and 26b_c, most of them are located in the upper half of the graph. This is also consistent with the finding of Durand (1953) and Wasp *et al* (1977).

In Fitton (2007) it was observed that an increased flow rate results in steeper equilibrium slopes. Interestingly, the same behaviour was not observed in this case. From Figure 37, it is shown that an increased flow rate caused flatter equilibrium slope. The reason behind the previous counter-intuitive observation is that the particles were depositing in the feed line rather than the testing glass pipe. However, such phenomenon was not observed in this set up where majority of the particles went through the glass pipe without any difficulties. It was suspected that the particle concentration for the previous study was not as high as 20%.

Moreover, the nature of the particle is also different; in Fitton (2007) glass particles were used whereas in current study sand particles were used.

4.4.7 Rheological analysis

The 11 non-Newtonian fluids used in the flume were tested in Rheosys Merlin II rheometer with bob and cup measurement system. Rheograms for the fluid 1307 is presented in Figure 38 with the rheological model curves inscribed. Error bars are presented on one of the tests of the fluid for a 95% confidence interval. 't1,t2 and t3' in the legend mean the fluid was tested for three times. It is seen from the figure that the rheological model fits well within the error limits. Figure 39 presents the same data sets as Figure 38 but on a viscosity versus shear rate plot. It is quite obvious that fluid 1307 shows shear thinning behaviour. Individual graphical fits of the rheological model curves for all the fluids are presented in Appendix. The shear rates applied to the fluid ranged from 2 to 800 1/s. The testing fluid was kept at a temperature of 18^{o}C.

Table 6 presents the rheological parameters for the 11 non-Newtonian fluids used in the experiment. *K* and *n* values are also presented.

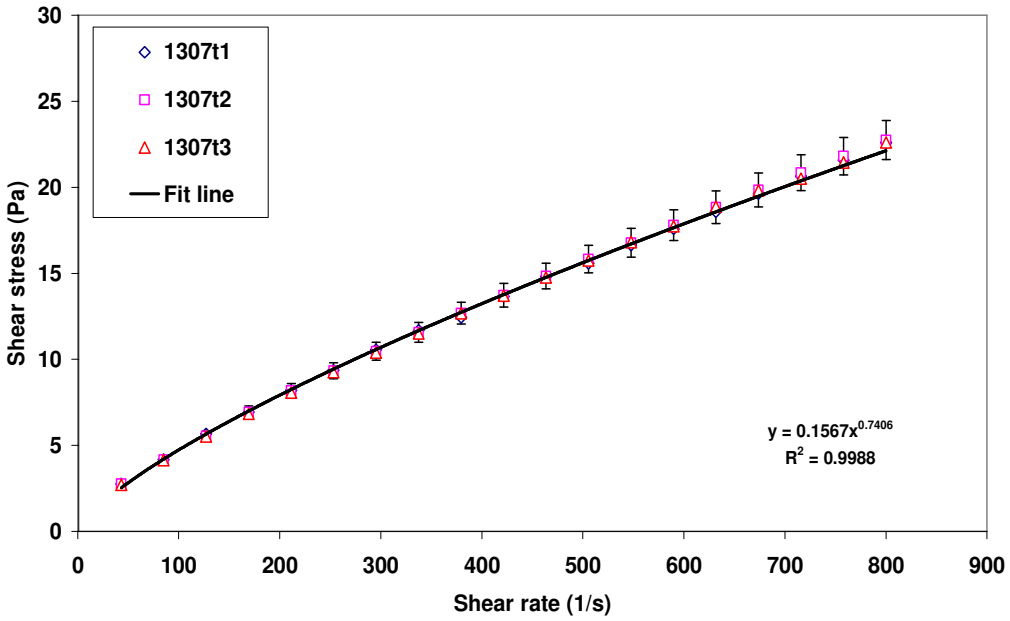

Figure 38 Rheograms for fluid 1307 with the rheological model fit curve inscribed

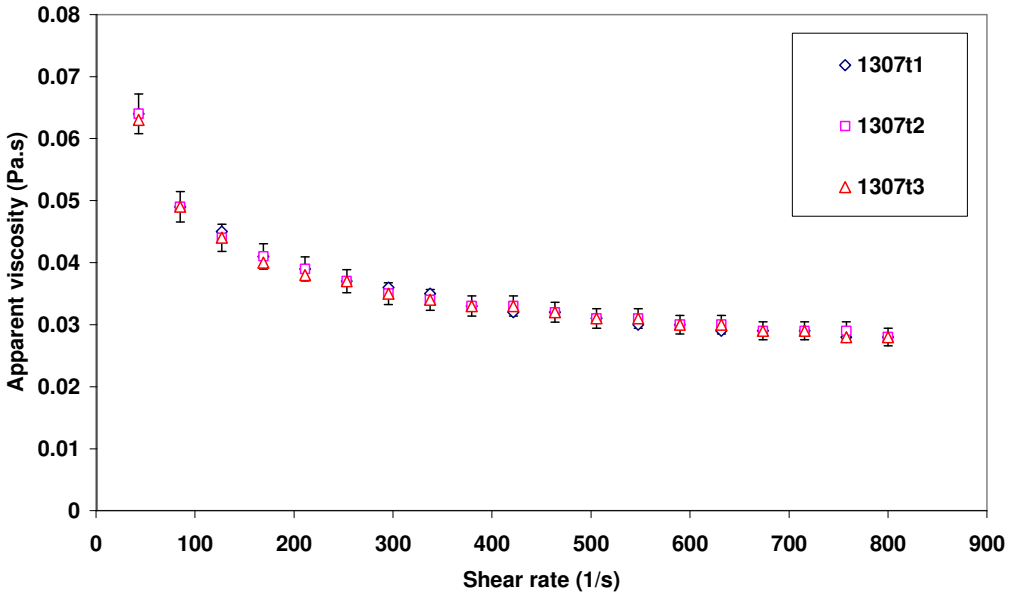

Figure 39 Apparent viscosity against shear rate of fluid tested

Table 6 Power law parameters for the non-Newtonian fluids tested

Fluid	*K* (Pa.S^n)	*n*
1307	0.156	0.741
1407a	0.113	0.78
1407b	0.11	0.749
1507a	0.141	0.885
1507b	0.131	0.851
1907	0.108	0.782
2007a	0.108	0.73
2007b	0.108	0.706
2107	0.112	0.808
2607a	0.107	0.755
2607b	0.376	0.507

4.5 Error in experimental results

Experimental errors have been analysed by two different methods. Firstly, statistical analysis of the data was undertaken to estimate the random error for different measurements. Secondly, an estimation of instrument and human errors was also undertaken for different measurements.

4.5.1 Random error analysis

Random errors arise from the fluctuations that are easily observed by multiple readings of a given measurement. There are different ways to make a reasonable estimate of the random error in a particular measurement. The best way to estimate the random error is to calculate the mean $\bar{x}$, and the standard deviation from the data.

The standard deviation is defined as

$$\sigma_x = \left(\frac{1}{N} \sum_{i=1}^{N} \left(x_i - \bar{x} \right)^2 \right)^{0.5} \quad \textbf{(65)}$$

Where σ is the standard deviation, N is the number of measurements, and x_i is the result of the i^{th} measurement.

Further, the random error can be presented in terms of a confidence interval.

$$\bar{x} \pm P\left(\frac{\sigma}{\sqrt{N}} \right) \quad \textbf{(66)}$$

Where P is the area under a normal distribution curve.

For the first phase experiment, it was quite difficult to set a consistent flow rate from the pump speed controller. When the speed of the pump was adjusted, it would take a minute to achieve a steady flow rate. With a larger increase of the pump speed, longer time was needed to stabilise the flow rate. The results of the random error analysis are presented in Table 7. It shows that the random error for the flow rate can be presented as $Q \pm 0.96\%$, which covers all three different flow rate.

The shear stress measured at a shear rate of 125/s was chosen as the test statistic from the rheological data. Higher shear rate measurement does not show an appropriate representation of the typical shear rates experienced in the experiment. The results of the random error

analysis of rheological data from the first phase experiment are presented in Table 8. It shows that the random error for the rheological data can be presented as ± 2.4% of shear stress value.

Table 7 Summary of first phase experiment flow rate random errors

Mean flow rate	95% Confidence level	CL/Mean
8.62	0.083	0.0096
7.50	0.013	0.0017
10.55	0.10	0.0096

Table 8 Summary of mean shear stress and confidence limit statistics for the four different fluids tested in first phase experiment

Name	Mean τ at 125/s	95% Confidence level	CL/Mean
0405.1100	3.48	0.039	0.011
0405.1200	3.32	0.078	0.024
0405.1400	3.84	0.001	0.0003
0405.1500	3.75	0.071	0.019

The shear stress measured at a shear rate of 134/s was chosen as the test statistic for the data collected from the small flume experiment. The results of the random error analysis of rheological data from the small flume experiment are presented in Table 9. It shows that the random error for the rheological data can be described as ± 3.4% of shear stress value.

Table 9 Summary of mean shear stress and confidence limit statistics for the seven different fluids tested in small flume experiment

Name	Mean τ at 134/s	95% Confidence level	CL/Mean
1307	8.85	0.30	0.034
1407a	5.03	0.020	0.0040
1507a	12.21	0.13	0.011
1907	5.17	0.16	0.031
2007a	3.92	0.034	0.0087
2107	10.14	0.20	0.020
2607b	3.55	0.039	0.011

4.5.2 Instrument errors and human errors

Experimental errors have been identified as instrument errors and human errors. Usually the data recorded for each variable during the experimental work was done repeatedly. The accuracy of the individual measurements contributing to the logging of the recorded variable was estimated. For simplicity reasons, the estimates were just based on the resolution of the instrument.

Table 10 Summary of instrument errors and human errors for recorded variables

Variable	Description of measurement	Accuracy
	First phase experiment	
Flow rate	Magflo electromagnetic flowmeter	$\pm$0.5%
Depth	Ruler	$\pm$1 mm (1.6%)
	Vectrino velocimeter	$\pm$1 mm (1.6%)
Slope	Initial mark (ruler)	$\pm$1 mm
	Accuracy of level	$\pm$2 mm
	Finial measurement (ruler)	$\pm$1 mm
Position of the probe	Ruler	$\pm$1 mm
Temperature	Vectrino velocimeter	$\pm$0.1^{o}C
	Second phase experiment	
Flow rate	Measurement from coriolis meter	$\pm$0.15%
Depth	Ruler	$\pm$1 mm
Slope	Initial mark (ruler)	$\pm$1 mm
	Accuracy of level	$\pm$2 mm
	Final measurement (inclinometer)	$\pm$0.5^{o}
Temperature	Measurement from coriolis meter	$\pm$1^{o}C
Particle size	Sieves	$\pm$5%
	Rheological measurement	
Rheology	Rheosys Merlin II rheometer	$\pm$1%

4.6 Summary

The equipment discussed in this thesis was not particularly designed and built for this project. However, all the equipments were modified to fit the aim of this project. The equipments were equipped with the necessary instrumentation to measure flow rate, temperature, velocity and depth. All the equipments were commissioned with clear water tests. Calibration of the velocimeter was done to produce water flow data to establish the sample volume size and weak spot. Additional water flow tests were done in order to check whether the modified flume was working. Rheology tests were conducted on all test solutions to yield a rage of rheological properties. The random error analysis and experimental error estimation were also presented in this section.

Chapter 5: Numerical Modelling of Turbulent Flow in Open Channels with Semtex

5.1 Introduction

This is a parallel study of the experimental investigation presented in this thesis. A three-dimensional numerical procedure is presented for modelling the turbulent non-Newtonian open channel flow. The use of DNS provides a significant amount of information for scientist and researchers to better understand the physics of turbulent flows. Usually computational fluid dynamics simulations of turbulent flow are more difficult than laminar flow. Rudman and Blackburn (2006) developed a numerical model using Fourier method (SEM) for Direct Numerical Simulation (DNS) of the turbulent flow of non-Newtonian fluids. This computational code is referred to as Semtex in this study.

Spectral methods are usually implemented for the numerical simulations of three-dimensional and time-dependent flow. They are both very accurate (converging exponentially with mesh refinement) and efficient (allowing the use of fast solvers and Fourier transforms). The spectral methods are particularly suited for problems having many fine scales, such as turbulent flow simulations. Combining high accuracy (exponential convergence) with computational high efficiency has made spectral methods the methods of choice within high accuracy domains of applications such as homogeneous turbulence (Orszag and Patterson, 1972) and turbulence in a channel flow (Orszag and Kells, 1980).

The code used in this study - Semtex is a family of spectral Fourier simulation codes. Blackburn (2007) refers the spectral element method as a high order finite element technique that combines the geometric flexibility of finite elements with the high accuracy of spectral methods.

5.2 Numerical method

The spatial discretisation employs a spectral element - Fourier formulation, which allows arbitrary geometry in the (*x, y*) plane and assumes periodicity in *z* (axial) direction (Rudman *et al*, 2004). A second-order-in-time mixed explicit-implicit technique is employed for time integration of the incompressible momentum equations, which for a spatially variable viscosity η read as.

$$\partial t\vec{u} + \vec{N}\left(\vec{u}\right) = -\rho^{-1}\nabla P + \rho^{-1}\nabla\left[\eta\left\{\nabla\vec{u} + \left(\nabla\vec{u}\right)^{T}\right\}\right] \quad \textbf{(67)}$$

$$\nabla\cdot\vec{u} = 0 \quad \textbf{(68)}$$

The non-linear terms $\vec{N}\left(\vec{u}\right)$ are implemented in skew-symmetric form as this has been found to reduce aliasing errors.

The equations are written in the Cartesian coordinate system. *x, y* and *z* denote the spanwise, wall normal and axial directions respectively. The numerical scheme employed is detailed in Blackburn and Sherwin (2004). The velocity *u* can be directly projected onto a set of two-dimensional complex Fourier modes.

The time integration scheme is based on a second-order velocity-correction projection scheme by Guermond and Shen (2003) and Karniadakis *et al* (1991). The simulation used Fourier expansions in the channel axis direction referred as Cartesian simulation. To allow a semi-implicit treatment of the viscous terms, the non-Newtonian viscosity is decomposed into a spatially constant component, η_r, and a spatially varying component η-η_r. The basic concept is to ensure that the reference viscosity is larger than the local (varying) viscosity throughout most of the domain at most of the time. An initial estimate of the reference viscosity η_r is chosen. If the value of η_r leads to numerical instability, it can be adjusted during the computation without adverse effects. Too small a value of η_r will lead to most of the viscosity being treated explicitly with either stability problems or very small time steps. Choosing a large value of η_r may lead to instability for reasons that are not clearly understood (Rudman *et al*, 2004). In this case, it is found that η_r, should be increased as *n* decreases.

Since both of the power law and Herschel-Bulkley rheology models have a singular viscosity at zero shear rate, a 'cut-off' value is used, below which the shear rate is assumed to be constant when computing the viscosity. The cut-off value is chosen to be 10^{-5} times the mean shear rate.

Furthermore, in order to drive the flow in the axial (z) direction, a body force per unit mass equivalent to the pressure gradient measured in the experiments is applied to the z-momentum equation. This approach allows the pressure to be periodic in the axial direction.

The computations reported here were carried out using 16-32 processors on Tango cluster from VPAC (Victorian Partnership for Advanced Computing). Tango is a large AMD Opteron system and it is VPAC's fourth and largest cluster. Its final configuration has 96 compute nodes, each with two AMD Barcelona 2.3 GHz quad core processors for a total of 760 CPUs (VPAC, 2010).

5.3 Boundary condition

In Semtex, the boundary conditions can only be Dirichlet or Neumann type as the mixed boundary conditions are not implemented in the code yet. For the velocity field, the Dirichlet condition is applied on the side and bottom walls, and the Neumann condition is applied on the surface, except for the normal component of velocity (v) which is set to zero. Similarly, in Wu *et al* (2000), their free surface condition treatment is also to set the velocity normal to the surface to zero.

In Figure 40, <D> denotes Dirichlet condition and <N> denotes Neumann condition. For pressure, type <H> is used. It is an internally computed Neumann boundary condition as described in Kariadakis *et al* (1991). This is supplied at all places except on outflow boundaries. In Figure 40, it is clearly seen that Dirichlet condition is applied on the walls. In the surface section, Neumann condition is applied, except for the normal component of velocity (v) which is set to zero.

```
<BCS NUMBER=2>
        1       w       4
                        <D>     u = 0           </D>
                        <D>     v = 0           </D>
                        <D>     w = 0           </D>
                        <H>     p = 0           </H>
        2       s       4
                        <N>     u = 0           </N>
                        <D>     v = 0           </D>
                        <N>     w = 0           </N>
                        <H>     p = 0           </H>
</BCS>
```

Wall section

Surface section

Figure 40 Boundary condition section in Semtex session file

5.4 Mesh generation

In this code, unstructured mesh is used to define the cells on which flow variables are calculated throughout the computational domain. It means the elements of the mesh can be anywhere. The elements do not have to maintain a certain pattern but the connectivity of the elements are important. An illustration of a 2-D mesh is shown in Figure 41 and Figure 42. Figure 43 shows a hand drawn mesh with 38 elements. To construct this mesh, 10 nodes are specified on the bottom edge; these nodes correspond to nine intervals along these edges. Similarly sixteen nodes are specified on the surface, corresponding to fifteen intervals along these edges. An internal mesh is then generated by connecting nodes one-for-one across the domain such that rows and columns are defined.

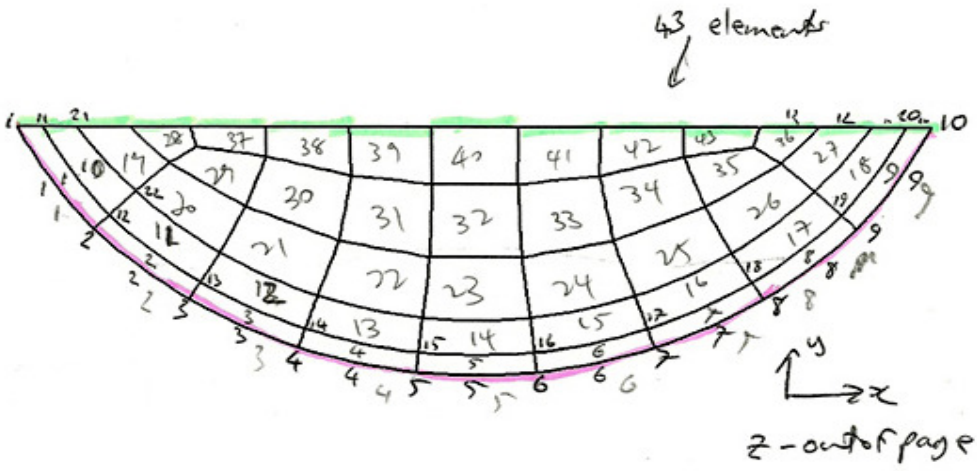

Figure 41 Sample structured 2-D mesh for 43 elements

Figure 42 Computer generated 2-D mesh for 43 elements

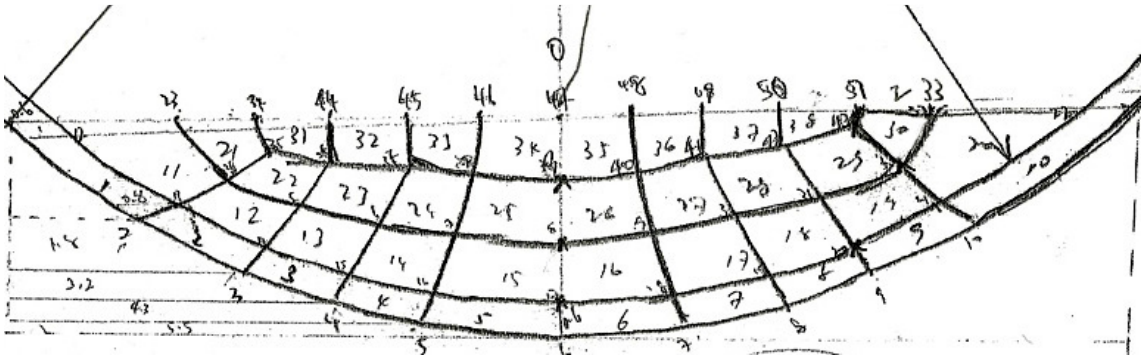

Figure 43 Hand drawing of 2-D mesh for 38 elements

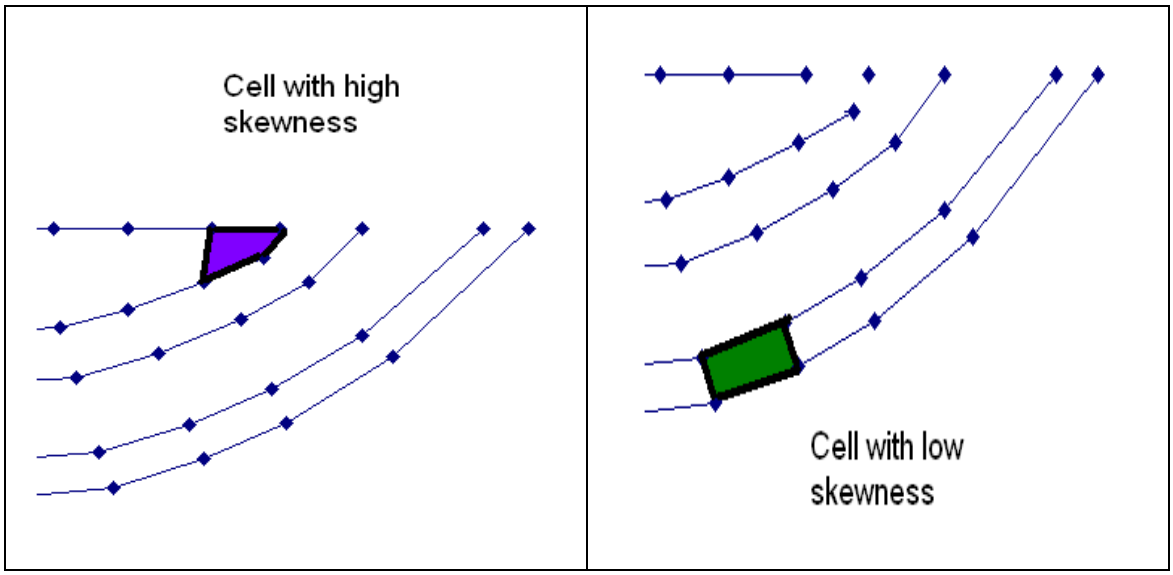

Figure 44 Elements with different skewness

However, if there is a cell with slightly skewness, the computational simulation would encounter some unexpected errors. Therefore, it is recommended that all the elements should be constructed with the lowest skewness as possible. In general, mesh generation is the most important procedure in the simulation.

5.5 Wall viscosity and wall unit

5.5.1 Wall viscosity

When the viscosity varies in space and time, the appropriate viscosity scale to use in order to define a Reynolds number is obvious. Therefore in this paper, the Reynolds number is defined by mean wall viscosity. It is calculated from the mean wall shear stress, τ_w. It is determined directly from the applied axial pressure gradient.

$$\tau_w = \frac{\delta p}{\delta z} \rho \frac{A}{C} \tag{69}$$

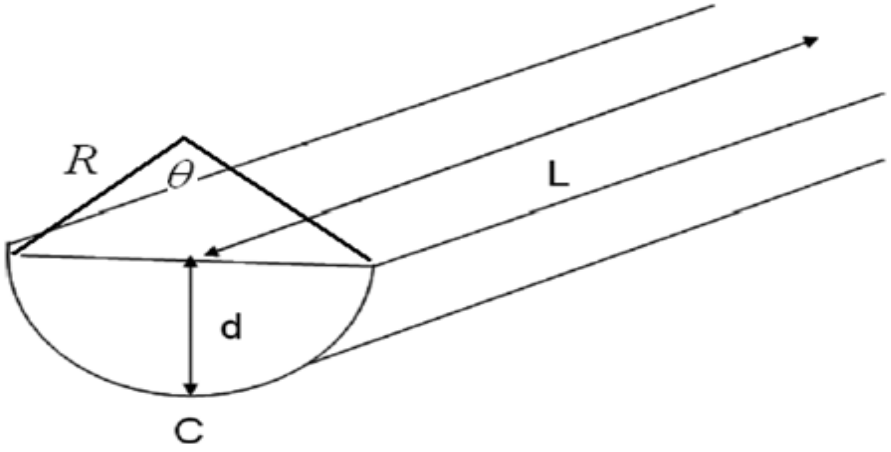

Figure 45 Simulation channel geometry

Where

$$C = R\theta \tag{70}$$

A is the cross-sectional area.

Assuming a Herschel-Bulkley rheology,

$$\eta_w = K^{1/n} \frac{\tau_w}{(\tau_w - \tau_y)^{1/n}} \tag{71}$$

For a power law rheology

$$\eta_w = K^{1/n} \tau_w^{(1-1/n)} \tag{72}$$

5.5.2 Wall units

Wall units are introduced with the wall viscosity replacing of the non-Newtonian viscosity. Therefore the friction velocity is defined as $U^* = \sqrt{\tau_w / \rho}$, the non-dimensional velocity is $U^+ = U/U^*$ and the non-dimensional distance from the wall is written $y^+ = (\rho U^* / \eta_w) y$.

5.6 Session file

In session file, a number of variables need to be identified. In this section, second-order accurate time integration is selected (N_TIME = 2) and the number of Lagrange knot points along the side of each element is set to desired value (N_P = 15). The code will integrate for a number time steps (N_STEP) with a time step of a value (D_T).

```
<TOKENS>
        N_TIME    = 2
        N_P       = 15
        N_Z       = 384
        BETA      = 4.0
        N_STEP    = 10000
        D_T       = 0.00001
        PowerLaw  = 0
        HB        = 1
        HB_K      = 0.000038
        HB_N      = 0.781
        HB_ZERO   = 0.00001
        YIELD_STRESS = 0.0014
        PL_K      = HB_K
        PL_N      = HB_N
        PL_ZERO = 0
        KINVIS = PL_K
        REFVIS = 0.8*HB_K
        Rad       = 0.5
        Q         = 0.0
        FFZ       = 0.147
        AVERAGE    = 2
        CHKPOINT  = 1
        ITERATIVE = 1
        IO_HIS    = 20
        IO_CFL    = 5
        IO_FLD    = 1000
```

Figure 46 Part of session file

The shape of the mesh is defined by the NODES and ELEMENTS sections. Each element obtained by connecting the corner nodes. The *x, y,* and *z* locations of the nodes are given. The SURFACE section describes how the edges of elements which define the boundary of the solution domain are dealt with.

5.7 Wall fluxes and modal energies

Figure 47 and Figure 48 show the total stress profile of the simulation of a set of Herschel-Bulkley rheological parameter over a period of time. The file containing stress data is called .flx file. The .flx file contains the volume integrated pressure and viscous terms in the three

coordinate directions. This file has nine columns of data after the time column. It includes pressure, viscosity, and total stress in the *x*-direction, *y*-direction and *z*-direction. Figure 47 shows a stress file of a simulation with constant oscillation. This means the simulation result is converged and the iteration could be stopped. In Figure 48 the stress curve shows an increasing trend thus it means that the simulation needs to keep running until the curve starts constant oscillation.

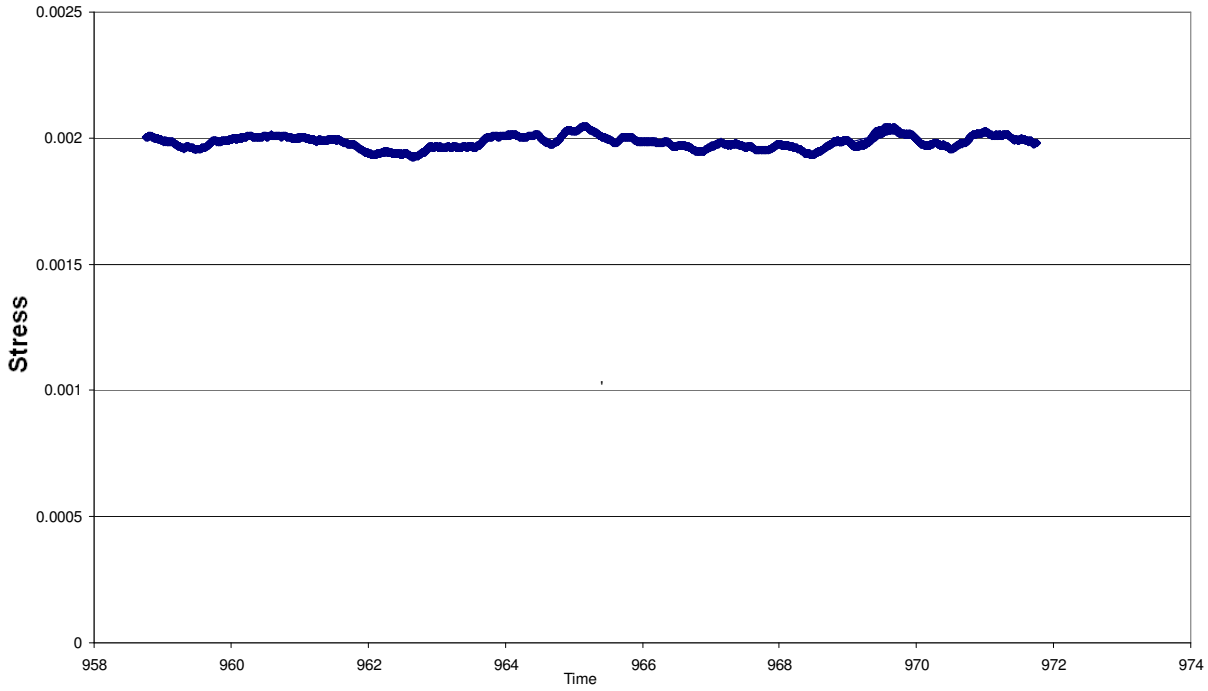

Figure 47 Simulation stress profile over a period of time (converged)

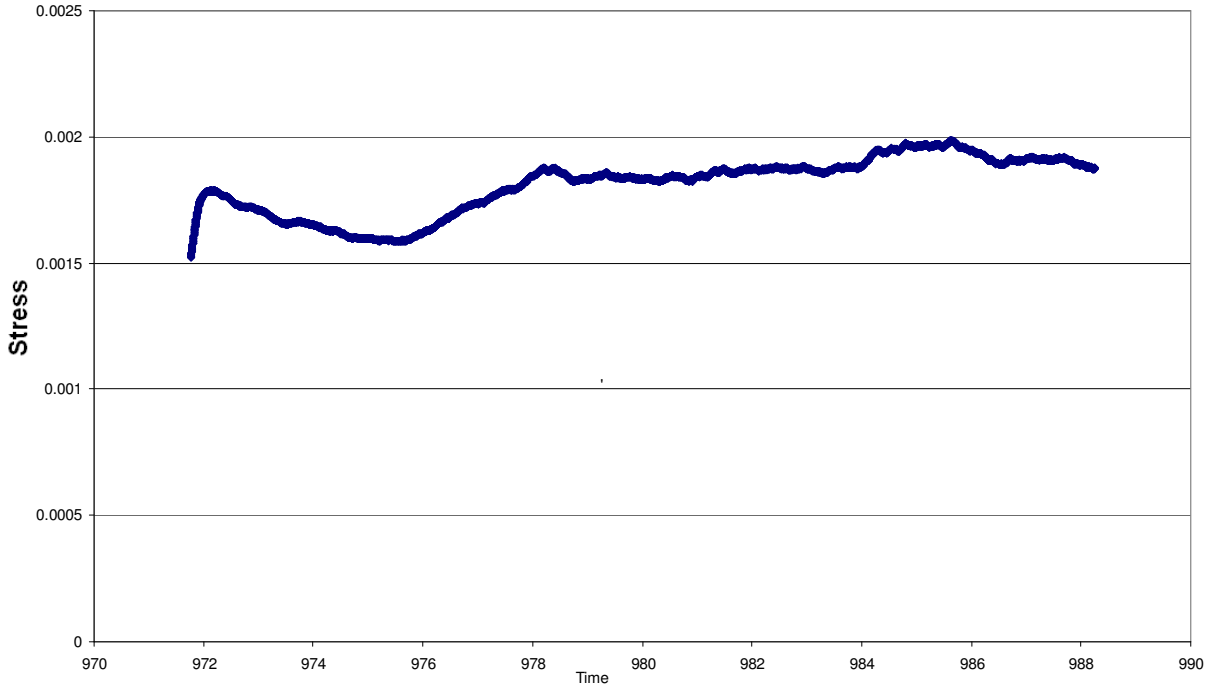

Figure 48 Simulation stress profile over a period of time (not converged)

Figure 49 and Figure 50 illustrate the same behaviour with the simulation's modal energy profile. The modal energy output file is called the .mdl file. This file has the energy in each of the Fourier modes in the z-direction. This is one of the time consuming task for this numerical simulation. Sometimes the simulation takes weeks get converged results. Once the data points begin constant oscillation, the simulation could be stopped and the next step would be data extraction.

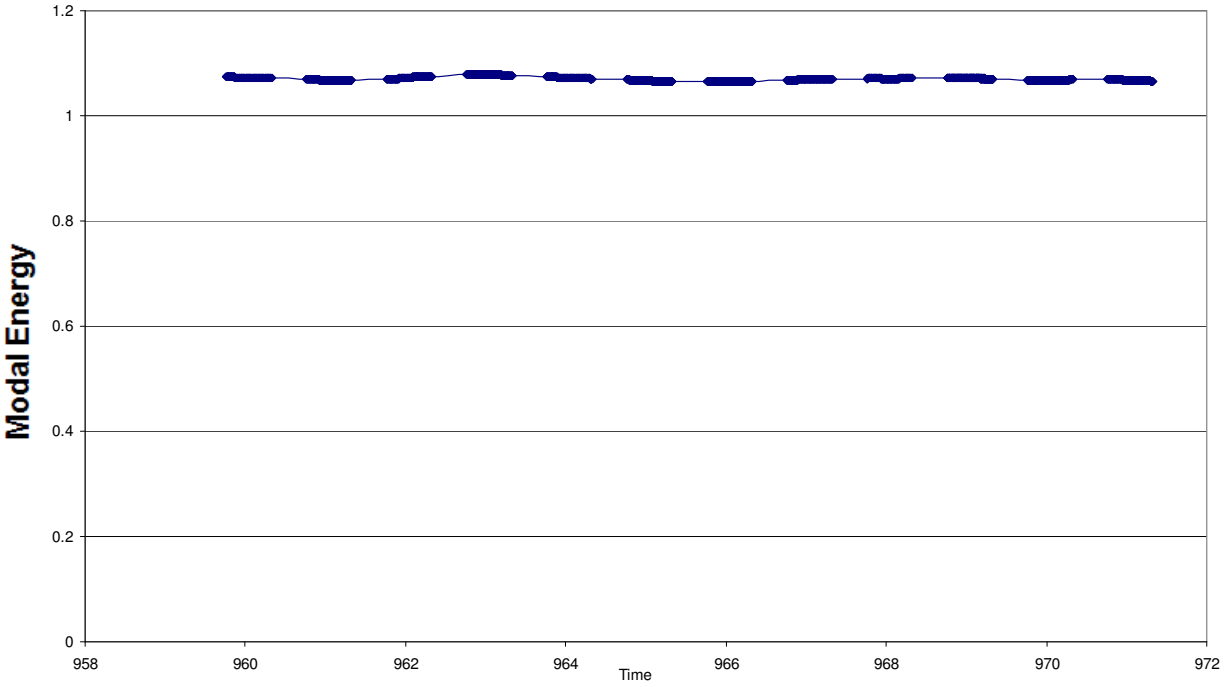

Figure 49 Simulation energy profile (converged)

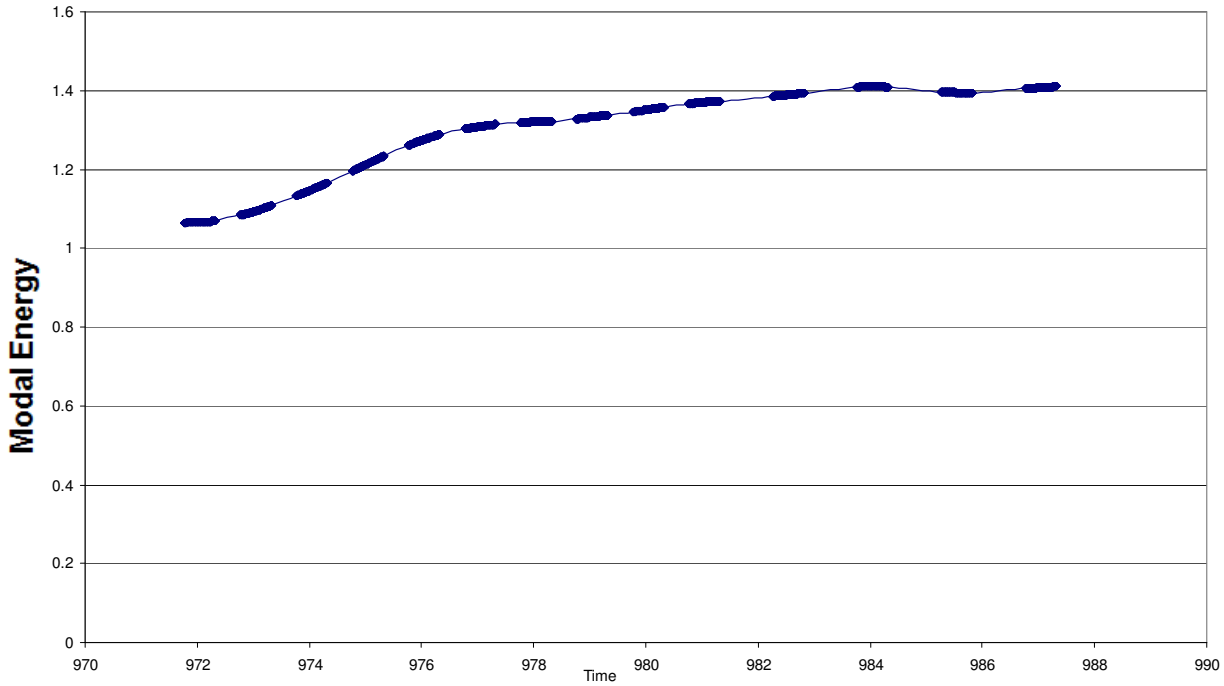

Figure 50 Simulation energy profile (not converged)

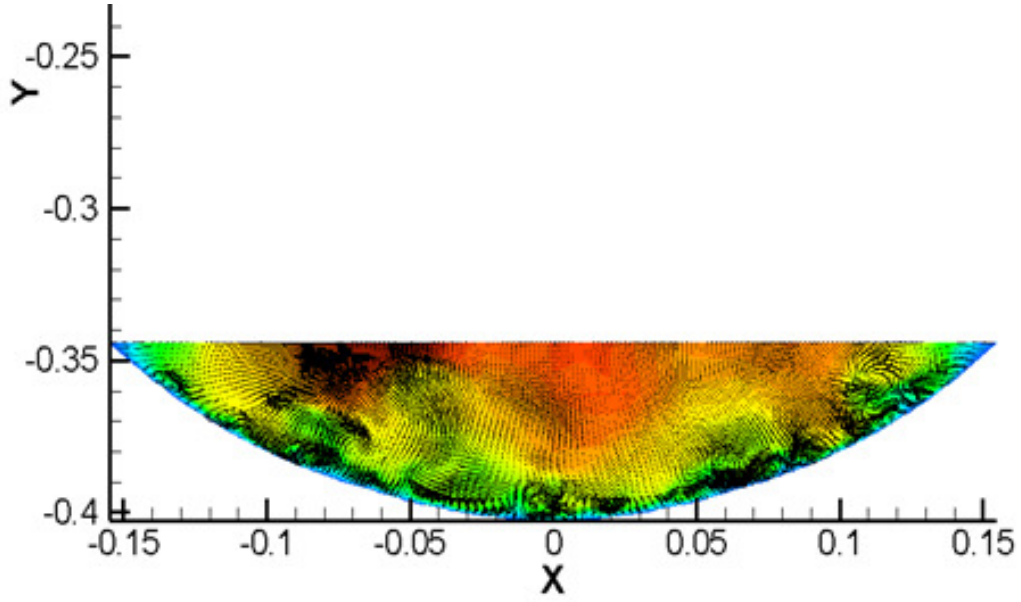

Figure 51 Instantaneous contours of z plane velocity vectors for the channel flow

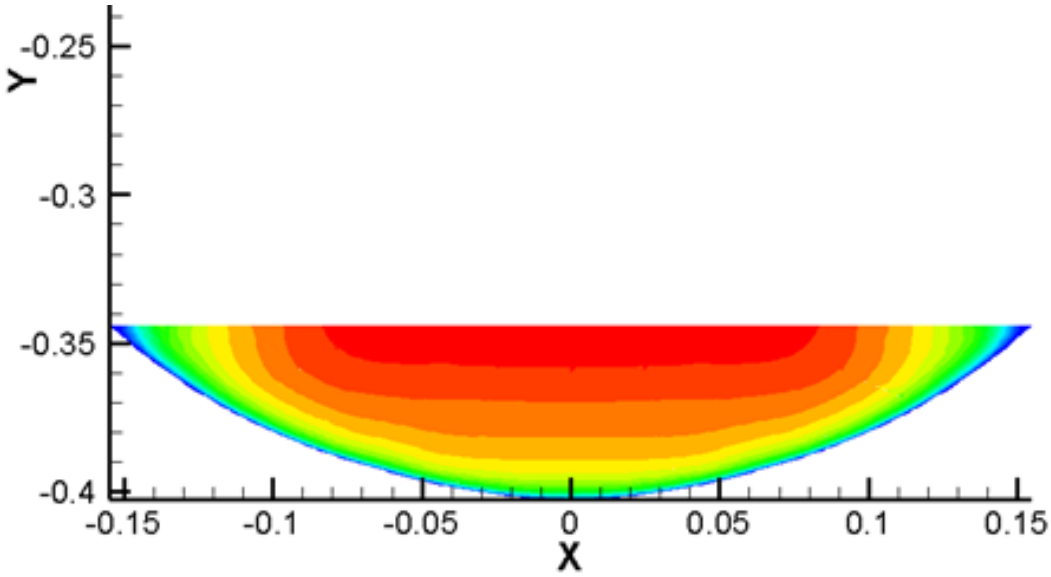

Figure 52 Symmetrised z plane velocity u

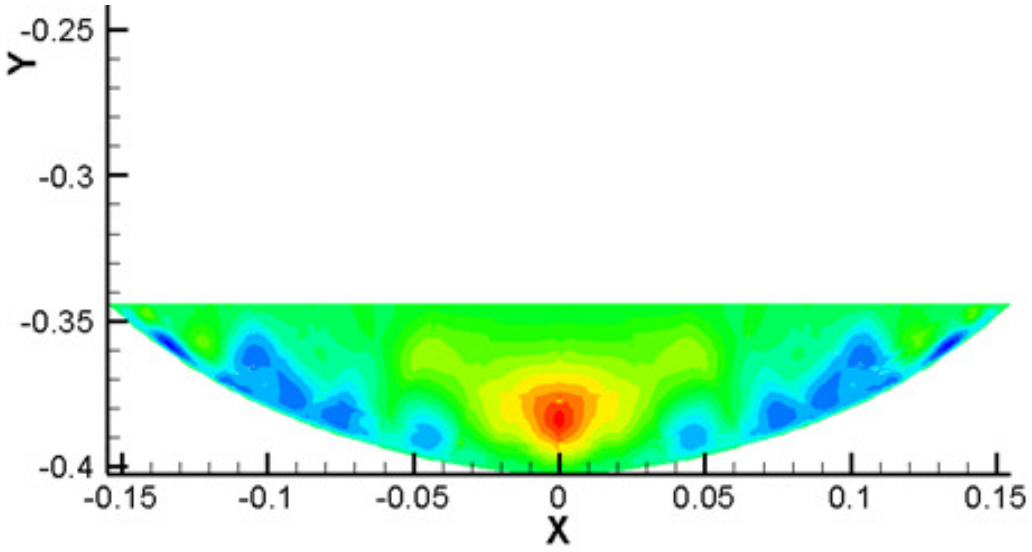

Figure 53 Symmetrised y plane velocity v

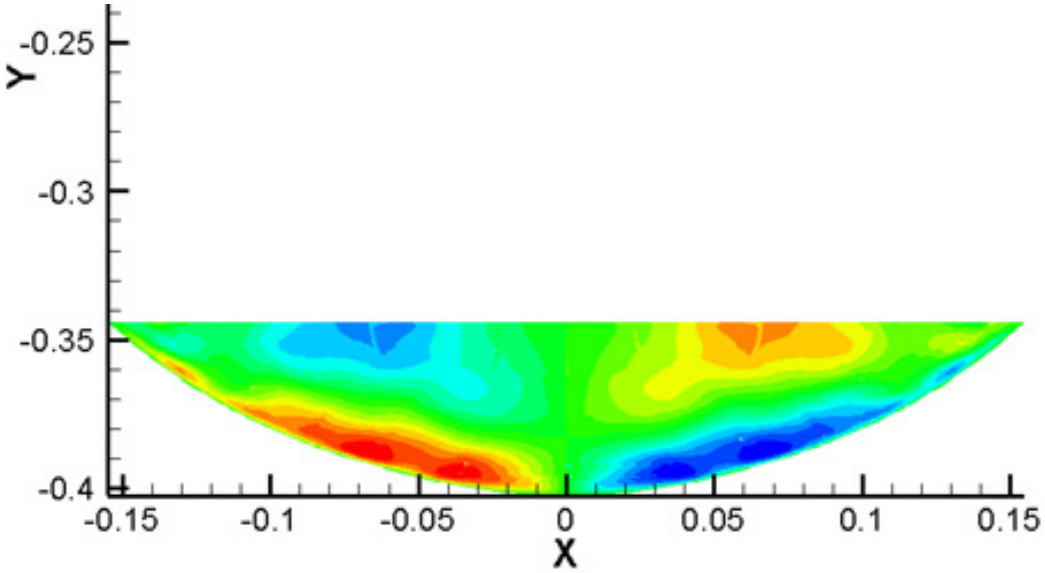

Figure 54 Symmetrised x plane velocity w

Tecplot360 (commercial software by Tecplot Inc.) is used to visualise the numerical simulation data. Figure 51 to Figure 54 show symmetrised plot of the simulation velocity. The geometry and boundary conditions of the simulation has been set up as symmetric. Therefore the expected time mean flow should also be symmetric. However, the actually simulated flow was not as symmetrical as expected. It is suggested that it could be a fundamental oddity in the flow or the simulation has not be averaged for long enough. By symmetrising the flow, a better averaged velocity can be obtained.

5.8 Summary

In this chapter, a three-dimensional numerical procedure is developed for modelling the turbulent non-Newtonian open channel flow. Computational modelling of non-Newtonian fluids using DNS shows good signs in helping to understand the physics of turbulent flows. More results of validation of the code and other simulation with different rheological parameters are shown in Chapter 6.

Chapter 6: Experimental results and simulation results

6.1 Introduction

This chapter will be divided into five different parts.

- Discussion of initial experimental results
- Presentation and discussion of experimental results
- Validation of simulation results
- Investigation of different simulation variables
- Secondary flow effect

The simulation parameter is mainly based on the actual experimental conditions and tested rheology parameters from Fitton (2007) due to current experimental limitations.

6.2 Initial calculation

6.2.1 Initial prediction

Before the actual commission of the experiment, it is essential to check whether the proposed setup could achieve turbulent condition. Therefore, this section shows a method to predict the turbulent condition in open channel flows. The variables in this calculation are slope of the channel and fluid flow rate. The tested diameter of this calculation is 200mm. It is assumed that in this calculation, the testing pipe is filled at half capacity therefore it would have the characteristic of an open channel, i.e. a free surface. The maximum flow rate used in this calculation was assumed to be 25 l/s. Figure 3 shows the diagram of the open channel shape use in this experiment. The shear thinning non-Newtonian fluids used in this experiment are CMC solutions. Three different CMC solutions are chosen for predicting flow conditions.

Table 11 presents the rheological parameters for the CMC used in the experiment. Yield stress, K and n values are also presented.

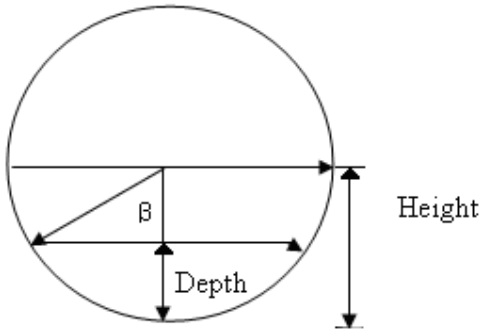

Figure 3 Schematic illustration of the cross-sectional view of open channel flow in a circular flume

Table 11 CMC solution parameter

CMC	Yield stress (Pa)	*K* (Pa.s^n)	*n*
A	0	0.23	0.60
B	0	0.125	0.70
C	0	0.09	0.70

A non-Newtonian fluid was investigated using Reynolds number in non-Newtonian open channel flow proposed by Haldenwang *et al* (2004). In this case, *D* was replaced by R_h for open channel conditions.

$$\mathrm{Re} = \frac{8\rho V^2}{\tau_y + K(\frac{2V}{R_h})^n} \qquad (20)$$

Where *V* is the mean velocity, ρ is the fluid density, τ_y, *K*, and *n* are fluid parameters and R_h is the hydraulic radius.

The literature values of Reynolds number for the onset of transition to turbulent flow in open-channels vary greatly (800 to 2000) for Newtonian fluids and are ill defined for non-Newtonian fluids. Transition to turbulence for non-Newtonian fluid in channel flow is still a practical problem. One method that addresses this confusion is that of Haldenwang *et al* (2004), draws a locus of transition points, which is a function of channel slope.

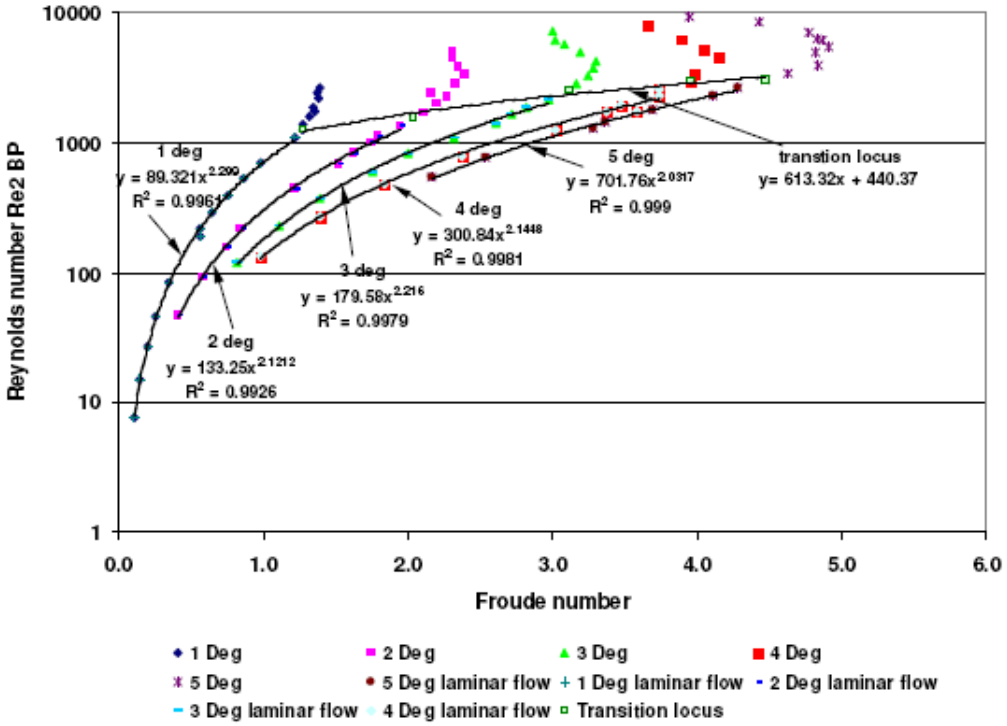

Figure 55 Haldenwang *et al* (2004) transition locus for open channel flow (4.6% bentonite in 150 mm flume)

Figure 55 shows a Reynolds number against Froude number graph for 4.6% bentonite in 150 mm flume from Haldenwang *et al* (2004) paper. The bentonite data was fitted with Bingham plastic rheology model. Haldenwang's locus indicates the start of transition from laminar to turbulent and the bend at higher Reynolds number indicates full turbulence. This shows a relationship between the Reynolds number and Froude number for each slope tested. The points of inflection were connected and Haldenwang *et al* (2004) established a linear relationship between these points. However, it appears that these are both speculative as the means of determining the presence of turbulence is not outlined in the paper. The model is only an empirical correlation. In this study, Haldenwang's locus is used to predict turbulent for the experiment because it is easy to apply on non-Newtonian open channel flow.

The prediction method is presented here for predicting flow condition in an open channel flow.

1. Chose an initial for channel depth
2. Calculate the free board and the angle

3. Calculate cross sectional area of the flow and the wetted perimeter in order to calculate R_h
4. Calculate average velocity (Q/A)
5. Calculate Reynolds number by using equation (20)
6. Calculate friction factor. It is discovered that due to the implicit nature of the Colebrook-White equation, the friction factor should be determined by an explicit relation developed by Haaland in 1983 (Wilson, 1988)

$$\frac{1}{\sqrt{f}} = -1.8\log\left[\left(\frac{\frac{\varepsilon}{D}}{3.7}\right)^{1.11} + \frac{6.9}{\mathrm{Re}}\right] \quad \textbf{(73)}$$

7. Calculate friction factor using Colebrook-White equation (equation (16))
8. Calculate R_h from the friction factor value calculate from step 7
9. Adjust the initial depth value until the two R_h values calculated in steps 3 and 7 equate
10. Calculate the channel width from R_h value calculate from step 9
11. Calculate Froude number as

$$Fr = \frac{V}{\left(g\frac{A}{B}\right)^{0.5}} \quad \textbf{(74)}$$

Different flow rates were used to obtain a range of Reynolds number and Froude number. The maximum flow rate 25 l/s used in the calculation is based on the maximum capacity of the proposed pump. The plot of Reynolds number against Froude number with CMC solution A is shown in Figure 56. The Haldenwang locus is drawn in relation to channel slope. In Figure 56 different groups of plots present different slopes. In this investigation, 2%, 5%, 10% and 20% slopes were chosen. With a slope of 2%, the CMC solution A can reach Haldenwang's locus without any difficulty. It means that with the pipe operating at half capacity i.e. half pipe, it is quite easy to get the flow into turbulent region. The plot with slope of 5%, 10% and 20% intersect with Haldenwang's locus and it can be predicted as the flow is in turbulent region. As there is a presence of a bend above Haldenwang's locus, a high Reynolds number also indicates the flow is turbulent. Similarly in Figure 57 and Figure 58 with CMC solution

B and CMC solution C, with a slope of more than 5%, most of the flow rate can easily bring the fluid to turbulent region according to Haldenwang's locus.

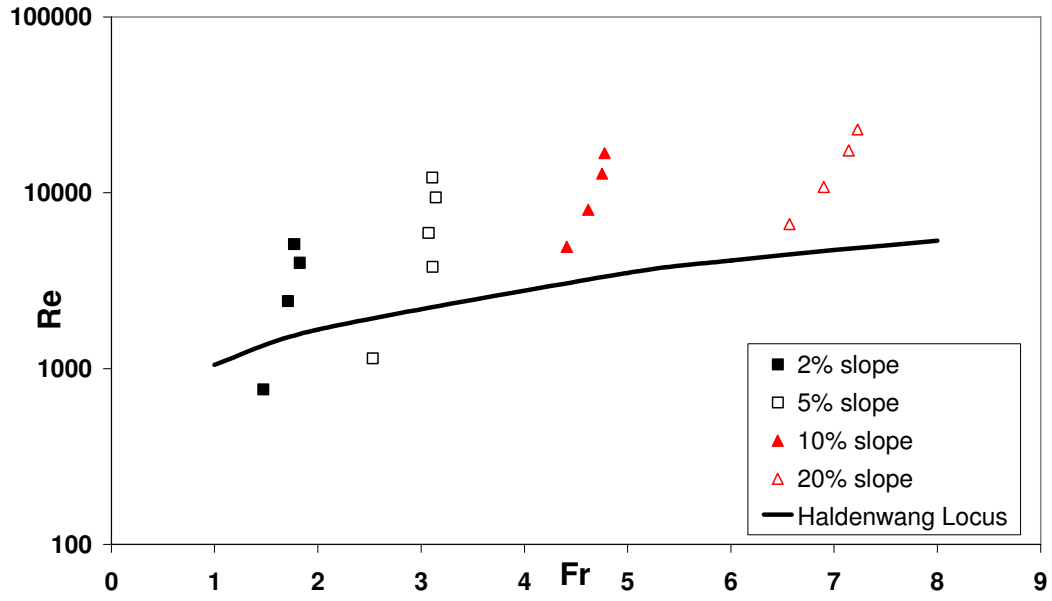

Figure 56 Predicted relationship for CMC solution A for different slopes. Haldenwang's locus is plotted and lies below the data points.

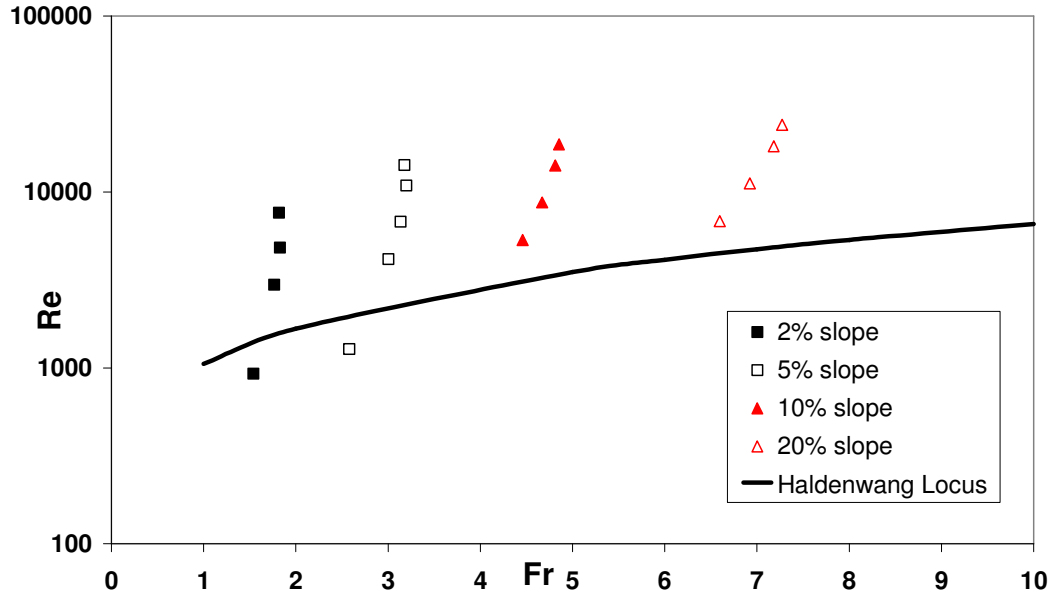

Figure 57 Predicted relationship for CMC solution B for different slopes. Haldenwang's locus is plotted and lies below the data points.

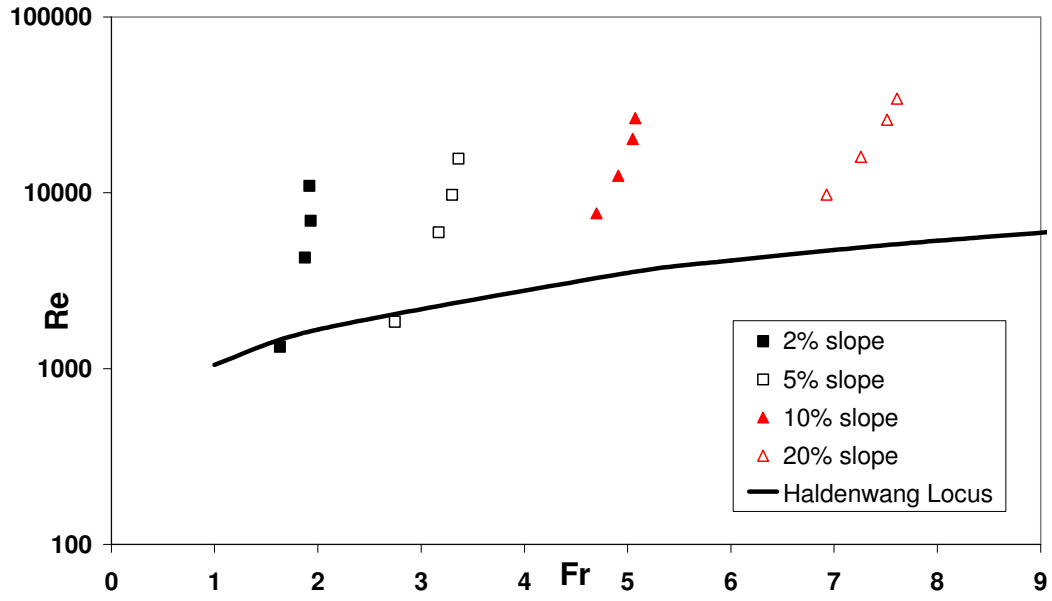

Figure 58 Predicted relationship for CMC solution C for different slopes. Haldenwang's locus is plotted and lies below the data points.

Furthermore, a group of Ultrez solution was also tested with the mentioned calculation method. The major difference between Ultrez solution and CMC solution is that the presence of yield stress in Ultrez solution.

Table 12 Rheological parameters for Ultrez solution

Ultrez	**Yield stress (Pa)**	***K* (Pa.s^n)**	***n***
0.1%	0.31	1.08	0.51
0.15%A	1.52	4.29	0.54
0.15%B	1.19	6.56	0.54

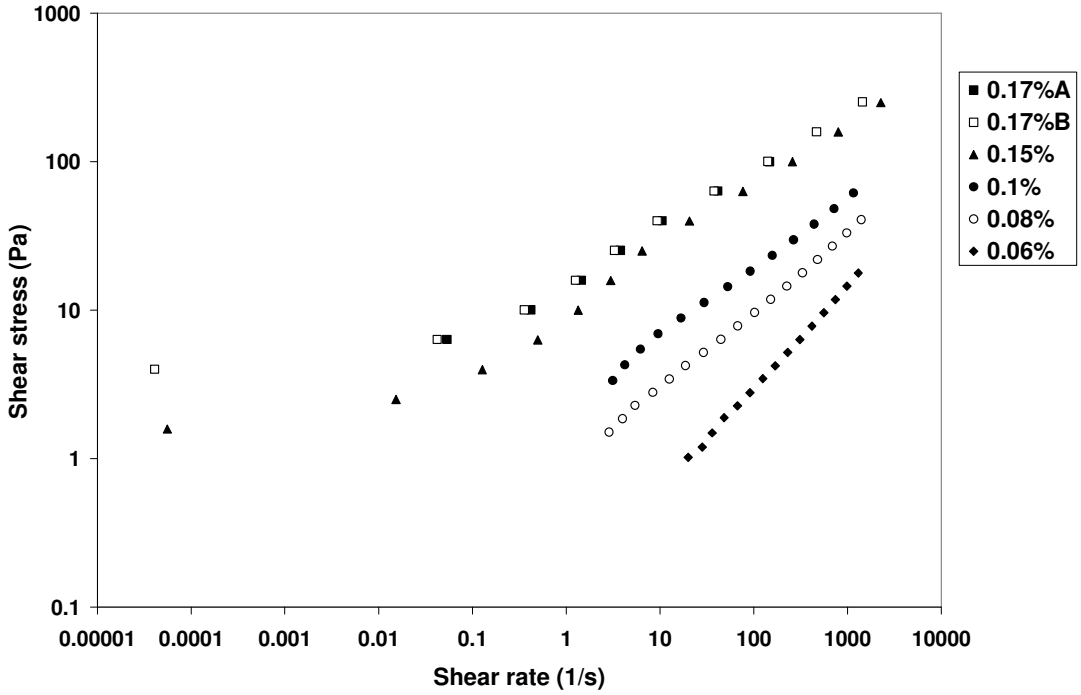

Figure 59 Rheogram of Ultrez solution tested

The plot of Reynolds number against Froude number for 0.1% Ultrez solution is shown in Figure 60. For slope of 2%, the 0.1% Ultrez solution could just reach Haldenwang's locus. This simply means that with 2% slope, this solution could not generate enough turbulence with the assumed maximum flow rate of 25 l/s. With the pipe operating at half capacity, it is very difficult to bring the flow into turbulent region. The plot with slope of 5%, 10% and 20% intersect with Haldenwang's locus and it can be predicted as turbulent flow. With high Reynolds number, it is determined that the flow is turbulent.

However, in Figure 61 and Figure 62, none of the calculated data can intersect with Haldenwang's locus. Even with 30% slope, 0.15% Ultrez B can only reach a Reynolds number approximately at 1000 from the formulas, which does not provide sufficient evidence for turbulence. Therefore it is concluded that with 0.15% Ultrez solution, turbulence cannot be achieved by increasing the flow rate without overflowing the pipe. It is suggested that a slope higher then 30% is very difficult to obtain because of the physical limitation of the equipment. Moreover, in Figure 61 and Figure 62, the curves of the predicted Ultrez solutions have small bends which are very similar to the bend presented in Haldenwang's data. However, all the data points were below the Haldenwang's locus. This suggests the locus may not be suitable for this set of solutions.

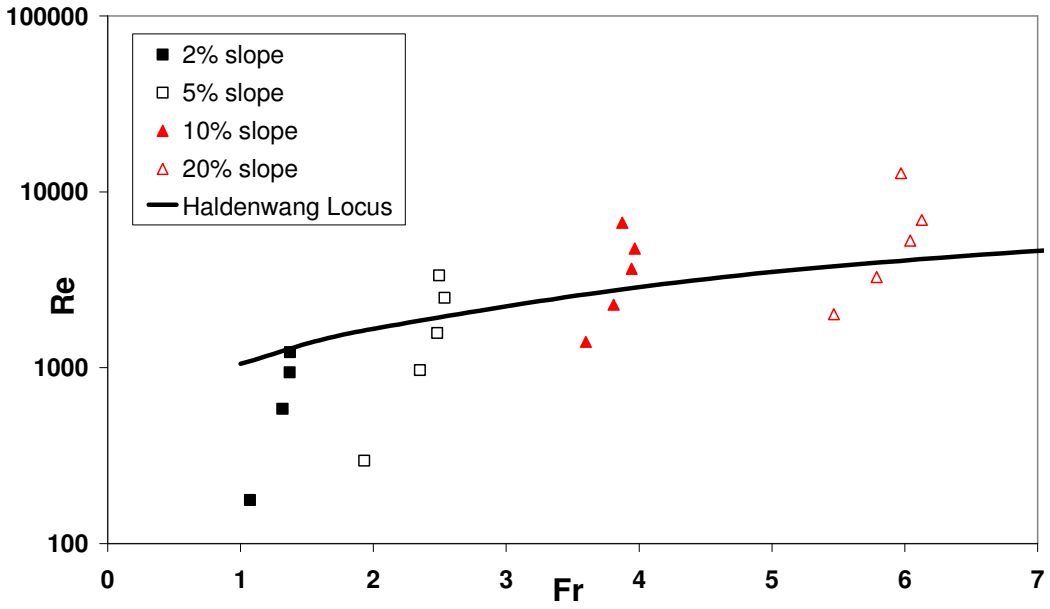

Figure 60 Prediction of turbulent region for 0.1% Ultrez solution

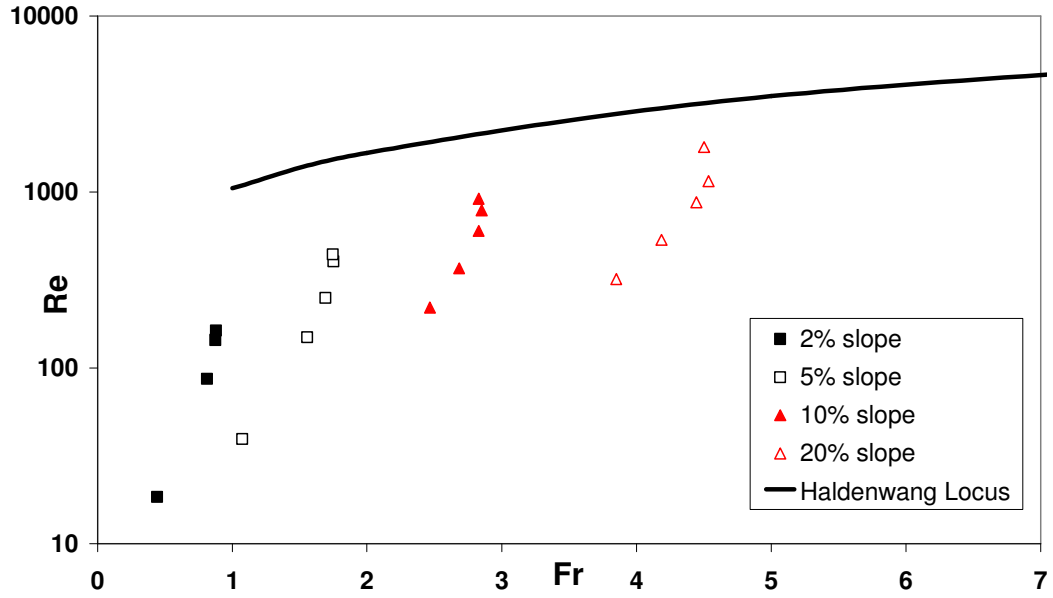

Figure 61 Prediction of turbulent region for 0.15% Ultrez A solution

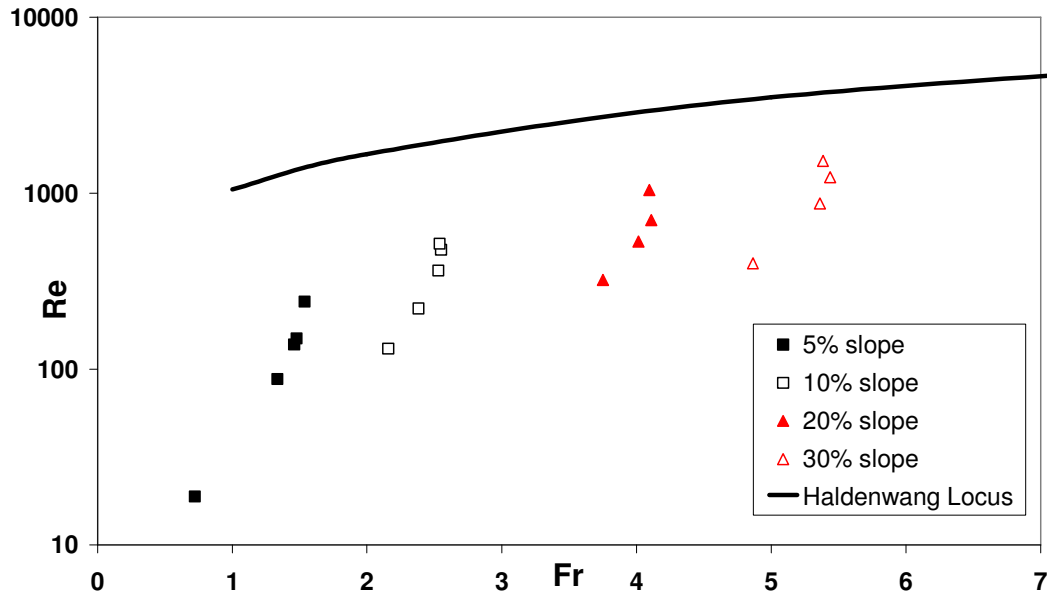

Figure 62 Prediction of turbulent region for 0.15% Ultrez B solution

6.2.1.1 Wang and Plate data (1996)

Wang and Plate (1996) used clay suspension to study the turbulence structure of non-Newtonian channel flow. They observed that transition from laminar to turbulent flows occurred when a Reynolds number *Re* is between 2000 and 10000. Their measurements of fluctuating velocity were obtained with a total pressure velocimeter. The measurements were carried out at the centre of the channel (Wang and Plate, 1996). The fluids used for this experiment were Clay-R (cohesive reservoir deposit) and Clay-W (from Wiesloch, Germany). Both of the fluids were tested to be Bingham fluid from Wang and Plate (1996).

Figure 63 is plotted from the data obtained by a smaller channel with the dimension (length × width × height) 10 m × 10 cm × 20 cm. Round shaped data points are plotted by previously discussed calculation method in section 6.2. Other black coloured data points were Wang and Plate (1996)'s measurements.

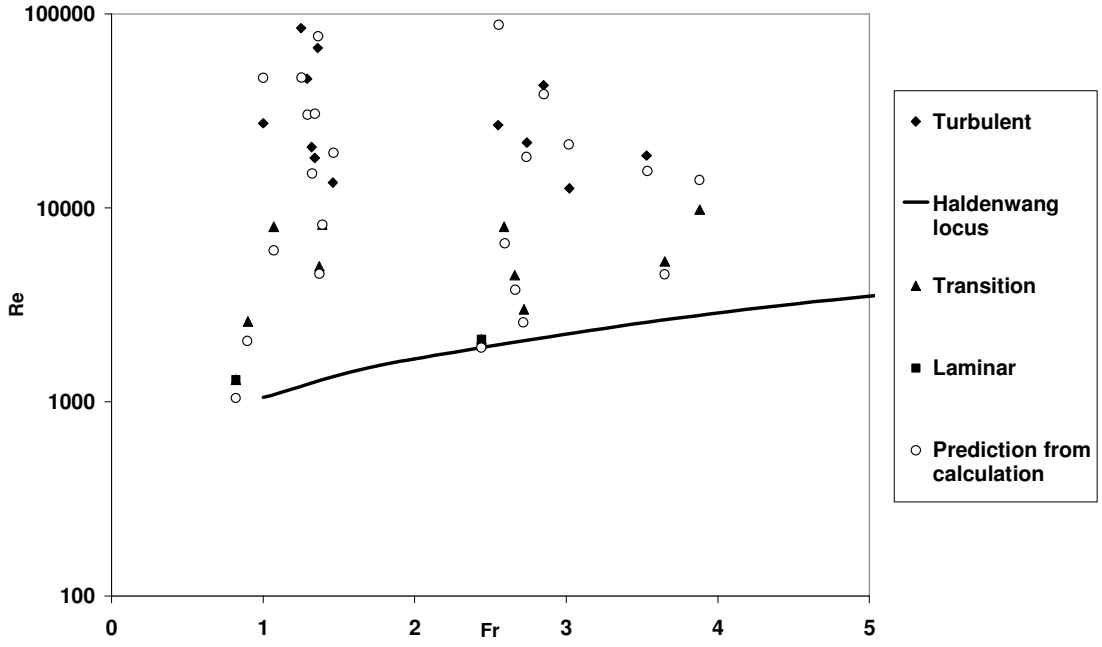

Figure 63 Combined Plot of Wang and Plate (1996) and calculated points by previous methodologies Small flume data

From Figure 63**,** the data points calculated by previous methodologies and Wang and Plate (1996)'s plot are almost identical. All the data points appeared above the Haldenwang's locus.

According to Haldenwang *et al* (2004), all the data in this plot should be in turbulent or transition region. This however shows some disagreement between Wang and Plate (1996)'s experimental results and Haldenwang's locus because some of the points from the laminar flow data of Wang and Plate (1996) fell into Haldenwang's turbulent and transition region.

Figure 64 uses Wang and Plate (1996)'s measurement from larger channel with the dimension of (length × width × height) 24 m × 60 cm × 65 cm. Round data points were obtained by the previous method (see section 6.2). Diamond shape and triangular shape data points were Wang and Plate (1996)'s measurement.

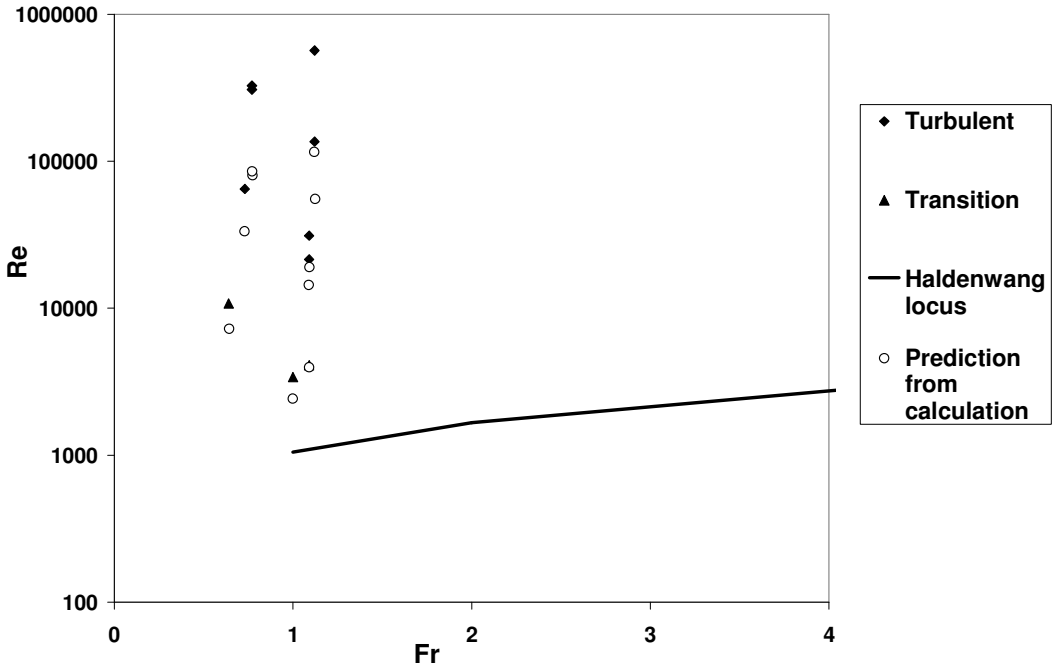

Figure 64 Combined Plot of Wang and Plate (1996) and calculated points by previous methodologies using large flume data

Reynolds number calculated by previous method do not fit particularly well with Wang and Plate (1996)'s data. Haldenwang's experiment was conducted with 3 different shaped flumes, a rectangle, a semi-circle and trapezoid; whereas Wang and Plate has only used rectangle shaped flumes. Therefore Kozicki and Tiu's shape factor can be used to check if the shape of the flume does affect the experimental result. The general trend of both turbulent and transition data sets are quite similar to the calculation. Therefore it is generally agreed that Haldenwang's locus can be used as a tool to predict flow conditions.

6.2.1.2 Kozicki and Tiu shape factor (1967)

Kozicki and Tiu (1967) investigated the effect of shape in laminar flow in open channels using.

$$\mathrm{Re} = \frac{\rho(U-u_0)^{2-n} R_h{}^n}{2^{n-3} K\left(\frac{a+bn}{n}\right)^n} \qquad (25)$$

Where a and b are the shape factors. For a semi-circular open channel, a = ¼ and b = ¾, and for rectangular open channel a = 0.2123 and b = 0.6759.

These shape factors however have not been tested against any valid experiment dataset. In fact, Kozicki and Tiu's shape factors can only predict the flow rate and maximum velocity in laminar flow of an incompressible, time-independent non-Newtonian fluid in a straight open channel (Kozicki and Tiu, 1967). Table 13 presents the rheological parameters for the Ultrez solution used in the calculation. Yield stress, K and n values are also presented.

Table 13 Rheological parameters of Ultrez solution

Ultrez	**Yield stress (Pa)**	***K* (Pa.s^n)**	***n***
0.06%	0.194	0.097	0.72
0.08%	0.72	0.61	0.58
0.10%	0	2.07	0.48
0.15%	1.56	6.65	0.49

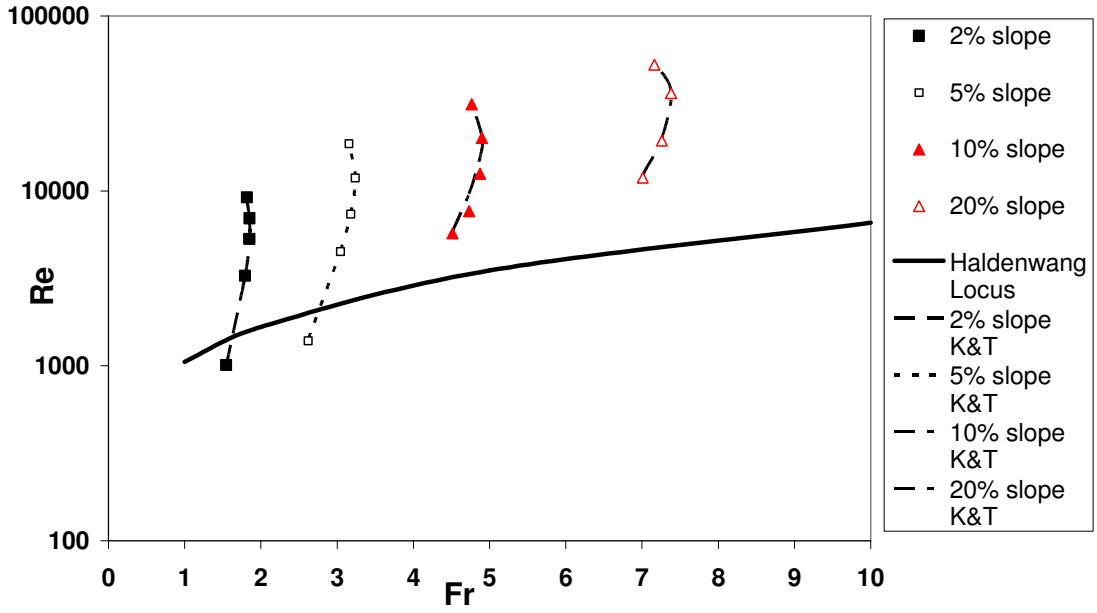

Figure 65 Prediction of turbulent region for 0.06% Ultrez solution with Kozicki and Tiu shape factor

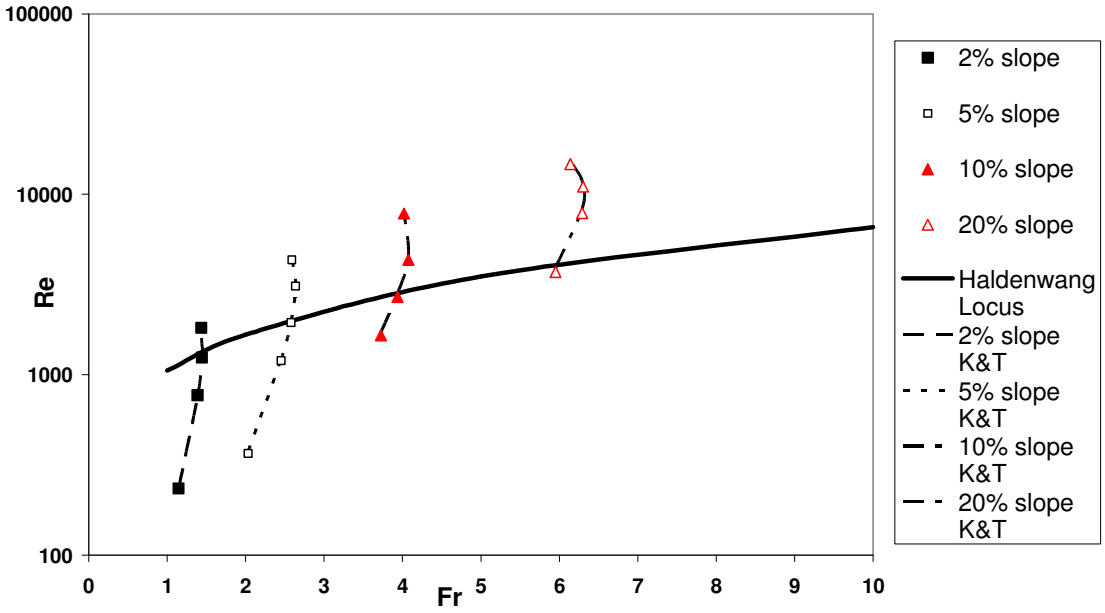

Figure 66 Prediction of turbulent region for 0.08% Ultrez solution with Kozicki and Tiu shape factor

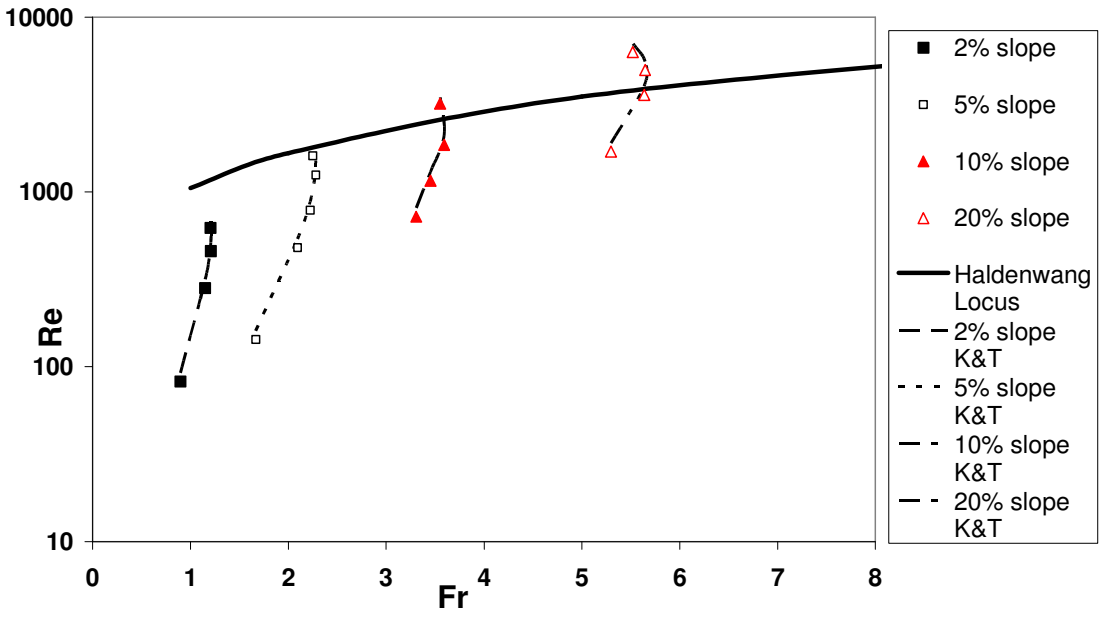

Figure 67 Prediction of turbulent region for 0.1% Ultrez solution with Kozicki and Tiu shape factor

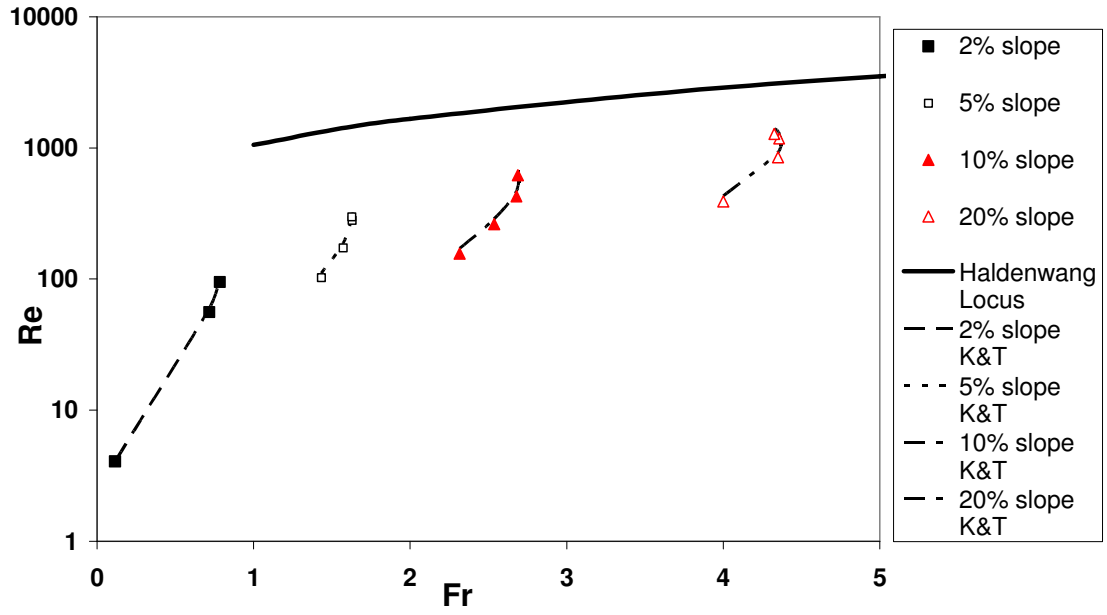

Figure 68 Prediction of turbulent region for 0.15% Ultrez solution with Kozicki and Tiu shape factor

Reynolds number is then calculated in consideration with Kozicki and Tiu's shape factor i.e. *a* and *b*. The points represent data calculated by using Kozicki and Tiu's shape factor with *a* =

0.25 and $b = 0.75$. The 'a' and 'b' values are approximate values from Kozicki and Tiu (1967) for semi-circular open channels only. In Figure 65 to Figure 68, the points present the calculated Reynolds number by the method described in section 6.2, the dotted lines present the Reynolds numbers calculated with Kozicki and Tiu's shape factor. From the graph, it is shown that the lines and points fitted quite well. The points didn't fit so well are mostly at the lower Reynolds number region, i.e. laminar region on the Haldenwang locus. The low yield stress of the 0.06%, 0.08% and 0.1% Ultrez solution may not have sufficient yield stress effect on power law based shape factor formula. Therefore the plot in Figure 65 to Figure 67 showed significant amount of similarities.

6.2.2 Entrance length debate

In the first phase of experiment, it was conducted in a 2 m long semi-circular channel. However, there is little information in the literature concerning turbulent entrance length for non-Newtonian fluid. Here, three different calculations were used to show the desirable entrance length for this experiment.

In Laufer (1952), the author worked on turbulent pipe flow and claimed that full flow development is at a length of 30 diameters based on "the measured mean velocity distribution" (p.421). Similarly, in Nikuradse (1966)'s paper, he concluded from a comparison of mean velocity profiles at successive streamwise lengths, that the flow was fully developed by 40 diameters.

In Lien *et al* (2004), the authors investigated fully developed turbulent flow in a smooth channel. It was estimated by Lien *et al* (2004) that the minimum length of 130h (h denote channel height) is required for flow to become constant with streamwise direction. However, the authors used air as the testing material in experimental channels.

Colwell and Shook (1988) presented a study of entrance length for sand slurries in pipelines. It was found that the entrance length required for horizontal turbulent slurry flow to become fully developed is around 50 pipe diameters for sand slurries. It was also found that with a high particle settling velocities; it requires shorter entrance lengths than that for intermediate settling velocities.

The most related paper for an effective entrance length is that of Shenoy and Mashelkar (1983). The authors proposed a design equation for estimating the turbulent entrance lengths for non-Newtonian fluids.

$$\frac{x_e}{D}\left[\frac{\psi_1}{(1+\beta_s n)\alpha_s \psi^2}\right]\mathrm{Re}^{\beta_s} \tag{75}$$

Where

$$\psi = \frac{[2-\beta_s(2-n)][2-\beta_s(2-n)]}{[1-\beta_s(1-n)][4-\beta_s(4-3n)]} \tag{76}$$

And

$$\psi_1 = \frac{[2-\beta_s(2-n)]}{[2-2\beta_s(1-n)]} - \frac{[2-\beta_s(2-n)]}{[2-\beta_s(2-3n)]} \tag{77}$$

In this case, $\alpha_s = 0.079$ and $\beta_s = 0.25$. And n is the flow behaviour index.

For all the entrance length calculations, R_h is used instead of diameter of pipe. Geometric conversion of $D = 4\ R_h$ is applied to all the calculations. $R_h = 0.0311$ for the first phase experiment. Reynolds number is calculated by equation (21)

Table 14 Summarised table for entrance length

	Calculated Entrance length
Laufer (1952)	3.73 m
Nikuradse (1966)	4.98 m
Colewell and Shook (1988)	6.22 m
Lien *et al* (2004)	7.15 m

Table 15 Entrance length calculated by Shenoy and Mashelkar (1983) equation

Reynolds number	Xe/D	Xe (m)
4000	10.09	1.25
4400	10.33	1.28
4840	10.58	1.31
5324	10.53	1.34
5856	11.10	1.38
6442	11.36	1.41
7086	11.64	1.45
7794	11.92	1.48
8574	12.21	1.52

Table 16 Entrance length calculated by Shenoy and Mashelkar (1983) equation

n **(Flow behaviour index)**	**Xe/D**	**Xe (m)**
0.50	7.96	0.99
0.55	8.61	1.07
0.61	9.30	1.15
0.67	10.02	1.27
0.73	10.77	1.34
0.81	11.57	1.44
0.88	12.40	1.54
0.97	13.26	1.65

Table 14 shows the calculated entrance length for this experiment with different methods. It is seen that by Laufer (1952) method, the entrance length needs to be 3.73 m and by Lien *et al* (2004) method; the entrance length needs to be at least 7.15 m. It is very surprising to see the large differences between the results. It is interesting to see that Shenoy and Mashelkar (1983) equation is Reynolds number and flow behaviour index dependent. Therefore in this investigation, Reynolds number and flow behaviour indices were varied in order to examine the full effect of these variables. Table 15 presents the calculated entrance length by Shenoy

and Mashelkar (1983)'s method. Reynolds number was calculated by equation (20). Table 16 presents similar information, the only difference is that Table 16's entrance lengths were calculated by a fixed Reynolds number of 4000 and different *n* values. It was found that the entrance length calculated by Shenoy and Mashelkar (1983) equation is sensitive to flow behaviour index of the fluid. When *n* increases by 10%, the entrance length would increase by 7-8%. However, when *n* approaches 1, the entrance length increases by a slightly smaller percentage. For example, when *n* increases from 0.5 to 0.55, the entrance length increases from 0.99 m to 1.07 m, that is around 8%. When *n* increases from 0.88 to 0.97, the entrance length increases from 1.54 m to 1.65 m, that is an increase of 7.1%. If there is a change in Reynolds number, the entrance length would change as well. In general, when Reynolds number increases by 10%, the entrance length increases about 2.4% with a fixed flow behaviour index *n*.

The length of the semi-circular channel used in the experiment is 2 metres. With the flow condition and rheology measurement, the entrance length calculated by Shenoy and Mashelkar (1982)'s equation is around 1.05 m. If the exit length in the flume is assumed to be equal to the entrance length, then the 2 metres long flume is extremely marginal for the experiment.

This analysis shows that entrance length of flume calculation varies significantly. Yet, there is a distinct scarcity of thorough investigations on the minimum entrance length of fully developed channel flow. Future investigation on this particular subject is much encouraged.

6.3 Experimental results

6.3.1 Presentation of initial results

This section will present the results obtained at CSIRO Highett lab where the first phase of experimental program took place. The amount of data obtained from ADV measurement is quite extensive. A number of figures have been plotted. The presentation and analysis of these data and some of these figures are given in this section. All the velocity measurements were collected with 4.70% slope.

6.3.1.1 Velocity measurements

Figure 69 shows the velocity against depth plot for measurement of 1405 (refer to Table 5) and 1705 at cross section of the channel. It can be seen that the velocity profiles are quite similar with the same flow rate. Figure 70 shows the rheogram for the solutions 1405 and 1705. It is seen that the 1705 solution had a lower viscosity compare to 1405 solution. There is a slight inconsistency in the rheogram at the high shear rate region. This could be caused by slippage at the high shear rate. Figure 69 also reflected the velocities for 1405 were about 15% less than 1705's velocity measurement at given height.

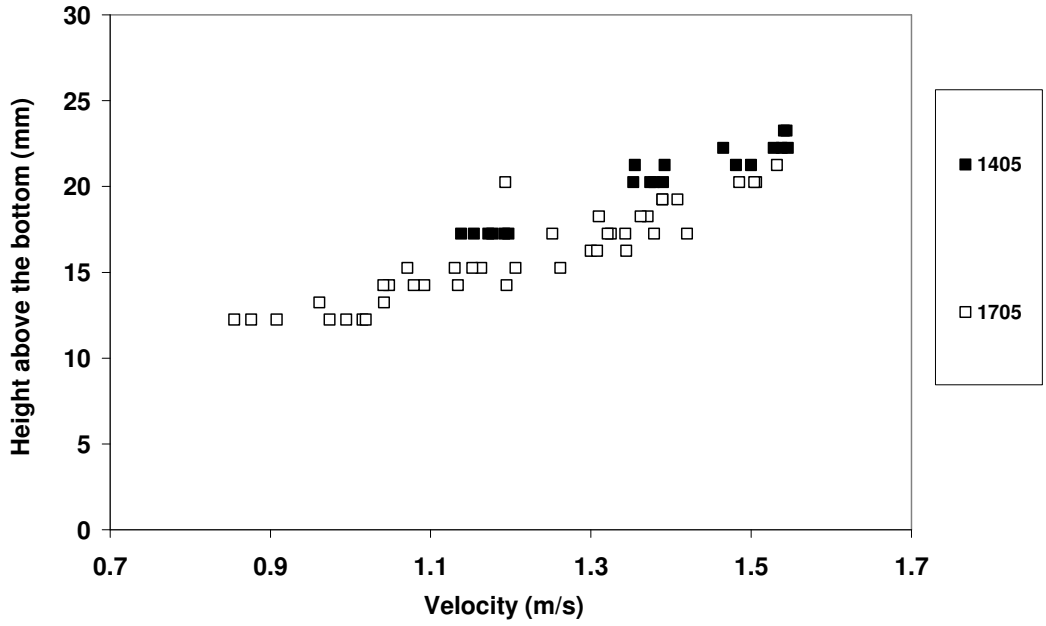

Figure 69 Velocity against depth plot at centreline of the channel for fluid samples 1405 and 1705 with slope equals 4.70%

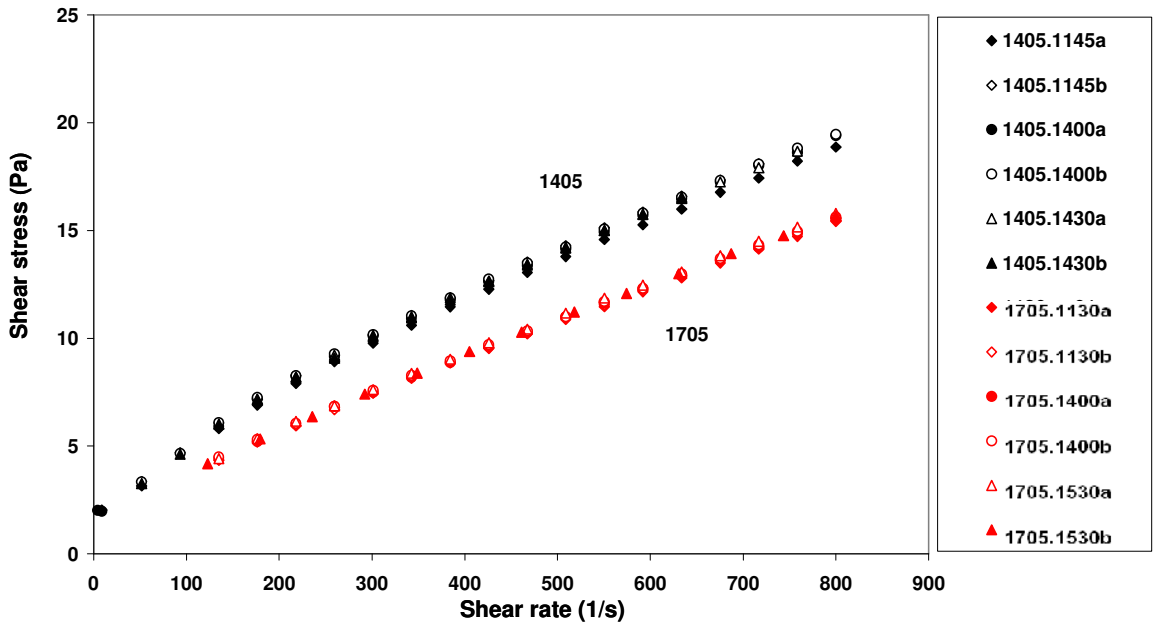

Figure 70 Rheogram for test samples 1405 and 1705 CMC solution at 18°C

Figure 71 shows the centreline velocity against depth plot for CMC solution (Test number. 1405, 1705 and 1805) at open channel cross section. It is seen that most of the velocities collapsed on a similar curve with small variation between them. In general, 1405 solution has a slight lower velocity than the other two solutions. From Figure 72, it is easy to see that the solutions viscosity slowly reduced with time over a scale of day. It is believed that some difference of solution viscosities might have contributed to the fluctuations in velocity measurements in Figure 71.

Figure 73 shows the velocity against normalised depth plot with different flow rates. The depths are normalised by maximum depth. It reinforces that higher flow rate causes a higher average velocity in the channel. One of the interesting aspects of the data in Figure 73 is that for 7 l/s flow rate, the velocities are lower than those for 8.5 l/s and 10 l/s. Whereas for flow rates of 8.5 l/s and 10 l/s, the difference in velocity profiles was less pronounced. The Reynolds number is then calculated for these three different flow rates. Reynolds numbers for 7 l/s, 8.5 l/s and 10 l/s flow rate are 3975, 4068 and 4325 respectively.

Further tests were conducted to see whether the flow is symmetrical in the channel. A number of measurements were recorded at different spanwise positions with a slope of 4.70% and flow rate at 7.30-7.50 l/s. The position for this measurement was 30 mm from the centreline of the channel. The exact distance was used to measure on both left and right side of the centreline. From Figure 74 it is interesting to see that there is not a vast difference between the different measurements from either left or right side from the channel centreline. The size of the velocimeter's transmit transducer prevented velocity measurement from being taken within about 50 mm of the boundaries of the half pipe. Therefore it was quite difficult to take any other measurements at a various spanwise positions.

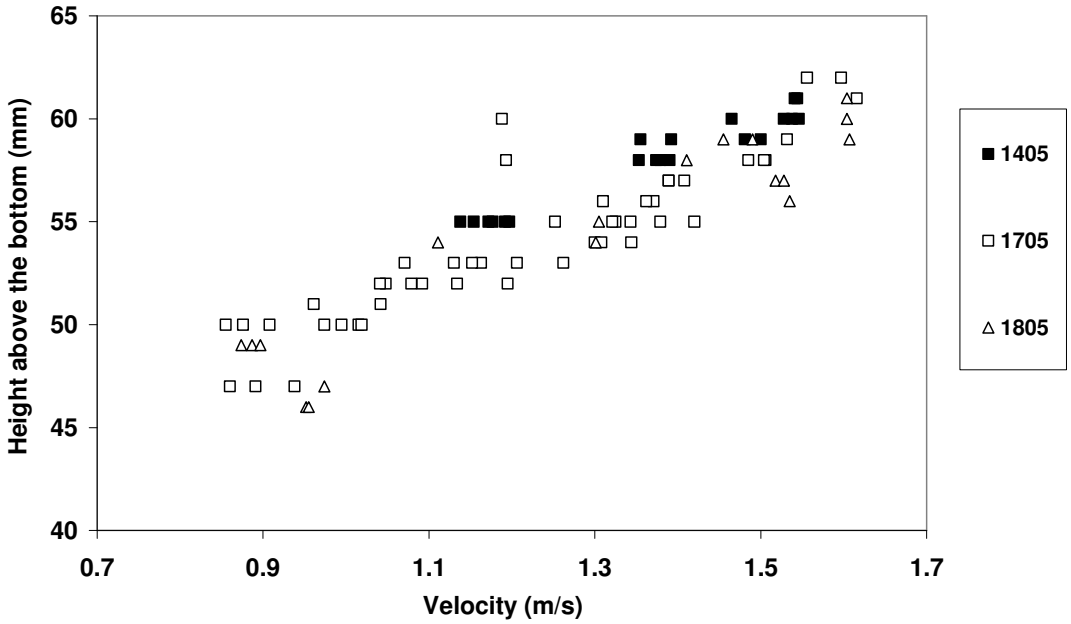

Figure 71 Velocity against depth plot at centreline of the channel for test samples 1405, 1705 and 1805 with slope equals 4.70%

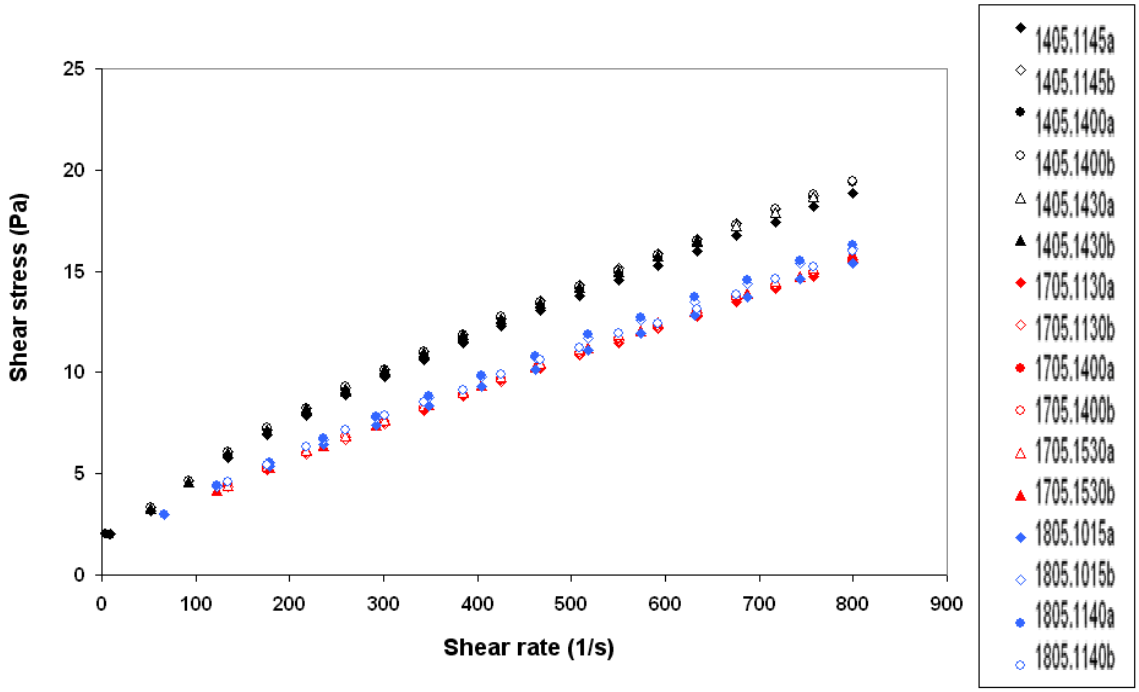

Figure 72 Rheogram for test samples 1405, 1705 and 1805 CMC solutions

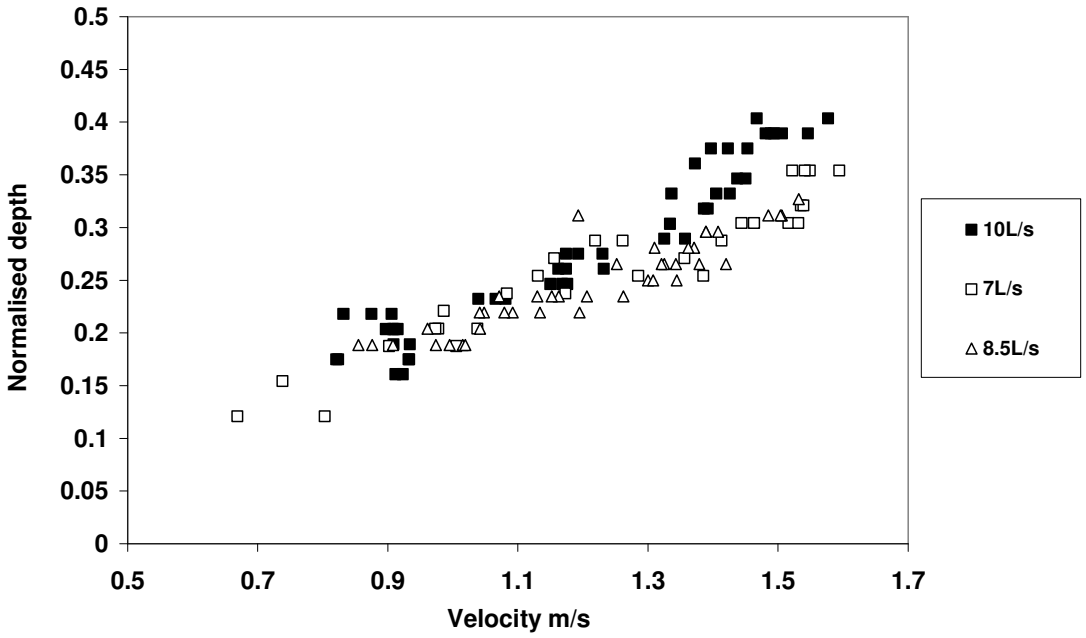

Figure 73 Velocity against normalised depth plot at centreline of the channel at different flow rate with slope equals 4.70%

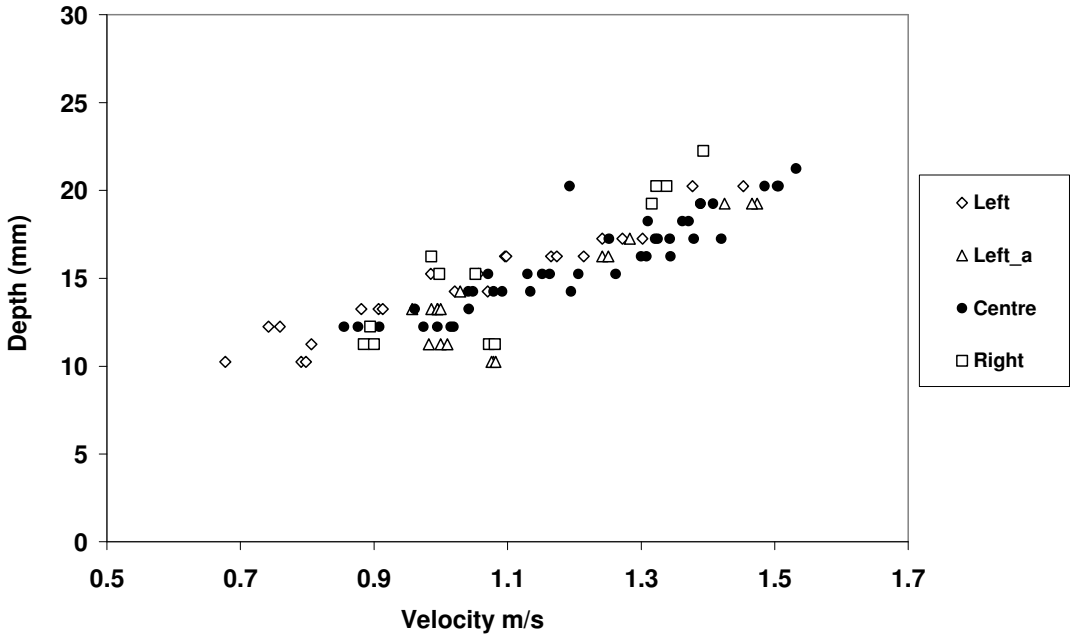

Figure 74 Velocity against depth plot at different positions of the channel with slope equals 4.70%

6.3.1.2 Summary of initial observations

From the above results, the discussion can be summarised as follows:

- With change in rheological parameters (thus a change in viscosity), the velocity profile will change. Increase in viscosity shows a slight decrease in velocity, decrease in viscosity shows an increase in velocity. This means rheology of the fluid is important in order to study turbulent behaviour in open channel flows.
- Figure 71 shows the velocity profile for solutions with different rheological parameters. It is interesting to see that the differences between the velocities are minimal for the different rheological parameters. It suggests that even when viscosity has changed by 15-20%, there has not been a significant change in velocity profile.
- With different flow rate, the velocity profile does not shift noticeably. The main reason for this is a minimum change in Reynolds number. It is shown earlier that Reynolds numbers for 7 l/s, 8.5 l/s and 10 l/s flow rate are 3975, 4068 and 4325 respectively.

- The flume's velocity at different spanwise position seemed to be symmetrical. A number of measurements were recorded at different positions. From Figure 74 it is seen that there is not a large difference between the different measurements. Due to the limitation of velocimeter and flume size, it was very hard to take velocity measurement at other spanwise positions.
- It was mentioned in the previous sections that there are limitations with the Vectrino acoustic Doppler velocimeter. Due to the velocity probe's limitations, the velocity probe's transmitter position needs to be at least 50 mm from the bottom of the flume. This was noticed in the initial water testing in the rectangular shaped flume. The depth of the rectangular flume is 154 mm yet the velocity measurement can only reach 100 mm. However in the semi-circular flume, the maximum depth of flow is only 70 mm. This means that to measure velocity very close to the wall, the velocimeter needs to be placed at least 50 mm from the channel wall. Therefore, the maximum vertical movement allowed for the velocimeter was 20 mm.
- Figure 75 shows the initial experimental measurements together with measurement data from Fitton (2007)'s experiment. From the plot, it's apparent that current measurement only covers a small range of the velocity profile. With Fitton (2007) measurements, a full velocity profile could be established.
- There was a considerable amount of air bubbles presented in the fluid. In the downstream end, when the fluid was pouring from flume into the holding tank, the splashing would create a lot air bubbles over time (Figure 76). When the air bubbles reached a certain concentration, the fluid turned from transparent to unclear (Figure 77). There is no easy method to totally eliminate the air bubbles. Usually when the flow rate equals to more than 3 l/s, the fluid would start to splash at downstream. The only possible way to eliminate some of the air bubbles is to fill the system up with large volume of fluid so the fluid in the holding tank would cover the flume's outlet in order to avoid splashing. This method was then implemented; however, the effect of elimination of air bubbles was minimal.

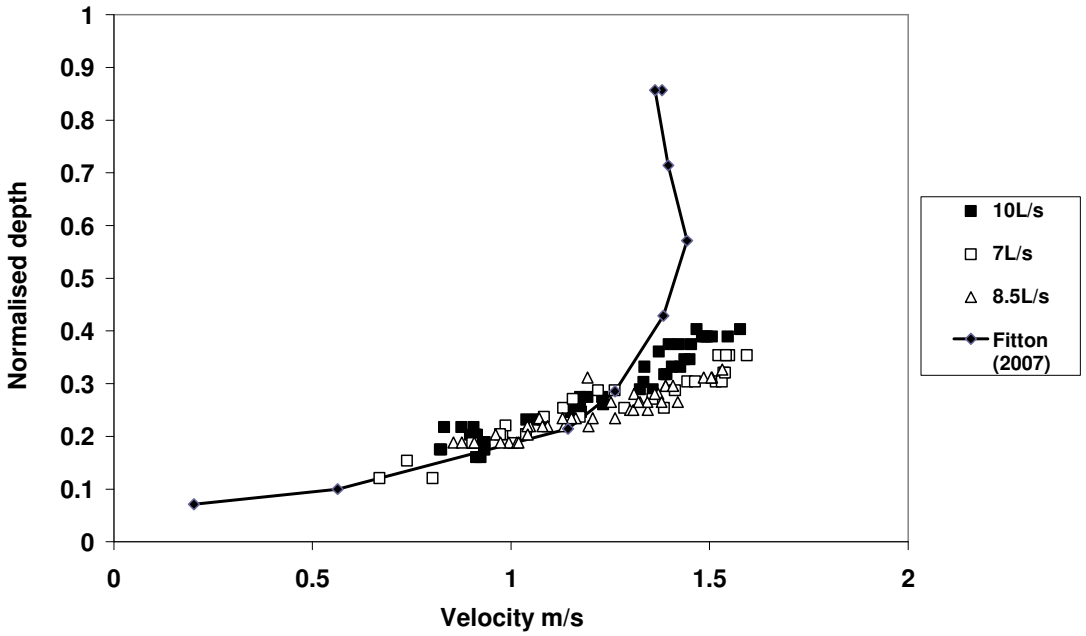

Figure 75 Velocity against depth plot at centreline of the channel for test samples 1405, 1705, 1805 and 2405 CMC solution with experimental data of Fitton (2007)

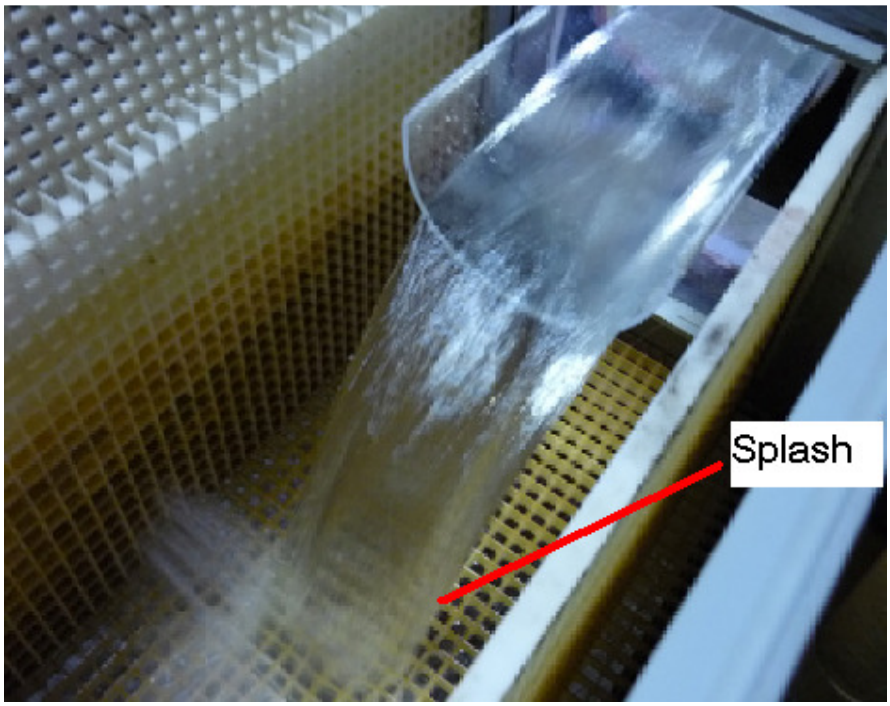

Figure 76 Splashing at downstream end of the experiment setup

Figure 77 Air bubbles caused unclearness in the fluid

6.4 Validation of Simulation results

6.4.1 Use of previous experimental data (Fitton, 2007)

Due to the limited range of data gathered from the experimental programme discussed above, a set of available data based on channel flow was chosen as simulation validation parameter. The experimental data were taken by a former RMIT PhD student, Tim Fitton in 2004. The experiment was conducted at the Sunrise Dam Gold Mine, in Western Australia. The experimental set up consisted of a flume channel of 340 mm internal diameter with semi-circular cross section. The tailings slurry was supplied to the plunge box which was located at the upstream end through a 150 mm HDPE pipe with an outlet 20 cm above the plunge box floor. A diaphragm valve was installed in the pipe to adjust the flow rate of the tailing. Further details of this experiment and associated instrumentation are given in Fitton (2007).

Rheometric analysis was performed on samples of the mineral slurries at different concentrations to determine its rheological parameters. This enabled the fitting of a Herschel-Bulkley rheological model. Rheological parameters based on the experimental data were used in the simulation. The modelling presented in the next section has been compared with experimental work presented by Fitton (2007)

6.4.2 Initial results

The simulation was originally designed to allow comparison to experiments undertaken in Fitton (2007) and the parameters were chosen to match with previous experiments. In this study, the computational domain consists of 51 fifteenth order elements in the channel cross section and 384 Fourier modes in the axial direction, with domain lengths of $0.5\pi D$. The reason for choosing a small domain length is because with a longer domain length and current number of planes (384) the simulation time would be too great. A larger number of z planes can increase the resolution of the contour thus the observation of the result become a lot easier. Therefore the domain length has been shortened to meet the demand of number of z planes. This is the summary of simulation parameter. This particular set of data was chosen because of the completeness of the data range and the quality of the data.

Table 17 Parameters for simulation 1

Model	n	K(Pa.s^n)	τ_y (Pa)	$\delta p/\delta z$	Length	Modes
Herschel-Bulkley	0.81	0.0506	2.249	0.147	$0.5\pi D$	384

In terms of wall units, the near-wall mesh spacing is $y^+ \approx 4.1$, $\theta^+ \approx 16$, and $z^+ \approx 25$. This resolution is quite marginal in y^+ and z^+. In Rudman *et al* (2004), the authors suggested that significantly increasing the streamwise resolution had little effect on the turbulence statistics. However, it would be interesting to see if y^+ can be reduced in future studies.

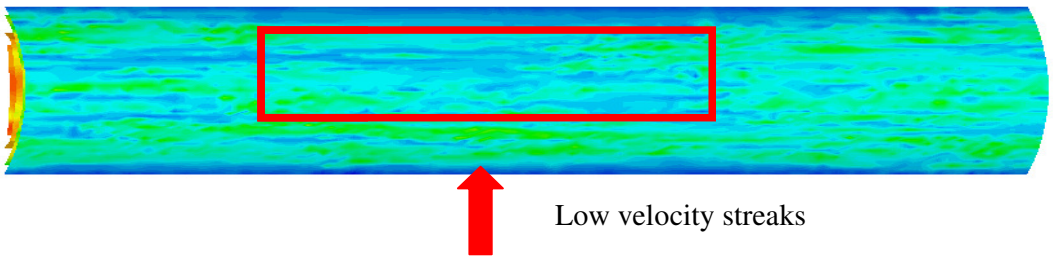

Figure 78 Near wall structure revealed in contours of streamwise velocity, red shows high velocity regions, blue shows low velocity regions

The average velocity calculated from the experiment is 1.06 m/s according to Fitton (2007). Based on the simulation, the average velocity for the channel flow is 1.39 m/s. The differences may be due to experimental error. With approximately 15% error of the flow

measurement from them (Fitton, 2007), the measured average velocity can go up to 1.355 m/s.

The simulated near wall structure of the channel flow is shown in Figure 78. The above diagram showed some wall streaks near bottom of the channel. The question needs to be answered is how may the wall structure have significant impact on particle transportation.

6.4.3 Velocity distribution

The instantaneous point velocity from the centreline is investigated to validate the computational method. In Figure 79, the plot represents velocity against depth along the centre line of the channel for the field experimental data from Fitton (2007). The depth measurement starts from 0 mm at the surface to 70 mm at the bottom of the channel. In Figure 79 depth starts from -0.34 m, that is 0.34 m below half of the channel height. The bottom of the channel is at -0.41 m which means the actual depth of the channel flow is still 70 mm overall. The field data shows a maximum velocity of 1.65 m/s at the channel surface. Whereas the simulation data shows around a maximum velocity of 1.80 m/s at the surface. The difference between the velocities could be caused by measurement error from the field experiment. Yet, both plots demonstrate similar pattern except for the small bend towards to the channel surface. More discussion on secondary current will be presented in the following sections. Thus, it is suggested that simulation and field experiment are of the same order of magnitude and it provided some agreement between the two results.

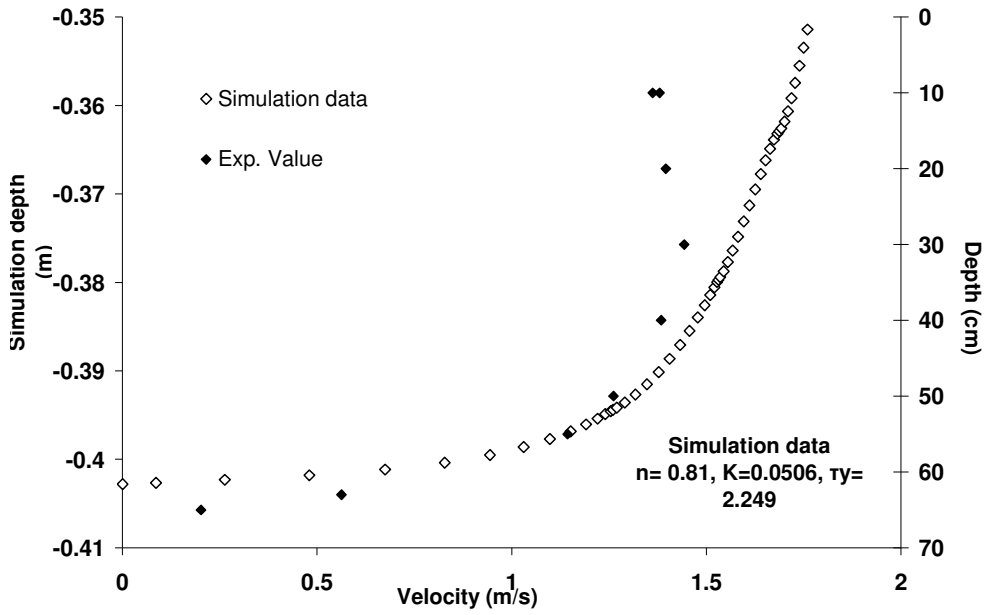

Figure 79 Instantaneous point velocity at the centre line of the channel

The velocity is then non-dimensionalised using the wall viscosity (equation (10)). The wall viscosity is calculated by wall shear stress. The wall shear stress is found from:

$$\tau_w = g \cdot \rho \cdot \sin\theta \cdot R_h \qquad \textbf{(10)}$$

In this case, the logarithmic profile used for the plot is:

$$U^+ = 5.5 + 2.5 \ln y^+ \qquad \textbf{(78)}$$

The mean axial velocity data at the centreline for the slurry is presented in Figure 80, in wall units, together with the logarithmic velocity profile. The experimentally measured velocity profile has a linear relationship between U^+ and y^+ in the near wall region. In the logarithmic region, the actual velocity profile for the slurry is slightly higher than the logarithmic velocity profile. At the free surface region, the measured velocity profile declined after a maximum. According to Joung *et al* (2007) and Nezu (2005), this could be concluded as a secondary flow effect where the lower velocity/momentum fluid has been dumped into the high velocity/momentum region. Therefore there is a dip in the axial velocity profile after maximum velocity has been reached. This happens regularly in non circular channel flow. It

is also suggested by Nezu and Nakagawa (1993) that this phenomenon is called the "velocity-dip", and it is peculiar to open channel flows.

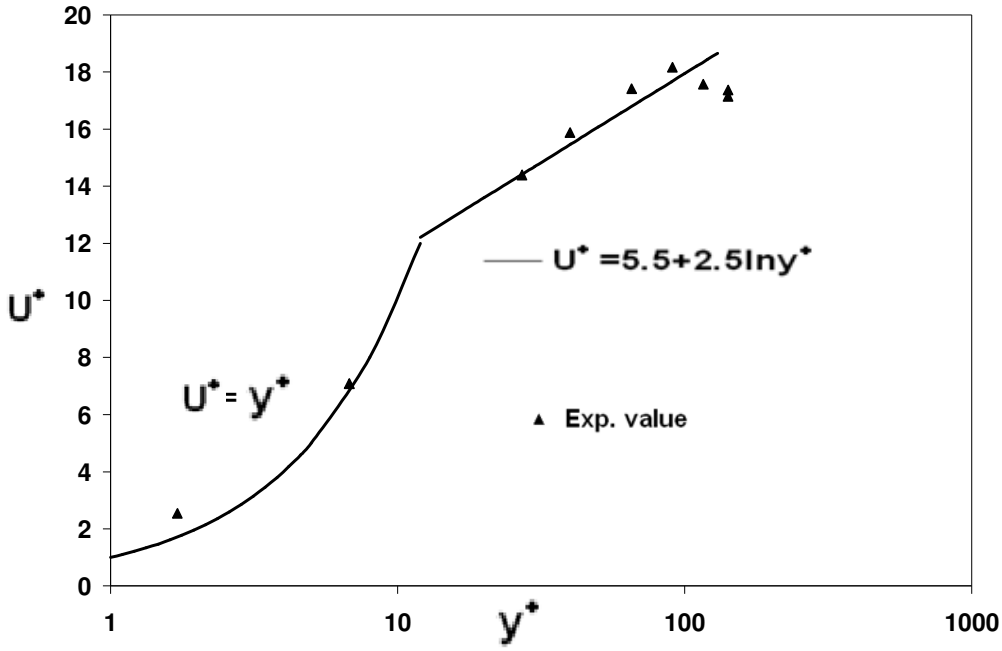

Figure 80 Experimentally measured velocity profile for slurry Fitton (2007).

The computationally predicted profile for the control Simulation at Reynolds number = 8182 is presented in Figure 81. The velocities have been non-dimensionalised. The non-dimensionalisation is undertaken using the wall viscosity give in equation (71). All profiles have a linear relationship between U^+ and y^+ in the near wall region. It is seen that some disagreements between simulation and measurement do exist. Not only is the predicted average bulk velocity is approximately 39% higher than experimental, but the velocity profile has somewhat different shape to the experimental profiles. The simulation profile and experimental profile have the same magnitude in the near wall region. In the free surface region, the simulation profile does not show any velocity dip.

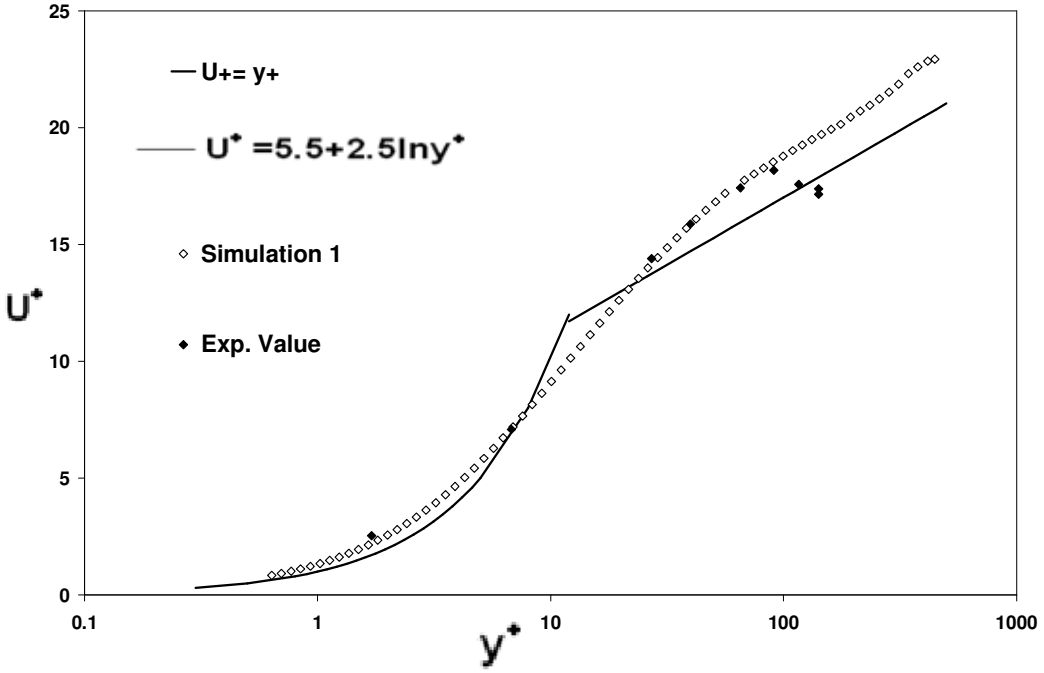

Figure 81 Experimentally measured velocity profile in conventional wall units for slurry in comparison of Simulation results

The next section will evaluate the data compiled for this thesis using the velocity profiles found in the literature review section.

6.4.3.1 Coles wake function (1956)

In Coles (1956) it was said that the log law equation (78) is only valid for the wall regions. The deviation of the velocity distribution in the outer region of open channel flows from the log-law can be accounted by adding a wake function.

$$U^+ = \frac{1}{k}\ln y^+ + A + w(\xi) \text{ with } w(\xi) = \frac{2\Pi}{k}\sin^2\left(\frac{\pi}{2}\xi\right) \quad \textbf{(38)}$$

Where $w(\xi)$ accounts for the deviation and termed the wake function, and Π is termed the Coles wake strength parameter. It was previously mentioned that Π is about zero at low Reynolds number < 500. At small values of *Re* but greater than 500, Π increases rapidly with Reynolds number *Re* and it remains nearly constant, i.e. Π =0.2 for *Re* > 2000. In this case, Π = 0.2 is used as the Reynolds number is well exceeding 2000.

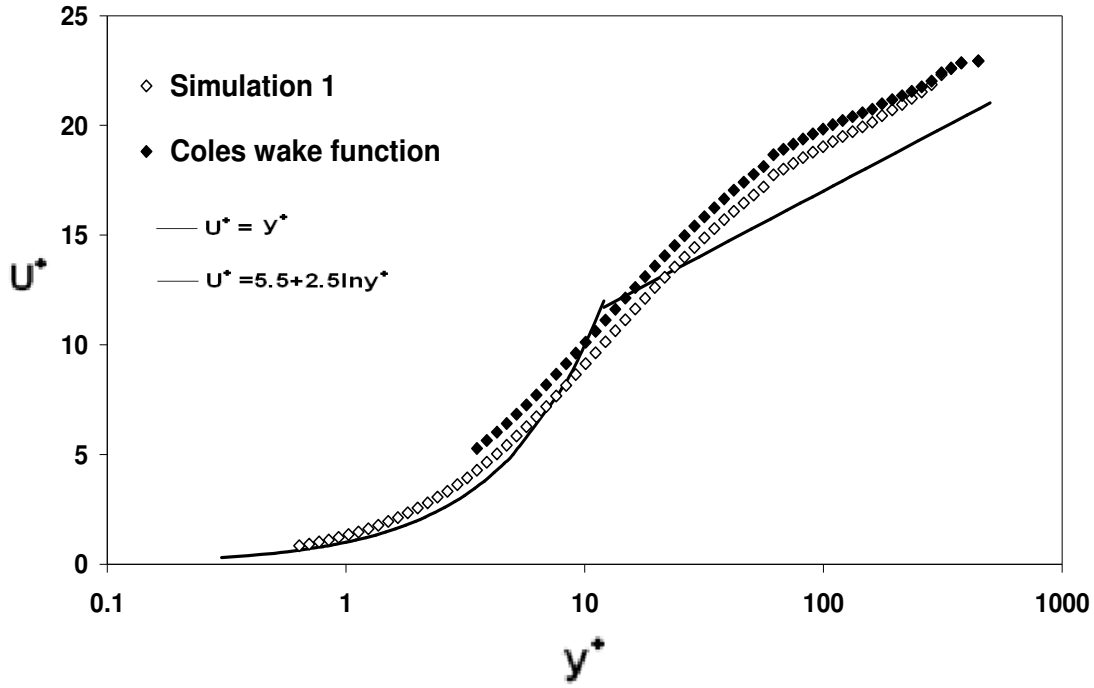

Figure 82 Simulation velocity profile in conventional wall units for slurry in comparison of Simulation results with Coles wake function

Figure 82 shows the Coles wake function from $y^+ > 5$. The wake function plot shows almost identical curvature when compared to the simulation velocity profile. Coles wake function plot is generally moving away from the logarithmic profile. This behaviour is also observed in Figure 83. From Figure 82 it shows that the Coles wake function overestimate the velocity slightly then converges with the simulation velocity profile at around $y^+ = 257$. There is a slight curvature towards $y^+ > 300$ from both the simulation profile and the wake function plot (Figure 83 and Figure 84). The magnitude of the curvature is very similar for both plots. This could be a presentation of very small secondary current but the magnitude of this small curvature is nothing compared to the visible experimental secondary current presented in Figure 81. It is certainly of interest to note that the simulation result suits quite well with Coles wake function in the outer region of the velocity profile plot. With the limited suitability of logarithmic velocity profiles, Coles wake function could be a better indication for channel flows. Despite the fact that the Coles wake function is used in water flows, it is observed here that the wake function also suits the outer region of non-Newtonian flow.

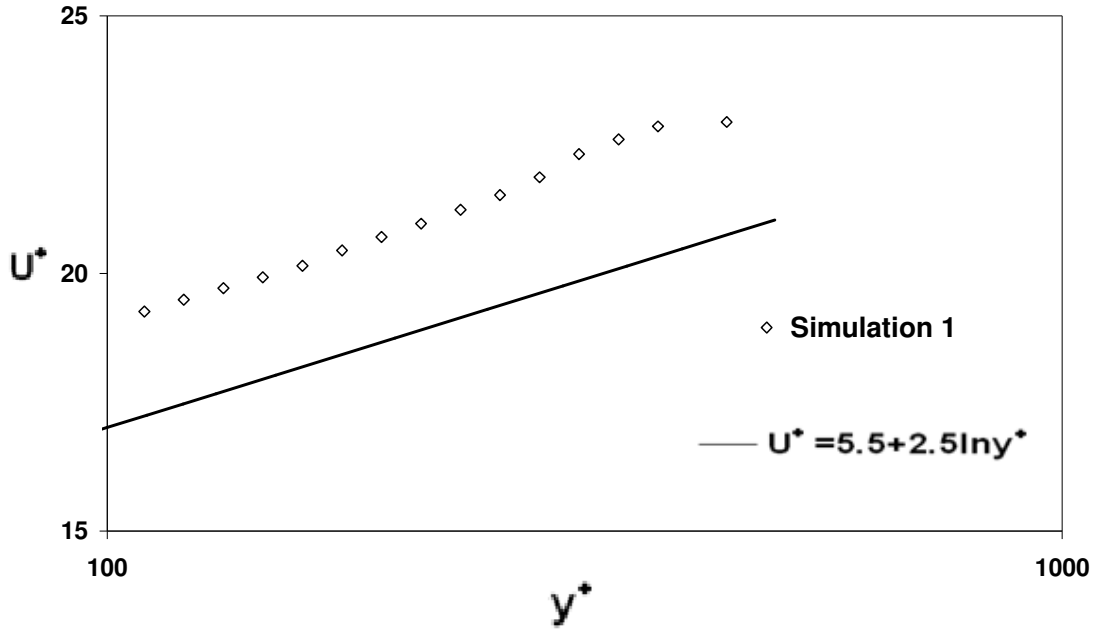

Figure 83 Enlarged plot for Simulation velocity profile in conventional wall units for slurry

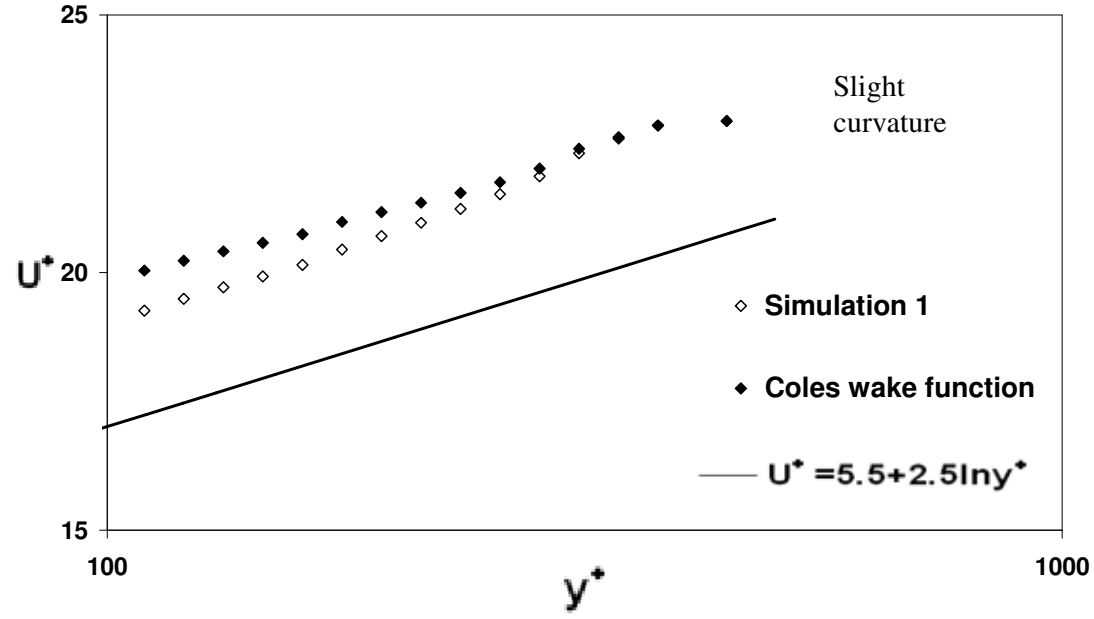

Figure 84 Enlarged plot for Simulation velocity profile in conventional wall units for slurry in comparison of Simulation results with Coles wake function

6.4.3.2 Clapp's velocity profile (1961)

Clapp (1961) reports the results of experimental measurements of the turbulent pipe flow of power law fluids with flow indices in the range of 0.698-0.813. Clapp determines that the logarithmic velocity profile for the turbulent flow of power law fluids is a function of the flow index, *n*, and satisfies

$$U^+ = \frac{A}{n} + \frac{B}{n}\ln y^+ \quad \textbf{(79)}$$

According to Clapp (1961), following the accepted division of turbulent flow of Newtonian fluids into three different regions, the laminar sublayer, the buffer layer and the turbulent core, the following equations and their limits are obtained for non-Newtonian fluid.

Viscous sublayer $$U^+ = \left(y^+\right)^{1/n},\ 0 < y^+ < 5^n \quad \textbf{(34)}$$

Buffer sublayer $$U^+ = \frac{5}{n}\ln y^+ - 3.05,\ 5^n < y^+ < y^+_2 \quad \textbf{(35)}$$

Turbulent layer $$U^+ = \frac{G}{n}\ln y^+ + H,\ y^+ > y^+_2 \quad \textbf{(36)}$$

Where *n* is the flow index, and *G* and *H* are empirical constants to be obtained. By Clapp's investigation, *G* and *H* are 2.78 and 3.8 respectively. y^+_2 = 30 is used for Clapp's (1961) paper; therefore it is also used in this calculation.

Using Clapp's velocity distribution equation and experimental rheology parameters, a new velocity profile is presented in Figure 85 with the mean axial velocity for the simulation. The simulation velocity profile is plotted with wall viscosity non-dimensionalisation. The simulation velocity profile showed reasonable agreement in term of overall shape. It is quite easy to distinguish all three separate regions i.e. laminar sublayer, buffer layer and turbulent core. In the laminar sublayer, the non-dimensionalised simulation velocity profile is a good fit to logarithmic profile. However, the velocity distribution curves in the buffer layer and turbulent core are much higher than the simulation data. Moreover, this velocity profile is based mainly on pipe experimental results. Therefore no secondary current related feature is considered in the velocity distribution equation. Lastly, Clapp (1961) only incorporated *n,* the flow behaviour index into the velocity distribution equations as the author only tested power

law fluids. In fact, it is expected that the yield stress of a non-Newtonian fluid will have some impact on velocity distribution.

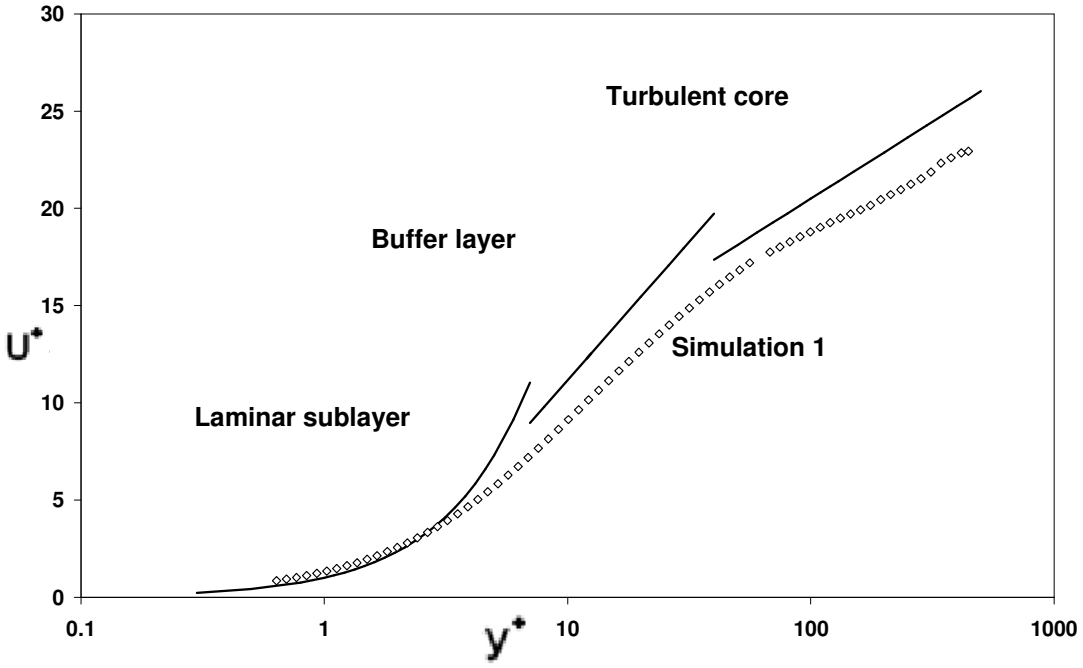

Figure 85 Simulation velocity profile in conventional wall units for slurry in comparison of Simulation results with Clapp's velocity distribution equation

6.4.3.3 Use of Yalin's roughness height k_s (1977)

In different pipe and channel flows, for a smooth surface, the no-slip condition requires that the relative velocity of the fluid at the surface of the pipe/channel to be zero. For a rough surface, the extension of the roughness elements into the flow complicates the interaction with the surface. A simplistic way to treat fully rough boundary layers is to replace the viscous length scale of the smooth wall with the mean roughness height, k_s. The mean velocity profile in the overlap region then becomes:

$$U^+ = \frac{1}{k}\ln\frac{y}{k_s} + B_s \qquad (80)$$

Yalin (1977) introduced a set velocity distribution equation in turbulent flow with roughness of the channel considered. The author stated that:

- if $U^* k_s/\upsilon < \approx 5$, then the velocity distribution is

$$U^+ = \frac{1}{k}\ln\frac{y}{k_s} + B_s,\ B_s = 2.5\ln\frac{U^* k_s}{\nu} + 5.5 \quad \textbf{(42)}$$

- if $U^* k_s/\upsilon > \approx 70$, then the velocity distribution is

$$U^+ = \frac{1}{k}\ln\frac{y}{k_s} + B_s,\ B_s = 8.5 \quad \textbf{(43)}$$

Where k_s is Nikuradse's original uniform sand grain roughness factor; it represents the equivalent sand roughness for any type of rough surface. B_s is a dimensionless property of the flow in the vicinity of the bed.

In an open channel, especially in a self formed open channel, the channel has been eroded into a deposit of tailings. The roughness of the channel boundaries must be defined by the size of the grains in the channel bed material. Abulnaga (2002) mentioned that k_s in an open channel is equal to twice the grain diameter. Ikeda *et al* (1988) also stated an approximation for k_s as equal to $1.5 \times d_{90}$. In Yalin (1977); the author used the absolute size of the grain for k_s. Therefore, in this investigation, the following value will be used for the roughness k_s. k_s is calculated using the particle characteristic from Fitton (2007).

- $k_s = d_{50} = 14$ μm
- $k_s = 2 \times d_{50} = 28$ μm
- $k_s = d_{90} = 170$ μm
- $k_s = 1.5 \times d_{90} = 255$ μm
- $k_s = 2 \times d_{90} = 340$ μm

With B_s less than 5, equation (42) was used to create the velocity profiles in Figure 86. The mean velocity profiles in outer coordinates and normalised by the friction velocity are shown in Figure 86. This shows a simulation velocity profile and velocity profiles with roughness considered. For the simulation results, no roughness value was used. All the other velocity profile with roughness value considered exhibit downward shift with respect to the log law. This finding is very similar to the work done by Bergstrom *et al* (2002) which involves air flow in a wind tunnel. $k_s = d_{50}$ shows the smallest shift from the simulation data while $k_s = 2 \times d_{90}$ shows the highest roughness shift. Therefore it is concluded that the roughness of the

channel does have an effect on mean velocity profile. The roughness effects actually penetrate into the overlap region, and the outer region velocity profile suggests that the turbulence model for rough wall flows needs to incorporate the effects of roughness at the surface. However, due to data limitation, the results presented here only show the same specific roughness geometry (shape) and same roughness conditions.

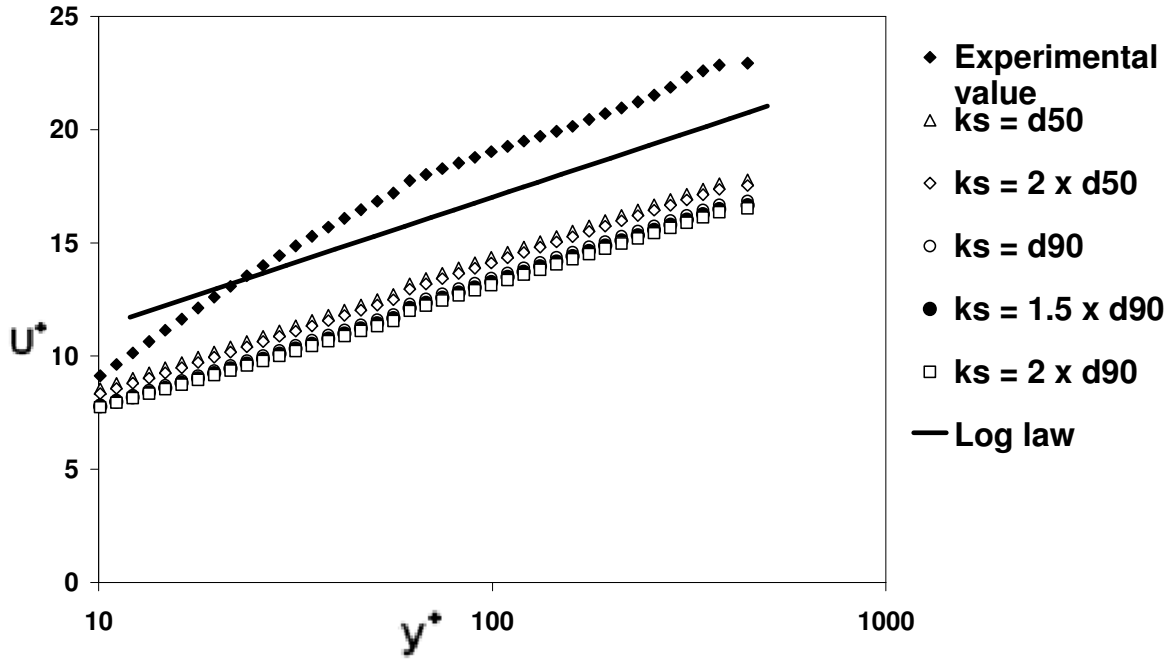

Figure 86 Simulation mean velocity profile with different roughness value

6.4.3.4 Barenblatt's Power law profile (1993)

Barenblatt (1993) introduced a specific power law for the velocity profile in pipe flow. These equations are presented in chapter 2 as equations (39) to (41) and are repeated below:

$$U^+ = Ay^{+\alpha} \tag{39}$$

$$A(\mathrm{Re}_d) = \frac{5}{2} + \frac{1}{\sqrt{3}}\ln \mathrm{Re}_d \tag{40}$$

$$\alpha(\mathrm{Re}_d) = \frac{3}{2\ln \mathrm{Re}_d} \tag{41}$$

Where $Re_d = Vd/\upsilon$. The Re_d is based on the average pipe velocity V and the pipe diameter d = 2R. For open channel flow, the hydraulic radius is used to replace the pipe diameter in the equations. In this case, the Reynolds number used in equation (40) and (41) is based on equation (22). From the calculation, A = 7.70 and α = 0.166. The velocity profile is then compared with the simulation profile as well as the conventional logarithmic velocity profile. From Figure 87 it is of interest to note that the power law velocity profile in the overlap region and turbulent region is very similar to the logarithmic law. The power law profile is slightly curved and positioned below the simulation velocity profile. The outer region of the conventional logarithmic velocity profile almost overlaps with power law profile.

It is found that the value of α decrease with increasing Reynolds number. However, even with a large increase in Reynolds number, the velocity profile does not shift significantly. Figure 88 shows the simulation results with different yield stresses. Reynolds numbers for +50% yield stress simulation and -50% yield stress simulation are 6481 and 9258 respectively. As yield stress τ_y increases, the velocity profiles for the simulation are moving away from the logarithmic profile. Power law profiles for these two different simulations are also drawn in the same graph. The power law profiles are almost identical for these two different flows with quite different Reynolds number 6481 and 9258. It is suspected that this power law velocity profile is not very sensitive to change of rheological parameters. The power law profile gives quite accurate results for turbulent flow through a pipe. However, it may not be appropriate for non-Newtonian open channel flow.

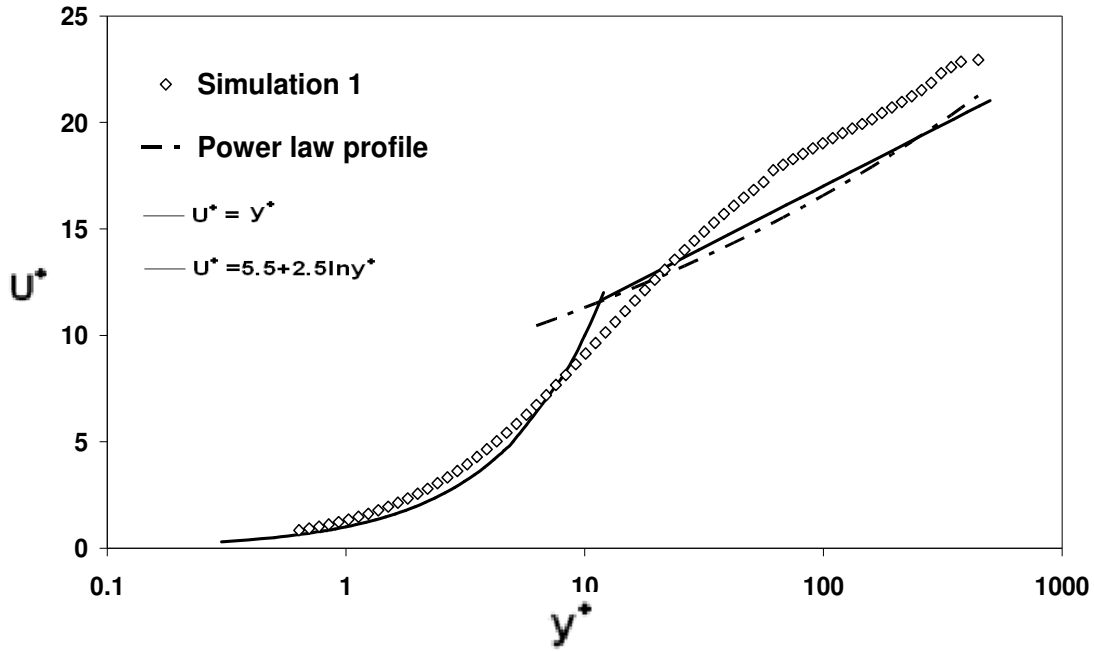

Figure 87 Simulation velocity profile in conventional wall units for slurry in comparison to Simulation results with Barenblatt (1993)'s power law velocity profile

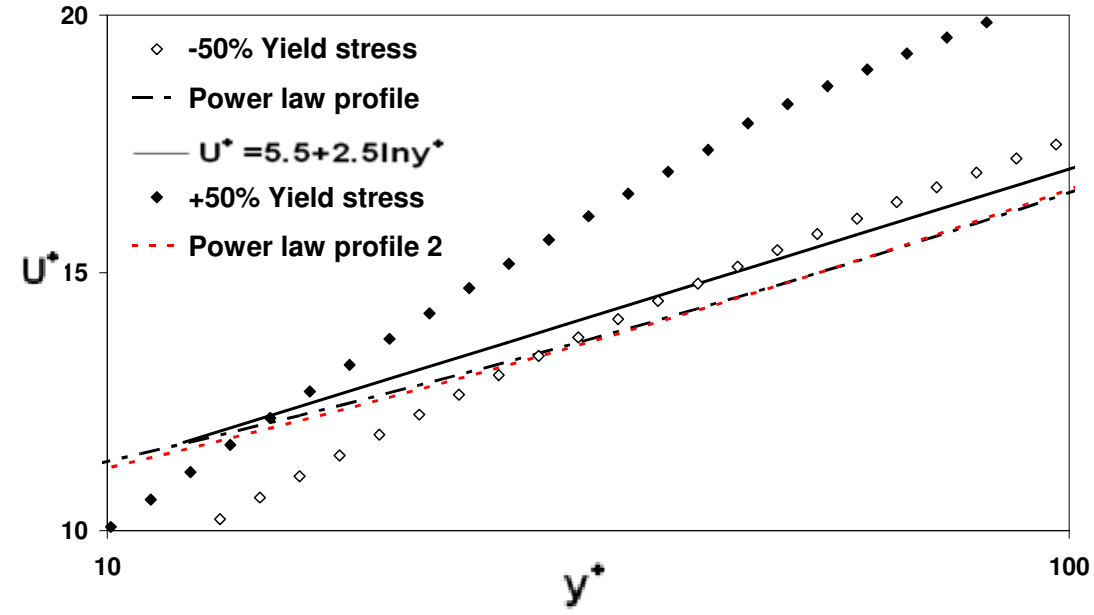

Figure 88 Different simulation velocity profiles with different yield stresses in comparison to Barenblatt (1993)'s power law velocity profile

6.4.3.5 Best fit model

From above sections, it is easily seen that the mean velocity distribution of turbulent channel flow is been studied in different conditions. In this section, a combined velocity distribution method is proposed to suit different velocity profiles in different conditions.

Firstly, in the viscous layer, all profiles have a linear relationship between U^+ and y^+ in the near wall region. Therefore, the best fit velocity distribution equation is still the $U^+ = y^+$ model.

In Clapp's paper, the author renamed the buffer layer, overlap layer and outer layer into just buffer layer and the turbulent core. From Figure 85, the simulation velocity profile shows good agreement in terms of shape. The velocity distribution profiles calculated by Clapp's equations are much higher than the actual simulation profile with $n = 0.81$. With a different n value, Clapp's velocity distribution profile does fit the simulation in different ways. In Figure 89, velocity profile of $n = 0.79$ is plotted with Clapp's velocity distribution equation. In this plot, velocity profile in the turbulent core region fits very well with Clapp's velocity profile. The buffer layer crosses with each other around $y^+ = 10$, which is an improvement from Figure 85. The difference in laminar sublayer can be an error in the simulation. This is further discussed in latter sections. Overall, Clapp's velocity distribution fits better with a slight decrease in flow behaviour index. It can be concluded that Clapp's velocity distribution equation can capture the variation in flow behaviour index quite well. However, it ignores the existence of the flow consistency index and yield stress.

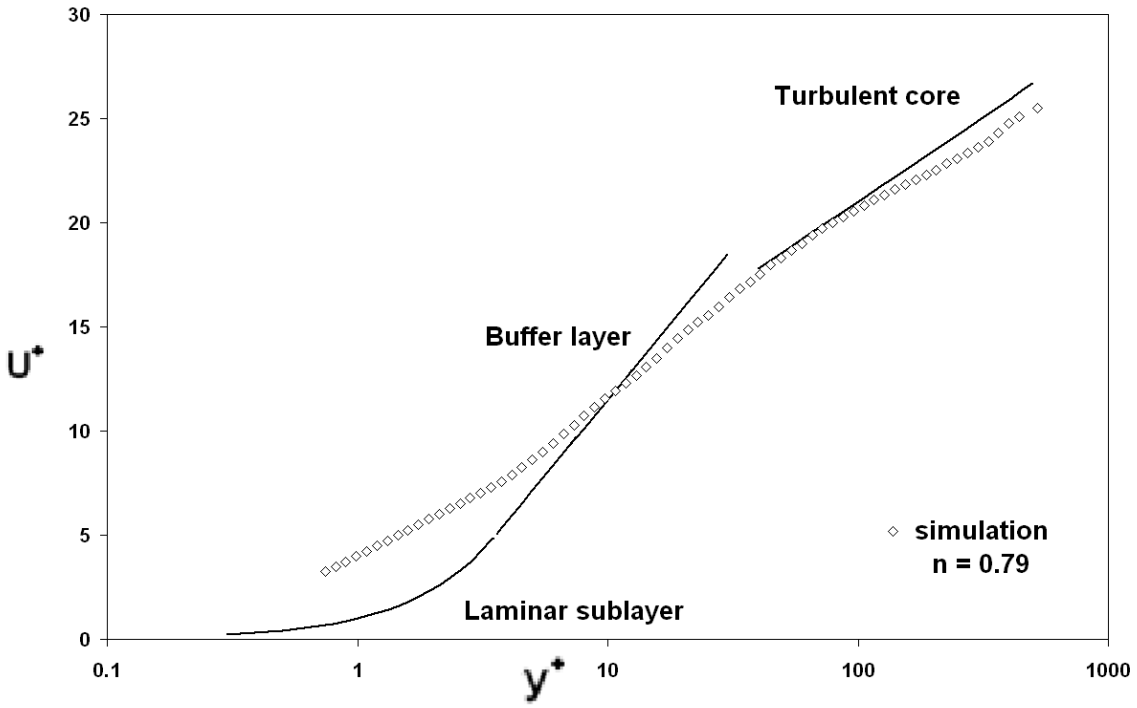

Figure 89 Simulation velocity profile in conventional wall units with Clapp's velocity distribution equation

With secondary flow effect, it was previously mentioned in the literature review that Yang *et al* (2004) proposed a velocity distribution profile for secondary current in rectangular open channel.

$$U^{+}=\frac{1}{k}\ln\left(\frac{y}{y_o}\right)+\frac{\alpha}{k}\ln\left(1-\frac{y}{h}\right) \quad \textbf{(48)}$$

Where α is the factor to predict secondary current, and is given by

$$\alpha=1.3\exp\left(-\frac{b}{2h}\right) \quad \textbf{(49)}$$

When $\alpha = 0$, then the above equation reverts to the classical log law. The second term on the RHS plays an important role in the outer region. However, it is negligible in the inner region as $\ln(1-y/h) \approx 0$. So if it is plotted for the outer layer instead of Clapp's turbulent core, the new velocity profile will appear as presented in Figure 90.

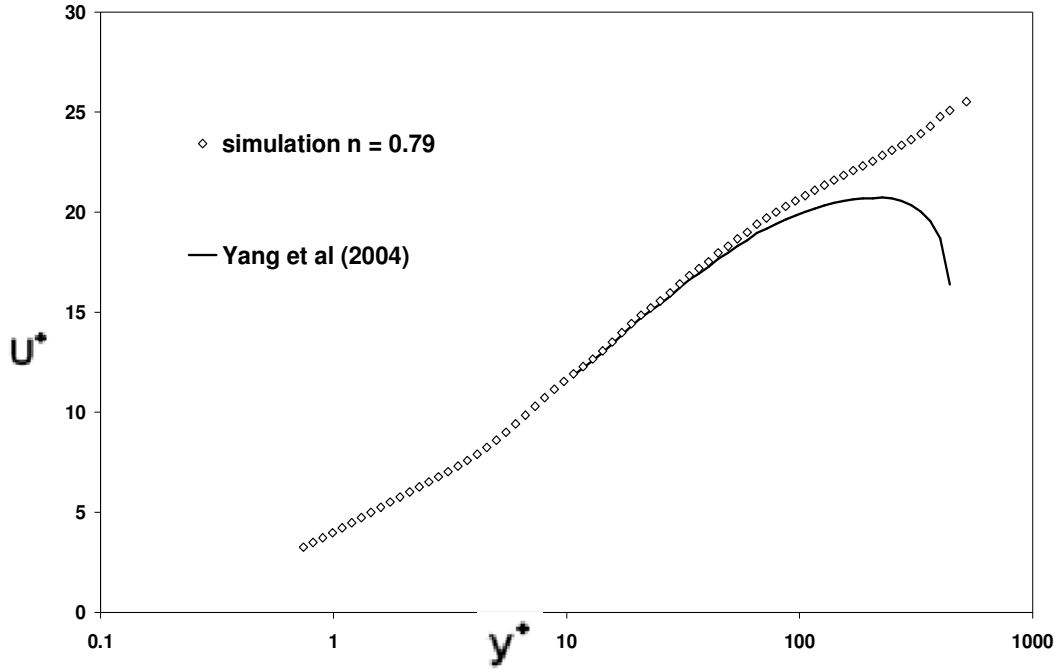

Figure 90 Simulation velocity profile of n = 0.79 and Yang *et al* (2004) equation

With a large velocity dip presented around the outer layer, this should fully capture the real effect of secondary current. However, Yang *et al* (2004)'s equation can be only used in the outer regions. Therefore it would be better if the combination of Clapp's equation and Yang's equation are used to plot the velocity profile. In Figure 91, Clapp's turbulent core equation is replaced by Yang's secondary flow equation. The velocity dip is fully presented in the graph. It is recommended that when plotting non-Newtonian channel flow velocity profile, both of Clapp and Yang's equation should be applied.

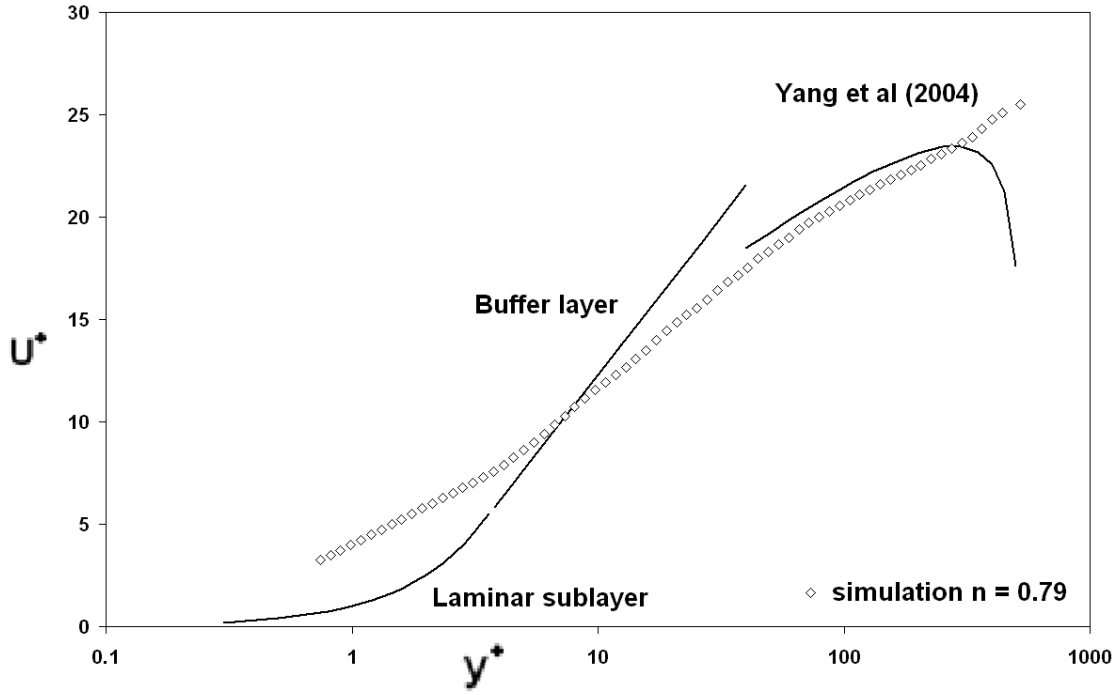

Figure 91 Simulation velocity profile in conventional wall units with Clapp's velocity distribution equation and Yang *et al* (2004) equation

Furthermore, for a more accurate plot, the mean velocity gradient of (dU^+/dy^+) should be used. First of all, the logarithmic velocity distribution equation is presented as

$$U^+ = \frac{1}{k}\ln\left(y^+\right) + A \tag{30}$$

Therefore

$$k = \left[y^+ \frac{dU^+}{dy^+} \right]^{-1} \tag{81}$$

$$A = U^+ - \frac{1}{k}\ln\left(y^+\right)$$

In Zanoun *et al* (2003), the authors used this method to calculate k and A. Their values of k = 0.37 ($\approx 1/e$) and A = 3.7 ($\approx 10/e$) are independent of Reynolds number. Hence, the same method is used to see if the results are any better than the previous methods.

In the viscous layer, the original $U^+ = y^+$ is still applied; therefore it is not shown in Figure 92. The calculated velocity profile in Figure 92 is constructed by calculating k and A using the existing simulation results. It is only applied in the buffer and overlap layer. With k = 0.34 and A = 3.4, the calculated velocity profile fits the original logarithmic profile better than the simulation profile. In general the calculated velocity profile shows general agreement with the shape and shows no secondary current feature. However, with this method, the calculated profile would have a very close fit to the results because the values of k and A are calculated by dU^+/dy^+. Therefore, this method only provides a good way to calculate values of k and A according to existing data rather than a velocity distribution model.

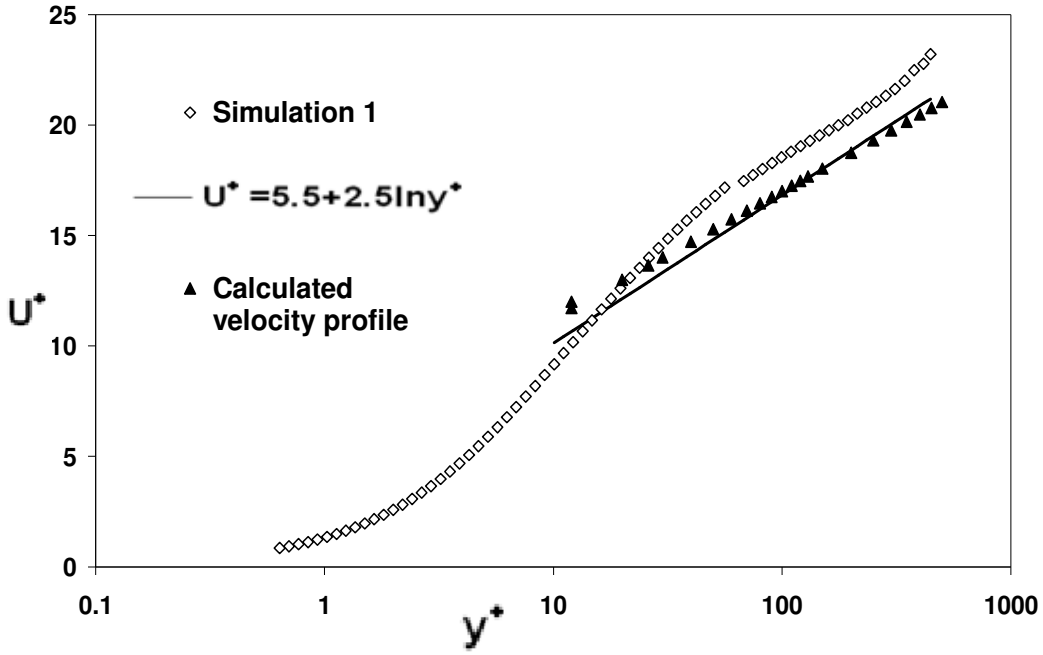

Figure 92 Simulation velocity profile in conventional wall units with calculated velocity profile

6.4.4 Experimental and simulation results from literature

The purposes of this section are to examine:

- If the simulation data is reasonable when compared with other published data and
- If there is any secondary current feature and velocity dips presented in any of the published open channel data?

6.4.4.1 Wallace et al (1972) data

In this paper, the author used oil as the test fluid in open channel flow. The channel used in the experiment was of a rectangular shape. Hot film anemometer probe was used for extensive turbulence measurements. Figure 93 shows the experimental measurement, simulation results and also data from Wallace *et al* (1972). The Reynolds number for Wallace *et al* (1972) experiment was around 7150 based on the width of the channel and the centreline velocity. This is equivalent to a pipe Reynolds number 11000. It can be seen from the plot that Wallace *et al* (1972) data have a good fit from the viscous region to the overlap region of logarithmic velocity profile. It can be noted that some of the data are scattered around in the viscous region; this may be caused by measuring toward in the wall region of the channel. In the region close to the surface, there is no visible secondary current feature (i.e. the velocity dip).

In Wallace *et al* (1972) paper, the authors did not report any secondary flow and velocity dip phenomenon. From the channel dimensions given in the paper, the aspect ratio is 0.25 which is less than the critical value 5. From Nezu (2005), it was predicted that with aspect ratio less than 5, some secondary currents should be noticed close to the surface as well as corner flows. However the experiment failed to capture any velocity dip features. It is noted that Wallace *et al* (1972) paper's focus was mainly on the turbulent characteristics of the channel flow rather than details of any secondary current.

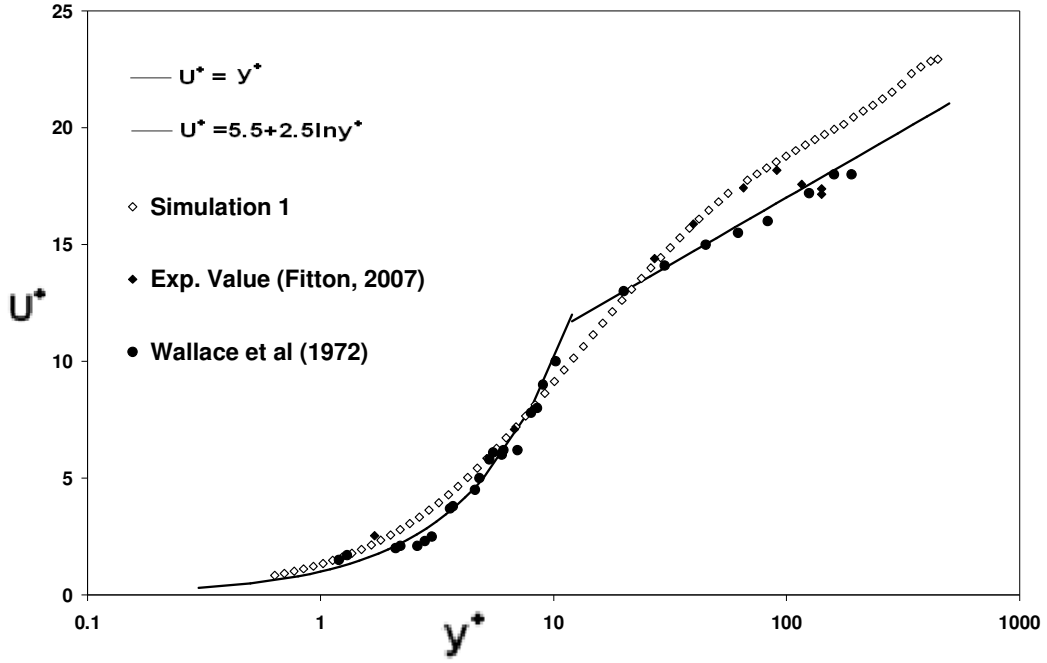

Figure 93 Experimentally measured velocity profile in conventional wall units for slurry and in comparison of Simulation results (Wallace *et al,* 1972)

6.4.4.2 Eckelmann (1974) data

Eckelmann (1974) used similar experimental setups to Wallace *et al* (1972)'s experiment. The flume was 22 cm wide and 1 m deep. It was filled with oil to 0.85 m deep. The Reynolds number based on channel width was 8200. The equivalent pipe Reynolds number was about 15000 based on the pipe radius. Figure 94 shows the experimental measurement, simulation results here compare to data from Eckelmann (1974). Eckelmann (1974) data also have a very good fit in the viscous region of logarithmic velocity profile. Their data in the viscous region is almost perfect fit to the logarithmic profile. Interestingly, Ecklemann (1974) profile overlaps the simulation profile rather than the overlap region of the logarithmic profile. With very similar experiment, Ecklemann (1974) and Wallace *et al* (1972) do not agree with each other on the velocity profile. Wallace *et al* (1972) are closer to the logarithmic profile whereas Ecklemann (1974) data are closer to the present simulation results. The only major difference between the data is Reynolds number. Ecklemann (1974) reported to have a larger Reynolds number of 8200 whereas Wallace *et al* (1972) reported a slightly smaller Reynolds number of 7150.

Similar to Wallace *et al* (1972) paper, the Ecklemann study also did not account for any velocity dip phenomena. Eckelmann (1974) reported an aspect ratio of 0.25, which is also less than the critical value (refer to section 2.4.2) reported by Nezu (2005). It is therefore concluded that the author have not observed the velocity dip phenomena in their paper.

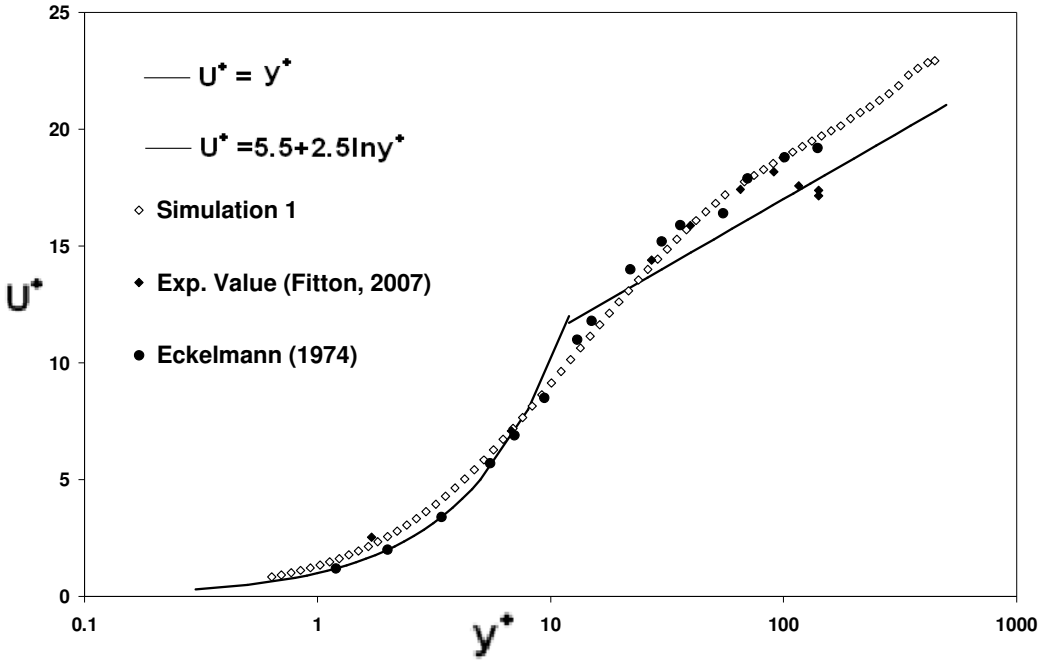

Figure 94 Experimentally measured velocity profile in conventional wall units for slurry in comparison to the Simulation results and Eckelmann (1974) data

6.4.4.3 Kastrinakis and Eckelmann (1983) data

In this paper, the author used a vorticity probe to measure the streamwise velocity component at the centreline. The experiment was carried out in the turbulent channel flow of a wind tunnel. The centreline velocity with the channel width results in a Reynolds number of 25200, which is a lot higher than the previous two papers. The flume was in a rectangular shape. Figure 95 shows the experimental measurement from Fitton (2007), simulation results and also data from Kastrinakis and Eckelmann (1983). Surprisingly, they did not take sufficient amount of data points close to the channel wall. Most of the data were taken at overlap and the outer region. In the overlap and outer region, the data are scattered. However, the general agreement between the data is quite good with limiting values at the wall. Similarly, the

authors did not mention anything about secondary current in their paper as the paper's main purpose was the measurement of streamwise vorticity fluctuations.

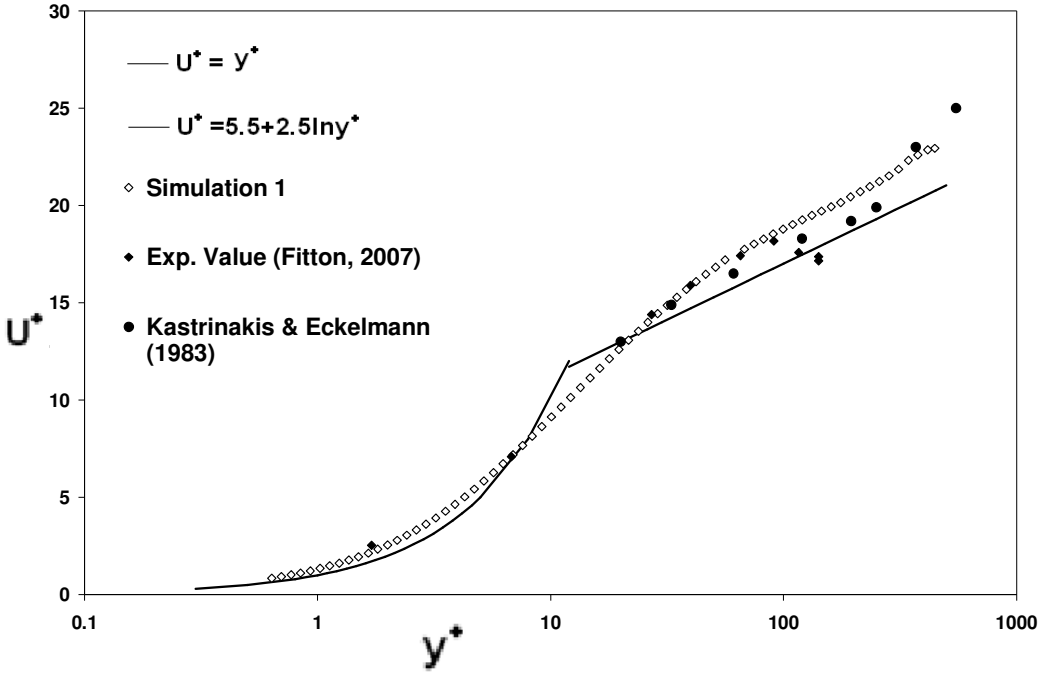

Figure 95 Experimentally measured velocity profile in conventional wall units for slurry in comparison to the Simulation results and Kastrinakis and Eckelmann (1983) data

6.4.4.4 Antonia et al (1992) data

In Antonia *et al* (1992) paper, the authors investigated channel flow by both experiments and simulation. The aspect ratio of the channel is 18 which is quite large when compare to other papers. The fluid used for simulation was Newtonian in nature. Velocity measurements were made at four different Reynolds number values ranging from 3300 – 21500. The authors used channel half width to calculate Reynolds number.

Simulations performed by Antonian *et al* (1993) were carried out at Reynolds number = 3300 and 7900. The numerical algorithm used was the same as that of Kim *et al* (1987).

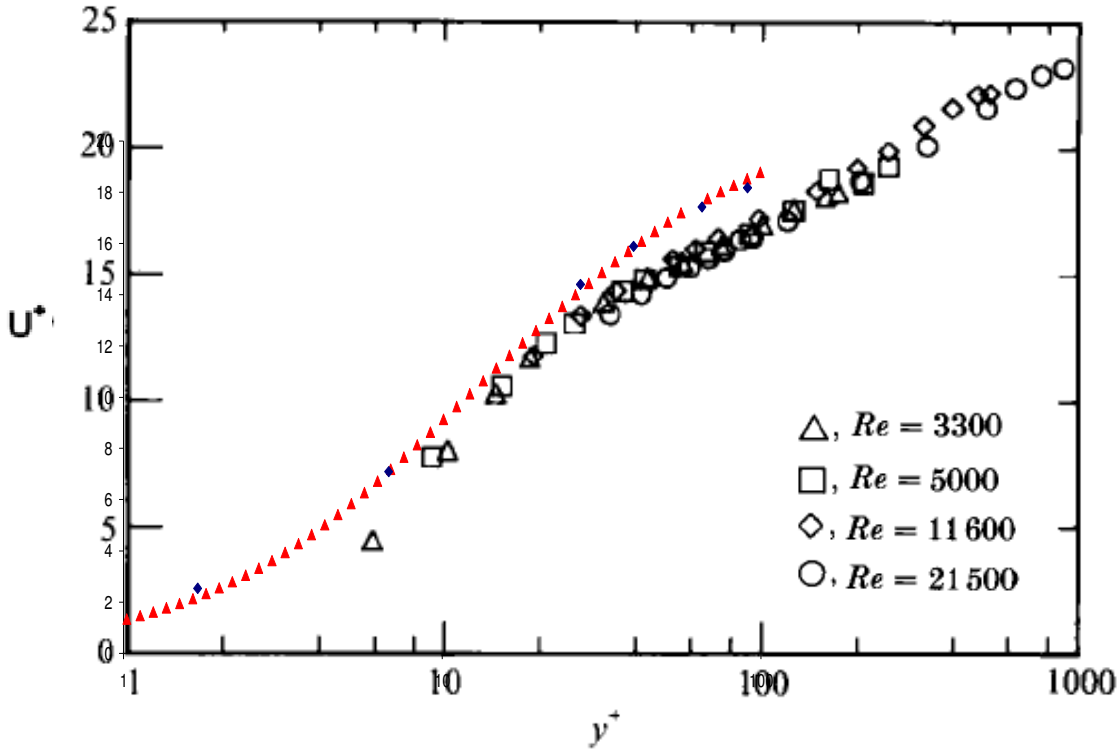

Figure 96 Simulation velocity profile in conventional wall units for slurry in comparison to the experimental data (Antonia *et al,* 1993)

It is seen first from Figure 96 that in the viscous region, the measured velocities from Antonia *et al* (1993) agree reasonably well with current experimental and simulation results. However, there are not many data points around viscous region. This could be due to equipment limitation, yet the authors did not comment on this. The DNS profile from Antonia *et al* (1993) also is in reasonable agreement with the measured velocity profile. From Figure 96 and Figure 97, it is noted that both profiles fell below the simulation results obtained here for non-Newtonian slurry's velocity profile. From Figure 97, it is seen that the high Reynolds number velocity profile (Re = 7900) is located lower than Re = 3300 profile. The Re = 7900 profile is expected to be closer to the overlap region of logarithmic velocity profile.

Figure 96 and Figure 97 show that, there are no obvious secondary current patterns observed from both experiments and simulations.

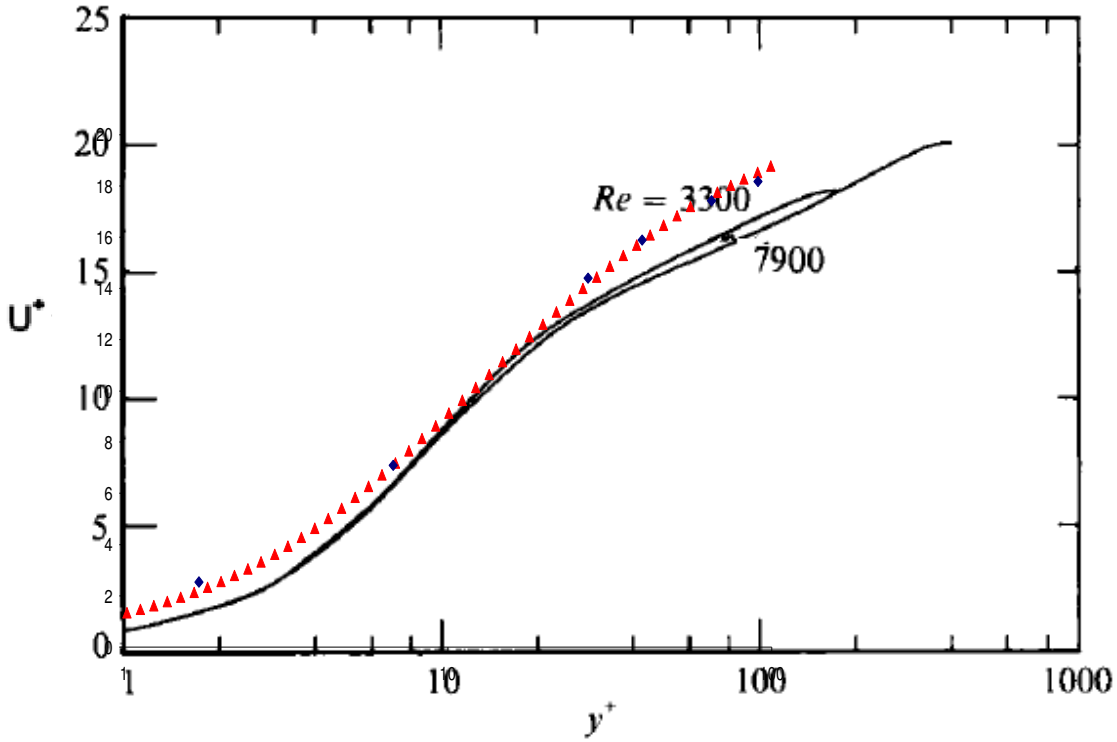

Figure 97 Simulation velocity profile in conventional wall units for slurry in comparison to the simulation data (Antonia *et al,* 1993)

6.4.4.5 Rudman et al (2004) data

Rudman *et al* (2004) reported some interesting findings from direct numerical simulation results of a power law fluid. The authors investigated a weakly turbulent pipe flow simulation. The simulation domain consisted of 105 eighth-order elements in the pipe cross section and 80-128 Fourier modes in the axial direction. The domain length was around 4-5 πD depending on Reynolds number and flow index n (Rudman *et al,* 2004). The Reynolds number was maintained at a similar range from 5252 – 5514. The authors used mean wall viscosity and pipe diameter to calculate Reynolds number. From Figure 98, it is seen that as index n increases, the profiles for the power law fluids approach the Newtonian profile. The results for n = 0.5 fall above the Newtonian profile. For the current simulation result, n = 0.81 almost overlap with Rudman *et al* (2004)'s n = 0.75 velocity profile. Clearly seen in this figure is that all the DNS results have similar profile and agree quite well in general despite the actual difference in simulation parameters. The current simulation was simulated for channel flow

whereas Rudman *et al* (2004) investigated pipe flow. Hence, there are no secondary current features predicted from the data provided by Rudman *et al* (2004).

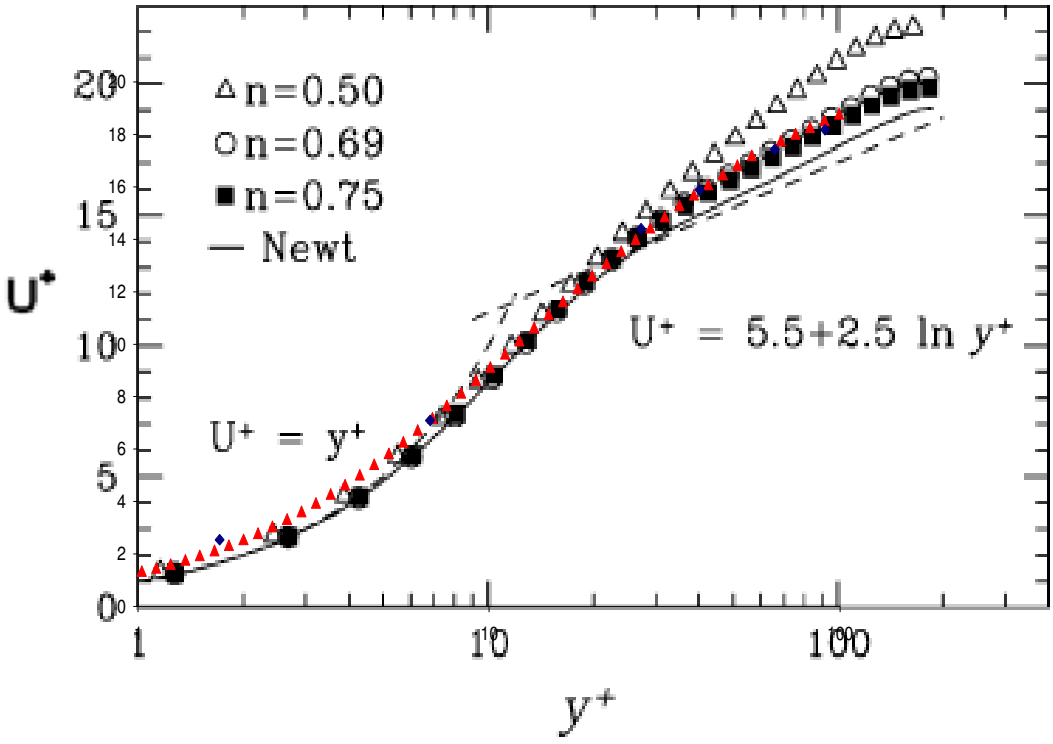

Figure 98 Simulation velocity profile in conventional wall units for slurry in comparison to Rudman *et al* (2004) data

6.5 Further DNS investigation of current simulation results

From the previous section, the simulation results showed general agreement with other data gathered from literature. However, it is possible that the Herchel-Bulkley model is not a true representation of the flow behaviour. None of previous velocity distribution profile presented in section 6.4.3 and section 6.4.4 can explain the slight discrepancy between simulation results and Fitton (2007)'s experimental results. Further, the average velocity for simulation is 1.48 m/s which is higher than the actual experimental value (Fitton, 2007) of 1.06 m/s. At this point, the cause of the discrepancy is uncertain. Therefore, investigations were conducted by changing various simulation parameters, including three different rheological parameters, change of depth, change of measurement positions, and change of mesh resolution to see if the cause of the velocity difference can be explained.

6.5.1 Reynolds number used

It was mentioned earlier that the Reynolds number is defined by mean wall viscosity. The main reasons for using mean wall viscosity instead of average viscosity are:

- The near-wall scaling is no longer $U^+ = y^+$
- The value of the Reynolds number for flows that are transitional and weakly turbulent falls below the Newtonian transitional Reynolds number of 2100 for some fluids
- The turbulence statistics do not collapse as neatly

(Rudman *et al*, 2004)

The wall viscosity is calculated from the mean wall shear stress, τ_w. It is determined directly from the applied axial pressure gradient. Assuming a Herschel-Bulkley rheology, the wall viscosity is calculated as follows:

$$\eta_w = K^{1/n} \frac{\tau_w}{(\tau_w - \tau_y)^{1/n}} \quad \textbf{(71)}$$

Therefore Reynolds number is calculated as follows:

$$\mathrm{Re} = \frac{\rho V(depth)}{K^{1/n} \dfrac{\tau_w}{(\tau_w - \tau_y)^{1/n}}} \quad \textbf{(82)}$$

Usually the bulk velocity and flow depth are used to calculate the Reynolds number for simulations. Both Broglia *et al* (2003) and Joung and Choi (2010) used bulk velocity and flow depth in their Reynolds number calculation. The Reynolds number used in this study is proposed in Rudman *et al* (2004) and has also been compared with that of Haldenwang's (2003) study. Friction factor used here is calculated by modified Fanning friction factor for open channels:

$$f = \frac{2gR_h \sin\alpha}{V^2} \quad \textbf{(83)}$$

Where g is the constant of gravity, R_h is the hydraulic radius and V is the bulk velocity of the flow. The deviation of the friction factor from the 16/*Re* line, used for the laminar region, was

calculated and compared for different Reynolds numbers. Blasius equation for flume flow is used for Reynolds number from transition region to fully developed flow region with Reynolds number up to 10^6. It is show as follows:

$$f = \frac{0.079}{\mathrm{Re}^{0.25}} \qquad \textbf{(84)}$$

Three non-Newtonian fluids were used in Haldenwang (2003) study. Kaolin was classified as a yield pseudoplastic fluid; CMC as a pseudoplastic fluid and bentonite as a Bingham fluid. The following is an example of 4.5% bentonite in the 300 mm flume from Haldenwang (2003). It is seen in Figure 99 that Rudman's Reynolds number has very similar values in comparison to Haldenwang's Reynolds number in the transition and turbulent regions. However, in the laminar region, Rudman's Reynolds number falls below the 16/*Re* line. This is more obvious in the laminar region in Figure 100. Likewise, the Reynolds number values calculated by Rudman's method and Haldenwang's method are similar in the turbulent region.

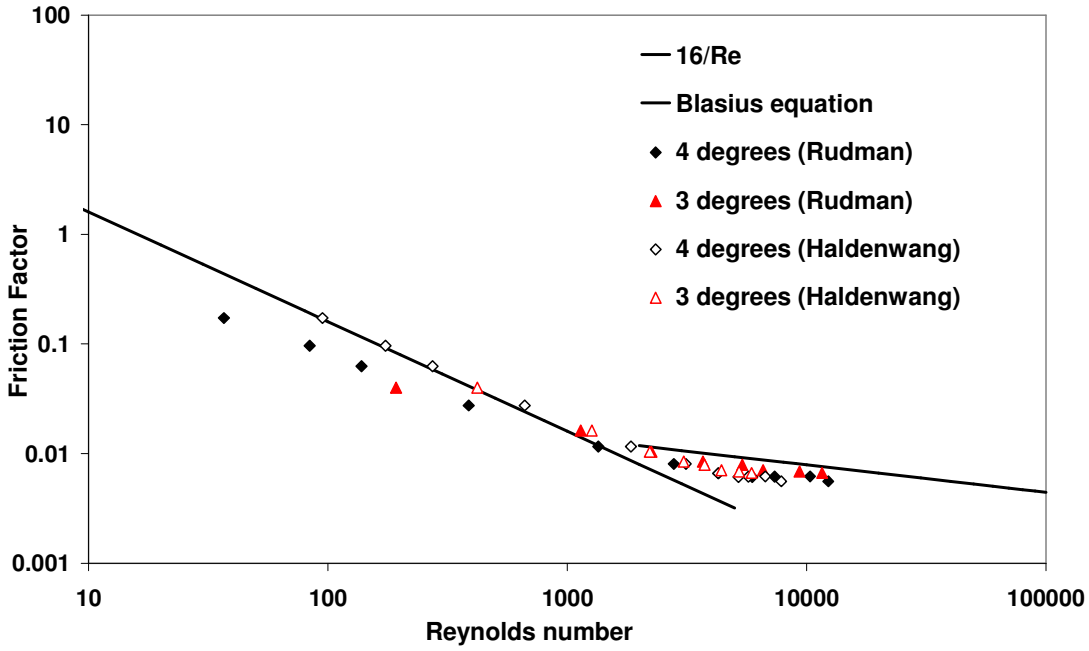

Figure 99 Comparison of Haldenwang Reynolds number with Rudman Reynolds number for 4.5% Bentonite in 300 mm flume

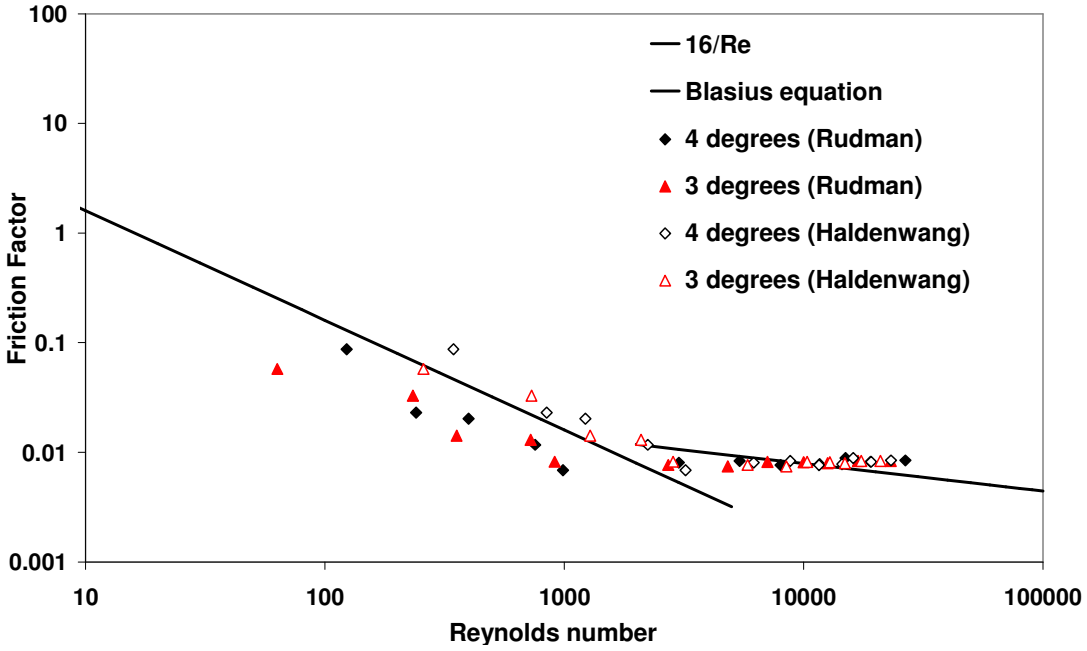

Figure 100 Comparison of Haldenwang Reynolds number with Rudman Reynolds number for 1.0% CMC in 300 mm flume

With 6% of Kaolin in 150 mm flume, calculated Rudman's Reynolds number shows reasonable fits in the turbulent region in Figure 101. In the laminar region, the Reynolds numbers show some slight differences. Interestingly in Figure 101, the Rudmans's Reynolds numbers extended to higher values (i.e.10^5) in the turbulent region, whereas Haldenwang's values reach to a maximum around 10^4. The nature of this discrepancy may be due to the use of different definitions of Reynolds number. This aspect should be further explored. However, the current study is mainly based on turbulent region of the flow; therefore Rudman's Reynolds number is used here for the analysis of the simulation.

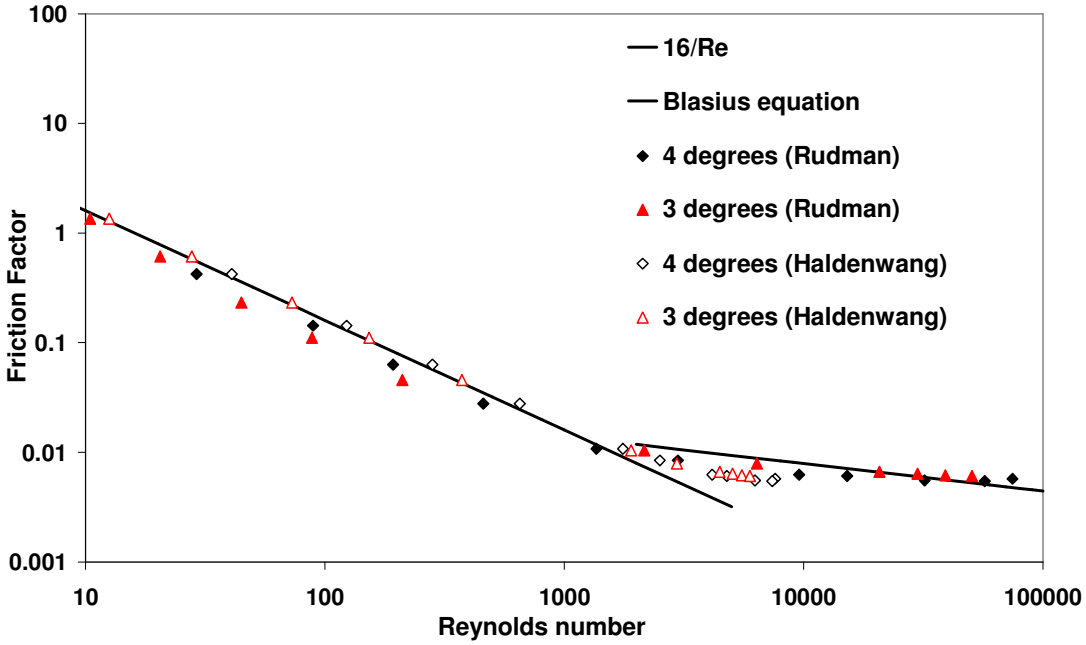

Figure 101 Comparison of Haldenwang Reynolds number with Rudman Reynolds number for 6.0% Kaolin in 150 mm flume

6.5.2 Yield stress effect

The results from six simulations are presented here. For these simulations, six different yield stresses (see Table 18) were used. Simulation A, B and C have yield stresses increased by 20%, 30% and 50% respectively. Simulation D, E and F have yield stresses decreased by 20%, 30% and 50% respectively. The six simulations are carried out at generalised Reynolds number of 6500-9300. Although simulations are undertaken in a Cartesian coordinate system, all results are presented in a cylindrical coordinate system in which the axial velocity is denoted by U, the radial velocity by V and the azimuthal velocity by W.

This is the summary of simulation parameters.

Table 18 Parameters for simulation

Simulation run	n	K (Pa.s^n)	τ_y (Pa)	Reynolds number	Wall viscosity
Control Simulation - Simulation result based on Fitton (2007) experiment	0.81	0.0506	2.249	8182	0.01998
Simulation A Yield stress +20%	0.81	0.0506	2.698	7295	0.02149
Simulation B Yield stress +30%	0.81	0.0506	2.923	7022	0.02232
Simulation C Yield stress +50%	0.81	0.0506	3.374	6481	0.02419
Simulation D Yield stress -20%	0.81	0.0506	1.799	8405	0.01865
Simulation E Yield stress -30%	0.81	0.0506	1.574	8688	0.01805
Simulation F Yield stress -50%	0.81	0.0506	1.124	9258	0.01693

Increased Yield Stress

Mean flow profile

The mean axial velocity for these three simulations for τ_y = 2.698, 2.923, 3.374 are shown in Figure 102. They are plotted with conventional 'law of the wall' non-dimensionalisation and are compared to control yield stress profile. As yield stress τ_y increases, the profiles are moving away from the logarithmic profile obtained by theoretical analysis. All three simulations plus the control simulation show indications of a log-layer profile with a greater slope than the theoretical logarithmic profile. The results for τ_y = 3.374 fall above the theoretical profile.

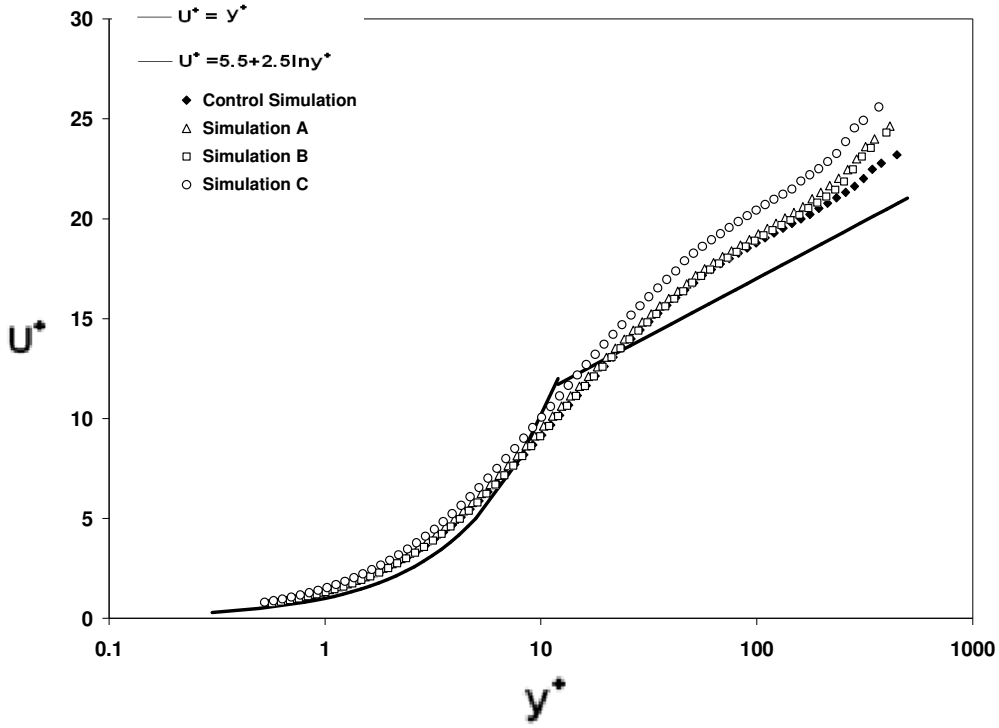

Figure 102 Mean axial velocity profiles for the turbulent flow of three different Herschel-Bulkley fluids. The profiles have been non-dimensionalised using the conventional non-dimensionalisation with the mean wall viscosity taking the place of the Newtonian viscosity

Turbulence statistics

The turbulence intensities and turbulence production are plotted in Figure 103 to Figure 106 in wall units and in Appendix F 1 to Appendix F 4 to in physical coordinates. The root-mean-square of the turbulent velocity fluctuations were used as turbulence intensities. In fact for turbulent intensities, simulation C and the control simulation are very similar. With azimuthal velocity and radial velocity fluctuations, both are lower than Newtonian case. This is in agreement with results in Rudman *et al* (2004). In fact, the axial velocity fluctuations are slightly higher than the Newtonian case with increase of yield stress. The differences are insignificant, as all the axial turbulence intensities are close together.

After non-dimensionalisation, low and high Reynolds number flows produce almost identical axial, radial and azimuthal velocity fluctuations. However, from Rudman and Blackburn (2006), it is discovered that the presence of a yield stress has the effect of reducing the cross-stream intensities more. From Figure 105, it is clearly seen that the azimuthal velocity fluctuations actually increased slightly with the increase of yield stress. It could be a result of

not fixing the Reynolds number to a certain value. In theory, with increased yield stress, the flows should be less developed in the channel.

The production of turbulence is given by

$$P_{zr} = \overline{U'V'}\frac{\partial \overline{U}}{\partial r} \tag{85}$$

and it is plotted in Figure 106**.** From Figure 106**,** the maximum production occurs at a value of $y^+ \approx 6.5$ for these simulations. In Rudman *et al* (2004), it was concluded that the maximum production in wall unit decreased slightly with a decreased n value. In their case, the maximum turbulent production occurs at $y^+ \approx 10$. From Figure 106, Simulation C has shifted the maximum to a slightly smaller y^+ value.

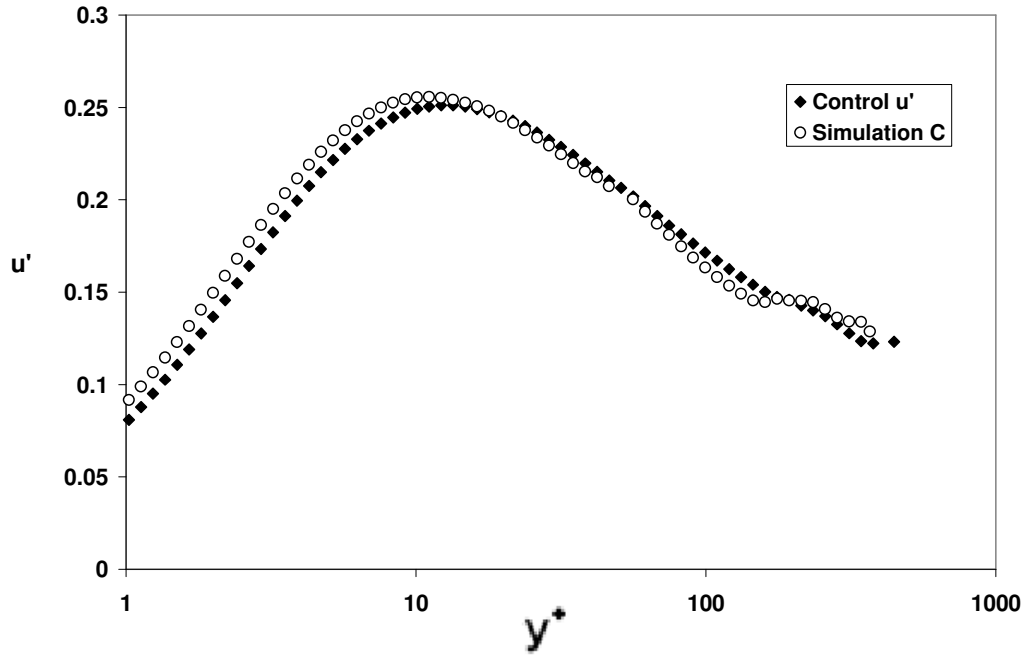

Figure 103 Axial turbulence intensities plotted in wall coordinates

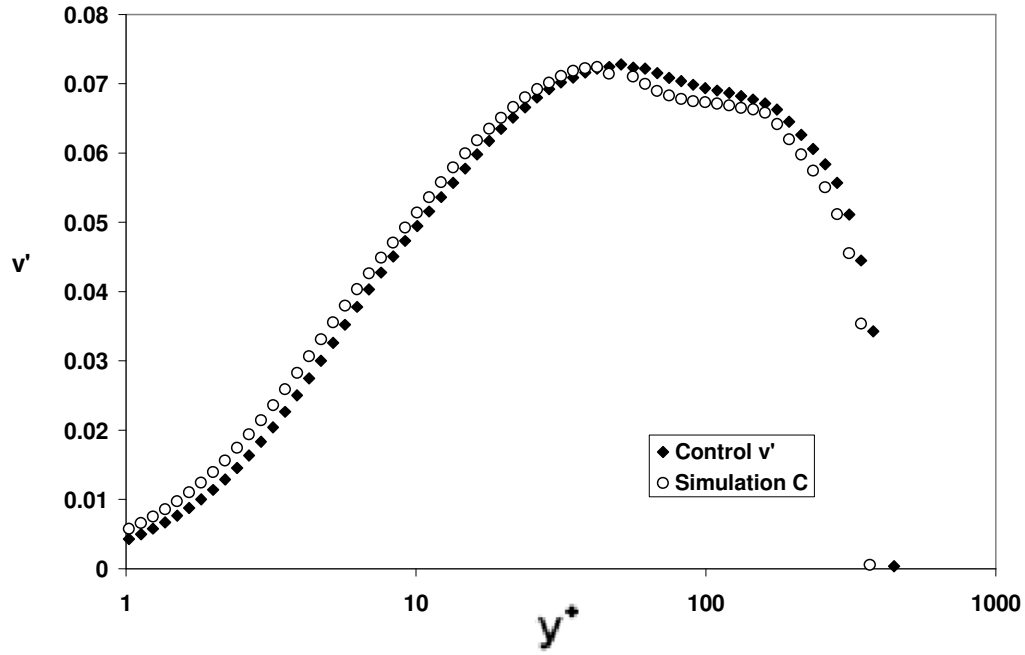

Figure 104 Radial turbulence intensities plotted in wall coordinates

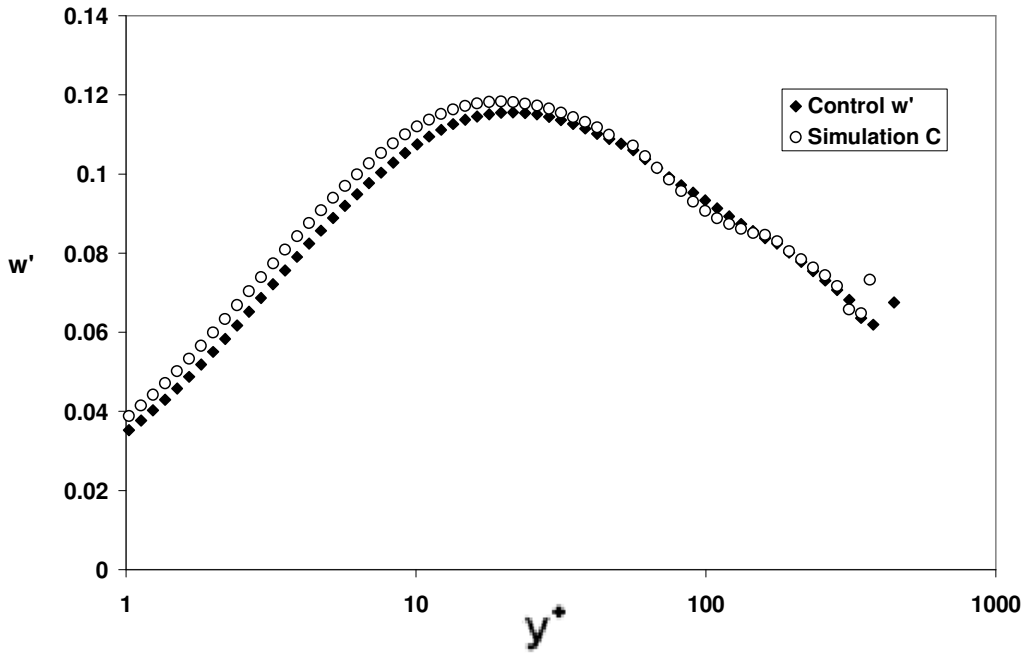

Figure 105 Azimuthal turbulence intensities plotted in wall coordinates

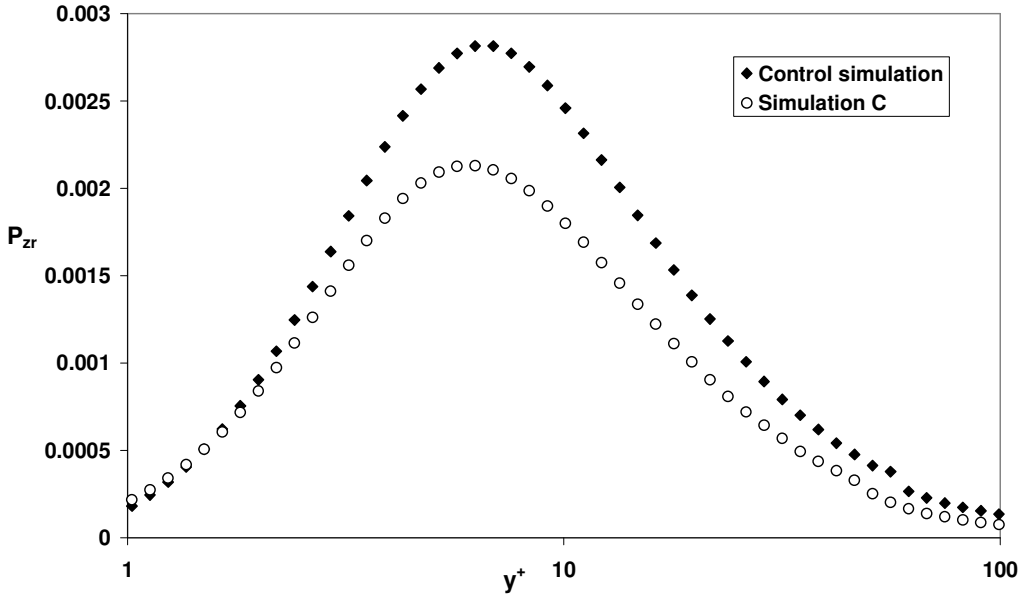

Figure 106 Turbulence production plotted in wall coordinates

Contours of axial velocity at $y^+ = 8$ are shown in Figure 107. These black structures (Figure 107) represent low velocity streaks. As the yield stress increases, the turbulent structures in simulation C are longer than the control simulation. In simulation A and B (Appendix F 5), the difference between the velocity streaks is quite similar to the control simulation. These black structures (Figure 107) represent low velocity streaks. It is more obvious to see in simulation C that the streaks are longer and wider. Therefore it is further suggested that the flow is not yet fully developed for the Herschel-Bulkley fluid. The structure in the Newtonian case is small scale and more random; this indicates the flow is more developed. However, in simulation C the streaks are becoming wider and larger; it would be recommended to increase the simulation domain length. In certain cases, longer domain length simulations were not feasible because of computational usage limitation.

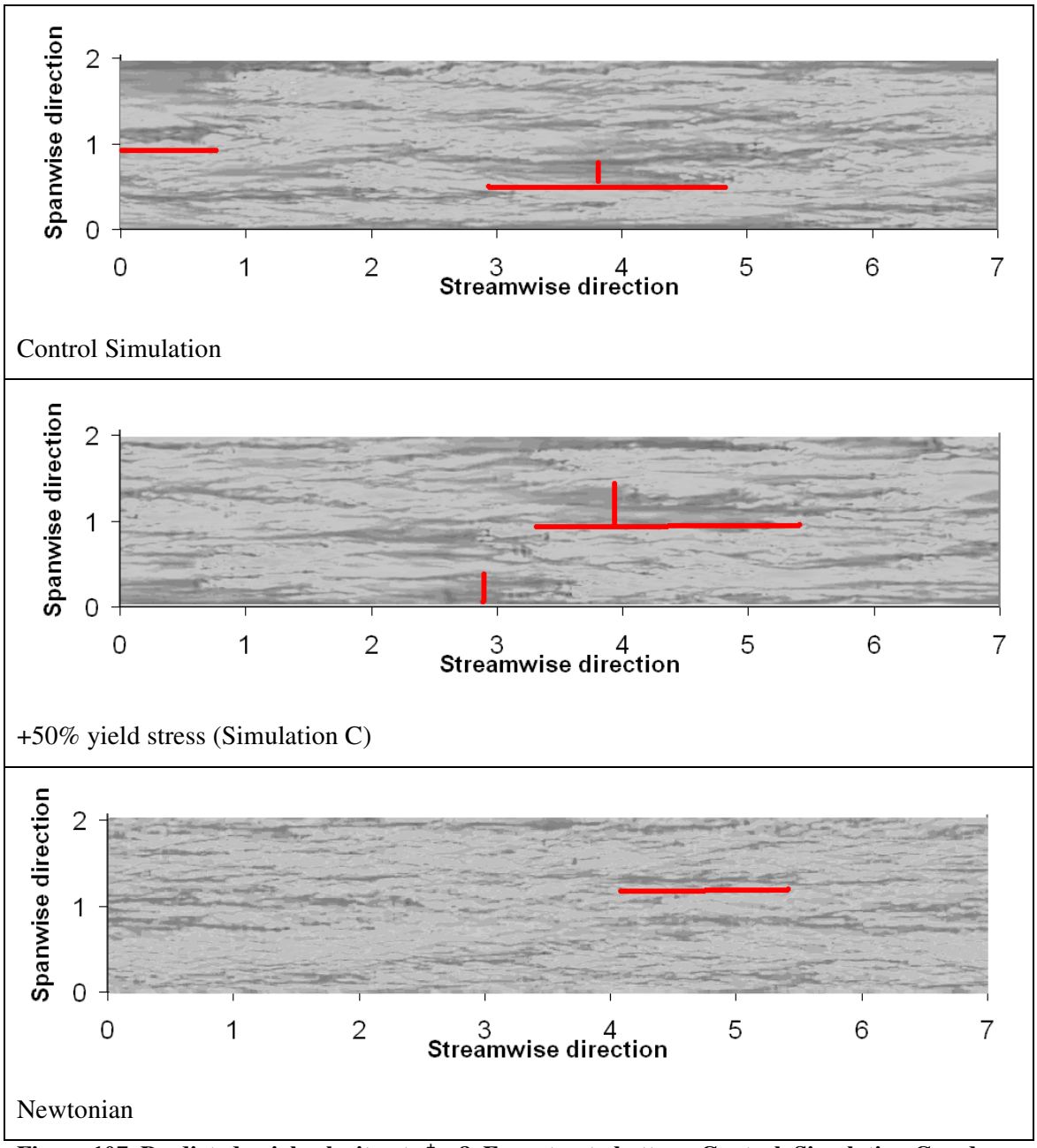

Figure 107 Predicted axial velocity at $y^+ \approx 8$. From top to bottom, Control, Simulation C and Newtonian simulation. White represents high velocity and black represents low velocity.

Table 19 Velocity streak size comparison

Simulation run	Typical velocity streak length	Typical velocity streak width
Control- Simulation result based on experiment (Fitton, 2007)	2 units	0.5 units
Simulation C +50% Yield stress	2.2 units	0.6 units
Newtonian Simulation	1.4 units	0.1~0.2 units

Table 19 shows a comparison between different simulation velocity streaks size and length. Newtonian simulation obviously has the smallest low velocity streaks length and width. There is not a significant qualitative difference between control simulation and simulation C's velocity streaks. In general, simulation C's velocity streaks are long and wider than the control simulation. This may reinforce that with an increase of yield stress, the flow is not as developed as the control simulation.

Contours of the axial velocity on a cross-section for one instant in time are presented in Figure 108. A low resolution of plotting of the velocity vectors is also plotted. According to the legend, the red colour represents velocity at a 2 m/s range, blue colour represents low velocity range. Simulation C shows very similar axial velocity contours when compared with the control simulation. However, with the low resolution in-plane velocities, there is not as much turbulence presented in simulation C plot. Note, there are two localised groups of eddies observed in the control simulation plot. The one on the left is very close to the surface and the other group is close to the bottom of the channel. In simulation C plot, there is no obvious localised eddies close to the channel surface. The only noticeable disturbance is the group close to the channel wall. With a smaller Reynolds number and very small disturbance along the channel wall, it is concluded that with +50% yield stress, the flow becomes less developed than the control simulation.

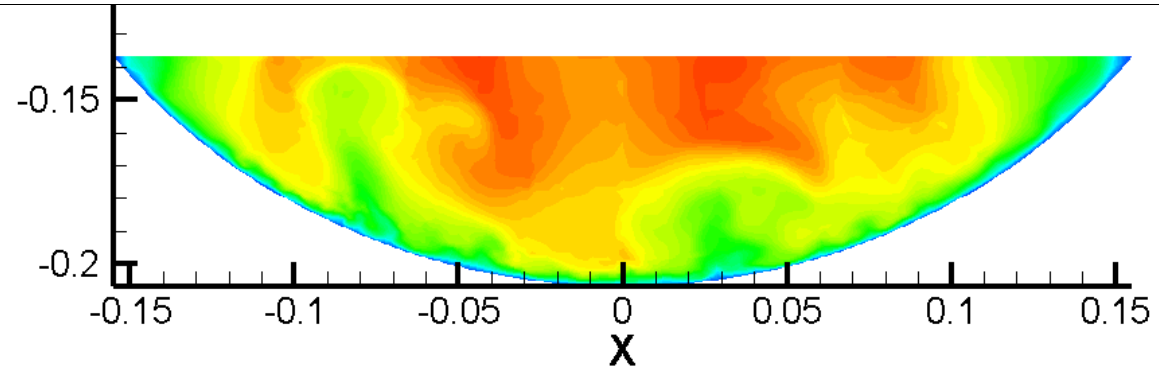

Axial velocity

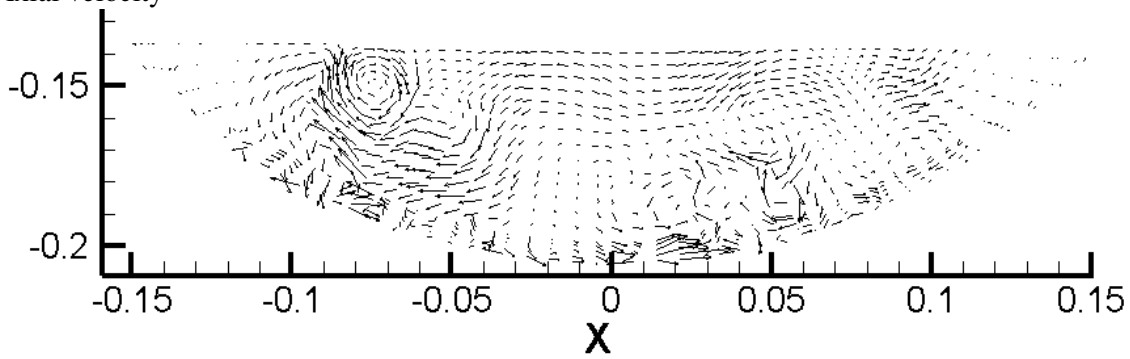

In-plane velocities (low resolution)

Control Simulation

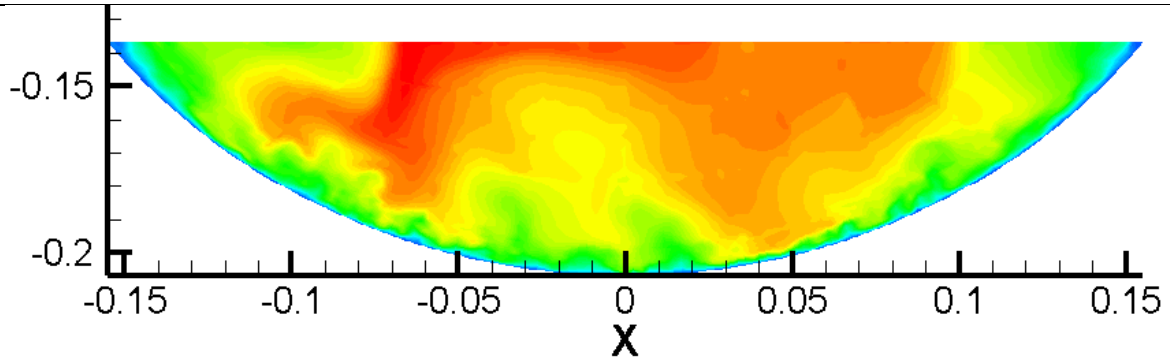

Axial velocity

Figure 108 continued

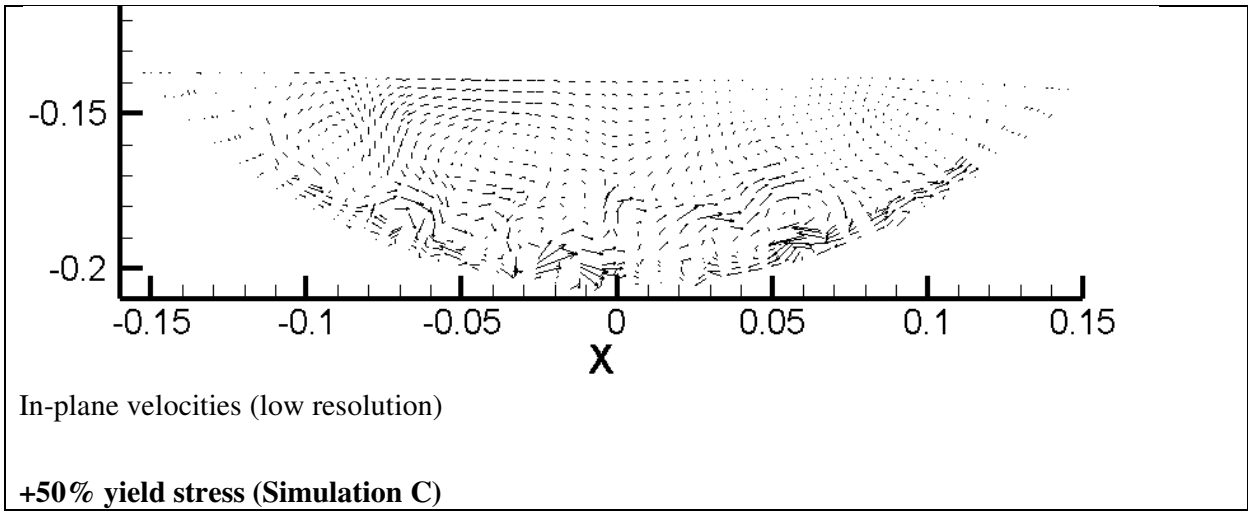

In-plane velocities (low resolution)

+50% yield stress (Simulation C)

Figure 108 Contours of instantaneous axial velocity and in-plane velocity vectors

Decreased Yield Stress

Mean flow profile for Herschel-Bulkley fluids

The mean axial velocity for these three simulations for τ_y = 1.799, 1.574, 1.125 are shown in Figure 109. They are plotted with conventional 'law of the wall' non-dimensionalisation and are compared to control yield stress profile using the code. As yield stress τ_y decreases, the profiles for the Herschel-Bulkley fluids move closer to the theoretical logarithmic profile. From Figure 109, it is quite obvious that Simulation F (which represents -50% yield stress) is closer to the logarithmic profile than the other two simulations (Simulation D and Simulation E).

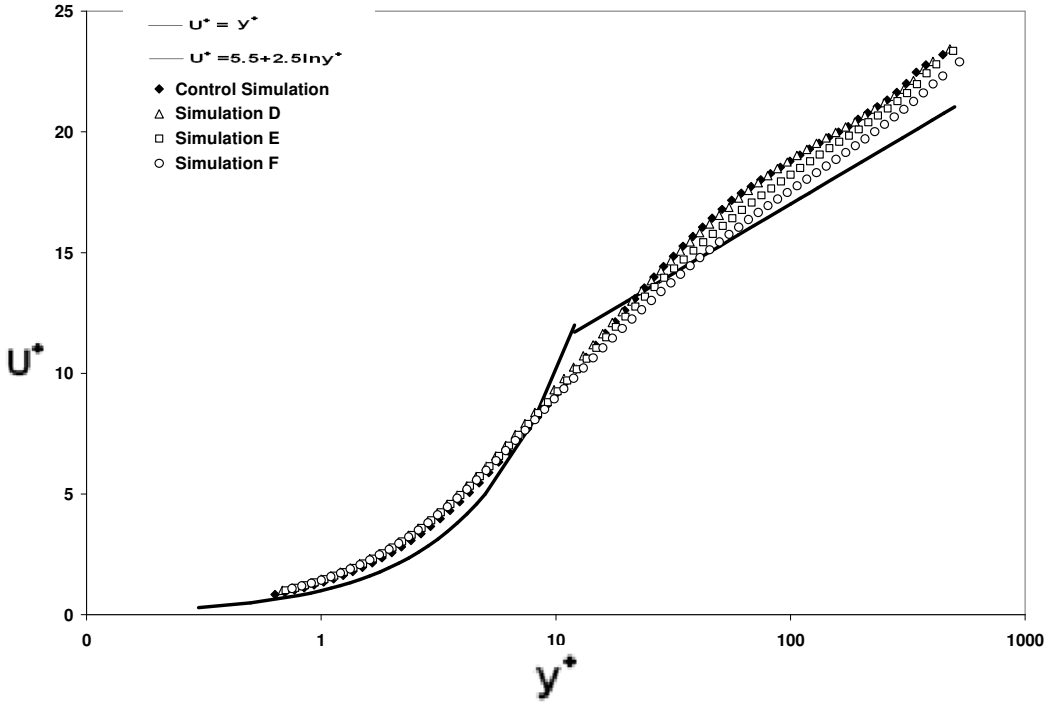

Figure 109 Mean axial velocity profiles for the turbulent flow of three different Herschel-Bulkley fluids

Turbulence statistics

Turbulence intensities and turbulence production are plotted in Figure 110 to Figure 113 in wall units and Appendix F 6 to Appendix F 9 in physical coordinates. For axial velocity fluctuations, the decreased yield stress simulations and the control simulations are very similar. Moser *et al* (1999) have done direct numerical simulation for turbulent channel flow with Re_τ = 590 based on friction velocity (where as Re_τ is around 900 for this simulation). They have discovered that with an increase in Reynolds number, from 180 to 500, the peak of u' increased by 4.5%. Also, the u' profile appears to be the same as the high Reynolds number for $y^+ > 80$ in Moser *et al* (1999). In Figure 110, the u' profile for Simulation F is shifted slightly to the left. Despite the shift, the shape and magnitude of the profile is quite similar to the control simulation. With azimuthal velocity and radial velocity fluctuations, both are quite higher than control simulation. In radial velocity fluctuation, Simulation F is closely approaching Newtonian case, especially in the wall regions. Interestingly, with a decreased yield stress, the axial velocity fluctuations are lower than the control simulation but closer to Newtonian case.

From both turbulent production plots, the maximum production occurs at a value of $y^+ \approx 6$ to 6.5. From Figure 113, it is noted that the simulation with smaller yield stress has higher turbulent production values than the control simulation. Simulation F has maximum turbulent production at similar y^+ value. When the turbulent production values are compared together in Figure 114, simulation C has lower turbulent production value in comparison with simulation F. This also shows in Table 18, where simulation C has a relatively low Reynolds number than simulation F.

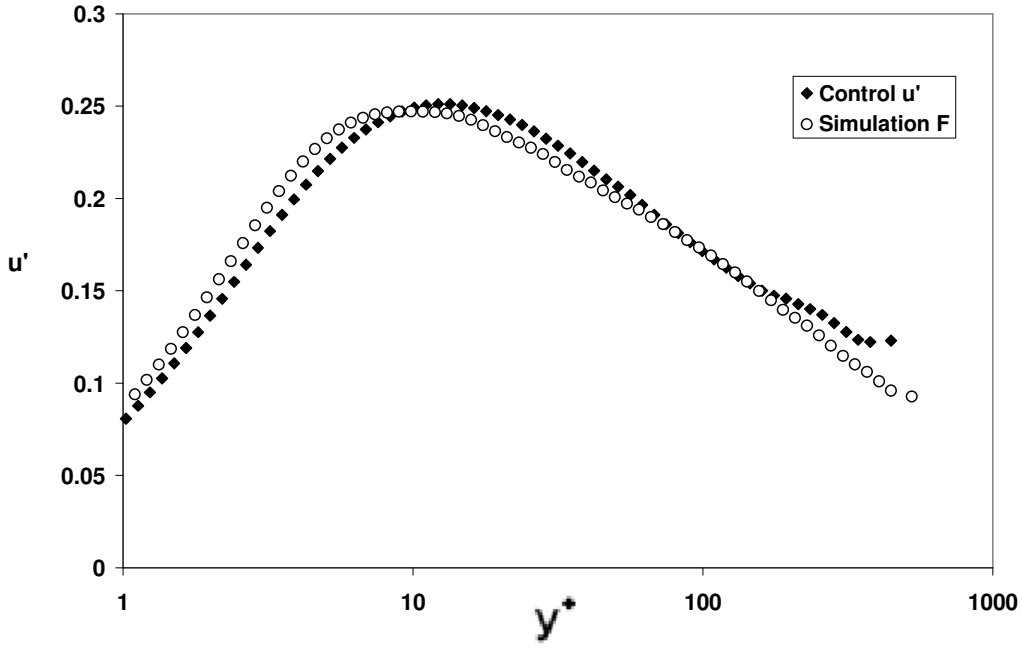

Figure 110 Axial turbulence intensities plotted in wall coordinates

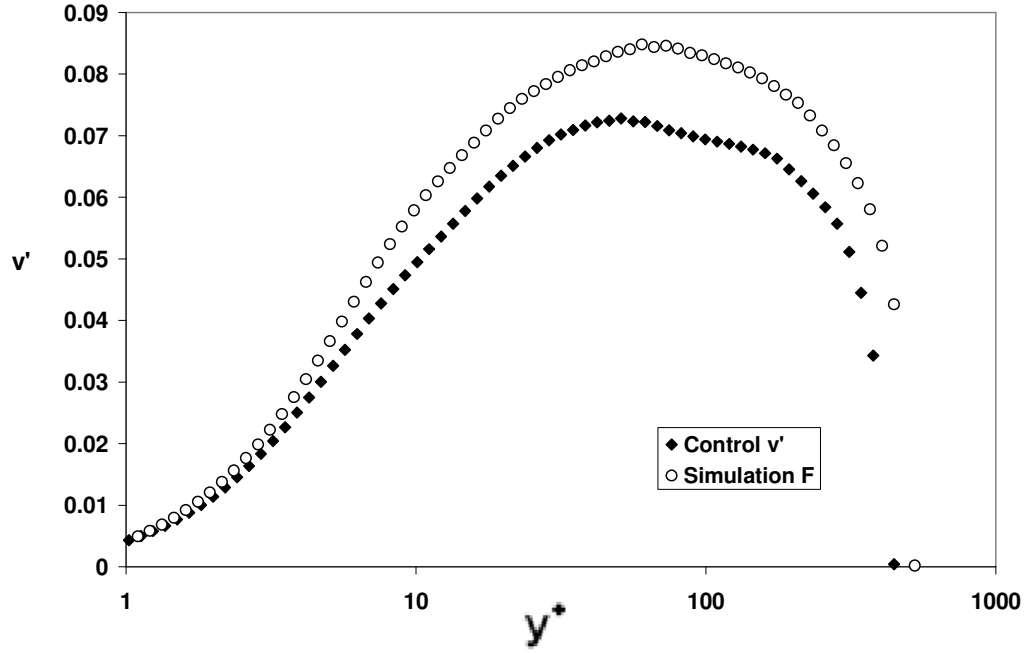

Figure 111 Radial turbulence intensities plotted in wall coordinates

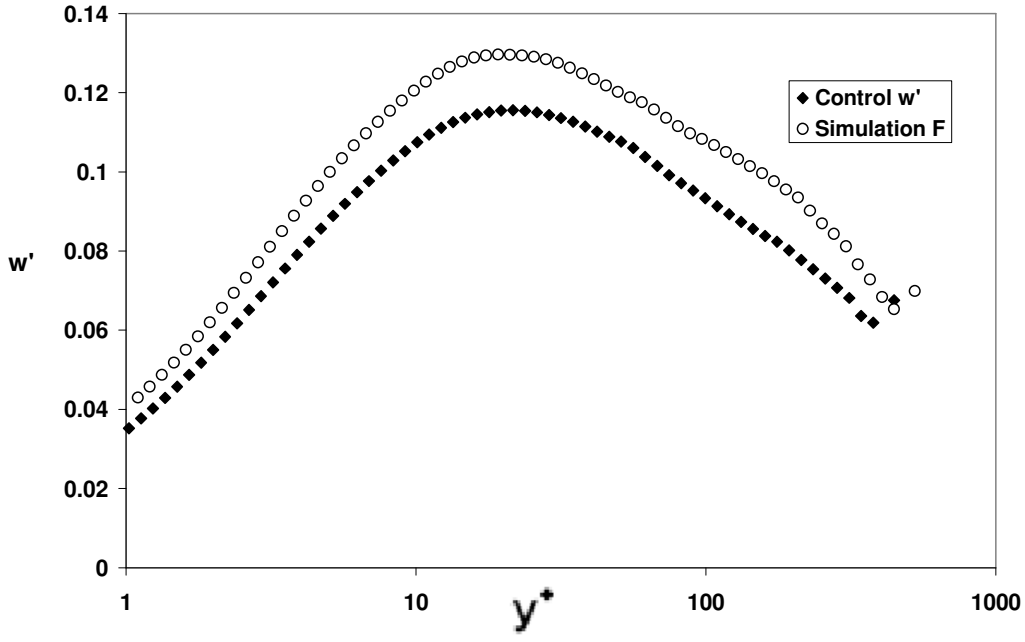

Figure 112 Azimuthal turbulence intensities plotted in wall coordinates

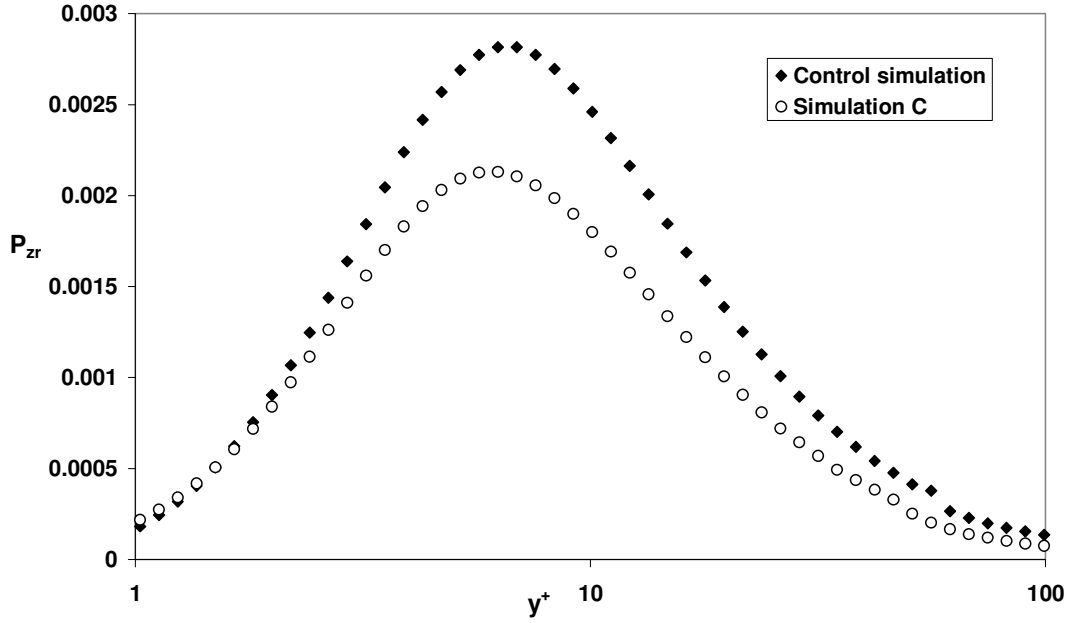

Figure 113 Turbulence production plotted in wall coordinates

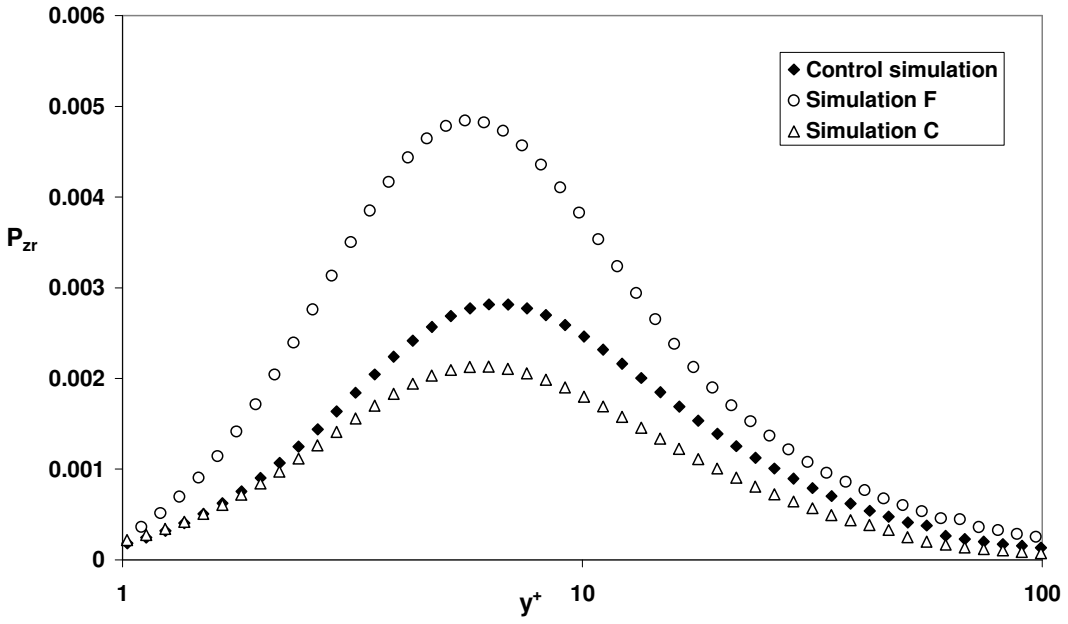

Figure 114 Turbulence production of control simulation and simulation C and F plotted in wall coordinates

Contours of axial velocity at $y^+ = 8$ are shown in Figure 115. The distribution of wall streaks becomes more homogeneous as the yield stress decreases. The velocity streaks in simulation F are shorter and more random than the control simulation. Simulation F shows a higher degree of unsteadiness in the flow compared with the control simulation. Hence it is suggested that as the yield stress decreases, the flow exhibits shorter and random flow structures. Simulation F's contour is not completely Newtonian like, yet, the flow tends to become more developed compared to the control simulation. With the current domain length, a full length turbulent structure can be observed in Figure 115. This shows that the domain length used here is adequate and reasonable.

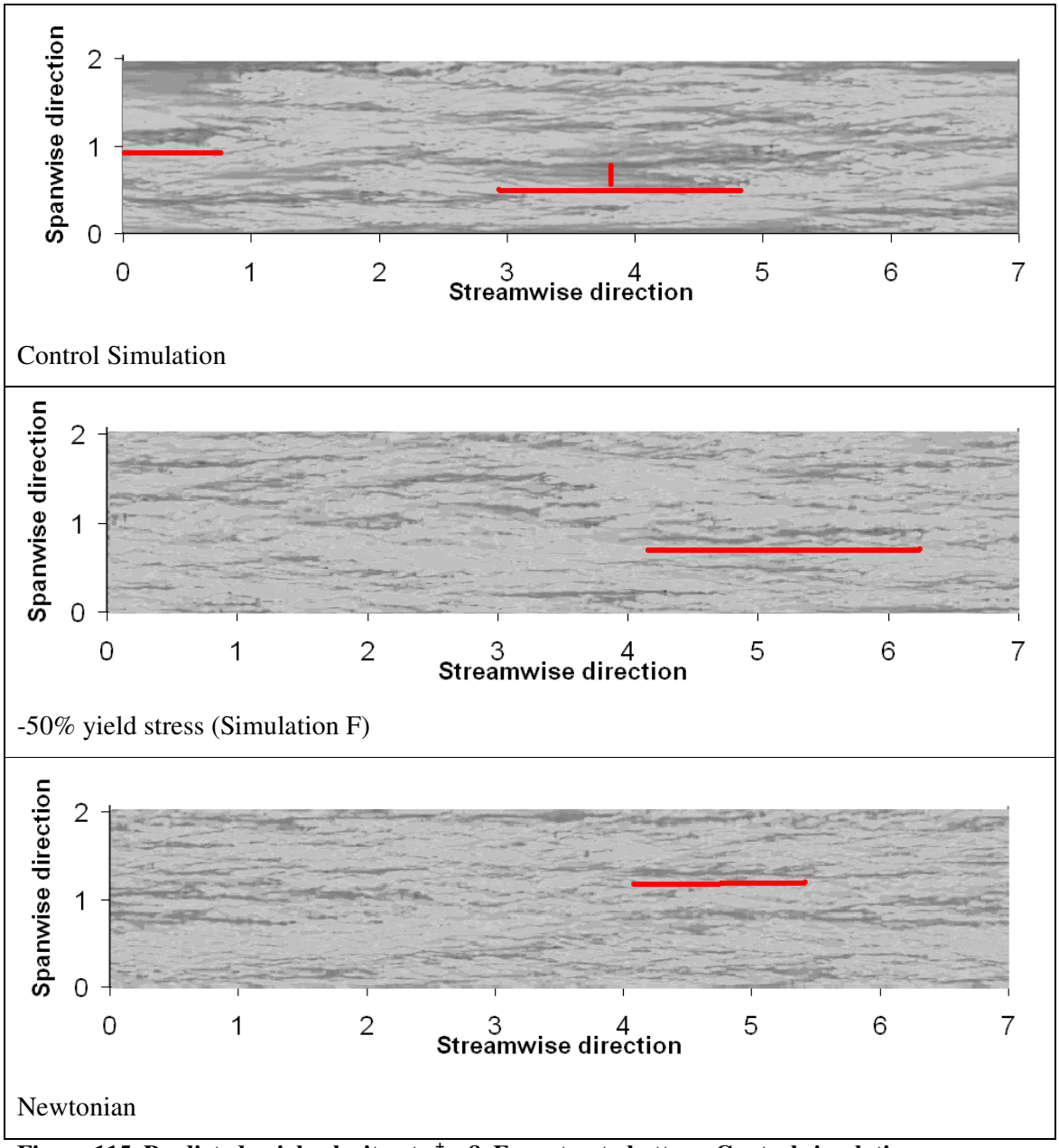

Figure 115 Predicted axial velocity at $y^+ \approx 8$. From top to bottom, Control simulation, Simulation F and Newtonian simulation. White represents high velocity and black represents low velocity.

Table 20 Velocity streak size comparison

Simulation run	Typical velocity streak length	Typical velocity streak width
Control- Simulation result based on experiment	2 units	0.5 units
Simulation F -50% Yield stress	2.2 units	0.2~0.3 units
Newtonian Simulation	1.4 units	0.1~0.2 units

Table 20 shows a comparison between different simulations' velocity streak size and length. Similar to Table 19 Newtonian simulation has the smallest low velocity streaks length and width. From observation, simulation F's velocity streaks' intensity and occurrence are very alike in the Newtonian case. Further, simulation F's velocity streak's length is longer than Newtonian simulation as well as control simulation. This information combines with Figure 115 reinforce that with a decrease of yield stress, the flow is more developed than the control simulation.

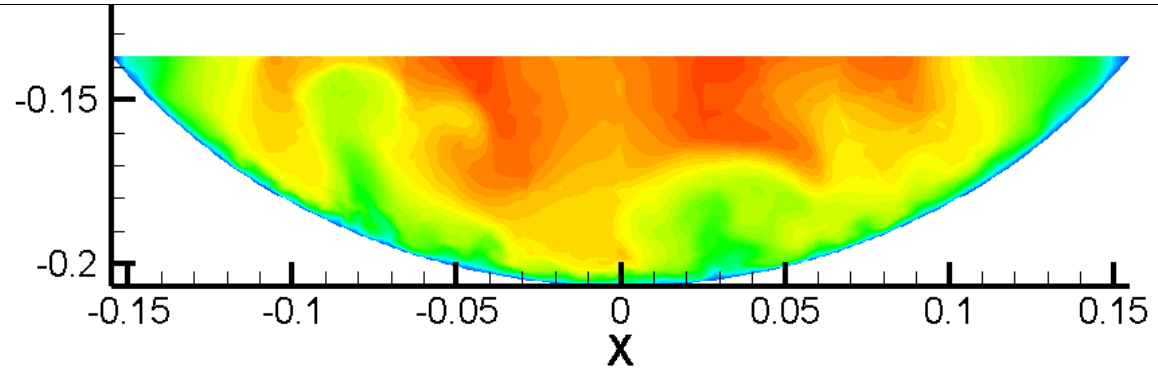

Axial velocity

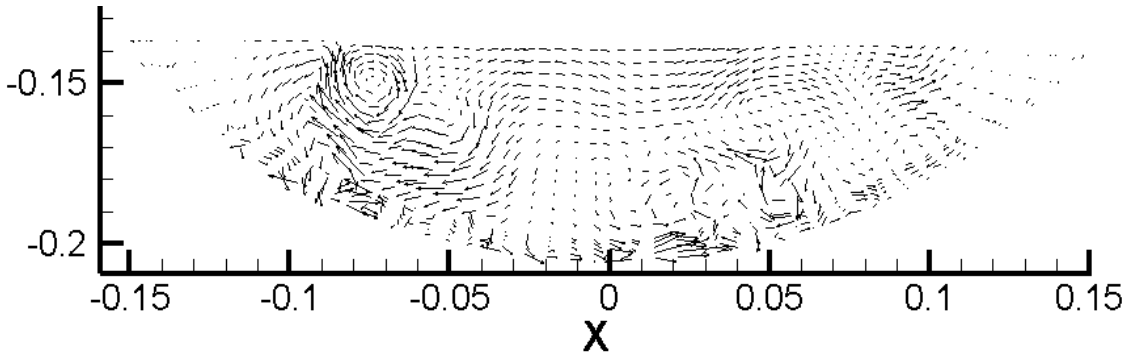

In-plane velocities (low resolution)

Control Simulation

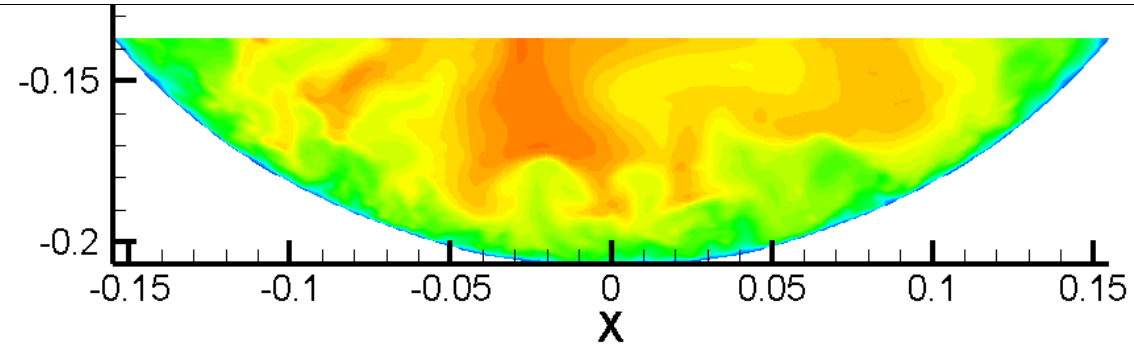

Axial velocity

Figure 116 continued

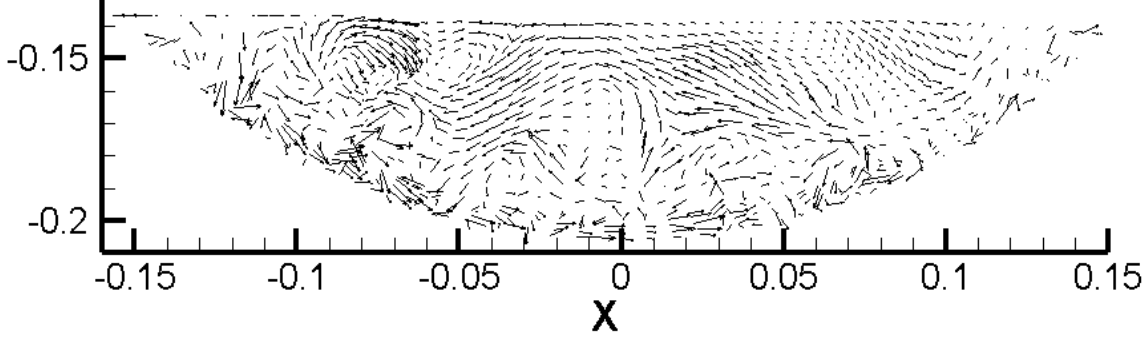

In-plane velocities (low resolution)

-50% yield stress (Simulation E)

Figure 116 Contours of instantaneous axial velocity and in-plane velocity vectors

Cross sections of velocity contour and velocity vectors are presented in Figure 116. With -50% yield stress, Simulation E shows slightly different axial velocity contours when compared with the control simulation. From axial velocity contour, the high velocity regions' colour is less intense in Simulation E plot. This means Simulation E has a smaller average velocity than control simulation.

In the low resolution in-plane velocity plot, there are many of small clusters of eddies presented in simulation E. Majority of them are locating next to the channel wall. From the high resolution plot, these eddies are much more intense than these eddies in the control simulation. There is also one large localised eddy structure sitting very close to the channel surface. Simulation E has a larger Reynolds number and the flow should be more developed than the control simulation. Combined with Figure 115 it is then concluded for -50% yield stress, the flow is more turbulent with more eddies and high turbulent production.

The bulk velocity for changing yield stress simulations vary between 1.50 m/s and 1.60 m/s. It is still a lot higher than the bulk velocity recorded by Fitton (2007) of 1.06 m/s. Therefore change in yield stress does not explain the velocity discrepancy in the bulk velocity. From observation, it is seen that increased yield stress decreases Reynolds number hence the flow will become less developed. Decreased yield stress increases Reynolds number therefore the flow will become more turbulent.

6.5.3 Flow behaviour index (*n*) effect

The results from four simulations with different flow behaviour indices are presented here. The values of *n* chosen are presented in Table 21. Any *n* values that is less than 0.75 or larger than 0.90 was not chosen for the simulation. From previous experience, with *n* decreasing, the simulation would get very unstable. These four simulations are carried out at generalised Reynolds number of 4200-12900.

The mean axial velocity profiles for n = 0.75 and 0.79 are shown in Figure 117. It is also plotted with conventional 'law of the wall' non-dimensionalisation and is compared to base-case flow behaviour index profile. In the overlap region, the profile of n = 0.79 is above the control profile as well as theoretical logarithmic profile. This is consistent with results presented in Pinho and Whitelaw (1989) for different concentration of CMC solutions. However, in Pinho and Whitelaw (1989), the authors did not comment on the near wall region of the velocity profile. Further, the most puzzling feature of Figure 117 is the n = 0.75 velocity profile. This velocity profile is sitting between n = 0.79 profile and control simulation profile. This is disagreed with Rudman and Blackburn (2003) paper where a number of power law fluid was tested. The authors claimed that with a decreased *n,* the smaller *n* velocity profile should fall above larger *n* velocity profile. It is therefore expected to have n = 0.75 profile fall above n = 0.79 profile as well as control profile. It is still unknown why the velocity profiles behave in an unexpected way. It is also extremely surprising to see the velocity profile did not follow the linear profile $U^+ = y^+$ in the viscous region. This could be an error caused by a very high Reynolds number because the resolution of simulation is insufficient to obtain good results. In Rudman and Blackburn (2003), the Reynolds number was kept at a constant value with changing *n*.

Table 21 Parameters for simulation

Simulation run	n	K (Pa.s^n)	τ_y (Pa)	Reynolds number	Wall viscosity
Control Simulation - Simulation result based on Fitton (2007) experiment	0.81	0.0506	2.249	8182	0.01998
n **=** 0.75	0.75	0.0506	2.249	12910	0.0124
n **=** 0.79	0.79	0.0506	2.249	9185	0.0171
n **=** 0.85	0.85	0.0506	2.249	5853	0.0267
n **=** 0.90	0.90	0.0506	2.249	4210	0.0370

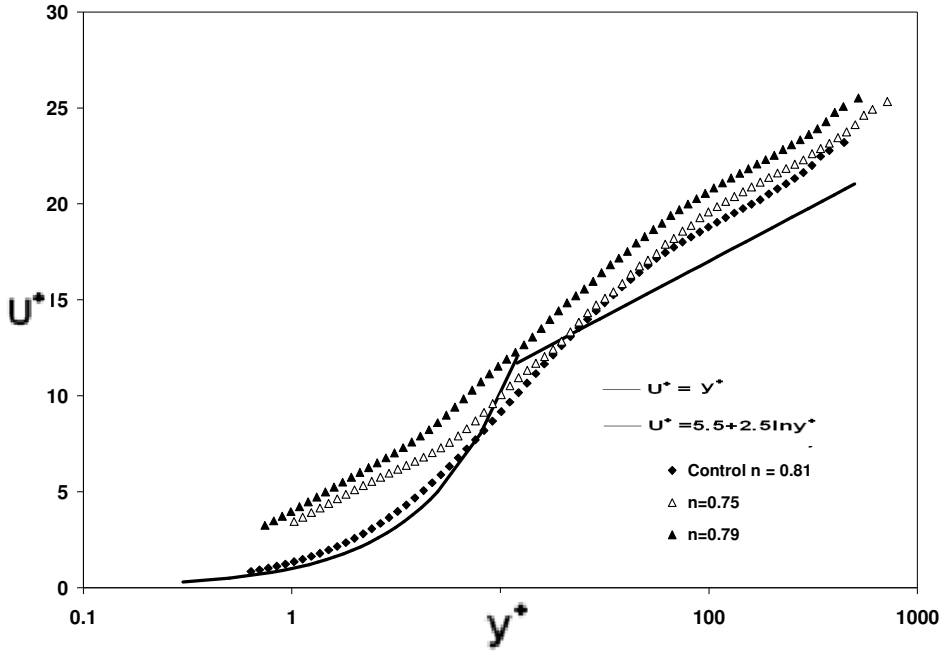

Figure 117 Mean axial velocity profile for the turbulent flow of *n* = 0.75 and 0.79

The mean axial velocity profiles for n = 0.85 and 0.90 are shown in Figure 118. As the flow behaviour index n increases, the profile for the Herschel-Bulkley fluids shifted upward from the logarithmic profile. The results for n = 0.90 fall above control simulation whereas n = 0.85 fall in between the other two velocity profiles. Rudman *et al* (2001) showed similar result with weakly turbulent flow of a power law pipe flow. It was concluded by Rudman *et al* (2001) that the mean flow profile approaches the theoretical profile as Reynolds number increases. In Rudman *et al* (2001) paper, the Re = 3,964 velocity profile also fell above their

control simulation Re = 5500. In this case, the Reynolds number for n = 0.90 simulation is 4,636, which is considerably smaller than the control simulation i.e. 8182. However, it is very difficult to make any comparison with different n values with changing Reynolds number. For velocity profiles, if n decreases, then velocity profile would shift upwards. If Reynolds number decreases, the velocity profile also would shift upwards. Therefore, to have a better understanding of changing of n values, Reynolds number must be kept at a relatively constant value.

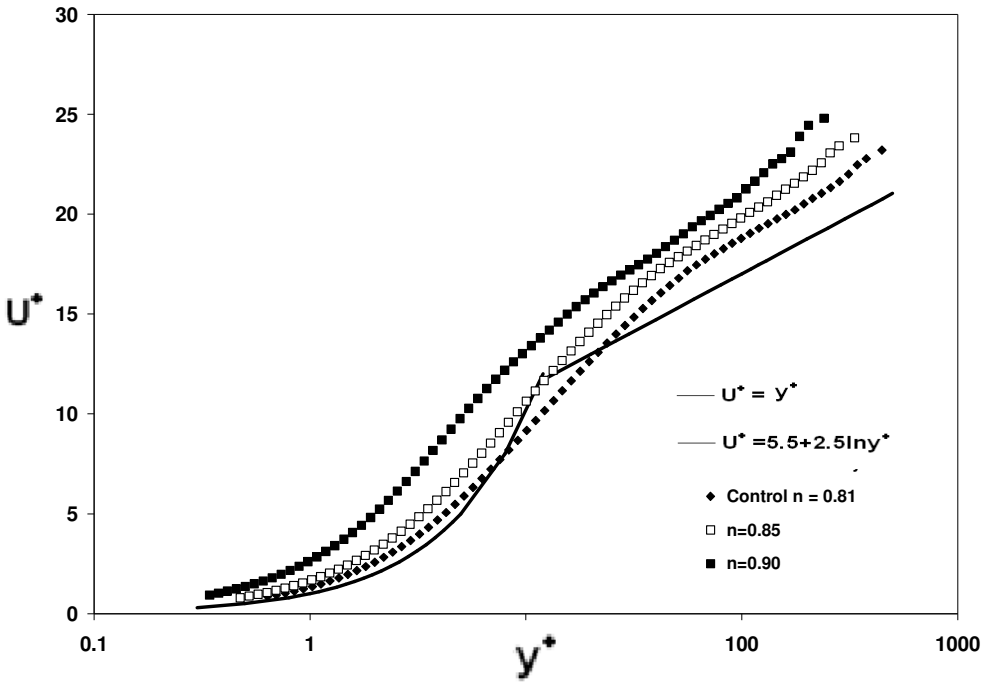

Figure 118 Mean axial velocity profile for the turbulent flow of n = 0.85 and n = 0.90

n = 0.85, 0.79, and control simulation's turbulent intensities are plotted in Figure 119 to Figure 121 in wall units and Appendix G 1 to Appendix G 3 in physical coordinates. In Appendix G 1 the axial turbulent intensity of n = 0.79 is higher than the control simulation from h/R = 0 to 1. For radial and azimuthal turbulent intensity, it is only higher than control simulation in the region where h/R = 0 to 0.2. In Figure 119 to Figure 121, when $y^+ < 10$, turbulent intensities for n = 0.79 are at least 50-100% higher than the control simulation. When $y^+ > 10$, turbulent intensities decrease dramatically. In Figure 120 and Figure 121, the radial and azimuthal turbulent intensities are almost identical to the control simulation.

Therefore, it is concluded that when n is smaller, the wall region is mostly affected by the change of n, especially in the region $0 < y^+ < 10$.

On the other hand, when n = 0.85, turbulent intensities are almost identical to the control simulation. For the radial turbulent intensity, it is lower than control simulation's radial intensity at h/R < 0.2 - 0.25 then increased to just below control simulation. However, the magnitude of the downward shift is considerably smaller than the upward shift resulted by n = 0.79. With a Reynolds number of 5853, n = 0.85 is expected to have smaller turbulent intensities than the control simulation. In Figure 119 to Figure 121, turbulent intensities for n = 0.85 are always higher than the control simulation at $y^+ < 10$. After it reaches a peak, the turbulent intensities then decrease to values lower than the control simulation turbulent intensities. This is observed in all three different turbulent intensity plots.

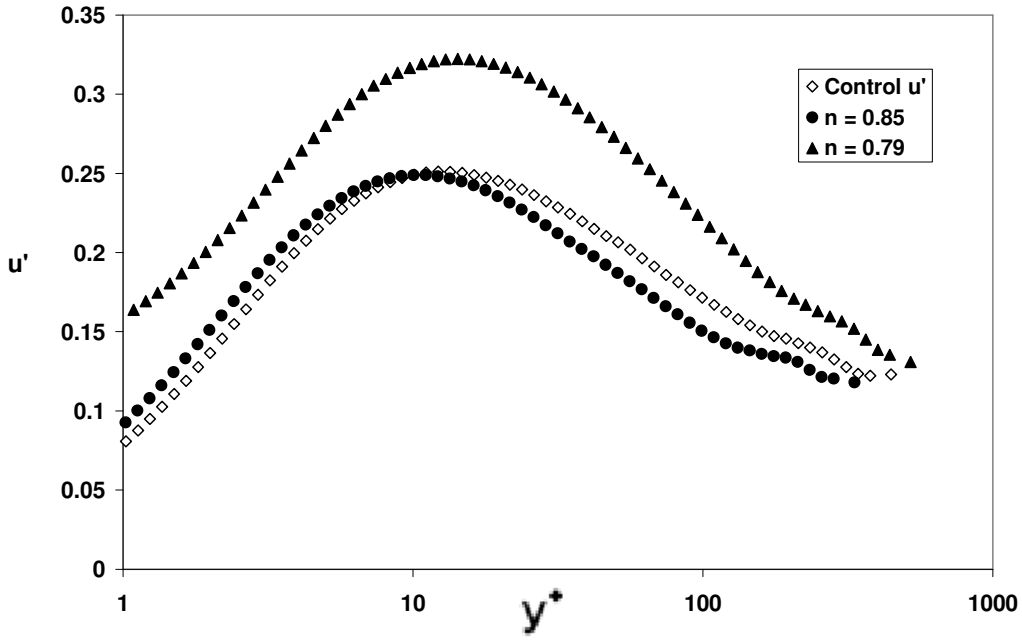

Figure 119 Axial turbulence intensities plotted in wall coordinates

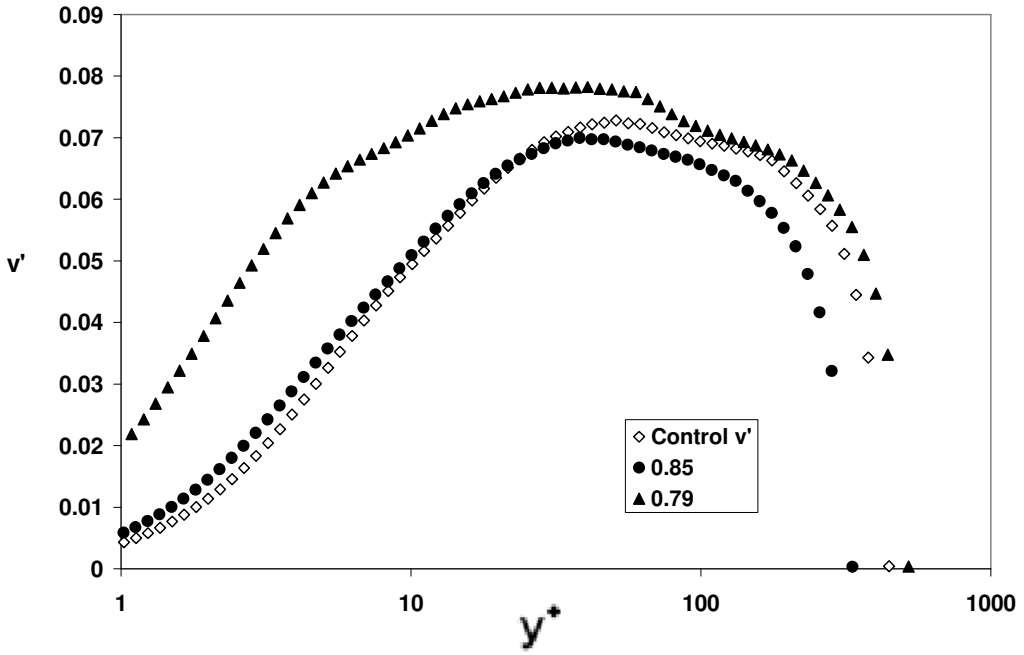

Figure 120 Radial turbulence intensities plotted in wall coordinates

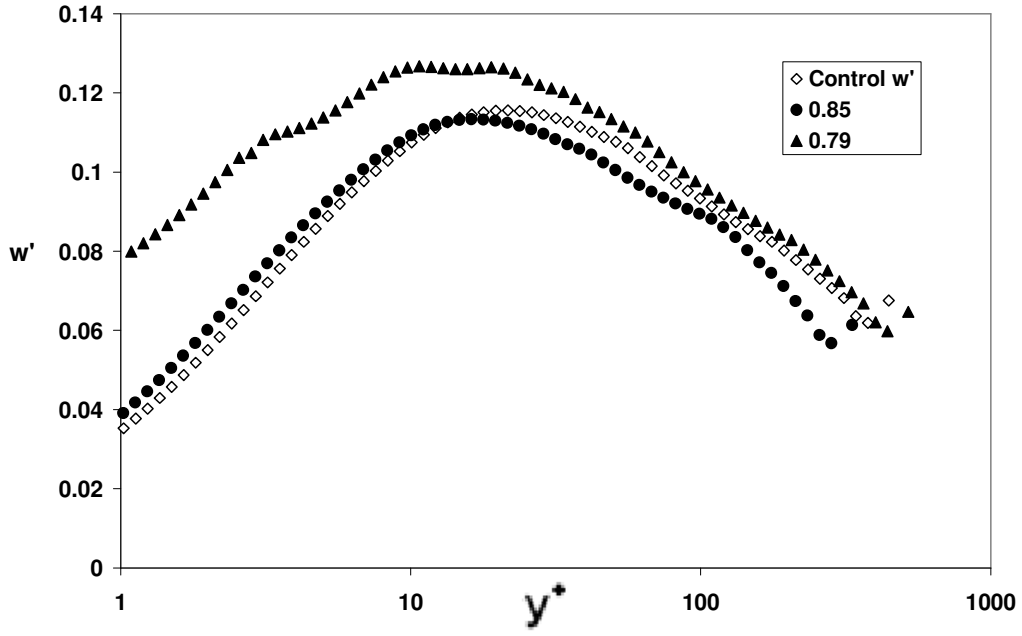

Figure 121 Azimuthal turbulence intensities plotted in wall coordinates

Contours of axial velocity of control simulation and all four different n simulations plus Newtonian simulation at $y^+ = 8$ are shown in Figure 122. For $n = 0.90$ contour, it is seen that a large region of turbulent activity exists from the left of the domain to the middle of the domain. The region near the right of the flow is devoid of unsteady structure. As the n increases, the low speed streak (the grey/black shaded area) in simulation $n = 0.90$ are more visible than the control simulation. It is further suggested that the flow is not fully developed for the Herschel-Bulkley fluid. For contours of $n = 0.85$ and 0.79, the reduction of low velocity streaks is clear and visible. In $n = 0.75$ velocity contour, the black/grey coloured low velocity streaks are almost invisible. The low velocity streaks in $n = 0.75$ velocity contour is very short and have a small width. There are also weak white spots presenting in $n = 0.75$ velocity contours which represent the high velocity streaks. A higher volume of high velocity streaks denote a more turbulent flow characteristic.

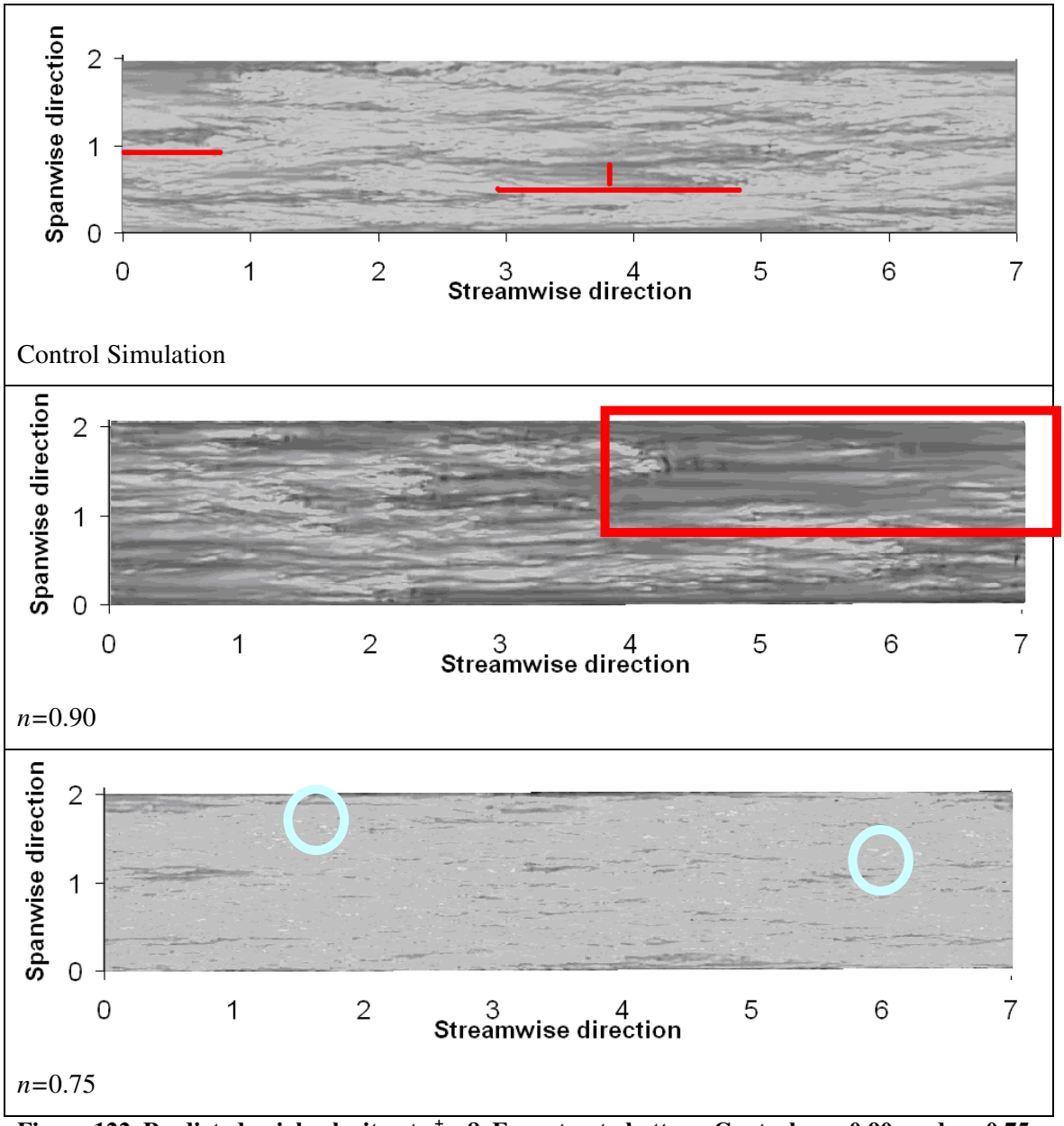

Figure 122 Predicted axial velocity at $y^+ \approx 8$. From top to bottom, Control, n = 0.90, and n =0.75. White streaks represent high velocity and black streaks represent low velocity.

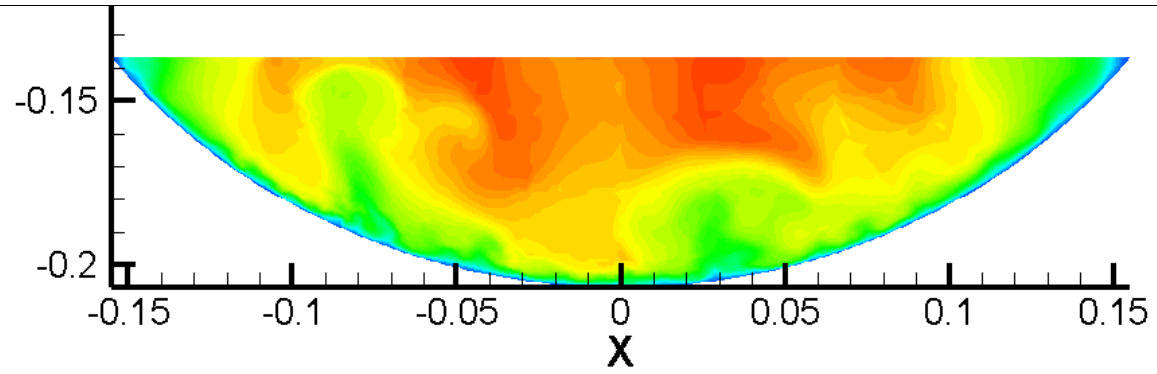

Axial velocity

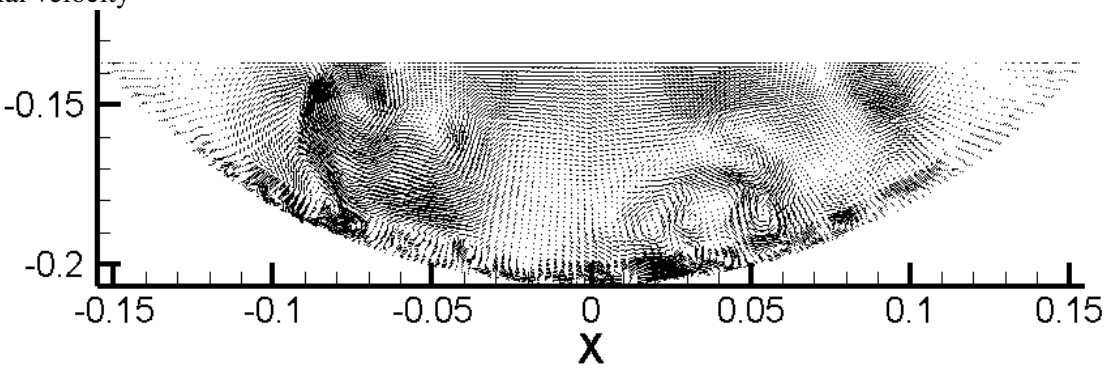

In-plan velocities

Control Simulation

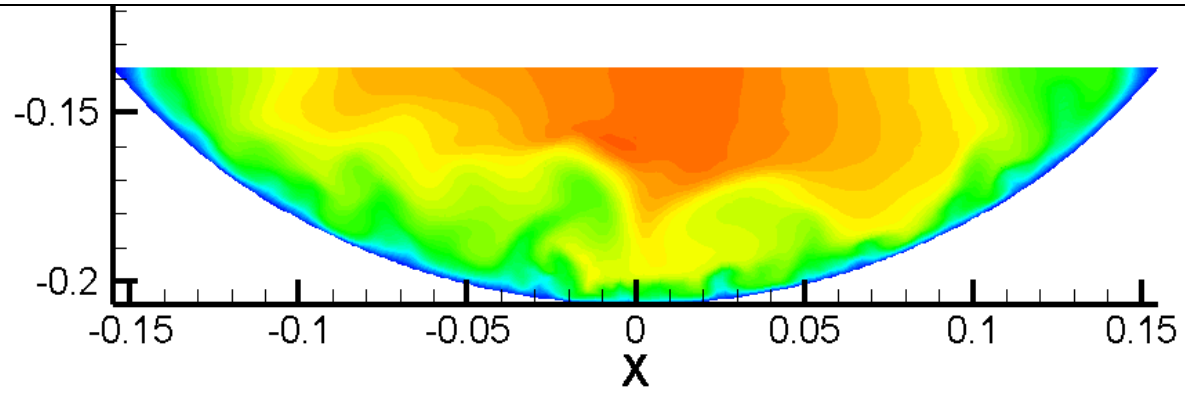

Axial velocity

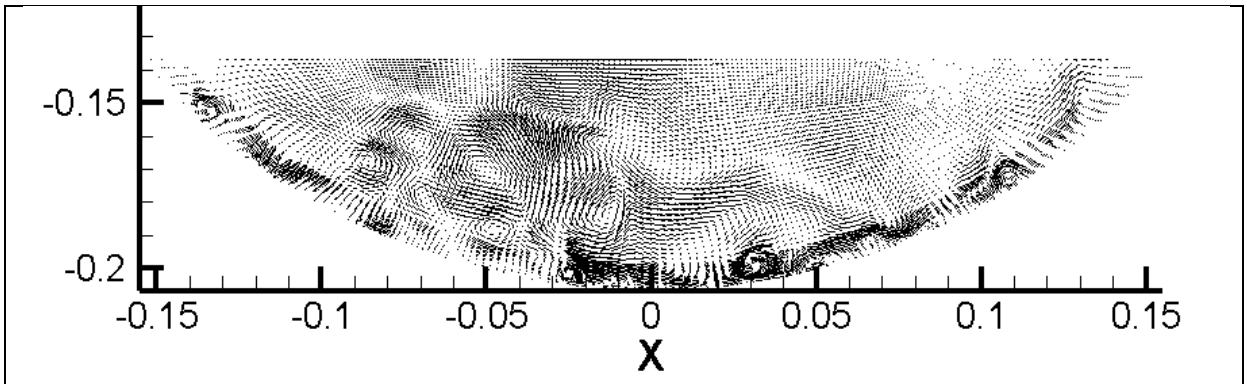

In-plan velocities

***n* = 0.90, Re = 4210**

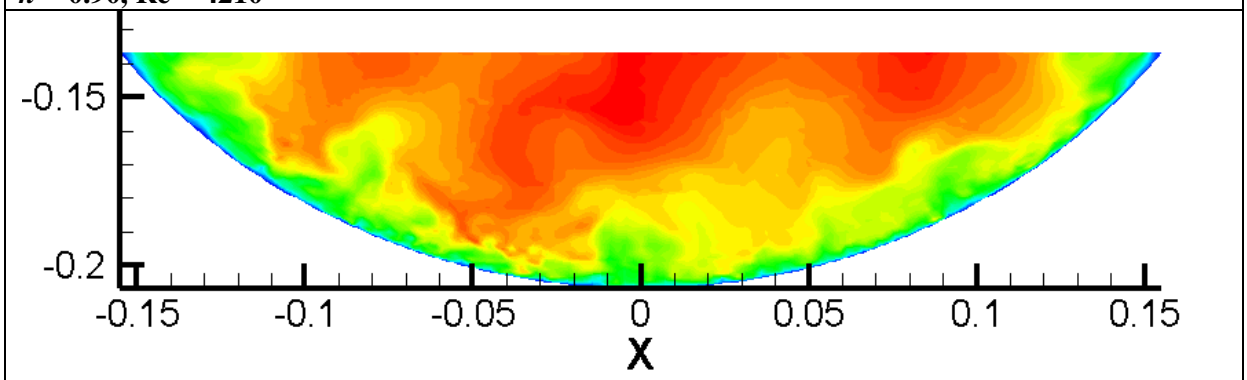

Axial velocity

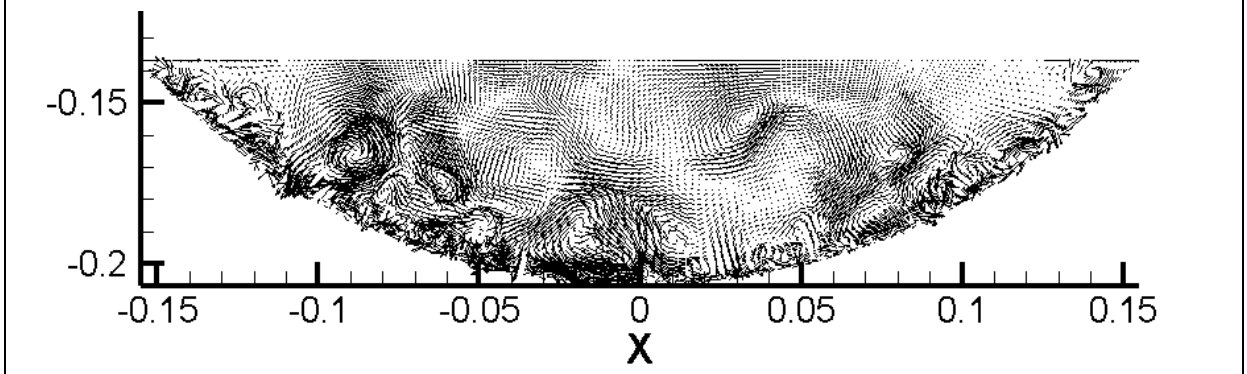

In-plan velocities

***n* = 0.75, Re = 12910**

Figure 123 Contours of instantaneous axial velocity and in-plane velocity vectors

Cross sections of velocity contour and velocity vectors are presented in Figure 123. For n = 0.90, the axial velocity's colour is less intense with a bulk velocity of 1.55 m/s and the in-

plane velocity vectors plot has only small size eddies along the bottom of the channel. In Appendix G 5**,** the plots corresponding to n = 0.85 do not share any recognisable difference when compared with control simulation. Similarly, plots for n = 0.79 shows similar axial velocity contours when compared with the control simulation. The most dissimilar plot out of the above five sets is where n = 0.75 with a Reynolds number of 12910. In n = 0.75 in-plane velocity vector plot, there is a number of strong turbulent eddies at the bottom of the channel. This observation is also supported by the turbulent intensity profile from Figure 119 to Figure 121 that the turbulent intensity peak at $y^+ \approx 10$ - 50 which is very close to the channel wall. Further, this simply means that the instantaneous velocity for n = 0.75 is the highest among these five sets of plots. Obviously all of this is expected as n = 0.75 simulation has a relatively high Reynolds number of 12910.

The simulated bulk velocity for n = 0.79 and n = 0.85 is 1.61 m/s and 1.54 m/s respectively. These velocities are higher than the experimental value of 1.48 m/s. However, with all the mean velocity profiles showing shifting velocity profile upward in this investigation, it is very difficult to see the real effect of flow behaviour index in relation to bulk velocity. Therefore change in flow behaviour index is not one of the contributing factors of the different bulk velocity between simulation and experiment.

Table 22 shows a comparison between changes in n value with change in Reynolds number. From this table, it is easily seen that a small decrease of n can result a large increase in Reynolds number. That is why the simulations were getting very unsteady during the n = 0.75 and 0.79 investigation.

Table 22 Changes in *n* value in relation to change in Reynolds number

n	Change in *n* (%)	Change in Reynolds number (%)
0.75	-7.5%	+57.8%
0.79	-2.5%	+12.3%
0.85	+5.0%	-28.5%
0.90	+11.1%	-48.5%

6.5.4 Fluid consistency index (*K*) effect

The results from four simulations with different flow consistency indices are presented here. The values of *K* chosen are presented in Table 23. These four simulations are carried out at generalised Reynolds number of 4200-12900.

Table 23 Parameters for simulation

Simulation run	*n*	*K* (Pa.s^n)	τ_y (Pa)	Reynolds number	Wall viscosity
Control Simulation - Simulation result based on Fitton (2007) experiment	0.81	0.0506	2.249	8182	0.01998
***K* +20%**	0.81	0.0608	2.249	6781	0.025
***K* +50%**	0.81	0.0760	2.249	5635	0.033
***K* -20%**	0.81	0.0405	2.249	11450	0.015
***K* -50%**	0.81	0.0253	2.249	21991	0.0085

The mean axial velocity profiles for $K = 0.0608$ and 0.0405 is shown in Figure 124. It is also plotted with conventional 'law of the wall' non-dimensionalisation and is compared to controlled fluid consistency index profile. In viscous region, both of $K = 0.0608$ and 0.0405 velocity profile fit very well with the simulation velocity profile. This actually reinforces that there are some errors associated with flow behaviour index investigation where there is a shift in velocity profile in the viscous region. In the literature reviewed, all of the velocity profile shifts happen in the overlap region rather than viscous region.

In the overlap region, the general trend of $K = 0.0608$ and 0.0405 velocity profile almost matches with the control simulation. The profile for $K = 0.0608$ is above the control profile as well as theoretical logarithmic profile whereas the profile for $K = 0.0405$ falls below the control simulation profile. From Rudman *et al* (2001), it was discovered that mean flow profile approaches the logarithmic profile as Reynolds number increase. From Table 23, for $K = 0.0608$ it has a higher Reynolds number of 11450 than for $K = 0.0405$, where Reynolds number is 6781. Therefore, the plot is consistent with Rudman *et al* (2001)'s statement.

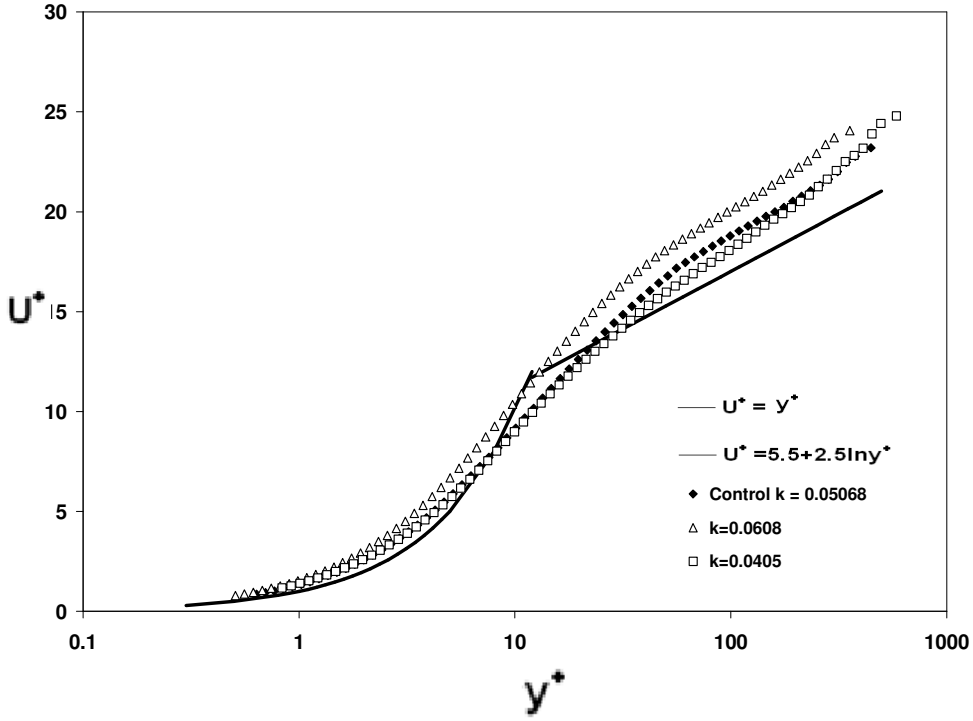

Figure 124 Mean axial velocity profiles for the turbulent flow of two fluids with different *K*

The production of turbulence is given by

$$P_{zr} = \overline{U'V'}\frac{\partial \overline{U}}{\partial r} \qquad \textbf{(85)}$$

Turbulent production plotted as a function of wall unit can be seen in Figure 125. From all simulations, the maximum production occurs at a value of $y^+ \approx 10$. From Figure 125, the simulation with smaller K has higher turbulent production values than the control simulation. In this case, when K = 0.0405 (-20%), the Reynolds number is 11450. Therefore at this point, it can be concluded that with K = 0.0405 (-20%), the turbulent production is the highest compared with control simulation.

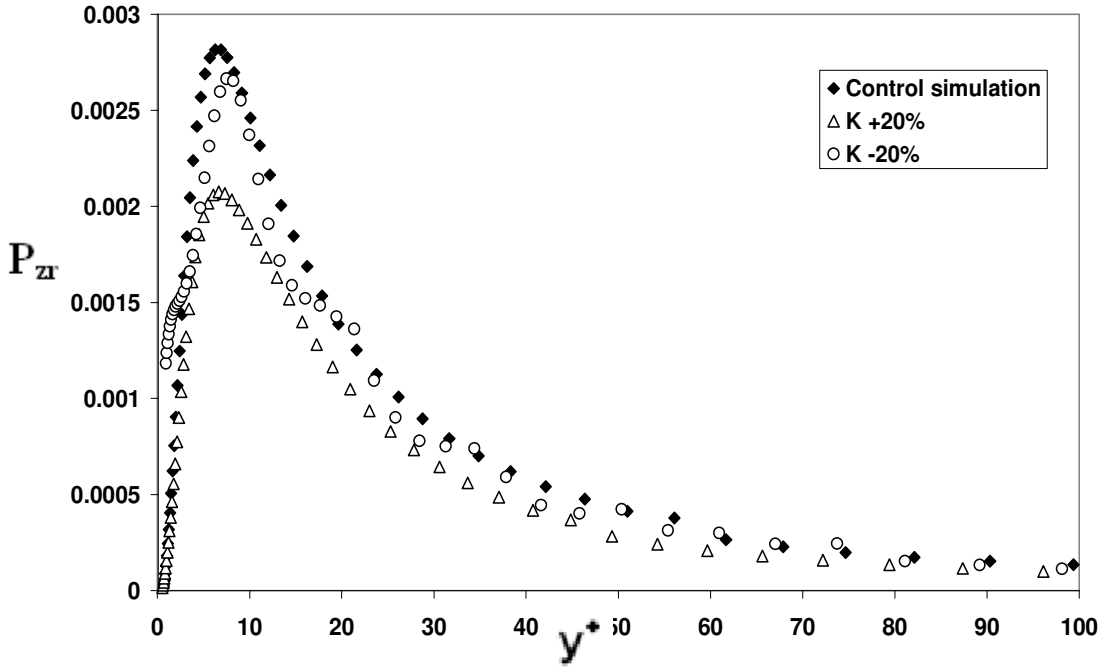

Figure 125 Turbulence production plotted as a function of wall unit

Contours of axial velocity of control simulation and all four different *K* simulations plus Newtonian simulation at $y^+ = 8$ are shown in Figure 126.

For *K* + 20% and *K* +50% contour, it is seen that the low velocity streaks are very thick, wide and very long. Especially on the side of the channel, these low velocity streak almost runs through the majority of the domain length. It is further suggested that the flow is not fully developed for increased *K* values. As *K* decreases, the low velocity streaks gradually disappear and become invisible. The low velocity streaks in *K* -20% velocity contour is short and have a small width. With *K* - 20%, the Reynolds number is already reaching 11450. This means the flow is very turbulent. In the next plot, there are some bright white spots present in *K* - 50% velocity contour which represent the high velocity streaks. This is not seen in the previous four velocity contours. This basically shows a more turbulent flow characteristic for *K* -20% and *K* -50% velocity contour.

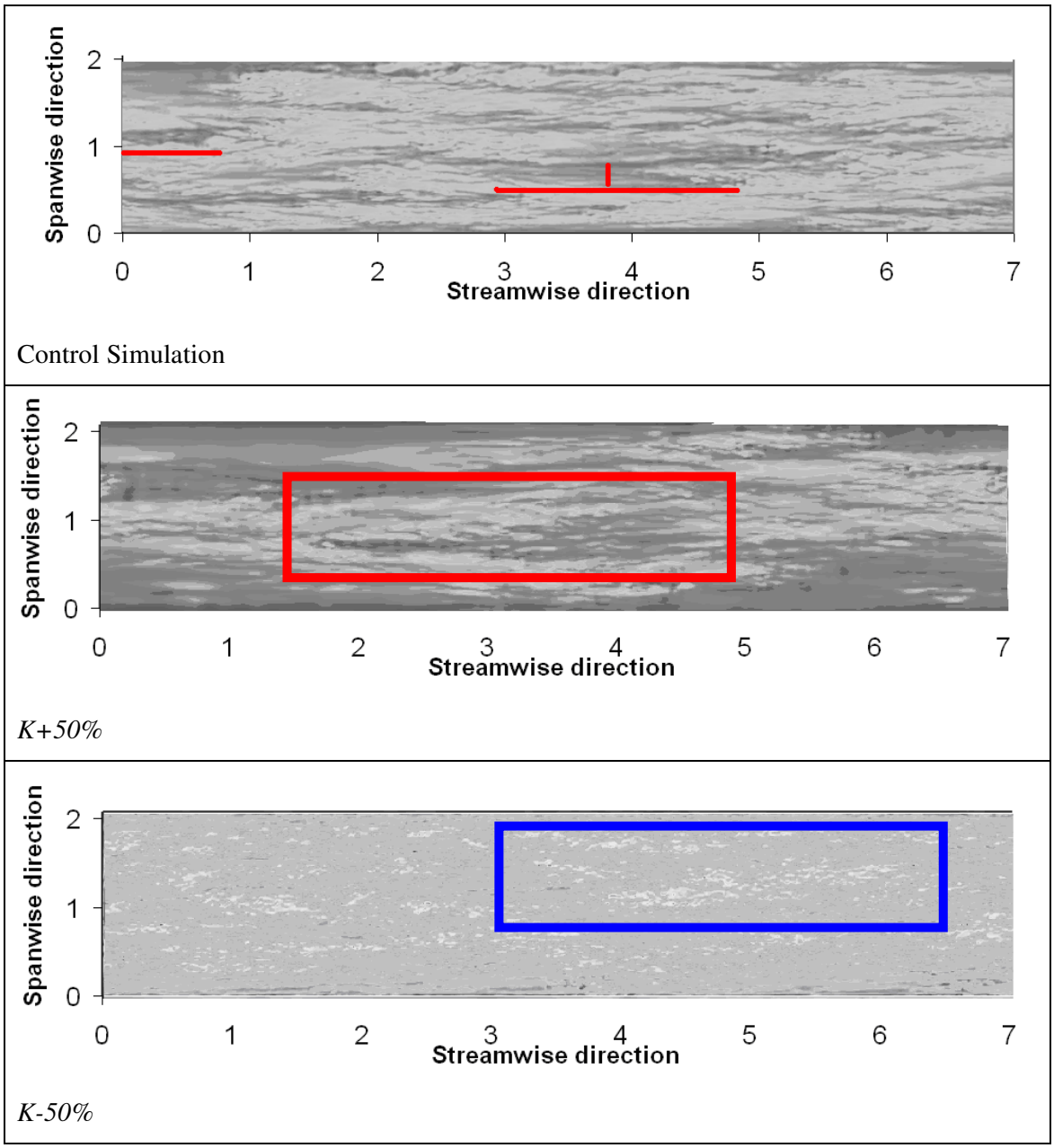

Figure 126 Predicted axial velocity at $y^+ \approx 8$. From top to bottom, Control simulation, *K* +50%, and *K* -50%. White represents high velocity and black represents low velocity.

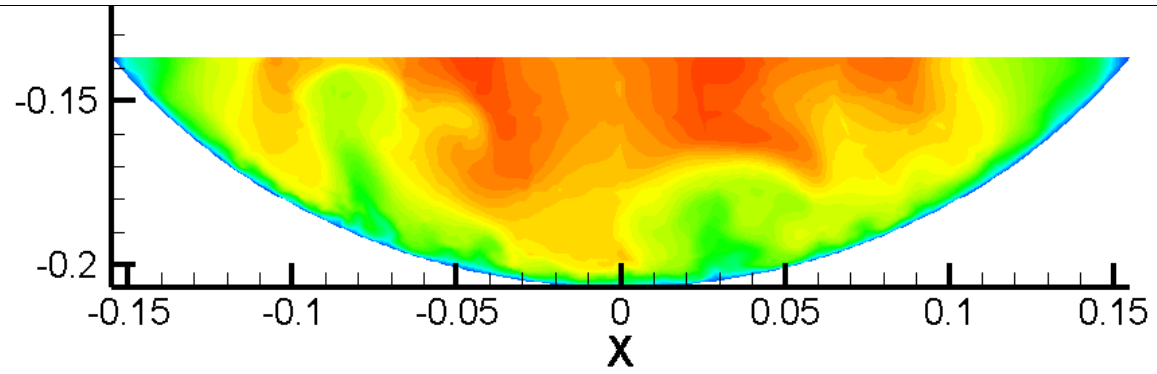

Axial velocity

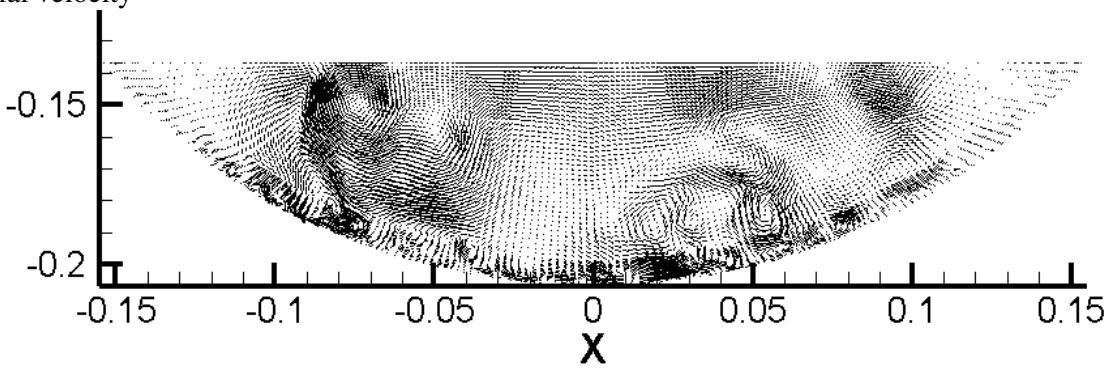

In-plane velocities

Control Simulation, Re = 8182

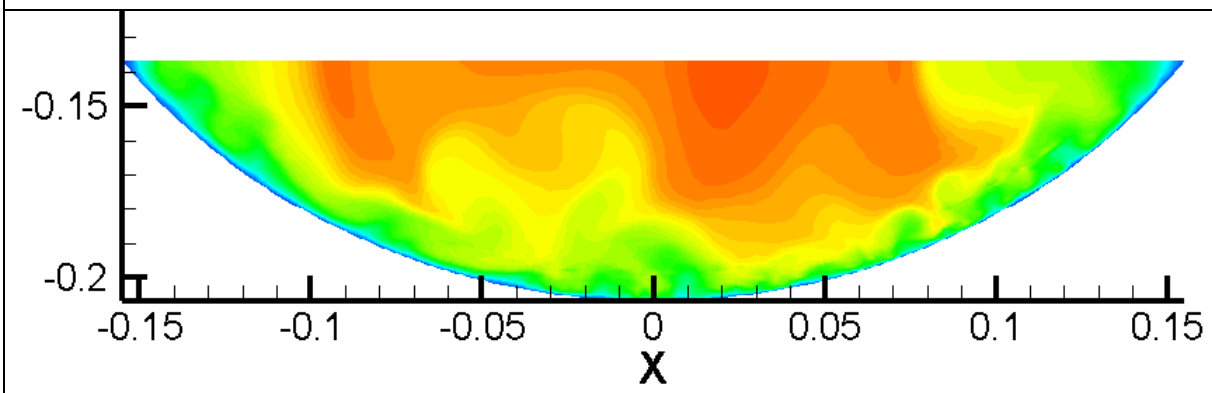

Axial velocity

Figure 127 continued

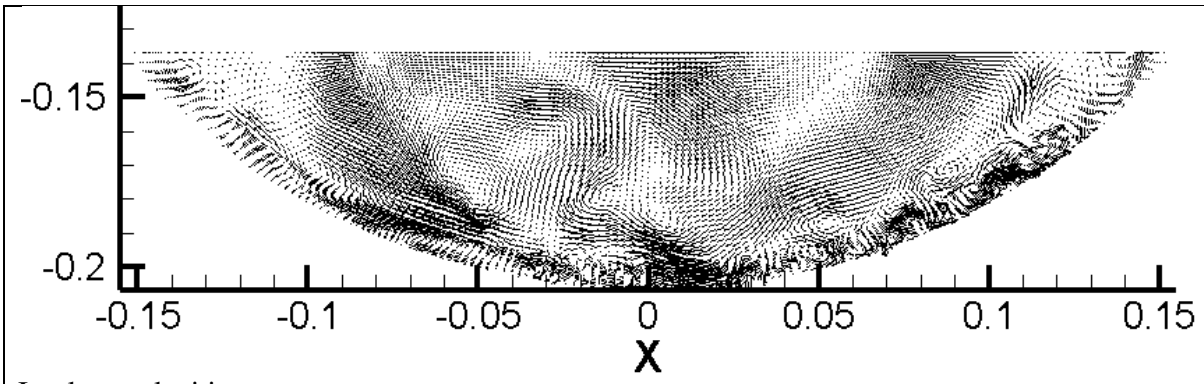

In-plane velocities

***K* +50%, Re = 5635**

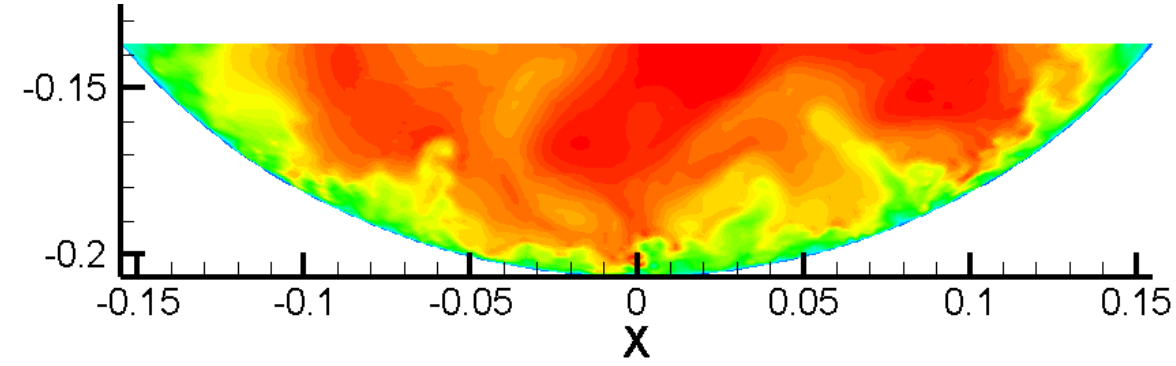

Axial velocity

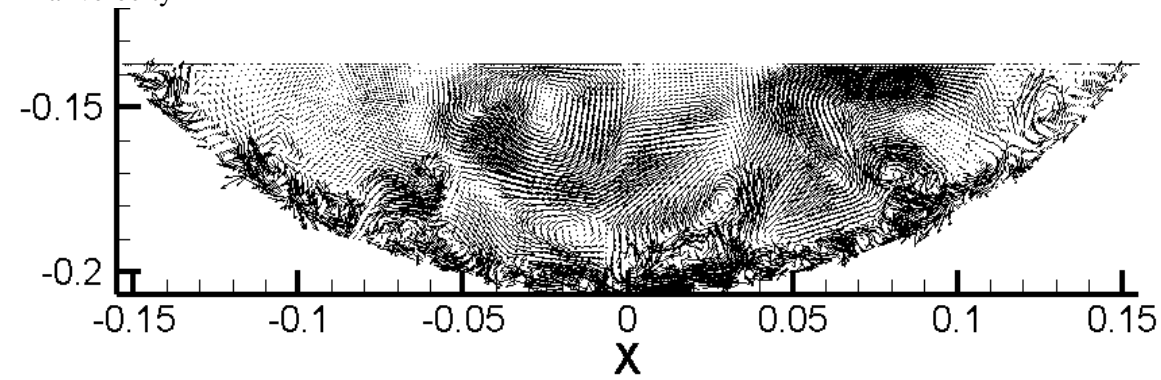

In-plane velocities

***K* -50%, Re = 21991**

Figure 127 Contours of instantaneous axial velocity and in-plane velocity vectors

Cross sections of velocity contours and velocity vectors are presented in Figure 127. The in-plane velocity vector plot for *K* +20% shows some small disturbance along the channel wall. Other than that, there is little to distinguish the plot from when compared with control simulation. Overall, the contour scales are identical for each *K* and the magnitude of the

cross-sectional velocity scales are equal. In *K* -20% in-plane plot, there is a large cluster of eddies in the left side of the channel. There is a significantly increased degree of structure in the core region of the *K* -50% plot where Reynolds number = 21991. This means that the instantaneous velocity for *K* -50% is highest among these five sets of plots with a bulk velocity of 1.67 m/s. However, it is also noted that with the Reynolds number at 21991, the resolution is insufficient to obtain good results from the simulation.

Fixed Reynolds number

Parallel investigation was conducted with similar Reynolds number. A number of *K* values were chosen for these simulations. *K* values of +50% and -50% of *K* values were not chosen because from previous experience, these simulations might become very unstable. However, *n* values also needed to be changed in order to have a relatively constant Reynolds number.

Table 24 Parameters for simulation

Simulation run	*n*	*K* (Pa.s^n)	τ_y (Pa)	Reynolds number	Wall viscosity
Control Simulation - Simulation result based on Fitton (2007) experiment	0.81	0.0506	2.249	8182	0.01998
***K* +20%**	0.781	0.0608	2.249	8278	0.0200
***K* +30%**	0.763	0.0659	2.249	8630	0.0192
***K* -20%**	0.846	0.0405	2.249	8295	0.0200
***K* -30%**	0.861	0.0354	2.249	8682	0.0191

The mean axial velocity profiles for *K* = 0.0608 and 0.0658 are shown in Figure 128. In the viscous region, *K* = 0.0608 velocity profile fits very well with the control simulation velocity profile. In the overlap region, *K* = 0.0608 velocity profile is slightly higher than the control simulation velocity profile. On the other hand, *K* = 0.0658 velocity profile falls above control simulation velocity profile as well as *K* = 0.0608 velocity profile. The general shape of the velocity profile fits very well with each other. Even with the *K* = 0.0658 velocity profile shifted upward, the shape of this profile is exactly the same as the other two profiles. From this plot, it is expected that with increase of *K,* the velocity profile will shift upward in both viscous region and overlap region. However, more values need to be tested in order to make the conclusion valid.

In Figure 129, the mean axial velocity profiles for K = 0.0405 and 0.0354 are plotted. In the overlap region, K = 0.0405 velocity profile fits quite well with the control simulation velocity profile. In the viscous region, K = 0.0405 velocity profile is slightly higher than the control simulation velocity profile. Surprisingly, K = 0.0354 velocity profile falls sufficiently above control simulation velocity profile as well as that of K = 0.0354 velocity profile. One of the distinct features of the K = 0.0354 velocity profile is that the shape of the profile is quite different to the other velocity profiles. There is no curvature in the viscous region for K = 0.0354 velocity profile. This could be a problem with simulation itself caused by simulation instability. This is also much unexpected as the Reynolds numbers are kept at a similar value. Other than that, the general shape of the rest of the velocity profiles fit very well. As stated previously, more values need to be tested in future work.

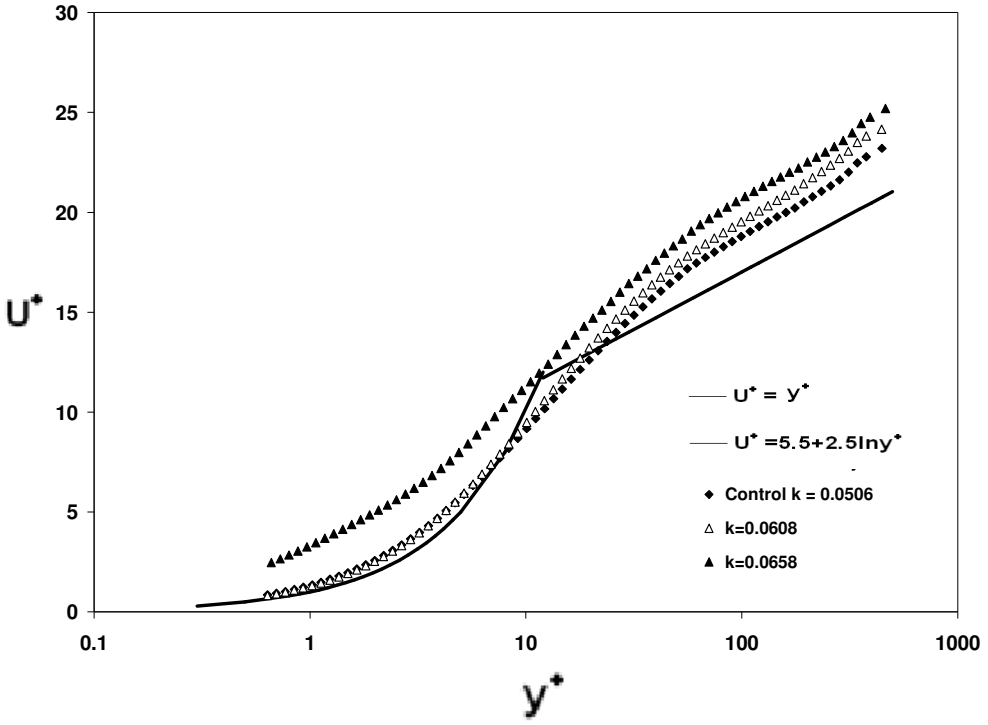

Figure 128 Mean axial velocity profiles for the turbulent flow of two fluids with different K values

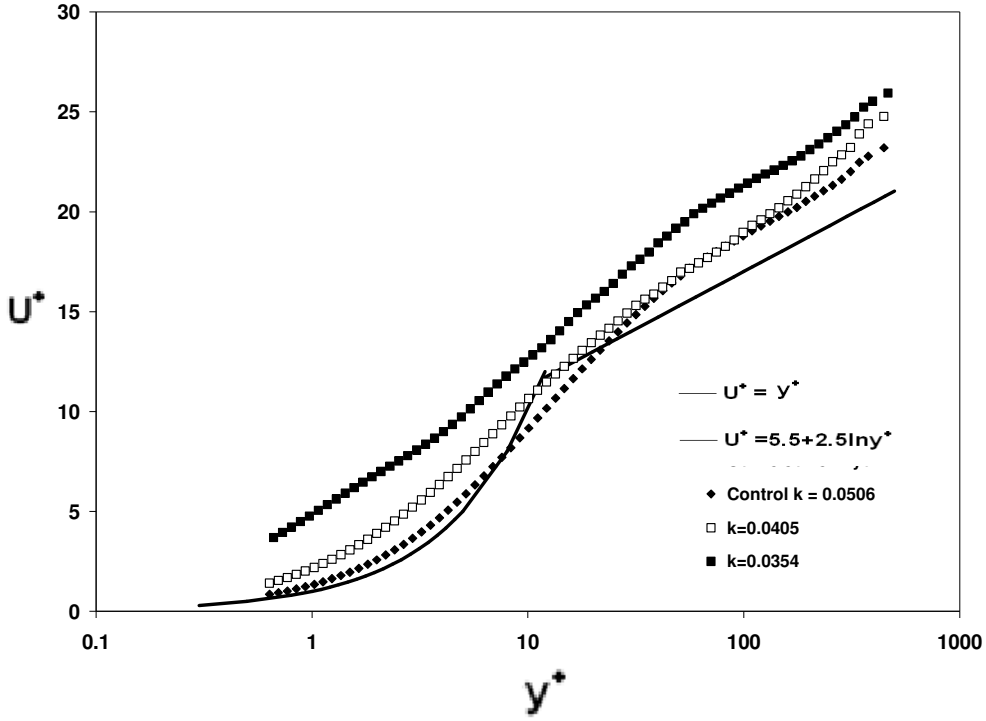

Figure 129 Mean axial velocity profiles for the turbulent flow of two fluids with different *K* values

Turbulent production plotted as a function of wall unit can be seen in Figure 130. From all simulations, the maximum production occurs at a value of wall unit ≈ 5. From Figure 130, the simulation with smaller *K* value has higher turbulent production values than the control simulation. In this case, Reynolds number for both simulations is very similar. Hence, the difference in turbulent production is caused by change in *K* values only. Therefore at this point, it can be concluded that with decreased *K* value, the turbulent production will increase in comparison with control simulation. With increased *K* value, the turbulent production will decrease in comparison with control simulation.

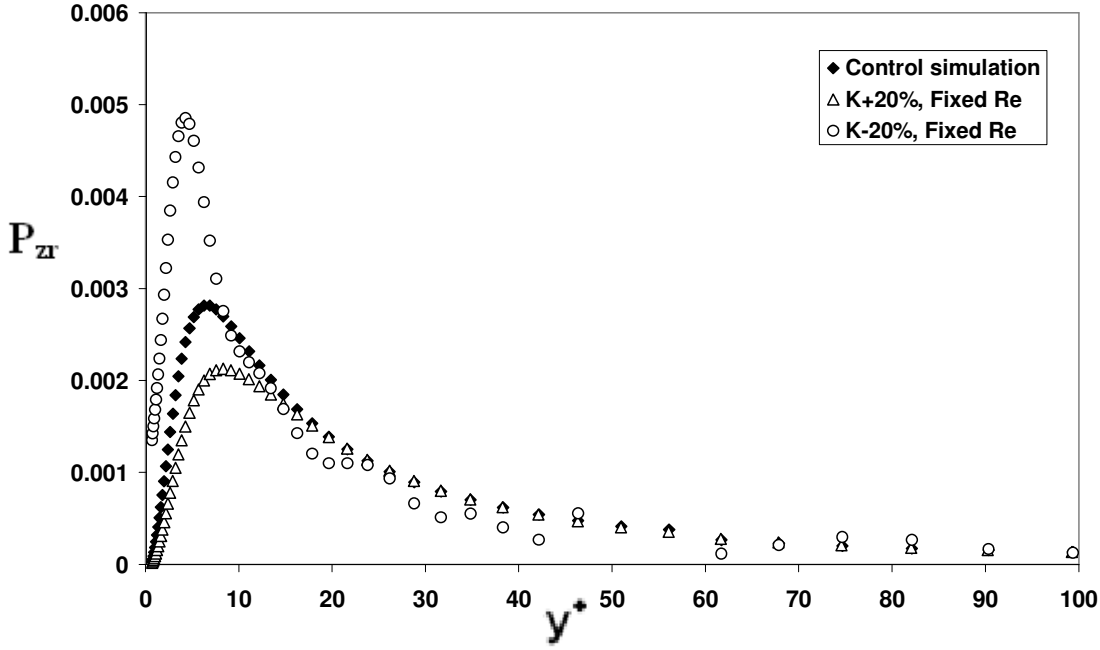

Figure 130 Turbulent production plotted as a function of wall unit

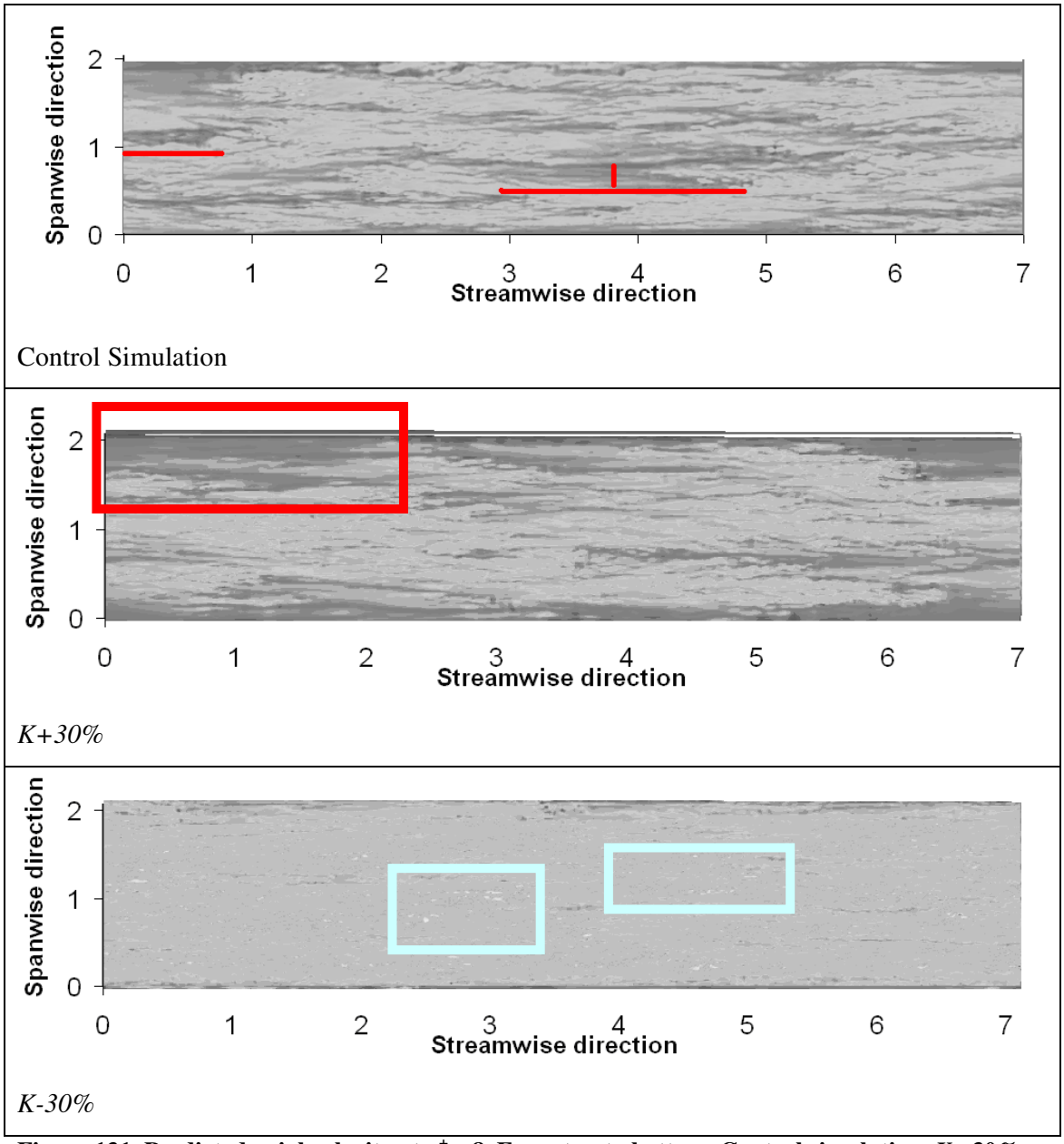

Figure 131 Predicted axial velocity at $y^+ \approx 8$. From top to bottom, Control simulation, *K* +30%, and *K* -30%. White represents high velocity and black represents low velocity.

Contours of axial velocity of control simulation *K* +30% and *K* -30% simulations plus Newtonian simulation at $y^+ = 8$ are shown in Figure 131. Contours of axial velocity of control simulation *K* +20% and *K* -20% simulations at $y^+ = 8$ are shown in Appendix H 3.

In Appendix H 3 and Figure 131, for *K* + 20% and *K* +30% contour, it is seen that a large region of low velocity streaks exists towards both end of the domain. The streaks are very

thick and very wide. It is very interesting to see that with a similar Reynolds number (around 8200-8600), the flow structures are still somewhat different. From *K* + 20% and *K* +30% contours, it is further suggested that the flow is not fully developed for increased *K* values.

Similar to Figure 126, as *K* decreases, the low velocity streaks gradually disappear and high velocity streaks appear. From Appendix H 3 with Reynolds number at around 8200, the low velocity streaks in *K* -20% velocity contour is quite short and random. This means regardless of Reynolds number effect, the flow is still very turbulent. In Figure 131, the bright white spots in *K* -30% velocity contour represent the high velocity streaks. This is not seen in the previous four velocity contours. This plot simply shows a more turbulent flow characteristic for *K* -20% and *K* -30% velocity contour. Moreover, the *K* -50% in Figure 126 and *K* -30% in Figure 131 show very similar velocity contours. Both of them have a number of high velocity streaks yet the Reynolds number for those two simulations is extremely different. This shows that without Reynolds number effect, a decreased *K* value will give more developed and more turbulent flows.

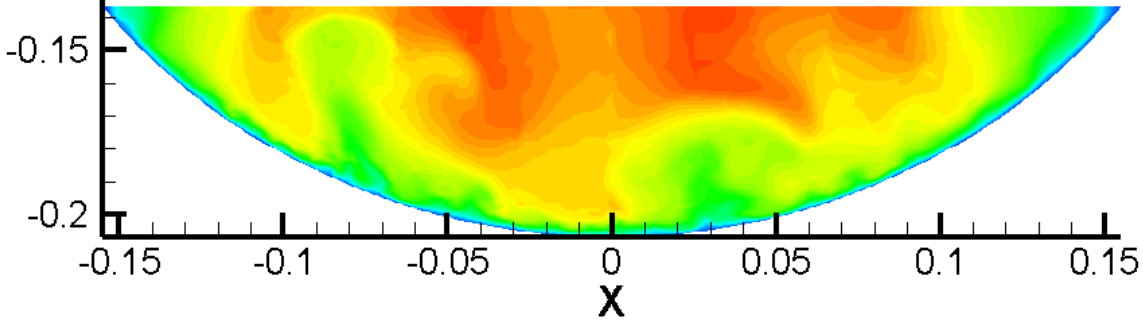

Axial velocity

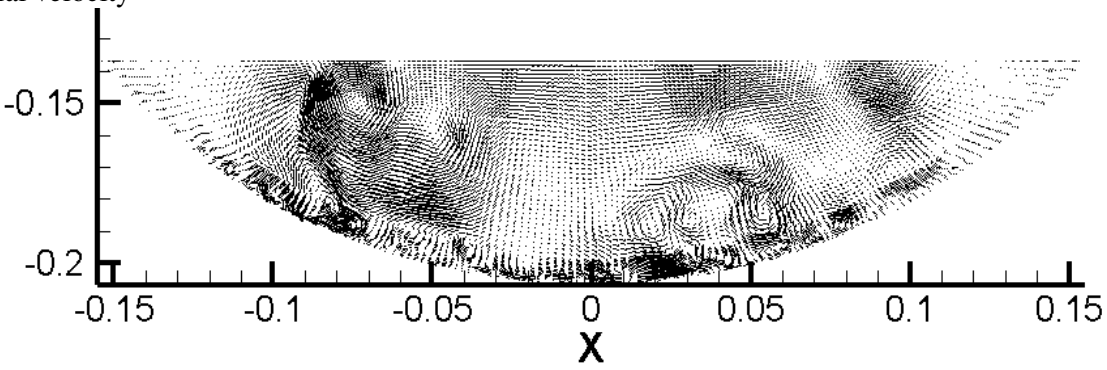

In-plane velocities

Control Simulation

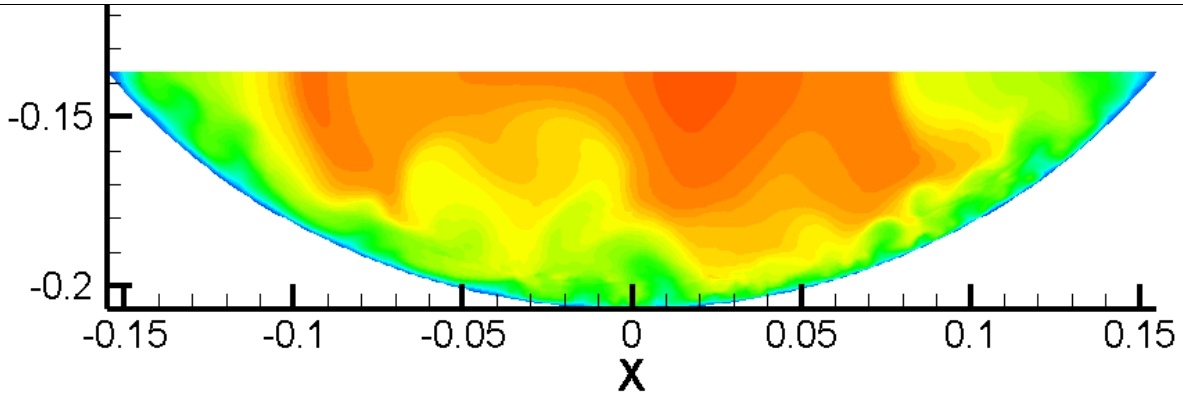

Axial velocity

Figure 132 continued

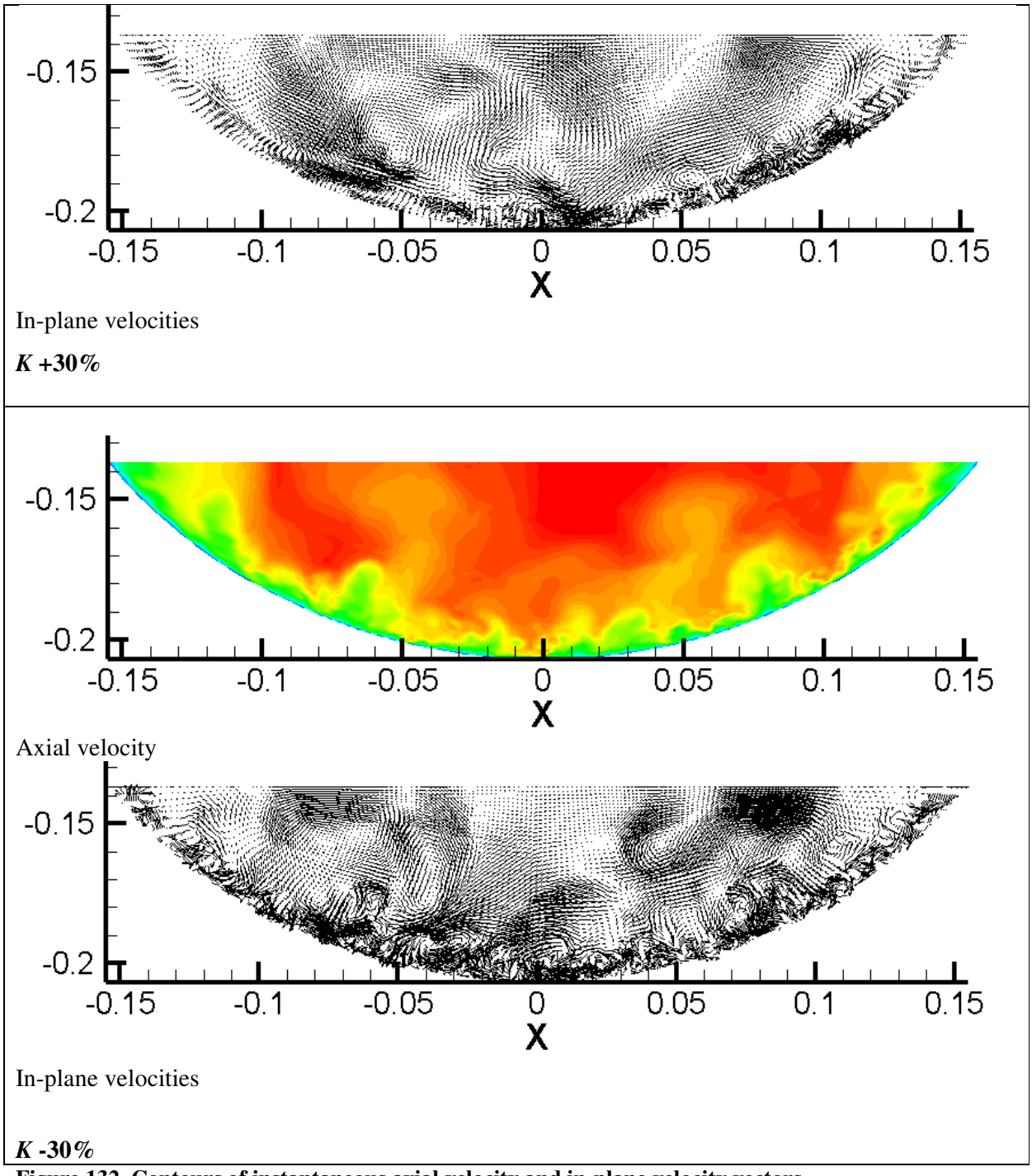

Figure 132 Contours of instantaneous axial velocity and in-plane velocity vectors

Cross sections of velocity contours and velocity vectors are presented in Figure 132**.** In-plane velocity vector plot for *K* +20% shows some small cluster of eddies along the channel wall. The axial velocity contour looks the same as the control simulation on both intensity and

shape. In *K* +30% plot, the in-plane velocity vector shows the smallest disturbance out of all five plots. This means that with increased *K* value, and increased viscosity in the core region, the turbulence is not as fully developed. Overall, the contour scales are identical for each *K* and the magnitude of the cross-sectional velocity scales are equal. In *K* -20% in-plane plot, there is a large cluster of eddies in the left side of the channel, which means the flow is becoming more turbulent. There is a significantly increased degree of structure in the core region of the *K* -30%. In the axial velocity plot, the velocity is around 2 m/s whereas in other simulations velocities are in a range of 1.6-1.8 m/s. This means that the instantaneous velocity for *K* -30% is the highest among these five sets of plots. This further shows the full effect of *K* without the effect of Reynolds number.

Table 25 shows a small comparison between changes in *K* values with change in Reynolds number. From this table, it is easily seen that a small decrease of *K* can results a large increase in Reynolds number. And an increase of *K* value can result in a large decrease in Reynolds number.

Table 25 Changes in *K* values in relation to change in Reynolds number

K	Change in *K* (%)	Change in Reynolds number (%)
0.0608	+20%	-17.1%
0.0659	+50%	-31.1%
0.0405	-20%	+40.0%
0.0354	-50%	+168.7%

6.5.5 Depth effect

In the experiment, the flow rate is usually set and depth is estimated. In the simulation, it is the opposite that the geometry is set (i.e. fixed depth) and Reynolds number (i.e. flow rate) is estimated. Different depths cause different Reynolds numbers therefore different flow rate can be recorded with unchanged forcing (i.e. slope). However, because of the nature of simulation and assumed grid, the depth is fixed under different conditions.

The question is quite obvious: If the depth is changing and rheology stays the same, how does the Reynolds number change and how does the bulk velocity change? Hence, depth of 0.06 m and 0.08 m were chosen to be tested in this investigation.

Table 26 Parameters for simulation

Simulation run	Bulk velocity (m/s)	Depth (m)	Hydraulic radius (m)	Cross-sectional Area (m^2)	Reynolds number
Control Simulation - Simulation result based on Fitton (2007) experiment	1.48	0.07	0.0429	0.0151	8182
Depth = 0.08 m Increased depth	1.46	0.08	0.0484	0.0182	10024
Depth = 0.06 m Decreased depth	1.52	0.06	0.0372	0.0120	6663

The mean axial velocity profiles for depth = 0.06 m and 0.08 m is shown in Figure 133. In the viscous region, the velocity profile for depth = 0.06 m is identical with control simulation. Whereas for depth = 0.08 m the velocity profile is sitting above the control simulation profile. In the overlap region, for depth = 0.06 m the velocity profile is moving above the base simulation profile whereas for depth = 0.08 m the velocity profile is falling below. However, there is no clear explanation on this behaviour as the general trend of the velocity profile is almost identical.

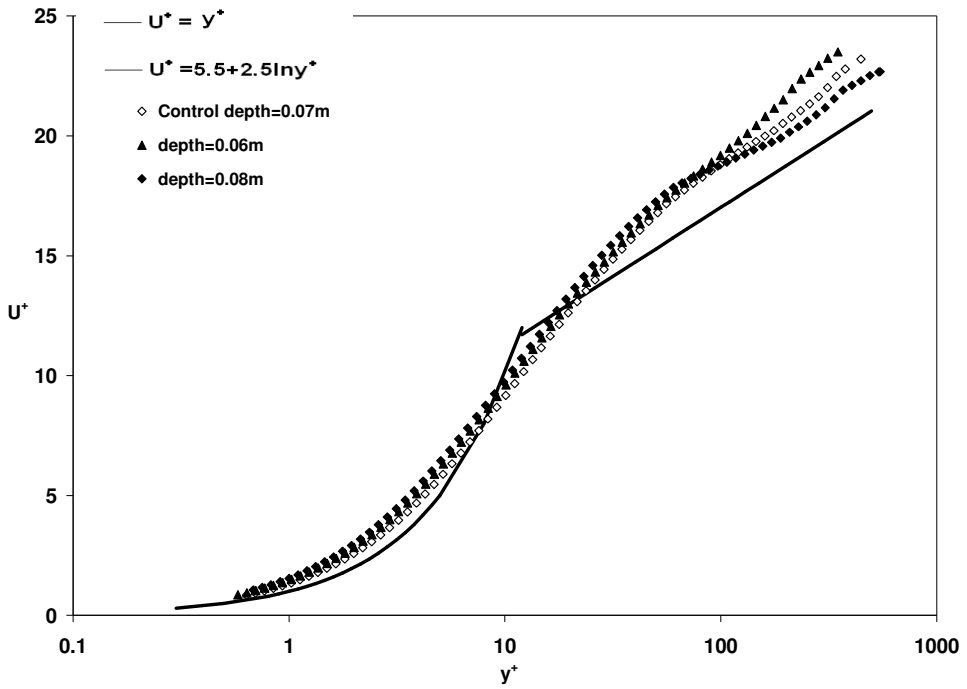

Figure 133 Mean axial velocity profiles for the turbulent flow of two fluids with different depths

It is also interesting to see the real effect of Reynolds number to the simulation. In this investigation, all the rheological parameters and slope are kept consistent; the only variable is the flow depth. So if the slope is not changing, change in depth will change the flow rate hence the Reynolds number of the flow.

Contours of axial velocity at $y^+ = 8$ are shown in Figure 134. As the Reynolds number increases, the low velocity streaks in the simulation of depth equals to 0.08 m are less in quantity than the control simulation. This is expected as the flow become more turbulent thus the instantaneous velocity increases. As the Reynolds number decreases, the low velocity streaks in the simulation of depth equals to 0.06 m are slightly apparent than the control simulation especially around the side of the channel. However, with Reynolds number of 6663 for depth equates 0.06 m, the flow is still quite turbulent.

According to Table 26, with an increased depth (i.e. Increasing from 0.07 m to 0.08 m), the bulk velocity changed from 1.48 m/s to 1.46 m/s. In this case, when the depth of the flow increases; the area of the flow increases by 20.5% and the estimated flow rate increases by 16.6%. With fixed flow rate, an increase in depth would lead to a decrease in bulk velocity. In

the current simulation, with a decreased bulk velocity, the estimated flow rate is still higher than the control simulation. There is no likely explanation for such behaviour. Comparing the bulk velocity from simulation with that of experimental value (Fitton, 2007); it is found that the simulation value is still a lot higher than 1.06 m/s. The bulk velocity difference between simulation and experiment changed from 39% to 37% by change the depth. It is very unlikely that the measurement error is this large during the experiment. Therefore depth measurement error is not the major contributing factor of the different bulk velocity between simulation and experiment.

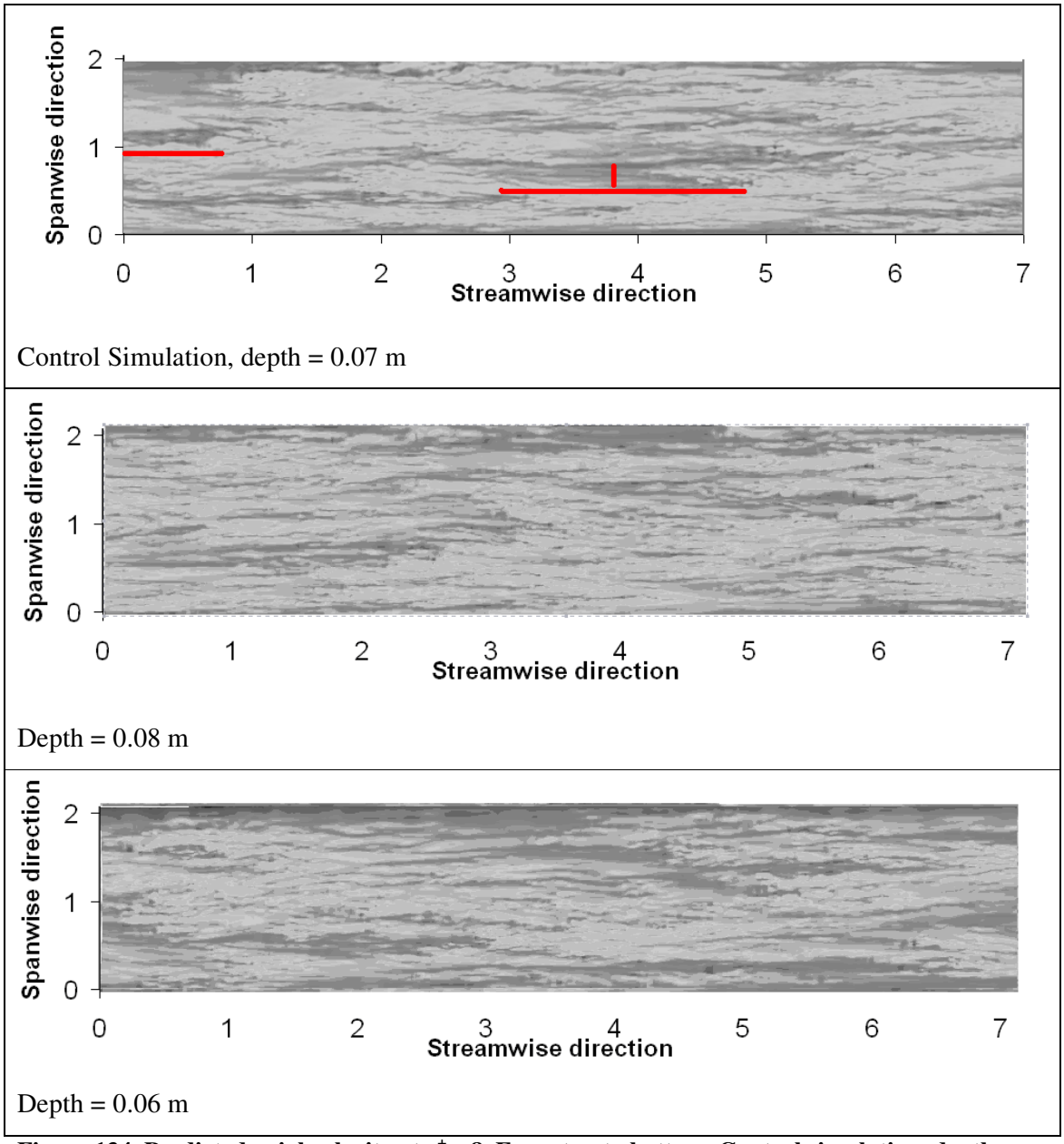

Figure 134 Predicted axial velocity at $y^+ \approx 8$. From top to bottom, Control simulation, depth = 0.08 m and depth = 0.06 m. White represents high velocity and black represents low velocity

6.5.6 Side measurements

From previous sections, all the simulation velocity profiles were obtained from channel's centre line. So what is the magnitude of velocity in different x (side) locations?

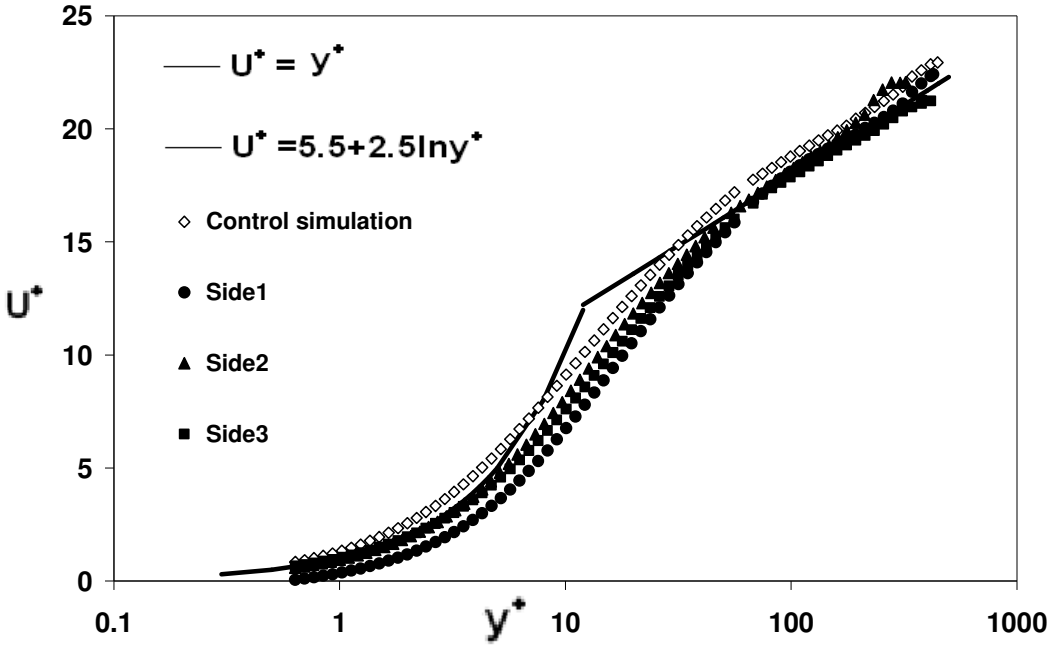

Figure 135 Mean axial velocity profiles for the turbulent flow of with different side measurements

Three different x positions x = 0.04 m, 0.065 m and 0.088 m were chosen in this investigation. The mean axial velocity profiles for all three different x positions and the centreline velocity profile is shown in Figure 135. All three x positions measurements fall below of the centreline velocity profile. This should be expected as the centreline velocity is the highest in the channel flow. Interestingly, in Figure 137 and Figure 139, there is a small velocity dip appearing at y^+ close to 230-300. It was suspected previously that in the centreline velocity profile, there was a very small velocity dip. With x moving out from the centreline, the velocity profile's velocity dip becomes more apparent and visible. Nevertheless, this could also be a possible feature of secondary current. More discussion of the secondary current phenomena will be presented in latter sections. In conclusion, with different x position measurements, the velocity is decreased with x shifting away from the centreline. Velocity dipping also appeared with x moving out towards to the channel boundary.

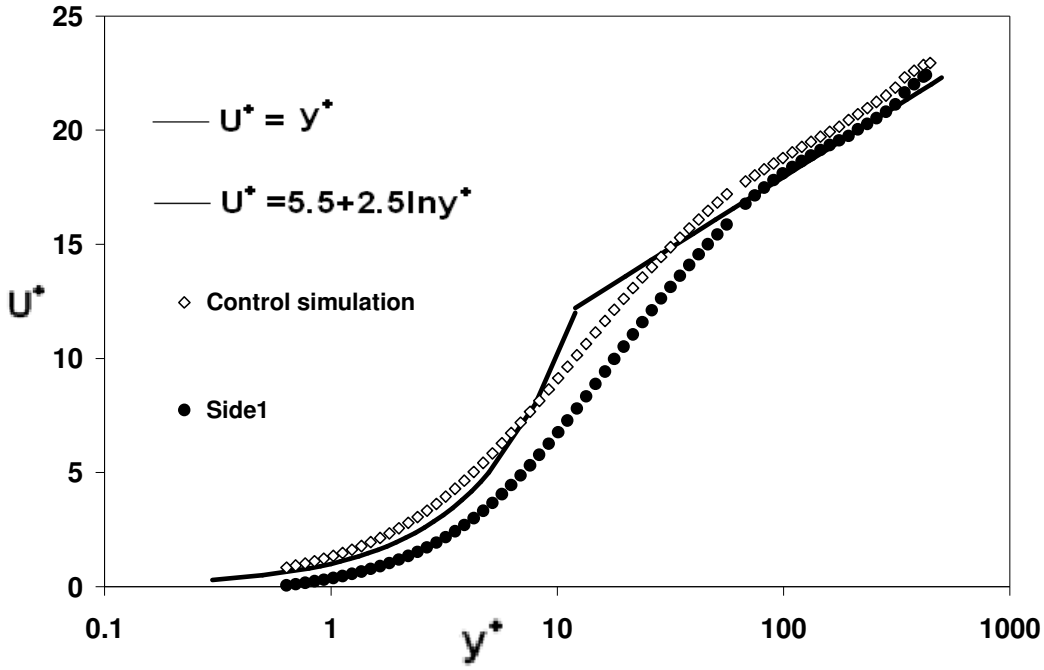

Figure 136 Mean axial velocity profiles for the turbulent flow at x = 0.04 m

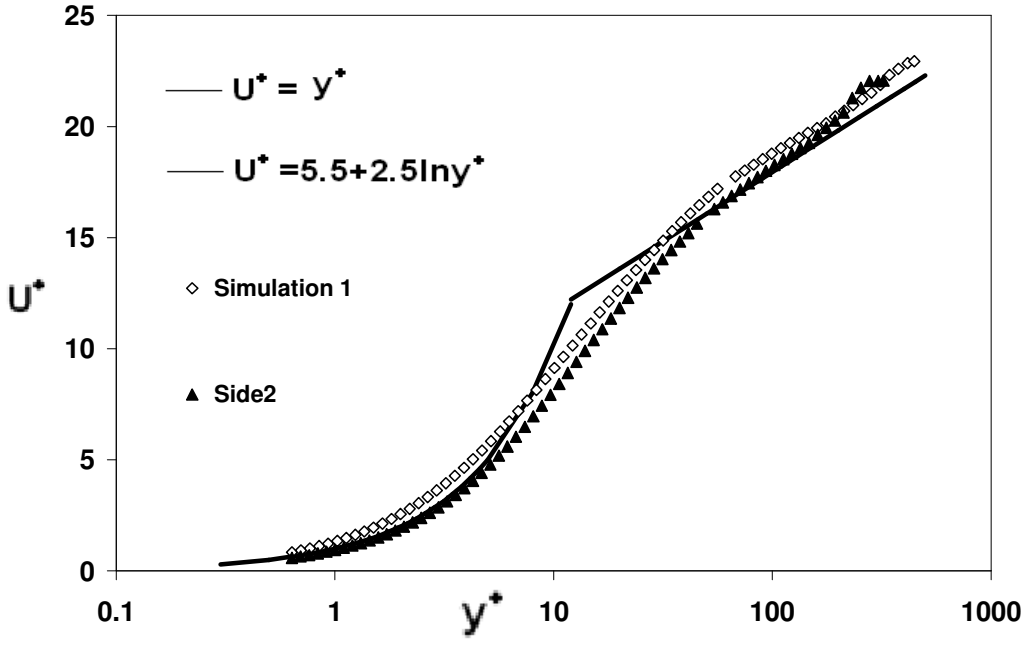

Figure 137 Mean axial velocity profiles for the turbulent flow at x = 0.065 m

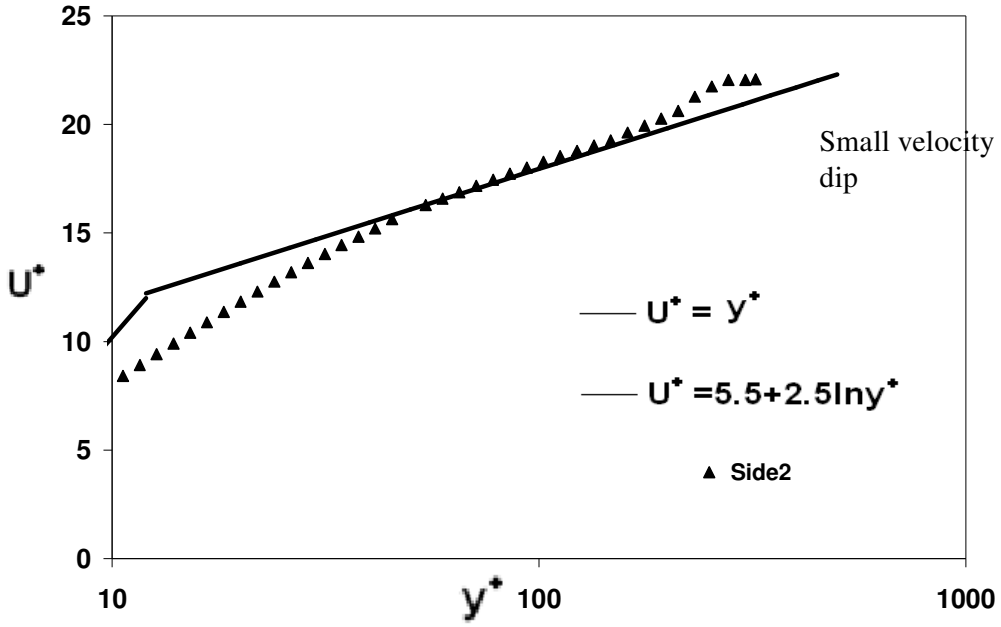

Figure 138 Mean axial velocity profiles for the turbulent flow at x = 0.065 m. 10 < y^+ <100

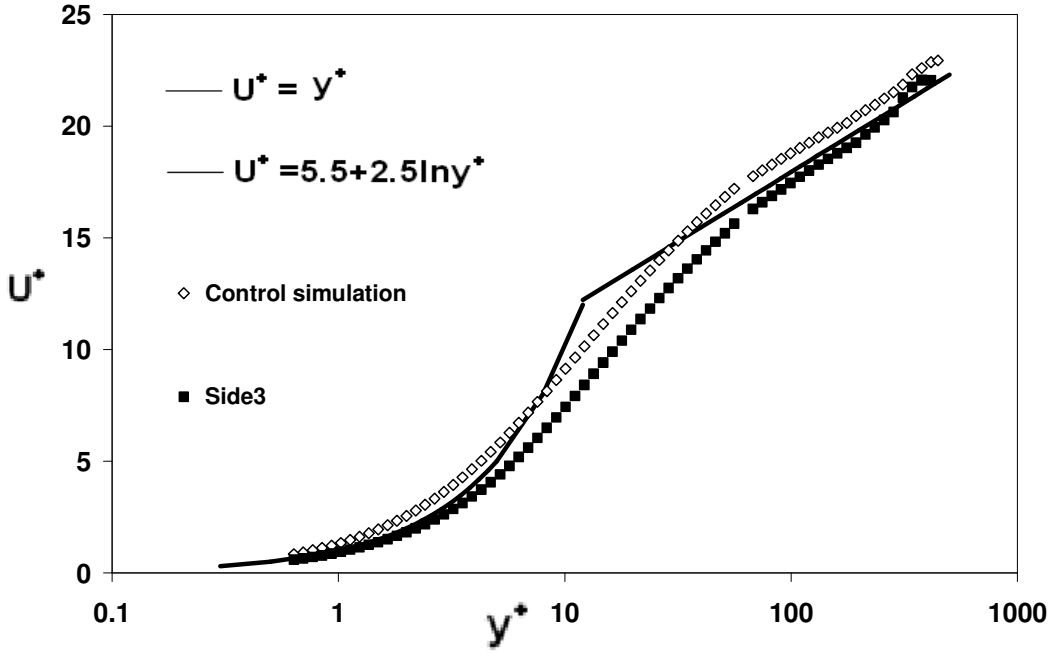

Figure 139 Mean axial velocity profiles for the turbulent flow at x = 0.088 m

6.5.7 Finer mesh effect

Previously, the computational domain consisted of 51 fifteenth order elements in the channel cross section and 384 Fourier modes in the axial direction, with domain lengths of $0.5\pi D$. In the finer mesh, the computational domain changed to 177 twelfth order elements in the channel cross section and 256 Fourier modes in the axial direct, with domain lengths unchanged. The Fourier modes were already decreased, however; this simulation took at least double the time consumed for the previous mesh. Figure 140 and Figure 141 show the coordinates of the old mesh and finer mesh respectively. It is easy to see from Figure 141 that the mesh has a lot more coordinate points than Figure 140.

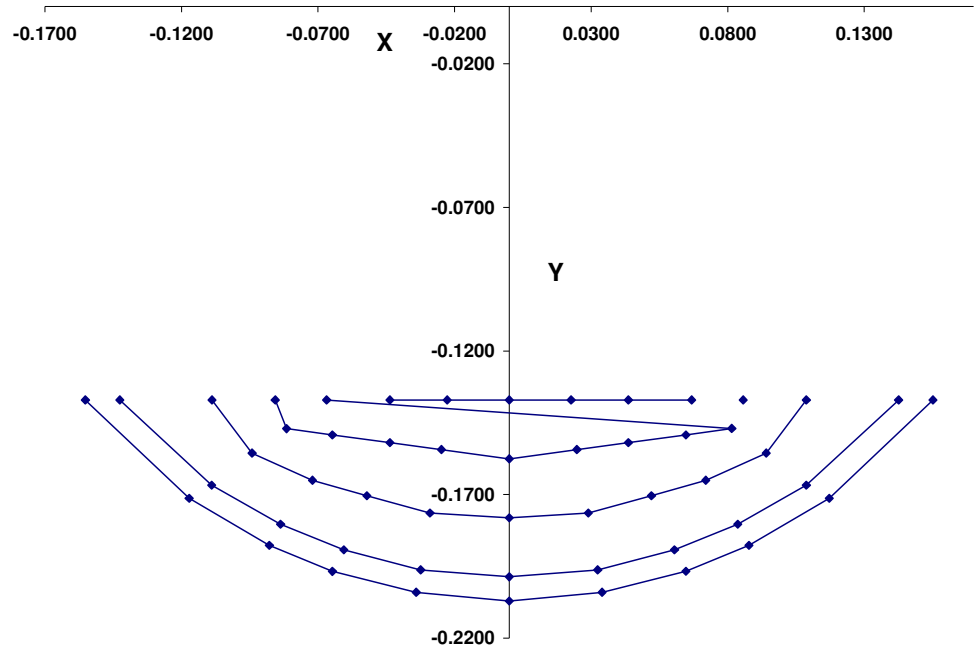

Figure 140 Coordinates of old simulation mesh

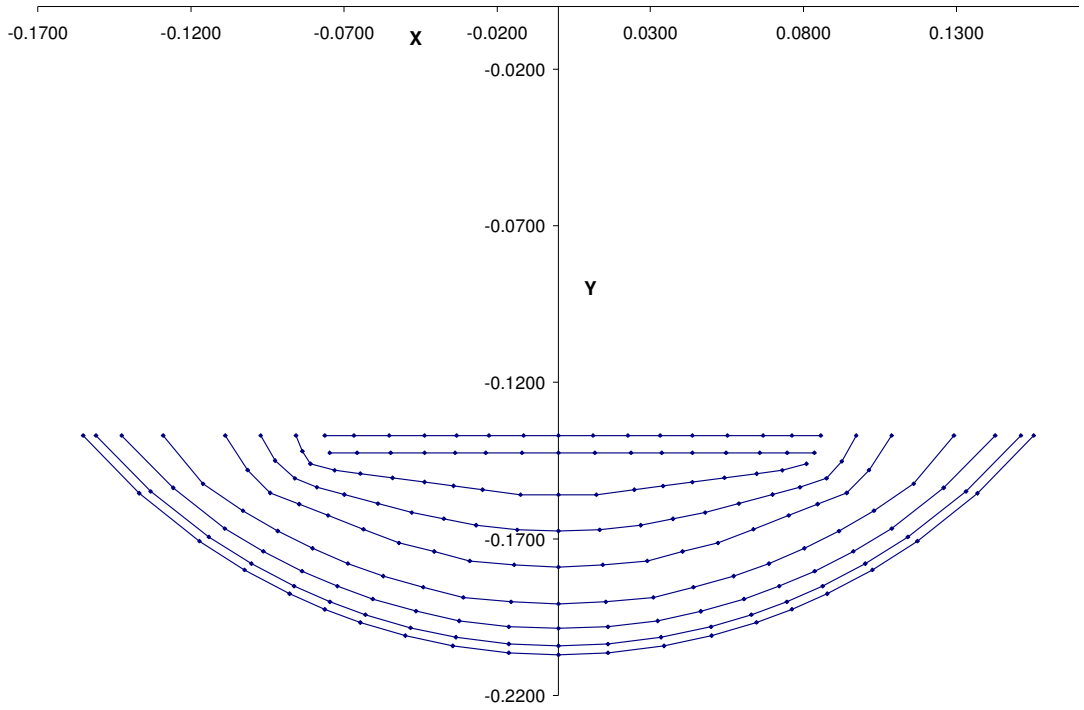

Figure 141 Coordinates of finer simulation mesh

The mean axial velocity profiles for two different meshes are shown in Figure 142. From the plot, it is seen that in the viscous region, the velocity profile for the finer mesh is below the older mesh (control simulation) velocity profile. It is very likely that the finer mesh can have a better resolution in the wall region because of redefined mesh. However, in the overlap region, both meshes produce identical velocity profile. There is also a small velocity dip at y^+ equal to around 450.

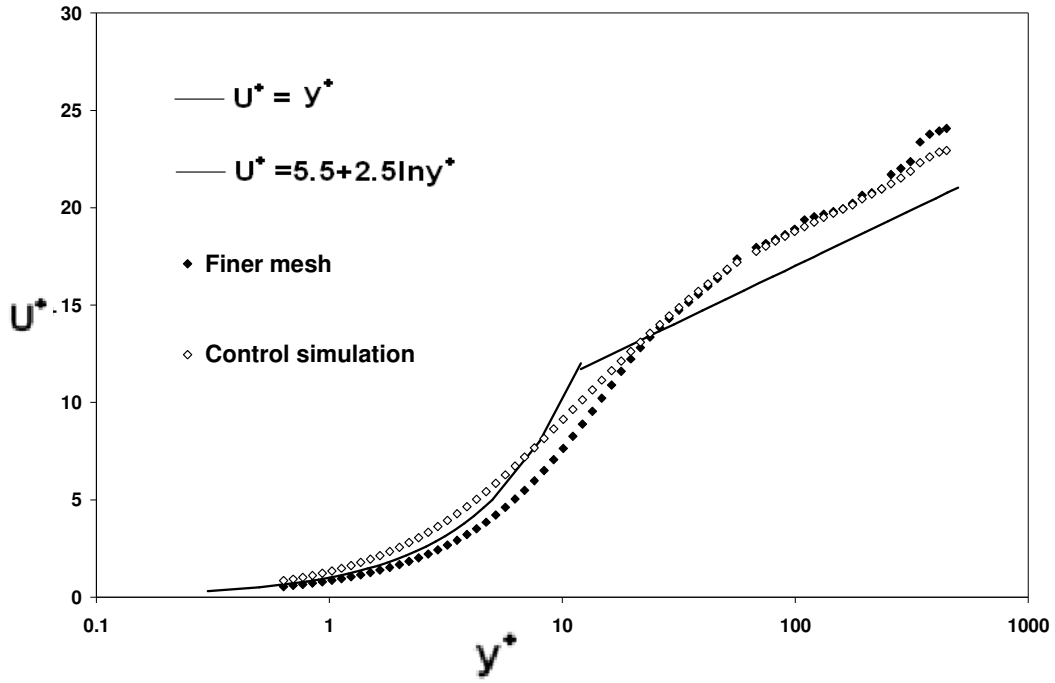

Figure 142 Mean axial velocity profiles for the turbulent flow of two different meshes

The finer mesh simulation and control simulation's turbulent intensities are plotted in Figure 143 to Figure 145. All the plots show very similar trend with the finer mesh turbulence intensities fall below the control simulation. In Figure 143 and Figure 144, the turbulence intensities are not fully converged. In the radial turbulence intensities plot, finer mesh curve shows a smoother look than the control simulation curve. The small differences in turbulent intensities showing that the coarse mesh is not fully resolved, however the differences are not significant.

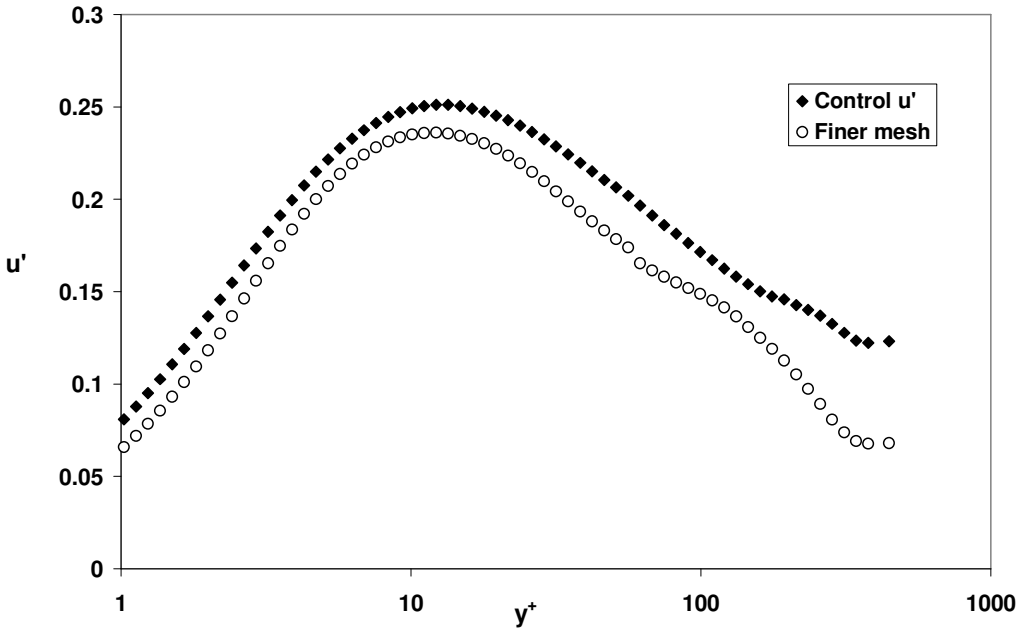

Figure 143 Axial turbulence intensities plotted in wall coordinates

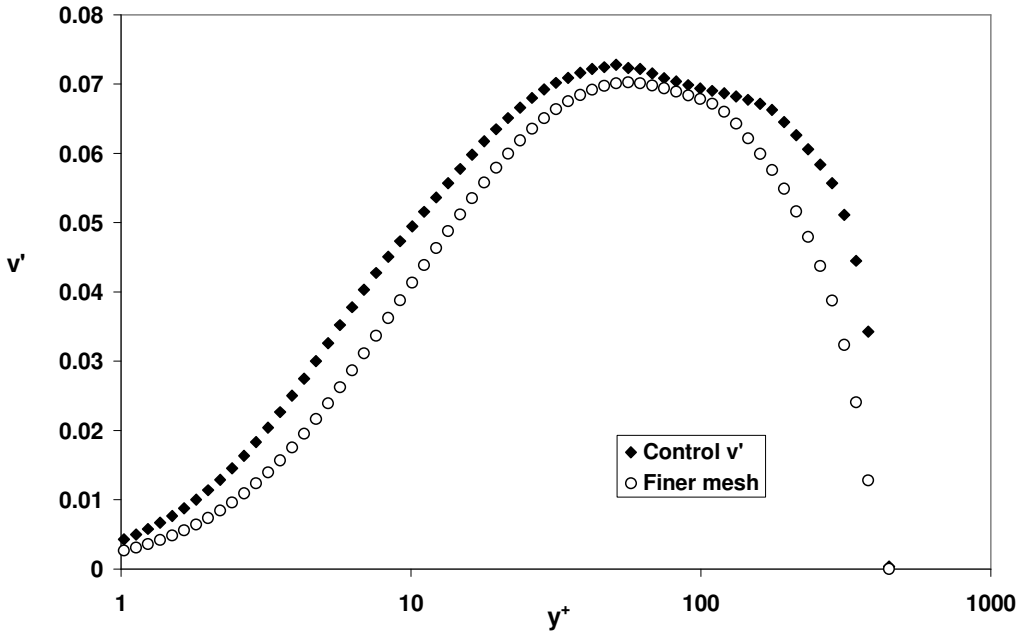

Figure 144 Radial turbulence intensities plotted in wall coordinates

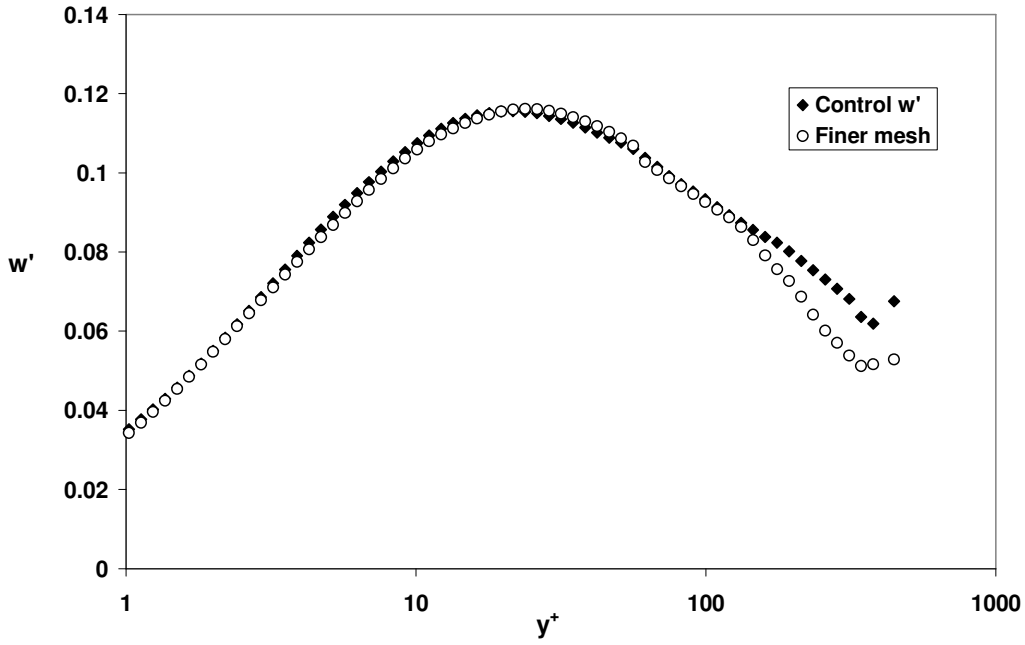

Figure 145 Azimuthal turbulence intensities plotted in wall coordinates

This is suggesting that the coarse mesh should give acceptable results. With no significant difference in velocity profiles, there is no reason to spend very high computational usage for the same simulation with the same result. Therefore the coarser mesh is still the preferred choice for this study.

6.6 Secondary flow effect

In the previous section 6.4.4, none of mentioned experimental and simulation results in open channel showed any secondary current features or velocity dip phenomenon. Hence, it is important to see if there is any possibility to achieve any sort of secondary current patterns from the simulation.

In the literature, secondary current is normally defined as the temporal mean of currents which occur in the plane normal to the local axis of the primary flow (Gulliver and Halverson, 1987). Secondary current can influence the mean turbulence quantities; this includes properties of the sweep and ejection cycle. Moreover, the secondary current plays an essential role in the lateral transfer of momentum, energy, heat and mass in a channel. This section

addresses the type of secondary current which occurs in turbulent noncircular open channel. They are called secondary flows of Prandtl's second kind (eds. Oertel, 2004).

It was mentioned in the literature review that Yang *et al* (2004) proposed a velocity distribution profile for secondary current in rectangular open channel.

$$U^{+}=\frac{1}{k}\ln\left(\frac{y}{y_o}\right)+\frac{\alpha}{k}\ln\left(1-\frac{y}{h}\right) \quad \textbf{(48)}$$

Where α is the factor to predict secondary current, and is given by

$$\alpha=1.3\exp\left(-\frac{b}{2h}\right) \quad \textbf{(49)}$$

In Heays *et al* (2010), the authors used a flume that was 0.45 m wide, 0.5 m deep and 19 m long. The test section comprised of a fixed bed with a vertically adjustable recess filled with graded gravels. Obviously in the experiment, the authors used water as the testing medium. The authors provided the raw data for investigation via private communication. The velocity against depth plot is presented in Figure 146. The *b/h* ratio is at around 2.25. According to Nezu (2005) the secondary flow phenomenon occurs if *b/h* is less than a critical value of 5. Hence, a possible secondary current is expected to be visible in the experiment. However, from Figure 146 it is seen that there is no visible secondary current feature presented in plot. It is extremely surprising that with a low *b/h* ratio and a Newtonian fluid, there is still no secondary current present.

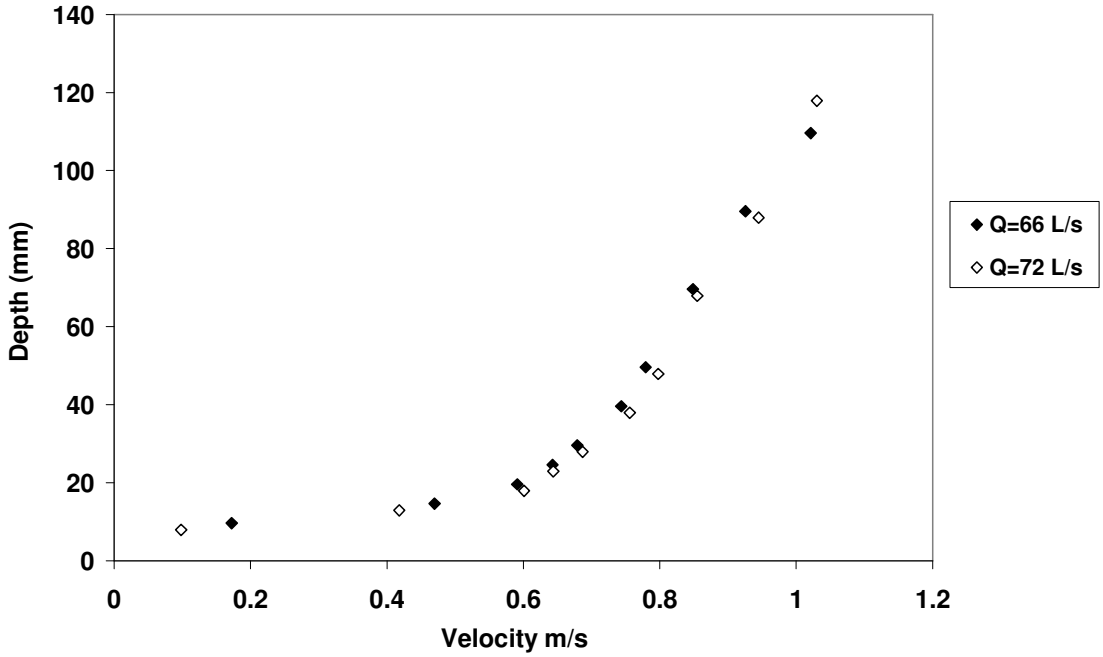

Figure 146 Field experimental velocity (Heays, 2010) against depth plot at centreline of the channel

Equation (48) and (49) are used to generate two new plots in Figure 147. It can be seen from Figure 147 the new plots have curved away from the measured profile at around $y^+ = 100$. This shows that if secondary current is present, there should be a velocity dip after the maximum velocity. There is also a possibility that the acoustic doppler velocimeter used by Heays *et al* (2010) has a similar measuring limitation as the current study. However, the detailed equipment limitation was not specified in the Heays *et al* (2010) paper.

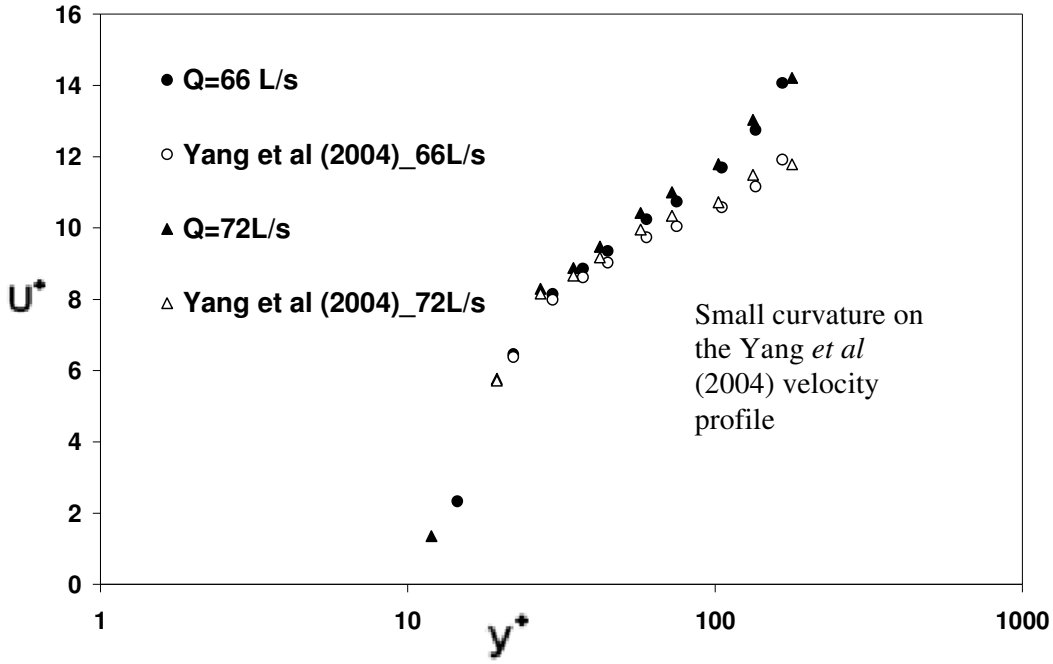

Figure 147 Non-dimensionalised experimentally measured velocity profile

The mean axial velocity data at the centreline for the slurry (Fitton, 2007) is presented in Figure 148 in wall units, together with the logarithmic velocity profile. The experimentally measured velocity profile has a linear relationship between U^+ and y^+ in the near wall region. In the logarithmic region, the actual velocity profile for the slurry is slightly higher than the logarithmic velocity profile. The computationally predicted profile for the control Simulation at Reynolds number = 8182 is presented in Figure 149. The velocities have been non-dimensionalised. The non-dimensionalisation is undertaken using the wall viscosity gives in equation (71). It is seen that the simulation result does not show any velocity dip or secondary current features. As described earlier, the secondary current features show that the maximum velocity appears not at the free surface but rather just below it in open-channel flows. Nezu (2005) found that the velocity-dip phenomenon occurs if *b/h* is less than a critical value. The geometry of this open channel from Fitton (2007) gives a *b/h* ratio of 4.4 which is very close to the critical value proposed by Nezu (2005). Another plot generated by Yang *et al* (2004)'s equation showed similar secondary current features as the experimental results of Fitton (2007). This new line shows a similar maximum velocity at a slightly higher y^+ value. The general trend of the new line and Fitton's experimental results is quite the same. This shows

that experiment measurement from Fitton (2007) is valid and reasonably accurate. So did the simulation completely ignore the secondary current feature?

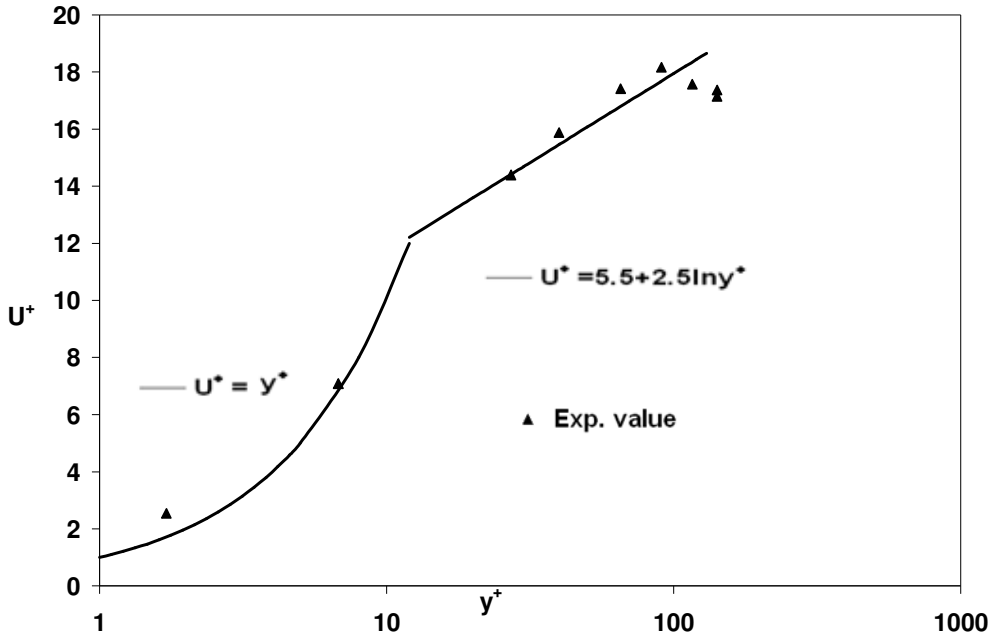

Figure 148 Non-dimensionalised experimentally measured velocity profile (Fitton, 2007)

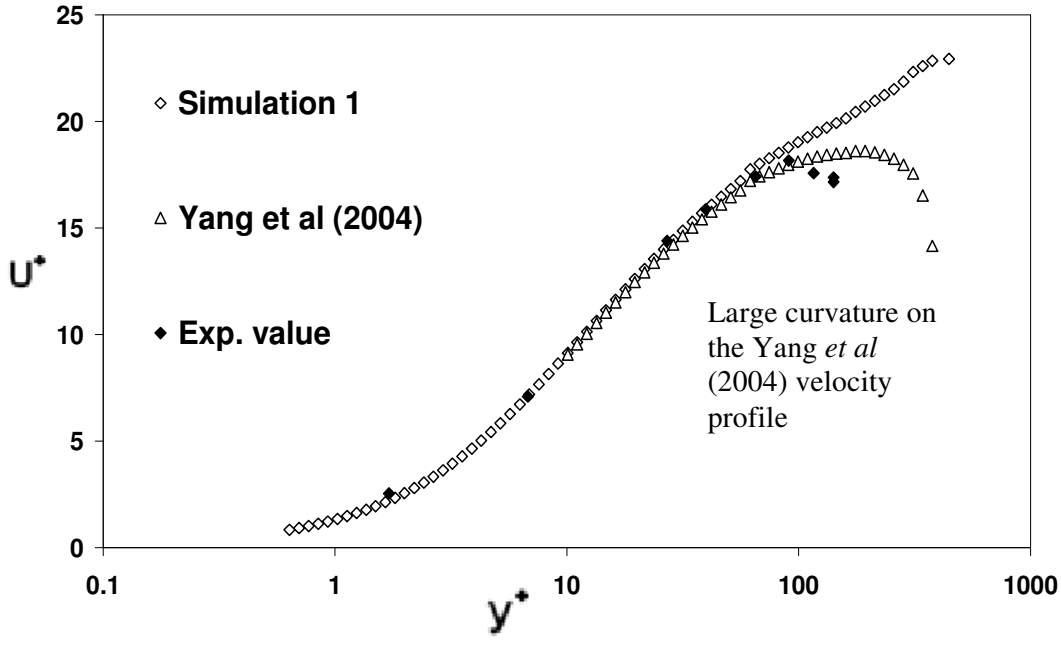

Figure 149 Non-dimensionalised experimentally measured velocity profile, simulation profile and Yang *et al* (2004) equation

In section 6.5.6, an investigation of velocity measurement at different x positions was conducted. Three different x positions x = 0.04 m, 0.065 m and 0.088 m were chosen in this investigation. The mean axial velocity profiles for all three different x positions and the centreline velocity profile is already shown in Figure 135. All three x positions measurements fall below of the centreline velocity profile. This should be expected as the centreline velocity is the highest in the channel flow. It is found that there is a small velocity dip appearing at y^+ close to 230-300 in Figure 153 and Figure 155. With x moving out from the centreline, the velocity dip of the velocity profile becomes more apparent and visible. From Figure 150, the average velocity vectors are plotted with a red line at x = 0.04 m. The two secondary current patterns are very clear and visible. The red line at x = 0.04 m is just touching the outside boundary of the secondary current cell. In Figure 151, there is a very small velocity dip in the outer region of the velocity profile.

From Figure 152, the average velocity vectors are plotted with a red line at x = 0.065 m. The red line at x = 0.065 m goes through the side of the secondary current cell. Interestingly, Figure 153 shows a little clearer velocity dip in the outer region of the velocity profile. Likewise, in Figure 154, the average velocity vectors are plotted with a red line at x = 0.088 m. The red line at x = 0.088 m goes through the centre of the secondary current cell. Without surprise, Figure 155 shows a clearer velocity dip in the outer region of the velocity profile. With these figures, it is concluded that measurements at different x positions could capture the very weak secondary current.

In Figure 150, the secondary current cells are very far apart. Their influence on the centreline velocity is almost minimal. However, when measurements were taken from various x positions, the velocity dip or secondary current became more apparent. Therefore it is concluded, the position of the secondary cells does have a significant effect on the secondary current feature in mean velocity profiles.

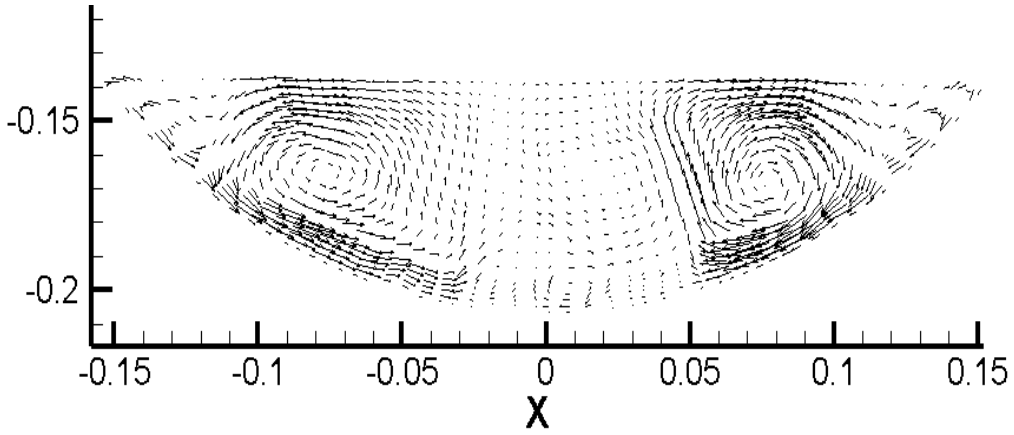

Figure 150 Illustration of velocity measurement (red line) taken at x = 0.04 m

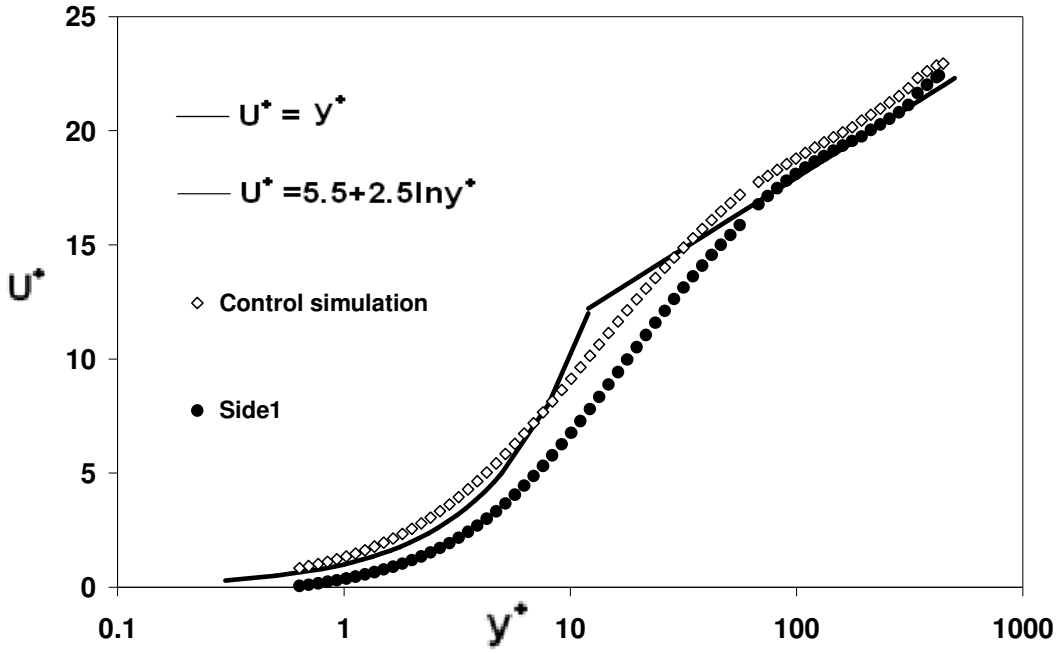

Figure 151 Mean axial velocity profiles for the turbulent flow at x = 0.04 m

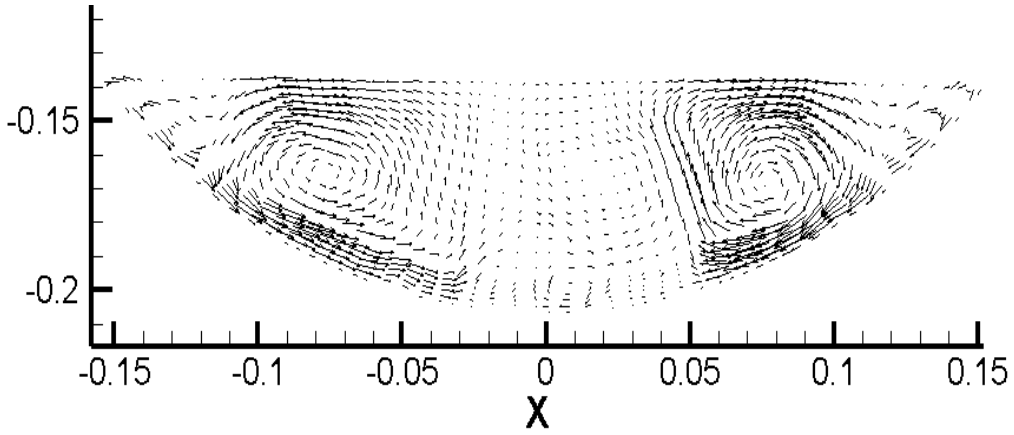

Figure 152 Illustration of velocity measurement taken at x = 0.065 m

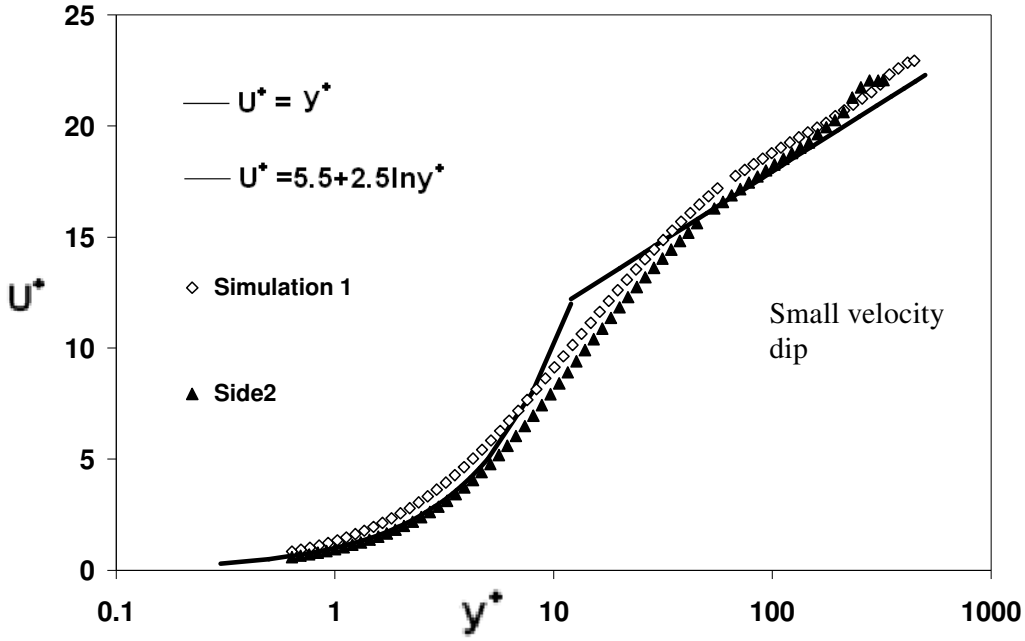

Figure 153 Mean axial velocity profiles for the turbulent flow at x = 0.065 m

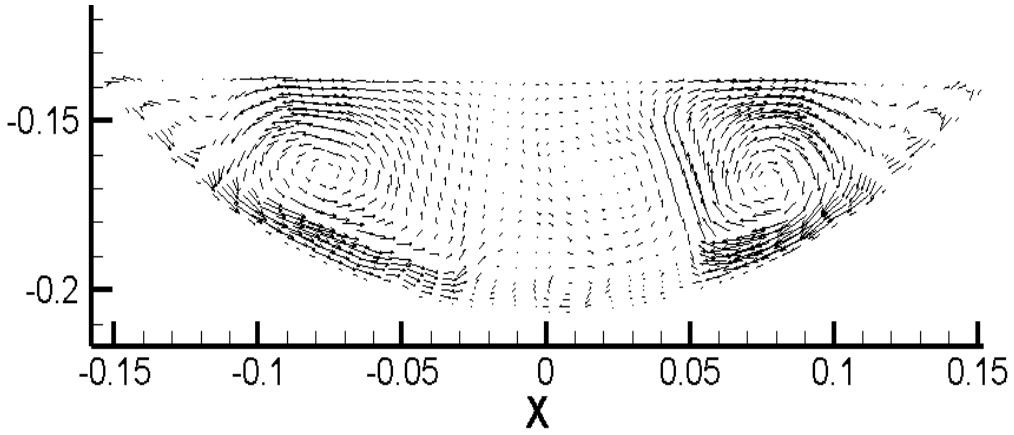

Figure 154 Illustration of velocity measurement taken at x = 0.088 m

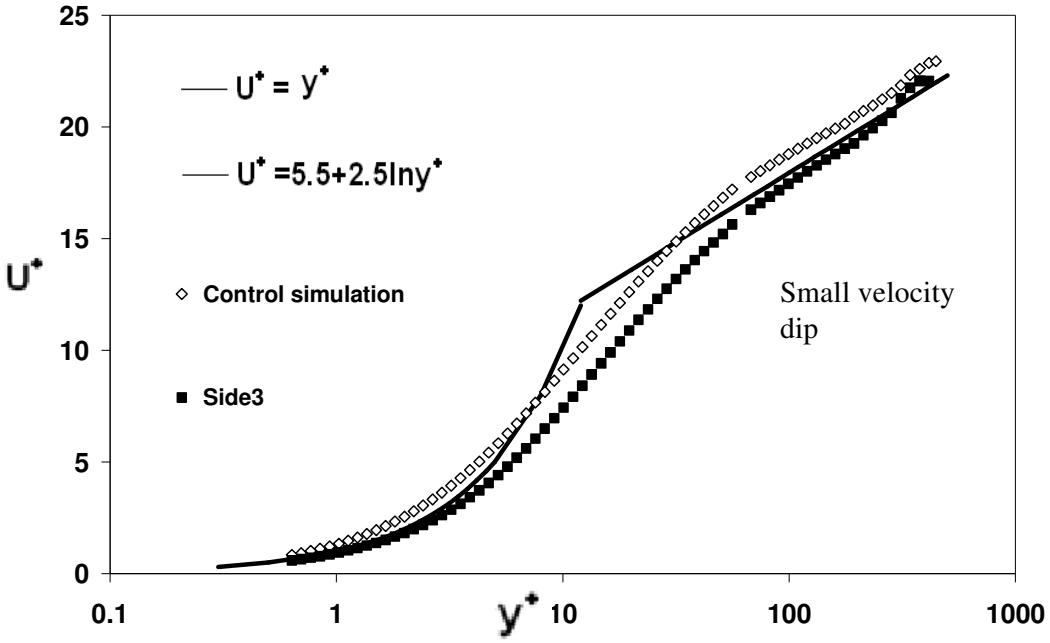

Figure 155 Mean axial velocity profiles for the turbulent flow at x = 0.088 m

Moreover, more tests were conducted with different simulation parameters; first, with a half pipe simulation of a power law fluid where the width and depth ratio is 2. Secondary current feature from the simulation is still not as obvious as expected. In Figure 156 the half pipe simulation reaches a maximum velocity at $y^+ = 100$ and then declines.

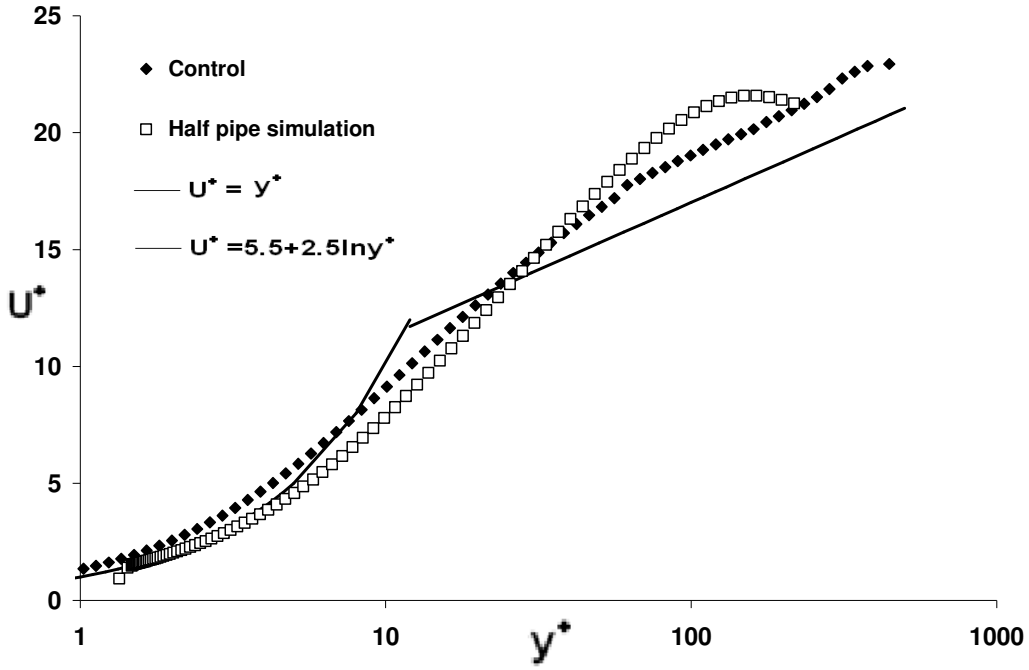

Figure 156 Simulation velocity profile in conventional wall units for slurry in comparison of half pipe simulation.

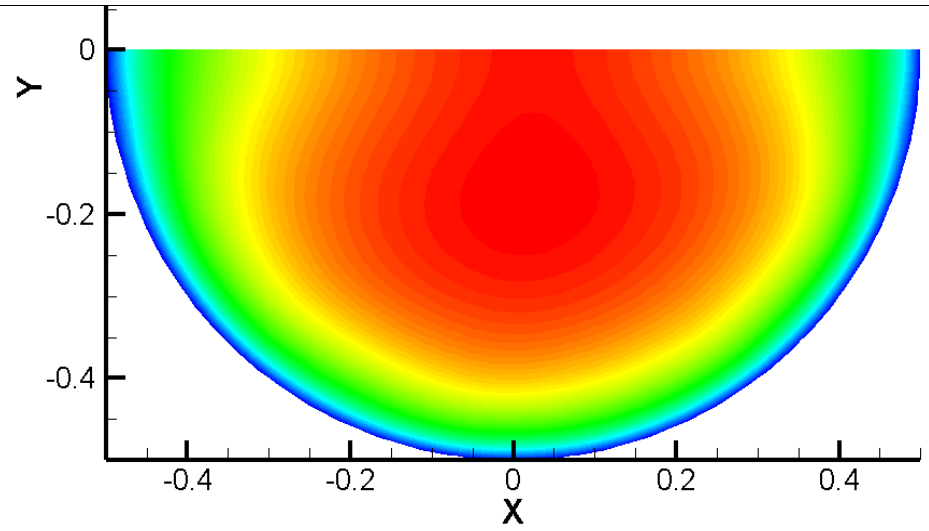

Figure 157 continues

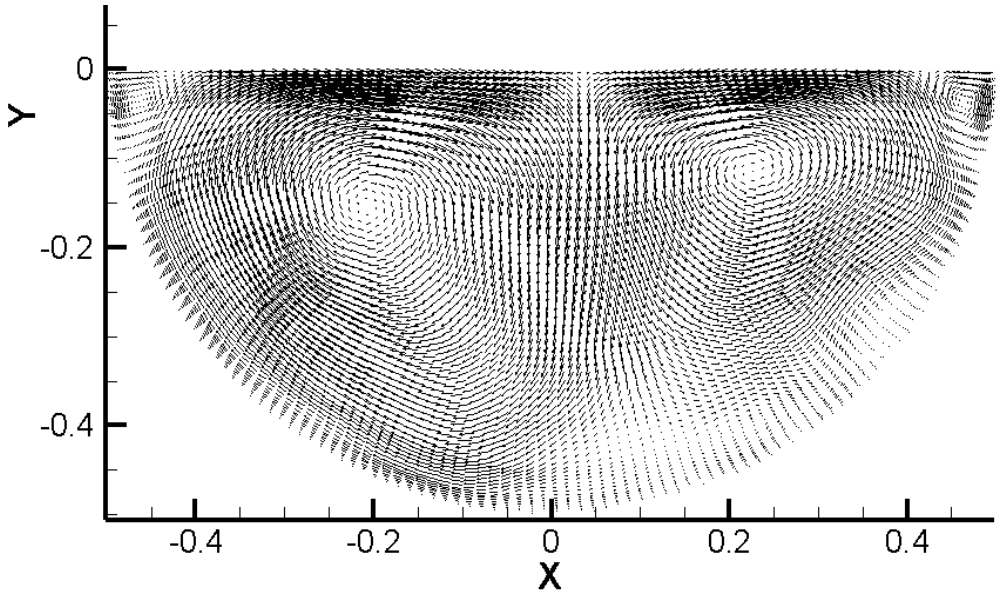

Half pipe simulation contour with power law model

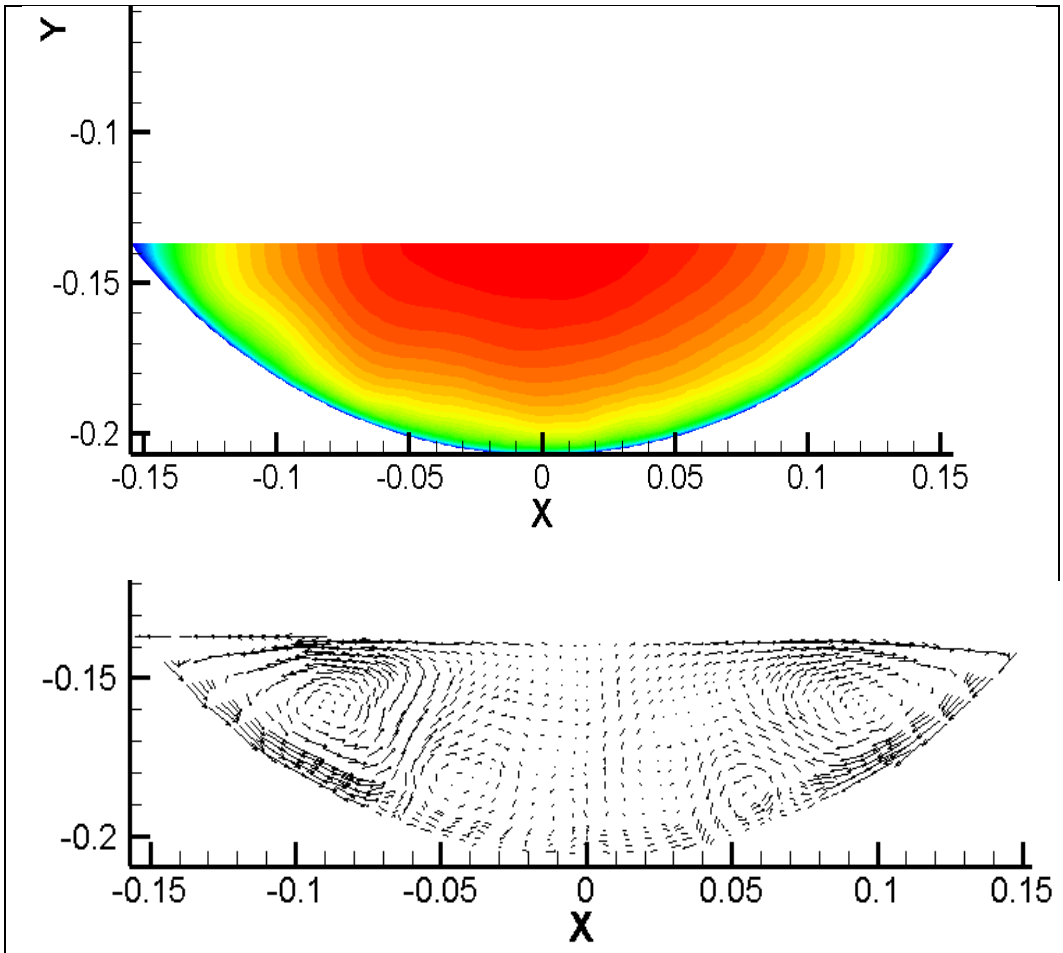

Newtonian simulation contour

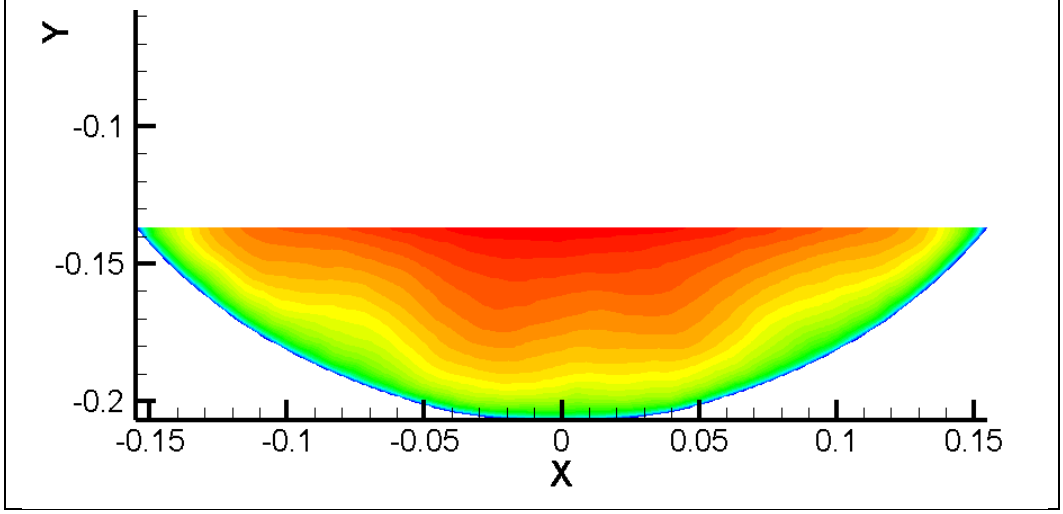

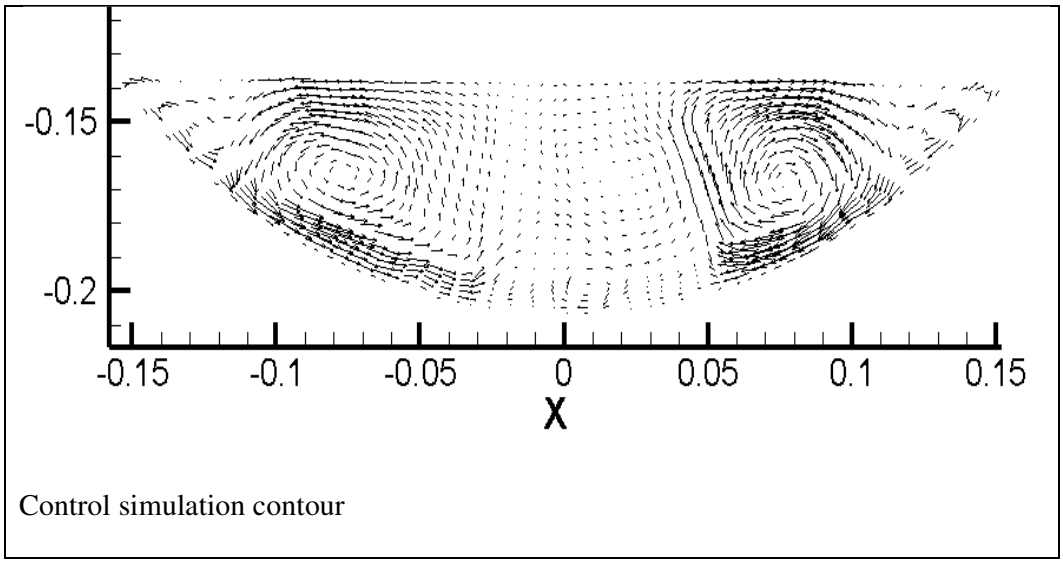

Figure 157 Axial velocity contours for half pipe simulation, Newtonian simulation and control simulation

Comparison of different axial velocity contours for half pipe power law simulation, a Newtonian fluid simulation and the control simulation are presented in Figure 157. From this figure, half pipe simulation shows the most obvious secondary current pattern, in both velocity contour and velocity vectors. In the half pipe contour map, the location of the maximum stremwise velocity occurs below the free surface. This shows the velocity-dip phenomenon, which is unique to turbulent open channel flow (Nezu and Nakagawa, 1993). As seen in Figure 157, the maximum velocity in the half pipe flow is just located below the free surface whereas the Newtonian simulation and control simulation do not exhibit the same behaviour. However, in the control simulation average velocity vectors, the secondary current cells are visible.

In the Newtonian channel flow, two pairs of counter-rotating vortices can be observed in the channel. Close to the centreline, the size of pair of vortices is smaller than the pair close to the boundary of the channel. However, with non-Newtonian flow, only one large pair of vortices is observed. With the same aspect ratio, only possible explanation for the disappearance of one pair of vortices is because of change of rheology. However, the actual cause of this observation is still not fully understood.

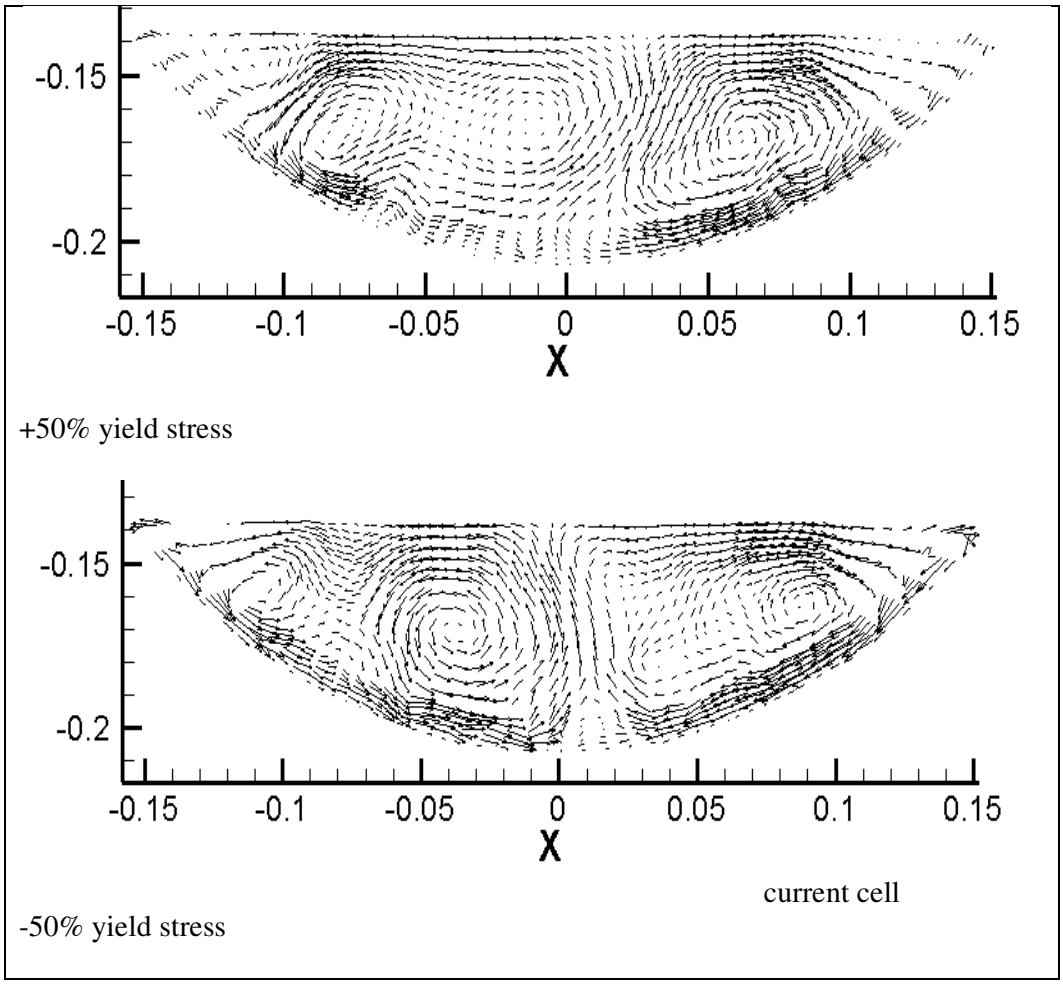

Figure 158 Velocity vectors for different simulations with different yield stress

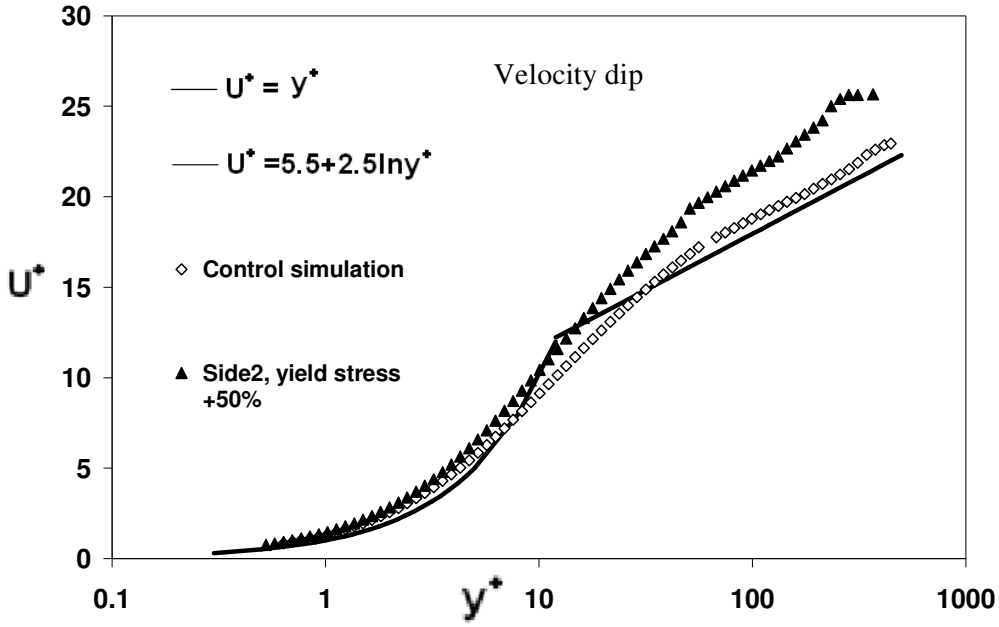

Figure 159 Mean axial velocity profiles for the turbulent flow at x = 0.065 m.

Further test was conducted to see if there is any chance to get secondary current in the simulation at all. First, in Figure 158, average velocity vectors of control simulation and two different yield stress simulation are presented. From the plot, all three simulations show some kind of secondary current features. The most symmetrical secondary cell appeared in the control simulation. In +50% yield stress simulation, there are three cells located in the channel. One on the right is similar to the secondary current cell in control simulation; the other two is located at the left side of the channel. The next plot shows the -50% yield stress simulation. This plot has a slightly off centre secondary current cells. The general shape of the secondary current cells is still very much the same as the control simulation. In Joung and Choi (2010), it was mentioned that the asymmetrical secondary current cells are caused by the free surface. From above plots, it can be concluded that an increase in yield stress could result an asymmetrical secondary current cell placement. Figure 159 shows the mean axial velocity profile for +50% yield stress at x = 0.065 m. A small velocity dip shows in the outer region of the velocity profile and it was not present in Figure 102. This shows that a small secondary current is been simulated.

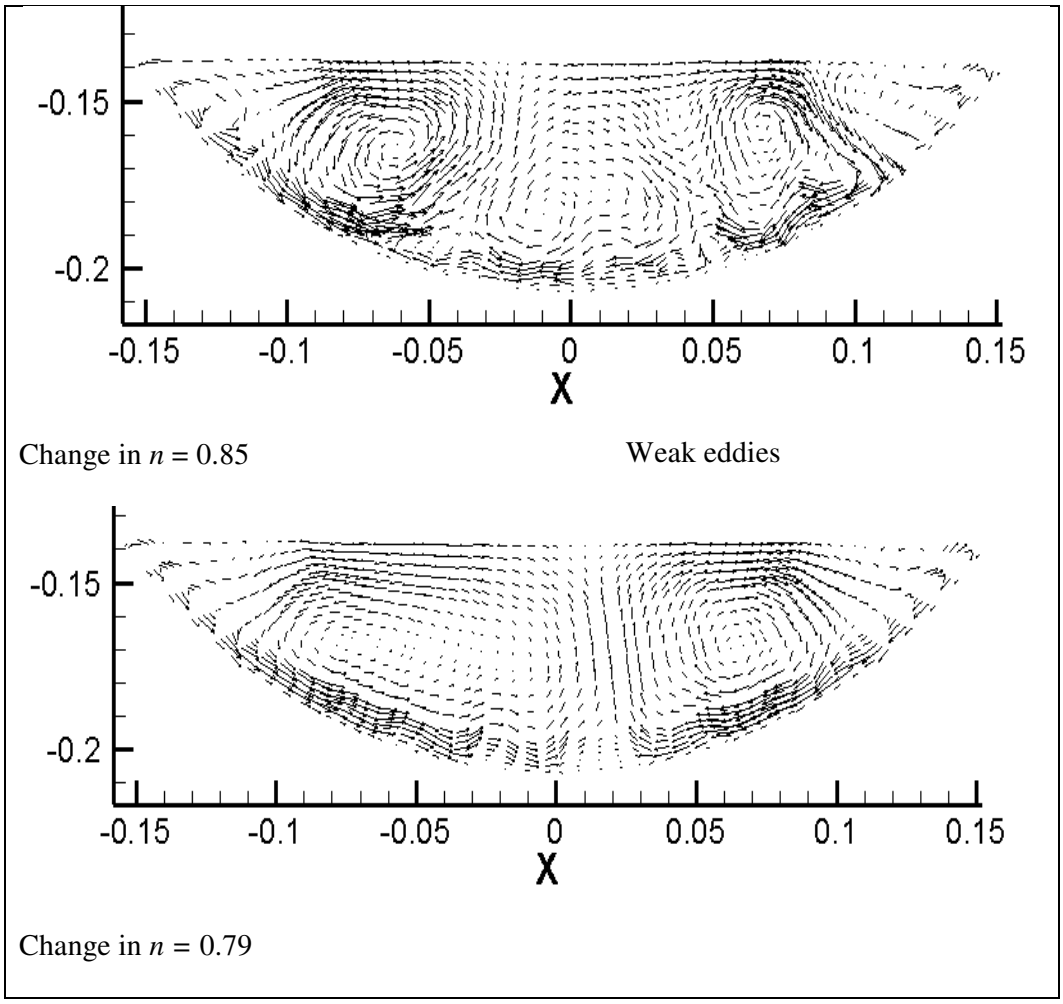

Figure 160 Velocity vectors for different simulations with different *n*

In Figure 160, average velocity vectors of control simulation and two different *n* simulations are presented. From all these three plots, secondary currents are apparent and observable. In *n* = 0.85 plot, other than the two secondary current cells, there is a weak turbulent region in the middle of the channel. Interestingly, this simulation has a smaller Reynolds number than the control simulation. The weak turbulent region could be caused by possible transitional behaviour in the channel. This is also observed in Figure 122 that there is a large region of unsteady structure present in the velocity contour.

For *n* = 0.79 simulation, the secondary current cells have a similar size compared with control simulation. However, the left secondary current cell has a smaller intensity than the right secondary current cell. It seems that the energy of the cell is already dissipated.

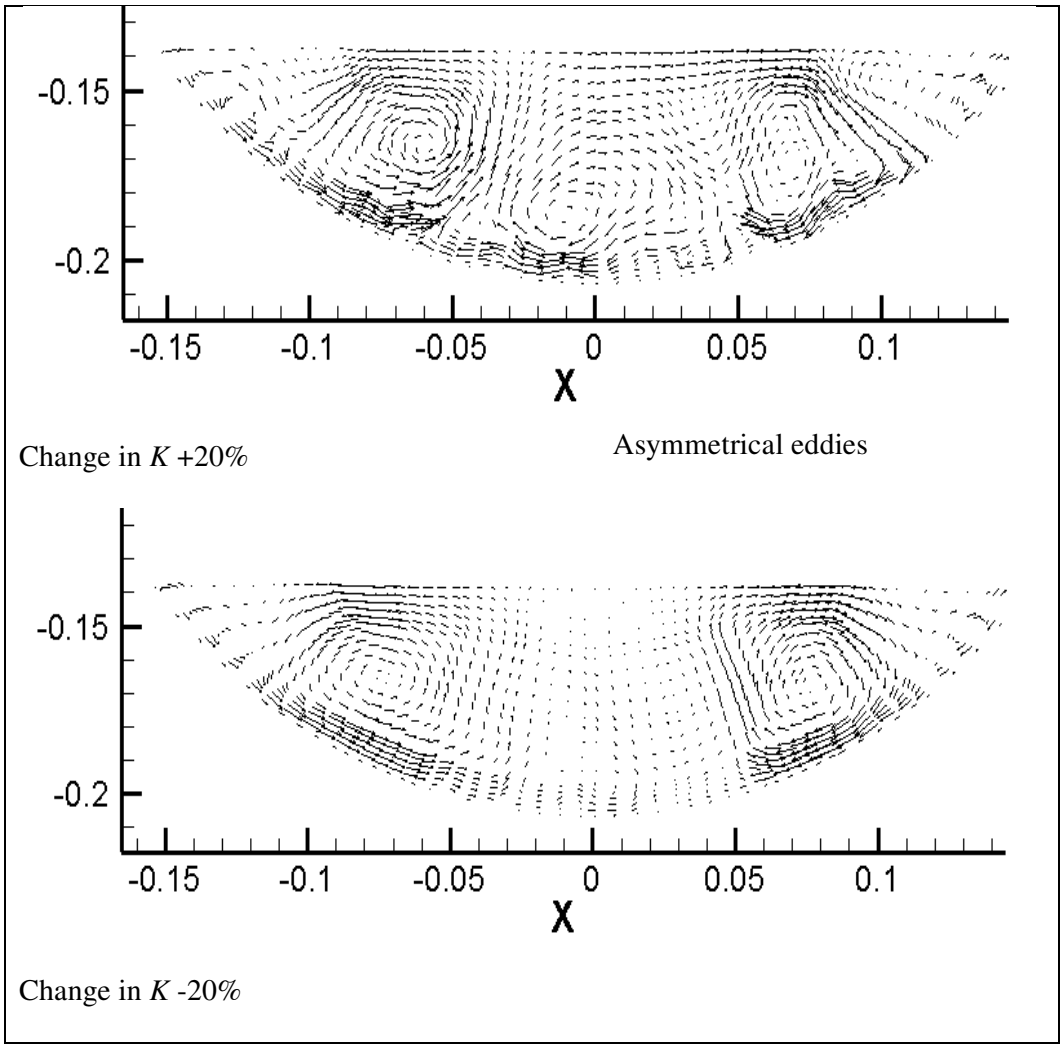

Figure 161 Velocity vectors for different simulations with different *K*

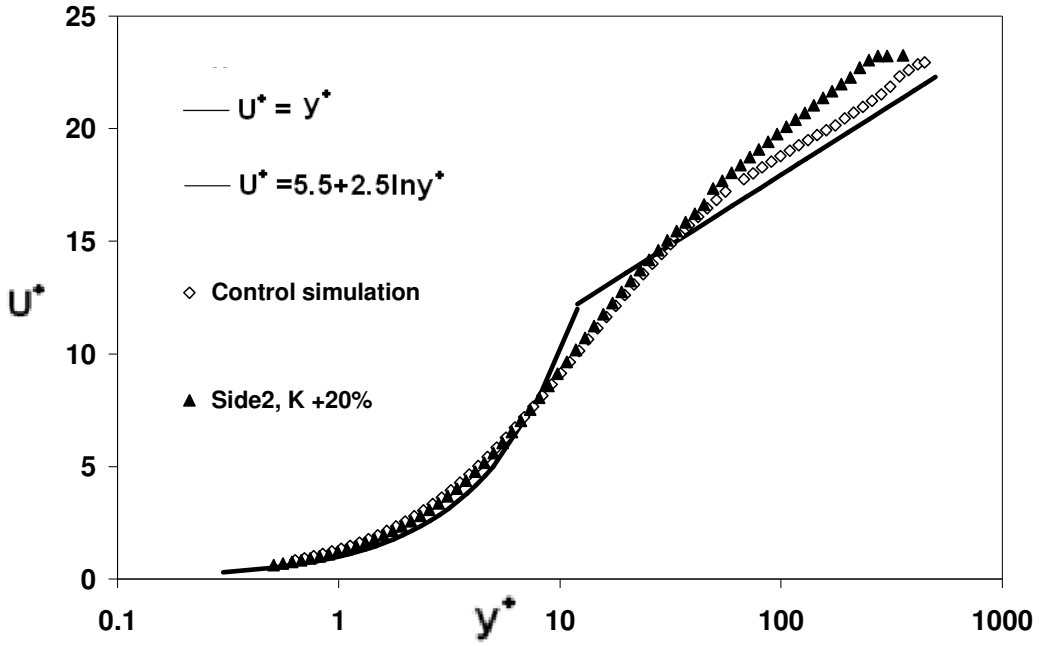

Figure 162 Mean axial velocity profiles for the turbulent flow at x=0.065 m.

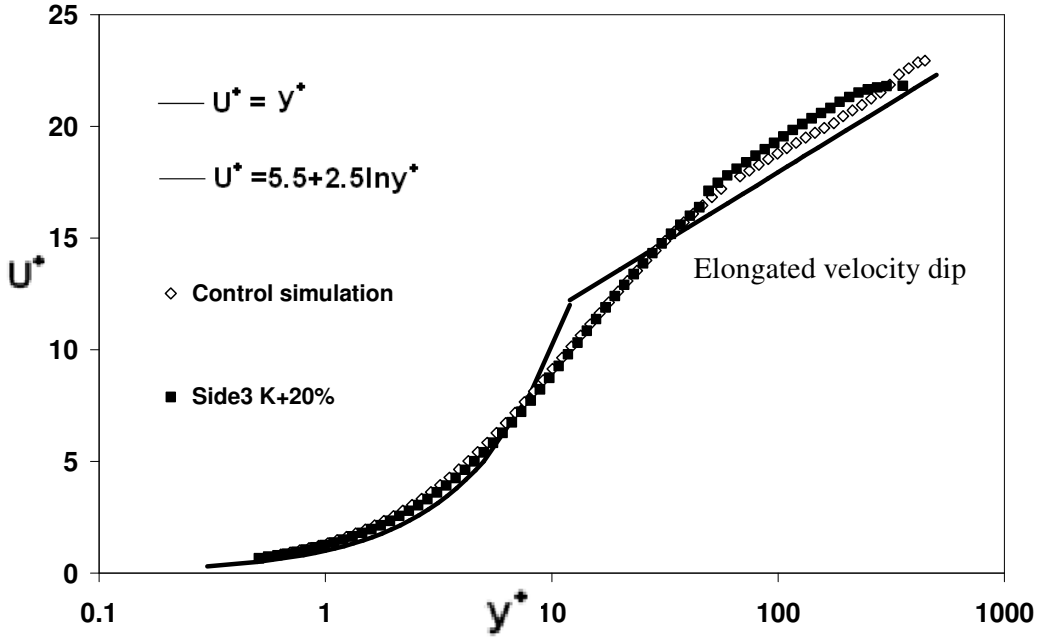

Figure 163 Mean axial velocity profiles for the turbulent flow at x=0.088 m.

Average velocity vectors of control simulation and two different *K* simulations are presented in Figure 161. In *K* +20% plot, similar to the *n* = 0.85 plot, there is a weak turbulent region in

the middle of the channel. The other similarity between these two plots is that both of these simulations have a smaller Reynolds number than the control simulation. This could mean that with a smaller Reynolds number, there are large turbulent puffs present in the flow which are similar to the transitional regime in Newtonian fluids.

The next plot shows the K -20% yield stress simulation. The secondary current cells have a similar size when compared with control simulation. This is very similar to n = 0.79 plot where there are only two noticeable secondary current cells located in the channel without other small disturbances. Both of these plots have high Reynolds numbers of 9185 and 11450 respectively.

Figure 162 and Figure 163 show the mean axial velocity profile for K +20% at x = 0.065 m and 0.088 m respectively. A small velocity dip shows in the outer region of the velocity profile, which was not observed in Figure 124. There is a noticeable difference between the intensity of these velocity dips in Figure 162 and Figure 163. Figure 162 has a more recognizable velocity dip feature whereas in Figure 163 the velocity dip is very weak and is extended into the majority of the overlap region. From these x positions (i.e. x = 0.065 m and x = 0.088 m), it appears that there is a little difference because both positions would only obtain the velocity at the boundary of the secondary current cells. So far, there is no likely explanation for such behaviour. More investigation needs to be conducted in future work.

Another interesting observation from the secondary current cells is that the cell on the left hand side always has counter-clockwise rotation; the cell on the right hand side always has clockwise rotation. This is observed in all simulation results. No matter the size of the cell and other disturbances, the rotation directions are always counter-clockwise on the left and clockwise on the right. It is found that the flow is always driven to move along side wall to leave from the edges (close to the surface). This basically means that the secondary current transports the momentum and energy from the middle of the channel to the corners.

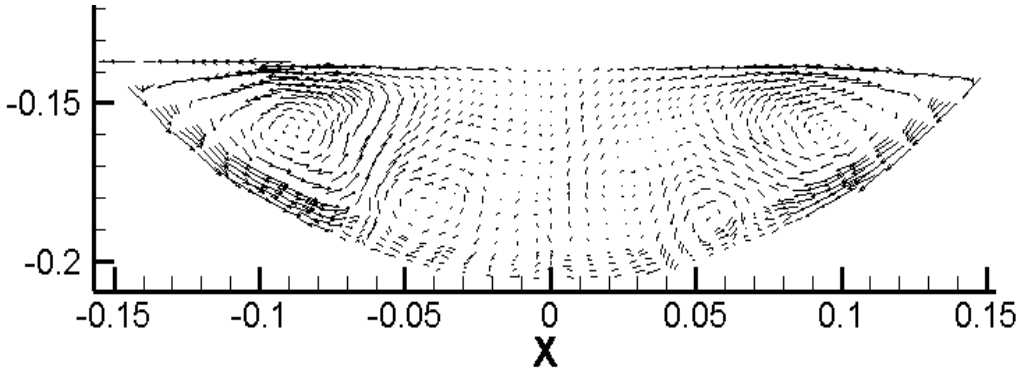

Figure 164 Velocity vectors for Newtonian simulation

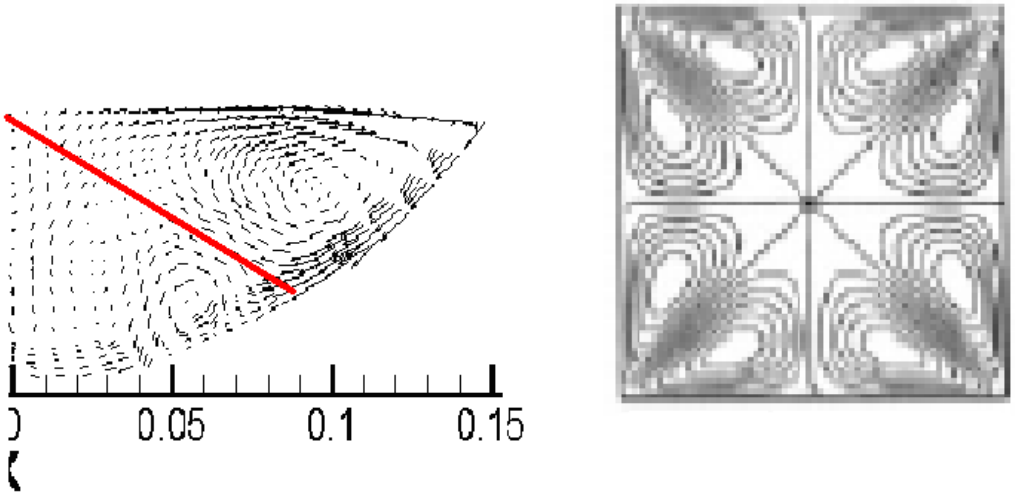

Figure 165 Velocity vectors for Newtonian simulation and rectangular duct flow from Yang (2009)

In conclusion, at different x positions, small velocity dip can be observed from the mean axial velocity plot. With in-plane average velocity vectors plot, secondary current cells can be detected. In general, with a smaller Reynolds number, weak but large turbulent structures appear in the middle region of the channel. This is observed with increased yield stress, decreased *n,* and increased *K* plots. With a larger Reynolds number, the secondary current cells tend to be stable and located at the side of the channel. This is observed in decreased yield stress, increased *n*, and decreased *K* plots. The sizes of the secondary current cells are quite similar for the above plots. One interesting finding from the Newtonian simulation is that there are four different secondary current cells present in the channel. Two larger ones are

on both left and right sides and another two smaller ones are located near the bottom. This is not observed in any non-Newtonian plots presented in this study. There is a possibility that there is a bisector separating the two secondary current cells. However, such bisector was only found in rectangular shaped channels (Figure 165, Yang, 2009). Further investigation needs to be conducted to explain this observation.

6.7 Summary

In this chapter, result of initial calculation for the experiment was first presented. Current experimental results were also presented and discussed. Computational simulation was validated against a number of different experimental and computational results. Different velocity distributions were tested to see the validity of the simulation. Major investigations were conducted to observe the effects of different rheological parameters to the simulation results. Some other variables were tested to further understand the discrepancy between the simulation and the experiments. It is believed that the simulation can produce reasonably good results for non-Newtonian turbulent open channel flow.

Moreover, this simulation method provides the opportunity to examine the effect of changing one rheology parameter while keeping the other parameters constant. It is such an advantage in the study of viscous behaviour of the tailings material.

A further investigation on secondary current was also conducted. It appears that with a smaller Reynolds number, weak and large size turbulent structures appear in the middle region of the channel. This is observed with increased yield stress, decreased n, and increased K plots. This could be a result of increased viscosity of the non-Newtonian fluid. With a larger Reynolds number, the secondary current cells tend to be stable and locate at either side of the channel. This is observed with decreased yield stress, increased n and decreased K plots.

Chapter 7: Particle transportation characteristics

7.1 Introduction

In this section, several particle transportation parameters and their effect on particles transportation are discussed. This includes Stokes number, particle behaviour in relation to wall streaks and a possible relationship between particle behaviour and different quadrants of turbulence.

7.2 Stokes number

In literature review section, Stokes number was introduced by Crowe *et al* (1993). The authors proposed a Stokes number defined as:

$$St = \frac{\tau_s}{\tau_F} \tag{50}$$

From Crowe *et al* (1993), it stated that if Stokes number is less than 1, then the particles will follow the fluid path lines. In terms of fluid flow, it means that the particles will follow the fluid vortex or eddy. If Stokes number is roughly equal to one, then the particles will be centrifuged by the cortices structures. If Stokes number is larger than one, the particles will continue its path and eventually settle via gravity. Similarly, in Rogers and Eaton (1991) the authors also mentioned that with small Stokes numbers $St < 0.01$, the particles will follow the flow exactly. For particles with large Stokes numbers $St > 100$, they will not respond significantly to turbulent velocity fluctuations. So with current simulation and experimental (Fitton, 2007) value, what is Stokes number for the particles in the flow?

7.2.1 Particle behaviour and Stokes number

In equation (52) δ is the size of the fluid structure. According to Nezu *et al* (2004), the size of the structure is defined as mixing length in the calculation. The first assumption needs to be made is the mixing length. It was introduced by Prandtl for the concept of the mixing length *l,*

which is related to the average size of the eddies. However, this concept is very limited because l is not constant for a given flow. Therefore, mixing length is written as a function of different variables, mostly a function of average flow variables and distance from the wall.

From Nezu *et al* (2004), the mixing length (non-dimensionalised) l^+ is obtained by using van Driest damping function:

$$l^+ = ky^+\Gamma \tag{53}$$

Where k is the von Karman constant and has a universal value of 0.412. y^+ is the distance from the wall. This method is also used in Aydin (2009) for open channel flow.

$$\Gamma = 1 - \exp(-y^+/26) \tag{54}$$

Stokes numbers are calculated using the particle characteristic from Fitton (2007). The d_{85} particle size is 14 μm for the all the Stokes number calculation. Streamwise velocity fluctuating components was chosen for ΔU values. Firstly in Figure 166, Stokes number for the control simulation and two different simulations with increased yield stress is plotted against distance from the wall. All three lines are very close to each other. The values of Stokes number near the bed in this graph are at the maximum and decrease higher in the flow. With increased yield stresses, only the simulation with increased 50% yield stress has a slightly lower Stokes number. In previous section 6.5.2, increased 50% yield stress showed a decrease in Reynolds number hence a decrease in the turbulent characteristics. Therefore the value of Stokes number is decreasing slightly as well.

Stokes number for decreased yield stress is presented in Figure 167. In this case, the magnitude of the Stokes number values is quite similar to the previous figure. Decreased 50% yield stress simulation has the largest Stokes number and the control simulation has the smallest Stokes number. With a high Reynolds number for decreased 50% yield stress simulation, a high Stokes number is likely. However, with very small Stokes number (i.e. $St <$ 0.01); particles will follow the direction of the flow regardless.

In Figure 168, Stokes numbers for $n = 0.75$ and $n = 0.85$ are plotted against distance from the wall. This time $n = 0.75$ simulation has a higher Stokes number than the other two plots. It is also observed that $n = 0.85$ simulation possess a smaller Stokes number than the control simulation. This is expected as $n = 0.75$ has a larger Reynolds number and $n = 0.85$ has a smaller Reynolds number in comparison to control simulation. In fact, Stokes number is increased around 33% for the smaller n simulation. The increase of Stokes number for $n = 0.75$ is expected to be higher as the average mean axial velocity plot in section 6.5.2 is significantly higher than the control velocity profile. It is also discovered from Rajitha *et al* (2006) that with flow behaviour index decrease below 1; the drag also decreases under the same Reynolds number. With less drag from the fluid, the particles would follow more the non-Newtonian fluid behaviour. However with a change in mixing length, the increase in Stokes number was not as much as expected.

Stokes numbers for the control simulation and two different flow consistency index simulations are plotted against distance from the wall in Figure 169. The magnitude of the Stokes number values is also quite similar for all three plots. It is very difficult to differentiate the plotted points. Interestingly, the Reynolds number difference between these two simulations (increased and decreased K) is quite large. Yet, in Figure 169 the difference between Stokes numbers is minimal. On the other hand, Stokes numbers for two different flow consistency index simulations with fixed Reynolds number are plotted in Figure 170. With very similar Reynolds number, K +20% simulation has a higher Stokes number and K -20% simulation has a smaller Stokes number. In this particular case, K +20% simulation makes the fluid more non-Newtonian like, than for K -20% simulation. Thus it is likely the particles would follow the fluid rather than settling in the fluid.

In general, Stokes number increases with increase of Reynolds number because of increased turbulent characteristics. From above discussion, it can be concluded that change in yield stress (up to 50% of current value) does not affect Stokes number significantly. Change in flow consistency index also affects Stokes number in a limited way. Change in flow behaviour index causes noticeable change in Stokes number. Yet, with current values, Stokes numbers are quite small (i.e. $St < 0.01$). However, several errors may be associated with calculation of Stokes number, such as selection of appropriate mixing length formula. This

suggests the need for further experimental studies to more precisely define the value of Stokes number.

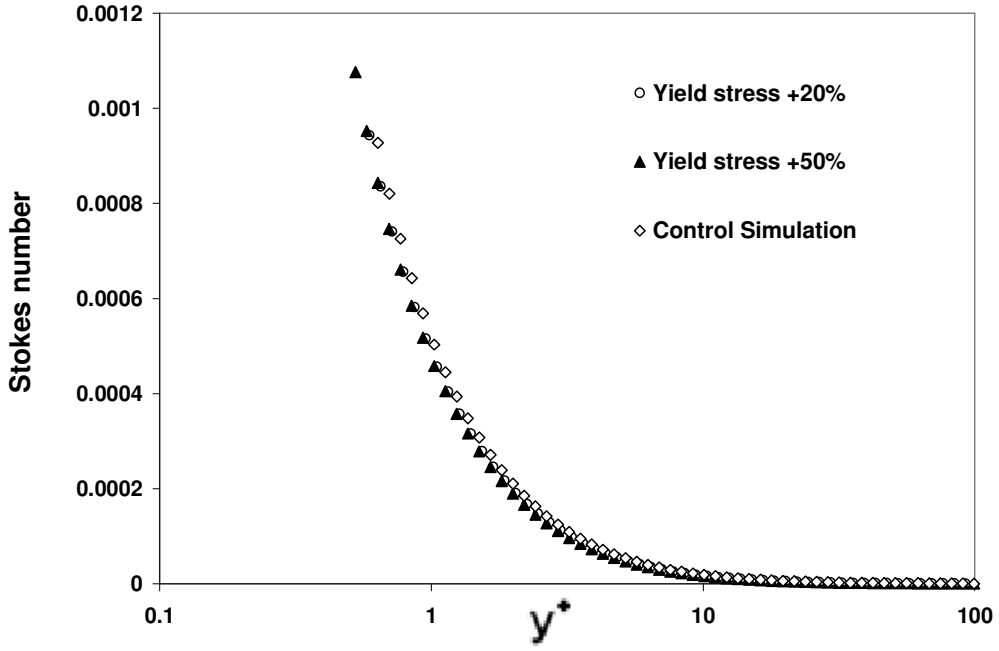

Figure 166 Stokes number plotted as a function of distance from the wall with different increased yield stress

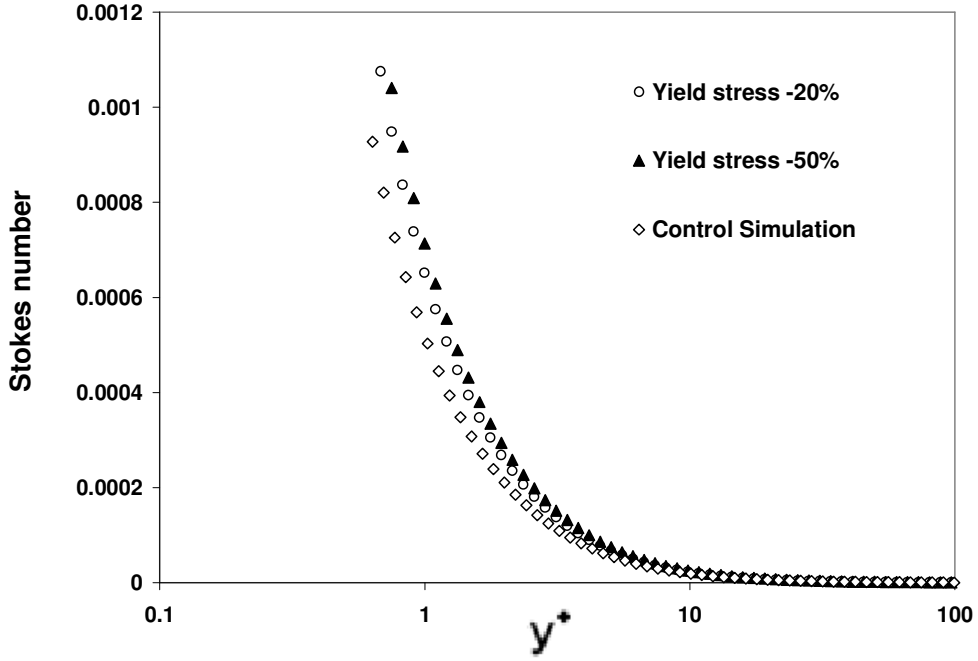

Figure 167 Stokes number plotted as a function of distance from the wall with different decreased yield stress

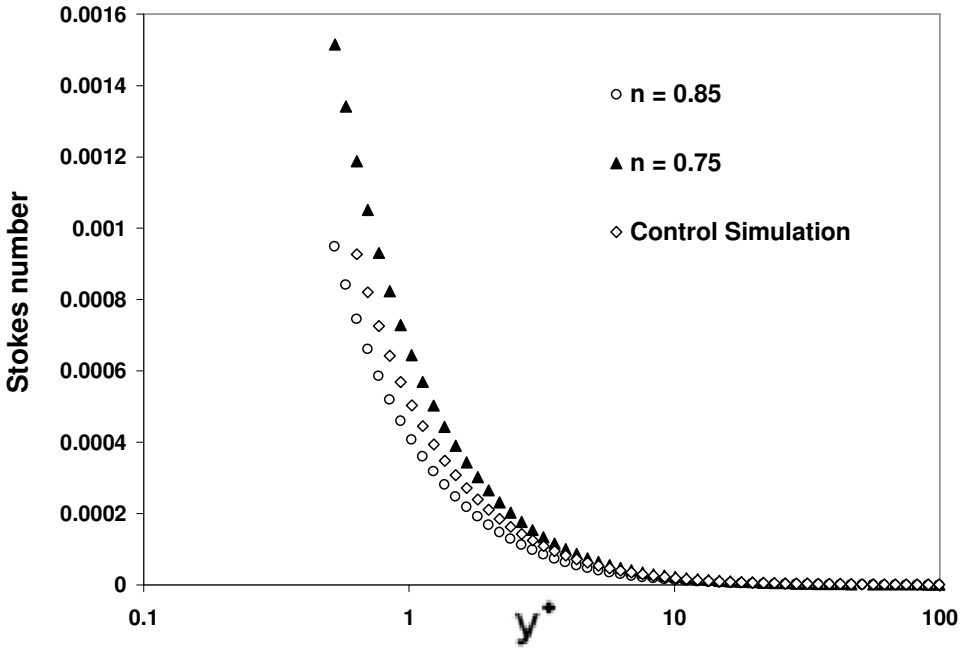

Figure 168 Stokes number plotted as a function of distance from the wall with two different *n* values

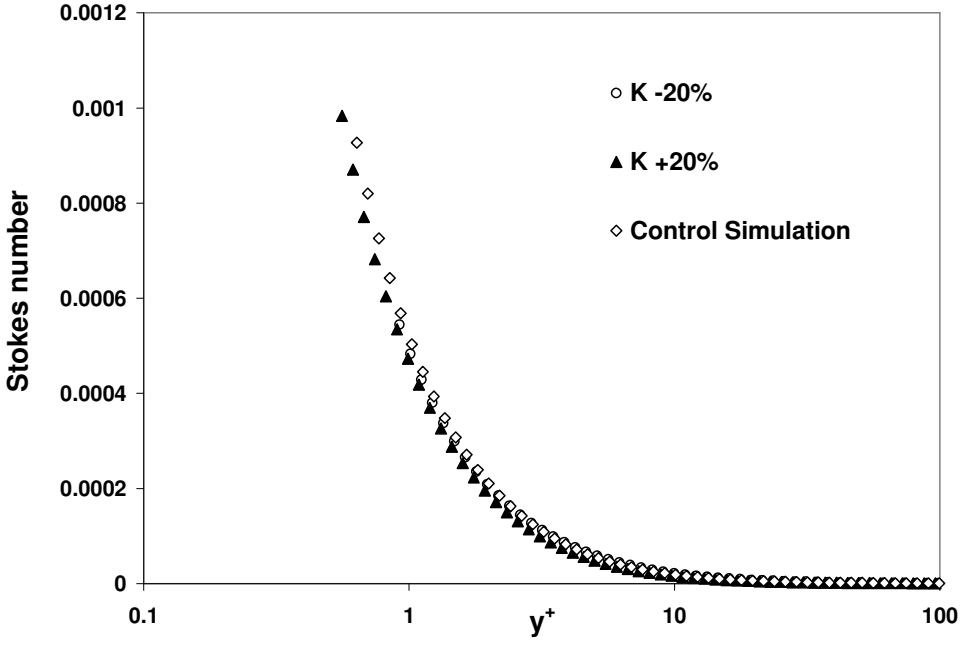

Figure 169 Stokes number plotted as a function of distance from the wall with two different *K* values

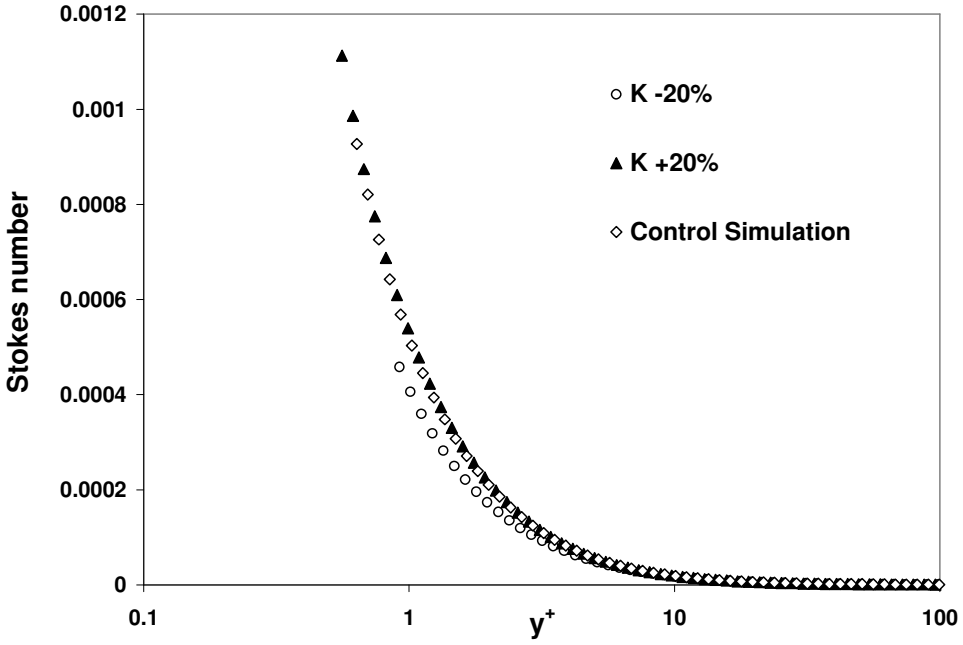

Figure 170 Stokes number plotted as a function of distance from the wall with two different *K* values with fixed Reynolds number

7.3 Particle behaviour and flow relationship

From literature, three different types of coherent wall structures have been observed. One type consists of low velocity streaks very close to the wall. The second is streamwise and quasistreamwise vortices and the third type is 'active' periods usually referred as 'bursts' (Kaftori *et al*, 1995). Bursts consist of sequences of ejections from the wall layer into the outer flow and sweeps of fluid from the outer region toward the wall. In this section, low velocity streaks and ejection/sweeps events will be investigated.

7.3.1 Wall velocity streaks

7.3.1.1 Minimum velocity

In the simulation, low velocity streaks are very observable from the velocity contours. These low velocity streaks are quite regular and persistent at the bottom of the channel. The low velocity streaks form as a result of circulation in the viscous boundary layer. Generally, they have been seen in the viscous sublayer and to some extent in the logarithmic region (Lim and Banerjee, 1992). In here, viscous sublayer is the region $0 \leq y^+ \leq 5$. There is another region

called generation region above the viscous sublayer. The generation region overlapped with the position of the majority of the ejection and sweep events (Sumer and Oguz, 1978). According to Sumer and Oguz (1978), the generation region is $5 \leq y^+ \leq 70$.

From Kaftori *et al* (1995) and Narayanan and Lakehal (2003), it was discovered that particles tend to accumulate in low velocity streaks near the wall. So it is interesting to see what is the level of magnitude of the minimum velocities in these wall streaks. Different simulation contours were tested by Tecplot software. The minimum velocity in the wall streaks was obtained by the probing function of the software. The velocity layers tested were in between $y^+ = 4$ and $y^+ = 8$. Velocities at $y^+ = 0$ to 4 were not mentioned here because the velocity presented in the very bottom of the channel is approaching zero for all contours and thus lacked comparability. The minimum velocities for 13 different simulations are presented in Table 27. The question is: are there any differences in velocity of different simulation's wall streaks?

It is quite obvious to see the velocity difference in Table 27. First for the yield stress simulations, +50% yield stress simulation have a smaller minimum velocity than -50% yield stress in the wall streaks. This is expected as the Reynolds number is higher for -50% yield stress simulation. It simply means at the same y^+ position, -50% yield stress simulation has a higher velocity to transport particles close to the wall. With +50% yield stress, as the fluid becomes more non-Newtonian like, the velocity close to the wall decreases.

For the next two simulations, simulation 3 ($n = 0.75$) has a higher minimum velocity than simulation 4 ($n = 0.90$). Such finding is quite surprising as simulation 3 makes the fluid more non- Newtonian like. However, with a high Reynolds number, it is very likely for simulation 3 to have a higher minimum velocity than simulation 4. Furthermore, from velocity contour, simulation 4 has a smaller minimum velocity than the control simulation. There is no valid explanation for this as simulation 4 has a lower Reynolds number than the control simulation. The velocity difference for these two simulations is very small and can be neglected for this instance.

The next four simulations consist of change in the rheology parameter *K*. When *K* increases, the simulation produces a smaller minimum velocity in the wall streaks. When *K* decreases,

the simulation produces a larger minimum velocity than the control simulation. One interesting aspect of the result is that the increase of *K* caused a 53% decrease of the minimum velocity, and the decrease of *K* caused a maximum of 40% increase of minimum velocity.

The minimum velocity for *K* +20% and +50% is very close. This means once *K* increased above 20%, the difference between the simulation velocity contours is not as noticeable. However, with only *K* +50% as the upper limit of the investigation, the full impact on increase in *K* is yet to be concluded. When *K* decreased by 20%, the change in minimum velocity is very small when compared with control simulation. Similar minimum velocity values are obtained from the last four simulations with relatively constant Reynolds number. Without Reynolds number effect, the minimum velocity values show the same trend with the change in *K* simulations. Therefore, it is concluded that with increase in *K,* minimum velocity would decrease but the percentage of decrease declines when *K* move towards to +50%. On the other hand, with decrease in *K*, minimum velocity would increase slightly first then increase up 40%.

In summary, high Reynolds number gives a higher velocity in velocity streaks. Lower Reynolds number gives a slightly lower velocity in velocity streaks. With a more constant Reynolds number (simulations 9 -12), the minimum velocity in the wall streaks behaves in the same ways as simulations 5 - 8. However, there is no way to measure the randomness of the ejection event by the simulation.

Table 27 Minimum velocity in low velocity streaks

Simulation		Minimum velocity (m/s)	Reynolds number
0	Control simulation	0.0739	8182
1	+50% yield stress simulation	0.0563	6481
2	-50% yield stress simulation	0.0840	9258
3	n = 0.75	0.127	12910
4	n = 0.90	0.0756	4210
5	K +20%	0.0357	6781
6	K +50%	0.0343	5635
7	K -20%	0.0750	11450
8	K -50%	0.104	21991
9	K +20% (with fixed Re)	0.0366	8278
10	K +50% (with fixed Re)	0.0305	8630
11	K -20% (with fixed Re)	0.0790	8295
12	K -50% (with fixed Re)	0.0920	8682

7.3.1.2 Wall velocity streak size

The wall streaks sizes for 14 different simulations (includes control simulation and Newtonian simulation) are presented in Table 28.

It is seen from Table 28 that, there is not a significant quantitative difference between control simulation and simulation 1 and 2. In general, the velocity streaks for simulation 1 are longer and wider than the control simulation. This means that with an increase of yield stress, the flow is not as developed as the control simulation. From observation, the velocity streaks intensity for simulation 2 and occurrence are very similar to the Newtonian case. This means with a decrease of yield stress, the flow is more developed than the control simulation.

Simulations 3 and 4 show some extreme cases of the velocity streaks. Simulation 3 has very small low velocity streaks compared with the control simulation. For simulation 3, the low velocity streaks are less than 0.5 units in length, and less than 0.2 units in width. In Figure

171, the black coloured low velocity streaks are not very noticeable. Instead, there are spotted weak white high velocity streaks present in the velocity contour. Usually, a higher volume of high velocity streaks indicate a more turbulent fluid flow. For simulation 4, it is seen that a large region of turbulent activity exists from the left of the domain to the middle of the domain. It is further suggested that the flow is not fully developed for the Herschel-Bulkley fluid.

For simulation 5 and 6, the velocity streaks have a length larger than 4 units and width of 1 unit. It has also been illustrated in Figure 126 that most of the low velocity streaks were located on the side of the channel. These low velocity streaks were very long and some of them run through the whole domain length. The main reason for this behaviour is that the Reynolds number is a lot lower than the control simulation. As K decreases, the low velocity streaks gradually disappear and become less visible. In Figure 126, the low velocity streaks in simulation 7 are short in the middle but longer and wider toward to the channel side wall. In general, there are less low velocity streaks in simulation 7 than 5 and 6. Once again in Figure 126, for simulation 8, there are some bright white high velocity streaks. The low velocity streaks in simulation 8 are extremely small and it is very difficult to quantify. This simply illustrates a more turbulent flow characteristic for simulations 7 and 8 than simulations for 5 and 6.

With a similar Reynolds number value, for simulation 9 and 10, the streaks are very thick and very wide. Size wise, simulation 9 and 10 have a smaller length than simulation 5 and 6. It confirms that Reynolds number effect is more significant than just change K. From simulation 9 and 10, it is further suggested that the flow is not fully developed for increased K values. As K decreases, the low velocity streaks gradually disappear and high velocity streaks emerge. With very similar Reynolds number value, the low velocity streaks in simulation 11 have a length of 2 units but a very small width at 0.1-0.2 units. This means regardless of Reynolds number effect, the flow is still very turbulent. Similar to simulation 8, simulation 12 has some bright white high velocity streaks in spots in Figure 131.

In summary, these low velocity streaks are strongly Reynolds number dependent. The flow with high Reynolds number simply exhibit shorter and smaller low velocity streaks and the flow with low Reynolds numbers show longer and wider low velocity streaks. With this

comparison between simulation 5-8 and simulation 9-12, it is also found that Reynolds number has more evident effect on the size of the low velocity streaks.

Table 28 Velocity streak size comparison

Simulation		**Typical velocity streak length**	**Typical velocity streak width**
Control- Simulation result based on experiment (Fitton, 2007)		2 units	0.5 units
1	+50% Yield stress	2.2 units	0.6 units
2	-50% Yield stress	2.2 units	0.2~0.3 units
3	n = 0.75	< 0.5 units	< 0.2 units
4	n = 0.90	>4.5 units	1-1.5 units
5	K +20%	4-4.5 units	0.5 units
6	K +50%	4.5 units	0.5 units
7	K -20%	2 units	0.2 units
8	K -50%	Very small	Very small
9	K +20% (with fixed Re)	3.5 units	0.5 units
10	K +50% (with fixed Re)	3.5 units	0.5 units
11	K -20% (with fixed Re)	2 units	0.1-0.2 units
12	K -50% (with fixed Re)	Very small	Very small
13	Newtonian simulation	1.4 units	0.1~0.2 units

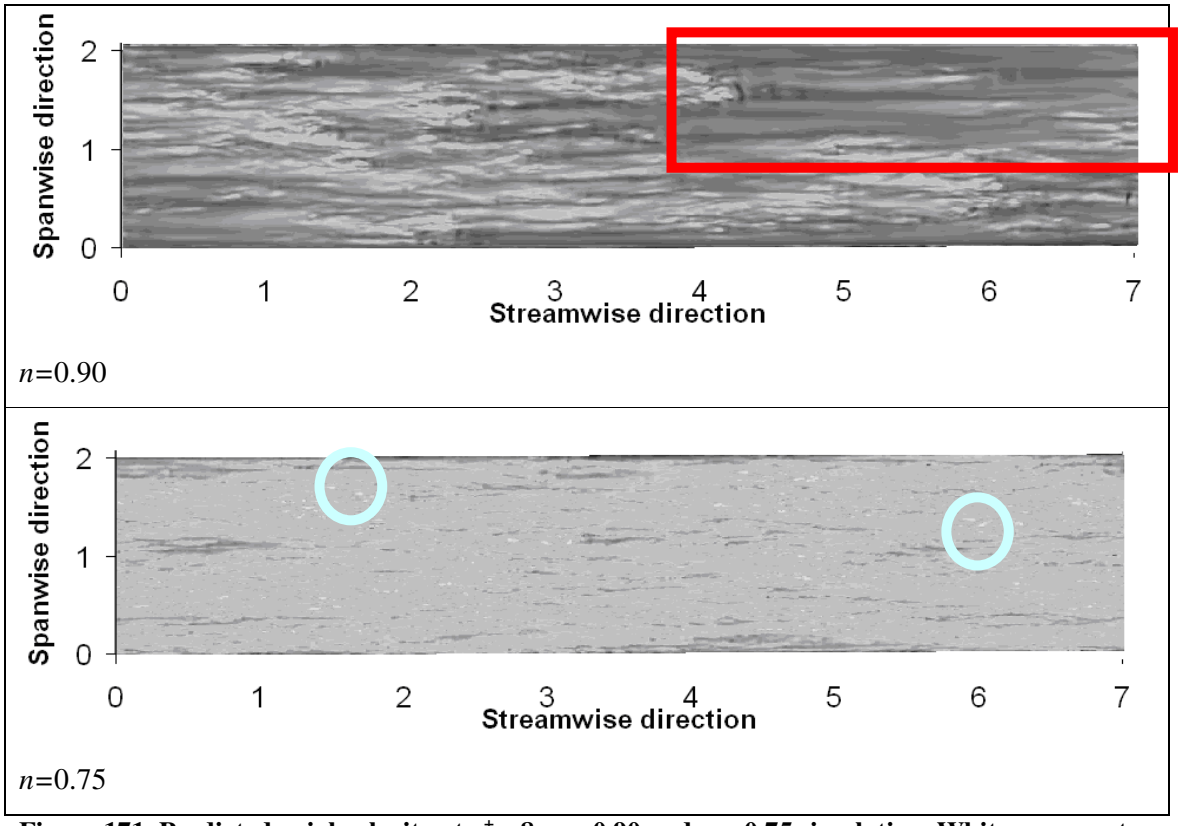

Figure 171 Predicted axial velocity at $y^+ \approx 8$. n = 0.90 and n = 0.75 simulation. White represents high velocity and black represents low velocity.

7.3.1.3 Eddy behaviour and Reynolds number

This section provides more information about the properties of the turbulent eddies. The importance of this result is that it could provide physical basis for the development of different schemes to control turbulence.

Cross sections of a typical eddy are viewed in Figure 172. The instantaneous velocity vectors at different z planes from z = 28 to z = 33 in streamwise direction are shown. The turbulent producing eddy is indicated by the highlighted square in Figure 172. This highlighted eddy has diameter of 0.024 – 0.026 m. The original eddy is generated from the wall by small vortices attached to the wall. In this case, the size of the eddy does not change much. This eddy moves upward from the bottom of the channel toward to the middle. During the move, smaller eddies appear at the bottom of the large eddy, and increase in size gradually. It is

possible that the turbulence is generated by these small eddies as they transport high momentum fluid to the wall and bring low momentum fluid away from the bottom and wall. Further downstream, the eddy shifts to the left, and the size does not change with the movement.

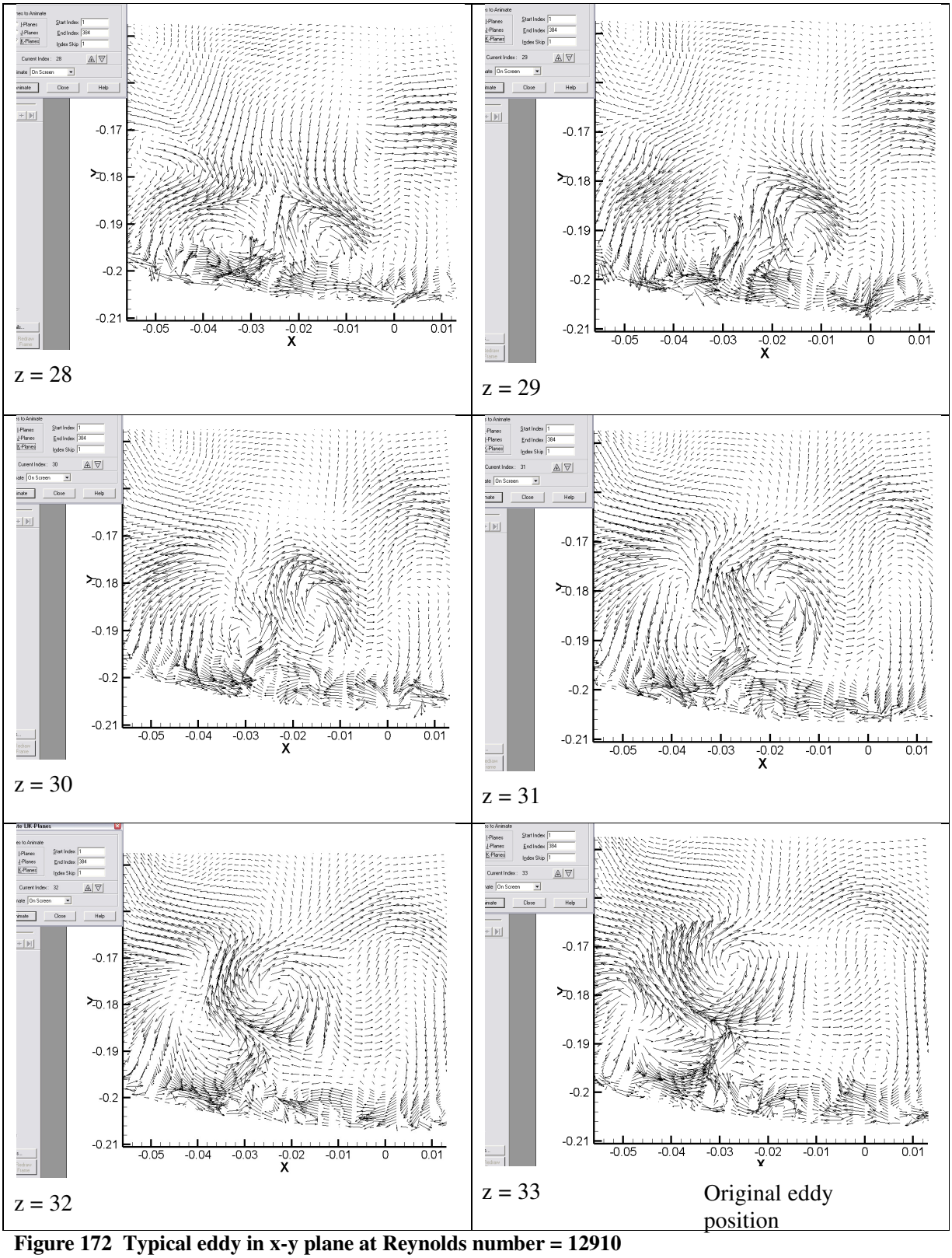

Figure 172 Typical eddy in x-y plane at Reynolds number = 12910

In Figure 173, the instantaneous velocity vectors at different z planes from z = 22 to z = 36 in streamwise direction are shown. This shows where a turbulence producing eddy appears to terminate at a given time. The eddy highlighted by red lines is produced with the disappearance of a previous eddy. Most of the wall generated eddies are well documented from the literature. However, according to the observations from this simulation results, there are many instances of an eddy disappearing and another one just generated below or next to the disappearing eddy. The old eddy grows in size then disintegrates into the surroundings. It is also argued that the 'birth' of one eddy is associated with the 'death' of another. Therefore, it is possible that the path of an eddy should end at a location where another eddy just begins. As shown in Figure 173, when the old eddy (highlighted by red lines) disintegrates, another eddy (highlighted by blue lines) lifts up from the wall region. This confirms that the claim of the 'birth' and 'death' of an eddy.

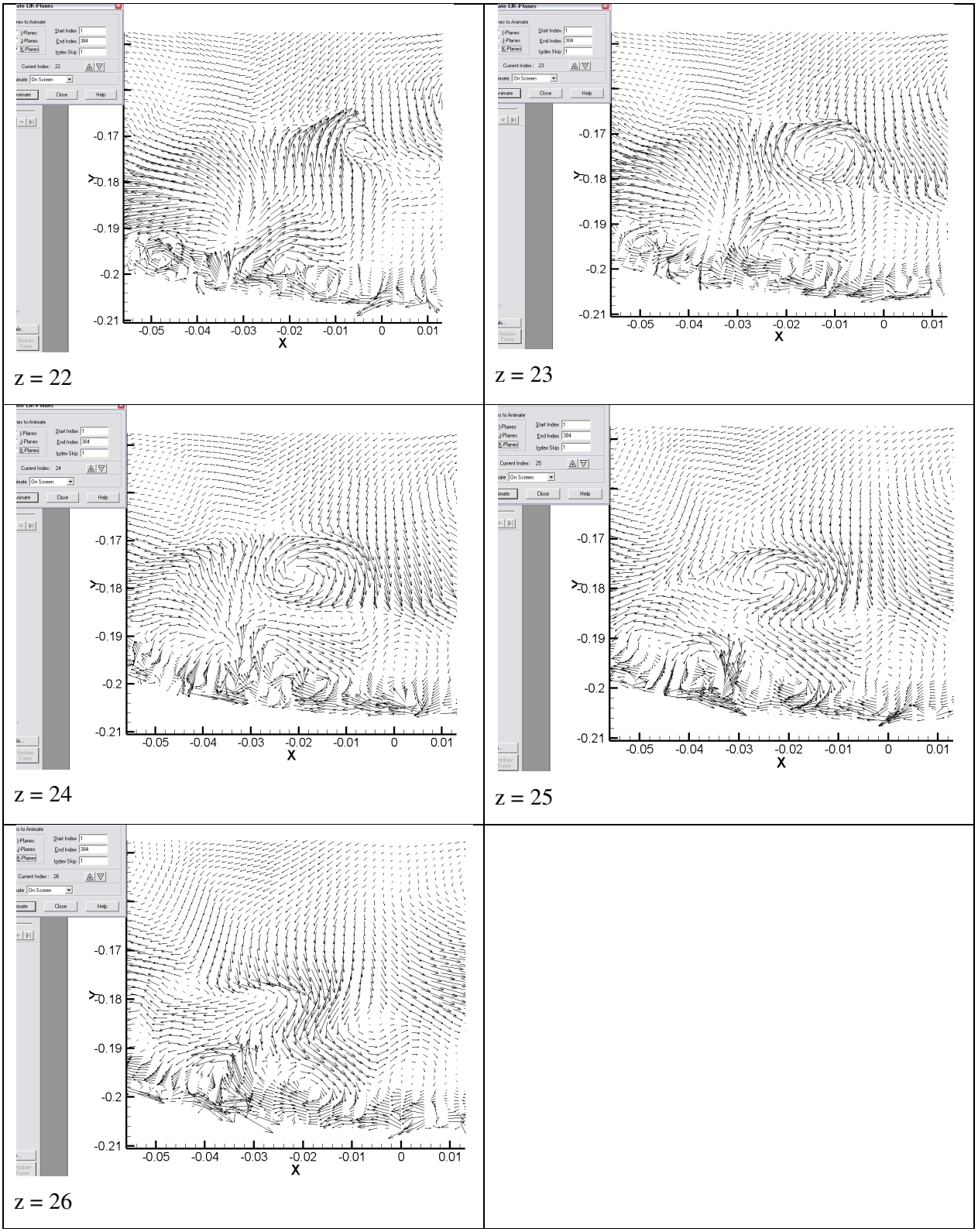

Figure 173 Typical eddy in x-y plane at Reynolds number = 12910

In Figure 174, the instantaneous velocity vectors at different z planes from z = 151 to z = 168 in streamwise direction are shown. This basically shows the 'birth' and 'death' of one eddy. At z = 151, the eddy just generates from the wall region, then it moves upward at z = 157. This eddy gradually grows in size from z = 157 to z = 160. At z = 160, a small eddy lifts up from the wall region and follows the former large eddy. The small eddy also moves upward in a slow motion, and the large eddy moves toward the surface and slowly disintegrates.

Furthermore, from Figure 172 and Figure 173, it is also observed that the speed of eddy movement is faster than that of Figure 174. For Figure 172, the centre of eddy moves from x,y = (-0.016, -0.186) to (-0.028, -0.176) in six z-planes. That is a movement of 0.0026 m per one z-plane. For Figure 174, the centre of eddy moves from x,y = (-0.028, -0.19) to (-0.008, -0.172) in 18 z-planes. By calculation, it shows a movement of 0.0015 per one z-plane. This is most likely caused by the different simulation Reynolds number. For Figure 172 and Figure 173, the Reynolds number equals 12910 whereas Figure 174 has a Reynolds number of only 5635. Other than the speed of eddy movement, it is also seen that Figure 172 and Figure 173 has larger and more intensified velocity vectors whereas in Figure 174 the velocity vectors are much organised and less random. Therefore it can be concluded that eddy's movement is Reynolds number dependent.

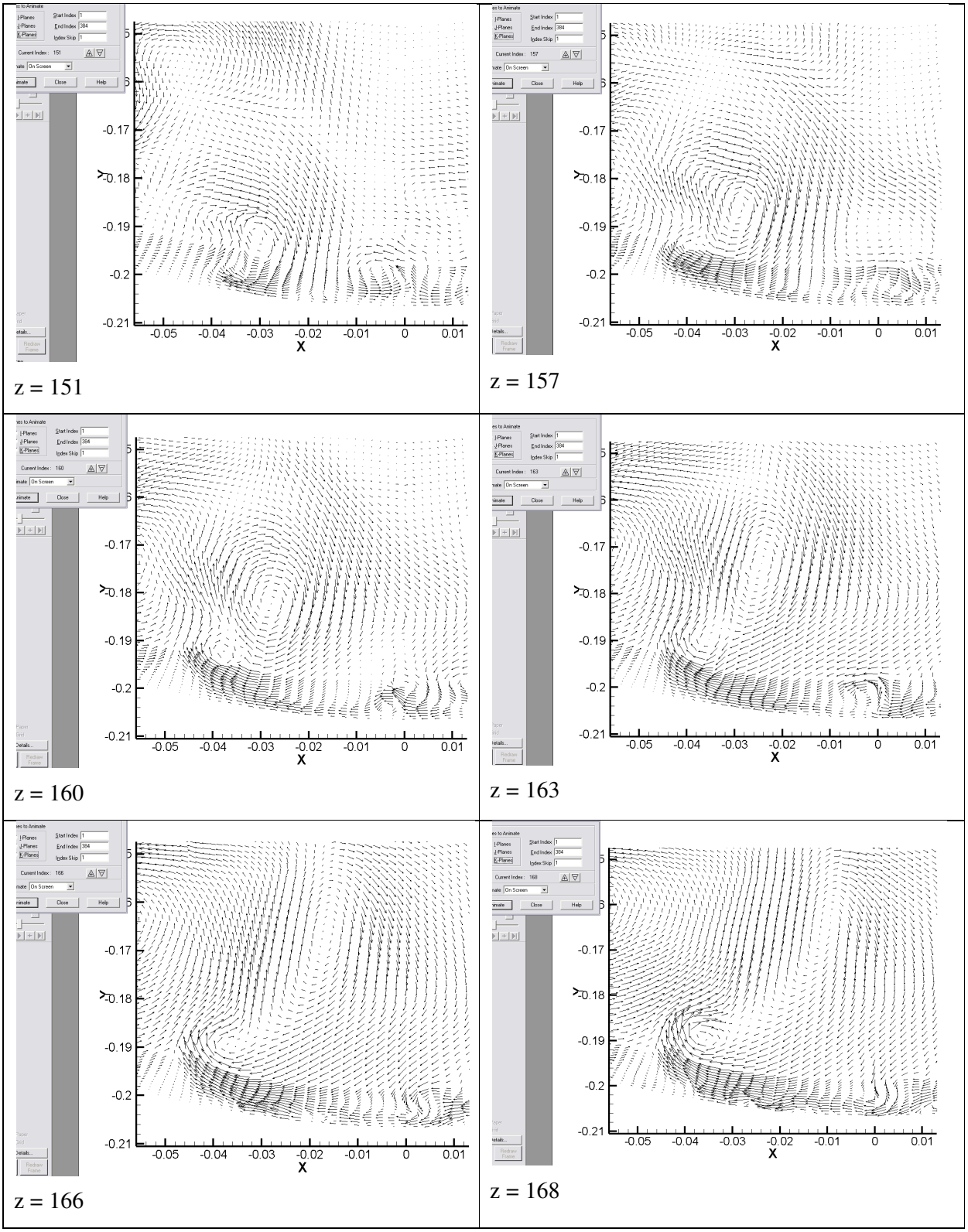

Figure 174 Typical eddy in x-y plane at Reynolds number = 5635

7.3.2 Particle suspension and quadrant analysis

Quadrant analysis was introduced earlier in the literature review section. It is used to investigate the Reynolds stress structures and features of the large eddy. In this research, quadrant analysis is used as a tool to quantify the near boundary behaviour of the fluid.

Basically, quadrant analysis sorts out contributions to the Reynolds shear stress $u'v'$ into quadrants of the u-v plane. The largest positive contributions to the turbulent energy were provided by the ejection ($u'<0$, $v'>0$) and sweep quadrants ($u'>0$, $v'<0$), while small and negative contributions were made by the interaction quadrants ($u'<0$, $v'<0$ and $u'>0$, $v'>0$). The first quadrant $u'>0$, $v'>0$, contains outward motion of high-speed fluid. The second quadrant $u'<0$, $v'>0$ contains the motion associated with ejections of low-speed fluid away from the wall. The third quadrant $u'<0$, $v'<0$ contains inward motion of low-speed fluid. The fourth quadrant $u'>0$, $v'<0$ contains an inrush of high-speed fluid (Kim *et al,* 1987). Figure 175 shows a typical quadrant map for one of the channel velocity measurement at a specified position. The different quadrants are also shown in this plot.

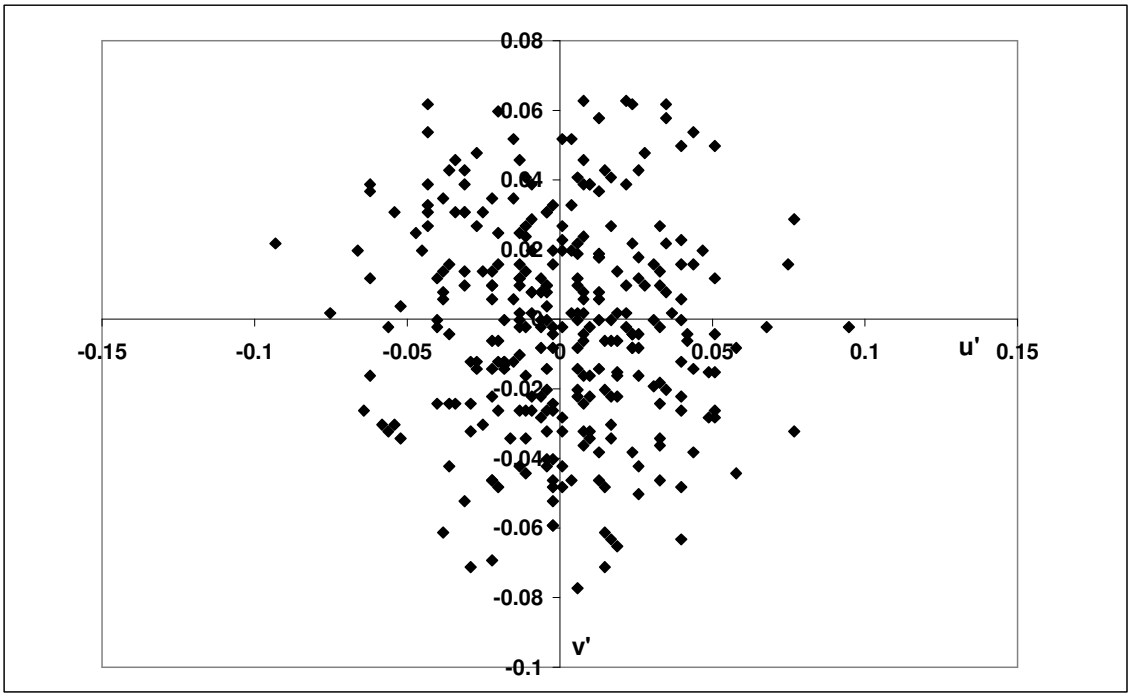

Figure 175 Typical quadrant map

Figure 176 to Figure 184 illustrate the quadrant analysis for the experimental data from Fitton (2007). These particular experiment parameters were also used for the simulation result. x represents different spanwise positions. Firstly, for Figure 176 to Figure 178, there is no noticeable Q2 and Q4 percentage different on average. However, analysing the result locally, it is clear from Figure 176, that there is a large percentage of Q4 at x = 0 cm (centreline) and depth = 60 cm. This equals around y/h = 0.14. Nezu and Azuma (2004) mentioned that the fluid particle interactions and bursting phenomena both occur in inner wall region of y/h < 0.2. However, measurement from just one position could not provide a satisfactory conclusion.

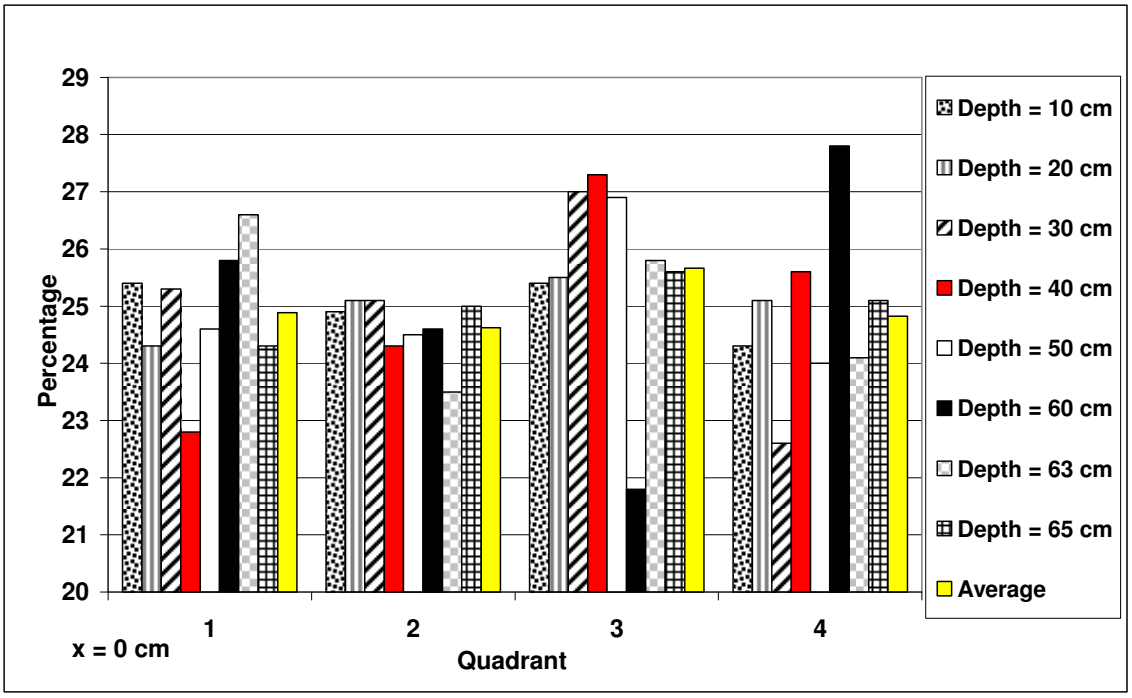

Figure 176 Quadrant analysis at x = 0 cm

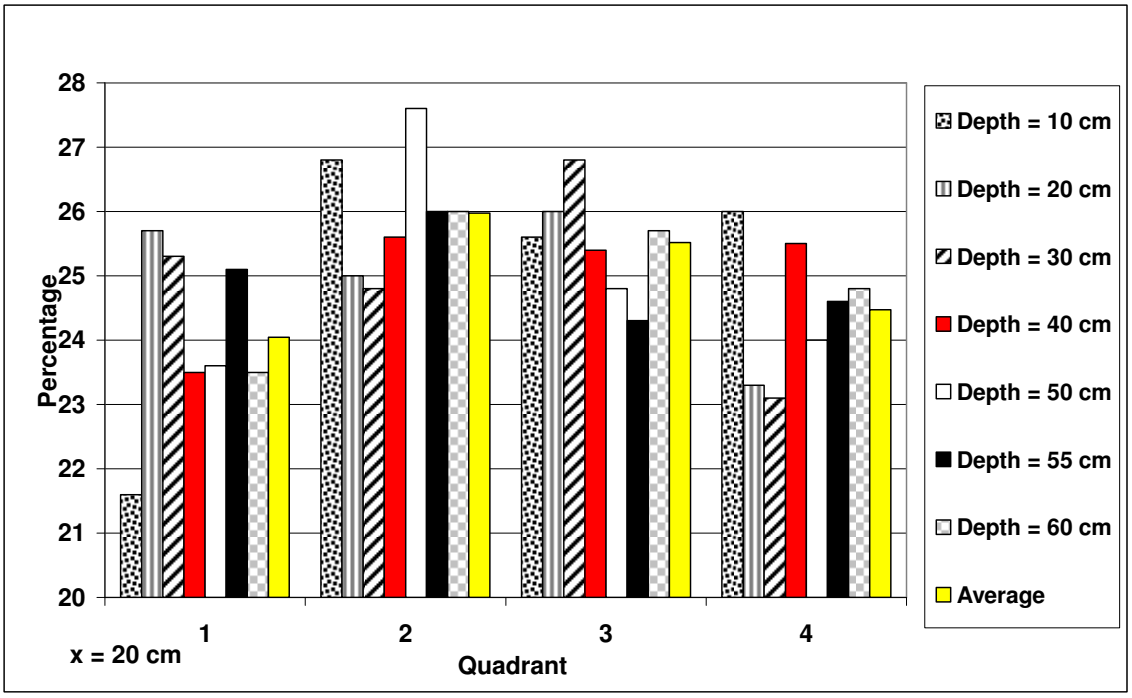

Figure 177 Quadrant analysis at x = 20 cm

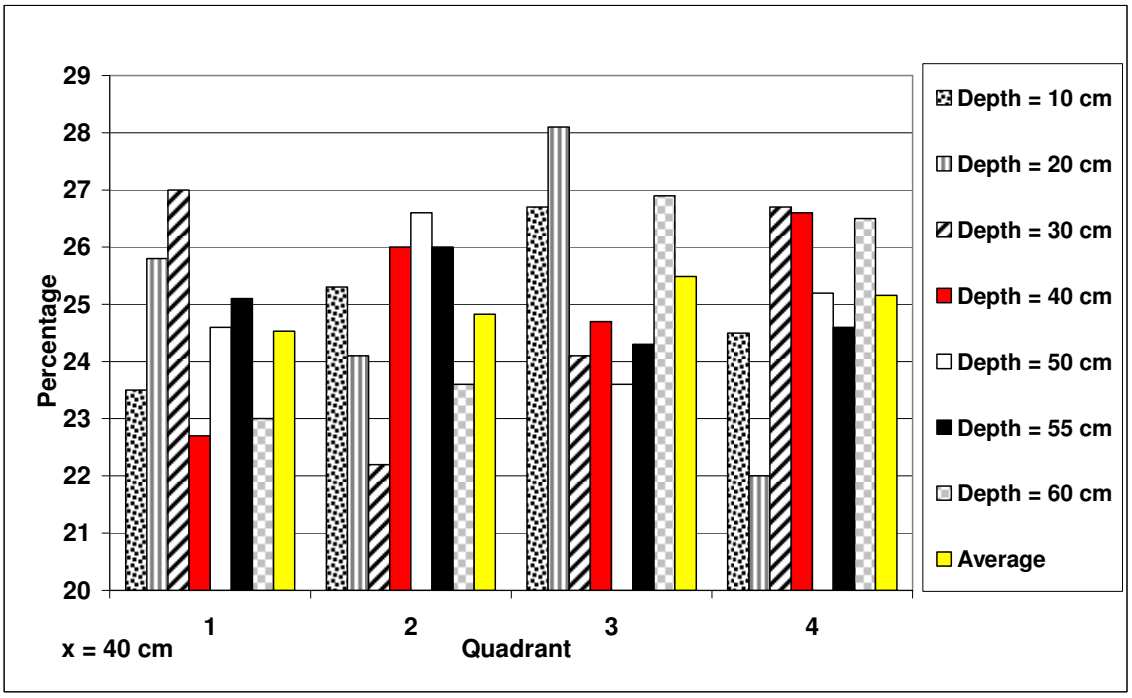

Figure 178 Quadrant analysis at x = 40 cm

In Figure 177 and Figure 178, there is no large Q2 and Q4 percentage change. It can be seen by the yellow coloured average bar in the graph, there is not a significant difference between

all four quadrants. In Figure 179, there is a large percentage of Q2 and Q4 action at depth = 50 cm. At x = 60 cm and depth = 50 cm, it can be seen that 29.1% of the total event is the ejection event and 29.7% of the total event is the sweep (Q4) event. This indicates that the ejection and sweep event is dominant in the region at y/h = 0.28 which is just outside of Nezu and Azuma (2004)'s value of 0.2.

This is a very interesting finding because from Figure 180, this measurement at x = 60 cm just passes through the secondary current cell boundary. The green circle pinpointed the position of x = 60, depth = 50 cm. It can be seen that the point is just located in the middle of some very intense velocity vectors. This could be one of the factors why Q2 and Q4 events dominate this particular region.

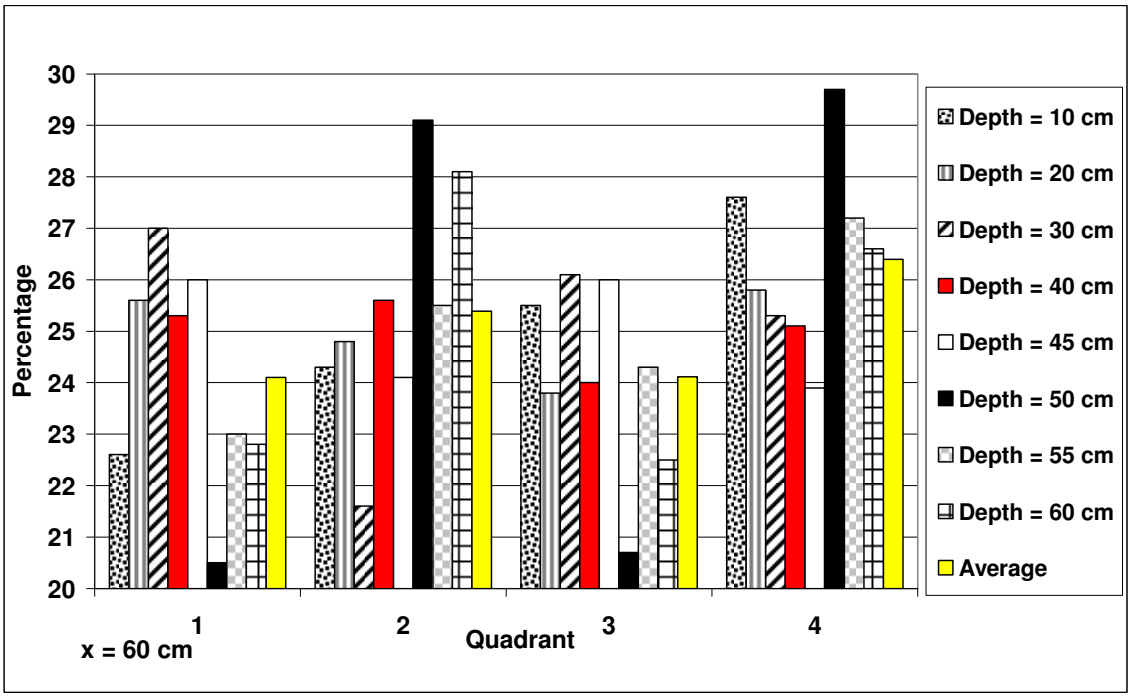

Figure 179 Quadrant analysis at x = 60 cm

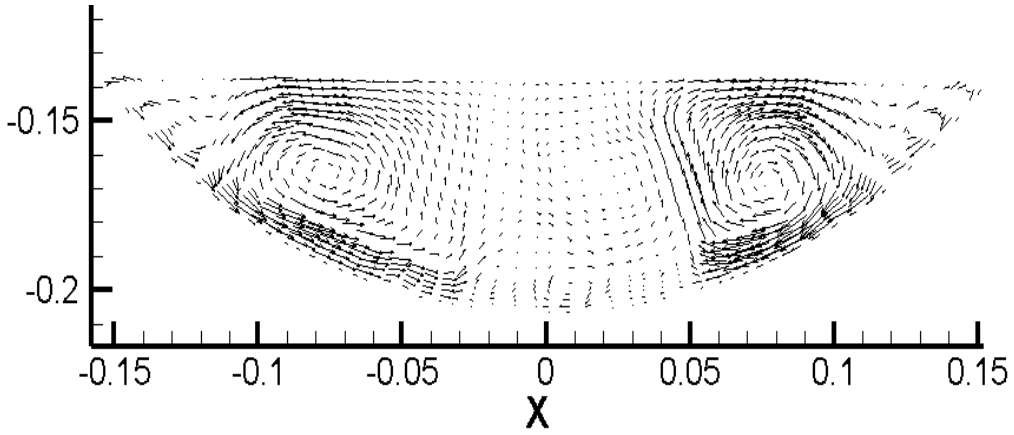

Figure 180 Illustration of velocity measurement taken at x = 60 m and depth = 50 cm

In Figure 181, there is a large percentage of Q2 and Q4 action at depth = 10 and 20 cm. At x = 80 cm and depth = 10 cm, it can be seen that 25.8% of the total event is the ejection event and 28.3% of the total event is the sweep event. At x = 80 cm and depth = 20 cm, there is 27.0% of the total event is the ejection event and 27.0% of the total event is the sweep (Q4) event. From literature (Nezu and Azuma, 2004), it is said that the ejection process transports the wall fluid toward the free surface. Therefore, the Q2 and Q4 events at close to the free surface is likely as ejection can interact with the free surface when wall ejections become more prominent.

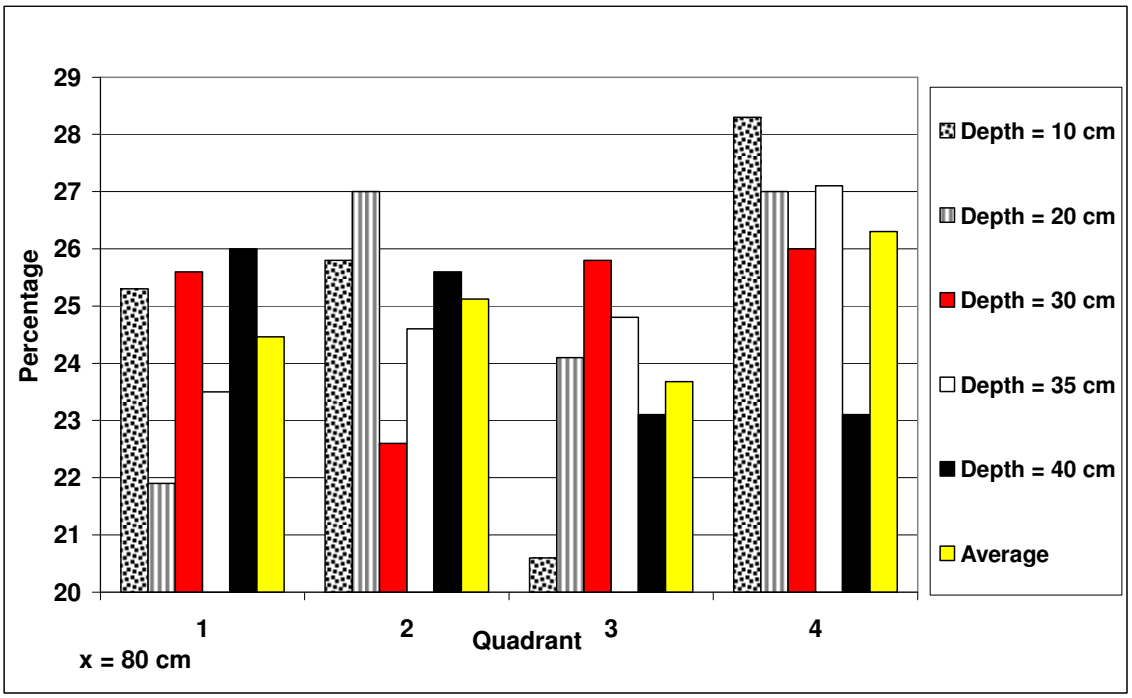

Figure 181 Quadrant analysis at x = 80 cm

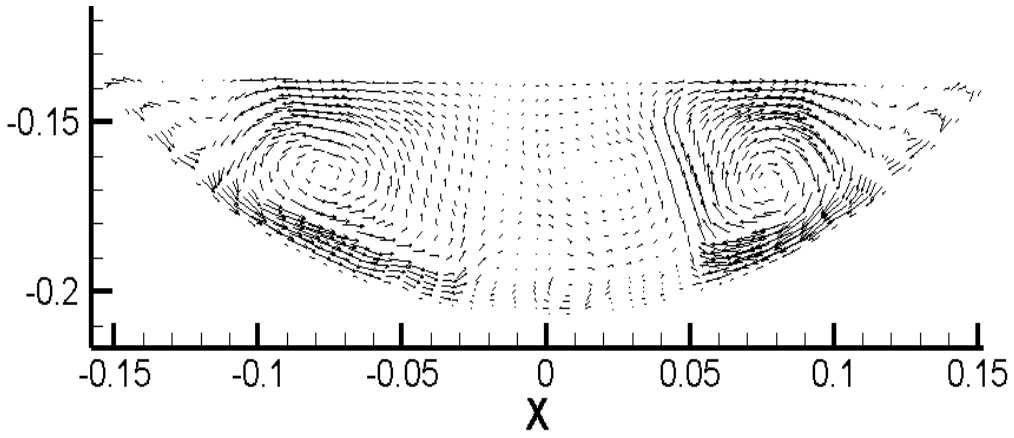

Figure 182 Illustration of velocity measurement taken at x = 80 m and depth = 10 cm

Figure 183 and Figure 184 show similar trends with large percentage for Q2 and Q4 action closer to the surface. At x = 90 cm and depth = 10 and 20 cm, it can be seen that 27.1% and 26.8% of the total event is the ejection event; 28.2% and 27.2% of the total even is the sweep event. At x = 100 cm and depth = 15 and 20 cm, there is 28.5% and 25.6% of the total event is the ejection event; 25.6% and 26.2% of the total event is the sweep event. Both Figure 183 and Figure 184 show that there are Q2 and Q4 events closer to the surface. This reinforces the claim that ejection and sweep do interact with the surface as well as at position y/h = 0.2.

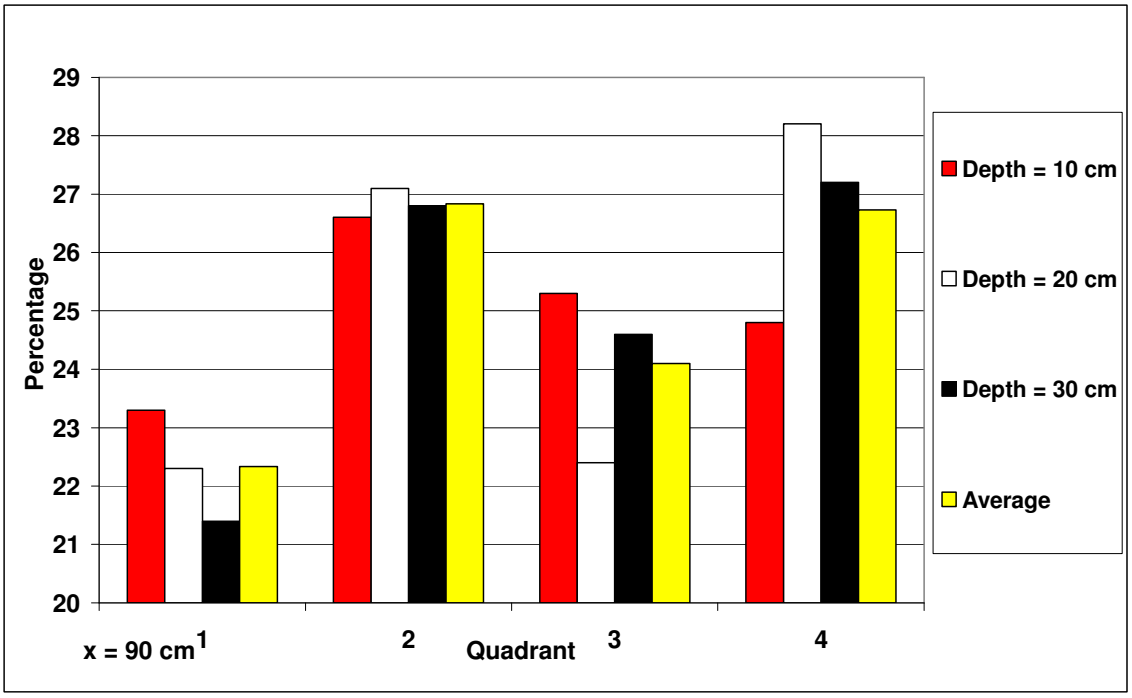

Figure 183 Quadrant analysis at x = 90 cm

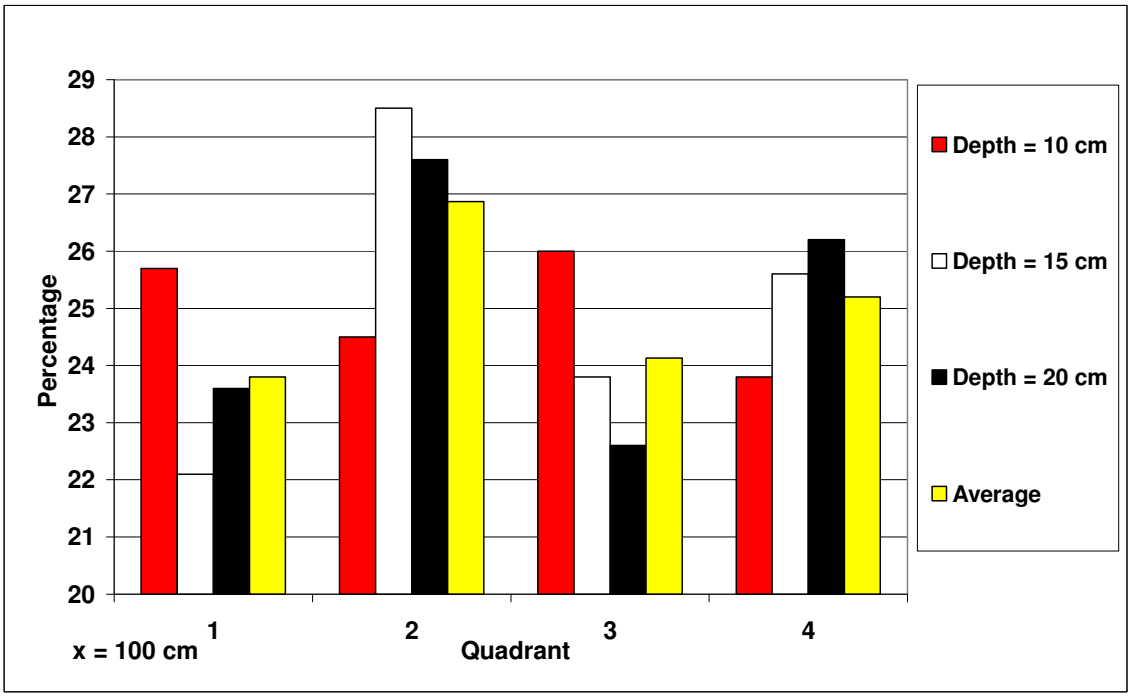

Figure 184 Quadrant analysis at x = 100 cm

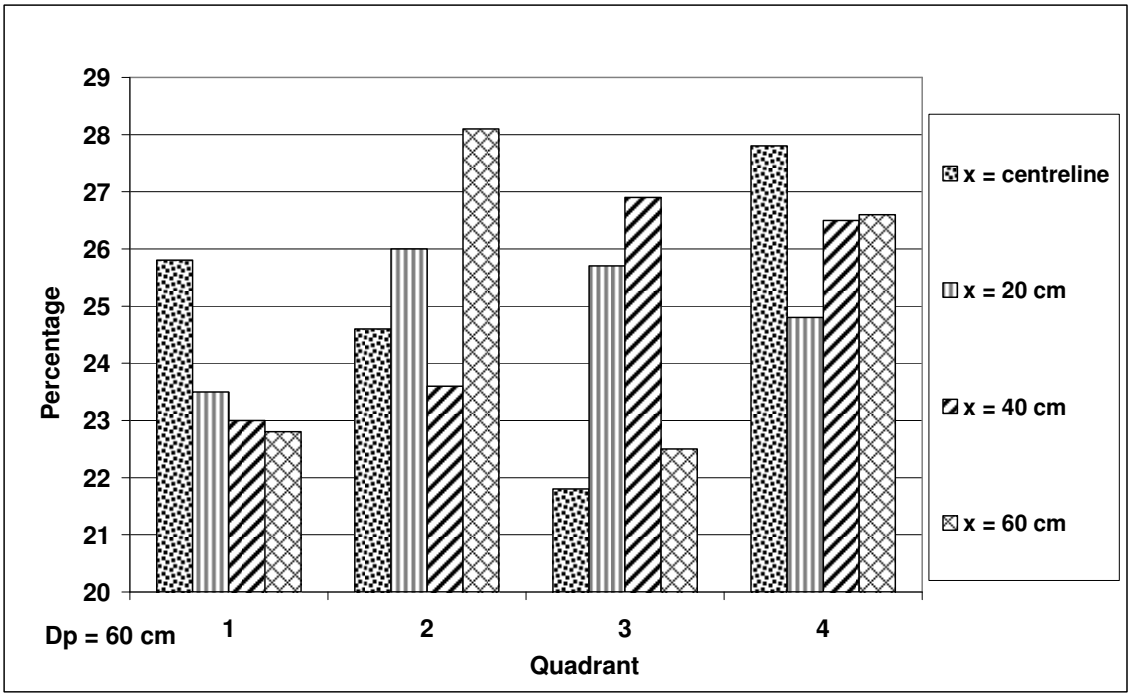

Figure 185 Quadrant analysis at depth = 60 cm

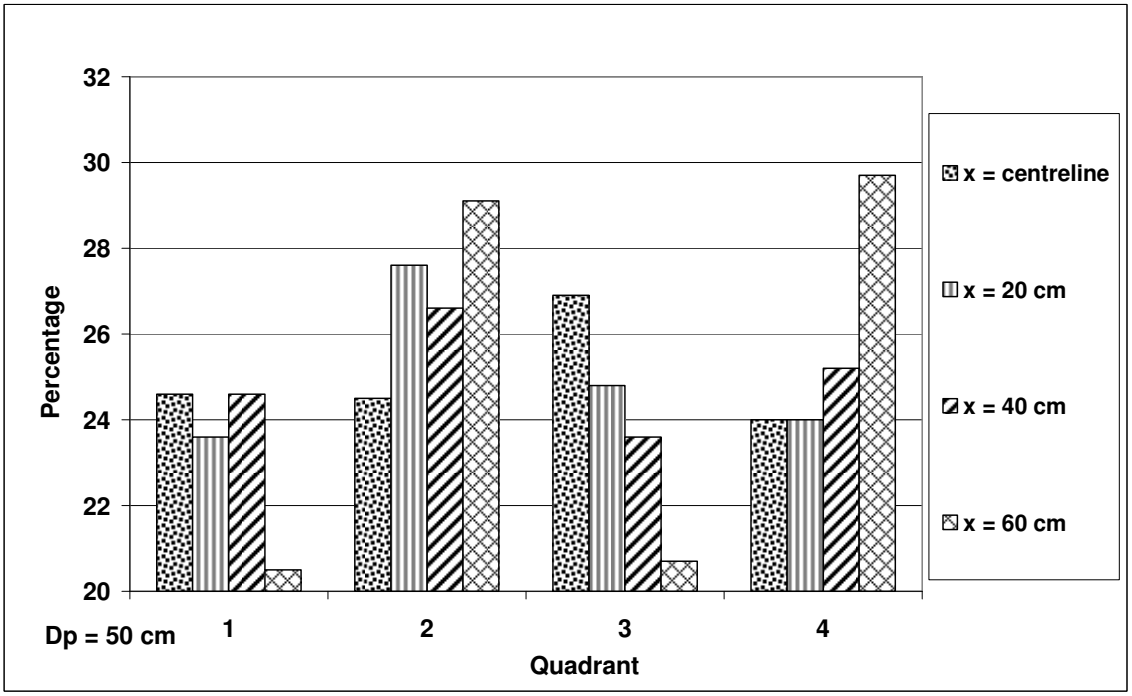

Figure 186 Quadrant analysis at depth = 50 cm

At depth = 60 cm, which is very close to the wall at *y/h* = 0.14, Q2 and Q4 events are very strong at x = 0 and 60 cm. similarly at depth = 50 cm, where *y/h* = 0.28, Q2 and Q4 events are

also quite strong at x = 20, 40 and especially at 60 cm. Ejection and sweeps are the foundation of the bursting process. From Sumer and Oguz (1978), the authors mentioned that the whole sequence of a burst started with the ejection. The ejection's upwelling motion lifts up particles from the bottom of the channel. Then as the ejection progresses, the lifted fluid will move away from the wall and grow in size. Later, the lifted fluid breaks up as it interacts with the next ejection and the whole sequence of events repeats in a cycle.

In simple words, particles rise by ejection, then terminates and the particle starts to return to the neighbourhood of the wall. On the way back to the wall, it is expected to meet new lifting fluid due to the next burst. This process makes it possible for the particle to stay in suspension. It is said that the bursting phenomenon has been shown to be responsible for most of the turbulence energy production and to be the major contributor to the transport of particles. (Sumer and Deigaard, 1981)

Other than the interactions near the free surface, the rest of the ejection and sweep events can be said as bursting cycles. Without the bursting cycle, particles cannot be suspended in the fluid. Therefore, ejections and sweeps are essential for particle suspension in an open channel. From previous discussions, it is known that particles tend to deposit in the low velocity wall streaks. Figure 187 shows simulation carried out by Pan and Banerjee (1996) that the particles tend to segregate in the low velocity streaks. This behaviour is well observed experimentally by Kaftori *et al* (1995) and Pedinotti *et al* (1992). With a larger, longer and wider wall streaks, it is easier for particles to deposit and settle than the smaller and more random wall streaks.

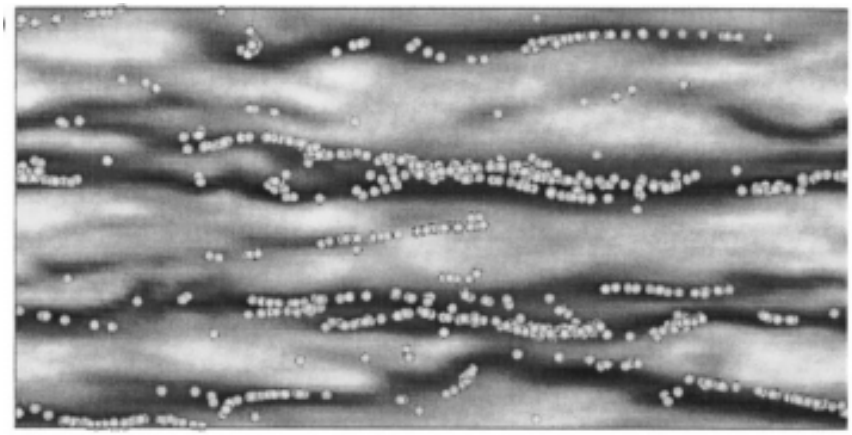

Figure 187 Particle distribution on a horizontal plane at $y^+ = 3.6$ from the wall (Pan and Banerjee, 1996)

From this section, it is seen that the largest percentage of ejection and sweep events occurred at x = 60 cm, depth = 50-60 cm. It is possible that particles are more easily suspended and re-suspended in those areas. It appears that particle transport is mainly controlled by the ejection events from the lift up and break-down of the low velocity streaks in the wall regions.

Moreover, there is a secondary current cell located at the same position as the occurrence of largest ejection and sweep events. This begs the question: is there any relationship between secondary current and particle suspension?

7.3.2.1 Particle suspension and secondary current

There appears to be no research on secondary currents in a semi-circular open channel. Most of the research is associated with square or rectangular channel. Within the current investigation, the most interesting finding is that the majority of the ejection and sweep events occurred in areas surrounding of a secondary current cell.

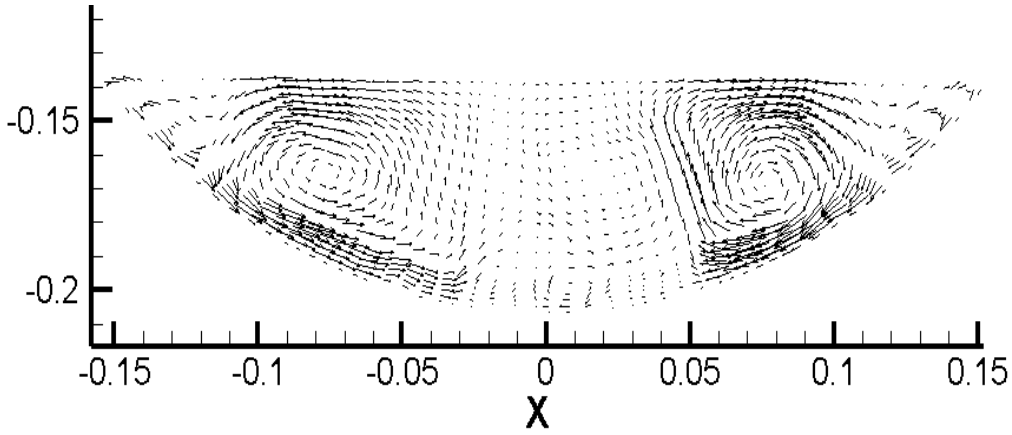

Figure 188 Average velocity vectors for control simulation

It is found that these secondary motions act to transfer fluid momentum from the centre of the channel to the side therefore causing a swelling of the streamwise velocity towards to the side of the channel. From previous section, it is seen that the secondary cell provides a mean upwards velocity at the bottom of the channel (see Figure 188). This creates a large percentage of ejection and sweeps events. Moreover, from Sumer and Oguz (1978), it is found that with continuous ejection and sweep (bursting cycle); particles can be suspended and re-suspended. It is also seen in Yao and Fairweather (2009) that the re-suspension is dominant in two regions, one close to the wall ($y^+ = 0$), and one close to the side walls. Yao and Fairweather (2009) used square duct geometry, however, secondary currents were also observed in the corner of their square duct. Their results also showed that the secondary current provided strong upward motion which is very similar to this study. Therefore, this secondary current cell has the potential to assist the re-suspension of particles.

However, the relationship between the size of the secondary current as well as the strength of re-suspension is not investigated in this study.

7.4 Summary

In summary, Stokes number increases with increase of Reynolds number because of increased turbulent characteristics. Simulation with high Reynolds number gives a higher velocity in the velocity streaks. Flow with lower Reynolds number gives a slightly lower velocity in the velocity streaks. The low velocity streaks are very Reynolds number dependent. Simulation

with high Reynolds number exhibits shorter and smaller low velocity streaks and low Reynolds number shows longer and wider low velocity streaks. It is also concluded that Reynolds number has a more significant effect on the low velocity streak size.

With the help of quadrant analysis, it is found that the largest percentage of ejection and sweep events occurred at away from the centreline at x = 60 cm, and close to the wall at a height 10-20 cm from the bottom. In theory the particles become easier to be suspended and re-suspended in those areas. Furthermore, it also reinforced that the secondary current cell can assist the re-suspension of particles.

Chapter 8: Conclusion and recommendation

8.1 Conclusion

The fundamentals of non-Newtonian open channel suspension flow have been investigated in this work. The following conclusions are based on both experimental and simulation work:

- Simulation results show good agreement with literature data. This includes the work of: Wallace *et al* (1972), Eckelmann (1974), Kastrinakis and Eckelmann (1983), Antonia *et al* (1992) and Rudman *et al* (2004).
- Computational results show good agreement with experimental data from Fitton (2007) except for the velocity dip phenomenon.
- Change in yield stress does not show any large change in the flow characteristics. Increase in yield stress decreases Reynolds number under the same simulation condition hence the flow becomes less developed. Decrease in yield stress increases Reynolds number therefore the flow becomes more turbulent. It is found that the yield stress does not have a major effect on the bulk velocity.
- For change in flow behaviour index, all the mean velocity profiles show shifting velocity profile upward in the simulation. It is still very difficult to see the real effect of flow behaviour index in relation to bulk velocity. With the help from velocity contour, it is concluded that increase in flow behaviour index makes the flow more developed under the same simulation condition. Decrease in flow behaviour index makes the flow less developed. The bulk velocity changes only slightly with change in flow behaviour index.
- Increase in fluid consistency index causes less developed flow. Decrease in fluid consistency index shows bright white high velocity streaks in the velocity contour. Hence this suggests that decrease in fluid consistency index would present a more turbulent flow characteristic for the fluid.
- With a more constant Reynolds number value, increase in fluid consistency index still suggests that the flow is not fully developed. Decrease in fluid consistency index also shows similar bright white high velocity streaks in the velocity contour. The same

conclusion can be made for flow without Reynolds number effect and the change in fluid consistency index with change in Reynolds number. From simulation, there is no significant change in bulk velocity with change in fluid consistency index.

- This simulation method provides the opportunity to examine the effect of changing one rheology parameter while keeping the other parameters constant. In practice, this kind of investigation is impossible to conduct. This is a major contribution to the study in rheological behaviour in tailings transportation.
- With an increased depth (i.e. Increasing from 0.07 m to 0.08 m), the bulk velocity changes from 1.48 m/s to 1.46 m/s. With a decreased depth, the bulk velocity increases to 1.52 m/s. However, there is no significant difference in velocity profile between increase or decrease in depth.
- With different x position measurements, velocity decreases with x moving away from the centreline. Velocity dipping also appears with x moving out towards the channel boundary.
- With a high resolution mesh, the result shows no significant difference in velocity profile and turbulence intensities.
- For secondary current, with smaller Reynolds number, weak and large size turbulent structures appear in the middle region of the channel. This is observed with increased yield stress, increased *n,* and increased *K* plots. This could be a result of increased viscosity of the non-Newtonian fluid. With a larger Reynolds number, the secondary current cells tend to be stable and locate at either side of the channel. This is observed in decreased yield stress, decreased *n* and decreased *K* plots.
- Stokes number increases with increase of Reynolds number because of increased turbulent characteristics. It is concluded that change in yield stress (up to 50% of current value) does not affect Stokes number significantly. Change in flow consistency index also affects Stokes number in a limited way. Change in flow behaviour index causes noticeable change in Stokes number.
- Simulation with high Reynolds number gives a higher velocity in velocity streaks. Simulation with lower Reynolds number gives a slightly lower velocity in velocity streaks. It is found that there is no major difference between simulation results with different Reynolds number and simulation results with relative constant Reynolds number.

- It is found that the size of low velocity streaks is very Reynolds number dependent. The flow with high Reynolds number demonstrates small and random low velocity streaks and low Reynolds number shows longer and wider low velocity streaks. With the comparison between simulation results with different Reynolds number and simulation results with relative constant Reynolds number, it is also found that Reynolds number has more significant effect on the size of the low velocity streaks.
- With quadrant analysis on available data, it is concluded that the largest percentage of ejection and sweep events occurs away from centreline and close to the wall at a height of 10-20 cm from the bottom. In theory the particles could be easily suspended and re-suspended in those areas.
- It is seen that the secondary cell provides a mean upward velocity at the bottom of the channel (see Figure 188). Therefore, in theory, this secondary current cell could assist the re-suspension of particles.

8.2 Recommendation

The following aspects, which are not covered in this thesis, should be further investigated for adding more benefit in related areas.

- Test in a larger and longer channel that is able to run large flow rate from 30L/s. This is the magnitude of the discharge in large mine sites.
- A longer domain length will influence the results. However, the implication of this change is unknown. A longer domain length could be adopted in the future, yet this may take a long time to simulate.
- More research on secondary current with different size semi-circular flume would be of value. This would add further knowledge on the size of secondary current cells and their implications.
- More research on different rheological parameters should be carried out. For example: high yield stress material and shear thickening material.
- More research on re-suspension should be followed by the development of a relationship between particle size, and re-suspension. PIV technology should be used to conduct future research. This would be extremely helpful to see the particle re-suspension in different fluids. However, the use of non-Newtonian fluid could make this more difficult.

- More research should be carried out to examine the effect of secondary current on re-suspension, and to establish a relationship between secondary flow and re-suspension. This would be of benefit to the mining industry as secondary current has a significant influence on particle suspension and re-suspension.
- More research should be carried out to examine the particle settling in non-Newtonian suspension under shear. This could be extremely helpful to the mining industry as this may lead to more accurate design of the structure of the tailing stack.

Chapter 9: Reference

Abe, H., Kawamura, H., Matsuo, Y., 2001, Direct numerical simulation of a fully developed turbulent channel flow with respect to the Reynolds number dependence, *Transactions of the ASME,* vol.123, pp 382-393.

Abulnaga, B., 2002, *Slurry systems handbook*, McGraw Hill, United States of America.

Alfredsson, P., Johansson, A., 1984, On the detection of turbulence-generating events, *Journal of Fluid Mechanics,* vol.139, pp 325.

Angelis, E., Casciola, C., Piva, 2002, DNS of wall turbulence: dilute polymers and self-sustaining mechanisms, *Computer and Fluids,* vol.31, pp 495-507.

Antonia, R., Browne, L., 1987, Quadrant analysis in the turbulent far-wake of a cylinder, *Fluid Dynamics Research,* vol.2, pp 3-14.

Antonia, R., Teitel, M., Kim, J., Browne, L, 1992, Low-Reynolds-number effects in a fully developed turbulent channel flow, *Journal of Fluid Mechanics,* vol.236, pp 579-605.

Aydin, I., 2009, Nonlinear mixing length model for prediction of secondary currents in uniform channel flows, *Journal of Hydraulic Engineering,* vol.135, No.2, pp 146-153.

Barenblatt, G., 1993, Scaling laws for fully developed turbulent shear flows. Part 1: basic hypothysis and analysis, *Journal of Fluid Mechanics,* vol.248, pp 513-520.

Barnes, H., Hutton, J., Walters, K., 1989, *An introduction to rheology,* Elsevier, New York.

Baron, A., Sibilla, S., 1998, DNS of the turbulent channel flow of a dilute polymer solution, *Applied Scientific Research,* vol.59, pp 331-362.

Bergstrom, D., Kotey, N,m Tachie, M., 2002, The effects of surface roughness on the mean velocity profile in a turbulent boundary layer, *Transactions of the ASME,* vol.124, pp 664-670.

Bhattacharya, S., 2001, *Rheology Fundamentals and Measurements,* Royal Melbourne Institute of Technology, Melbourne.

Biddinika, M., 2010, Clarification of ejection and sweep in rectangular channel turbulent flow, *ICONE-18,* Xi'an, China.

Blackburn, H., 2007, *Using Semtex*, Monash University, Melbourne.

Blackburn, H., Sherwin, S., 2004, Formulation of a Galerkin spectral element – Fourier method for three dimensional imcompressible flows in cylindrical geometries, *J. Comput. Phys.,* vol.197, No.2, pp 759-778.

Blackwelder, R., Kaplan, R., 1976, On the wall structure of the turbulent boundary layer, *Journal of Fluid Mechanics,* vol.76, pp 89-112.

Bogue, D.C. and Metzner, A.B., 1963, Velocity profiles in turbulent pipe flow, *Industrial and Engineering Chemistry Fundamentals,* vol.2, No.2, pp143-149.

Bradshaw, P., 1978, *Topics in applied physics-turbulence*, Springer-Verlag, Berlin Heidelberg.

Broglia, R., Pascarelli, A., Piomelli, U., 2003, Large-eddy simulations of ducts with a free surface, *Journal Fluid Mechanics,* vol.484, pp 223-253.

Brook, J., Hanratty, T., 1993, Origin of turbulence-producing eddies in a channel flow, *Phys. Fluids A,* vol.5, No.4.

Cancela, M., Alvarez, E., Maceiras, R., 2005, Effect of temperature and concentration on carboxymethylcellulose with sucrose rheology, *Journal of Food Engineering,* vol.71, pp419-424.

Cargnelutti, M., Portela, L., 2007, Influence of the turbulence structure on the particle sedimentation in wall-bounded flow, *in Particle Laden Flow: From Geophysical to Kolmogorov Scales,* Springer, Netherlands.

Cengel, Y., Cimbala, J., 2006, *Fluid Mechanics Fundamentals and Applications,* McGraw Hill, New York.

Chanson, H., 1999, *The hydraulics of Open Channel Flow,* Arnold, London.

Chhabra, R., Richardson, J., 2008, *Non-Newtonian Flow and Applied Rheology: Engineering Applications,* Butterworth-Heinemann, UK.

Chiu, C.L., Tung, N.C., 2002, Maximum velocity and regularities in Open-channel flow, *Jounral of Hydraulic Engineering,* vol.128, No.4, pp390-398.

Chow, V., 1959, *Open-channel Hydraulics,* McGraw-Hill, New York.

Chryss, A.G., Fitton, T.G., Bhattacharya, S.N., 2006, Turbulent flow of non-Newtonian tailings in self formed channels on tailing stacks, Jewell, R.J., Lawson, S., Newman, P.(eds), 2006, *Paste 2006*, Australian Centre for Geomechanics, Perth.

Clapp, R., 1961, Turbulent heat transfer in pseudoplastic non-Newtonian fluids, *Int. Dev. Heat Transfer Part III*, New York.

Coles, D., 1956, The law of the wake in turbulent boundary layer, *Journal of Fluid Mechanics,* vol.1, pp 191-226.

Coles, D., 1968, The turbulent boundary layers in a compressible flow, *The Physics of Fluids,* vol.7, No.9, pp 1403-1432.

Coleman, N., 1981, Velocity profiles with suspended sediment, *Journal of Hydraulic Research,* vol.19, pp 221-229.

Coleman, N., Alonson, C., 1983, Two-dimensional channel flows over rough surfaces, *Journal of Hydraulic Engineering, ASCE,* vol.109, pp 175-188.

Colwell, J., Shook, C., 1988, The entry length for slurries in horizontal pipeline flow, *The Canadian Journal of Chemical Engineering,* vol.66, pp714-720.

Coussot, P., 1994, Steady laminar flow of concentrated mud suspensions in open channels, *Journal of Hydraulic Research,* vol.32, No.4, pp 535-558

Crowe, C., Chung, J., Troutt, T., 1993, "Particle dispersion by organized turbulent structures", in Roco, M.C, *Particulate two phase flow,* Butterworth-Heineman, Boston.

Davies, J., 1972, *Turbulence Phenomena*, Academic Press Inc, New York.

De Angelis, E., Casciola, C., Piva, R., 2002, DNS of wall turbulence: dilute polymers and self-sustaining mechanisms, *Computers and Fluids,* vol.31, pp 495-507.

Dean, R., 1978, Reynolds number dependence of skin friction and other bulk flow variables in two-dimensional rectangular duct flow, *Journal of Fluids Engineering,* vol.100, pp 215-223.

Dimitropoulos, C., Dubief, Y., Shaqfeh, E., Moin, P., Lele, S., 2004, Direct numerical simulation of polymer-induced drag reduction in turbulent boundary layer flow, *Physics of Fluids,* vol.17, 011705.

Dodge, D., Metzner, A., 1959, Turbulent Flow of Non-Newtonian Systems, *A.I.Ch.E Journal,* vol.5, No.2, pp189-204.

Druzhinin, O., 2000, On the stability of a stationary solution of the Tchen's equation, *Physics of Fluids*, vol.12, No.7, pp1878-1880

Durand, R., 1953, Basic relationships of the transportation of solids in pipes – experimental research, *Minnesota International Hydraulics Convention,* Minnesota, USA.

Eckelmann, H., 1974, The structure of viscous sublayer and the adjacent wall region in a turbulent channel, *Journal of Fluid Mechanics,* vol.65, pp 439-459.

Eggels, J., Unger, F., Weiss, M., Westerweel, J., Adrian, R., Friedrich, R., Nieuwstadt, F., 1994, Fully developed turbulent pipe flow: a comparison between direct numerical simulation and experiment, *Journal of Fluid Mechanics,* vol.268, pp 175-209.

Einstein, H., Li, H., 1958, Secondary currents in straight channels, *Transactions – American Geophysical Union,* vol.39, No.6, pp 1085-1088.

Escudier, M., Poole, R., Presti, F., Dales, C., Nouar, C., Desaubry, C., Graham, L., Pullum, L., 2005, Observations of asymmetrical flow behaviour in transitional pipe flow of yield-stress and other shear-thinning liquids, *Journal of Non-Newtonian Fluid Mechanics,* vol.127, pp143-155.

Escudier, M., Smith, S., 2001, Fully developed turbulent flow of non-Newtonian liquids through a square duct, *Proc. R. Soc. Lond. A,* vol.457, pp911-936.

Faddick, R., 1986, Slurry flume design, *10th International Conference on the Hydraulic Transport of Solids in Pipes,* Hydrotransport 10, Innsbruck, Austria.

Fitton, T., Chryss, A., Bhattacharya, S.N, 2006, Tailings beach slope prediction: a new rheological method, *International Journal of Mining, Reclamation and Environment,* vol.20, No.3, pp181-202.

Fitton, T., 2007, *Tailings beach slope prediction,* PhD thesis, RMIT, Australia

French, R., 1982, *Open channel hydraulics,* McGraw-Hill Book Company, New York.

Freeze, B., Smolentsev, S., Morley, N., Abdou, M., 2003, Characterization of the effect of Froude number on surface waves and heat transfer in inclined turbulent open channel wave flows, *International Journal of Heat and Mass transfer*, vol.46, pp3765-3775.

Friedlander, S., Johnstone, H., 1957, Deposition of suspended particles from turbulent gas streams, *Industrial and Engineering Chemistry Research,* vol.49, No.7, pp 1151-1156.

Garcia, C., Cantero, M., Nino, Y., Garcia, M., 2005, Turbulence measurements with Acoustic Doppler Velocimeter, *Journal of hydraulic Engineering,* vol. 131, No.12, pp1062-1073.

Gessner, F., 1973, The origin of secondary flow in turbulent flow along a corner, *Journal of Fluid Mechanics,* vol.58, No.01, pp1-25.

Gillies, R., Schaan, J., Sumner, R., McKibben, M., Shook, C., 2000, Deposition velocities for Newtonian slurries in turbulent flow, *The Canadian Journal of Chemical Engineering,* vol.78.

Govier, G., Aziz, K., 1972, *The flow of Complex Mixtures in Pipes,* Litton Educational Publishing, U.S

Graham, L., Pullum, L., Chryss, A., Rudman, M., 2001, Transition to turbulence in non-Newtonian pipe flow, *6th World congress of chemical engineering,* Melbourne, Australia, 23-27 September 2001.

Guermond, J., Shen, J., 2003, Velocity-correction projection methods for incompressible flows, *SIAM Journal on Numerical Analysis.*, vol.41, pp 112 -134.

Gulliver, J., Halverson, M., 1987, Measurements of large streamwise vortices in an open channel flow, *Water resources research,* vol.23, No.1, pp115-123.

Haldenwang, R., 2003, *Flow of non-Newtonian fluids in open channels*, PhD thesis, Cape Technikon, South Africa.

Haldenwang, R., Slatter P., Chhabra, R., 2002, Laminar and Transitional flow in Open Channels for non-Newtonian Fluids, *15th International Conference on Hydrotransport,* Banff, Canada. pp755-768.

Haldenwang. R., Slatter, P., Chhabra R., 2004, Prediction of transition for non-Newtonian open channel flow, *12th international conference on transport and sedimentation of solid particles,* Prague, Czech Republic. pp387-396.

Haldenwang, R., Slatter, P., Chhabra, R., 2004, The thin film approximation for laminar flow in open channels for non-Newtonian fluids, *International Seminar on Paste and Thickened Tailings,* Paste and Thickened Tailings Paste 2004.

Heays, K., Friedrich, H., Melville, B., 2010, Change of particle size distribution during cluster evolution, *IAHR APD,* Auckland.

Henderson, F., 1966, *Open Channel Flow,* MacMillan, New York.

Hetsroni, G., 1993, The effect of particles on the turbulence in a boundary layer*,* in Roco, M.C, *Particulate two phase flow,* Butterworth-Heineman, Boston.

Hetsroni, G., Rozenblit, R., 1994, Heat transfer to a liquid solid mixture in a flume, *Int. J. Multiphase Flow*, vol.20, pp671

Hogan, R., Cuzzi, J., 2001, Stokes and Reynolds number dependence of preferential particle concentration in simulated three-dimensional turbulent, *Physics of Fluids,* vol.13, No.10, pp2938-2945.

Hu, Z., Morfey, C., Sandham, N., 2006, Wall pressure and shear stress spectra from Direct Simulations of channel flow, *AIAA Journal,* vol.44, No.7, pp 1541-1549.

Ikeda, S., Parker, G., Kimura, Y., 1988, Stable width and depth of straight gravel rivers with heterogeneous bed materials, *Water Resources Research,* vol.24, No.5, pp 713-722.

Jeong, J., Hussain, F., Schoppa, W., Kim, J., 1997, Coherent structures near the wall in a turbulent channel flow, *Journal of Fluid Mechanics,* vol.332, pp 185-214.

Joung, Y., Choi, S., 2010, Direct numerical simulation of low Reynolds number flows in an open-channel with sidewalls, *International Journal for Numerical Methods in Fluids,* vol.62, pp 854-874.

Joung, Y., Choi, S., Choi, J., 2007, Direct numerical simulation of turbulent flow in a square duct: analysis of secondary flows, *Journal of Engineering Mechanics,* vol.133, No. 2, pp 213-221.

Kaftori, D., Hetsroni, G., Banerjee, S., 1995, Particle behaviour in the turbulent boundary layer. II. Velocity and distribution profiles, *Physics of Fluids*, vol.7, No.5, pp1107-1121.

Kaftori, D., Hetsroni, G., Banerjee, S., 1998, The effect of particles on wall turbulence, *Int. J. Multiphase Flow*, vol.24, No.3, pp359-386.

Kang, S., Tanahashi, M., Miyauchi, T., 2007, Dynamics of fine scale eddy clusters in turbulent channel flow, *Journal of Turbulence,* vol.8, No.52, pp 1-20.

Kastrinakis, E., Eckelmann, H., 1983, Measurement of streamwise vorticity fluctuations in a turbulent channel flow, *Journal of Fluid Mechanics,* vol.137, pp 165-186.

Karniadakis, G., Israeli, M., Orszag, S., 1991, High-order splitting methods for the incompressible navier-Stokes equations, *Journal of Computational Physics,* vol .97, pp 414-443

Kiger, K., Pan, C., 2002, Suspension and turbulence modification effects of solid particulates on a horizontal turbulent channel flow, *Journal of Turbulence,* vol.3, No.19, pp 1-21.

Kim, J., Baek, S., Sung, H., 2002, An implicit velocity decoupling procedure for the incompressible Navier-Stokes equations, *International Journal of Numerical Methods Fluids,* vol.38, No.2, pp 125-138.

Kim, J., Moin, P., Moser, R., 1987, Turbulence statistics in fully developed channel flow at low Reynolds number, *Journal Fluid Mechanics,* vol.177, pp 133-186.

Kirkgoez, M., 1988, Turbulent velocity profiles for smooth and rough open channel flow, *Journal of Hydraulic Engineering,* vol.115, No.11, pp 1543-1561.

Kirkgoez, M., Ardichoglu, M., 1997, Velocity profiles of developing and developed open channel flow, *Journal of Hydraulic Engineering,* vol.123, No.12, pp 1099-1105.

Klipp, C., Wang, Y., Chang, S., Williamson, C., Huynh, G., Garvey, D., 2006, Surface layer counter-gradient motion in and around an urban area, *14th Joint Conference on the Applications of Air Pollution Meteorology with Air and Waste Management Associates,* 2006.

Kneen, T., Strauss, W., 1969, Deposition of dust from turbulent gas streams, *Atoms. Environ.* vol.3, No.1, pp 55-67.

Knight, D., Demetriou, J., Hamed, M., 1984, Boundary shear in smooth rectangular channels, *Journal of Hydraulic Engineering,* vol.110, No.4, pp 405-422.

Knight, D., Sterling, M., 2000, Boundary shear in circular pipes running partially full, *Journal of Hydraulic Engineering,* vol.126, No.4, pp 263-275.

Kozicki, W., Tiu, C., 1967, Non-Newtonian flow through open channels, *The Canadian journal of Chemical Engineering,* vol.45, pp127-134.

Kreplin, H., Eckelmann, H., 1979, Behaviour of the three fluctuating velocity components in the wall region of a turbulent channel flow, *Phys. Fluids,* vol.22, pp 1233-1239.

Kumar, S., Gupta, R., Banerjee, S., 1998, An experimental investigation of the characteristics of free-surface turbulence in channel flow, *Physics of fluids,* vol.10, No.2, pp 454-456.

Lam, K., Banerjee, S., 1992, On the condition of streak formation in a bounded turbulent flow, *Physics of Fluids A,* vol.4, No.2, pp 306-320.

Laufer, J., 1952, The structure of turbulence in fully developed pipe flow, *NAVA Report,* No.1174, pp 417-434.

Li, C., Gupta, V., Sureshkumar, R., Khomami, B., 2006, Turbulent channel flow of dilute polymeric solutions: Drag reduction scaling and an eddy viscosity model, *Journal of Non-Newtonian Mechanics,* vol.139, pp 177-189.

Lien, K., Monty, J., Chong, M., Ooi, A., 2004, The entrance length of fully developed turbulent channel flow, *15th Australiasian Fluid Mechanics Conference,* The University of Sydney, 13-17 December 2004.

Lim, K., Banerjee, S., 1992, On the condition of streak formation in a bounded turbulent flow, *Physics of Fluids A,* vol.4, No.2, pp 306-320.

Liu, Z., Adrian, R., Hanratty, T., 2001, Large-scale modes of turbulent channel flow: transport and structure, *Journal of Fluid Mechanics,* vol.448, pp 53-80.

Liu, B., Agarwal, J., 1974, Experimental observation of aerosol deposition in turbulent flow, *Journal of Aerosol Science,* vol.5, No.2, pp 145-155.

Ljus, C., Johansson, B., Almstedt, A., 2002, Turbulence modification by particles in a horizontal pipe flow, *International Journal of Multiphase Flow*, vol. 28, pp1075-1090.

Lohrmann, A., Cabrera, R., Nicholas, C., Kraus, M., 1994, Acoustic- Doppler Velocimeter (ADV) for laboratory use, *Fundamentals and Advancements in Hydraulic Measurement and Experimentation Proceedings,* Hydraulic Division/ASCE, August 1-5, 1994, New York.

Mathieu, J., Scott, J., 2000, *An introduction to Turbulent Flow*, Cambridge University Press, Cambridge.

McCoy, D., Hanratty, T., 1977, Rate of deposition of droplets in annular two-phase flow, *International Journal of Multiphase Flow,* vol.3, No.4, pp 319-331.

McIver, D., Blackburn, H., Nathan, G., 2000, Spectral element-Fourier method applied to simulation of turbulent pipe flow, *ANZIAM Journal,* vol.42, pp C954-C977.

Mei, C., Yuhi, M., 2001, Slow flow of a Bingham fluid in a shallow channel of finite width, *Journal of Fluid Mechanics,* vol.431, pp 135-159.

.

Metzger, T., 1998, *A little course in Rheology Part 1. Physica,* Messtechnik GmbH, Stuttgart, Germany.

Metzner, A.B., Reed, J.C., 1955, Flow of Non-Newtonian fluids- Correlation of the laminar, transition and turbulent flow regions, *American Inst. Chem Eng J,* vol.1, pp 434-440.

Mishra, P., Tripathi, G., 1971, Transition from laminar to turbulent flow of purely viscous non-Newtonian fluids in tubes, *Chemical Engineering Science,* vol.26, pp 915-921.

Moser, R., Kim, J., Mansour, N., 1999, Direct numerical simulation of turbulent channel flow up to $Re\tau$ =590, *Physics of Fluids,* vol.111, No.4, pp 943-945.

Muste, M., Patel, V., 1997, Velocity profiles for particles and liquid in open channel flow with suspended sediment, *Journal of Hydraulic Engineering,* vol.123, No.9, pp 742-751.

Narayanan, C., Lakehal, D., 2003, Mechanisms of particle deposition in a fully developed turbulent open channel flow, *Physics of Fluids,* vol.15, No.3, pp 763-775.

Nezu, I., 2005, Open-Channel flow turbulence and its research prospect in the 21st century, *Journal of Hydraulic Engineering,* vol.131, No.4, pp229-246.

Nezu, I., Azuma, R., 2004, Turbulence characteristic and interaction between particles and fluid in particle-laden open channel flow, *Journal of Hydraulic Engineering,* October, 2004.

Nezu, I., Nagakawa, H., 1993, *Turbulence in Open Channel Flows,* IAHR AIRH, Netherlands.

Nezu, I., Rodi, W,. 1985, Experimental study on secondary currents in open channel flow, *21st IAHR congress*, Melbourne, Australia, pp114-119.

Nikuradse, J., 1932, Gesetzmassigkeiten der turbulenten stromung in glatten rohren, *Forschung auf dem Gebiet de Ingenieurwesens,* vol.3, pp 1-36, (Translated in NASA TTF-10, 359, 1966).

Nortek AS, 2004*, Vectrino Velocimeter user guide*, Nortek AS, Vangkriken, Norway.

Oertel, H.(eds), 2004, *Prandtl's essentials of fluid mechanics,* Sprinder Verlag New York, United States of America.

Orszag, S., Kells, L., 1980, Transition to turbulence in plane Poiseuille and plane Couette flow, *Journal of Fluid Mechanics,* vol.96, pp 159-205.

Orszag, S., Patterson, G., 1972, Numerical simulation of three-dimensional homogeneous isotropic turbulence, *Phys.Rev.Lett.,*vol.28, pp 76-79.

Owen, P., 1969, Pneumatic transport, *Journal of Fluid Mechanics,* vol.39, No.2, pp 407-432.

Pan, Y., Banerjee, S., 1996, Numerical simulation of particle interactions with wall turbulence, *Physics and Fluids,* vol.8, No.10, pp 2733-2755.

Pedinotti, S., Mariotti, G., Banerjee, S., 1992, Direct numerical simulation of particle behaviour in the wall region of turbulent flows in horizontal channels, *Int.J.Multiphase Flow,* vol.18, No.6, pp 927-941.

Rajagopalan, S., Antonia, R., 1982, Use of a quadrant analysis technique to identify coherent structures in a turbulent boundary layer, *Physics of Fluids,* vol.25, No.6, pp 949-956.

Rajitha, P., Chharbra, R., Sabiri, N., Comiti, J., 2006, Drag on non-spherical particles in power law non-Newtonian media, *International Journal of Miner. Process,* vol.78, pp 110-121.

Rashidi, D., Banerjee, S., 1988, Turbulence structure in free-surface channel flows, *Physics of Fluids,* vol.31, pp 2491-2503.

Rashidi, D., Hetsroni, G., Banerjee, S., 1990, Particle-Turbulence interaction in a boundary layer, *Int. J. Multiphase Flow*, vol.16, No.6, pp 935-949.

Righetti, M., Romano, G., 2004, Particle-fluid interactions in a plane near-wall turbulent flow, *Journal of Fluid Mechanics,* vol.5, pp 93-121

Robinson, S., 1991, Coherent motions in the turbulent boundary layer, *Annu.Rev.Fluid Mech.* vol.23, pp 601-639.

Rodi, W., 2006, DNS and LES of come engineering flows, *Fluid Dynamics Research,* vol.38, pp 145-173.

Roger, C., Eaton, J., 1991, The effect of small particles on fluid turbulence in a flat-plate, turbulent boundary layer in air, *Physics of Fluids A,* vol.3, pp 928-937.

Rouson, D., Eaton, J., 2001, On the preferential concentration of solid particles in turbulent channel flow, *Journal of Fluid Mechanics,* vol.428, pp 149-169.

Rudman, M., Blackburn, H., 1999, Large eddy simulation of turbulent pipe low, *Second International Conference on CFD in the Minerals and Process Industries,* pp 503-508.

Rudman, M., Blackburn, H.M., 2003, The effect of shear thinning behaviour on turbulent pipe flow, *Third International Conference on CFD in the Minerals and Process Industries*, CSIRO, Melbourne, Australia.

Rudman, M., Blackburn, H.M., 2006, Direct numerical simulation of turbulent non-Newtonian flow using a spectral element method, *Applied Mathematical Modelling*, vol.30, pp 1229-1248.

Rudman, M., Blackburn, H,M., Graham, L, J., Pullum, L., 2001, Weakly turbulent pipe flow of a Power law fluid*, 14th Australiasian Fluid Mechanics Conference*, Adelaide, Australia.

Rudman, M., Blackburn, H,M., Graham, L, J., Pullum, L., 2004, Turbulent pipe flow of shear-thinning fluids, *J. Non-Newtonian Fluid Mech*, vol.118, pp 33-48.

Sarimeseli, A., 2002, Sedimentation of particles in developed turbulent flow in rough pipes, *Powder Technology,* vol.127, pp 144-148.

Schaflinger, U., Acrivos, A., Zheng, K., 1995, Viscous resuspension of a sediment within a laminar and stratified flow, *International Journal of Multiphase Flow,* vol.16, No.4, pp 567-578.

Shah, S., El Fadili, Y., Chhabra, R., 2007, New model for single spherical particle settling velocity in power law (visco-inelastic) fluids, *International Jounral of Multiphase Flow,* vol.33, pp 51-66.

Shan, H., Ma, B., Zhang, Z., Nieuwstadt, F., 1999, Direct numerical simulation of a puff and a slug in transitional cylindrical pipe flow, *Journal of Fluid Mechanics,* vol.387, pp 39-60.

Sharma, G., Phares, D., 2006, Turbulent transport of particles in a straight square, *International Journal of Multiphase Flow,* vol.32, pp 823-837.

Shenoy, A., Mashelkar, R., 1983, Engieering estimate of hydrodynamic entrance lengths in non-Newtonian turbulent flow, *Ind. Eng. Chem. Process Des. Dev,* vol.22, pp 165-168.

Shvidchenko, A., Pender, G., 2001, Macroturbulent structure of open-channel flow over gravel beds, *Water Resources Research,* vol.37, No.3, pp 709-719.

Slatter, P., 1995. *Transitional and turbulent flow of non-Newtonian slurries in pipes,* phD thesis, University of Cape Town.

Smagorinsky, J., 1965, Numerical simulation of the atmosphere's general circulation, *Large-scale problem in physics,* IBM scientific computing symposium, Yorktwon Heights, New York, pp 141-144.

Sreenivas, K., No Date, *Free shear flows,* Engineering Mechanics Unit, JNCASR Bangalore.

Stevenson, P., Thorpe, R., Davidson, J., 2002, Incipient motion of a small particle in the viscous boundary layer at a pipe wall, *Chemical Engineering Science,* vol.57, pp 4505-4520.

Straub, L.G., Silberman, E., Nelson, H., 1958, Open channel flow at small Reynolds numbers, *Trans ASCE,* vol.123, pp 685-714.

Sumer, M., Deigaard, R., 1981, Particle motions near the bottom in turbulent flow in an open channel. Part 2, *Journal of Fluid Mechanics,* vol.109, pp 311-337.

Sumer, M., Oguz, B., 1978, Particle motions near the bottom in turbulent flow in an open channel, *Journal of Fluid Mechanics,* vol.86, pp 109-127.

Sureshkumar, R., Beris, A., Handler, R., 1997, Direct numerical simulation of the turbulent channel flow of a polymer solution, *American Institute of Physics,* vol.9, pp 743-755.

Tsukahara, T., Seki, Y., Kawamura, H., 2005, DNS of turbulent channel flow at very low Reynolds numbers, *Thermal Science and Engineering,* vol.13, No.4, pp 81-86.

Van Driest, E., 1955, On turbulent flow near a wall, *Journal of the Aeronautical Sciences,* vol.23, No.11, pp 1007-1011.

Van Rijn, L., 1984, Sediment transport, Part II: suspended load transport, *Journal of Hydraulic Engineering,* vol.110, No.11, pp 1613-1641.

VPAC, 2010, *Tango Specification,* viewed 16 March 2010, http://www.vpac.org/services/supercomputers/tango.

Verbanck, M., 2000, Computing near-bed solids transport in sewers and similar sediment-carrying open channel flows, *Urban Water,* vol.2, pp277-284.

Wallace, J., Eckelmann, H., Brodkey, R., 1972, The wall region in turbulent shear flow, *Journal of Fluid Mechanics,* vol.54, Part 1, pp 39-48.

Wallingford, H., Barr, D., 1994, *Tables for the hydraulic design of pipes, sewers and channels, volume 2,* Thomas Telford publishing, London.

Wang, Z,Y., Plate, E,J., 1996, A preliminary study on the turbulence structure of flows of non-Newtonian fluid, *Journal of Hydraulic Research,* vol.34, No.3.

Wasp, E., Kenney, J., Gandhi, R., 1977, *Solid-liquid flow slurry pipeline transportation,* Trans Tech Publications, Germany.

Willmarth, W., Lu, S., 1972, Structure of the Reynolds stress near the wall, *Journal of Fluid Mechanics*, vol.55, pp 65-92.

Wilson, K., 1988, *Slurry transport in flumes,* Slurry handling design of solid-liquid systems, Brown, N., and Heywood, N., (eds), Elsevier, London, pp167-179.

Winterwerp, J., de Groot, M., Mastbergen, D., Verwoert, H., 1990, Hyperconcentrated sand-water mixture flows over flat bed, *Journal of Hydraulic Engineering,* vol.116, pp36-54.

Wu, W., Rodi, W., Wenka, T., 2000, 3D Numerical modelling of flow and sediment transport in open channels, *Journal of Hydraulic Engineering,* vol.126, No.1, pp 4-15.

Wygnanski, I., Champagne, F., 1973, On transition in a pipe. Part 1. The origin of puffs and slugs and the flow in a turbulent slug, *Journal of Fluid Mechanics.*, vol.59, pp 281-335.

Yalin, M.S., 1977, *Mechanics of Sediment Transport,* Pergamon Press, Great Britain.

Yang, S.Q., 2009, Mechanism for initiating secondary currents in channel flows, *Can.Journal.Civ.Engieering,* vol.36, pp 1506-1516.

Yang, S.Q., Tan, S.K., Lim, S.Y., 2004, Velocity distribution and dip-phenomenon in smooth uniform open channel flows, *Journal of Hydraulic Engineering,* vol.130, No.12, pp 1179-1186.

Yao, J., Fairweather, M., 2009, Mechanisms of inertial particle re-suspension in a turbulent square duct flow, *Turbulence, Heat and Mass Transfer,* vol.6, pp 1-12.

Zanoun, E., Durst, F., 2003, Evaluating the law of the wall in two-dimensional fully developed turbulent channel flows, *Physics of Fluids,* vol.15, No.10, pp 3079-3089.

Appendix A Highett experimental data

This appendix contains the detailed log of measurements made during Highett experiment. Statistical analysis for this set of data is also presented in this appendix.

Date	04/05/2010					
					slope	
Name	Depth (cm)	Nominal velocity (m/s)	Temp(°C)	Flow rate (L/s)	2.23%	
110620	4.5	1.2	18.1	8.22		
110759	4.4	1.8		8.23		
110945	4.5	2.4	18.27	8.24		
111207	4.8	1.2	18.27	8.22		
111349	4.8	1.8		8.17		
111523	4.8	2.4		8.18		
111722	5	1.2		8.22		
111845	5.1	1.8		8.23		
112040	4.9	2.4	18.61	8.47		
112225	5.4	1.2	18.44	8.16		
112420	5.4	1.8		8.26		
112615	5.3	2.4	18.61	8.26		
112828	5.9	1.2	18.44	8.19		
112955	5.9	1.8	18.61	8.31		
113118	5.7	2.4		8.3		
113319	6	1.2	18.78	8.58		
113513	6.1	1.8	18.61	8.46		
113704	6	2.4		8.41		
113847	6.3	1.2		8.67		
114035	6.9	1.8	18.78	8.93		
114223	6.9	2.4		8.5		
114449	6.8	1.2	18.78	8.47		
114629	6.8	1.8		8.68		
114752	7.5	2.4		8.85	Entry	Exit
					4.4	4
114943	8	1.2	18.78	8.89		
115123	7.1	1.8		8.73		
115331	8.1	2.4	18.96	8.85		
115619	5.3	1.2	18.96	8.33		
115744	5.2	1.8		8.39		
115925	4.7	2.4		8.35		

120110	5.1	1.2	19.13	8.57
120314	5.2	1.8		8.15
120452	5.2	2.4		8.3
120658	5.5	1.2	19.13	8.36
120845	5.5	1.8		8.27
121013	5.5	2.4	19.3	8.56
121340	5.9	1.2	19.3	8.61
121522	5.8	1.8		8.4
121645	5.8	2.4		8.33
121826	6.1	1.2	19.3	8.66
121951	6.1	1.8		8.45
122116	6.1	2.4		8.4
122330	6.3	1.2	19.3	8.84
122455	6.3	1.8		8.63
122624	6.4	2.4		8.8
122844	6.6	1.2	19.3	8.69
123003	6.5	1.8		8.75
123127	6.6	2.4	19.47	8.76
123442	6.3	1.2	19.47	8.76
123603	6.3	1.8		9.12
123733	6.7	2.4		8.9
133714	4.5	1.2	19.47	8.1
134010	4.4	1.8		8.24
134218	4.4	2.4		8.46
134405	4.6	1.2	19.47	8.27
131531	4.7	1.8	19.64	8.34
134656	4.6	2.4		8.33
134908	5	1.2	19.64	8.16
135047	5	1.8		8.33
135323	5	2.4		8.38
135542	5.2	1.2	19.81	8.39
140154	5.1	1.8	19.81	8.25
140350	5.1	2.4		8.42
140611	5.3	1.2	19.81	8.25
140802	5.3	1.8		8.5
140943	5.3	2.4	19.99	8.39
141159	5.5	1.2	19.81	8.62
141343	5.6	1.8		8.51
141505	5.6	2.4		8.64
141712	5.8	1.2	19.99	8.67

Entry	Exit
4.3	3.8
Slope	
4.70%	

141850	5.7	1.8		8.57	Entry	Exit	
142023	5.5	2.4		8.71	4.5		5.5
143647	4.6	1.2	20.33	8.48			5.3
143811	4.6	1.8		8.5			
143942	4.6	2.4	20.16	8.56			
144156	4.9	1.2	20.33	8.43			
144428	4.9	1.8	20.5	8.39			
144602	4.8	2.4		8.43			
144758	5.2	1.2	20.33	8.5			
144957	5.2	1.8	20.5	8.33			
145125	5.1	2.4		8.51			
145319	5.4	1.2	20.5	8.5			
145441	5.4	1.8		8.49			
145602	5.4	2.4		8.62			

Date 07/05/2010

Name	depth (cm)	Nominal velocity (m/s)	Temp (°C)	Flow rate (L/s)	slope 5.70%	
102746	4.9	1.2	16.91	7.44		
102910	4.8	1.8	17.08	7.5	Entry	Exit
103035	4.8	2.4	16.91	7.55	5.4	4.4
103806	4.9	1.2	17.08	8.42		
104005	4.9	1.8		8.5		
105501	5	2.4		8.39		
105643	4.8	1.2	17.25	8.55		
105946	4.9	1.8		8.57		
110125	5	2.4		8.74		
110320	5.3	1.2	17.25	8.74		
110445	5.3	1.8		8.74		
110621	5.4	2.4	17.42	8.77		
111439	5.7	1.2	17.42	9.09		
111608	5.7	1.8		9.12		
111755	5.7	2.4		8.62		
					slope	
112449	5.7	1.2	17.59	8.78	4.70%	
112716	5.7	1.8		8.87		
112841	5.7	2.4	17.76	8.8		
113103	5.4	1.2	17.76	8.4		
113288	5.3	1.8		8.45		
113421	5.3	2.4		8.51		
113841	5	1.2	17.93	8.59		
114031	5	1.8	17.76	8.57		
114151	5	2.4		8.55		
114827	4.7	1.2	17.93	8.4		
114952	4.7	1.8		8.45		
115105	4.7	2.4		8.4		

Date 11/05/2010

Name	depth (cm)	Nominal velocity (m/s)	Temp (°C)	Flow rate (L/s)
103938	5.1	1.2	17.08	8.79
104111	5	1.8		8.65
104251	5.2	2.4		8.85
104458	5.4	1.2	17.08	8.74
104640	5.4	1.8		8.66
104821	5.4	2.4		8.85
105406	5.7	1.2	17.08	8.7
105547	5.6	1.8		8.75
105808	5.7	2.4		8.72
110143	5.9	1.2	17.08	8.95
110513	5.9	1.8		8.8
110642	6	2.4	17.25	8.89
111110	5.9	1.2	17.25	8.85
111249	5.9	1.8		8.83
111414	5.9	2.4		9.08
111614	5.7	1.2	17.25	8.85
111937	5.7	1.8		8.91
112111	5.6	2.4	17.42	8.66
112300	5.4	1.2	17.42	8.82
112424	5.5	1.8		8.73
112524	5.4	2.4		8.99
132915	5.2	1.2	17.08	8.67
133042	5.2	1.8		8.8
133219	5.3	2.4		8.62
133429	5.7	1.2	17.08	8.66
133558	5.7	1.8		8.77
133727	5.7	2.4		8.95
133912	6	1.2	17.08	8.79
134058	6	1.8		8.93
134224	6	2.4		8.76
134335	5.9	1.2	17.08	8.86
134528	6	1.8		8.77
134710	6	2.4		8.81
134857	5.7	1.2	17.08	8.89
135033	5.7	1.8		8.74
135207	5.8	2.4	17.25	8.65

slope 4.70%

Entry	Exit
4.8	4.3

135343	5.5	1.2	17.25	8.84
135513	5.5	1.8		8.8
135630	5.5	2.4		8.76
135809	5.3	1.2	17.25	8.8
135927	5.3	1.8		8.83
140055	5.3	2.4		8.76
140541	5.4	1.2	17.25	8.97
140659	5.4	1.8		8.82
140908	5.5	2.4		8.75
141101	5.7	1.2	17.42	8.73
141250	5.7	1.8		8.75
141408	5.7	2.4		8.71
141602	5.9	1.2	17.25	8.99
141728	5.9	1.8		8.86
141851	5.9	2.4		8.96
142110	6	1.2	17.25	9
142323	6.1	1.8		8.92
142456	6	2.4		8.86
142757	6.1	1.2	17.42	8.85
143318	5.8	1.8		8.77
143519	5.8	2.4		8.7
143700	5.6	1.2	17.42	8.85
143828	5.5	1.8		8.81
144007	5.6	2.4		8.74
144145	5.4	1.2	17.42	8.83
144312	5.3	1.8		8.73

Date 14/05/2010

Name	depth (cm)	Nominal velocity (m/s)	Temp (°C)	Flow rate (L/s)	slope 4.70%	
115717	5.9	1.2	16.4	8.89		
115932	5.9	1.8		8.86	Entry	Exit
120153	5.9	2.4		8.84	6.8	6.3
133644	5.5	1.2	16.4	8.69		
134134	5.5	1.8		8.67		
134456		2.4	16.57	8.65		
134625	5.5	1.2	16.57	8.61		
134759	5.5	1.8		8.6		
134935	5.5	2.4		8.59		
135121	5.8	1.2	16.57	8.59		
135257	5.8	1.8		8.56		
135436	5.8	2.4		8.6		
135612	5.9	1.2	16.57	8.58		
135746	5.8	1.8		8.57		
135914	5.9	2.4		8.59		
140209	6	1.2	16.57	8.58		
141922	6.1	1.8		9.2		
142059	6.1	2.4		8.8		
142223	6	1.2	16.57	8.83		
142408	6	1.8		8.85		
142534	6	2.4		8.85		
142730	5.9	1.2	16.74	8.84		
142850	5.9	1.8		8.84		
143017	5.9	2.4		8.85		

Date 17/05/2010

Name	depth (cm)	Nominal velocity (m/s)	Temp (°C)	Flow rate (L/s)	slope 4.70%	
113905	5.9	1.2	15.21	8.47		
114036	5.9	1.8		8.44	Entry	Exit
114219	5.9	2.4	15.38	8.44	6.1	5.1
114353	6	1.2	15.38	8.45		
114525	5.9	1.8		8.45		
114659	5.9	2.4		8.47		
114845	5.7	1.2	15.38	8.44		
115039	5.7	1.8		8.45		
115222	5.7	2.4		8.45		
115408	5.4	1.2	15.38	8.47		
115531	5.4	1.8		8.49		
115722	5.5	2.4		8.46		
115900	5.1	1.2	15.38	8.45		
120027	5.2	1.8		8.4		
120219	5.2	2.4		8.45		
120708	5.2	1.2	15.38	8.44		
120830	5.2	1.8		8.27		
120956	5.2	2.4		8.48		
121134	5.4	1.2	15.38	8.49		
121301	5.6	1.8		8.47		
121428	5.5	2.4		8.45		
121608	5.8	1.2	15.38	8.47		
121755	6	1.8		8.45		
121914	5.8	2.4		8.46		
133428	5.8	1.2	15.38	8.46		
133548	5.8	1.8		8.45		
133726	5.9	2.4		8.53		
133901	5.4	1.2	15.38	8.56		
134042	5.4	1.8		8.51		
134225	5.5	2.4		8.53		
134421	5.3	1.2	15.38	8.52		
134549	5.2	1.8	15.55	8.53		
134716	5.3	2.4		8.53		
134900	5	1.2	15.55	8.42		
135030	5	1.8		8.45		
135207	5	2.4		8.43		
135353	4.7	1.2	15.55	8.2		

135515	4.7	1.8		8.2
135640	4.7	2.4		8.4
135930	5	1.2	15.55	8.42
140118	5	1.8		8.53
140239	5	2.4		8.42
140419	5.2	1.2	15.55	8.66
140543	5.3	1.8		8.7
140704	5.2	2.4		8.77
141028	5.5	1.2	15.55	8.8
141157	5.5	1.8		8.82
141334	5.5	2.4		8.84
144622	5.7	1.2	15.55	8.69
144803	5.7	1.8		8.84
145044	5.7	2.4	15.55	8.81
145243	6.2	1.2	15.55	8.85
145500	6.2	1.8		8.85
145623	6.1	2.4		8.82
145755	5.6	1.2	15.72	8.83
145926	5.5	1.8		8.83
150048	5.6	2.4		8.84
150223	5.3	1.2	15.72	8.64
150403	5.3	1.8		8.74
150528	5.3	2.4		8.66
150712	5.1	1.2	15.72	8.42
150851	5.1	1.8		8.45
151030	5	2.4		8.43
				side 1
151509	4.9	1.2	15.72	8.41
151634	5	1.8		8.25
151800	4.9	2.4		8.46
151934	5.2	1.2	15.72	8.5
152102	5.2	1.8		8.56
152305	5.2	2.4		8.55
153214	5.4	1.2	15.72	8.44
153336	5.5	1.8		8.46
153453	5.4	2.4		8.56
153633	5.6	1.2	15.72	8.57
153756	5.5	1.8		8.58
153928	5.6	2.4		8.57
154058	5.6	1.2	15.72	8.59
154234	5.5	1.8		8.6

Date 18/05/2010

Name	depth (cm)	Nominal velocity (m/s)	Temp (°C)	Flow rate (L/s)	slope 4.70%	
101003	4.6	1.2	15.04	8.12		
101130	4.6	1.8		8.13		
101258	4.7	2.4		8.15		
101557	4.9	1.2	15.04	8.17		
101718	4.9	1.8		8.2		
101837	4.9	2.4		8.28		
105038	5.4	1.2	15.04	8.79		
102219	5.4	1.8		8.78		
102338	5.5	2.4		8.74		
102524	5.7	1.2	15.04	8.75		
102654	5.6	1.8		8.77		
102814	5.7	2.4		8.77		
102949	6	1.2	15.04	8.77		
103140	6	1.8		8.81		
103304	5.9	2.4		8.83		
103434	5.9	1.2	15.04	8.83		
103603	5.8	1.8		8.85		
103721	5.9	2.4		8.85		
104006	4.7	1.2	15.04	10.06	Entry	Exit
104150	4.6	1.8		10.02	7.5	7
104308	4.7	2.4		10.17		
104449	4.9	1.2	15.04	10.14		
104620	5	1.8		10.11		
104807	4.9	2.4		10.12		
105024	5.2	1.2	15.04	10.12		
105159	5.1	1.8		10.14		
105309	5.1	2.4		10.05		
105442	5.5	1.2	15.04	10.01		
105554	5.5	1.8		9.9		
105716	5.5	2.4		10		
105843	5.8	1.2	15.04	10.45		
110003	5.9	1.8	15.21	10.25		
110155	5.8	2.4		10.14		
110435	6.1	1.2	15.21	10.33		
110558	6.2	1.8		10.24		
110719	6.2	2.4		10.29		

110435	6.1	1.2	15.21	10.33			
110558	6.2	1.8		10.24			
110719	6.2	2.4		10.29			
110851	6.5	1.2	15.21	10.71			
111007	6.5	1.8		10.25			
111153	6.6	2.4		10.38			
114042	4.7	1.2	15.21	7.5	Entry	Exit	
114221	4.7	1.8		7.55	6	5.5	
114336	4.5	2.4		7.64			
114500	4.9	1.2	15.21	7.92			
114704	4.9	1.8		7.78			
114824	5	2.4		7.82			
115006	5.3	1.2	15.21	7.82			
115122	5.4	1.8		7.82			
115234	5.3	2.4		7.82			
115414	5.9	1.2	15.21	7.84			
115524	5.9	1.8		7.83			
		2.4					
115818	6.4	1.2	15.21	10.3			
115945	6.4	1.8		10.3			
120103	6.5	2.4		10.32			
120241	6.1	1.2	15.21	10.15			
120402	6	1.8		10.15			
120532	6	2.4		10.49			
120654	5.7	1.2	15.21	9.91			
120813	5.6	1.8	15.38	10.16			
120941	5.7	2.4		10.35			
121225	5.4	1.2	15.38	10.31			
121353	5.4	1.8		10.12			
121517	5.4	2.4		10.26			
121644	5.2	1.2	15.8	10.31			
121756	5.2	1.8		10.18			
121910	5.2	2.4		10.2			

Date 18/05/2010

Name	depth (cm)	Nominal velocity (m/s)	Temp (°C)	Flow rate (L/s)	slope 4.70%	
124533	5	1.2	14.7	8.39		
124718	4.9	1.8		8.48		
124909	5	2.4		8.48		
125108	5.3	1.2	14.7	8.52	Entry	Exit
125237	5.1	1.8		8.49	6.5	6
125413	5.3	2.4		8.52		
125612	5.4	1.2	14.7	8.52		
125738	5.3	1.8		8.51		
125913	5.3	2.4		8.54		
130100	5.8	1.2	14.7	8.5		
130324	5.8	1.8		8.48		
130449	5.8	2.4		8.51		
130657	6.1	1.2	14.7	8.52		
130839	6	1.8		8.51		
133411	6.2	2.4		8.22		
133707	6.2	1.2	14.7	8.43		
133833	6	1.8		8.43		
133955	6.2	2.4		8.45		
134221	5.7	1.2	14.7	8.57		
134356	5.7	1.8	14.87	8.58		
134514	5.7	2.4		8.56		
134715	5.4	1.2	14.87	8.56		
134847	5.4	1.8		8.57		
135009	5.4	2.4		8.61		
135245	5.1	1.2	14.87	8.41		
135405	5	1.8		8.41		
135535	4.9	2.4		8.34		
135757	5	1.2	14.87	7.5	Entry	Exit
135940	5.1	1.8		7.5	6	5.5
140101	5	2.4		7.48		
140304	5.2	1.2	14.87	7.51		
140428	5.3	1.8		7.51		
140542	5.2	2.4		7.5		
140740	5.5	1.2	14.87	7.5		
140913	5.6	1.8		7.4		
141045	5.6	2.4		7.45		
141238	5.9	1.2	14.87	7.53		

141404	5.7	1.8		7.5		
141526	5.9	2.4		7.54		
141646	5.6	1.2	14.87	7.49		
141807	5.6	1.8		7.51		
141928	5.7	2.4		7.53		
143049	5.4	1.2	15.04	7.52		
143215	5.5	1.8		7.54		
144113	5.5	2.4		7.51		
144302	5	1.2	15.04	7.51		
144423	5	1.8		7.5		
144544	5	2.4		7.52		
144936	5	1.2	15.04	10.63	Entry	Exit
145103	5	1.8		10.35	7.5	8
145221	5	2.4		10.21		
145358	5.3	1.2	15.04	10.16		
145532	5.3	1.8		10.55		
145654	5.3	2.4		10.5		
145848	5.7	1.2	15.04	10.51		
150007	5.6	1.8		10.33		
150131	5.6	2.4		10.7		
150320	6.3	1.2	15.04	10.71		
150432	6.4	1.8		10.65		
150541	6.1	2.4		10.74		
150726	6.6	1.2	15.04	10.74		
150842	6.5	1.8		10.74		
151007	6.5	2.4		10.74		

Date 28/05/2010

Name	depth (cm)	Nominal velocity (m/s)	Temp (°C)	Flow rate (L/s)	slope 4.70%	
105540	5	1.2	15.89	8.52		
105657	5	1.8		8.53	Entry	Exit
105815	5	2.4		8.47	6.5	6
110022	5.3	1.2	15.89	8.49		
110156	5.2	1.8		8.45		
110315	5.2	2.4		8.44		
110455	5.5	1.2	15.89	8.46		
110623	5.5	1.8		8.47		
110747	5.5	2.4		8.5		
112939	5.8	1.2	15.89	8.65		
113105	5.8	1.8		8.5		
113222	5.8	2.4		8.62		
115558	5.4	1.2	16.06	8.63		
115720	5.4	1.8		8.63		
115855	5.4	2.4		8.65		
120034	5.1	1.2	16.06	8.62		
120202	5.1	1.8		8.62		
120329	5.1	2.4		8.61		
120505	4.8	1.2	16.23	8.74		
120622	4.8	1.8		8.75		
120753	4.8	2.4		8.75		
120937	5	1.2	16.23	8.73		
121102	5	1.8		8.74		
121225	4.9	2.4		8.73		
121414	5.3	1.2	16.23	8.76		
121545	5.4	1.8		8.75		
121713	5.4	2.4		8.76		
122240	4.9	1.2	16.23	8.67	side1	
122407	4.7	1.8		8.75		
122554	4.5	2.4		8.76		
122733	4.5	1.2	16.23	8.76		
122851	4.6	1.8		8.75		
123031	4.7	2.4		8.75		
123257	4.7	1.2	16.23	8.78		
123435	4.9	1.8	16.4	8.76		
123653	4.9	2.4		8.77		
123918	5	1.2	16.4	8.76		

124120	4.9	1.8		8.75	
124300	4.9	2.4		8.76	
124459	5.4	1.2	16.4	8.76	
124625	5.3	1.8		8.77	
124809	5.3	2.4		8.75	
125021	5.7	1.2	16.4	8.75	
125148	5.8	1.8		8.77	
125350	5.8	2.4		8.75	
125910	4.8	1.2	16.4	8.75	side2
130044	4.8	1.8		8.77	
130217	4.8	2.4		8.76	
130408	5.1	1.2	16.4	8.79	
130531	5.1	1.8		8.78	
130652	5.2	2.4		8.8	
130831	5.4	1.2	16.4	8.77	
130947	5.4	1.8		8.78	
131107	5.5	2.4		8.75	
131239	5.7	1.2	16.4	8.75	
131358	5.7	1.8		8.81	
131514	5.7	2.4		8.8	
131646	5.1	1.2	16.57	8.82	
131809	5.1	1.8		8.8	
131923	5.1	2.4		8.83	
132047	4.9	1.2	16.57	8.87	
132205	4.9	1.8		8.77	
132327	4.9	2.4		8.78	

Table 29 to Table 31 present three different flow measurements that were recorded in the first phase experiment. Each series of measurement was recorded for a different flow rate.

Table 29 Random error analysis on flow rate measured on 7/5/2010

Date	7/05/2010					
Name	depth (cm)	Nominal velocity (m/s)	Flow rate (L/s)		Mean	8.625833
103806	4.9	1.2	8.42		Standard deviation	0.207928
104005	4.9	1.8	8.5		Count	24
105501	5	2.4	8.39		Alpha	0.05
105643	4.8	1.2	8.55		Confidence level (95%)	0.083187
105946	4.9	1.8	8.57		CL/Mean	0.009644
110125	5	2.4	8.74			
110320	5.3	1.2	8.74			
110445	5.3	1.8	8.74			
110621	5.4	2.4	8.77			
111439	5.7	1.2	9.09			
111608	5.7	1.8	9.12			
111755	5.7	2.4	8.62			
112449	5.7	1.2	8.78			
112716	5.7	1.8	8.87			
112841	5.7	2.4	8.8			
113103	5.4	1.2	8.4			
113288	5.3	1.8	8.45			
113421	5.3	2.4	8.51			
113841	5	1.2	8.59			
114031	5	1.8	8.57			
114151	5	2.4	8.55			
114827	4.7	1.2	8.4			
114952	4.7	1.8	8.45			
115105	4.7	2.4	8.4			

Table 30 Random error analysis on flow rate measured on 18/5/2010

Date	18/05/2010					
Name	depth (cm)	Nominal velocity (m/s)	Flow rate (L/s)		Mean	7.502381
135757	5	1.2	7.5		Standard deviation	0.030968
135940	5.1	1.8	7.5		Count	21
140101	5	2.4	7.48		Alpha	0.05
140304	5.2	1.2	7.51		Confidence level (95%)	0.013245
140428	5.3	1.8	7.51		CL/Mean	0.001765
140542	5.2	2.4	7.5			
140740	5.5	1.2	7.5			
140913	5.6	1.8	7.4			
141045	5.6	2.4	7.45			
141238	5.9	1.2	7.53			
141404	5.7	1.8	7.5			
141526	5.9	2.4	7.54			
141646	5.6	1.2	7.49			
141807	5.6	1.8	7.51			
141928	5.7	2.4	7.53			
143049	5.4	1.2	7.52			
143215	5.5	1.8	7.54			
144113	5.5	2.4	7.51			
144302	5	1.2	7.51			
144423	5	1.8	7.5			
144544	5	2.4	7.52			

Table 31 Random error analysis on flow rate measured on 18/5/2010

Date	18/05/2010					
Name	depth (cm)	Nominal velocity (m/s)	Flow rate (L/s)		Mean	10.55067
144936	5	1.2	10.63		Standard deviation	0.201617
145103	5	1.8	10.35		Count	15
145221	5	2.4	10.21		Alpha	0.05
145358	5.3	1.2	10.16		Confidence level (95%)	0.102031
145532	5.3	1.8	10.55		CL/Mean	0.009671
145654	5.3	2.4	10.5			
145848	5.7	1.2	10.51			
150007	5.6	1.8	10.33			
150131	5.6	2.4	10.7			
150320	6.3	1.2	10.71			
150432	6.4	1.8	10.65			
150541	6.1	2.4	10.74			
150726	6.6	1.2	10.74			
150842	6.5	1.8	10.74			
151007	6.5	2.4	10.74			

Appendix B Tensor converting from Cartesian format to cylindrical format

If S is a tensor, with components

$$S \equiv \begin{bmatrix} S_{rr} & S_{r\theta} & S_{rz} \\ S_{\theta r} & S_{\theta\theta} & S_{\theta z} \\ S_{zr} & S_{z\theta} & S_{zz} \end{bmatrix} \equiv \begin{bmatrix} S_{xx} & S_{xy} & S_{xz} \\ S_{yx} & S_{yy} & S_{yz} \\ S_{zx} & S_{xy} & S_{zz} \end{bmatrix} \tag{86}$$

In the cylindrical-polar basis and the Cartesian basis respectively. These two sets of components are related by

$$\begin{bmatrix} S_{xx} & S_{xy} & S_{xz} \\ S_{yx} & S_{yy} & S_{yz} \\ S_{zx} & S_{xy} & S_{zz} \end{bmatrix} = \begin{bmatrix} \cos\theta & -\sin\theta & 0 \\ \sin\theta & \cos\theta & 0 \\ 0 & 0 & 1 \end{bmatrix} \begin{bmatrix} S_{rr} & S_{r\theta} & S_{rz} \\ S_{\theta r} & S_{\theta\theta} & S_{\theta z} \\ S_{zr} & S_{z\theta} & S_{zz} \end{bmatrix} \begin{bmatrix} \cos\theta & \sin\theta & 0 \\ -\sin\theta & \cos\theta & 0 \\ 0 & 0 & 1 \end{bmatrix} \tag{87}$$

$$\begin{bmatrix} S_{rr} & S_{r\theta} & S_{rz} \\ S_{\theta r} & S_{\theta\theta} & S_{\theta z} \\ S_{zr} & S_{z\theta} & S_{zz} \end{bmatrix} = \begin{bmatrix} \cos\theta & \sin\theta & 0 \\ -\sin\theta & \cos\theta & 0 \\ 0 & 0 & 1 \end{bmatrix} \begin{bmatrix} S_{xx} & S_{xy} & S_{xz} \\ S_{yx} & S_{yy} & S_{yz} \\ S_{zx} & S_{xy} & S_{zz} \end{bmatrix} \begin{bmatrix} \cos\theta & -\sin\theta & 0 \\ \sin\theta & \cos\theta & 0 \\ 0 & 0 & 1 \end{bmatrix} \tag{88}$$

The simulation produces results in Cartesian format, therefore all the components needs to be converted into cylindrical format for plotting purpose.

Appendix C Mesh spacing calculation

This is the sample calculation for mesh spacing.

$$z = \frac{L}{nz}$$

$$L = \frac{2\pi}{\beta}$$

$$\beta = 4$$

$$L = \frac{2\pi}{4}$$

$$nz = 384$$

$$\therefore z = \frac{\frac{2\pi}{4}}{384} = 0.004$$

$$\theta = \frac{C}{(15-1)*10(cells)} = \frac{R\theta}{140} = 0.0025$$

$$r = \frac{d}{np-1} = \frac{0.009}{14} = 0.00064$$

In term of wall unit

$$z^+ = (\frac{\rho U_z}{\eta w}) * z$$

$$= \frac{1600 * 0.079424}{0.01998} * 0.004 = 25.4$$

$$\theta^+ = 16$$

$$r^+ = 4.07$$

Appendix D Highett experimental rheological data and model fitting

This appendix contains all of the rheograms that were recorded for the tested fluids used in Highett experiments. The rheology testing was conducted at the same temperature that it was under the laboratory flume. Statistical analysis for this set of data is also presented in this appendix.

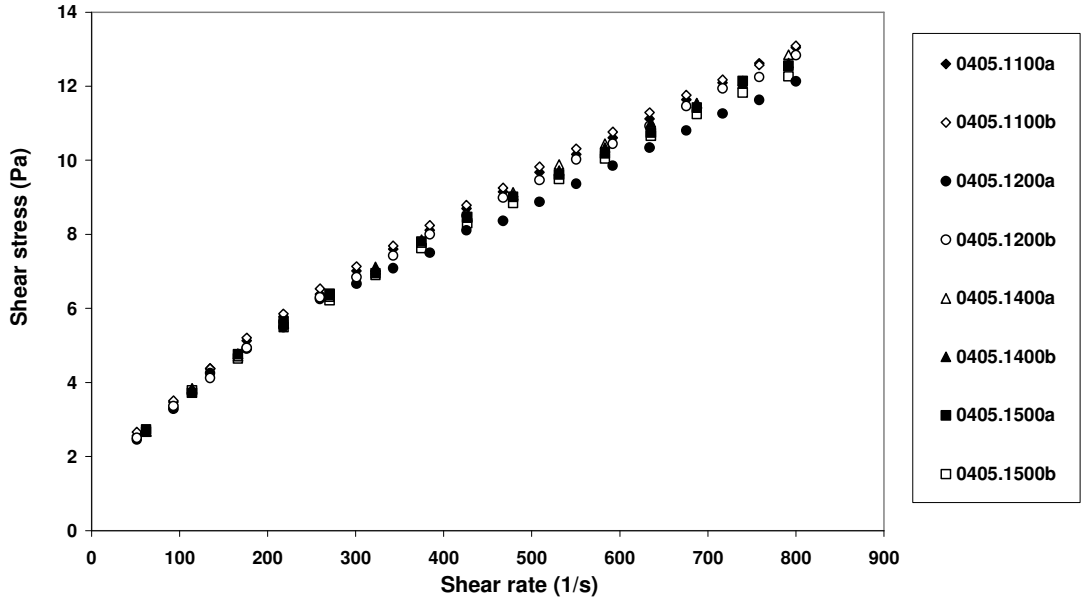

Appendix D 1 Rheograms for fluid 0405 from Highett experiment

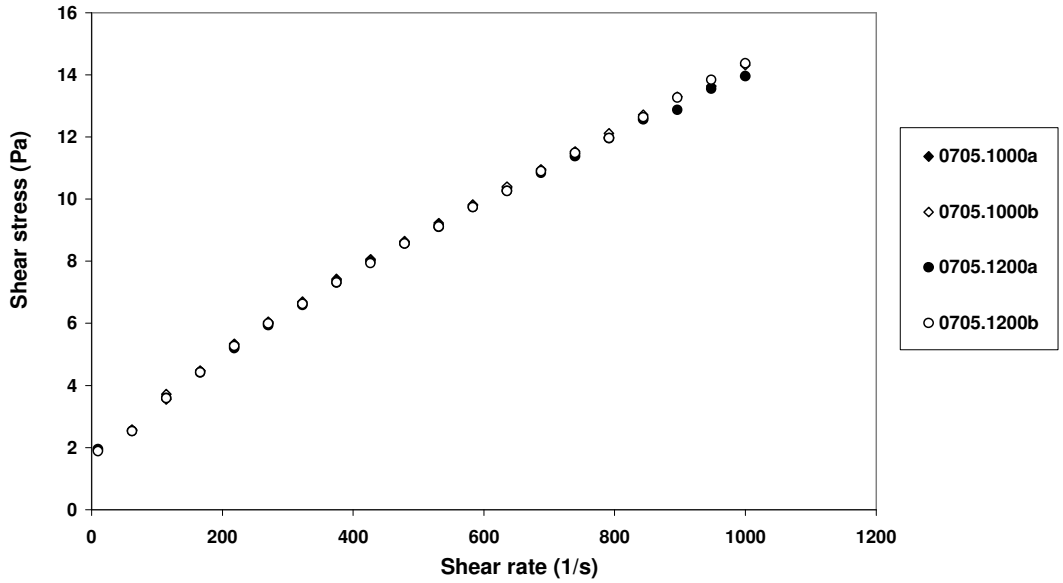

Appendix D 2 Rheograms for fluid 0705 from Highett experiment

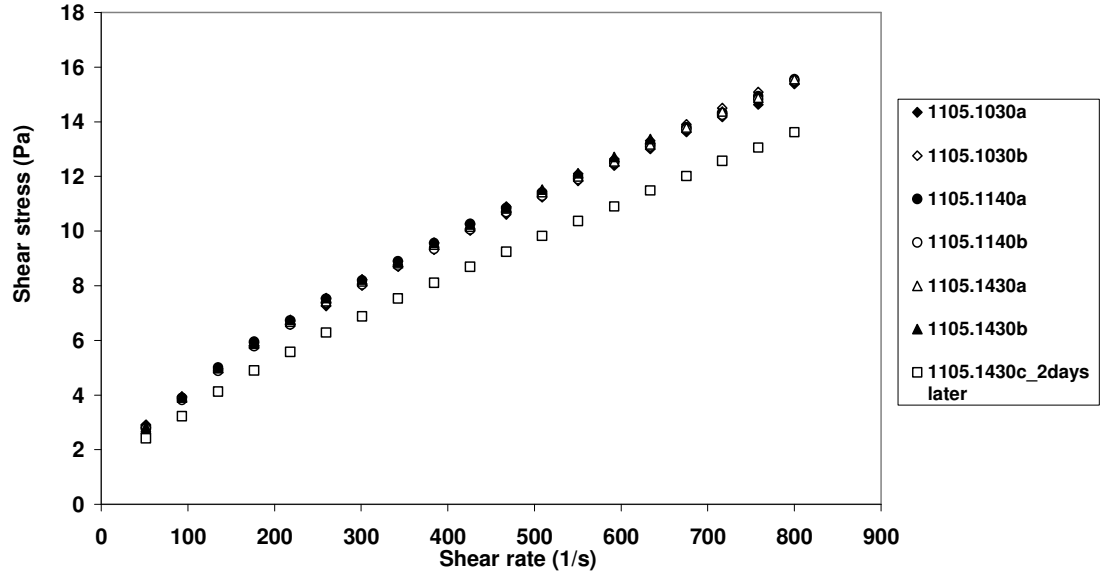

Appendix D 3 Rheograms for fluid 1105 from Highett experiment

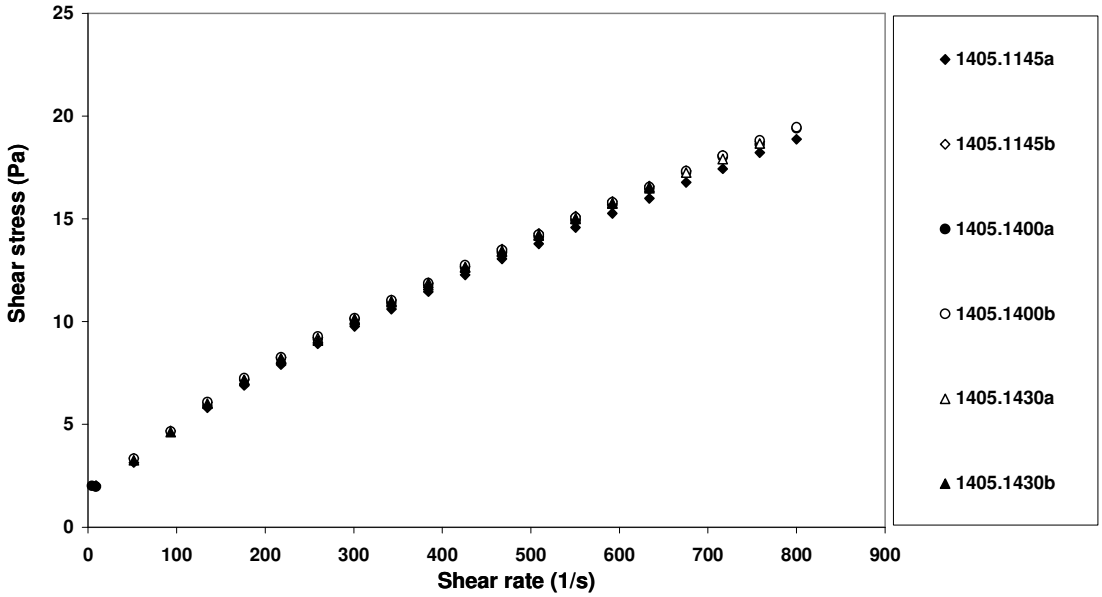

Appendix D 4 Rheograms for fluid 1405 from Highett experiment

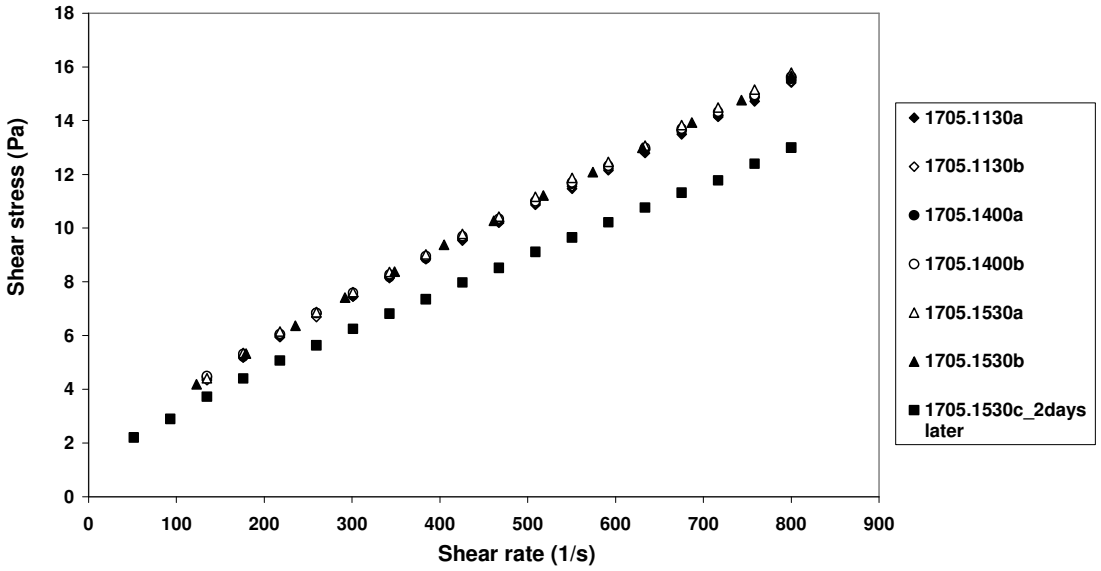

Appendix D 5 Rheograms for fluid 1705 from Highett experiment

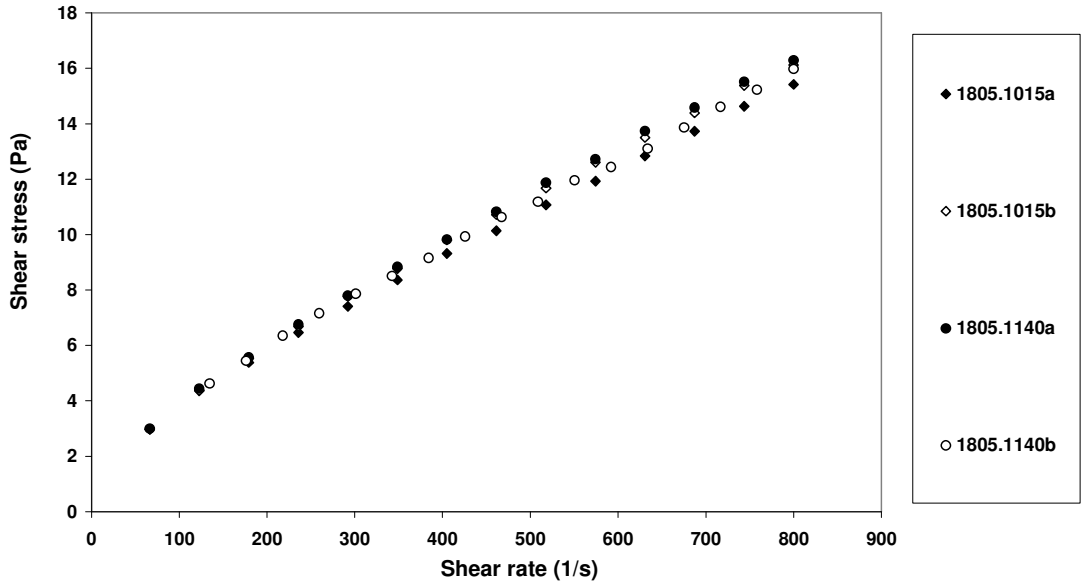

Appendix D 6 Rheograms for fluid 1805 from Highett experiment

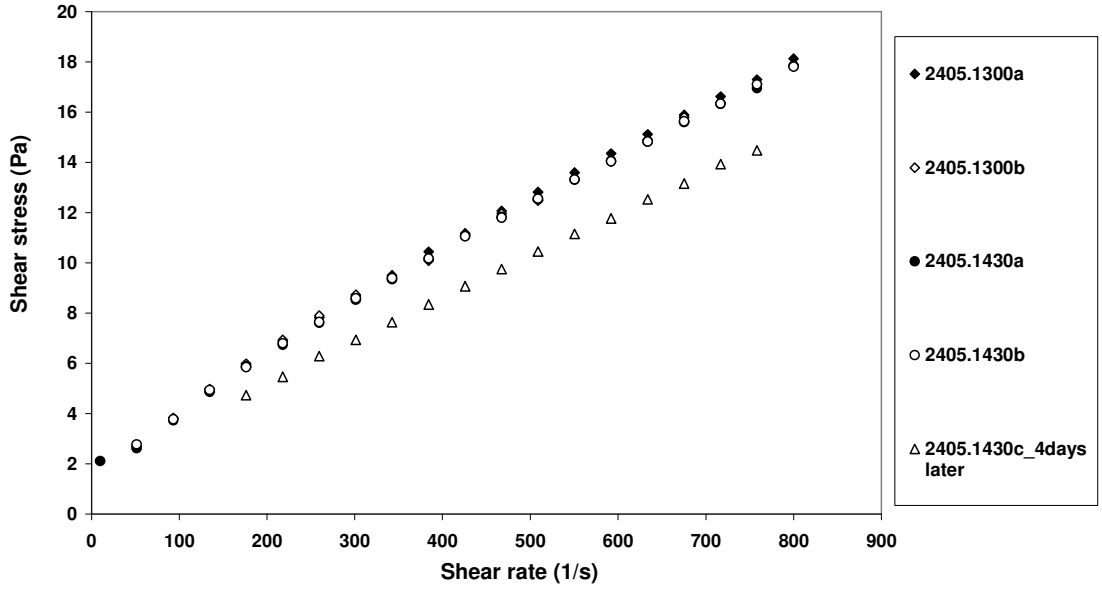

Appendix D 7 Rheograms for fluid 2405 from Highett experiment

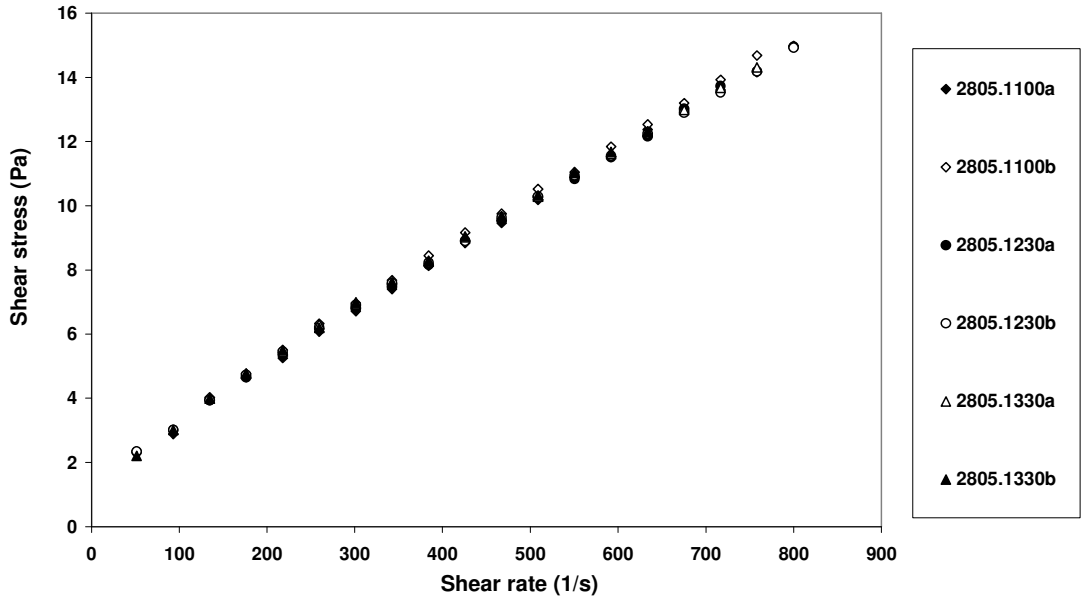

Appendix D 8 Rheograms for fluid 2805 from Highett experiment

Table 32 to Table 35 present rheological data that was measured by Rheosys Merlin II rheometer at RMIT University. Each sample was tested twice. The 95% confidence level is showed in each table.

Table 32 Rheological data for first phase experimental 0405.1100

	0405.1100a	0405.1100b			
Shear Rate (1/s)	Shear stress (Pa)	Shear stress (Pa)		Mean	3.489
0.985	2.009	2.059		Standard deviation	0.028284
51.552	2.569	2.66		Count	2
93.145	3.469	3.509		Alpha	0.05
134.737	4.379	4.375		95% CL	0.039199
176.329	5.128	5.204		CL/Mean	0.011235
217.921	5.781	5.852			
259.513	6.387	6.531			
301.105	7.008	7.131			
342.588	7.603	7.688			
384.18	8.11	8.245			
425.773	8.696	8.787			
467.365	9.147	9.252			
508.847	9.679	9.821			
550.44	10.161	10.309			
592.032	10.607	10.765			
633.733	11.123	11.288			
675.326	11.638	11.759			
716.808	12.093	12.175			
758.4	12.619	12.57			
799.993	13.048	13.088			

Table 33 Rheological data for first phase experimental 0405.1200

	0405.1200a	0405.1200b			
Shear Rate (1/s)	Shear stress (Pa)	Shear stress (Pa)		Mean	3.328
0.985	2	1.989		Standard deviation	0.056569
51.552	2.454	2.508		Count	2
93.145	3.288	3.368		Alpha	0.05
134.737	4.254	4.121		95% CL	0.078399
176.329	4.91	4.935		CL/Mean	0.023557
217.921	5.497	5.646			
259.513	6.253	6.299			
301.105	6.667	6.843			
342.588	7.086	7.426			
384.18	7.503	8.003			
425.773	8.105	8.507			
467.365	8.366	8.994			
508.847	8.879	9.466			
550.44	9.367	10.026			
592.032	9.855	10.446			
633.733	10.339	10.923			
675.326	10.802	11.463			
716.808	11.261	11.943			
758.4	11.63	12.247			
799.993	12.134	12.836			

Table 34 Rheological data for first phase experimental 0405.1400

	0405.1400a	0405.1400b			
Shear Rate (1/s)	Shear stress (Pa)	Shear stress (Pa)		Mean	3.8335
0.985	2.109	1.879		Standard deviation	0.000707
51.552	2.67	2.678		Count	2
93.145	3.834	3.833		Alpha	0.05
134.737	4.775	4.708		95% CL	0.00098
176.329	5.594	5.598		CL/Mean	0.000256
217.921	6.368	6.319			
259.513	7.121	7.056			
301.105	7.855	7.777			
342.588	8.491	8.45			
384.18	9.06	9.139			
425.773	9.723	9.887			
467.365	10.34	10.446			
508.847	11.014	10.948			
550.44	11.527	11.544			
592.032	12.072	12.136			
633.733	12.625	12.853			
675.326	13.339	13.442			
716.808	13.891	13.877			
758.4	14.407	14.292			
799.993	14.91	14.893			

Table 35 Rheological data for first phase experimental 0405.1500

	0405.1500a	0405.1500b			
Shear Rate (1/s)	Shear stress (Pa)	Shear stress (Pa)		Mean	3.753
0.985	2.053	2.035		Standard deviation	0.050912
51.552	2.735	2.674		Count	2
93.145	3.717	3.789		Alpha	0.05
134.737	4.764	4.65		95% CL	0.070559
176.329	5.633	5.492		CL/Mean	0.018801
217.921	6.396	6.222			
259.513	6.95	6.905			
301.105	7.806	7.623			
342.588	8.468	8.297			
384.18	9.012	8.846			
425.773	9.613	9.494			
467.365	10.185	10.052			
508.847	10.745	10.662			
550.44	11.425	11.249			
592.032	12.143	11.827			
633.733	12.554	12.266			
675.326	13.088	12.853			
716.808	13.639	13.475			
758.4	14.481	14.079			
799.993	14.879	14.547			

Appendix E Small flume experiments rheological data

This appendix contains all of the rheograms that were recorded for the tested fluids used in RMIT small flume experiments. The rheological model curve was also fitted. Each of the fluids was tested 3 times in the rheometer at the same temperature that it was under the laboratory flume. Statistical analysis for this set of data is also presented in this appendix.

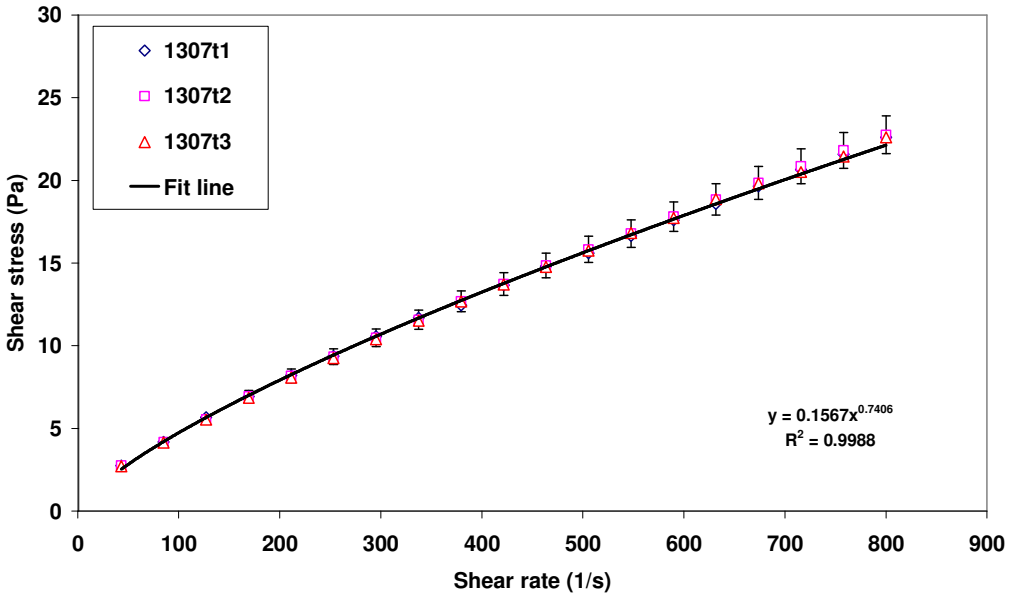

Appendix E 1 Rheograms for fluid 1307 from small flume experiment

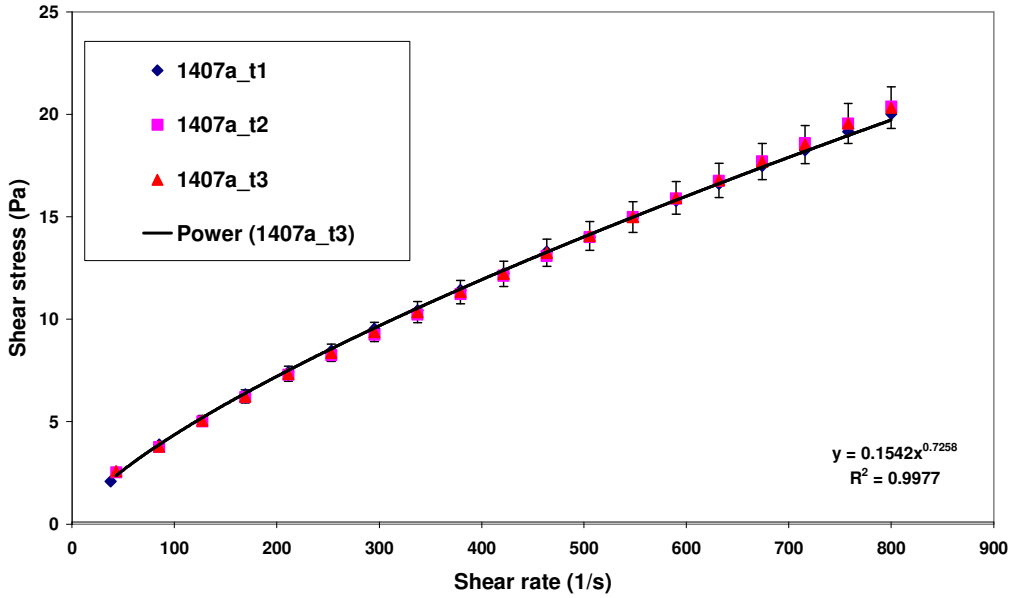

Appendix E 2 Rheograms for fluid 1407a from small flume experiment

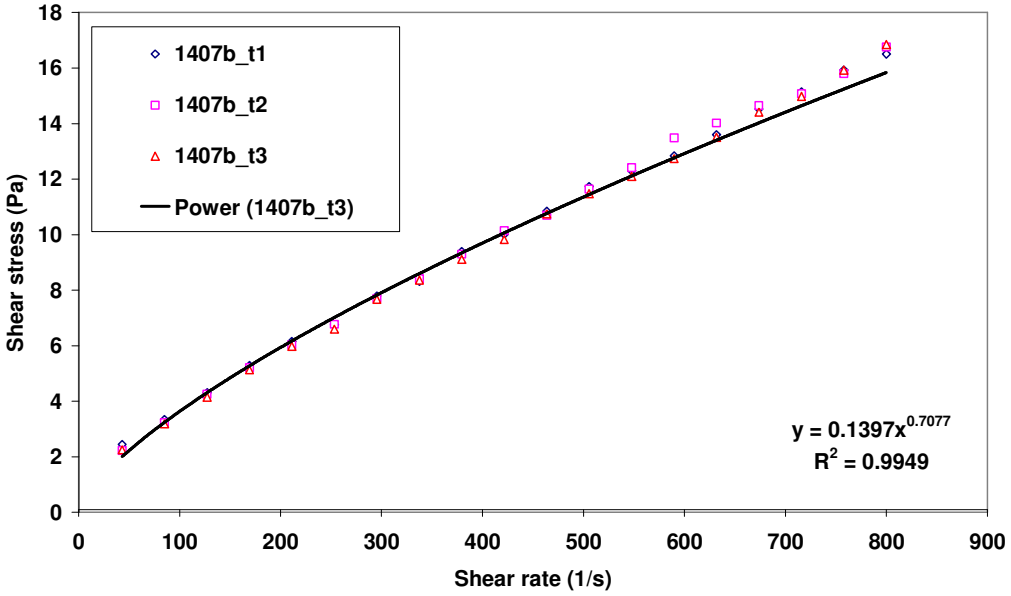

Appendix E 3 Rheograms for fluid 1407b from small flume experiment

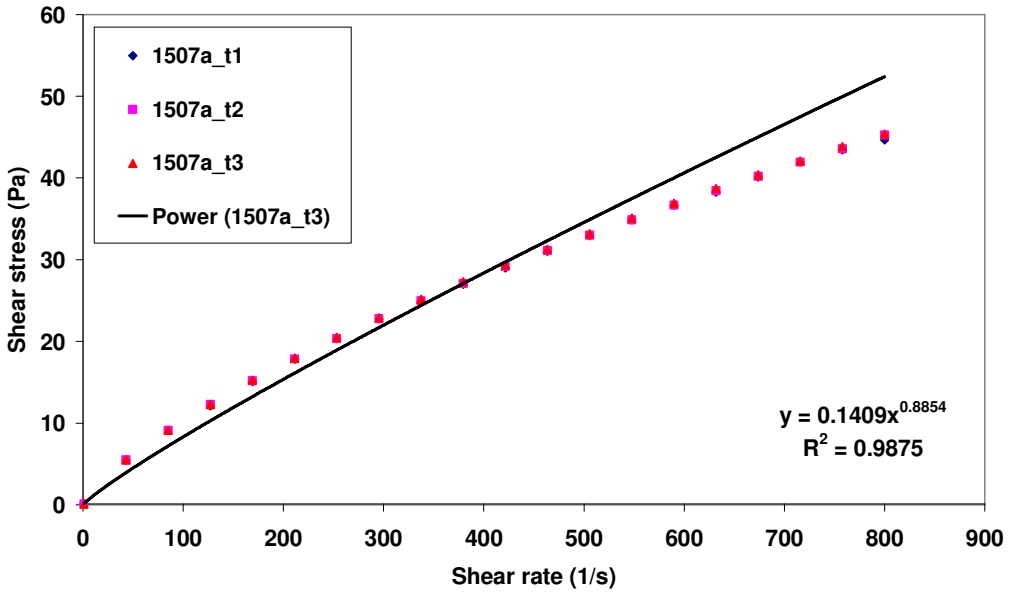

Appendix E 4 Rheograms for fluid 1507a from small flume experiment

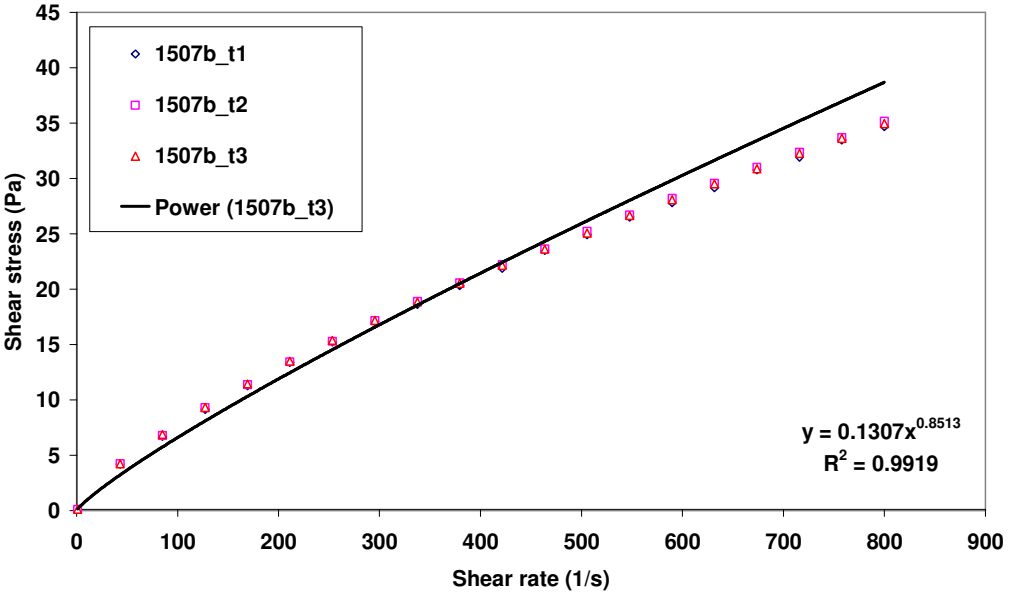

Appendix E 5 Rheograms for fluid 1507b from small flume experiment

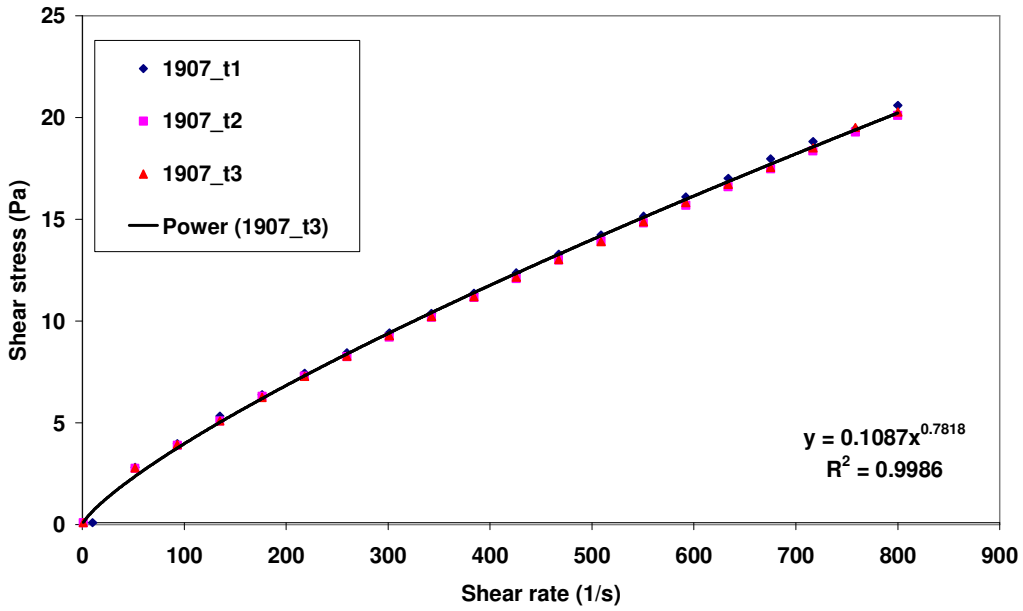

Appendix E 6 Rheograms for fluid 1907 from small flume experiment

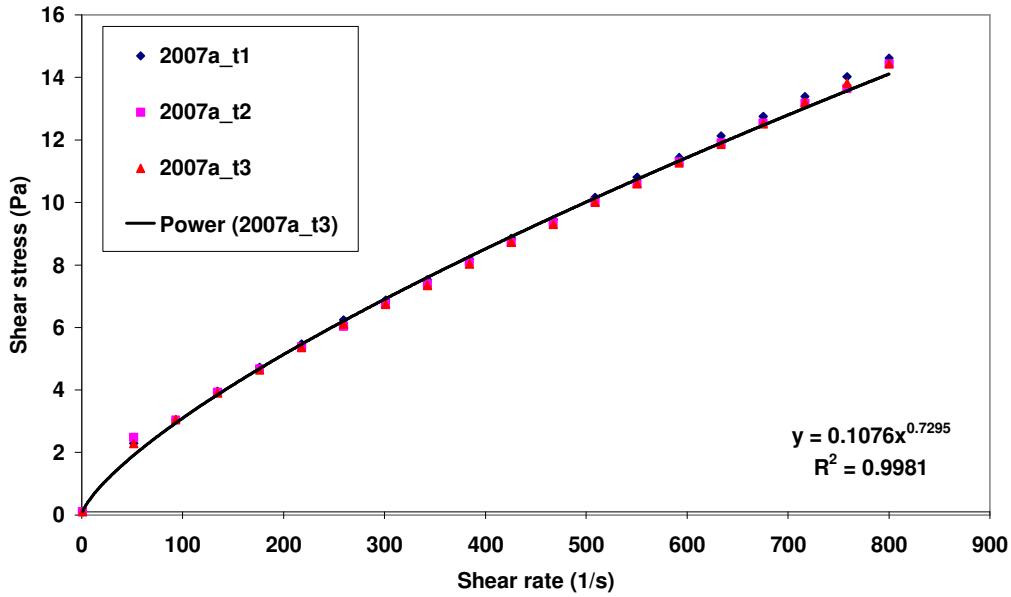

Appendix E 7 Rheograms for fluid 2007a from small flume experiment

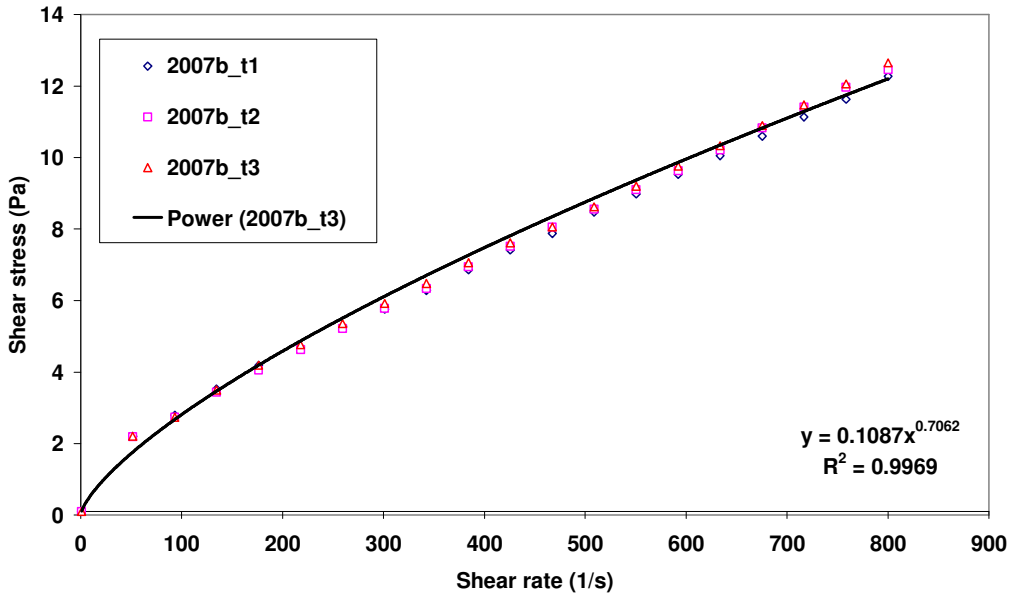

Appendix E 8 Rheograms for fluid 2007b from small flume experiment

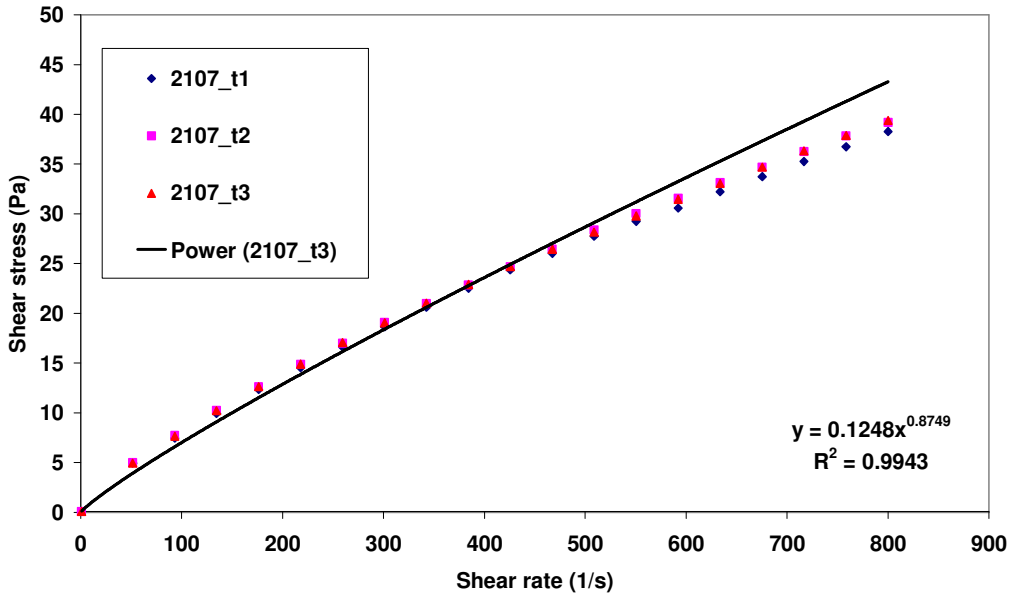

Appendix E 9 Rheograms for fluid 2107 from small flume experiment

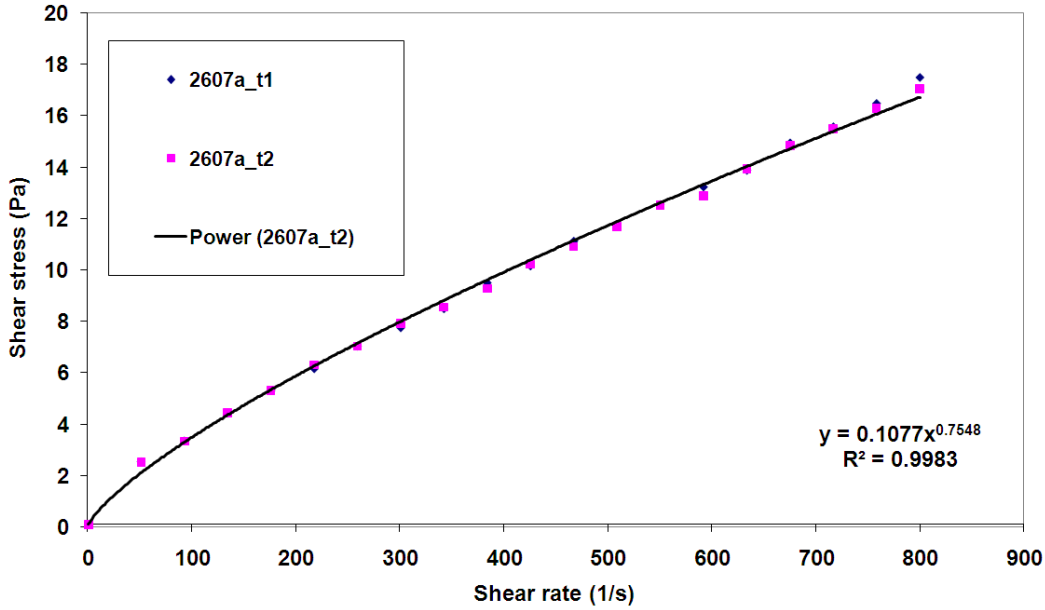

Appendix E 10 Rheograms for fluid 2607a from small flume experiment

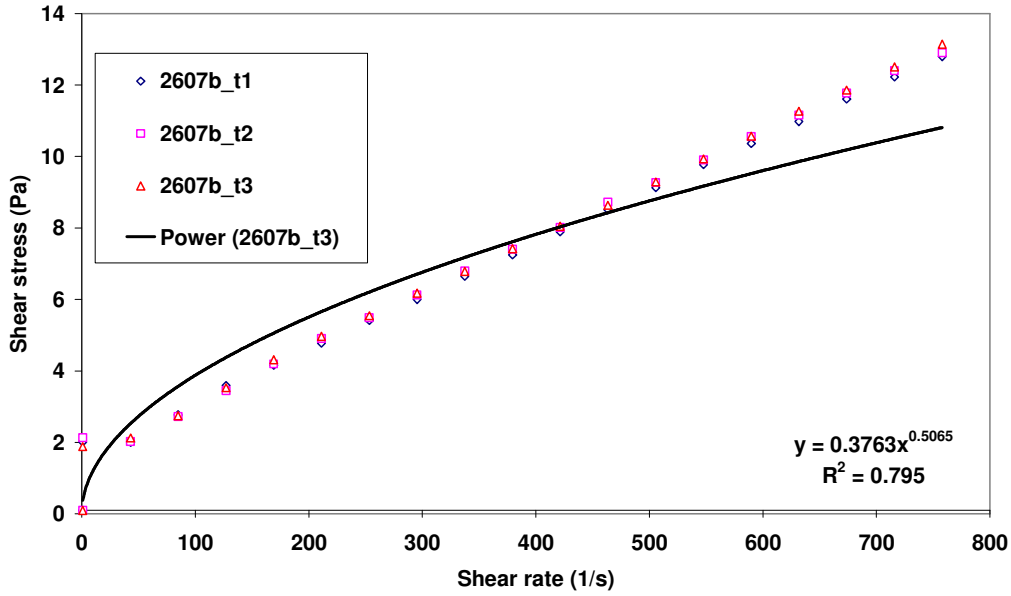

Appendix E 11 Rheograms for fluid 2607b from small flume experiment

Table 36 to Table 42 present rheological data that was measured by Rheosys Merlin II rheometer at RMIT University. Each sample was tested three times. The 95% confidence level is shown in each table.

Table 36 Rheological data for first phase experimental 1307

Run	1	2	3		
Shear Rate (1/s)	Shear Stress (Pa)	Shear Stress (Pa)	Shear Stress (Pa)	Mean	8.858667
0.985	0	0	0	Standard deviation	0.264162
43.125	4.183	3.972	4.011	Count	3
85.045	6.748	6.365	6.544	Alpha	0.05
127.184	9.128	8.6	8.848	95% CL	0.298921
169.214	11.469	10.695	11.12	CL/Mean	0.033743
211.244	13.516	12.669	13.244		
253.274	15.337	14.441	15.118		
295.414	17.309	16.181	16.963		
337.444	18.8	17.874	18.669		
379.474	20.561	19.457	20.358		
421.504	22.281	21.018	22.071		
463.534	23.918	22.595	23.648		
505.564	25.477	23.989	25.206		
547.703	26.987	25.493	26.705		
589.733	28.508	26.896	28.201		
631.763	30.048	28.271	29.671		
673.793	31.47	29.664	31.049		
715.823	32.712	30.966	32.503		
757.853	33.825	32.229	34.014		
799.993	35.184	33.865	35.304		

Table 37 Rheological data for first phase experimental 1407a

Run	1	2	3		
Shear Rate (1/s)	Shear Stress (Pa)	Shear Stress (Pa)	Shear Stress (Pa)	Mean	5.03333
0.985	0	0	0	Standard deviation	0.01795
43.125	2.085	2.527	2.581	Count	3
85.045	3.886	3.762	3.779	Alpha	0.05
127.184	5.04	5.013	5.047	95% CL	0.02032
169.214	6.335	6.196	6.233	CL/Mean	0.00404
211.244	7.425	7.285	7.339		
253.274	8.458	8.245	8.37		
295.414	9.529	9.24	9.376		
337.444	10.427	10.235	10.353		
379.474	11.423	11.218	11.325		
421.504	12.245	12.122	12.214		
463.534	13.292	13.075	13.244		
505.564	13.999	14.006	14.061		
547.703	14.982	14.984	14.986		
589.733	15.779	15.888	15.921		
631.763	16.618	16.755	16.777		
673.793	17.479	17.704	17.691		
715.823	18.245	18.6	18.524		
757.853	19.151	19.542	19.551		
799.993	20.004	20.373	20.321		

Table 38 Rheological data for first phase experimental 1507a

Run	1	2	3		
Shear Rate (1/s)	Shear Stress (Pa)	Shear Stress (Pa)	Shear Stress (Pa)	Mean	12.21367
0.985	0.1	0.1	0.1	Standard deviation	0.114028
43.125	5.448	5.506	5.501	Count	3
85.045	9.135	9.113	9.126	Alpha	0.05
127.184	12.082	12.28	12.279	95% CL	0.129032
169.214	15.072	15.157	15.249	CL/Mean	0.010565
211.244	17.806	17.864	17.957		
253.274	20.324	20.337	20.511		
295.414	22.756	22.752	22.906		
337.444	24.875	24.971	25.16		
379.474	27.012	27.061	27.298		
421.504	28.98	29.146	29.319		
463.534	31.013	31.127	31.279		
505.564	32.962	33.003	33.171		
547.703	34.861	34.88	35.094		
589.733	36.672	36.674	36.923		
631.763	38.258	38.424	38.715		
673.793	40.123	40.203	40.393		
715.823	41.942	41.938	42.093		
757.853	43.41	43.589	43.865		
799.993	44.641	45.241	45.381		

Table 39 Rheological data for first phase experimental 1907

Run	1	2	3		
Shear Rate (1/s)	Shear Stress (Pa)	Shear Stress (Pa)	Shear Stress (Pa)	Mean	5.179667
0.985	0.1	0.1	0.1	Standard deviation	0.139733
43.125	2.819	2.764	2.789	Count	3
85.045	3.984	3.9	3.937	Alpha	0.05
127.184	5.341	5.097	5.101	95% CL	0.15812
169.214	6.391	6.302	6.248	CL/Mean	0.030527
211.244	7.439	7.294	7.287		
253.274	8.444	8.261	8.274		
295.414	9.419	9.213	9.28		
337.444	10.383	10.192	10.232		
379.474	11.371	11.164	11.206		
421.504	12.364	12.086	12.159		
463.534	13.287	12.996	13.014		
505.564	14.224	13.924	13.903		
547.703	15.15	14.826	14.884		
589.733	16.103	15.689	15.815		
631.763	17.017	16.601	16.714		
673.793	17.972	17.489	17.555		
715.823	18.821	18.359	18.508		
757.853	19.44	19.284	19.518		
799.993	20.6	20.115	20.278		

Table 40 Rheological data for first phase experimental 2007a

Run	1	2	3		
Shear Rate (1/s)	Shear Stress (Pa)	Shear Stress (Pa)	Shear Stress (Pa)	Mean	3.927
0.985	0.1	0.1	0.1	Standard deviation	0.03005
43.125	2.292	2.48	2.28	Count	3
85.045	3.047	3.029	3.058	Alpha	0.05
127.184	3.958	3.925	3.898	95% CL	0.034004
169.214	4.721	4.67	4.631	CL/Mean	0.008659
211.244	5.473	5.377	5.351		
253.274	6.245	6.035	6.099		
295.414	6.877	6.749	6.731		
337.444	7.526	7.396	7.342		
379.474	8.187	8.089	8.028		
421.504	8.848	8.713	8.726		
463.534	9.457	9.357	9.293		
505.564	10.162	10.025	10		
547.703	10.807	10.601	10.59		
589.733	11.439	11.293	11.26		
631.763	12.127	11.895	11.854		
673.793	12.75	12.541	12.51		
715.823	13.39	13.167	13.198		
757.853	14.029	13.643	13.82		
799.993	14.617	14.434	14.432		

Table 41 Rheological data for first phase experimental 2107

Run	1	2	3		
Shear Rate (1/s)	Shear Stress (Pa)	Shear Stress (Pa)	Shear Stress (Pa)	Mean	10.14133
0.985	0.1	0.1	0.1	Standard deviation	0.179305
43.125	4.949	4.997	4.944	Count	3
85.045	7.481	7.741	7.652	Alpha	0.05
127.184	9.936	10.267	10.221	95% CL	0.202899
169.214	12.345	12.643	12.646	CL/Mean	0.020007
211.244	14.529	14.87	14.906		
253.274	16.627	17.013	17.078		
295.414	18.652	19.075	19.048		
337.444	20.624	20.968	21.022		
379.474	22.524	22.839	22.903		
421.504	24.385	24.708	24.705		
463.534	26.028	26.436	26.434		
505.564	27.747	28.386	28.167		
547.703	29.259	30.033	29.803		
589.733	30.582	31.571	31.466		
631.763	32.224	33.152	33.053		
673.793	33.738	34.707	34.709		
715.823	35.255	36.266	36.336		
757.853	36.738	37.847	37.875		
799.993	38.27	39.202	39.384		

Table 42 Rheological data for first phase experimental 2607b

Run	1	2	3		
Shear Rate (1/s)	Shear Stress (Pa)	Shear Stress (Pa)	Shear Stress (Pa)	Mean	3.552
0.985	2.013	1.881	1.881	Standard deviation	0.034641
43.125	2.009	2.126	2.126	Count	3
85.045	2.771	2.747	2.747	Alpha	0.05
127.184	3.592	3.532	3.532	95% CL	0.039199
169.214	4.158	4.317	4.317	CL/Mean	0.011036
211.244	4.781	4.968	4.968		
253.274	5.417	5.544	5.544		
295.414	6.001	6.177	6.177		
337.444	6.651	6.788	6.788		
379.474	7.251	7.424	7.424		
421.504	7.893	8.048	8.048		
463.534	8.512	8.637	8.637		
505.564	9.128	9.29	9.29		
547.703	9.774	9.934	9.934		
589.733	10.368	10.569	10.569		
631.763	10.979	11.27	11.27		
673.793	11.609	11.856	11.856		
715.823	12.229	12.508	12.508		
757.853	12.795	13.145	13.145		
799.993	13.563	13.846	13.846		

Appendix F Additional figures for investigation of change of yield stress

Additional figures from section 6.5.2 for investigation of increase yield stress effect.

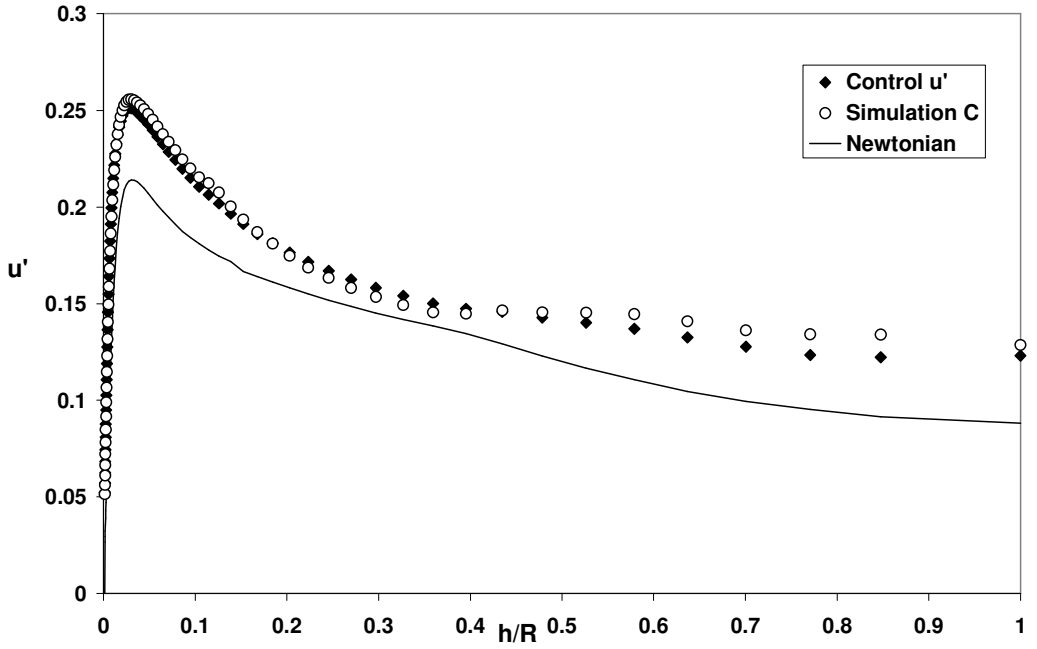

Appendix F 1 Axial turbulence intensities plotted as a function of h/R. (Solid line for Newtonian DNS)

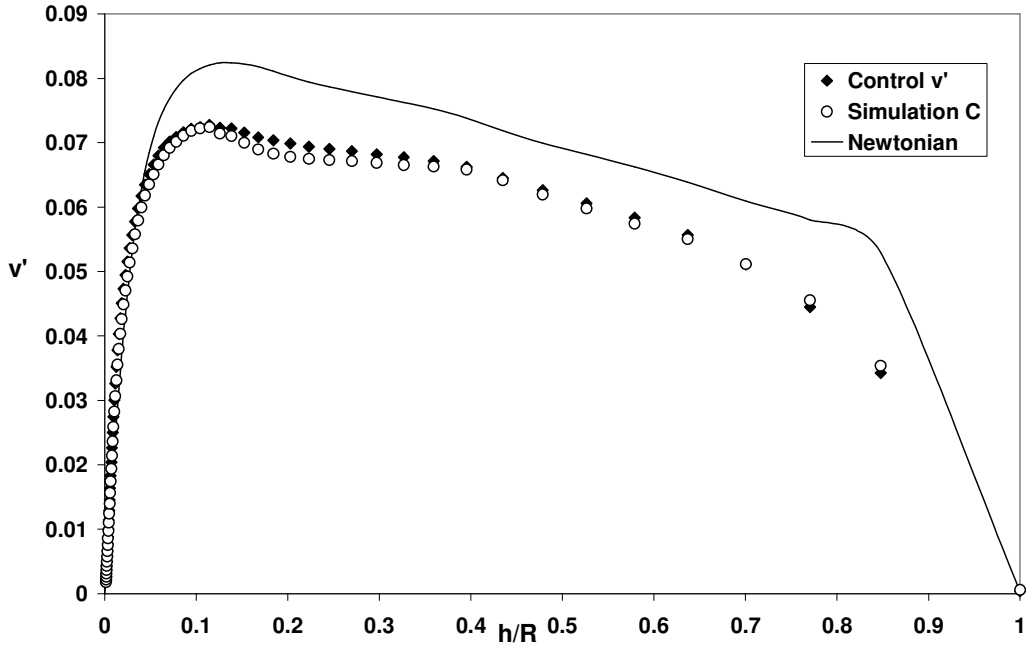

Appendix F 2 Radial turbulence intensities plotted as a function of h/R. (Solid line for Newtonian DNS)

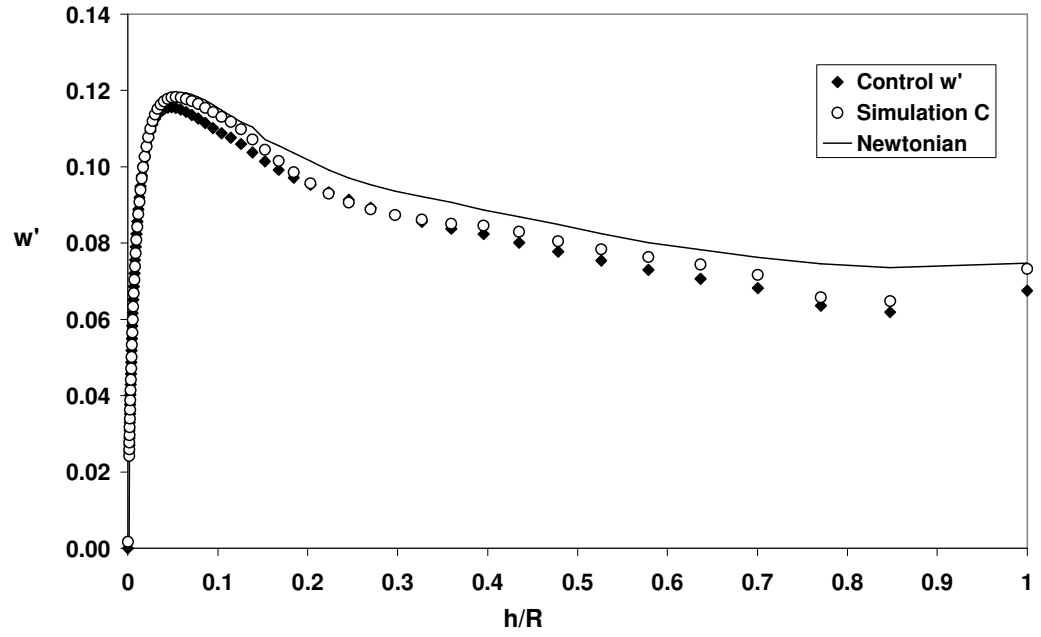

Appendix F 3 Azimuthal turbulence intensities plotted as a function of h/R. (Solid line for Newtonian DNS)

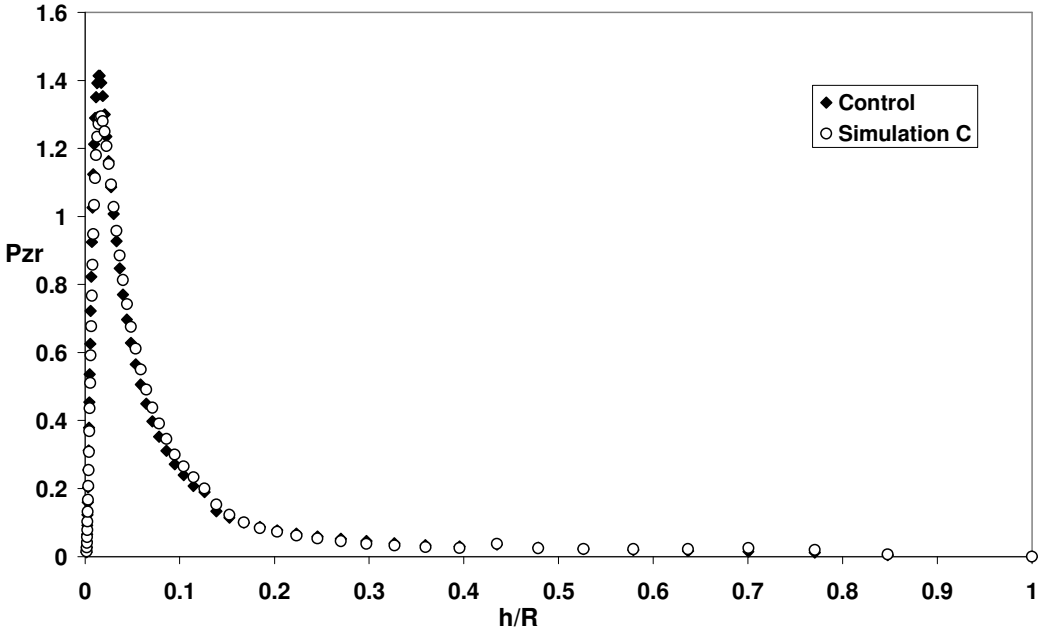

Appendix F 4 Turbulence production plotted as a function of h/R

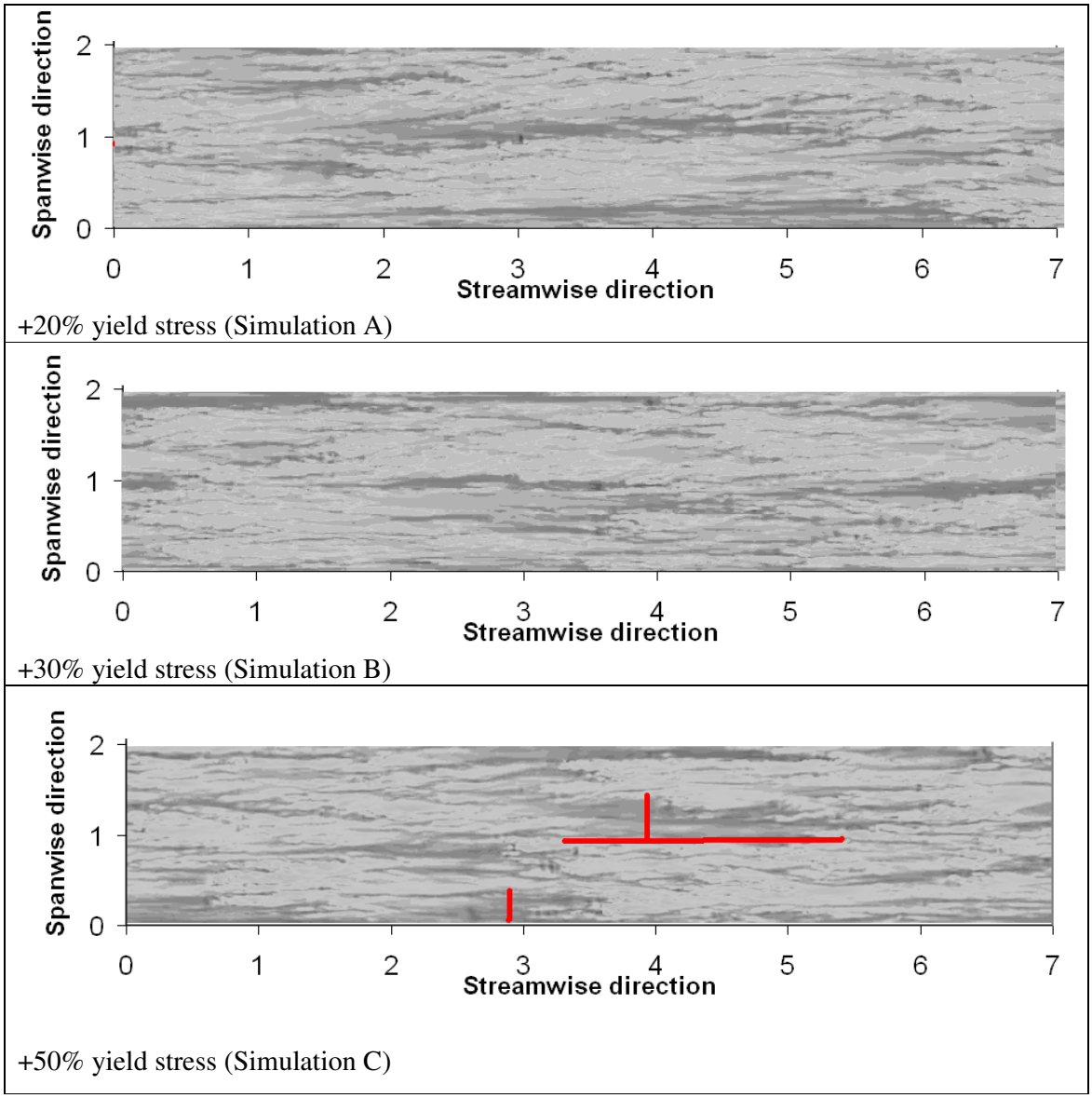

+20% yield stress (Simulation A)

+30% yield stress (Simulation B)

+50% yield stress (Simulation C)

Appendix F 5 Predicted axial velocity at $y^+ \approx 8$. From top to bottom, Simulation A, B and C. White represents high velocity and black represents low velocity.

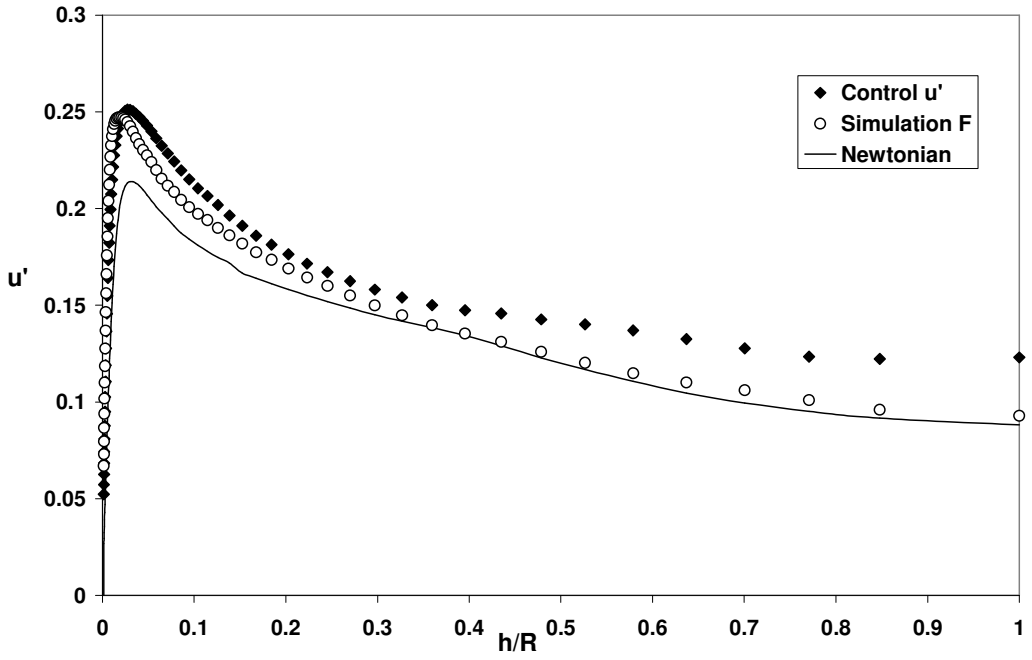

Appendix F 6 Axial turbulence intensities plotted as a function of h/R. (Solid line for Newtonian DNS)

Additional figures for investigation of decrease yield stress effect

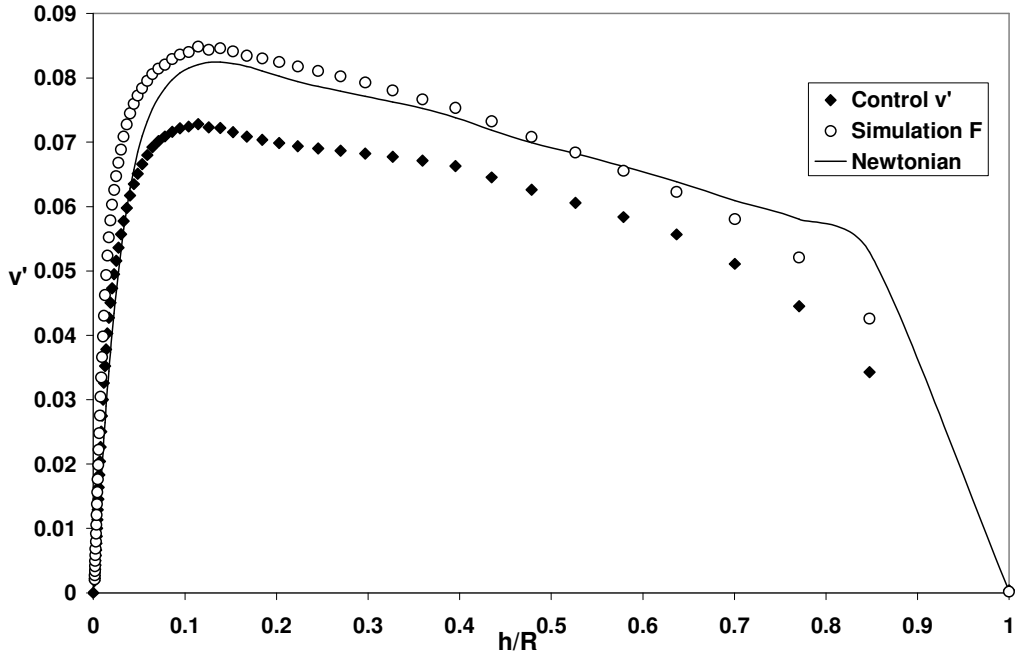

Appendix F 7 Radial turbulence intensities plotted as a function of h/R. (Solid line for Newtonian DNS)

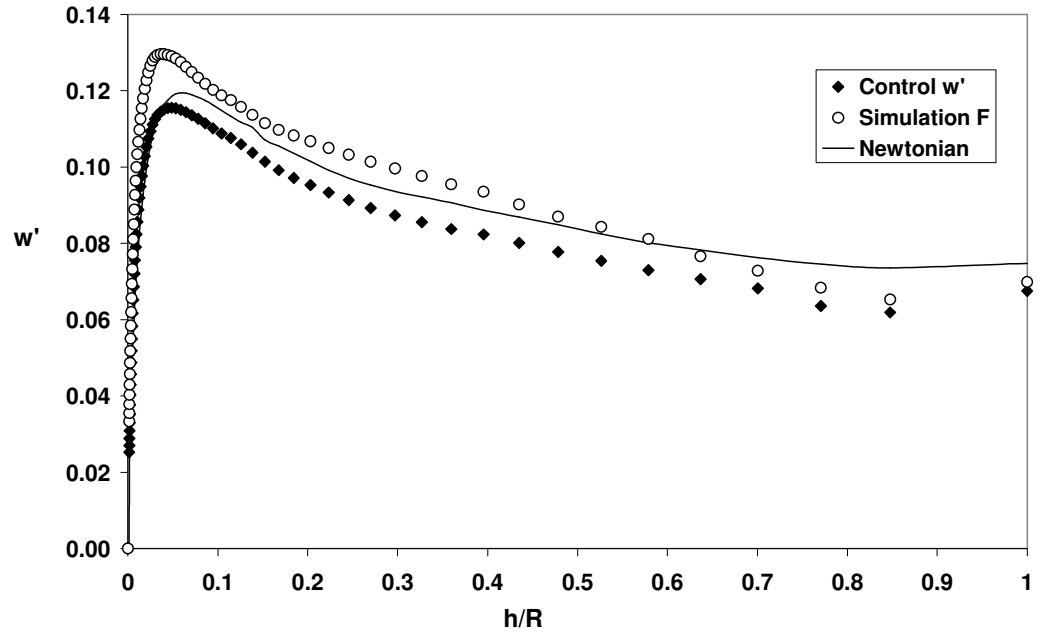

Appendix F 8 Azimuthal turbulence intensities plotted as a function of h/R. (Solid line for Newtonian DNS)

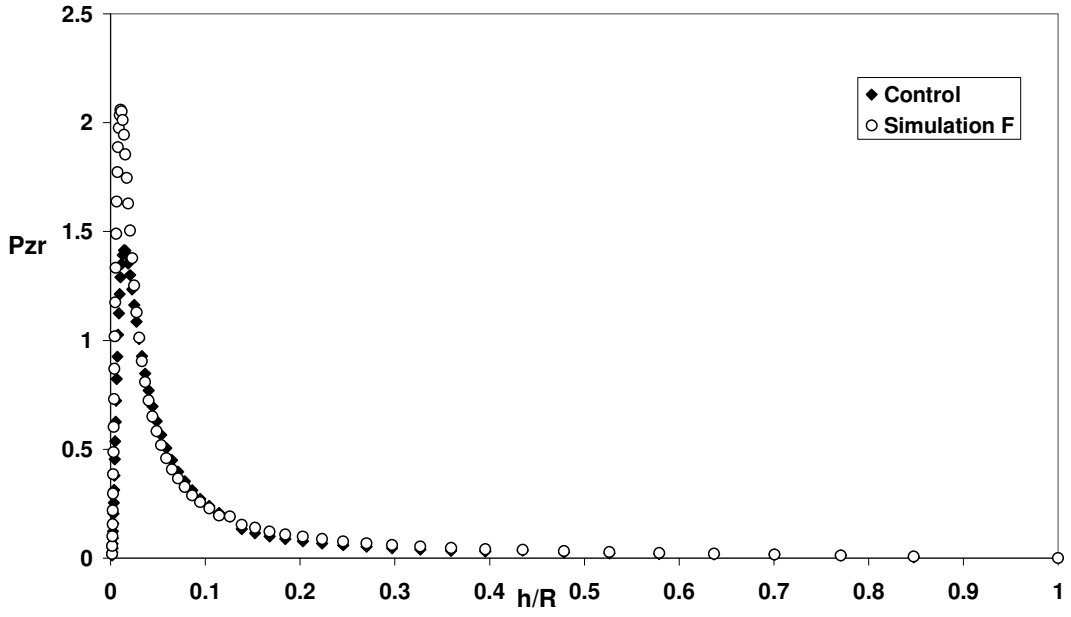

Appendix F 9 Turbulence production plotted as a function of h/R

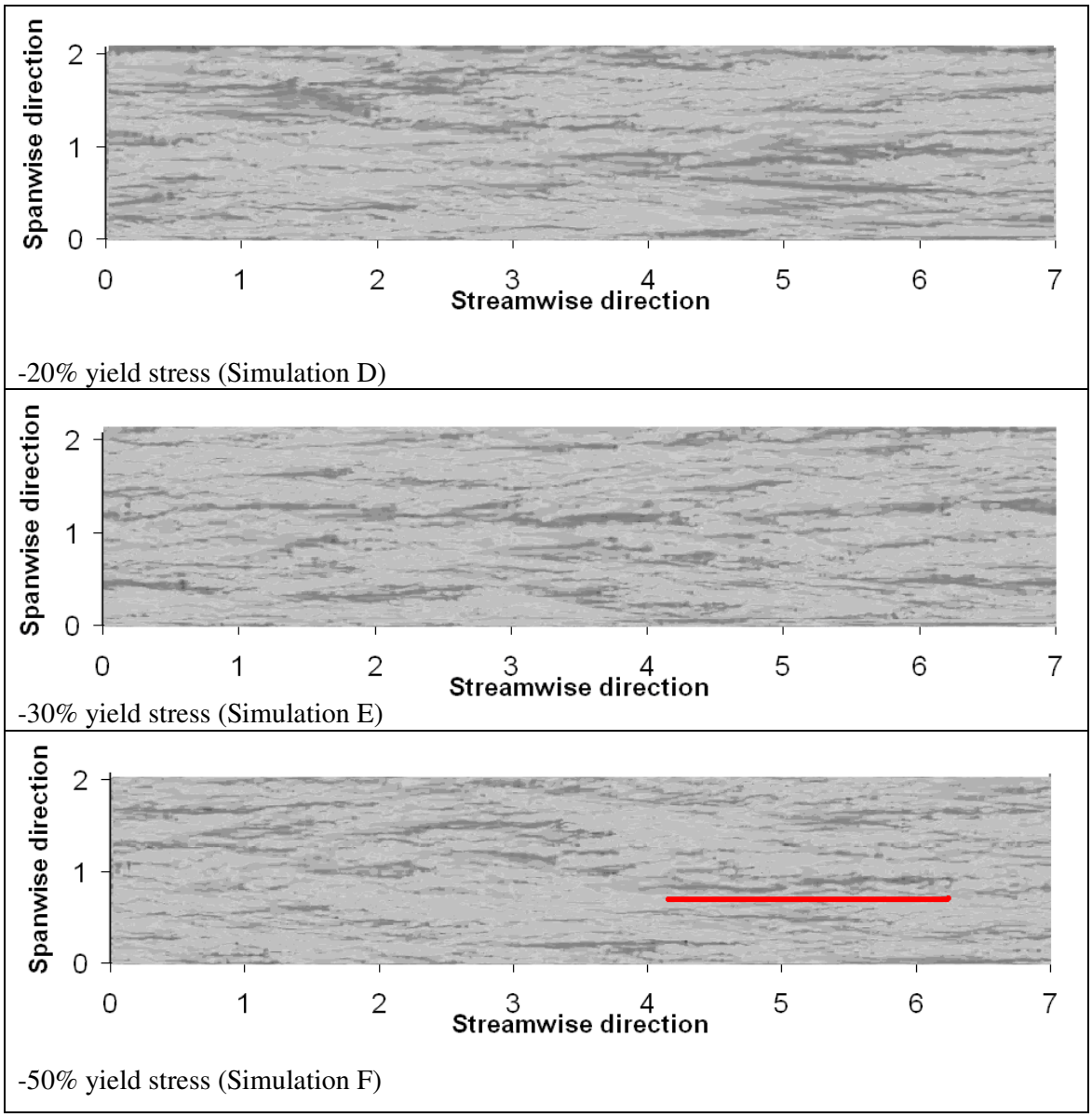

-20% yield stress (Simulation D)

-30% yield stress (Simulation E)

-50% yield stress (Simulation F)

Appendix F 10 Predicted axial velocity at $y^+ \approx 8$. From top to bottom, Simulation D, E and F. White represents high velocity and black represents low velocity.

Appendix G Additional figures for investigation of change of flow behaviour index

Additional figures from section 6.5.3 for investigation of increase flow behaviour index effect.

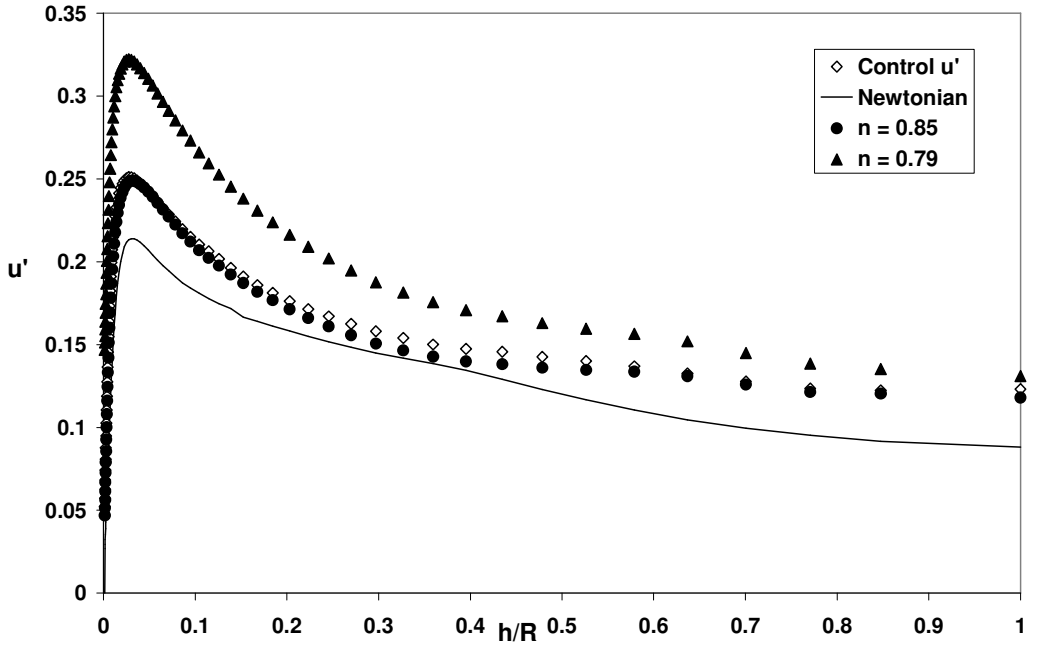

Appendix G 1 Axial turbulence intensities plotted as a function of h/R. (Solid line for Newtonian DNS)

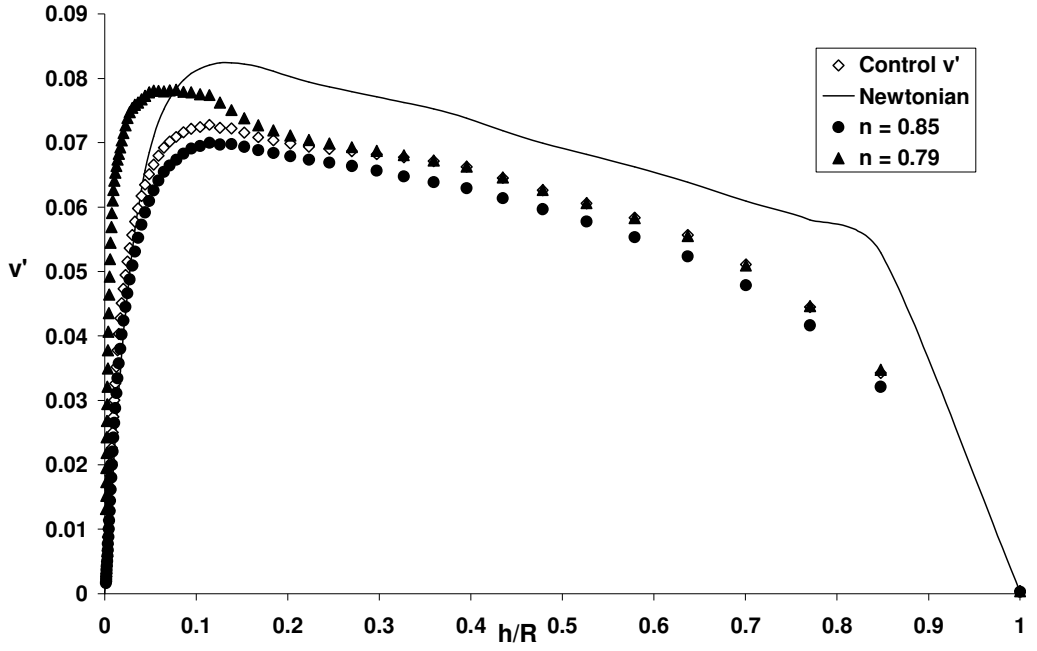

Appendix G 2 Radial turbulence intensities plotted as a function of h/R. (Solid line for Newtonian DNS)

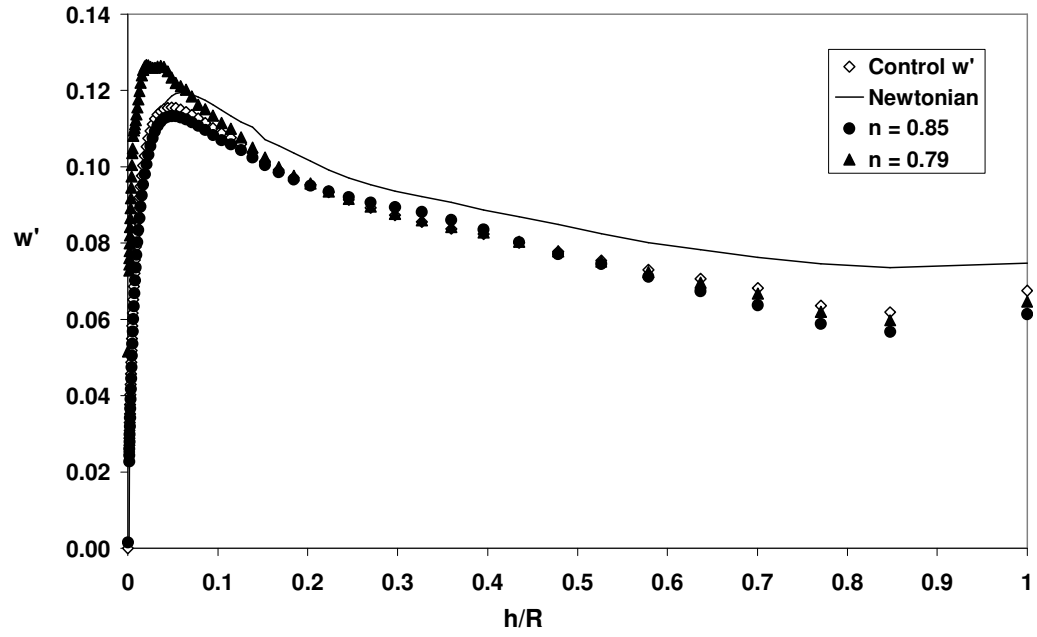

Appendix G 3 Azimuthal turbulence intensities plotted as a function of h/R. (Solid line for Newtonian DNS)

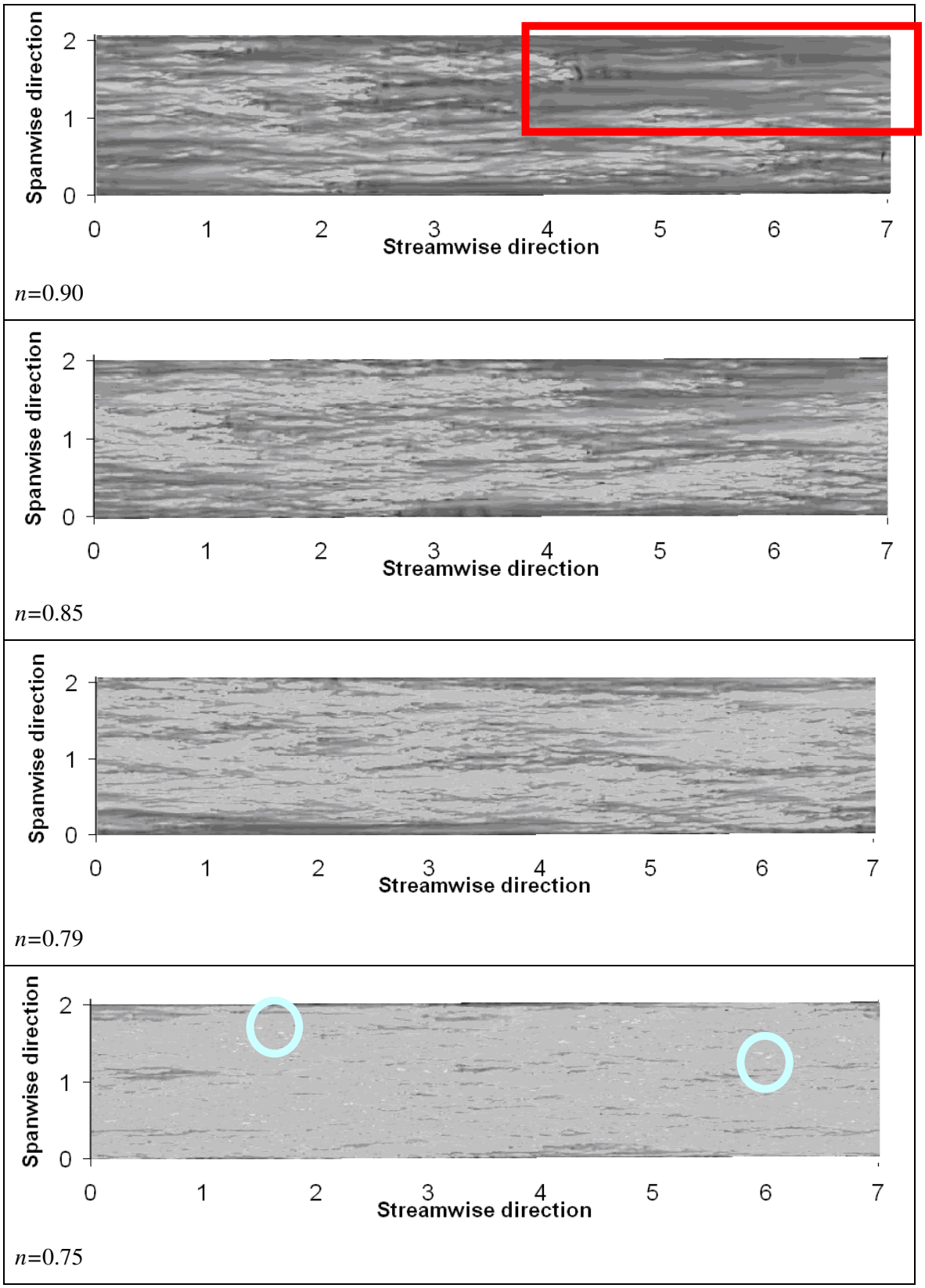

Appendix G 4 Predicted axial velocity at $y^+ \approx 8$. From top to bottom, n=0.90, n=0.85, n=0.79, and n=0.75. White represents high velocity and black represents low velocity.

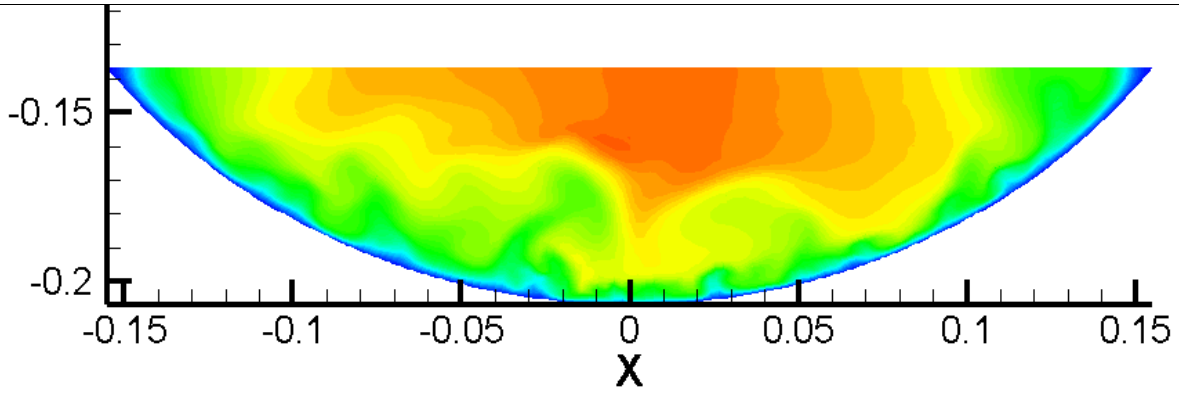

Axial velocity

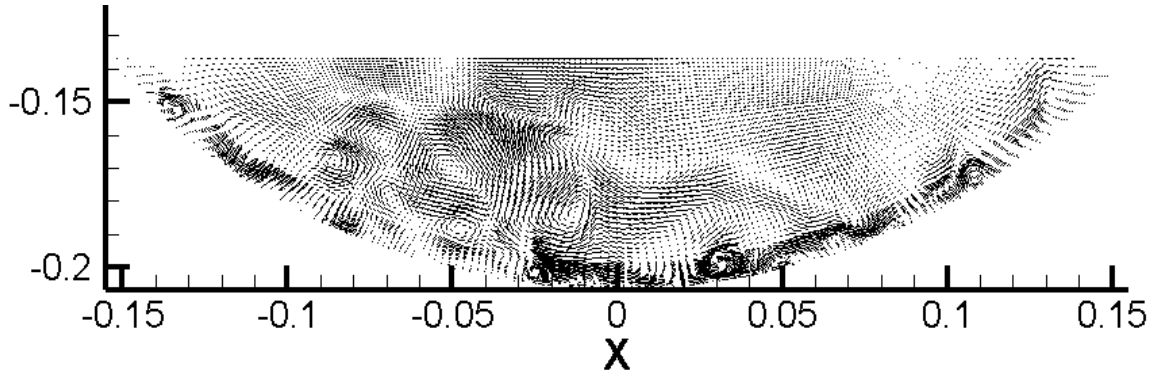

In-plan velocities

***n* = 0.90, Re = 4210**

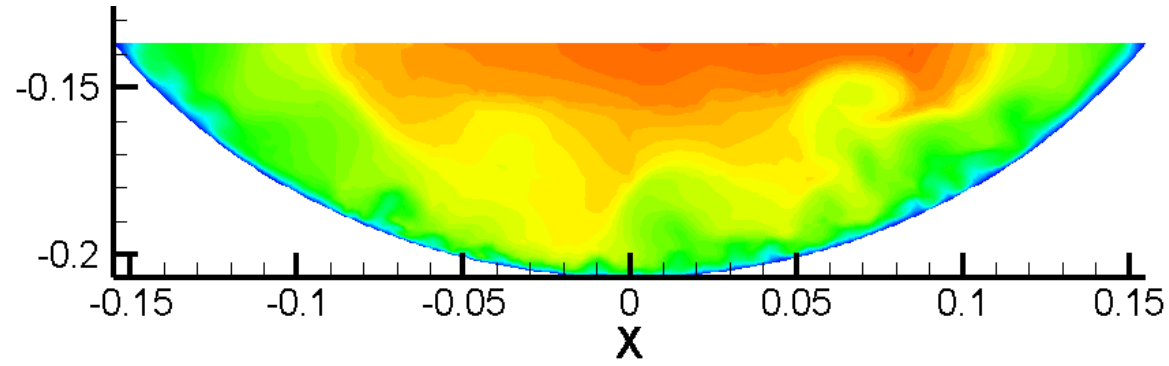

Axial velocity

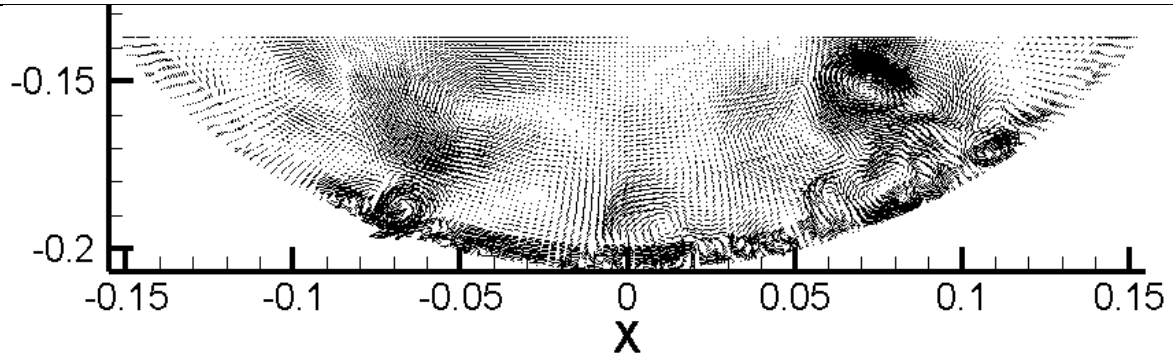

In-plane velocities

***n* = 0.85, Re = 5853**

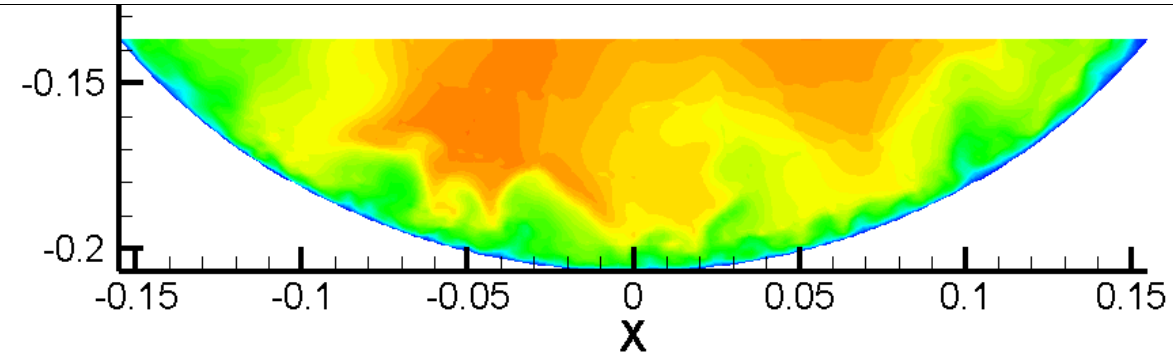

Axial velocity

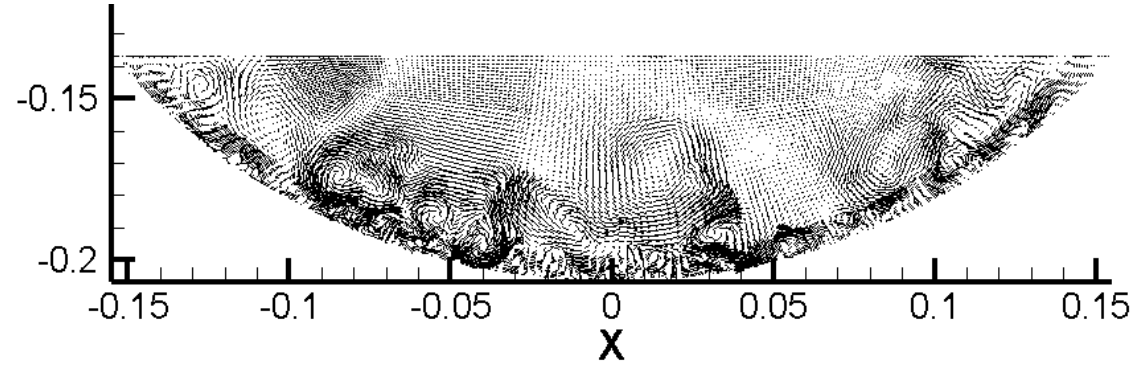

In-plan velocities

***n* = 0.79, Re = 9185**

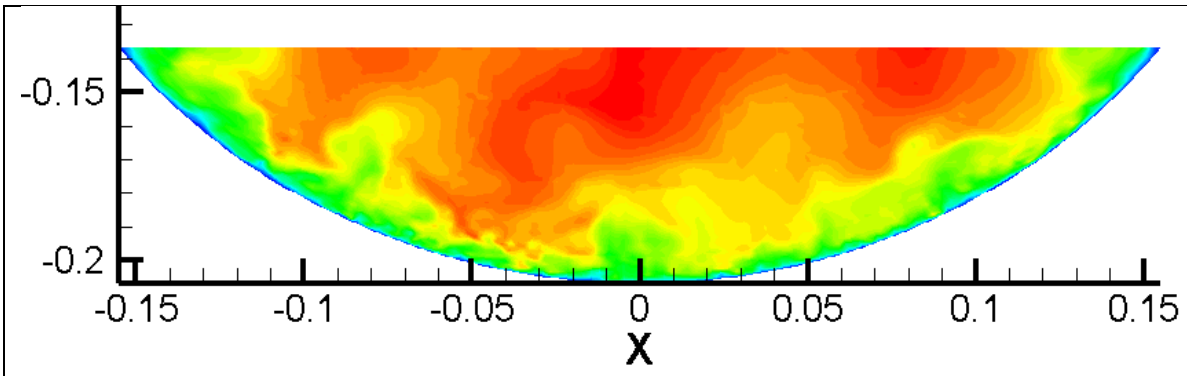

Axial velocity

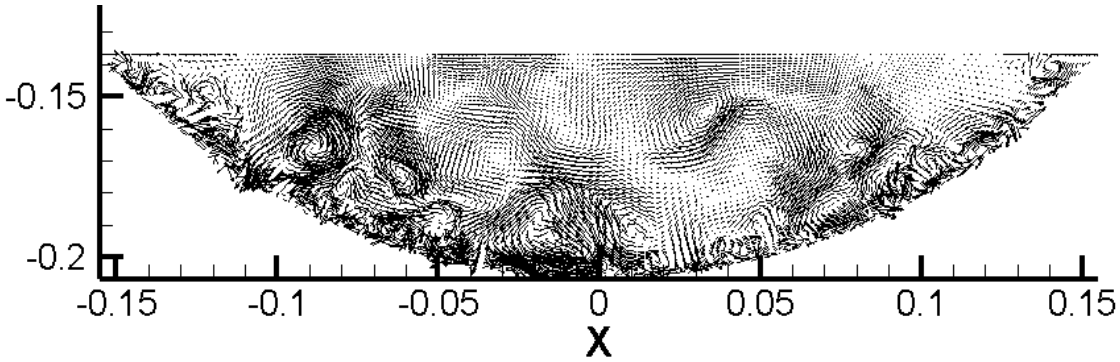

In-plan velocities

***n* = 0.75, Re = 12910**

Appendix G 5 Contours of instantaneous axial velocity and in-plane velocity vectors

Appendix H Additional figures for investigation of change of flow consistency index

Additional figures from section 6.5.4 for investigation of change of flow consistency index (with different Reynolds number).

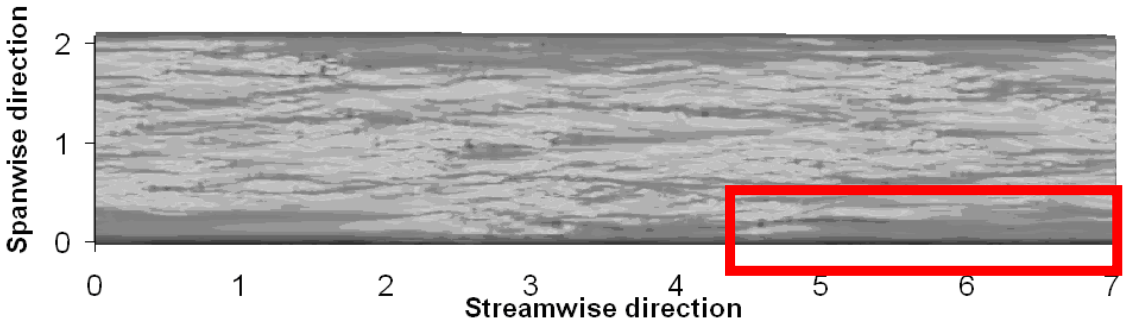

K+20%

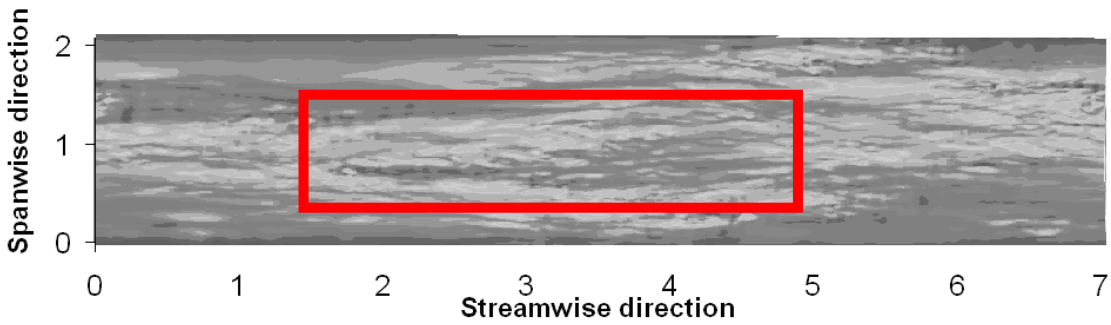

K+50%

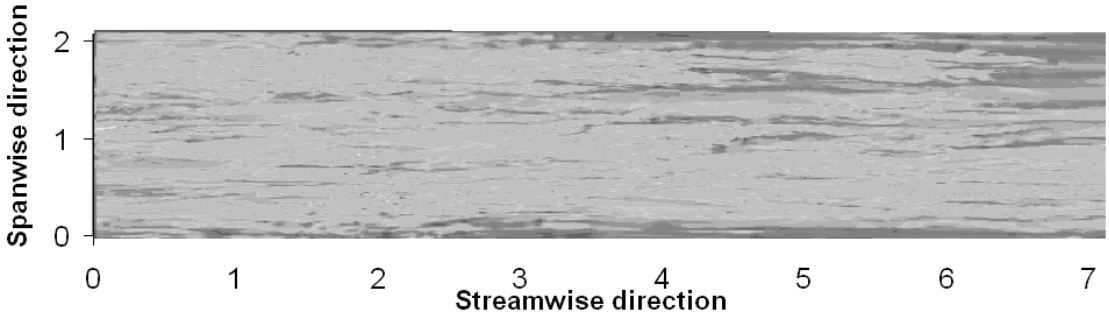

K-20%

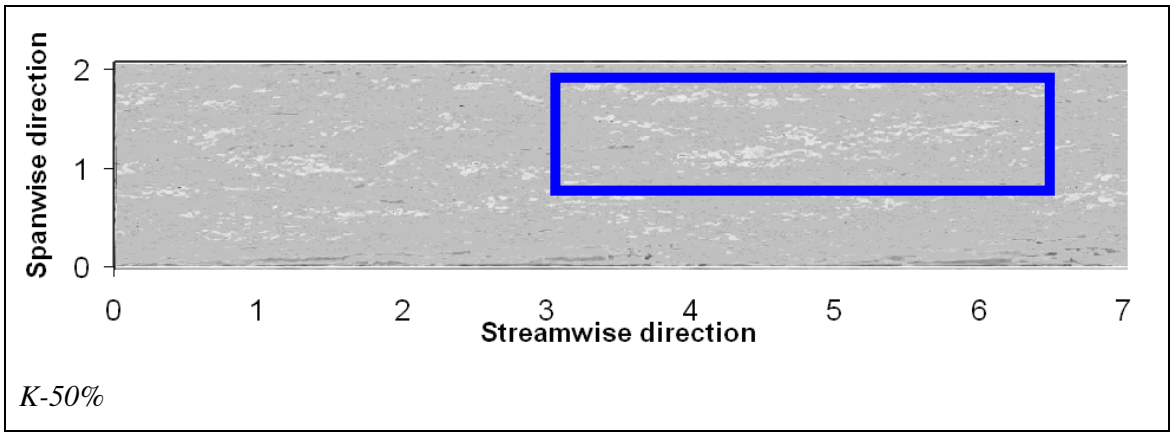

K-50%

Appendix H 1 Predicted axial velocity at $y^+ \approx 8$. From top to bottom, *K*+20%, *K*+50%, *K*-20%, and *K*-50%. White represents high velocity and black represents low velocity.

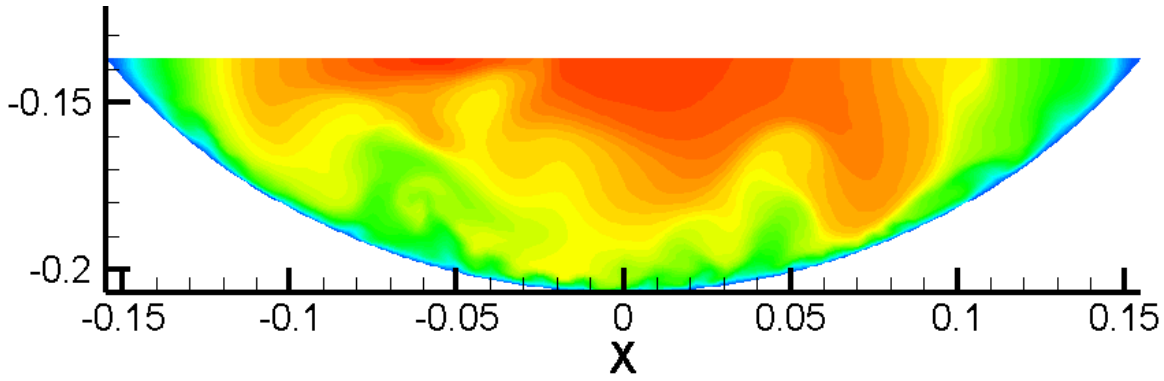

Axial velocity

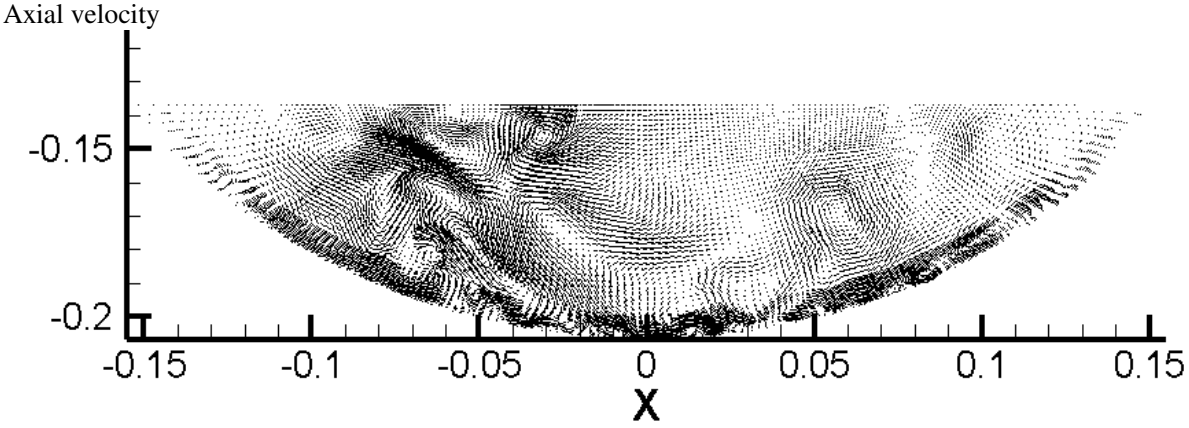

In-plane velocities

***K* +20%, Re = 6781**

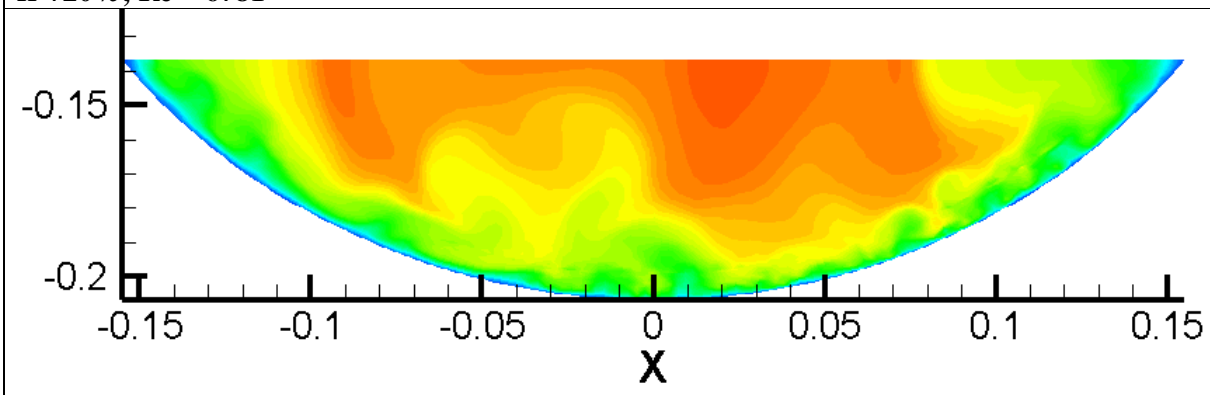

Axial velocity

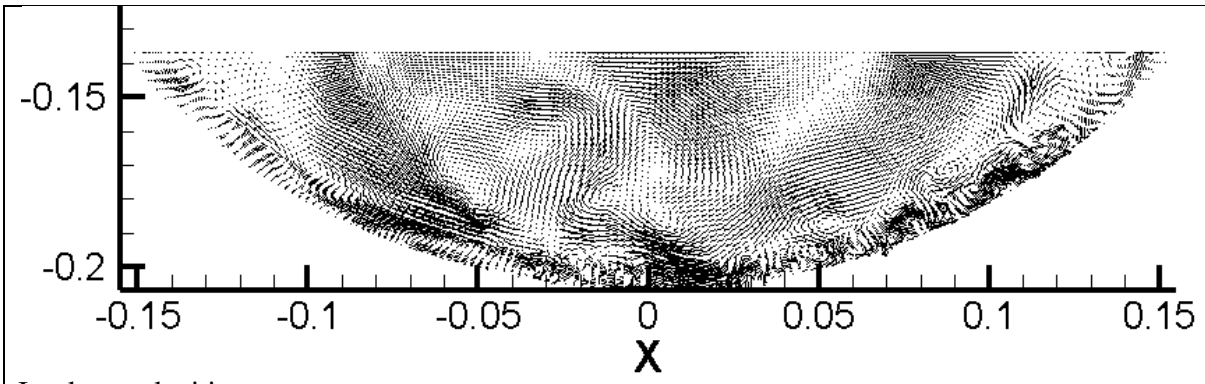

In-plane velocities

***K* +50%, Re = 5635**

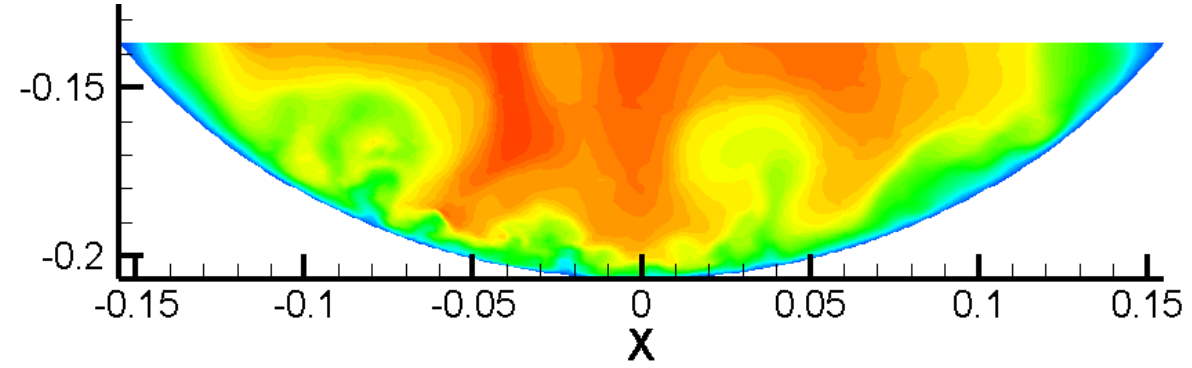

Axial velocity

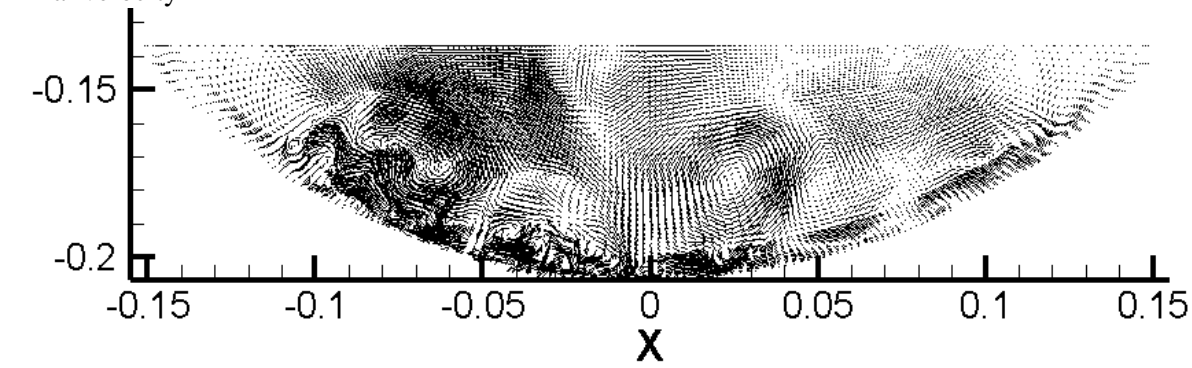

In-plane velocities

***K* -20%, Re = 11450**

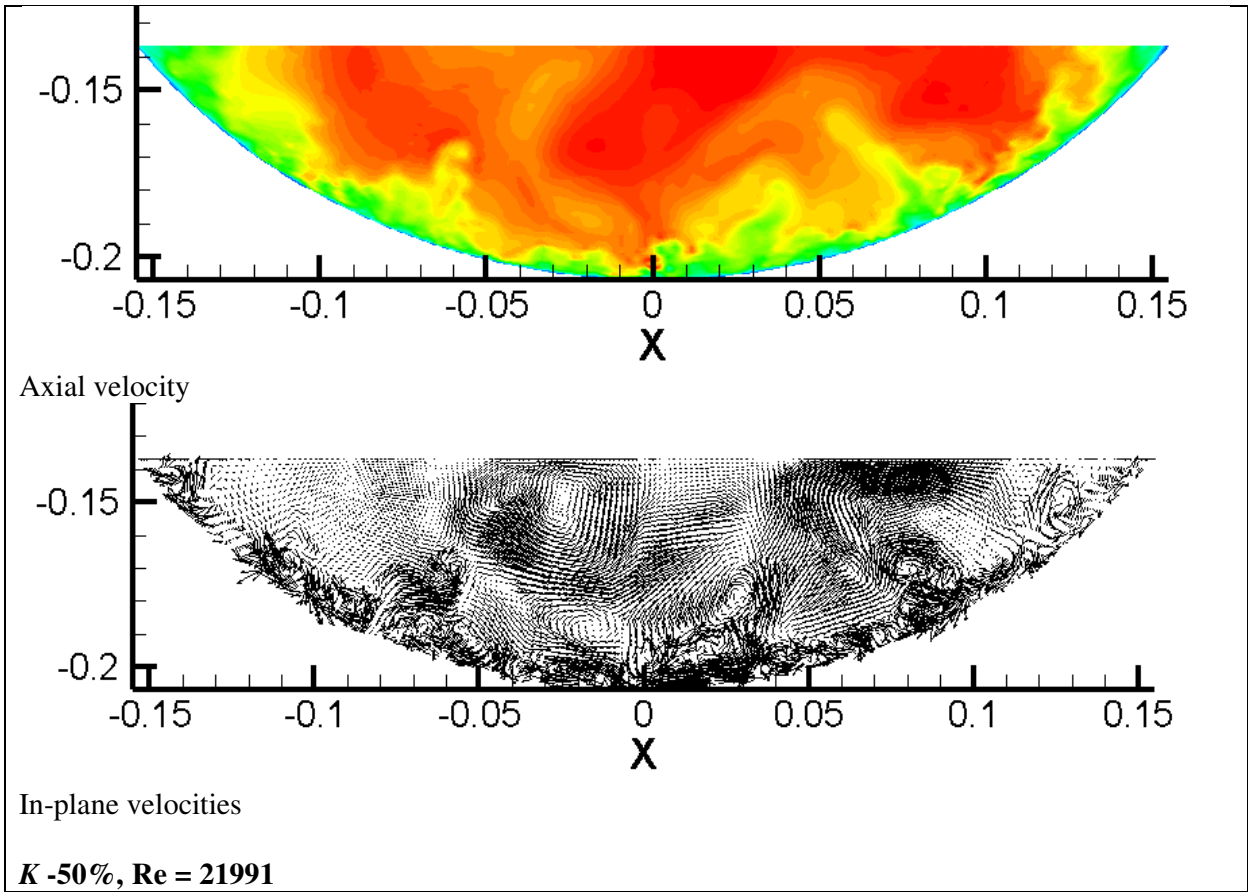

Appendix H 2 Contours of instantaneous axial velocity and in-plane velocity vectors

Additional figures for investigation of change of flow consistency index (with fixed Reynolds number).

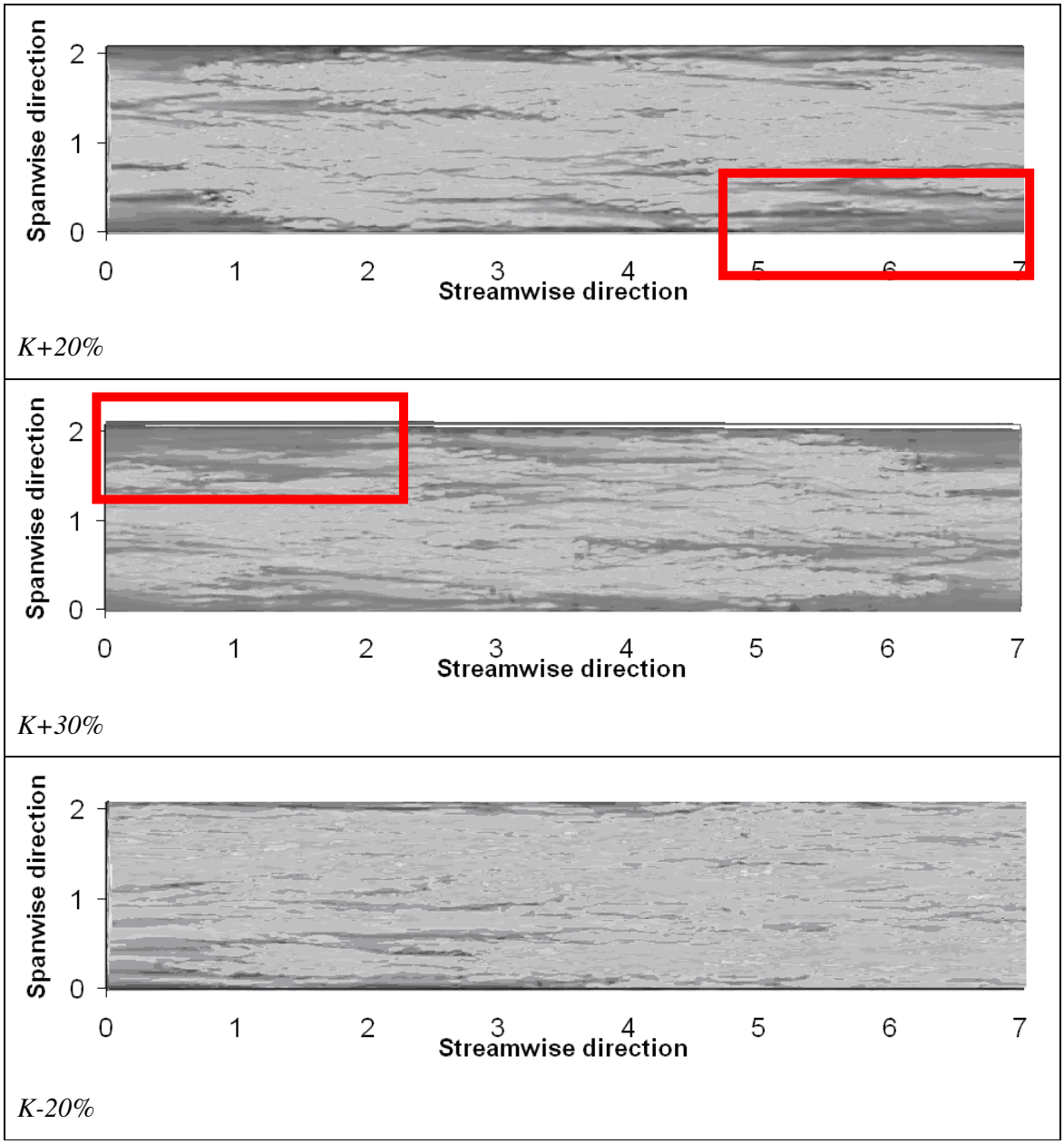

K+20%

K+30%

K-20%

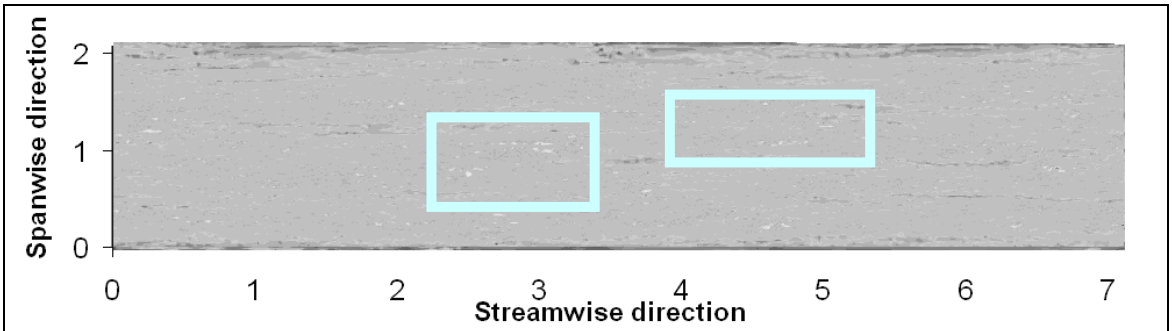

K-30%

Appendix H 3 Predicted axial velocity at $y^+ \approx 8$. From top to bottom, *K*+20%, *K*+30%, *K*-20%, and *K*-30%. White represents high velocity and black represents low velocity.

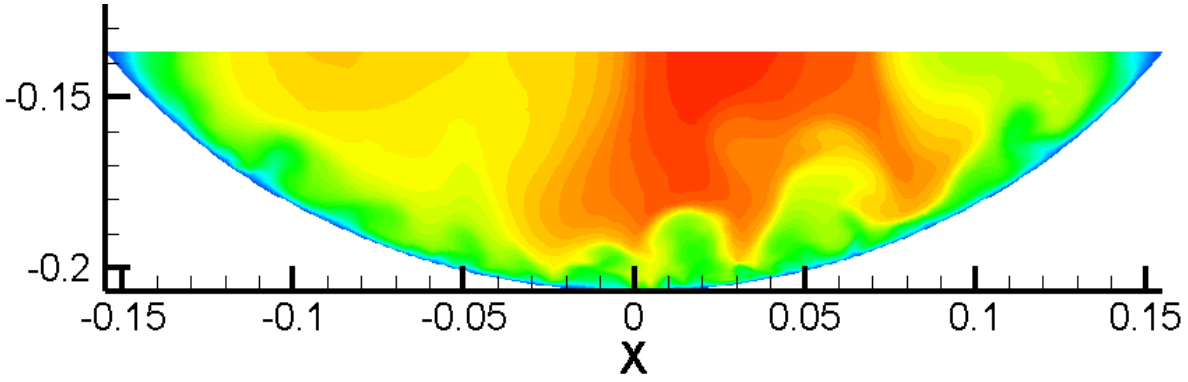

Axial velocity

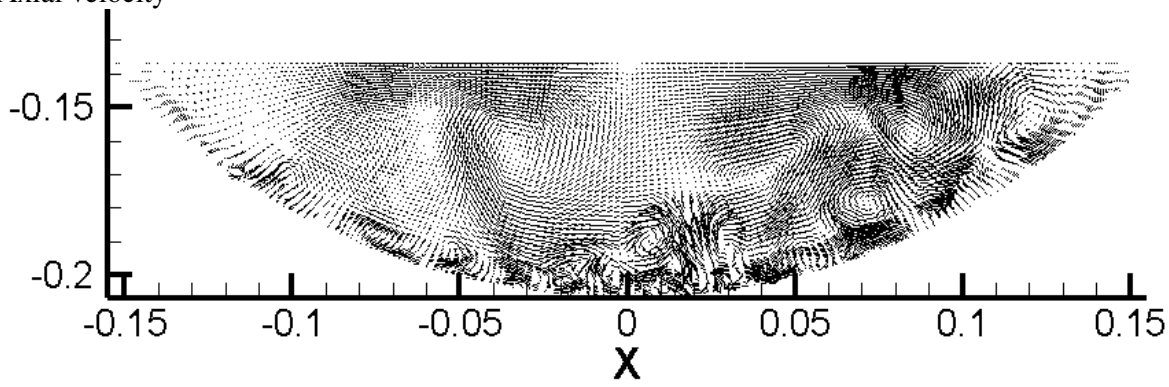

In-plane velocities

***K* +20%**

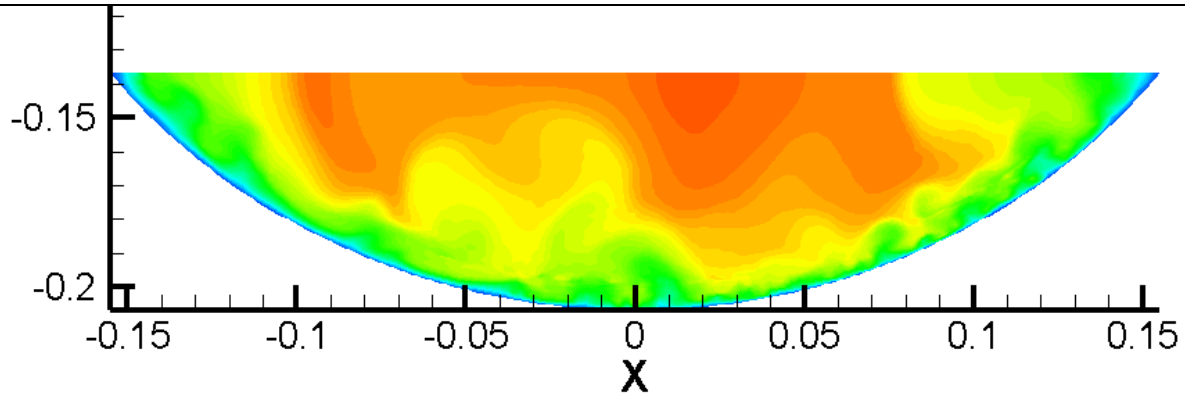

Axial velocity

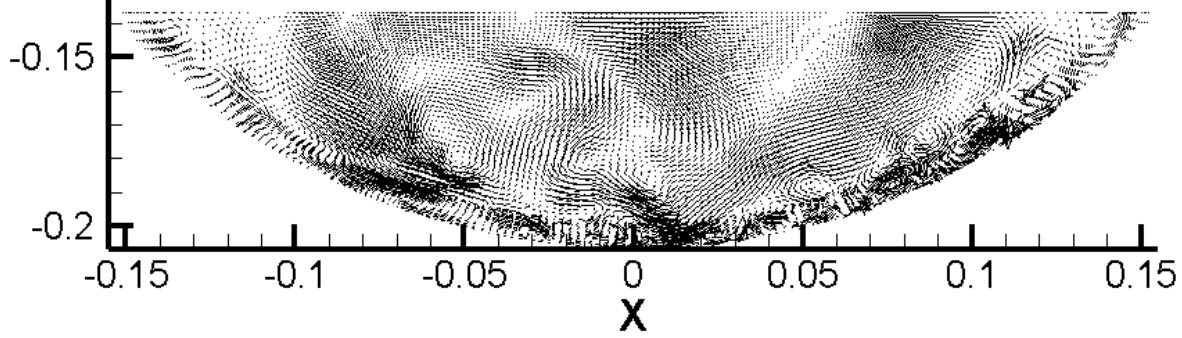

In-plane velocities

***K* +30%**

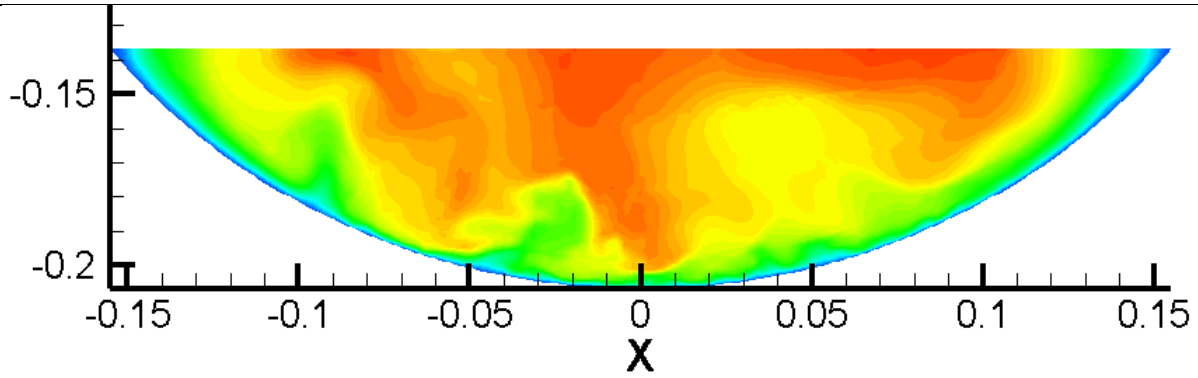

Axial velocity

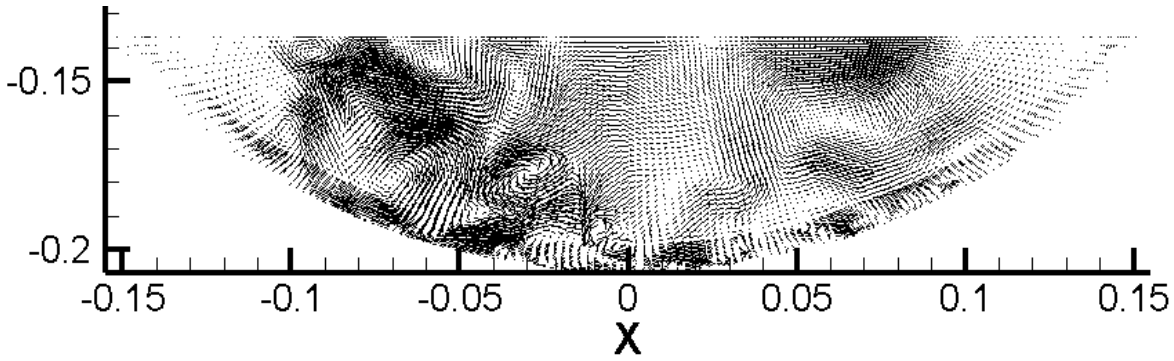

In-plane velocities

***K* -20%**

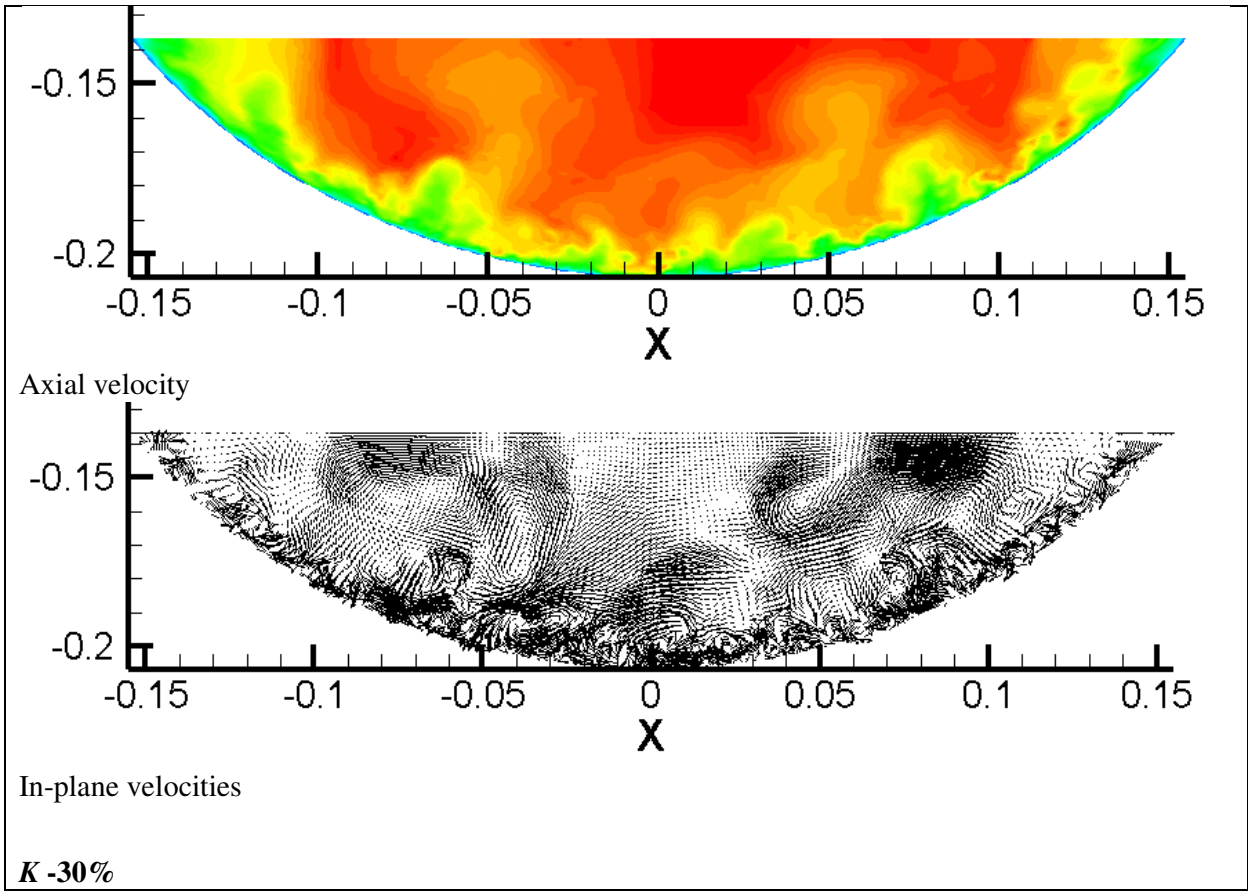

***K* -30%**

Appendix H 4 Contours of instantaneous axial velocity and in-plane velocity vectors